AUGUST 1, 1989

Analytical CHEMISTRY

SOLID-SURFACE LUMINESCENCE SPECTROMETRY

889 A

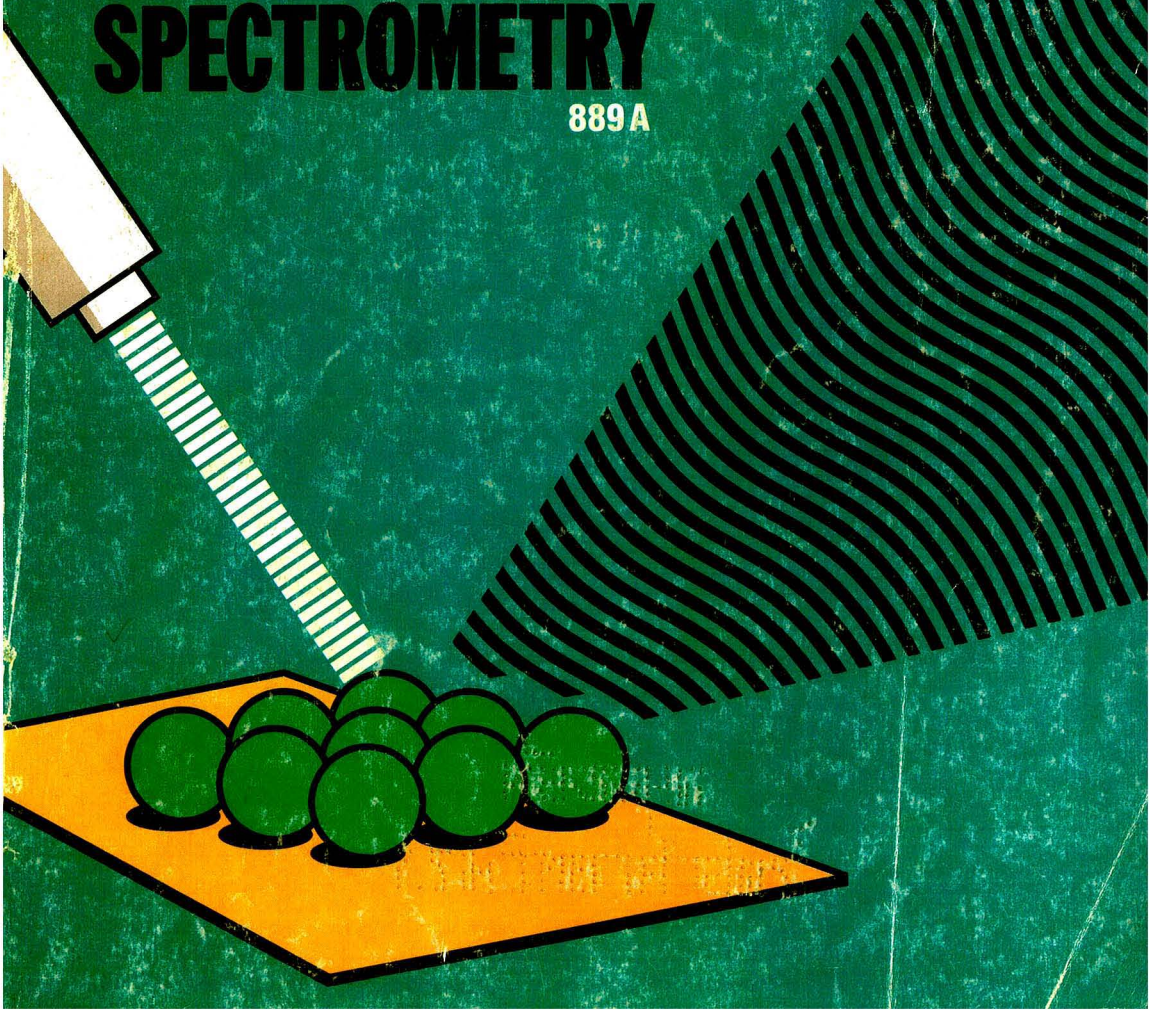

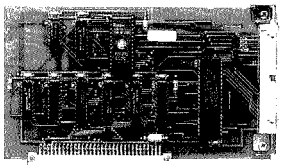

NB-DIO-24 $245
Macintosh II Digital I/O Interface
- 24 TTL Digital I/O Lines Organized into 3 8-bit Ports
- 50-pin Digital I/O Connector
- Transfer rates up to 300K Bytes/Sec

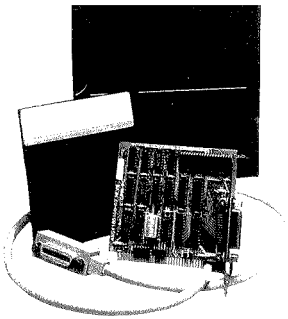

GPIB-PC II/IIA From $395
Interface for IBM PC
- Transfer rates over 300K Bytes/Sec
- RF-Shielded IEEE-488 Receptacle
- Choice of 3 DMA Channels
- Transparent DMA Enabling/Disabling

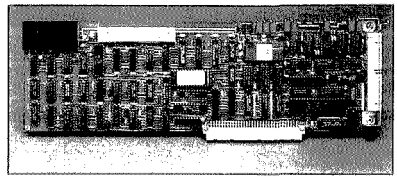

NB-MIO-16 From $1195
Macintosh II Multifunction Input/Output Board
- Fast 12-bit A/D Converter
- 2 Multiplying 12-bit D/A Converters
- 16 Word FIFO A/D Buffer
- 8 Digital I/O Lines
- Other Models Available for PC/AT and PS/2 Computers

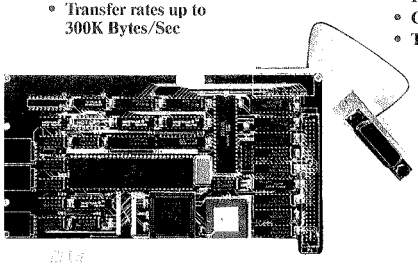

GPIB-SE From $495
GPIB Interface for Macintosh SE
- Onboard Turbo 488 Custom IC
- DMA Rates as High as 1M Bytes/Sec
- High-speed CMOS Technology

OMEGA Introduces IEEE Computer Interfaces

NEW!

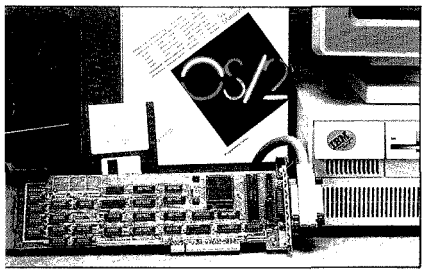

MC-GPIB $495
IEEE-488 Interface for IBM Personal System/2
- Turbo 488 Custom IC
- 1M Bytes/Sec GPIB Reads
- 700K Bytes/Sec GPIB Writes

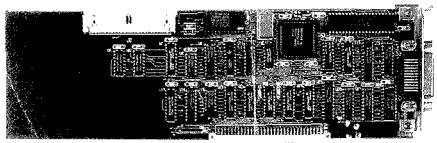

NB-GPIB $495
PC NuBus IEEE-488 Interface for Macintosh II
- High-Performance RTSI Bus Interface
- Onboard ROM for Configuration Information
- I/O Data Rates as High as 400K Bytes/Sec

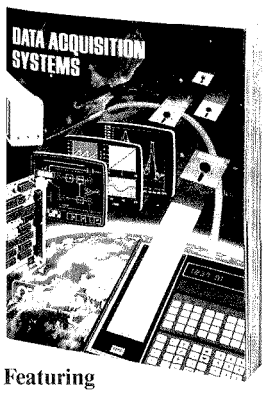

Featuring
- Data Acquisition
- Software
- Data Logging Systems
- Recorders

CIRCLE 120 ON READER SERVICE CARD

Dial (203)359-RUSH to Request Your Free Handbooks

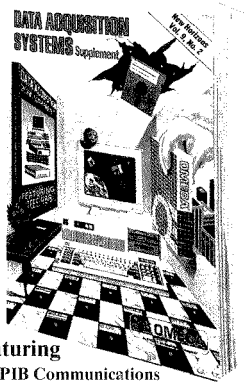

Featuring
- GPIB Communications
- Data Acquisition
- Accessories
- Software
- All Made-In-USA!
  - All Full Color Pages
  - All Prices Listed
  - Complete Technical Information Included
  - In-Stock for Fast Delivery

OMEGA
An OMEGA Technologies Company

One Omega Drive, Box 4047, Stamford, CT 06907
Telex 996404 Cable OMEGA FAX (203) 359-7700

To Order Products, Call Toll Free

1-800-TC OMEGA
1-800-82 66342

IN CT (203) 359-1660

How HP HPLC lightens your workload.

1976 HP advances HPLC with new standards in precision flow control.

1978 HP advances HPLC with the first scanning variable wavelength detector.

1982 HP advances HPLC with the first commercial diode-array detector.

1983 HP advances HPLC with the first system optimized for low dispersion LC.

1986 HP advances HPLC with first on-line pre-column derivatization.

1988 HP advances HPLC with particle beam LC/MS.

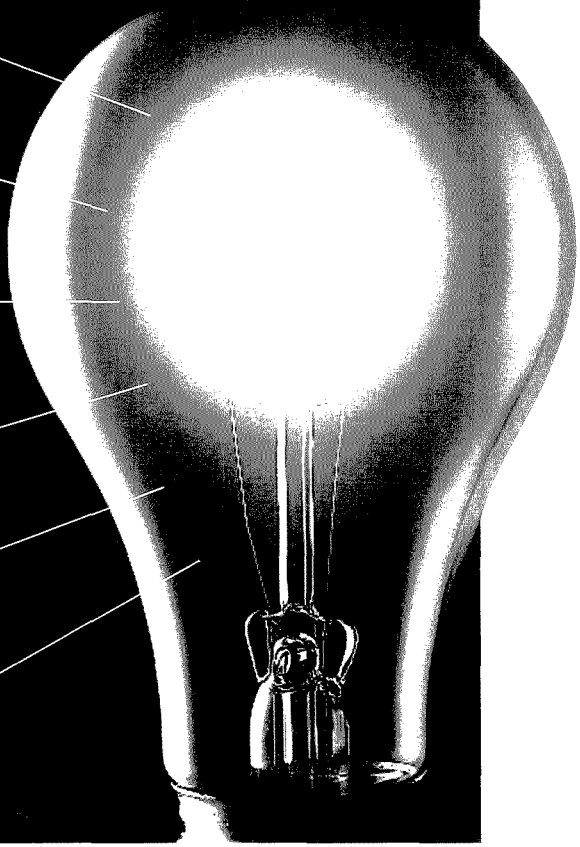

Why are more and more chromatographers switching to HP HPLC? *Superior technology that makes your job much easier and more productive!*

Year after year, Hewlett-Packard introduces some of the brightest ideas in HPLC. Things like high precision solvent flow. Instant spectra. Push button operation. Full automation with diagnostics. All of the advantages of low dispersion LC and particle beam LC/MS with true EI spectra. Not to mention the incredible reliability that made 99% uptime a practical reality.

Along with extraordinary power and versatility, HP offers a wide range of HPLC products. From economical modules to fully integrated systems. From a spectrum of detectors to application specific analyzers. From integrators to lab information and control systems. All from a single vendor.

To learn more call **1 800 556-1234, EXT 10211.** In California call **1 800 441-2345, EXT 10211.**

HEWLETT PACKARD

CIRCLE 65 ON READER SERVICE CARD

THE NEW AGE OF FREEDOM

Mattson Instruments' new Galaxy™ series spectrometers bestow freedoms never realized in the analytical laboratory before Mattson's Revolution of '89: freedom of bench space, freedom of compatibility, and freedom of proof.

Freedom of Bench Space

The recent availability of the revolutionary new, large-scale integrated 4326 circuit chip, enables Mattson's Galaxy spectrometers to pack more performance into less bench space. In fact, the 4326 chip has freed us to not only substantially reduce the size of the spectrometer, but enhance its performance and reliability as well. By the way, you'll find the 4326 and its compact performance capabilities only in Mattson's Galaxy series.

Freedom of Compatibility

All Galaxy spectrometers are designed to operate independently or with the computer — or computers — of your choice without sacrificing data acquisition speed. The Galaxy series' design enhances the speed of any computer to superbly execute any FTIR experiment — and allows display and data manipulation on virtually any computer in your system.

Freedom of Proof

We'll prove — in your own lab, with your own applications, with your own team — the freeing power of the Mattson Galaxy spectrometer best suited for your needs. Because Mattson Instruments is a full service FTIR company with strong regional support personnel, we can set up an on-site demonstration in minutes.

The Price of Freedom?

Half the price of comparable systems — though truly comparable systems simply don't exist. No other spectrometer series packs so much performance into such a manageable size, features Mattson's 4326 chip, offers such unlimited compatibility, or incorporates Mattson's unique cube corner optics, true optical null and long-term reliability. No other spectrometer series offers so much freedom at any price.

If you'd like to lead your lab into the New Age of Freedom, call Mattson Instruments today.

Mattson Instruments, Inc.
1001 Fourier Court
Madison, WI 53717 U.S.A.
Tel. (608) 831-5515
Telex: 262006
Fax: (608) 831-2093

Mattson Instruments, Ltd.
Linford Forum
Rockingham Drive
Linford Wood
Milton Keynes MK 14 6LY
England
Tel. (0908) 679961
Telex: 825264 Silbus G
Fax: (0908) 668974

Mattson

CIRCLE 94 ON READER SERVICE CARD

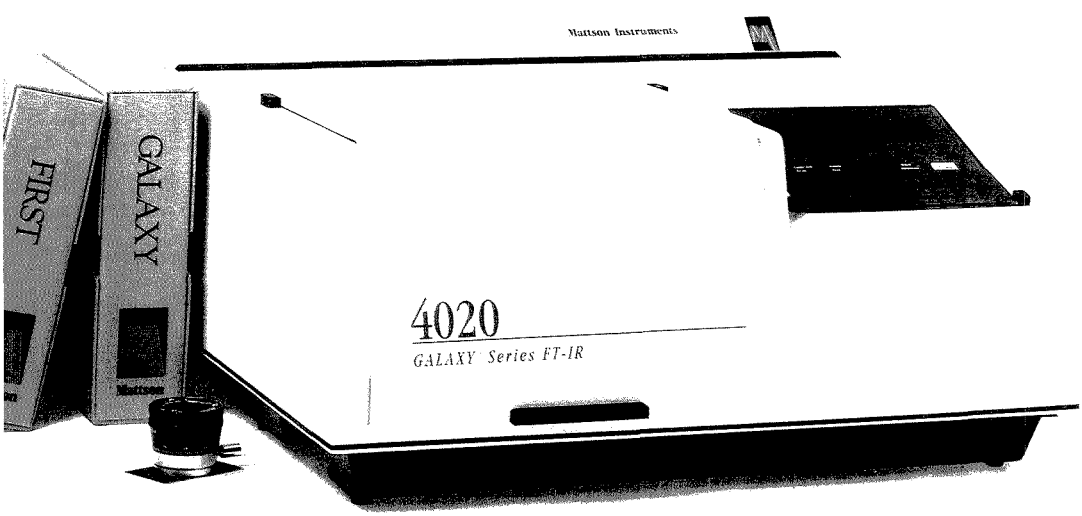

AUGUST 1, 1989
VOLUME 61
NUMBER 15

ANCHAM
61(15) 871A–930A/1601–1792 (1989)
ISSN 0003-2700

ANALYTICAL CHEMISTRY (ISSN 0003-2700) is published semimonthly by the American Chemical Society at 1155 16th St., N.W., Washington, DC 20036. Editorial offices are located at the same ACS address (202-872-4600; TDD 202-872-8733). Second-class postage paid at Washington, DC, and additional mailing offices. Postmaster: Send address changes to ANALYTICAL CHEMISTRY Member & Subscriber Services, P.O. Box 3337, Columbus, OH 43210.

Claims for missing numbers will not be allowed if loss was due to failure of notice of change of address to be received in the time specified; if claim is dated (a) North America: more than 90 days beyond issue date, (b) all other foreign: more than one year beyond issue date, or if the reason given is "missing from files."

Advertising Management: Centcom, Ltd., 500 Post Rd. East, Westport, CT 06880 (203-226-7131)

1989 subscription rates include air delivery outside the U.S., Canada, and Mexico

	1 yr	2 yr
Members		
Domestic	$ 27	$ 45
Canada and Mexico	56	103
Europe	83	157
All Other Countries	120	231
Nonmembers		
Domestic	49	83
Canada and Mexico	78	141
Europe	155	280
All Other Countries	192	354

Three-year and other rates contact: Member & Subscriber Services, ACS, P.O. Box 3337, Columbus, OH 43210 (614-447-3776 or 800-333-9511).

Subscription orders by phone may be charged to Visa, MasterCard, Barclay card, Access, or American Express. Call toll free at (800-ACS-5558) from anywhere in the continental United States; from Washington, DC, call 872-8065. Mail orders for new and renewal subscriptions should be sent with payment to the Business Management Division, ACS, P.O. Box 57136, West End Station, Washington, DC 20037.

Subscription service inquiries and changes of address (Include both old and new addresses with ZIP code and *recent mailing label*) should be directed to the ACS Columbus address noted above. Please allow six weeks for change of address to become effective.

ACS membership information: Lorraine Bowlin (202-872-4567)

Single issues, current year, $7.00 except review issue and LabGuide, $12.00; **back issues and volumes and microform editions** available by single volume or back issue collection. For information or to order, call (800-ACS-5558) or write the Microform & Back Issues Office at the Washington address.

Nonmembers rates in Japan: Rates above do not apply to nonmember subscribers in Japan, who must enter subscription orders with Maruzen Company Ltd., 3–10 Nihonbashi 2-chome, Chuo-ku, Tokyo 103, Japan. Tel: (03) 272-7211.

Analytical

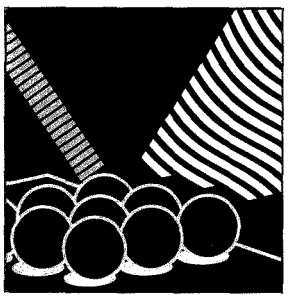

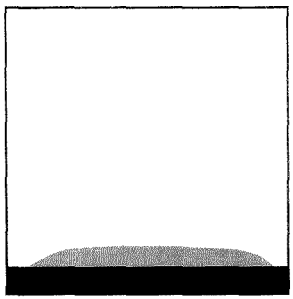

REPORT **889 A**

On the cover. **Solid-surface luminescence.** The speed, simplicity, sensitivity, selectivity, and moderate cost of solid-surface luminescence make it applicable to areas of interest ranging from column chromatography to the analysis of pharmaceutical tablets. Robert J. Hurtubise of the University of Wyoming discusses the principles of the technique, current applications, and prospects for future theoretical and instrumental developments

INSTRUMENTATION **897 A**

Fast thermolysis/FT-IR spectroscopy. By imposing a faster heating rate than conventional thermogravimetry, researchers can obtain information about relatively reactive molecules lost to side reactions at slower heating rates or with time delays in the detection step. Thomas B. Brill of the University of Delaware describes the technique, the instrumentation involved, and its application

BRIEFS **874 A**

EDITORIAL **885 A**

25th Anniversary of a classic paper. July marked the silver anniversary of the publication in this JOURNAL of Abraham Savitzky and Marcel Golay's landmark smoothing algorithm. This paper ushered in the use of data-processing and digital computer techniques that have had a profound effect on the practice of analytical chemistry

NEWS **887 A**

NIST establishes a **consortium for the development of automated analytical systems.** ▸ Identifying sulfur compounds in coal nondestructively. ▸ Drilling into a volcano

MEETINGS **909 A**

The 198th ACS fall national meeting will be held Sept. 10–15 in Miami Beach, FL. The Division of Analytical Chemistry's program will be highlighted by presentation of awards to Ralph Adams, M. Bonner Denton, Theodore Williams, and Gary Hieftje. ▸ Conferences. ▸ Short courses. ▸ Call for papers

FOCUS **921 A**

A **historic collaboration.** Abraham Savitzky recalls the genesis of the Savitzky–Golay algorithm. ▸ **Marcel Golay—a memorial**

NEW PRODUCTS & MANUFACTURERS' LITERATURE **924 A**

AUTHOR INDEX **1601**

BRIEFS

Perspective: Analytical Biotechnology

Isoelectric Focusing in Immobilized pH Gradients 1602

Recently a new generation of stable acrylamido buffers was described, leading to increased resolution and use over a wider pH range of the technique of isoelectric focusing in immobilized pH gradients. This "Perspective" highlights current knowledge and predicts that this separation method will become widely used, particularly in the fields of human and animal genetics.

Pier Giorgio Righetti*, Elisabetta Gianazza, Cecilia Gelfi, and Marcella Chiari, Chair of Biochemistry, Faculty of Pharmacy and Department of Biomedical Sciences and Technologies, University of Milan, Via Celoria 2, Milan 20133, Italy and **Pranav K. Sinha,** Institute of Clinical Chemistry and Biochemistry, Universitätsklinikum Rudolf Virchow, Spandauer Damm 130, D-1000 Berlin 19, FRG

Articles

Strategies for Background Subtraction in Electron Probe Microanalysis/X-ray Compositional Mapping 1612

The dependence of the bremsstrahlung on average atomic number can be used to make an indirect calculation of the background appropriate to each location in an X-ray compositional map.

Robert L. Myklebust*, Dale E. Newbury, and Ryna B. Marinenko, Room A121, Chemistry Building, National Institute of Standards and Technology, Gaithersburg, MD 20899

Alkali-Metal and Alkaline-Earth Cation and Proton Selectivities of Dibenzo-14-crown-4 and Its Derivatives in Polymeric Membranes 1618

The attachment of pendant groups (–OH, $-OCH_2CH_2OCH_3$, $-OCH_2CO_2H$) to the central carbon of a three-carbon bridge in dibenzo-14-crown-4 markedly alters the response of this ionophore to alkali metal cations, alkaline earth cations, and protons in solvent-polymeric membranes.

Uriel Olsher* and Felix Frolow, Department of Chemical Services, The Weizmann Institute of Science, Rehovot 76100, Israel, **Gil Shoham*,** Department of Analytical and Inorganic Chemistry, The Hebrew University of Jerusalem, Jerusalem, Israel, and **Gwi-Suk Heo and Richard A. Bartsch*,** Department of Chemistry and Biochemistry, Texas Tech University, Lubbock, TX 79409-1061

Electrochemical Study of the Mechanism of Cadmium Extraction with Dithizone 1621

An acetate-containing anionic cadmium dithizonate species, $CdDz_2(OAc)^-$, is identified as the species that transfers from water into dichloroethane under current scanning polarographic conditions.

Wei-hua Yu and H. Freiser*, Strategic Metals Recovery Research Facility, Department of Chemistry, University of Arizona, Tucson, AZ 85721

* Corresponding author

Analysis of Transient Currents and Interfacial Kinetics for Neutral Carrier Membranes 1624

General and simplified digital simulation schemes are used to generate current–time and component potential–time curves and carrier concentration profiles. Attempts to fit whole transients globally, with independently determined parameters, are partially successful.

James R. Sandifer*, Corporate Research Laboratories, Eastman Kodak Company, Rochester, NY 14650 and **Michael L. Iglehart and Richard P. Buck,** Department of Chemistry, University of North Carolina, Chapel Hill, NC 27514

Preparation and Electrochemical Characterization of Conical and Hemispherical Ultramicroelectrodes 1630

A fabrication technique allows the preparation of conical Pt–Ir ultramicroelectrodes with radii of 0.5–10 μm. The radius determines the geometry of the diffusional behavior. SEM, cyclic voltammetry, and chronoamperometry are used to characterize the electrodes.

Reginald M. Penner, Michael J. Heben, and Nathan S. Lewis*, Division of Chemistry and Chemical Engineering, California Institute of Technology, Pasadena, CA 91125

Quantitative Relationship between Electron Transfer Rate and Surface Microstructure of Laser-Modified Graphite Electrodes 1637

The electron transfer rate constant and capacitance of untreated and laser-activated highly ordered pyrolytic graphite surfaces are correlated with the fractional surface coverage of the edge plane, indicating that both are determined by the edge plane density.

Ronald J. Rice and Richard L. McCreery*, Department of Chemistry, The Ohio State University, 120 West 18th Avenue, Columbus, OH 43210

On-Line Radioisotope Detection for Capillary Electrophoresis 1642

Two detector systems are evaluated using synthetic mixtures of ^{32}P-labeled sample molecules. Flow programming extends the detection limit to the sub-nCi level.

Stephen L. Pentoney, Jr., and Richard N. Zare*, Department of Chemistry, Stanford University, Stanford, CA 94305 and **Jeff F. Quint,** Beckman Instruments, Inc., Scientific Instruments Division, Fullerton, CA 92634

Near-Infrared Surface-Enhanced Raman Spectroscopy Using a Diode Laser 1648

A diode laser using Ag and Cu electrodes is used to obtain SER spectra of 6-mM solutions of the highly luminescent compound tris(2,2′-bipyridyl)ruthenium(II). No luminescent interference is encountered.

Stanley M. Angel* and Michael L. Myrick, Environmental Sciences Division, Lawrence Livermore National Laboratory, Livermore, CA 94550

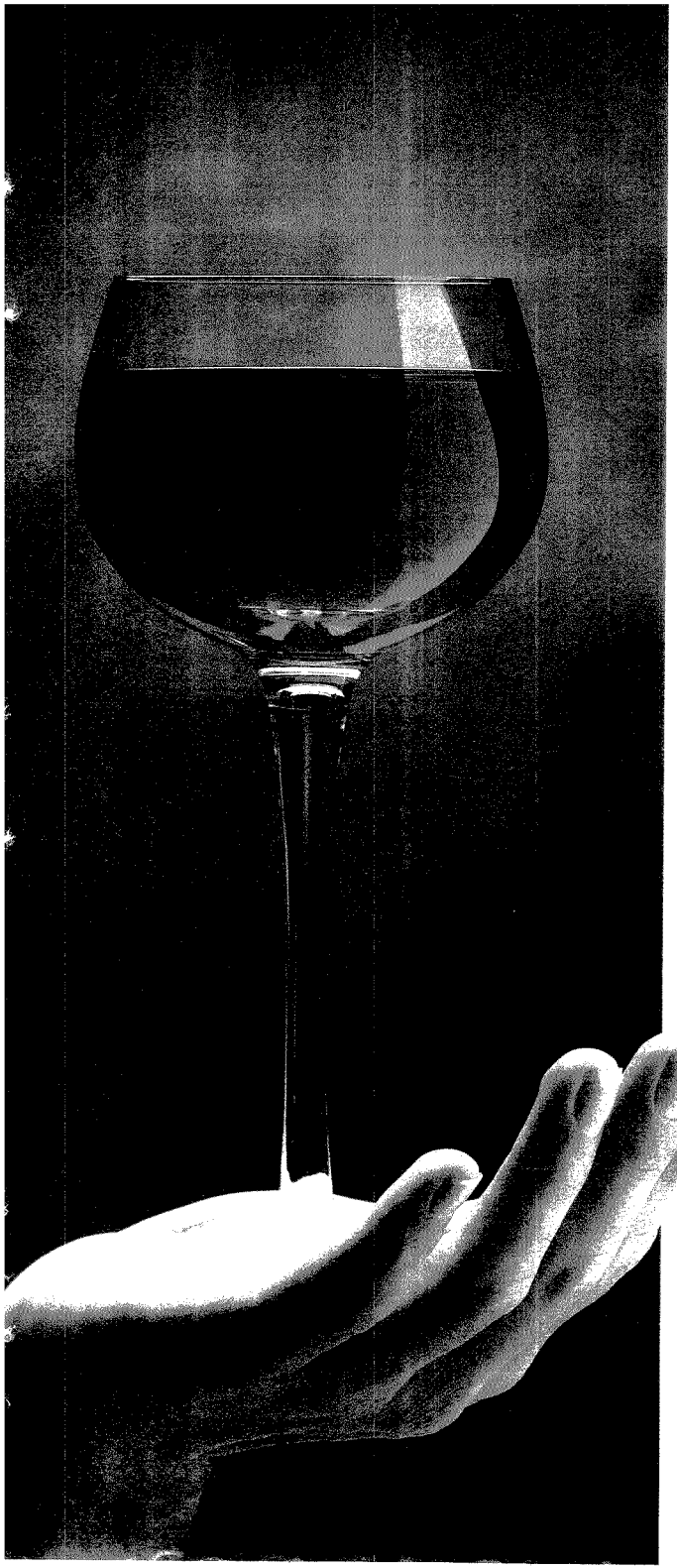

DABS brings stability to reversed phase amino acid analysis.

Stability. It's more than holding something steady for just a moment. It's *keeping* it that way. For a long, long time.

With DABS you won't measure derivative stability in minutes. Or even hours. DABS remains stable for weeks.

So you can do repeated runs from the same sample. Or go back days later and analyze a sample again using the same derivative, the same method — without changes.

And DABS only takes minutes to set up with our exclusive Dabsylation Kit.

Add the advantages of visible detection, and DABS is obviously the wise choice for high speed, high sensitivity amino acid analysis.

System Gold

And because you'll be using the world's easiest, most advanced HPLC — System Gold,™ the Personal™ Chromatograph — you'll have guaranteed methods and reference chromatograms available on disk.

To add stability to your reversed phase amino acid analyses, contact your local Beckman representative. Offices in major cities worldwide.

Call 800/742-2345 in the US. Or write Beckman Instruments, Inc., Altex Division, 2350 Camino Ramon, P.O. Box 5101, San Ramon, CA 94583.

BECKMAN

A SMITHKLINE BECKMAN COMPANY

Australia, Sydney **Austria**, Vienna **Canada**, Toronto **Denmark**, Birkerød **France**, Gagny **Germany**, Munich **Hong Kong**, Aberdeen **Italy**, Milano **Japan**, Tokyo **Mexico**, Mexico City **Netherlands**, Mijdrecht **Norway**, Oslo **Puerto Rico**, Carolina **Singapore South Africa**, Johannesburg **Spain**, Madrid **Sweden**, Bromma **Switzerland**, Nyon **Taiwan**, Taipei **United Kingdom**, High Wycombe **United States**, San Ramon AX88-1025

Circle 24 to send Representative and Literature.
Circle 25 for Literature only.

Studies of Sputtering Atomizers for Atomic Absorption Spectroscopy 1652

Factors influencing absorption sensitivity and reproducibility are investigated for several sputtering atomizers used in atomic absorption analysis of solid samples.

David S. Gough*, Peter Hannaford, and R. Martin Lowe, CSIRO Division of Materials Science and Technology, Locked Bag 33, Clayton, Victoria 3168, Australia

Identification of Immobilized Bacteria by Aminopeptidase Profiling 1656

Incorporating an immobilized cell technique into a standard bacterial identification method allows reduction in the cell concentration and incubation period without a loss in sensitivity. The total turnaround time is reduced from 2.5 days to 3–7 h.

K. D. Hughes and F. E. Lytle*, Department of Chemistry, Purdue University, West Lafayette, IN 47907 and **D. M. Huber*,** Department of Botany and Plant Pathology, Purdue University, West Lafayette, IN 47907

Water as a Unique Medium for Thermal Lens Measurements 1660

The effect of temperature on the thermal lens signal in water is exploited to produce photothermal focusing and defocusing and to enhance the sensitivity of the measurement.

Mladen Franko and Chieu D. Tran*, Department of Chemistry, Marquette University, Milwaukee, WI 53233

Spectrophotometric Method for the Analysis of Plutonium and Nitric Acid Using Partial Least-Squares Regression 1667

PLS regression is used to quantitate plutonium and nitric acid using the absorption spectra. Pu(III) (1.99–29.9 g/L) and nitric acid (0.5–3.0 M) are calibrated simultaneously with a standard error of 0.20 g/L and 0.18 M, respectively.

W. Patrick Carey and Lawrence E. Wangen, Chemical and Laser Science Division, G740, Los Alamos National Laboratory, Los Alamos, NM 87545 and **James T. Dyke*,** Material Science and Technology Division, E501, Los Alamos National Laboratory, Los Alamos, NM 87545

Continuum Source Atomic Absorption Spectrometry in a Graphite Furnace with Photodiode Array Detection 1670

An AA spectrometer that uses an Xe arc lamp as the source and an intensified photodiode array detector is described. The multiwavelength detection power allows simultaneous determination of several elements in a mixture and provides automatic background correction.

Bradley T. Jones, Ben W. Smith, and James D. Winefordner*, Department of Chemistry, University of Florida, Gainesville, FL 32611

Polymer-Coated Cylindrical Waveguide Absorption Sensor for High Acidities 1674

Molar concentrations of nitric and hydrochloric acids are detected using an in situ sensor composed of polymer-encapsulated indicators combined with cylindrical optical elements. Precision is 0.05 M.

W. Patrick Carey* and Michael D. DeGrandpre, Chemical and Laser Science Division, G740, Los Alamos National Laboratory, Los Alamos, NM 87545 and **Betty S. Jorgensen,** Material Science and Technology Division, E549, Los Alamos National Laboratory, Los Alamos, NM 87545

Picogram Level Quantitation of 2,3,7,8-Tetrachlorodibenzo-*p*-dioxin in Fish Extracts by Capillary Gas Chromatography/Matrix Isolation/Fourier Transform Infrared Spectrometry 1678

GC/MI/FT-IR spectrometry is used to confirm the identity and quantitate 2,3,7,8-tetrachlorodibenzo-*p*-dioxin in fish extracts in the 170–220-pg range (15–45 pg/g). Recovery averages 52%.

Magdi M. Mossoba*, Richard A. Niemann, and Jo-Yun T. Chen, Division of Contaminants Chemistry, Food and Drug Administration, 200 C St., S.W., Washington, DC 20204

Application of Cross-Correlation to Quantitative Analysis of Binary Mixtures Using Extended X-ray Absorption Fine Structure 1686

Using suitable standard spectra for calibration purposes, it is possible to extract percent composition information from EXAFS data of binary mixtures using cross-correlation analysis. Without such standards, semiquantitative trends can also be obtained.

Douglas P. Hoffmann, Andrew Proctor, Martin J. Fay, and David M. Hercules*, Department of Chemistry, University of Pittsburgh, Pittsburgh, PA 15260

Fourier Transform Atomic Absorption Flame Spectrometry with Continuum Source Excitation 1694

The design and performance of an FT-AA spectrometer using a 300-W Xe arc continuum source and a Michelson interferometer are presented. Detection limits for several elements are generally an order of magnitude poorer than those obtained by continuum AA methods that use echelle-grating spectrometers.

Mark R. Glick, Bradley T. Jones, Benjamin W. Smith, and James D. Winefordner*, Department of Chemistry, University of Florida, Gainesville, FL 32611

Mixture Analysis and Quantitative Determination of Nitrogen-Containing Organic Molecules by Surface-Enhanced Raman Spectrometry 1697

A correction procedure for standardization of measurements is proposed and evaluated to solve the problem of quantitation of adsorbate in SERS. The RSD is about 15%, and linearity is achieved up to 50 μg/mL aminoacridine.

J. J. Laserna, A. D. Campiglia, and J. D. Winefordner*, Department of Chemistry, University of Florida, Gainesville, FL 32611

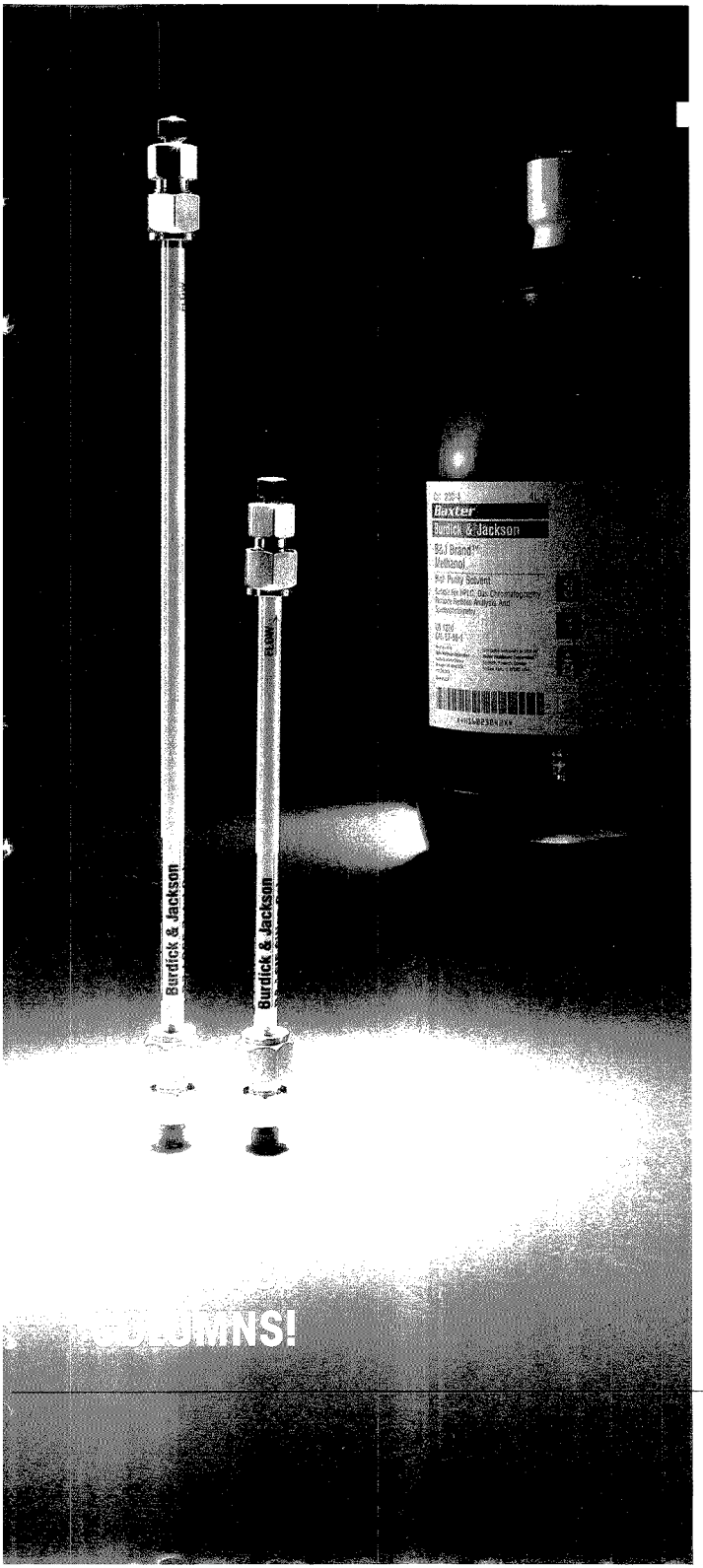

B&J solvents have always set the industry standard for quality and consistency.

The same philosophy is the cornerstone in developing an entire line of new B&J analytical HPLC columns. Now B&J offers a wide variety of normal and reversed phase supports, each with a rigorous set of specifications (N, α and skew) which guarantees reproducible column-to-column performance. Every column comes with a benchmark standard to verify initial column performance, a test chromatogram and a guide for use and storage.

All B&J packing materials are based on 5μ spherical silica. Columns are 15 cm or 25 cm in length with a 4.6 mm I.D.

The combination of B&J HPLC Columns and B&J Solvents gives you a dependable team which delivers the highest level of quality and consistency.

For more details, contact Baxter Healthcare Corporation, Burdick & Jackson Division, 1953 South Harvey Street, Muskegon, MI 49442 USA. For technical assistance, call us toll-free at 800.368.0050.

Redefining Quality Through Innovation

Distributed Exclusively in USA by
Baxter Healthcare Corporation
Scientific Products Division
Manufactured by
Baxter Healthcare Corporation
Burdick & Jackson Division

Baxter

CIRCLE 18 ON READER SERVICE CARD

Interpreting Mass Spectra of Multiply Charged Ions 1702

Two algorithms that extract molecular mass information from the spectra of multiply charged ions are applied to the spectra of small proteins (5–40 kD) obtained by electrospray MS. Accuracy and sources of error are discussed.

Matthias Mann, Chin Kai Meing, and John B. Fenn*, Department of Chemical Engineering, Yale University, New Haven, CT 06520-2159

On-Line Electrochemistry/Thermospray/Tandem Mass Spectrometry as a New Approach to the Study of Redox Reactions: The Oxidation of Uric Acid 1709

The on-line combination of electrochemistry and thermospray/tandem MS provides otherwise difficult to obtain information about redox and associated chemical reactions of biological molecules, such as the structure of reaction intermediates and products.

Kevin J. Volk, Richard A Yost*, and Anna Brajter-Toth*, Department of Chemistry, University of Florida, Gainesville, FL 32611

Determination of Serum Cholesterol by a Modification of the Isotope Dilution Mass Spectrometric Definitive Method 1718

Cholesterol is determined in seven pools of human serum, with a coefficient of variation of 0.22%. The modified method uses improved chromatographic separation and a new method of implementing selected ion monitoring.

Polly Ellerbe*, Stanley Meiselman, Lorna T. Sniegoski, Michael J. Welch, and Edward White V, Center for Analytical Chemistry, National Institute of Standards and Technology (formerly National Bureau of Standards), Gaithersburg, MD 20899

Desorption Chemical Ionization, Thermospray, and Fast Atom Bombardment Mass Spectrometry of Dihydropyridine ⇌ Pyridinium Salt-Type Redox Systems 1723

Trigonellyl-substituted (quaternary pyridinium salt-type) compounds and their dihydropyridine analogues undergo thermal decomposition, hydrolysis, and redox reactions under desorption ionization conditions.

László Prókai, Bih-Hsiung Hsu, Hassan Farag, and Nicholas Bodor*, Center for Drug Design and Delivery, College of Pharmacy, Box J-497, J. Hillis Miller Health Center, University of Florida, Gainesville, FL 32610

Potentiometric Homogeneous Enzyme-Linked Competitive Binding Assays Using Adenosine Deaminase as the Label 1728

The assay is based on the inhibition of an adenosine deaminase–biotin conjugate by avidin. Unlike conventional homogeneous enzyme immunoassays, this method uses an ammonium-selective electrode rather than a photometric detector.

Thea L. Kjellström and Leonidas G. Bachas*, Department of Chemistry, University of Kentucky, Lexington, KY 40506-0055

Quantification of Recombinant Interleukin-2 in Human Serum by a Specific Immunobioassay 1732

The detection limit is 2 units/mL using 0.1 mL serum. Interassay precision is 4.6%, whereas intraassay precision is 12.7%. Sensitivity, reproducibility, specificity, stability, and recovery are also discussed.

R. W. Nadeau*, N. F. Oldfield, W. A. Garland, and D. J. Liberato, Department of Drug Metabolism, Hoffmann-La Roche, Inc., Nutley, NJ 07110

Conductometric Transducers for Enzyme-Based Biosensors 1737

Transducers with Cu and Pt electrodes are constructed and characterized, and two enzyme immobilization methods are tested. A detection limit of 10^{-6} M and a linear range of 2 orders of magnitude are achieved.

Susan R. Mikkelsen and Garry A. Rechnitz*, Department of Chemistry, University of Delaware, Newark, DE 19716

Immobilized-Metal Affinity and Hydroxyapatite Chromatography of Genetically Engineered Subtilisin 1742

Subtilisin (MW 27500) single amino acid variants are separated by immobilized-metal affinity chromatography. Selectivity is demonstrated with the separation of two variants differing by only a methylene group.

Roman M. Chicz and Fred E. Regnier*, Department of Biochemistry, Purdue University, West Lafayette, IN 47907

Subambient Temperature Modification of Selectivity in Reversed-Phase Liquid Chromatography 1749

The effect of column temperature on selectivity is examined for monomeric and polymeric C_{18} phases. A model for temperature induced selectivity changes is presented.

Lane C. Sander* and Stephen A. Wise, Center for Analytical Chemistry, National Institute of Standards and Technology (formerly National Bureau of Standards), Gaithersburg, MD 20899

Cycling Technique for the Determination of Femtomole Amounts of Sulfite 1755

A micromethod for the fluorometric determination of sulfite is based on a coupled enzyme assay and enzymatic cycling. The method is linear with a detection limit of 150 fmol for standard and wine samples, and 290 fmol for extracts of freeze-dried needle tissue.

Regina Keil, Universität Tübingen, Institut für Botanik, Auf der Morgenstelle 1, D-7400 Tübingen, Federal Republic of Germany, **Rüdiger Hampp***, Universität Tübingen, Institut für Botanik, Auf der Morgenstelle 1, D-7400 Tübingen, Federal Republic of Germany, and **Hubert Ziegler,** Technische Universität München, Lehrstuhl für Botanik, Arcisstrasse 21, D-8000 München, Federal Republic of Germany

SIEMENS

Realize the full potential of Fundamental Parameter analysis in your lab

Siemens new Fundamental Parameter software fully integrates theoretical and empirical alphas within the SPECTRA AT package to provide superior results from elemental analysis by XRF.

- Easy to use.
- Requires fewer standards.
- Based on the work of Tertian and Broll (X-Ray Spectrometery, 1983, Vol. 12, No. 1).

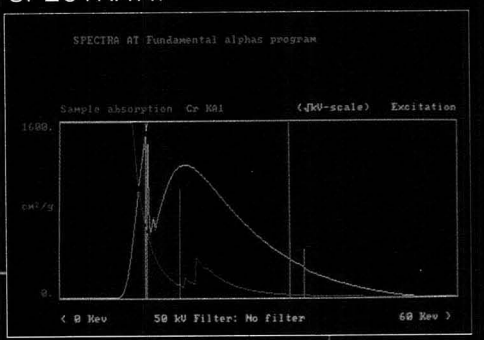

Excitation profile and absorption of sample.

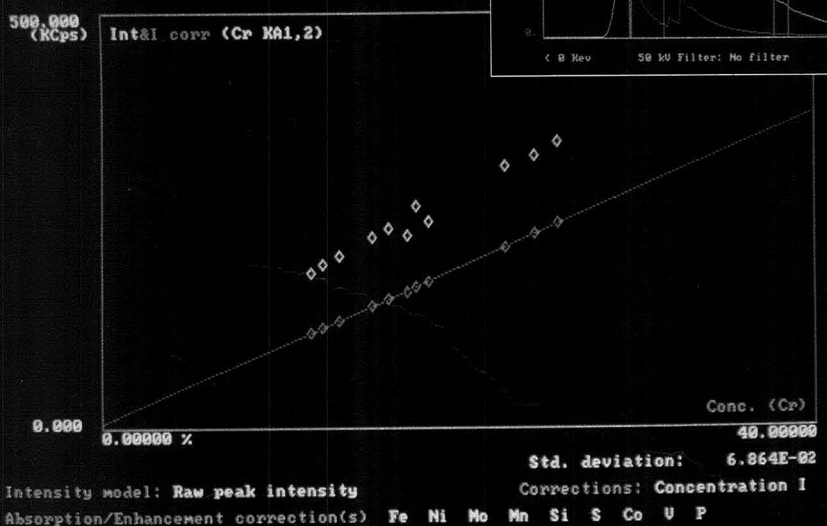

Results of calibration using theoretical alpha's.

The solution is Siemens.

In USA & Canada contact Siemens Analytical X-Ray Instruments, Inc., a joint venture of Siemens & Nicolet.
6300 Enterprise Lane • Madison, WI 53719-1173 • Tel. (608) 276-3000 • FAX (608) 276-3015
Worldwide Contact: Siemens AG, Analytical Systems E 689 • D 7500 Karlsruhe 21 • P.O. Box 21 1262 • Federal Republic of Germany • Tel. (0721) 595-4295

CIRCLE 154 ON READER SERVICE CARD

BRIEFS

Determination of Lead in Antarctic Ice at the Picogram-per-Gram Level by Laser Atomic Fluorescence Spectrometry 1758

LEAF allows direct analysis of decontaminated samples (20 μL) without preliminary chemical treatment or preconcentration. Results are compared with those previously obtained for the same samples by isotope dilution mass spectrometry.

Michail A. Bolshov, Claude F. Boutron*, and Aleksandr V. Zybin, Institute of Spectroscopy, USSR Academy of Sciences, Troitzk, 142092 Moscow Region, USSR, and Laboratoire de Glaciologie et Géophysique de l'Environment du CNRS, Domaine Universitaire, 2, rue Molière, B.P. 96, 38402 St. Martin d'Hères Cedex, France

Cyclic Voltammetry at Microhole Array Electrodes 1763

A reversible redox-electrode reaction at microhole array electrodes is discussed. The theoretical results are confirmed experimentally for the redox-electrode reaction of $[Fe(CN)_6]^{4-/3-}$ using cyclic voltammetry at carbon fiber–epoxy composite electrodes.

Koichi Tokuda*, Department of Electronic Chemistry, Graduate School at Nagatsuta, Tokyo Institute of Technology, Nagatsuta, Midori-ku, Yokohama 227, Japan and **Ken-ichi Morita** and **Yoshihiro Shimizu,** Basic Research Laboratories, Toray Industry, Inc., 1111 Tebiro, Kamakura 248, Japan

Fiber-Optic Time-Resolved Fluorescence Sensor for the Simultaneous Determination of Al^{3+} and Ga^{3+} or In^{3+} 1768

The sensor is based on a pool of chelator solution trapped behind an ion-permeable membrane. Time-resolved fluorimetric methods are used to determine the contribution of each of two complexes to the total fluorescence signal.

Mary K. Carroll, Frank V. Bright, and Gary M. Hieftje*, Department of Chemistry, Indiana University, Bloomington, IN 47405

Split Zone Flow Injection Analysis: An Approach to Automated Dilutions 1773

An overly concentrated sample can be automatically diluted up to 15,000-fold, independent of the sample's viscosity (up to 167 cP). The dilution conditions can be preset, and the extent of the dilution can be calculated.

Gregory D. Clark, Jaromir Ruzicka, and Gary D. Christian*, Center for Process Analytical Chemistry, Department of Chemistry, BG-10, University of Washington, Seattle, WA 98195

Titanium Dioxide Based Substrate for Optical Monitors in Surface-Enhanced Raman Scattering Analysis 1779

The use of Ag-coated TiO_2 substrates as optical monitors for SERS is investigated. The experimental parameters and analytical capabilities are reported, and its use for in situ trace organic analysis is demonstrated.

Job M. Bello, David L. Stokes, and Tuan Vo-Dinh*, Advanced Monitoring Development Group, Health and Safety Research Division, Oak Ridge National Laboratory, Oak Ridge, TN 37831-6101

The FT-IR's that are making waves.

We've upset the status quo!

For example, "old school FT-IRs" use obscure computer operating systems, maddeningly complex software and are barely compatible with the rest of the computer world. Analect, on the other hand, has made FT-IRs extremely easy to use. We've multiplied–not restricted–your options in third-party computer hardware and software by providing the IBM-compatible MS-DOS operating system. This mainstream operating system also handles FT-IR data with incredible speed.

And Analect doesn't go along with the "conventional wisdom" that an FT-IR must be pampered and frequently realigned. Our systems are so reliable and accurate that they may never need realignment or recalibration.

Like those waves? There's more.

While the competition offers a dead-end upgrade path, Analect provides modularity and upgradability throughout its entire family of instruments, from 2 wave to 1/8 wavenumber systems.

Isn't that the way you would design an FT-IR?

It's time to make some waves of your own.

Fill out the coupon or call our toll-free number for a free, absolutely no obligation demonstration of Analect FT-IRs.

CIRCLE 92 ON READER SERVICE CARD

Laser Precision Analytical.
17819 Gillette Ave., Irvine, CA 92714.
In CA: 714-660-8801.
Toll Free: 1-800-334-3433.

LASER PRECISION ANALYTICAL

Technology you can believe in.

Heinrich Emanuel Merck Award for Analytical Chemistry 1990

In 1988 E. Merck, Darmstadt, has granted the Heinrich Emanuel Merck award for the first time.
The award is endowed with DM 25,000 for the promotion of new developments in Analytical Chemistry, in particular for developing new methods in classical chemistry for sample preparation in trace analysis and their application in human environment.
The next award will be granted in the scope of the European Conference on Analytical Chemistry which will take place in Vienna, August 1990.

All young chemists up to the age of 45 are required to submit an original paper to the following adress; deadline will be the end of january 1990.

Herrn Prof. Dr. Günther Tölg
Institut für Spektrochemie und
Angewandte Spektroskopie
Postfach 10 13 52
Bunsen-Kirchhoff-Str. 11
D-4600 Dortmund 1

The winner of this award will be chosen by an international jury of renowned analytical chemists.

If you need more information please contact Prof. Dr. G. Tölg.

E. Merck · Frankfurter Strasse 250 · D-6100 Darmstadt 1

CIRCLE 98 ON READER SERVICE CARD

BRIEFS

Correspondence

Exchange of Comments on the Simplex Algorithm Culminating in Quadratic Convergence and Error Estimation 1783
Steven Brumby, Research School of Chemistry, Australian National University, G.P.O. Box 4, ACT 2601, Australia and **G. R. Phillips and E. M. Eyring*,** Department of Chemistry, University of Utah, Salt Lake City, UT 84112

Technical Notes

Construction of an Optically Transparent Thin-Layer-Electrode Cell for Use with Oxygen-Sensitive Species in Aqueous and Nonaqueous Solvents 1787
Matthew B. G. Pilkington, Barry A. Coles, and Richard G. Compton*, Physical Chemistry Laboratory, Oxford University, South Parks Road, Oxford OX1 3QZ, England

Application of a Nested-Loop System for the Simultaneous Determination of Thorium and Uranium by Flow Injection Analysis 1789
José Luis Pérez Pavón, Bernardo Moreno Cordero*, Jesús Hernández Méndez, and Rosa Maria Isidro Agudo, Department of Analytical Chemistry, Bromatology and Food Sciences, University of Salamanca, Salamanca, Spain

On-Line Dilution Scheme for Liquid Chromatography 1791
Javier N. Oquendo* and Joseph A. Leone*, ARCO Oil and Gas Company, Research and Technical Services, Plano, TX 75075

Lubricon, Beech Grove, IN, specializes in testing lubricants for private and private label companies. Lubricants from such diverse applications as large stationary engines, compressors, transmissions, shipping industry, drilling rigs, and natural gas engines are tested and the results analyzed as to the condition of the lubricant and the unit being lubricated.

Based on Lubricon's finding, the user knows whether to change the lubricant; to check for internal problems such as bearing wear or improper gear train mesh; or external problems such as poor air filtration, all of which could lead to premature failures requiring expensive and untimely maintenance.

Stan Leitz, Operations Manager for Lubricon, wanted a way of eliminating the inconvenience of changing tanks and the cost of nitrogen used to purge an FT-IR spectrometer being used in the analysis of lubricants. "We were going through a tank of nitrogen about every two days but we didn't want to mess with larger tanks or liquid nitrogen. We were looking at the possibility of putting together our own system of an air compressor and an air dryer to provide clean, dry, CO_2-free compressed air for the FT-IR", says Leitz.

When contacted by Lubricon, Balston, Inc., Lexington, MA, recommended the Balston Type 74 Clean Air Package. After reviewing the specifications for the Balston Clean Air Package, a self-contained unit consisting of an air compressor, after-cooler, prefilter and after filters, CO_2 remover and air dryer, Lubricon quickly decided it was exactly what they were looking for.

"The Balston Clean Air Package was simple to install. All we had to do was hook up the electrical power and connect a copper air supply line to the spectrometer. We let the Air Package run for a couple of hours to purge the supply line and we were in business", says Leitz. "Base line calibration tests are taken on a regular basis to check for CO_2 and moisture content in the purge. After two months of operation, we haven't detected any noticeable difference in calibration between the bottled nitrogen we were using and the air supplied by the Balston Clean Air Package".

"Based on what we were paying for bottled nitrogen, the Balston Clean Air Package will pay for itself in less than one year, after which we will be saving about $7,000 per year".

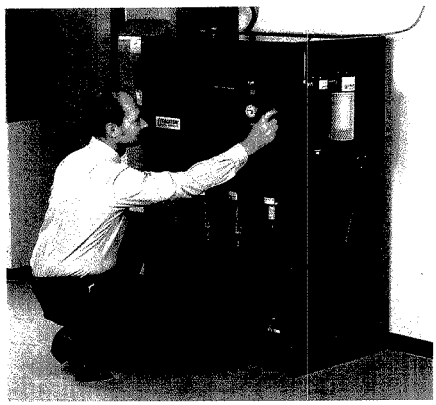

Balston Type 74 Clean Air Package eliminates bottled nitrogen gas and saves FT-IR Spectrometer user $7,000 per year

Other than replacing a small filter cartridge, no maintenance has been required on the system. "Every now and then we walk by and hear it running so we know it's working. We don't pay a great deal of attention to it. It's been sitting there running 24 hours a day, seven days a week ever since we put power to it".

There are other tests that Lubricon performs that also call for clean, dry air for which they now purchase bottled compressed air. Future plans call for running another supply line from the Balston Clean Air package to eliminate having to purchase the bottled air which will further reduce the payback period for the Balston Clean Air Package.

"The Balston Clean Air Package is paying for itself and has eliminated the hassle of changing tanks every two days. It's been working just like it was presented to us".

Discover
FT-IR 800

The new Nicolet System 800 shapes the future of FT-Spectroscopy

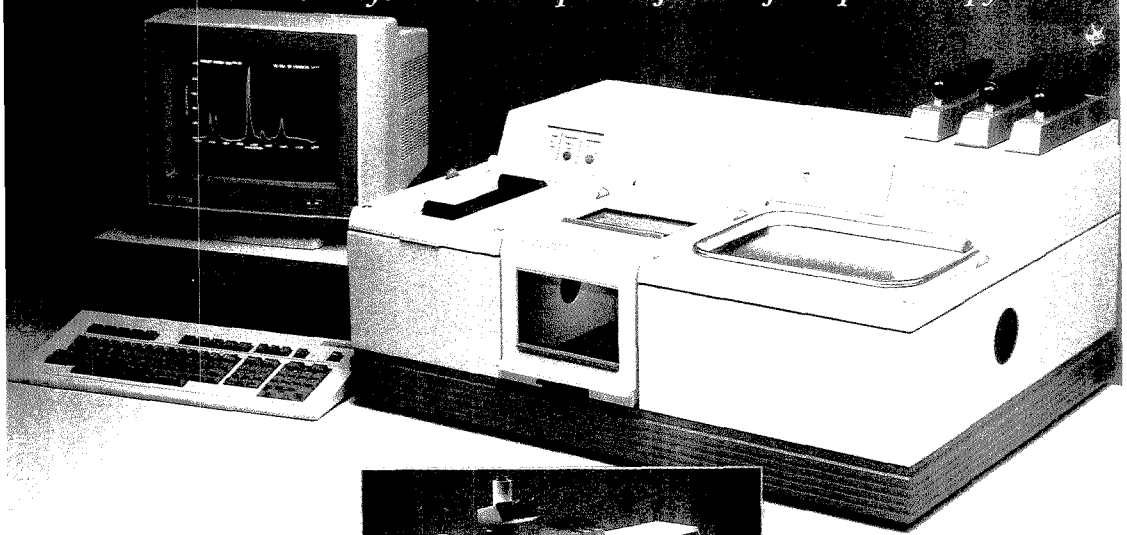

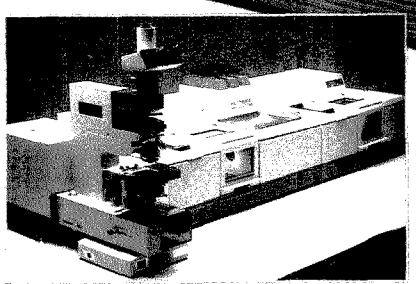

The System 800 represents the new generation in research tools. It is the synthesis of advances in optical, electronic and mechanical design. The System 800 combines an ultra-stable interferometer design with a unique dynamic alignment system, for superior data throughout the spectral range.

The System 800 provides the stability, signal-to-noise performance, and repeatability required for demanding applications. Whether your experiments involve long-term data acquisitions or rapid short-term dynamic spectroscopy applications, the 800 has the capabilities to solve your problems with confidence.

The System 800 incorporates the features demanded by leading research investigators throughout the world. Standard features include optical bench communications, optical bench configuration monitoring and status, rapid spectral range conversion, ultra-quiet electronics train, highest throughput optical design, dynamic alignment, fully expandable optical path, ultra high-output sources, and simplified experimental design for multiple modulation techniques.

The System 800 supports the full range of experiments including FT-Raman, Emission, Microspectroscopy, GC/FT-IR, SFC/FT-IR, and more. Multiple beam paths allow several different experiments or applications to be configured simultaneously.

Nicolet sets the standard for research performance. Let us show you the future of FT-Spectroscopy.

Nicolet

INSTRUMENTS OF DISCOVERY

Belgium: 02-762-2511	France: 1-30-81-3081	Japan: 06-863-1550	Switzerland: 056-834545
Canada: 416-625-8302	Germany: 069-837001	Netherlands: 03403-74754	United Kingdom: 0926-494111

Nicolet Analytical Instruments / 5225-1 Verona Rd. / Madison, WI 53711 / (608) 271-3333 / FAX: (608) 273-5046

To complement these direct Nicolet offices, Nicolet maintains a network of representatives in countries throughout the world.

CIRCLE 110 ON READER SERVICE CARD

EDITORIAL

25th Anniversary of a Classic Paper

This past month marked the 25th anniversary of the publication in ANALYTICAL CHEMISTRY of Abraham Savitzky and Marcel Golay's classic paper describing a smoothing algorithm that permits reduction of random noise from measured spectra (*Anal. Chem.* **1964**, *36*, 1627–39). In this issue's FOCUS article Abraham Savitzky provides the historic background for the writing of this important paper, which ushered in the use of data-processing and digital computer techniques that have had a profound effect on analytical chemistry. This collaboration between a chemist and an electrical engineer provided procedures that for the first time could be understood and used by mathematically unsophisticated chemists. The field has grown dramatically since this landmark paper was published, and today's chemometrics plays a vital role in most aspects of analytical chemistry.

The Savitzky–Golay algorithm, in all its simplicity, is sometimes overlooked in today's world of gigaflop machines and data-processing techniques that border on artificial intelligence. Perhaps we should all reexamine our data-massaging algorithms. Those that bludgeon our data into submission can often be replaced by shorter and faster ones. The simpler procedures, although usually considered less sophisticated, can provide information closer to the spirit of the raw data. We might then put all that computing power to better use in other applications.

As this FOCUS article was being prepared, we learned of the sudden death on April 27 of Marcel Golay shortly before his 87th birthday. The memorial to Dr. Golay in this issue describes his many important contributions to a broad scope of scientific areas. His landmark contributions to chromatography, spectroscopy, data processing, and image analysis have had a tremendous impact on the field of analytical chemistry. Few scientists can claim such a fruitful career, and he will be sorely missed.

G. H. Morrison

SOLUTIONS *Number I*

An Update on the State of the Art in Separations Technology

nhancements to Series 4500i Chromatographs provide more problem-solving power.

The chromatographer's problem-solving power for inorganic and organic ions and transition metals has just received a significant boost. Many compounds which were difficult to separate and detect by traditional approaches have become easier to analyze thanks to recent enhancements made to the Series 4500i Chromatographs.

The 4500i Gradient Pump and Chromatography Module now have *solvent-compatible PEEK tubing and ferrule fittings.* These allow you to use the most common chromatographic solvents for more versatility, in addition to assuring that no corrosion or metal contamination will occur with the metal-free 4500i systems.

The Series 4500i also features an all new *Spectral Array Detector,* which offers several benefits unavailable from photodiode array detectors.

This multi-wavelength UV/Vis detector is capable of monitoring 32 different wavelengths and gathers data at 96 points/sec. for excellent spectral resolution. Multiple-wavelength chromatograms can be displayed in 3-D format for rapid and accurate determination of peak purity and identity.

The new Spectral Array Detector's sensitivity and freedom from refractive index effects are equal to those of the best variable wavelength detectors.

The enhanced Series 4500i Chromatographs also adds new power to chemically suppressed conductivity detection. Now you can use both salts and solvent gradients in conjunction with MicroMembrane Suppressors to separate and detect an even broader range of inorganic and organic ions.

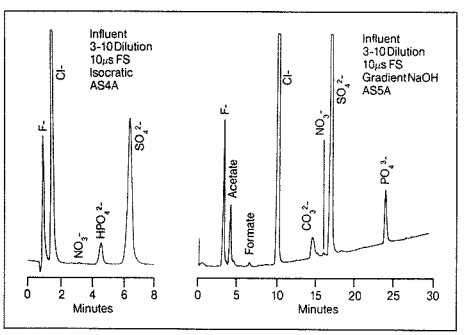

Sunnyvale Municipal Waste

nique OmniPac™ columns — a major advance over bonded silica.

Two Dimensional Chromatography with a Single Column

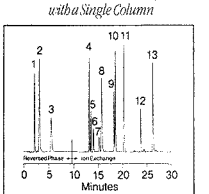

Column: OmniPac PAX-500
Peaks:
1. Benzylalcohol, 2. Diethyltoluamide, 3. Benzene, 4. Benzoic Acid, 5. Benzenesulfonic Acid, 6. Toluenesulfonic Acid, 7. p-Chlorobenzenesulfonic Acid, 8. p-Bromobenzoic Acid, 9. Phthalic Acid, 10. Terephthalic Acid, 11. p-Hydroxybenzenesulfonic Acid, 12. 1,3,5 Benzenetricarboxylic Acid, 13. 1,2,4,5 Benzenetetracarboxylic Acid

These remarkable polymeric, multi-dimensional columns combine 3 separation modes — ion exchange, ion pairing, and reversed phase. 100% solvent-and buffer-compatible, the OmniPac columns can work small miracles, such as

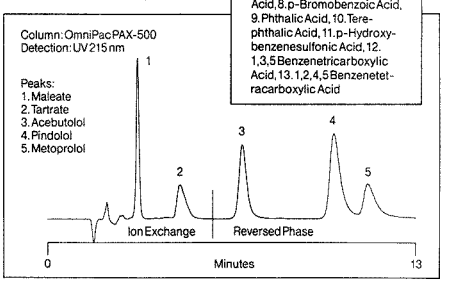

Carboxylic Acids and Adrenergic Drugs with One Column

combining sample preparation and analysis in one column, or separating ionic and non-ionic compounds in the same chromatogram.

The columns utilize solvents, pH, and ionic strength to affect selectivity or to elute both organics and inorganics in the same sample. Hydroxide eluants are used for increased sensitivity with chemically suppressed conductivity detection.

OmniPac columns have a pH stability of 0–14, allowing use of the full range of pH and ionic strength to optimize selectivity.

Add OmniPac columns to your array of separation tools to perform a full range of separations on a single column, with more resolution and maximum control of selectivity.

or complete information or to discuss your application, contact your local Dionex representative or (in U.S.A.) call 1-800-227-1817, ext. 42.

DIONEX
A BETTER SOLUTION

Nondestructive Coal Analysis

Using a new-generation electron spin resonance (ESR) spectrometer designed to improve analysis of biological and materials specimens, researchers at the University of Illinois at Urbana–Champaign have been able to identify, nondestructively, sulfur compounds inside coal. Whereas other, harsher procedures cause decomposition, generating many sulfur compounds in the process, ESR, according to Robert Clarkson of the Illinois ESR Research Center (IERC), finds only a few distinct species. This unexpected result has also been obtained recently by other researchers performing density gradient separations of sulfur compounds in coal.

The key to the Illinois observations is their new W-band spectrometer designed for microwave frequencies around 100 GHz. Compared with standard ESR spectrometers that operate at 9 GHz, or X-band frequencies, the W-band instrument offers significantly improved resolution. For instance, ESR of melanins, which show little structure or differentiation at X-band, are structured and clearly differentiated at W-band. Dibenzothiophene radical shows only a single asymmetric X-band ESR signal, but at W-band a low-field peak splits out about 30 G from the central line, revealing the sulfur heteroatom.

Clarkson, along with R. Linn Belford from IERC and the university's Department of Chemistry, has examined a series of model sulfur compounds with W-band ESR. Using peak locations and line shape analyses they can then identify similar species locked in coal samples. Says Clarkson, "My optimism on this technique has gone up 100%."

Clarkson, Belford, and co-workers at IERC are also pursuing differentiation of biological molecules with W-band and next plan to use it to explore catalyst and semiconductor surfaces. They hope to bridge the gap between high-vacuum surface work and "dirty" surfaces under practical reaction conditions.

Center for Automated Systems

In an effort to steer industrial, academic, and government research and development toward automated chemical analysis, the National Institute of Standards and Technology (NIST) has formed the Consortium on Automated Analytical Laboratory Systems (CAALS). An initial informational meeting of the consortium is scheduled for September 28 and 29 at NIST in Gaithersburg, MD.

According to NIST, the purpose of the consortium is to pool resources of various organizations and thereby offer a unified and common development base for the automation of chemical analysis. NIST hopes CAALS will lead to automated systems that are user-friendly, incorporate quality control into the components, and generate standard methods of analysis. Currently the task of integrating and automating different analytical techniques often exceeds the abilities of individual manufacturers or users.

For more information, contact H. M. Kingston, NIST, Inorganic Analytical Research Division, A349 Chemistry Building, Gaithersburg, MD 20899 (301-975-4142).

Going for Magma

This month researchers at Sandia National Laboratories should begin drilling a 6.1-km-deep well into a caldera—the collapsed crater of a volcano—near Mammoth Lakes, CA. Expected to take four years to complete, the project is aimed at investigating the caldera and the magma beneath the surface. For the first time, scientists will drill above an active magma chamber. With temperatures exceeding 600 °C, magma could someday become a clean, alternative energy source.

The $8 million project will require drilling in four stages, and samples will be collected regularly for analysis. The final stage of digging is expected to be completed in 1992.

The drill site is in the Inyo National Forest on a resurgent dome, a large, low, rounded hill that is produced by subsurface magma flow pushing on the caldera. Geophysicists estimate that the roof of the magma chamber lies 6 km below the dome. The actual drilling will not enter the chamber; it will stop when the borehole temperature reaches 500 °C or when a depth of 6.1 km is reached. Following the completion of drilling, Sandia will restore the site to near-original conditions.

For Your Information

For the analysis of fish and other fatty foods, NIST is offering **a standard cod liver oil reference solution** containing six chlorinated pesticides (hexachlorobenzene, α-hexachlorocyclohexane, *trans*-chlordane, *cis*-chlordane, *trans*-nonachlor, and dieldrin), five different PCBs, and vitamin E in the form of α-tocopherol. In addition, the reference material has uncertified concentrations of six dioxin compounds and octachlorodibenzofuran. For more information, contact the Office of Standard Reference Materials, NIST, B311 Chemistry Building, Gaithersburg, MD 20899 (301-975-6776).

To assist scientists investigating combustion or atmospheric chemistry, NIST has filled a personal computer floppy disk with **gas-phase rate constants for approximately 2000 reactions.** A special software option allows users to display all the rate constants determined for an individual reaction as a function of temperature. For more information, contact the Office of Standard Reference Data, NIST, A320 Physics Building, Gaithersburg, MD 20899 (301-975-2208).

The German Society for Clinical Chemistry is seeking applicants for the **Biochemical Analysis prize.** The award, worth DM 50,000, is given for outstanding and novel work in biochemical analysis or biochemical instrumentation. Applicants must submit papers covering one theme that were published or accepted for publication during the period between October 1, 1987, and September 30, 1989. Submissions are due before October 15, 1989, and should be addressed to H. Feldman, Institut für Physiologische Chemie der Universität, Goethestrasse 33, D-8000 München 2, FRG.

HRLC®: The Next Step Ahead

High Resolution Liquid Chromatography (HRLC) advances to a new level of speed, performance, and convenience.

Bio-Rad offers dramatic advances in HRLC with its new series 800 and 500 systems. Every single component of these systems, as well as the associated Windows® software, reflects the latest technology.

New multi-tasking data station
IBM®-based data station with menu-driven Bio-Rad software provides single-point control over system components. All components are controlled by the central computer.

Series 800 data stations generate virtually any gradient profile on two completely independent systems, collecting high-resolution data from up to four detectors and controlling up to 6 high-pressure pumps.

Powerful Windows software
Bio-Rad's new proprietary software supports every aspect of system operation, from control to calibration, to data analysis and storage. Mouse driven software with pull-

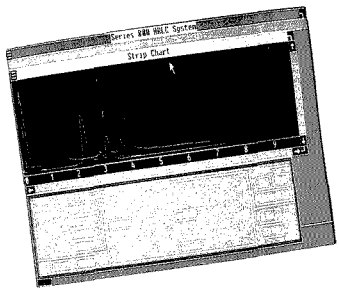

down menus simplifies methods development and provides many options. Together it makes your system function with unsurpassed ease.

Sophisticated data analysis
Display and process data with superimposable video strip charts and microvolt sensitivity.

Full range of color and monochrome graphics available, including a color printer for the series 800 system.

Customized systems
All HRLC systems are 100% upgradable, since all components are free-standing and compatible with the system's central computer. Start with a PC-integrator data analysis system; later you can upgrade to an isocratic, gradient, or multiple system easily and inexpensively.

An exceptionally wide range of options, including titanium construction, choice of 10 ml/min or 40 ml/min flow rates, detectors, pumps, and an unparalleled selection of column chemistries, allow us to tailor an isocratic or gradient system that suits you perfectly. All systems arrive pre-plumbed, pre-tested, and pre-assembled.

No conventional system can offer you as much capability and flexibility as our series 800 and 500 HRLC systems. And these systems are backed by three decades of chromatographic expertise. Let us show you how our systems can satisfy your applications needs.

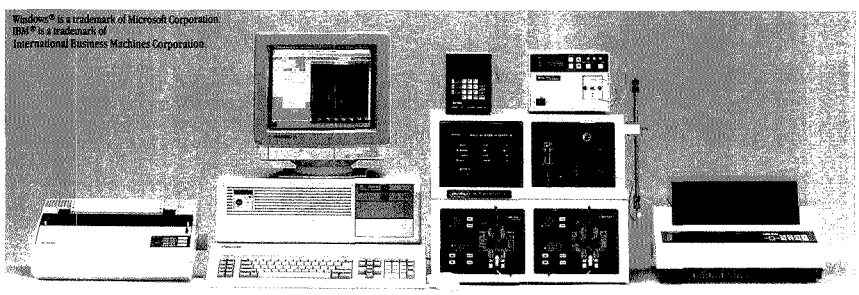

Chemical Division

1414 Harbour Way South
Richmond, CA 94804
(415) 232-7000
800-843-1412

Also in Rockville Centre, NY; Hornsby, Australia; Vienna, Austria; Brussels, Belgium; Mississauga, Canada; Watford, England; Paris, France; Munich, Germany; Hong Kong; Milan, Italy; Tokyo, Japan; Utrecht, The Netherlands; and Glattbrugg, Switzerland.

CIRCLE 16 ON READER SERVICE CARD

SOLID-SURFACE LUMINESCENCE SPECTROMETRY

REPORT

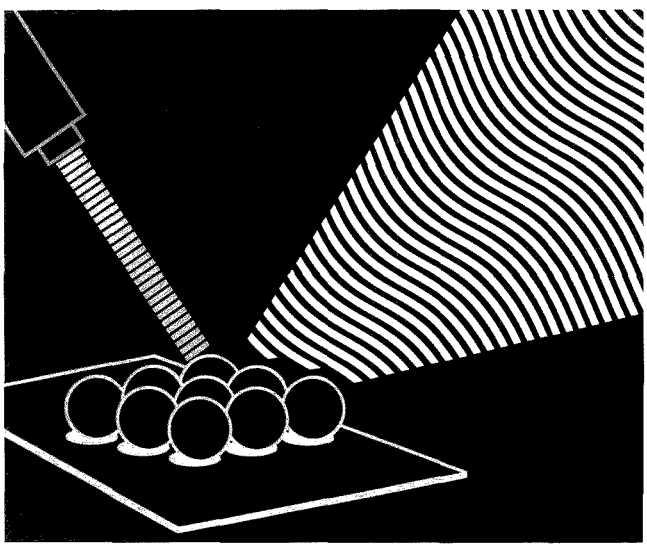

Robert J. Hurtubise
Chemistry Department
University of Wyoming
Laramie, WY 82071

In its broadest meaning, solid-surface luminescence spectrometry includes the theory and methodology involved in luminescence emitted from components adsorbed on or chemically bonded to solid matrices as well as luminescence emitted from solid compounds. The speed, simplicity, sensitivity, selectivity, and moderate cost of solid-surface luminescence make it applicable to many areas of chemical interest from column chromatography to the analysis of pharmaceutical tablets. Because both fluorescence and phosphorescence signals can be obtained at room temperature in many situations, their combined use can yield a substantial amount of luminescence information about a sample, particularly mixtures.

Principles of solid-surface luminescence

Several types of solid-surface luminescence techniques are suitable for a wide variety of applications (Figure 1). The term luminescence refers to both fluorescence and phosphorescence. Fluorescence results when a radiative transition occurs from the lowest vibrational level of the lowest excited singlet state to a singlet ground state of a molecule, whereas phosphorescence occurs when the transition is from the lowest vibrational level of the lowest triplet state to the singlet ground state (*1*). The transition from an excited singlet state to the singlet ground state (fluorescence) is spin-allowed and will thus occur with a high degree of probability. Fluorescence decay times range from approximately 10^{-9} to 10^{-7} s. The radiative transition from an excited triplet state to the singlet ground state (phosphorescence) is spin-forbidden, however, which results in long lifetimes (from approximately 10^{-4} to 10 s) for a triplet electronic state and greatly increases the probability of collisional transfer of energy with other molecules. Because collisional transfer of energy is efficient in solution at room temperature, micelle, sensitized, and solid-surface room-temperature phosphorescence are widely used for chemical analysis (*2*).

Theory, instrumentation, and applications of solid-surface luminescence are discussed in recent monographs (*3*, *4*), and will be covered only briefly here. Several solid materials, including filter paper, silica gel, aluminum oxide, silicone rubber, sodium acetate, potassium bromide, and cellulose, are used in solid-surface luminescence. In general, one of two methods is used to deposit luminescent components on solid surfaces. Syringes or micropipets have been employed that can deliver microliter amounts of solution to a solid surface such as filter paper. In addition, it has been possible to adsorb luminescent components on powders by mixing the powder with a solution of luminescent compounds and then evaporating the solution in which the components are dissolved. Various chemical reac-

0003-2700/89/0361-889A/$01.50/0

tions are carried out to chemically bond a luminescent species to a surface.

One obvious difference between solid-surface and solution luminescence is that in solid-surface luminescence the luminescent molecules are usually attached to small particles or a solid surface such as filter paper or silica gel, whereas in solution luminescence, the luminescent molecules are dissolved in a solvent. In solid-surface luminescence, both the source and luminescence radiation are scattered and diffusely reflected from the surface of the solid matrix. Radiation can also be transmitted through the solid material. Ordinarily the diffusely reflected luminescence is measured.

For adsorbed species, a fraction of the sample of interest penetrates into the solid matrix, and the sample luminescence is excited at the surface and within the solid matrix at a given depth, depending on the properties of the solid matrix. The most important breakthrough in solid-surface luminescence analysis in the past 15 years is the development of solid-surface room-temperature phosphorescence (RTP), which will be discussed later.

Why use solid-surface luminescence?

Solid-surface luminescence analysis is very sensitive and selective for organic trace analysis (*3*, *4*). Nanogram and subnanogram detection limits are easily obtained, and in many cases, picogram levels can be detected. In addition, solid-surface luminescence methodology is simple, inexpensive, and rapid, and it can be used selectively for mixture analysis.

Although solutions are most often used, a solid surface may be the only vehicle that can be employed. Small samples are easily handled by solid-surface luminescence techniques, a capability that can be important when toxic materials or biological samples are used. In solution phosphorimetry, it is usually necessary to cool the sample solution to liquid nitrogen temperature. However, with solid-surface RTP, the analysis can be performed at room temperature, which eliminates the need for cryogenic equipment. In addition, both fluorescence and phosphorescence data (rather than just solution fluorescence data) often can be obtained at room temperature from a sample adsorbed on a solid surface. In some cases, solid-surface luminescence is also more rapid than solution luminescence. It can be automated, used with HPLC, TLC, and paper chromatography, and readily adapted to field and process control work.

Any analytical approach has disadvantages, however, and solid-surface luminescence analysis is no exception. Although depositing a material on a surface is not as easy as dissolving a sample in solution, with a little practice excellent reproducibility can be achieved. Fluorescence and phosphorescence background signals emitted from the solid surface can raise the limits of detection and also adversely affect reproducibility. Moisture and oxygen quenching can be a problem in RTP analysis, but under the appropriate experimental conditions these problems can be minimized. Although the use of powders requires more sample preparation time than does a flat surface such as filter paper, the sensitivity and selectivity obtained with powders often outweigh the additional preparation time.

Solid-surface fluorescence

Some new developments in solid-surface fluorescence are considered in a recent review on solid-surface luminescence analysis (*5*). Many of the current applications center around the analysis of environmental and biological samples. Numerous applications of this type have appeared in the past and should appear in the future because of the simplicity of adsorbing a tiny aliquot (~1 μL or less) of a solution on a solid surface and because of the sensitivity that can be obtained by measuring the fluorescence of the adsorbed compounds.

A relatively simple and very sensitive laser fluorometric system has been described (*6*) with which a detection limit of ~8000 molecules of Rhodamine 6G was obtained. The Rhodamine 6G was adsorbed on silica spheres (10-μm diameter) that were viewed individually with a fluorescence microscope (Figure 2). A CW Ar-ion laser was used as an excitation source, and an optical fiber was used to direct the output of the laser to a quartz slide on which the silica spheres were spread. To obtain a calibration curve, the fluorescence emission was measured for each of 10 individual spheres and an average value and a percent relative standard deviation were calculated. The main advantages of this system are that there is no solvent fluorescence or Raman scattering, and particles are viewed from a stationary position. This fluorometer could be useful for the ultratrace measurements of polycyclic aromatic hydrocarbons on air particulates.

Several types of filter papers have been evaluated for use as substrates for solid-surface room-temperature fluorescence and photochemical fluores-

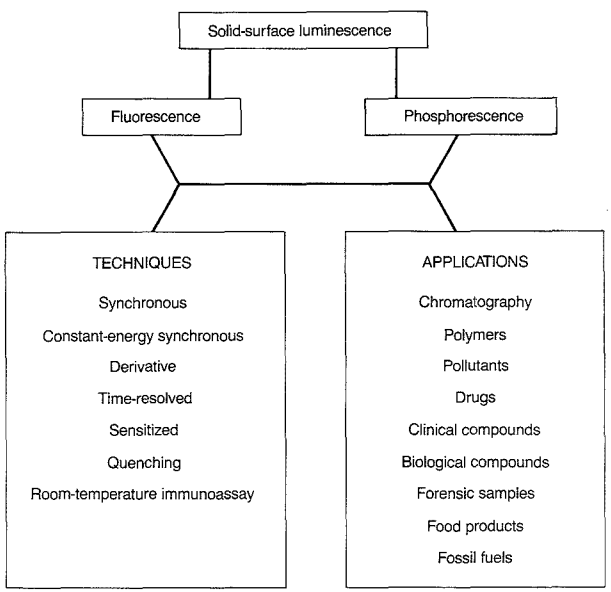

Figure 1. Solid-surface luminescence techniques and applications.

cence (7). Analyte fluorescence signals were two to four times higher on filter paper than on silica gel TLC plates, and absolute detection limits of between 0.6 and 40 ng were obtained by using Whatman filter papers. Based on these results, filter paper was determined to be a convenient, inexpensive, and easy-to-handle substrate for room-temperature fluorescence and photochemical fluorescence measurements.

An in situ fluorescence detection approach has been developed for polycyclic aromatic hydrocarbons preconcentrated on C_{18} chromatographic silica (8). Pyrene was employed as a model compound, and the analyte was preconcentrated from a methanol–water solution onto the C_{18} silica after appropriate adjustment of the solution composition. With an arc-lamp fluorometer the detection limit for pyrene was 15 pg/mL, whereas with a laser fluorometer, the detection limit dropped to 0.17 pg/mL. The concentration of pyrene sorbed on the surface can be related to the solution concentration by chromatographic retention values obtained from a column packed with the same C_{18} packing.

Bacon and Demas (9) used the oxygen quenching of the luminescence of tris(4,7-diphenyl-1,10-phenanthroline)ruthenium(II) perchlorate immobilized in silicone rubber to develop a method for measuring oxygen concentrations in both solutions and the gas phase. The quenching can be quantitated by either lifetime or intensity quenching measurements, and the degree of quenching of the excited complex is related to the partial pressure of oxygen in contact with the polymer film. Although essentially all small gaseous molecules penetrate the sensor film, only sulfur dioxide and chlorine interfere, and they do not degrade the sensor. This system can be used to analyze oxygen concentrations below 1 torr partial pressure of oxygen, and more sensitive sensors could be fabricated by using less permeable polymers or sensors with shorter excited-state lifetimes.

Several researchers recently employed fluorescence spectrometry to study fluorescent species that are chemically bonded or physically adsorbed to chromatographic stationary phases. Lochmüller et al. (10) studied the fluorescence of pyrene silane molecules chemically bonded to microparticulate silica gel at several surface concentrations. They were interested in determining the proximity and distribution of chemically bound molecules on the native silica gel. The fluorescence of the monomer and the excimer of the chemically bonded pyrene silane would thus have "clusters" of bonded alkyl ligands rather than a uniform distribution, as previously reported.

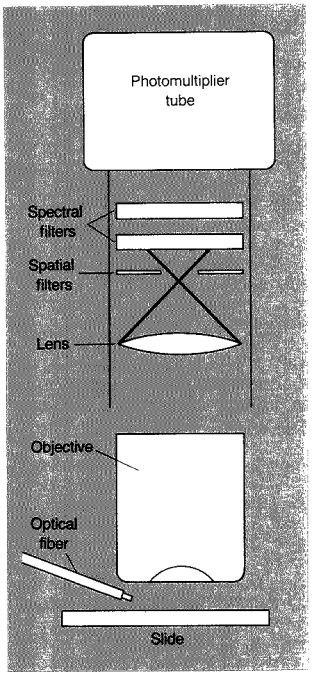

Figure 2. Schematic of the laser-excited microscopic fluorometer.
(Adapted from Reference 6.)

was measured as a function of surface concentration (Table I). As the percent carbon increases, the pyrene excimer-to-monomer ratio increases, which shows that pyrene molecules chemically bonded to microparticulate silica were not evenly distributed but were clustered into regions of high density. A reversed-phase stationary phase

The influence of the mobile phase on the environment and structure of the C_{18} stationary phase was explored by using pyrene fluorescence as a probe (11). The intensity ratios of the vibronic emission bands were used to study changes in the polarity around the pyrene sorbed to the C_{18} surface. In other experiments, the quenching of pyrene fluorescence by potassium iodide was used to correlate changes in polarity to exposure of pyrene to the mobile phase. With high concentrations of methanol, pyrene was partitioned or fully surrounded by alkyl chains, which were most likely well solvated by methanol. At lower methanol concentrations, the onset of quenching by solution-phase ions showed that some fraction of sorbed pyrene was exposed to the surrounding solvent as the stationary-phase volume collapsed.

Solid-surface fluorescence spectrometry has also been used to investigate interactions in normal-phase liquid chromatography (12) by studying the chromatographic interactions of benzo[*h*]quinoline with water-deactivated silica gel. The experimental conditions significantly affected the extent to which benzo[*h*]quinoline would undergo excited-state protonation with silica. Fluorescence data were obtained for benzo[*h*]quinoline as it migrated on water-deactivated silica gel packed into a quartz column. The results showed that some of the water was adsorbed on sites in silica that were incapable of proton donation to benzo[*h*]quinoline in its excited singlet state. By combining the fluorescence data with the chromatographic data, the mass balance was calculated for three benzo[*h*]quinoline species that were responsible for the chromato-

Table I. Monomer and excimer intensities as a function of percent carbon

Pyrene silica sample	Percent carbon	Monomer intensity (max. at 26,600 cm^{-1})	Excimer intensity (max. at 21,100 cm^{-1})	Excimer-to-monomer ratio	Log (excimer-to-monomer ratio)
A	1.1	483	78	0.16	−0.80
B	1.6	564	121	0.21	−0.68
C	2.6	316	459	1.45	0.16
D	4.4	115	505	4.39	0.64
E	5.4	69	536	7.77	0.89
F	8.2	14	653	46.64	1.67

Note. Adapted from Reference 10.

graphic bands (Figure 3). These results provided the first fluorescence data in support of the Snyder displacement model for liquid–solid chromatography (*13*).

Solid-surface phosphorescence

In the six years since ANALYTICAL CHEMISTRY published an INSTRUMENTATION article on phosphorimetry (*2*), considerable progress has been made in developing an understanding of interactions in solid-surface RTP, in obtaining analytical RTP data, and in applying RTP to important analytical areas (*4*, *5*). Fewer developments have occurred recently in instrumentation, however, because much of the instrumental development in solid-surface phosphorescence happened during the late 1970s and early 1980s.

Why does a phosphor give RTP when adsorbed on a particular surface? The answer is not an easy one; factors such as solution chemistry, evaporation of the solvent, drying of the solid surface, and phosphor–solid matrix interactions must be considered.

Schulman and Parker (*14*) were the first to study the effects of moisture, oxygen, and nature of the support–phosphor interactions. Their results showed that hydrogen bonding of the phosphor to the support was an important factor in preventing collisional deactivation of the excited phosphor and that the sample matrix resisted the penetration and quenching efforts of oxygen. Niday and Seybold (*15*) showed that packing filter paper with substances such as salts or sugars inhibited the internal motion of the adsorbed phosphor, and they suggested that the added substances "plugged up" the channels and interstices of the solid matrix and therefore decreased the oxygen and moisture permeability.

McAleese and Dunlap (*16*) proposed a matrix isolation mechanism for solid-surface RTP with filter paper based on the swelling property of cellulose in the presence of strongly polar solvents, such as when ethanol is used to deposit the phosphor on the solid surface. Swelling of filter paper would favor entry of phosphor molecules into the submicroscopic pores in the paper. After the solid matrix is dried, the molecules could become trapped between cellulose chains, providing the necessary rigidity for the adsorbed phosphor.

To pursue the interactions of phosphors with solid surfaces in more depth, a method has been developed for determining fluorescence and phosphorescence quantum yields for compounds adsorbed on a variety of solid surfaces (*17*). By using this method, one can calculate some fundamental luminescence parameters that yield insights into solid-surface RTP interactions. For example, solid-surface fluorescence quantum yield (ϕ_f) and phosphorescence quantum yield (ϕ_p) values along with phosphorescence lifetime (τ_p) values for the anion of *p*-aminobenzoic acid adsorbed on sodium ace-

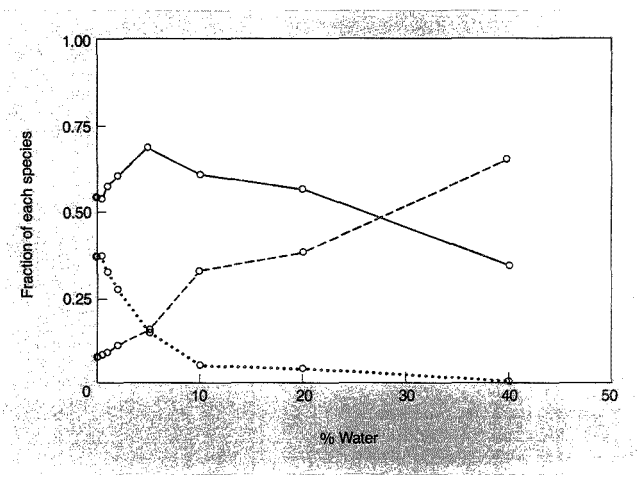

Figure 3. Fractional mass balance of 1-μg samples of benzo[*h*]quinoline migrating on water-deactivated silica gel.

Fraction of neutral benzo[*h*]quinoline in the mobile phase (- - -), fraction of protonated benzo[*h*]quinoline on the stationary phase (—), and fraction of neutral benzo[*h*]quinoline on the stationary phase (. . .). (Adapted from Reference 12.)

MODEL 305
Modular HPLC Pump

The new Gilson Model 305 Master Pump. For analytical or preparative HPLC in the isocratic, binary or ternary modes.

The Pump.

Now you can program gradients without a computer. Upgrade your isocratic system without major expense. Switch from analytical to preparative and back again. Use the special dispense mode for repetitive injection in automatic preparative systems.

The heads.

For micro-analytical up to laboratory preparative scale (0.025 - 200 mL/min). For aqueous or salt-concentrated solutions. In titanium for ion-free work. All completely interchangeable so you can choose the optimum combination for your separation.

This compact new pump (only 32 cm wide) can handle any HPLC application.

To find out more about Gilson's new Master Pump, please contact your nearest Gilson representative.

THE MASTER PUMP

with built-in gradient controller

GILSON

U.S.A. - Box 27, 3000 West Beltline Hwy - Middleton, WI 53562 - Tel. : 608-836-1551
Tlx : 26-5478 - Fax : 608-831-4451 - FRANCE - BP 45 - 95400 Villiers-le-Bel - Tel. : (1) 34 29 50 00
Tlx : 606 682 - Fax : (1) 39 94 51 83

CIRCLE 61 ON READER SERVICE CARD

tate have been obtained from 23 °C to −180 °C (*18*). The phosphorescence quantum yield increased as the temperature was lowered and the rate constant for the radiationless transition from the triplet state increased with increasing temperature, whereas the triplet formation efficiency (ϕ_t) remained constant, leading to the conclusion that a "rigidly held" mechanism was operative. The stronger the interaction between the phosphor and the solid matrix, the higher the phosphorescence quantum yield.

In other work, the anion of *p*-aminobenzoic acid was studied on several sodium acetate–sodium chloride mixtures (*19*). Again, ϕ_f, ϕ_p, and τ_f were obtained for the anion of *p*-aminobenzoic acid. To obtain strong RTP the dried matrix must be packed efficiently and a saturated sodium acetate solution must be used in the sample preparation step.

Mixtures of both α-cyclodextrin and β-cyclodextrin with sodium chloride have also been shown to induce strong RTP from a variety of adsorbed compounds (*20, 21*). By obtaining ϕ_f, ϕ_p, and ϕ_t values, it was possible to construct energy-level diagrams that showed how the absorbed energy was distributed radiatively and nonradiatively (*22*). It was assumed that quenching was minimal; however, even if it did occur, the extent of such quenching would show up in the "nonradiative" part of the diagram.

Figure 4 shows typical diagrams for 4-phenylphenol adsorbed on 80% α-cyclodextrin–NaCl at 23 °C and −180 °C. The percentage of fluorescence, of intersystem crossing from singlet to triplet state, of intersystem crossing from triplet to ground state, and of phosphorescence all increase with lower temperature, and internal conversion decreases to 0% at −180 °C. A sizable amount of the absorbed energy is lost through internal conversion from the singlet state at room temperature. By minimizing internal conversion from the singlet state, it is possible to make more energy available to increase ϕ_f or ϕ_t. If ϕ_t were increased, this could favor an increase in ϕ_p. Such energy diagrams can be useful for adjusting experimental conditions to maximize ϕ_p and for studying interactions in solid-surface RTP.

Filter paper is used extensively in solid-surface RTP. In recent work, temperature variation experiments were performed with the protonated form of benzo[*f*]quinoline adsorbed on filter paper (*23*). Several luminescence parameters were calculated, and a relationship was found between ϕ_p and the modulus (softness or stiffness) of cellulose. The modulus of the filter paper, which is related to the hydrogen bonding network in the paper, is an important factor in obtaining a high ϕ_p for a phosphor adsorbed on filter paper.

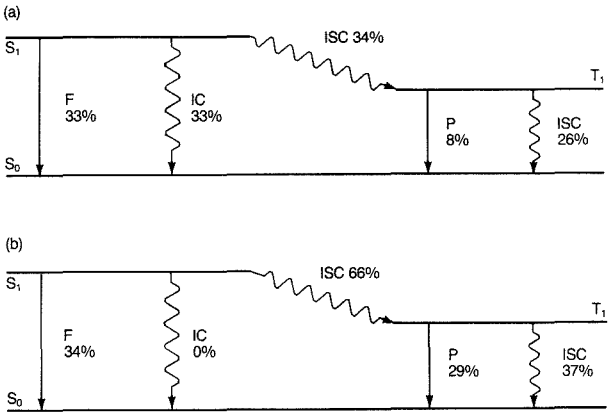

Figure 4. Energy diagrams for 4-phenylphenol adsorbed on α-cyclodextrin–NaCl mixtures.

(a) 80% α-cyclodextrin mixture at 23 °C and (b) 80% α-cyclodextrin mixture at −180 °C. S_0, ground state; S_1, singlet state; T_1, triplet state; F, fluorescence; IC, internal conversion; ISC, intersystem crossing; P, phosphorescence. (Adapted with permission from Reference 22.)

X-ray photoelectron spectroscopy (XPS) has been used to better understand the surface processes in RTP in the presence of a heavy-atom enhancer (*24*). XPS data were obtained before and after the spotting of a luminescent compound or a heavy-atom solution onto the surface of the filter paper. There was no evidence that a strong chemical interaction occurred between the heavy atom and the phosphor, and penetration into the bulk of the paper of both the heavy atoms and luminescent molecules was apparent.

A considerable amount of RTP research involves acquiring analytical data for model compounds in the hope of developing analytical applications. The effects of surfactants on RTP of several polyaromatic hydrocarbons and carbazole have been studied by using filter paper and thallium nitrate as a heavy atom (*25*). When an anionic surfactant was added or when phosphors were spotted from micellar solutions, sensitivity enhancements of 2–9 orders of magnitude were obtained. The RTP signal on filter paper was totally quenched, however, in the presence of a cationic surfactant.

Analysis of multicomponent mixtures using RTP without the need for separation has also been achieved by using mixtures prepared from four or five toxic substance standards (*26*). In other work, Long et al. (*27*) considered the feasibility of surface analysis of homogeneous tablets by RTP using propranolol, *p*-aminobenzoic acid, and acetylsalicylic acid as model compounds. For commercially prepared tablets, RTP can be employed in quality control work but correlation of RTP intensities with a reference method such as high-performance liquid chromatography is necessary.

A personal dosimeter badge based on molecular diffusion and direct detection by RTP of polynuclear aromatic pollutants has been developed (*28*). The dosimeter is a pen-sized device that does not require sample extraction prior to analysis. The paper substrate is simply removed from the badge and the RTP of the adsorbed components measured. The dosimeter badge has been used to detect various polynuclear aromatics (e.g., pyrene, phenanthrene, and quinoline) at the parts-per-billion level after 1 h of exposure.

White and Vo-Dinh (*29*) used RTP to determine potentially carcinogenic compounds that permeate protective clothing. RTP was used to analyze the surface of a filter paper substrate exposed to petroleum products that permeated protective glove samples. The petroleum product passes from a vial through a fine mesh wire screen to the protective clothing, permeates the clothing, and eventually contacts the filter paper disk. RTP spectra were obtained from the material on the filter

paper without the need for any sample extraction, illustrating the simplicity and cost-effectiveness of the RTP technique.

Future developments

The state of analytical theory in solid-surface luminescence requires further development. More complete theoretical equations are needed that describe luminescence reflected or transmitted from solid surfaces as a function of the amount of adsorbed luminescent components. Also, a more complete analytical model is required to describe the interactions between the luminescent compounds and the solid matrix that yield high luminescence.

Generally, commercial and research instruments are effective for obtaining solid-surface luminescence data. However, some instrumental improvements could be made. In some cases, incorrect positioning of the adsorbed sample can cause measurement errors. More extensive use of computers and digital electronics would minimize this source of error. Although laser sources have not yet been used much in solid-surface luminescence work, they have been used in fluorescence line-narrowing experiments with pyrene adsorbed on a TLC plate (*30*) and in obtaining fluorescence line-narrowing information on a polycyclic aromatic hydrocarbon–nucleoside adduct adsorbed on a TLC plate (*31*). Such use of laser sources should continue to increase.

Given the speed, simplicity, sensitivity, selectivity, and moderate cost of solid-surface luminescence, many applications should continue to appear. As advancements are made in theory and instrumentation, solid-surface luminescence should be exploited even more extensively to solve future analytical problems.

References

(1) Birks, J. B. *Photophysics of Aromatic Molecules;* Wiley: New York, 1970.
(2) Hurtubise, R. J. *Anal. Chem.* **1983,** *55,* 669 A.
(3) Hurtubise, R. J. *Solid-Surface Luminescence Analysis;* Dekker: New York, 1981.
(4) Vo-Dinh, T. *Room Temperature Phosphorimetry for Chemical Analysis;* Wiley: New York, 1984.
(5) Hurtubise, R. J. *Molecular Luminescence Spectroscopy: Methods and Applications—Part II;* Schulman, S. J., Ed.; Wiley: New York, 1988; Chapter 1.
(6) Kirsch, B.; Voigtman, E.; Winefordner, J. D. *Anal. Chem.* **1985,** *57,* 2007.
(7) Fidanza, J.; Aaron, J. J. *Talanta* **1986,** *33,* 215.
(8) Carr, J. W.; Harris, J. M. *Anal. Chem.* **1988,** *60,* 698.
(9) Bacon, J. R.; Demas, J. N. *Anal. Chem.* **1987,** *59,* 2780.
(10) Lochmüller, C. H.; Colborn, A. S.; Hunnicutt, M. L.; Harris, J. M. *Anal. Chem.* **1983,** *55,* 1344.
(11) Carr, J. W.; Harris, J. M. *Anal. Chem.* **1987,** *59,* 2546.
(12) Burrell, G. J.; Hurtubise, R. J. *Anal. Chem.* **1988,** *60,* 2178.
(13) Snyder, L. R. *High Performance Liquid Chromatography;* Horvath, C., Ed.; Academic: New York, 1983; Vol. 3.
(14) Schulman, E. M.; Parker, R. T. *J. Phys. Chem.* **1977,** *81,* 1932.
(15) Niday, G. J.; Seybold, P. G. *Anal. Chem.* **1978,** *50,* 1577.
(16) McAleese, D. L.; Dunlap, R. B. *Anal. Chem.* **1984,** *56,* 2244.
(17) Ramasamy, S. M.; Senthilnathan, V. P.; Hurtubise, R. J. *Anal. Chem.* **1986,** *58,* 612.
(18) Ramasamy, S. M.; Hurtubise, R. J. *Anal. Chem.* **1987,** *59,* 432.
(19) Ramasamy, S. M.; Hurtubise, R. J. *Anal. Chem.* **1987,** *59,* 2144.
(20) Bello, J. M.; Hurtubise, R. J. *Anal. Lett.* **1986,** *19,* 775.
(21) Richmond, M. R.; Hurtubise, R. J. *Appl. Spectrosc.,* in press.
(22) Bello, J. M.; Hurtubise, R. J. *Appl. Spectrosc.* **1988,** *42,* 619.
(23) Ramasamy, S. M.; Hurtubise, R. J. *Appl. Spectrosc.* **1989,** *43,* 616.
(24) Andino, M. M.; Kosinski, M. A.; Winefordner, J. D. *Anal. Chem.* **1986,** *58,* 1730.
(25) Ramos, G. R.; Alvarez-Coque, M.C.G.; O'Reilly, A. M.; Khasawneh, I. M.; Winefordner, J. D. *Anal. Chem.* **1988,** *60,* 416.
(26) Asafu-Adjaye, E. B.; Yun, J. I.; Su, S. Y. *Anal. Chem.* **1985,** *57,* 904.
(27) Long, W. J.; Su, S. Y.; Karnes, H. T. *Anal. Chim. Acta* **1988,** *205,* 279.
(28) Vo-Dinh, T. *Environ. Sci. Technol.* **1985,** *19,* 997.
(29) White, D. A.; Vo-Dinh, T. *Appl. Spectrosc.* **1988,** *42,* 285.
(30) Hofstraat, J. W.; Engelsma, M.; Cofino, W. P.; Hoornweg, G. Ph.; Gooijer, C.; Velthorst, N. H. *Anal. Chim. Acta* **1984,** *159,* 359.
(31) Cooper, R. S.; Jankowiak, R.; Hayes, J. M.; Pei-qi, L.; Small, G. J. *Anal. Chem.* **1988,** *60,* 2692.

Robert J. Hurtubise received his Ph.D. in analytical chemistry from Ohio University. After working at Rockhurst College and Pfizer Inc., he accepted a faculty position at the University of Wyoming, where he is professor of chemistry. His research interests include physical and chemical interactions in solid-surface luminescence analysis, the application of solid-surface luminescence to organic trace analysis, solute/mobile-phase and solute/stationary-phase interactions in liquid chromatography, and luminescence properties of polycyclic aromatic hydrocarbon–DNA adducts.

Beckman Sets the P/ACE for Automated Electrophoretic Separations...

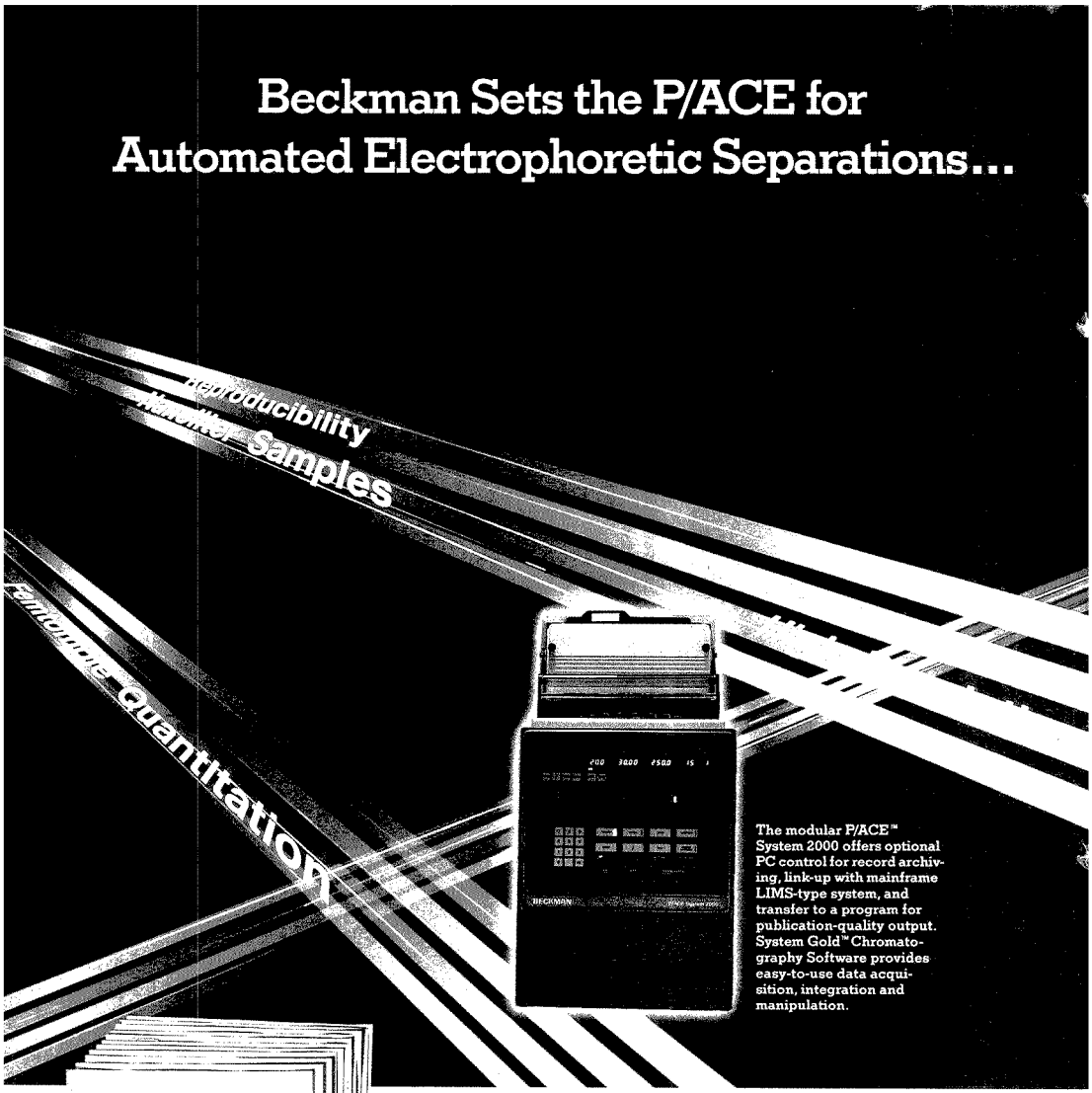

The modular P/ACE™ System 2000 offers optional PC control for record archiving, link-up with mainframe LIMS-type system, and transfer to a program for publication-quality output. System Gold™ Chromatography Software provides easy-to-use data acquisition, integration and manipulation.

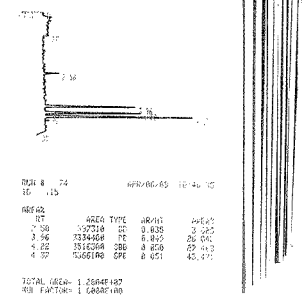

Shows 11 injections in 90 min from a total sample of 5 μL, accomplished with P/ACE™ Migration time CV less than .25%.

The P/ACE™ System 2000 from Beckman is designed for today *and* tomorrow. A modular system, P/ACE leads the evolution of capillary electrophoresis.

A removable detector allows multiple future detection options. Interchangeable cartridges let you change capillaries in minutes. Temperature control provides unmatched reproducibility. And sealed vials minimize sample evaporation. All unique to P/ACE. Unique too—the surprisingly affordable price.

Keep P/ACE with the latest in electrophoretic separation techniques! And achieve rapid success separating proteins, peptides, synthetic oligonucleotides, DNA fragments, and more. Call 800/742-2345, or write to Beckman Instruments, Inc., Spinco Division, Customer Service Department, 1050 Page Mill Rd., Palo Alto, CA 94304. Offices in major cities worldwide.

BECKMAN

A SMITHKLINE BECKMAN COMPANY

CIRCLE 20 ON READER SERVICE CARD

Fast Thermolysis/ FT-IR Spectroscopy

New Dimensions in Combined Thermal Analysis and Spectroscopy

Thomas B. Brill
Department of Chemistry
University of Delaware
Newark, DE 19716

Real-time analysis of dynamically changing chemical or physicochemical processes offers the opportunity to characterize events in a way only hinted at by static analysis. Of course, many dynamic analytical techniques exist, but few allow scientists to probe the neat reacting condensed phase in situ and in near-real-time at high heating rates. The high heating rate condition is relevant for fundamental research in combustion- and explosion-like environments, but it also provides a means (by thermolysis or pyrolysis) to analyze materials routinely by studying the gas products liberated.

Fast pyrolysis/FT-IR spectroscopy using filament heating was first described in 1976 by Liebman et al. (*1*). However, combining a thermal analysis technique with FT-IR spectroscopy generally implies TG (thermogravimetry)/FT-IR. (See Reference 2 for a review of modern thermogravimetry.) With TG/FT-IR, the mass change of the sample is monitored as a function of temperature while the evolved gases are channeled into an IR spectrometer beam (*3*). The relatively slow heating rate of TG (~20 °C/min) enhances thermal equilibration and facilitates quantifying the data. By imposing a faster heating rate (~170 °C/s), however, one gains a new dimension in combined thermal analysis and spectroscopy. Temperature and mass changes as well as IR active gases can still be measured, but they are measured as a function of time during the rapid heating phase. An advantage of the real-time/fast heating approach is the detection of some relatively reactive molecules that are lost to side reactions at slower heating rates or with time delays in the detection step. Thus reaction schemes different from those occurring with slow heating can be studied by fast heating. The technique becomes even more powerful because temperature and mass changes can be measured simultaneously.

The broad area described here is fast thermolysis/FT-IR spectroscopy (*4*). Variations on this basic theme include temperature profiling/FT-IR spectroscopy (*5*), in which the temperature changes of the condensed phase are measured simultaneously with the gas evolution; fast-heat-and-hold/FT-IR spectroscopy (*6*), in which isothermal decomposition is studied following rapid heating to a selected temperature; and SMATCH/FT-IR (*7*), in which *S*imultaneous *MA*ss and *T*emperature *CH*ange measurements are made along with the IR detection of the evolved gases at a high heating rate. The examples here come from the rocket propellant and explosives field, but the methods are applicable to any material that can be thermally decomposed.

Near real-time FT-IR spectra of gases from fast-heated compounds

When studying combustion and explosion phenomena, one needs to obtain thermal decomposition measurements at relevant heating rates and pressures. This information can be derived by using a fast-thermolysis cell (*4–5*, *8–9*), shown in Figure 1. The antireflection-coated 0.5″ × 1″ diameter ZnSe windows are held in a 3″ diameter aluminum cylinder by brass end caps. The cell was designed to withstand a static pressure of 5000 psi but is used only in the 1–1000-psi range. The filament is a creased nichrome IV ribbon (2.5 × 0.6 × 0.012 cm) supported on pressure-tight feedthrough insulators.

Although studies were not conducted on a variety of compounds, a detailed study of a sample of a liquid gun propellant expected to be especially sensitive to catalysis revealed little dependence of the thermolysis products on the filament material (*10*). Typically, 1–2 mg of sample (solid, liquid, or mixture) were heated using a Foxboro

0003-2700/89/0361-897A/$01.50/0

40 Pyrochem controller. The constant voltage–variable current aspect of the controller is useful for the temperature-profiling experiments discussed below. In principle, any reasonable heating rate of the sample could be achieved, but a rate < 400 °C/s was chosen because the spectral collection rate does not distinguish processes at higher heating rates. True combustion heating rates are thousands of degrees per second; thus, the heating rates of fast thermolysis/FT-IR fall between those of conventional thermal analysis and combustion. The argon gas pressure in the cell was adjusted as desired in the 1–1000 psi range.

Because of the importance of collecting IR spectra at high temporal resolution, the rapid-scan mode of a Nicolet 60SX FT-IR spectrometer was used in all of these studies. Typically, the instrument was operated at a rate of 10 scans/s, 2 spectra per file, and 4 cm^{-1} resolution. With the beam focused several millimeters above the filament surface, the IR-active gas products from the fast heated sample can be detected in near real time. No significant change in the pressure occurred from the evolved gases because of the small sample size. However, the gas composition can differ somewhat depending on whether the sample is thinly spread or heaped. Small samples that are thinly spread on the filament give more reproducible results.

In the above experiment only a small time delay exists between thermolysis and the detection of the evolved gases because the gases need only diffuse several millimeters from the sample to reach the IR beam. The argon atmosphere is relatively cool, so that the gases are in their ground states based on the P and R rotational branches. Figure 2 illustrates the good quality of the spectra that are obtained for a sample of RDX explosive. When heated at a rate $dT/dt \simeq 170$ °C/s from room temperature, the initial gases from RDX are first detected at about 1.15 s because thermal decomposition occurs at about 200 °C. By using the IR intensities and effective linewidths, the observed absorbances can be converted to the relative percent composition of the IR-active gases (*4*). The moderate temperature and relatively high pressure in the cell preclude the detection of unstable radicals and molecular fragments in the scan time available.

Figure 3 shows relative gas composition versus time profiles for RDX. H_2O, IR-inactive molecules, and any species for which the IR intensities are unknown (i.e., HNCO) are not included. The importance of near real-time analysis of the gas products in fast-ther-

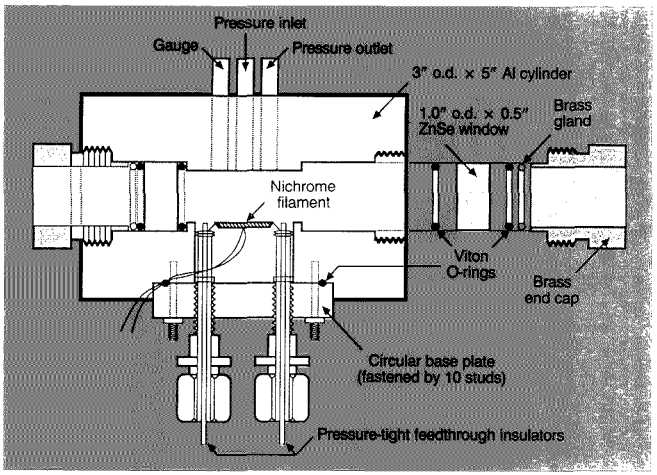

Figure 1. Basic fast thermolysis/FT-IR spectroscopy cell.
The pressure ports and gauge are drawn in abstraction.

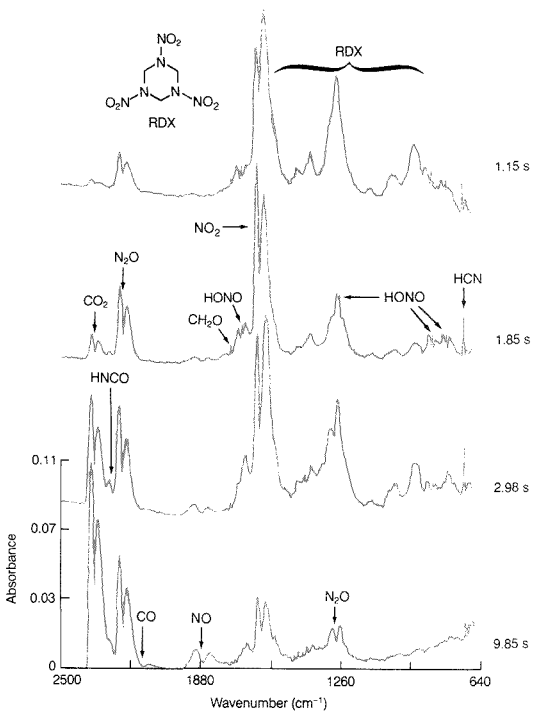

Figure 2. Selected absorption spectra of the gas products, along with a small amount of RDX aerosol, when 2 mg of RDX is heated at 170 °C/s under 15 psi N_2.
The times given are those following the onset of heating. Spectra were recorded at 4 cm^{-1} resolution, 2 spectra per file, and 10 scans/s.

molysis research is evident from Figure 3. NO_2 is the dominant early decomposition product of RDX, but, because of secondary redox reactions, it decreases rapidly in concentration whereas NO increases. Note that NO is negligible at the onset of decomposition. As a result, if the time delay between the analysis and the onset of thermolysis were to exceed 5 s, then different and potentially incorrect conclusions could be drawn about the thermal decomposition process of RDX. The changes in the gas concentrations with time indicate secondary reactions among the gases, whereas the initial gas composition most closely reflects the thermolysis of the parent molecule. Fast-thermolysis/FT-IR data as described here are mostly the result of condensed-phase chemistry.

Studies of the formation of HONO from secondary nitramines, R_2NNO_2 (R = $-CH_2-$) illustrate an advance made possible by fast thermolysis/FT-IR (*11*). HONO has been considered to be an important intermediate in the thermal decomposition of nitramines (*12*), but because of its reactivity, it was

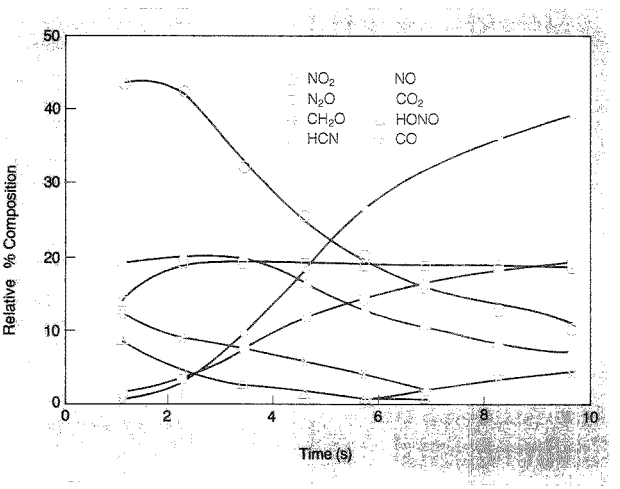

Figure 3. Relative percent composition versus time profile of the quantified gas products from RDX in Figure 2.
Any H_2O, HNCO, IR-inactive products, and RDX aerosol are not included. Note the strong time dependence of several products.

previously proposed from indirect evidence (*13, 14*). By using fast thermolysis/FT-IR, we can readily detect both *cis*- and *trans*-HONO in the IR spectrum of the gas from RDX (see the PQR pair at 700–900 cm^{-1} in Figure 2). However, as shown in Figure 3, HONO is transient under the conditions of the experiment. The initial concentrations most closely reflect the connection of the gas products to the composition of the parent molecule.

Figure 4 shows the quantity of HONO as a percentage of the initial gas products for various nitramines (*11*) versus the H/NO_2 ratio in the parent molecule. The general trend suggests that HONO arises from adventitious bimolecular encounters of $H^{\cdot}$ and $NO_2^{\cdot}$ radicals in the condensed phase (*11*) rather than from concerted decomposition of the 4- and 5-center intermediates (below) that may contribute in unimolecular gas-phase reactions (*15*).

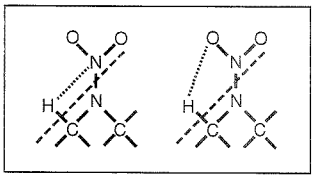

Fast thermolysis/FT-IR thus far also has made key contributions to uncovering relationships between the parent molecular structure and decomposition

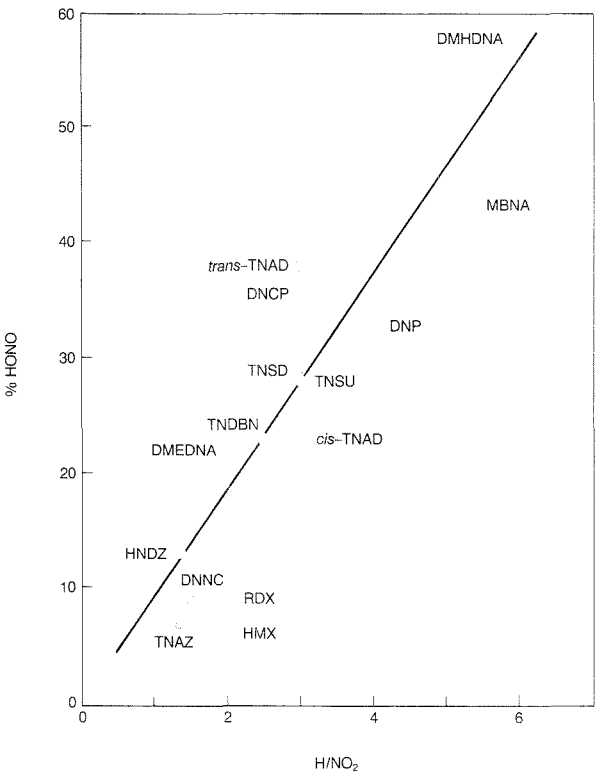

Figure 4. Plot of the initial relative percent concentration of HONO versus the H/NO_2 ratio in the parent molecule for a series of nitramine compounds.

DMHDNA = *N, N'*-dimethyl-*N, N'*-dinitro-1,6-hexanediamine; MBNA = *N*-methyl-*N*-nitro-1-butanamine; *trans*-TNAD = *trans*-decahydro-1,3,5,7-tetranitropyrimido[5.4-*d*]pyrimidine; DNCP = 1,3-dinitroimidazolidine; DNP = *N, N'*-dinitropiperidine; TNSD = 1,3,7,9-tetranitro-1,3,7,9-tetraazaspiro[4.5]decane; TNSU = 2,4,8,10-tetranitro-2,4,8,10-tetraazaspiro[5.5]undecane; TNDBN = 1,3,5,7-tetranitro-3,7-diazabicyclo[3.3.1]nonane; DMEDNA = *N, N'*-dimethyl-*N, N'*-dinitro-1,2-ethanediamine; *cis*-TNAD = *cis*-(±)-decahydro-1,3,5,7-tetranitropyrimido[5.4-*d*]pyrimidine; HNDZ = 1,3,3,5,7,7-hexanitro-1,5-diazacyclooctane; DNNC = 1,3,5,5-tetranitrohexahydropyrimidine; RDX = hexahydro-1,3,5-trinitro-1,3,5-triazine; TNAZ = 1,3,3-trinitroazetidine; HMX = octahydro-1,3,5,7-tetranitro-1,3,5,7-tetrazocine.

GET RICH QUICK.

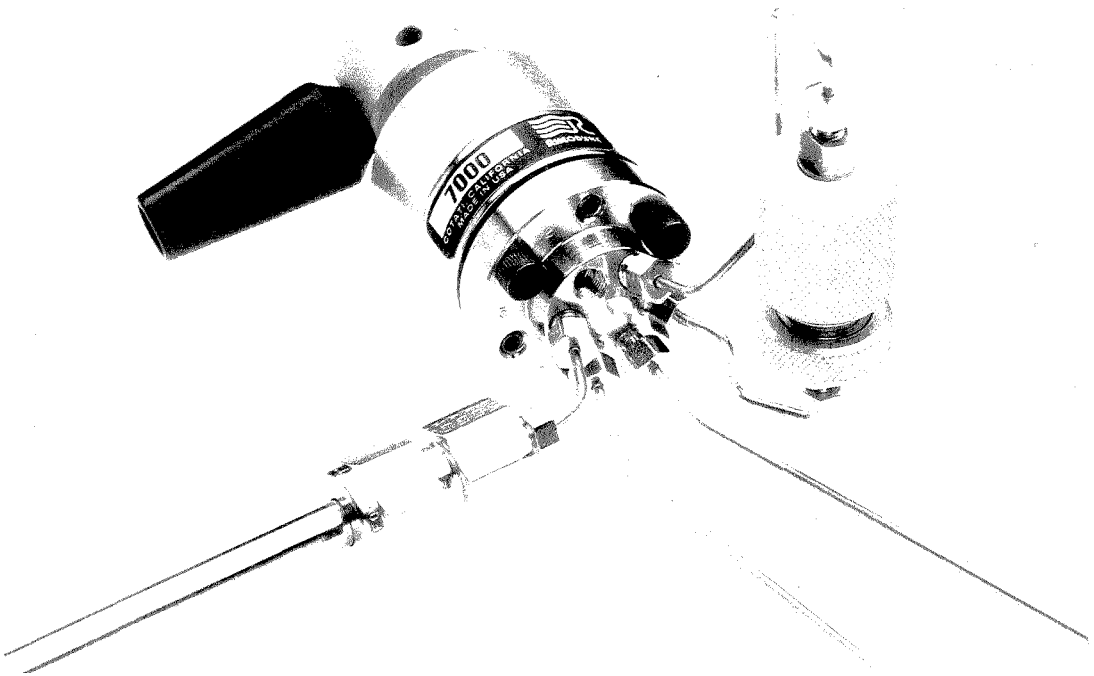

The quick way to enrich trace components in an LC sample is to do it on-line with a Rheodyne column switching valve.

The valve, connected after the injector, lets you concentrate the sample in a pre-column, then elute it onto the analytical column by simply turning the valve handle. You eliminate the task of collecting a batch of enriched sample outside the chromatographic system.

The valve also lets you perform sample cleanup on-line by a similar procedure. You can remove interfering proteins, or polymers, or small molecules present in high concentrations.

Using column switching for enrichment and cleanup is usually faster than batch processing when making repeated analyses. This is especially true when switching is automated under the control of the chromatograph. Indeed, many chromatographs and autosamplers offer automated column switching as an option, using Rheodyne valves for the purpose.

For more information phone your Rheodyne dealer. Or contact Rheodyne, Inc., P.O. Box 996, Cotati, California 94931, U.S.A. Phone (707) 664-9050.

RHEODYNE

CIRCLE 140 ON READER SERVICE CARD

gases such as HONO, NO_2 (*16*), CH_2O (*17, 18*), and NO (*11*). These gases are important in determining the ignition and flame chemistry as well as the hazards of the parent compounds at elevated temperature.

Temperature profiling/FT-IR spectroscopy

In the fast-thermolysis/FT-IR method discussed above, the final temperature and heating rate of the filament were established by spot-welding a type J thermocouple to the filament and recording its output on a digital oscilloscope. Subsequently it was found that by positioning a type E thermocouple on the underside of the filament opposite the sample and leaving it in place during the thermolysis experiment, the endothermic and exothermic events of the condensed phase were tracked simultaneously with the detection of the gas products. This led to the temperature profiling/FT-IR technique (*5*). Development of this technique was straightforward because the heating of the filament is under constant voltage–variable current control.

Figure 5 shows a block diagram of the circuit used for this temperature-profiling experiment. The 60-Hz noise on the filament was removed by a low-pass filter, and the signal was amplified by about 100× with a differential amplifier. The analog output was processed through a Metrabyte DAS-16 A/D converter to an IBM-PC. The "take data" cycle of the interferometer triggered the heater so that there is a direct correlation between the time, temperature, and interferogram. Four hundred data points were collected in the 10-s temperature measurement.

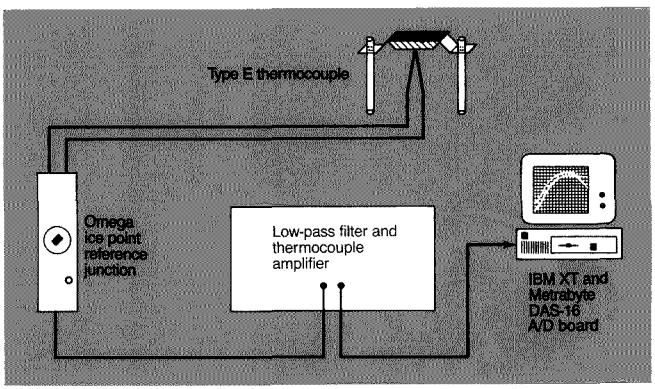

Figure 5. Block diagram of the circuit used for real-time filament temperature measurements in temperature profiling/FT-IR spectroscopy.

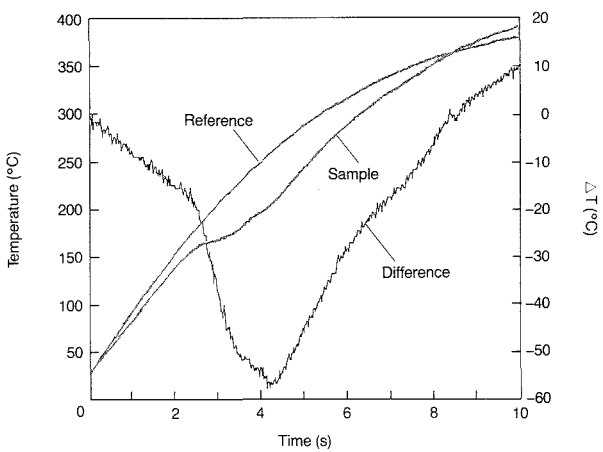

Figure 6. Filament temperature trace without sample (reference), the filament trace with 2 mg of ethylenediammonium dinitrate (EDD) spread on it (sample), and the difference thermal trace (sample trace minus reference trace).
The initial heating rate is about 70 °C/s, and the atmosphere is 15 psi Ar.

Figure 6 illustrates the type of results now available; the sample under study is ethylenediammonium dinitrate (EDD). A reference thermal trace (filament with no sample present) and a sample thermal trace (filament with 2 mg of EDD thinly spread on the center portion) are shown superimposed on the difference trace (sample trace minus reference trace). Most of the endotherms and exotherms are evident in the sample thermal trace, but the difference trace clearly shows an endotherm preceding an exotherm in the 300–330 °C range.

The temperature signature in Figure 6 will be explained below for EDD, but first let us consider several sources of endotherms and exotherms in the fast heating conditions used. Melting, sublimation or evaporation, evolution of decomposition gases, and endothermic chemical reactions in the condensed phase are common origins of endotherms. Exothermic chemistry in the condensed phase and filament "catch up" are sources of exotherms. Exothermic gas-phase chemistry makes a negligible contribution to the filament temperature in this experiment. Filament catch up results from the fact that the portion of the filament in contact with the sample and thermocouple can have a lower temperature than regions away from the sample. This is because the sample may leave the filament by endothermic decomposition off-gassing, evaporation, or sublimation. Toward the end of this process heat can flow rapidly from the hotter regions of the filament toward the cooler thermocouple area, resulting in a rapid temperature rise. Therefore, an apparent exotherm is sensed that may not be connected to an exothermic chemical event in the sample.

A true sample exotherm is a temperature rise that drives the sample thermal trace *above* that of the reference trace. An apparent exotherm that leaves the filament temperature below the reference trace may or may not be attributable to exothermic chemistry. In this case, a chemical event cannot be readily distinguished from catch up by

PHILIPS

PHILIPS

3,000 PARTICLES IN JUST 37 MINUTES!

Routine Particle-analysis at Record-breaking Speed

Philips Analytical

With PHAX-SCAN - Philips' High-speed Automatic X-ray analyser - sophisticated random-particle analyses take minutes... not hours! Whether you're involved in forensics, tribology or environmental monitoring, the benefits are the same: increased efficiency and cost savings, thanks to performance that allows full matrix corrected analysis of 16 elements in less than 0.1 second.

PHAX-SCAN is based upon Philips Series 500 scanning electron microscopes, a range of versatile instruments designed to allow easy functional integration of facilities such as X-ray and image analysers. This facilitates automation of complex procedures, through centralized and fully coordinated computer control of all analytical and data processing functions. To find out more about the remarkable PHAX-SCAN system, or other Philips electron microscopes, contact:

Write to Philips Analytical, Electron Optics Department, Building AAE, 5600 MD Eindhoven, The Netherlands. Or call your local supplier.
Austria (0222)-60101/1794; **Belgium** (02) - 5256273; **Denmark** (01) - 572222; **France** (1) - 49428141; **Germany** (0561) - 501543; **Great Britain** (0223) - 358866; **Italy** (02) - 644912; **Netherlands** (040) - 782773, **Norway** (02) - 6802000; **Spain** (01) - 4042206; **Sweden** (08) - 7821550; **Switzerland** (01) - 4882211; **U.S.A.** (201) - 5293800.

To find out more, contact us today.

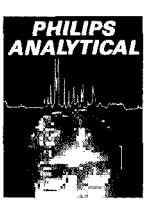

BIGGER IDEAS FOR BETTER ANALYSIS

1. *Single keystroke start*

2. *Automatic division of analysis field*

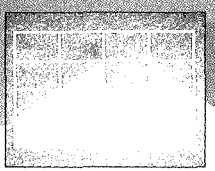

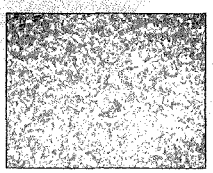

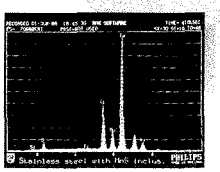

3. *Detection of valid particles*

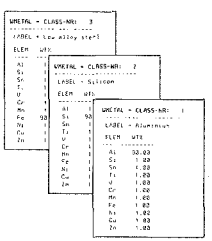

5. *X-ray analysis of each particle*

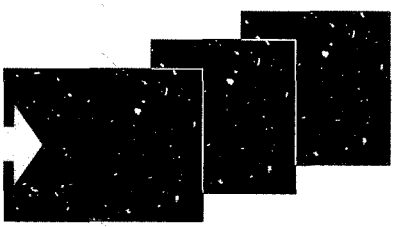

4. *Conversion of image to a binary map*

6. *Sorted results for 3,000 particles*

CLASS	NR	AREA	OOF	CLASS-LABELS:
1	64	3224	3062	Aluminium
2	612	8577	8185	Silicon
3	735	10898	10276	Low alloy steel
4	104	3954	3627	Stainless 1408
5	21	570	500	Stainless 1018
6	169	6812	6224	Stainless 1823
7	38	898	799	Aust.stainless 2647
8	123	12521	11873	Brass
9	510	18714	17531	Bronze
10	46	840	761	High tin bronze
11	3	33	28	High Chromium
12	130	8389	7566	Nickel based alloy

TOTAL DETECTED = 3072 REJECTED = 1243 ACC. 1555

TOTAL DETECTED AREA% = .62 TYPICAL PART. SIZE = 9.85 /U
AVERAGE PARTICLE AREA% = .56 AVER.PARTICLE SIZE = 3.48 /U

7. *On-line calculation of class averages and statistics*

8. *Full information on any particle*

9. *Results saved by Data Logger*

10. *Output of analysis results*

t=37 min.

a single thermocouple measurement. Detailed quantitation of the thermal trace, as is done in differential scanning calorimetry and differential thermal analysis measurements, is difficult because of the complexity of the heat transfer phenomena at these high heating rates. Nevertheless, much qualitative information is produced, and we are attempting to move toward more quantitation.

Returning to the description of the thermal decomposition of EDD, we see that Figure 7 shows the quantified gas products from EDD superimposed on the difference thermal trace (*19*). This permits chemical and physical events to be attached to the temperature deflections. The initially negative slope of the thermal trace results from the additional heat capacity of the filament with the sample present. The melting endotherm occurs at about 175–180 °C. At about 200 °C, melting is complete (not isothermal because of the rapid heating rate) and the liquid phase continues to heat to about 275 °C without evidence of decomposition off-gassing. At 275 °C, the first gas products are detected. These are HNO_3(g) formed by proton transfer and desorption, and a small quantity of NO_2(g), probably from thermal decomposition of HNO_3. NH_3(g) then appears, perhaps from C–N bond heterolysis.

The lag in the thermal trace shows that this stage of decomposition is, as expected, overall endothermic. However, above 330 °C, CO_2 from backbone oxidation and the more reduced nitrogen oxide products, NO and N_2O, can be detected. These products are created by exothermic reactions in the condensed phase, as evidenced by the increased heating rate of the filament. Thus the combination of real-time temperature record and near real-time observation of the gas products helps map the overall reaction sequence during the fast thermal decomposition of a complex material.

Pressure as a variable

Apart from its practical value for suppressing sublimation and evaporation of the sample when needed, pressure is a useful research variable. Because the initial pressure in the cell can be set as desired, we have found that performing thermolysis with the initial pressure as the major variable gives additional insight (*20*). Pressure differences affect gas diffusion rates; that is, the decomposition gases are forced to remain in contact with the condensed phase for different lengths of time. At lower pressure the most reactive gases (NO_2, HONO) usually are detected in high relative concentrations because they are able to diffuse away from the reaction zone. When the applied pressure is increased, these gases remain in the reaction zone longer and react to the extent that products having intermediate stability dominate (NO, HCN). At the highest pressures studied, the most

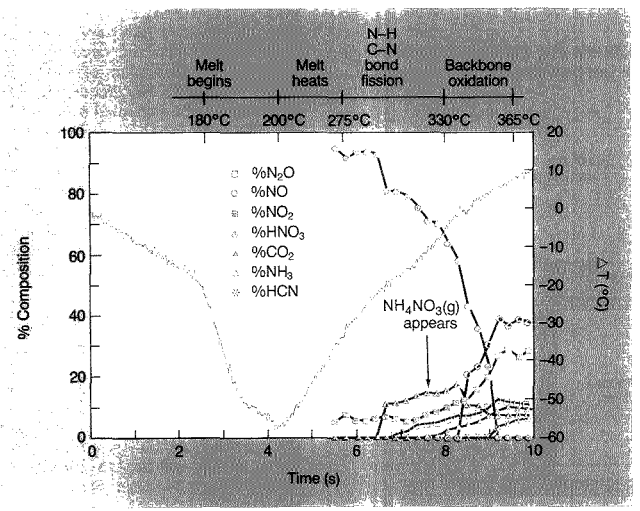

Figure 7. Difference thermal trace superimposed on the quantified gas products from EDD.

H_2O, NH_4NO_3 aerosol, and any IR-inactive gases are excluded.

thermally stable products dominate (CO,CO_2 and, undoubtedly, N_2). We do not believe that a change in the decomposition mechanism is implied by these results, but simply that the order of reactivity of the nitrogen compounds (NO_2>NO>N_2) and carbon compounds (CH_2O>CO,CO_2) in this environment is reflected in the length of time the gases remain in the reaction zone.

The thermal trace can also display pressure dependence. If the position of the exotherm is insensitive to pressure, it suggests that the exotherm is driven by condensed-phase reactions with little participation of the gas phase (*21*). Conversely, a significant temperature shift of the exotherm with pressure, as occurs with nitrate salts (*19*), implies that heterogeneous gas-phase–condensed-phase chemistry is important.

Isothermal decomposition studies following rapid heating

The uniformity and efficiency of heat transfer to the sample is enhanced and the complication of filament catch up is reduced by employing a much smaller filament (5.0 × 1.2 × 0.02 mm), smaller sample mass (200–300 μg), and a higher percent coverage of the filament by the sample (*6*). The center one-third of the filament was covered by a thin layer of sample about 0.2 mm thick. Upon melting, the sample layer becomes much thinner, which further enhances the efficiency of heat flow. The smaller filament is also more responsive to the heater circuit. This modification permits rapid heating to a specified temperature and then holding at that temperature. As before, the IR spectrum of the gas phase is monitored simultaneously with the temperature of the condensed phase.

The experiments were termed fast-heat-and-hold/FT-IR and can be used to simulate time-to-explosion tests of explosives (*6*). Hence, fast thermolysis/FT-IR can be used to investigate the explosion hazard of materials directly. Engineering tests, such as that described by Henkin (*22*) and the one-dimensional time to explosion (*23*), measure the time to explosion as a function of the sample temperature. A similar measurement, the time to exotherm, is made in the fast-heat-and-hold experiment (*6*) for the explosive HMX (Figure 8). An apparent activation energy can be calculated from these data.

In addition, the IR spectra of the gas products are obtained simultaneously, making the cell a spectroscopically instrumented thermal explosion test device. For instance, thermal decomposition gases almost always appear in advance of the exotherm, indicating that autocatalysis occurs to achieve the exotherm. For HMX, N_2O and NO_2 are the first detected gases and their appearance precedes the appearance of CH_2O. The formation of N_2O and CH_2O from HMX has frequently been considered to be a coupled process (*24, 25*). The sequence that we observe suggests that their formation is not necessarily coupled. Also, only a small difference exists in the gas-phase concentration profiles for all of the thermal traces in Figure 8, implying that there is no change in the thermal decomposition mechanisms over this range of temperatures.

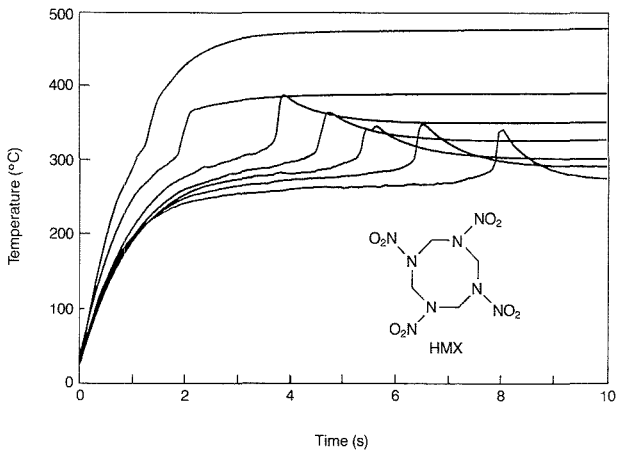

Figure 8. Temperature profiles of 200 μg of HMX showing the times to exotherm as a function of the sample temperature using the fast-heat-and-hold filament design.

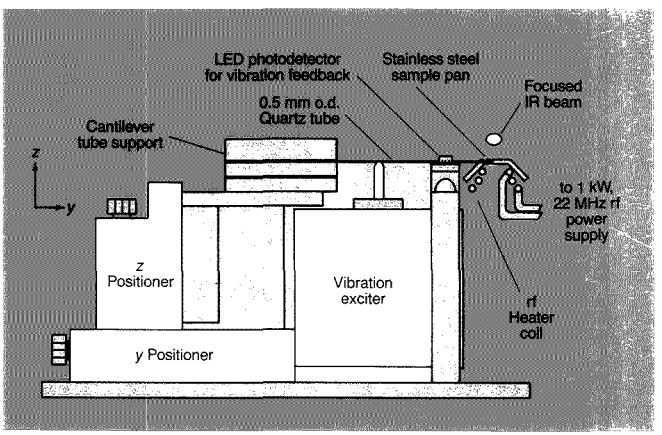

Figure 9. Sketch of the sample holder and cell region for SMATCH/FT-IR spectroscopy.

SMATCH/FT-IR spectroscopy

If more than one decomposition step occurs upon rapid heating, then there is a question about the amount of sample involved in each step. To address this question we recently developed the SMATCH/FT-IR technique, which, as the name implies, permits the mass and temperature change to be measured at high heating rates (*7*).

Figure 9 shows the essential features of the sample holder for SMATCH/FT-IR. The sample is coated onto a

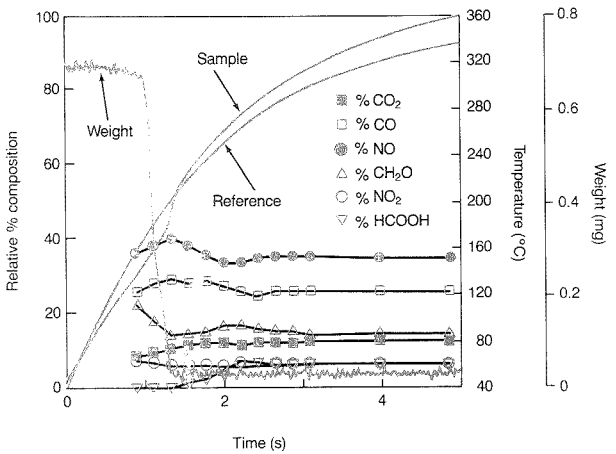

Figure 10. Plot of the simultaneously measured mass change, sample and reference filament temperature change, and evolved gases from nitrocellulose (13.4% N).
These data were measured simultaneously and in real time at the initial heating rate of about 100 °C/s.

stainless steel end tip attached to a quartz capillary tube. The tube is set into 130-Hz motion by the exciter piston. Heating of the metal end tip is effected by a 1-kW rf power source. The measurement of the mass change is based on the change in the vibrational frequency of the capillary tube as measured by the output of a phototransistor that senses the motion. The temperature change is measured by a type E thermocouple attached to the metal end tip. The gas products are evolved into a cell and detected by the IR spectrometer beam focused about 1 cm above the metal end tip. Although this experiment is more complicated than the other fast-thermolysis/FT-IR techniques described above, it gives even more detailed information about the fast-thermolysis process.

Figure 10 shows a result from the first study using SMATCH/FT-IR. It is a composite plot of the mass change, temperature change, and gas products from essentially fully nitrated nitrocellulose (13.4% N).

Conclusions

On the research front, fast-thermolysis/FT-IR spectroscopy gives considerable new mechanistic insight into the physicochemical processes that occur in materials undergoing rapid heating. The pressure and the composition of the atmosphere can be set as desired to gain an additional variable. The conditions of the experiment relate to fire and other combustion situations and explosions. The small sample size permits studies to be performed safely and with limited research materials. The sample can be a mixture, a pure material, a solid, or a liquid.

On the quality control and routine analysis front, the opportunities are excellent because samples can be studied with reasonably rapid turnover. Once established on an authentic sample, the gas product distribution is frequently characteristic and distinguishable among various materials. Because these techniques are applicable to any material that can be thermalized, the outlook for new insight into many important materials and situations is indeed bright.

Doctoral students Richard J. Karpowicz, Yoshio Oyumi, Stephen F. Palopoli, James T. Cronin, Thomas P. Russell, Peter J. Brush, and Jangkang Chen, and postdoctoral student Mark D. Timken took this field from dream to reality. The Air Force Office of Scientific Research (AFOSR-80-0258, AFOSR-85-0353, AFOSR-87-0033), the Army Research Office (DAAG29-84-K-0198), the Air Force Armament Laboratory (F08635-87-C-0130), and Morton-Thiokol, Inc., supported chemistry programs during which most of the methods described here were developed.

References

(1) Liebman, S. A.; Ahlstrom, D. H.; Griffiths, P. R. *Appl. Spectrosc.* **1976**, *30*, 355.
(2) Earnest, C. M. *Anal. Chem.* **1984**, *56*, 1471 A.
(3) Lephardt, J. O. *Appl. Spectrosc. Rev.* **1982**, *18*, 265.
(4) Oyumi, Y.; Brill, T. B. *Combust. Flame* **1985**, *62*, 213.
(5) Cronin, J. T.; Brill, T. B. *Appl. Spectrosc.* **1987**, *41*, 1147.
(6) Brill, T. B.; Brush, P. J. *Proc. Symp. (Int.) Detonation, 9th;* Portland, OR, in press.
(7) Timken, M. D.; Chen, J-K.; Brill, T. B., unpublished results.
(8) Karpowicz, R. J. Ph.D. Dissertation, University of Delaware, 1984.
(9) Cronin, J. T.; Brill, T. B. *Appl. Spectrosc.*, in press.
(10) Cronin, J. T.; Brill, T. B. *Combust. Flame* **1988**, *73*, 81.
(11) Brill, T. B.; Oyumi, Y. *J. Phys. Chem.* **1986**, *90*, 6848.
(12) Melius, C. F. *J. Phys.* **1987**, *48*, C4–341.
(13) Bulusu, S.; Axenrod, T.; Milne, G.W.A. *Org. Mass. Spectrom.* **1970**, *3*, 13.
(14) Farber, M.; Srivastava, R. D. *Chem. Phys. Lett.* **1979**, *64*, 307.
(15) Shaw, R.; Walker, F. E. *J. Phys. Chem.* **1977**, *81*, 2572.
(16) Brill, T. B.; Oyumi, Y. *J. Phys. Chem.* **1986**, *90*, 1970.
(17) Oyumi, Y.; Brill, T. B.; Rheingold, A. L. *J. Phys. Chem.* **1986**, *90*, 2526.
(18) Oyumi, Y.; Brill, T. B. *Prop. Explos. Pytech.* **1988**, *13*, 69.
(19) Russell, T. P.; Brill, T. B. *Combust. Flame* **1989**, *76*, 393.
(20) Oyumi, Y.; Brill, T. B. *Combust. Flame* **1987**, *68*, 209.
(21) Brill, T. B.; Subramanian, R. *Combust. Flame*, in press.
(22) Henkin, H.; McGill, R. *Indust. Eng. Chem.* **1952**, *44*, 1391.
(23) McGuire, R. R.; Tarver, C. M., *Proc. Symp. (Int.) Detonation, 7th;* U.S. Naval Academy: Annapolis, MD; 1981, 56.
(24) Schroeder, M. A. *Chemical Propulsion Information Agency Publication 308*, **1979**, *II*, 17.
(25) Schroeder, M. A. *Chemical Propulsion Information Agency Publication 347*, **1981**, *II*, 395.

Thomas B. Brill is professor of chemistry at the University of Delaware, where he has been a member of the faculty since 1970. He received his B.S. degree from the University of Montana in 1966 and his Ph.D. from the University of Minnesota in 1970. His research interests include the development of IR and Raman spectroscopy methods to investigate chemistry at high heating rates and elevated pressure conditions, structure/property/decomposition relationships, thermal explosions, combustion, supercritical water, the synthesis of energetic materials, and the Arbuzov reaction. He is the 1989 "Spectroscopist-of-the-Year" of the Society for Applied Spectroscopy, Delaware Valley Section.

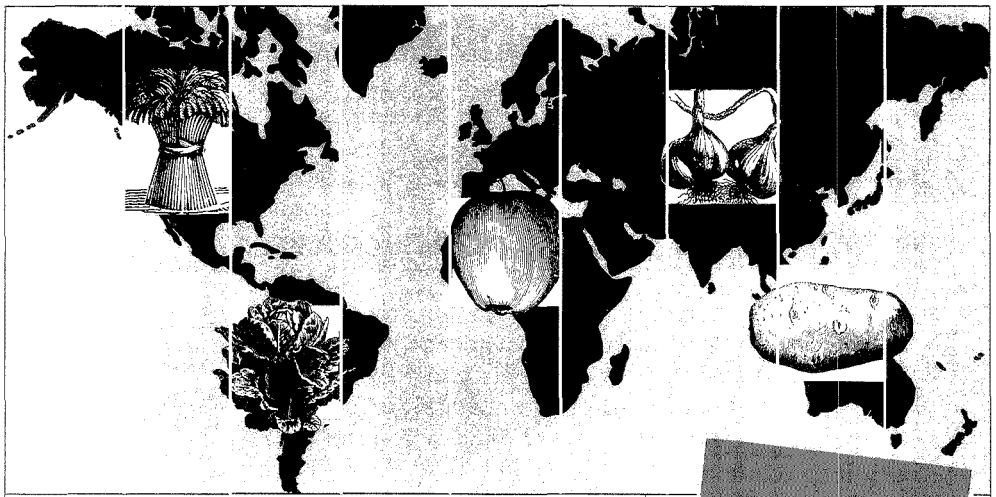

For the Most Current International Research in the Field . . .

Journal of Agricultural and Food Chemistry

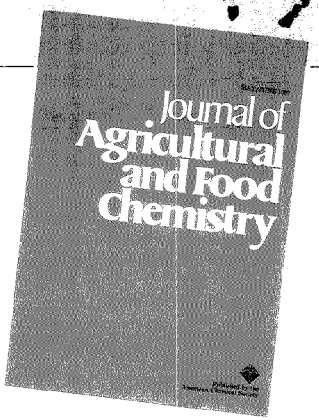

The bimonthly journal in the chemical disciplines targeted toward more efficient and economical production and greater safety of foods, feeds, fibers, and other agricultural products.

Designed to Meet Researchers' Needs . . .

The JOURNAL OF AGRICULTURAL AND FOOD CHEMISTRY keeps you up-to-date with timely, original research. You'll find reports on the chemical, biochemical, and nutritional aspects of foods and feedstuffs. More than 350 articles are published yearly on a broad range of topics such as:

- ☐ Woods
- ☐ Pesticides/Residues
- ☐ Fertilizers
- ☐ Flavor and Aroma
- ☐ Analytical Chemistry
- ☐ Pesticides/Metabolism
- ☐ Pesticides/Field Applications
- ☐ Biotechnology
- ☐ Toxicants
- ☐ Plant Nutrients and Regulators
- ☐ Food and Feed Processing
- ☐ Agricultural Products
- ☐ Compounds Isolated from Food Material
- ☐ And much more!

Subscribe to the JOURNAL OF AGRICULTURAL AND FOOD CHEMISTRY today! Join the thousands of your colleagues worldwide—who already depend on each bimonthly issue for the kind of research they can use in their day-to-day work.

JOURNAL OF AGRICULTURAL AND FOOD CHEMISTRY
Published Bimonthly. One volume per year.
Volume 37 (1989) ISSN 0021-8561

One Year Rate		U.S.	Canada and Mexico	Europe**	All Other Countries**
ACS Members*	1 year	☐ $ 25	☐ $ 33	☐ $ 45	☐ $ 49
Save 10%	2 years	☐ $ 45	☐ $ 61	☐ $ 85	☐ $ 93
Nonmembers		☐ $138	☐ $146	☐ $158	☐ $162

*Personal use only **Air service included. For nonmember rates in Japan, contact Maruzen Co., Ltd.

In a hurry?
Call Toll Free (800) 227-5558
and Charge Your Order! (U.S. Only)
Outside U.S. 202/872-4363
Telex: 440159 ACSP UI
89 2582 ACSPUBS
FAX: 202/872-4615

Or write:
American Chemical Society
Marketing Communications Department
1155 Sixteenth Street, NW
Washington, DC 20036 U.S.A.

Available on microfilm, microfiche, and electronically through CHEMICAL JOURNALS ONLINE on STN International.

The Challenge of Synthesis: Techniques and Strategies

An Audio Course produced by the American Chemical Society

Now you can get a complete and comprehensive understanding of synthetic strategies and reaction mechanisms with this unique new audiocassette course. Learn new skills and applications as you become familiar with new reagents, reactions, and catalysis, especially transition metal catalysis, as they relate to synthesis design.

WHAT YOU'LL LEARN

IF YOU ARE A CHEMIST who works in basic research, process research, or with developing new routes to known materials, you'll especially benefit from this in-depth look into synthetic reactions. Specifically, you'll gain insight to:

- chemo- and regioselectivity of reactions
- carbocyclic and heterocyclic chemistry
- stereocontrol of organic reactions
- correlation between new synthetic reactions and synthetic strategy
- asymmetric synthesis
- retrosynthetic analysis
- reaction mechanisms

and much more! Plus this challenging course includes self exercises, an extensive bibliography, primary literature references, and examples illustrating concepts.

BACKED BY THE ACS GUARANTEE

ACS guarantees you'll benefit from this course! If you're not completely satisfied with your audio course, simply return it within ten days of receipt for a full refund, charge credit, or cancellation of invoice.

HOW YOU'LL BENEFIT

Designed to improve your awareness of synthetically useful reactions, you'll enhance your chemical efficiency, learn new experimental techniques, improve your analytical ability in synthesis design, and develop an understanding of the correlation between new synthetic reactions and synthetic strategy.

ABOUT THE COURSE AUTHORS

Dr. Barry M. Trost is Professor of Chemistry at Stanford University. He is the recipient of the ACS Awards for Pure Chemistry and Creative Work in Synthetic Organic Chemistry. Dr. Edwin Vedejs is Professor of Chemistry at the University of Wisconsin, and is active in the synthesis of complex molecules.

PACKAGE *(Catalog No. 99)*

The course comes complete with six cassettes (7 hours playing time) and a 200-page manual for $485.00 (U.S. and Canada), $582.00 (export). Additional manuals may be purchased at $32.00 each (U.S. and Canada), $39.00 (export).

CALL TOLL FREE **1-800-227-5558!**

O • R • D • E • R F • O • R • M

Send this Order Form with your payment or purchase order to:
American Chemical Society, Distribution Office, Dept. 04
PO Box 57136, West End Station, Washington, DC 20037

	Qty.	US & Can Price	Export Price	Total Amount
The Challenge of Synthesis *(Cat. No. 99)*	____	$485.00	$582.00	$ ____
Additional Manuals	____	$ 32.00	$ 39.00	$ ____
			Total enclosed:	$ ____

Ship to:
Name ____
Organization ____
Address ____
____
City, State, Zip ____
Phone ____

Bill to:
Name ____
Organization ____
Address ____
____
City, State, Zip ____
Phone ____

☐ Payment enclosed (make checks payable to ACS). ☐ Purchase order enclosed. PO # ____
☐ Charge my ☐ MasterCard ☐ VISA ☐ American Express ☐ Barclaycard ☐ ACCESS ☐ Diners Club/Carte Blanche

Account # ____
Expires ____ Interbank # ____ (ACCESS & MC Only)
Name of Cardholder ____
Signature ____

198th ACS National Meeting

The 198th National Meeting of the American Chemical Society will be held in Miami Beach, FL, Sept. 10–15. At the meeting, the Division of Analytical Chemistry will sponsor or cosponsor technical sessions at which more than 180 presentations are scheduled. In addition to the technical program, the meeting will feature a presidential plenary session on atmospheric chemistry (Monday, Sept. 11), a career development tutorial (Sunday, Sept. 10 and Monday, Sept. 11), and a National Chemistry Week celebration (Tuesday, Sept. 12). Other features of interest will be meetings of the ACS council and board of directors; ACS short courses, a national employment clearinghouse; and a series of social events, including the ACS president's reception (Monday, Sept. 11), an ACS mixer (Wednesday, Sept. 13), an ACS alumni hour (Tuesday, Sept. 12), and the Division of Analytical Chemistry social hour and dinner (Tuesday, Sept. 12).

On-site registration facilities will be in the main lobby of the Miami Beach Convention Center and in the Grand Gallerie of the Fontainebleau Hilton. Registration hours will be Sunday, Sept. 10, from 2 to 7 P.M.; Monday, Sept. 11, through Thursday, Sept. 14, from 7:30 A.M. to 3:30 P.M.; and Friday, Sept. 15, from 7:30 to 10 A.M.

An exposition of instruments, chemicals, technical literature, and other products and services will run for three days in conjunction with the meeting. The exposition, which will be housed in the Miami Beach Convention Center, will be open Monday, Sept. 11, through Wednesday, Sept. 13, from 8:30 A.M. to 5 P.M.

The following Division of Analytical Chemistry symposia and sessions are scheduled: electrochemistry, capillary chromatography, ultrasensitive and ultraselective detectors in chromatography, 2D NMR spectroscopy, chromatography, analytical measurements based on piezoelectric crystal responses, expert systems in analytical chemistry, solid-state luminescence, supercritical fluid extraction and supercritical fluid chromatography, and general topics.

The Division's program will also include several award symposia. Ralph Adams, recipient of the Division of Analytical Chemistry Award in Electrochemistry, will deliver a talk on Tuesday, Sept. 12, titled "Properties of Pretreated Carbon Fiber Electrodes Pertinent to In Vivo Electrochemical Applications." The Division of Analytical Chemistry Award in Chemical Instrumentation will be presented to M. Bonner Denton, who will deliver a talk titled "Past Successes and Future Goals in Spectrochemical Analysis" on Monday, Sept. 11. Theodore Williams, this year's recipient of the Division of Analytical Chemistry Award for Excellence in Teaching, will deliver his award address titled "The Analysis of Ocular Tissues" on Monday, Sept. 11. Gary Hieftje will receive the Division of Analytical Chemistry Award in Spectrochemical Analysis on Tuesday, Sept. 12, and will deliver an address titled "Analytical Atomic Spectrometry—Is the End Near?"

The Division of Analytical Chemistry will cosponsor two additional symposia: chromatography of biopolymers (with the Division of Polymer Chemistry) and emerging technologies in analytical chemistry (with the Younger Chemists Committee).

The Division's dinner is scheduled for Tuesday, Sept. 12, at Fairmont Gardens, 1000 Collins Ave. The social hour begins at 6 P.M., followed by dinner at 7 P.M. Cost is $25. Ticket ordering information is available in the July 17 issue of *Chemical & Engineering News*.

The ACS Department of Continuing Education will offer a series of short courses at the meeting. Further information about these courses appears on p. 918 A of this issue.

Preregistration forms and additional information are available in the June 19 and July 17 issues of *Chemical & Engineering News*. The latter issue contains the complete final program for the meeting. The program that follows includes all sessions sponsored or cosponsored by the Division of Analytical Chemistry.

Program

DIVISION OF ANALYTICAL CHEMISTRY

Sam P. Perone, *Chairman*

MONDAY MORNING — SECTION A

Electrochemistry

V. Y. Young, *Presiding*

9:20 Twin Electrode Voltammetry at Gold Interdigitated Filar Microelectrodes. **M. S. Harrington,** L. B. Anderson
9:40 Direct Amperometric Biosensors from Enzyme-Containing Cross-Linked Redox Polymers Bound to Electrodes. **B. A. Gregg,** A. Heller
10:00 Nonlinear Responses of pH Glass Electrodes. **N. Ashraf,** K. L. Cheng
10:35 Capacitance of Membrane Electrodes. S.X.R. Yang, **K. L. Cheng**
10:55 Effect of Humidity on the ac Impedance of Thin Films of Hectorite. R. Venedam, M. E. Eastman, **M. P. Eastman,** B. L. Wheeler
11:15 Effect of Light on Pb ISE Powder Surfaces. M. L. Clay, **V. Y. Young**

SECTION B

Division of Analytical Chemistry Excellence in Teaching Award Symposium

K. Dolbow, *Presiding*

8:30 Introductory Remarks.
8:40 Analytical Chemistry and the Human Resources Pipeline. **H. N. Blount, III**
9:10 Studies of Cyclodextrin Complexes in the Presence of Nonionic Surfactants. **I. M. Warner,** G. Nelson, J. Zung, V. Smith
9:40 Receptor Signaling: The Basis for Hormone and Drug-Induced Physiological Effects. **L. E. Limbird**
10:25 Advances in Sequencing Peptides and Proteins by Tandem MS. **J. T. Stults**
10:55 Nitrogen Metabolism and Storage in Cyanobacteria: ^{15}N-Labeling of Arginine and Aspartic Acid in Cyanophycin Granule Polypeptide as Determined by GC/MS. **M. V. Merritt,** S. Bhattacharya, L. A. Brown, N. B. Elliott, H. W. Lee, B. M. O'Gorman, L. J. Szabo, M. M. Allen
11:25 Presentation of the Division of Analytical Chemistry Award for Excellence in Teaching to Theodore Williams
11:35 Award Address: The Analysis of Ocular Tissues. **T. R. Williams**

SECTION C

Symposium on Capillary Chromatography: The Applications—I

W. Jennings, *Presiding*

8:55 Introductory Remarks.
9:00 Column Equivalency in Environmental Methods. **G. L. Robertson,** J. Fisk
9:30 Applications of Capillary GC in Industrial Hygiene. **M. Przybyciel**
10:15 EPA Methods Using Parallel Megabore Columns with Common Detector. **V. Lopez-Avila,** W. Beckert
10:45 Analysis of PAHs and PAH Derivatives in Ambient Air Samples Using High-Resolution GC/MS. **J. Arey,** B. Zielinska, R. Atkinson
11:15 Measurement of Toxic Organic Compounds in Ambient Air Using EPA Method TO-14. **S. D. Hoyt**

SECTION D

General—I

E. P. Grimsrud, *Presiding*

9:00 Elimination of Unusual Negative Ions in Electron Capture MS by Use of Carbon Dioxide Buffer Gas. L. J. Sears, **E. P. Grimsrud**
9:20 Displacement Chromatography on Microbore Columns. L. H. Irgens, G. Farkas, **G. Vigh**
9:40 Sample Composition-Based Parameter Selection for the Optimization of Reversed-Phase Ion-Pair Chromatographic Separations. **A. Bartha,** G. Vigh
10:15 Determination of Argininosuccinate and Its Anhydrides by HPLC. **H. Liu,** H. G. Worthen
11:05 GPC Method for the Analysis of Polyurethane Prepolymers. **S. G. Taylor,** C. M. Thompson, W. W. McGee

MONDAY AFTERNOON — SECTION A

Division of Analytical Chemistry Award in Electrochemistry Symposium—I

J. Q. Chambers, *Presiding*

2:00 Nuances, Nuisances, and Propagational Adequacy: ABCs of Stimulation of Electrochemical Phenomena. **S. W. Feldberg**
2:30 Electrochemical Oxidative Decarboxylation of 3,4-Dihydroxy-mandelic Acid: Evidence Consistent with the Formation of a Quinone Methide Intermediate. T. H. Czapla, M. R. Claeys, T. D. Morgan, K. J. Kramer, T. L. Hopkins, **M. D. Hawley**
2:55 Interaction of Protons and Dimethylaniline in Ambient-Temperature Chloroaluminate Ionic Liquids. S-G. Park, R. T. Carlin, P. Trulove, **R. A. Osteryoung**
3:30 Mixed-Solvent Effects in Electrode Kinetics. **Z. Galus**
4:10 Surface Structure and Electron-Transfer Activity of Carbon Electrodes. **R. L. McCreery,** R. J. Bowling, R. Rice, N. Pontikas, C. Allred
4:35 Nernst Donnan Fermi Distribution Potential: Interfacial Potentials at Nonclassical Interfaces and Redox Diodes. **R. P. Buck**

continued on p. 913 A

PHOTO COURTESY OF GREATER MIAMI CONVENTION & VISITORS BUREAU

Miami Beach and boardwalk

SECTION B

Division of Analytical Chemistry Award in Chemical Instrumentation Symposium—I

R. B. Bilhorn, *Presiding*

2:00 Arrays of Data from Transient Analytical Discharges. **A. Scheeline**
2:30 Instrument Development and the Role of Analytical Scientists. **A. T. Zander**
3:10 Presentation of the Division of Analytical Chemistry Award in Chemical Instrumentation to M. Bonner Denton
3:20 Award Address: Past Successes and Future Goals in Spectrochemical Analysis. **M. B. Denton**
4:05 Improved Atomic and Molecular Spectroscopy with Slow-Scan Charge Transfer Device Cameras. **R. B. Bilhorn**
4:35 Spectroscopy—A Cost-Effective Medium for Process Control. **K. J. Leiper**

SECTION C

Symposium on Capillary Chromatography: The Applications—II

J. Nikelly, *Presiding*

2:00 Use of Capillary Chromatography in the Analysis of Environmental Tobacco Smoke. **M. W. Ogden**
2:30 Detection of Pesticides Using Large-Bore Capillary Columns. **P. J. Marsden,** M. Roby, F. Tsang
3:00 Fatty Foods Cleanup for Organochlorinated and Organophosphorus Pesticides by GPC and Chromatography by Wide-Bore Capillary Column GC. **E. R. Krout, Jr.,** K. Hornung
3:40 Use of Computerized Modeling To Develop New Capillary GC Column Stationary Phases for Optimum Separation of Chlorinated Dioxin/Dibenzofuran Isomers. **T. O. Tiernan,** J. H. Garrett, J. G. Solch, L. A. Harden, R.M.A. Lautamo, R. R. Freeman
4:10 Application of the Multidimensional Approach to Chromatographic Analysis of Environmental Samples. R. A. Cavalier, J. J. Kosman, R. G. Lukco, **S. A. Schmidt,** J. A. Yancey
4:40 Analysis of Trace Organics Using Coupled SFE/Capillary GC with Conventional On-Column and Split–Splitless Injectors. **S. B. Hawthorne,** D. J. Miller

SECTION D

Symposium on Ultrasensitive and Ultraselective Detectors in Chromatography

N. J. Dovichi, *Presiding*

1:30 New Detection Schemes in Capillary Chromatography and Capillary Electrophoresis. **E. S. Yeung**
2:00 Single-Molecule Detection in Flowing Sample Streams as an Approach to DNA Sequencing. J. H. Jett, **R. A. Keller,** J. C. Martin, N. K. Seitzinger, E. B. Shera
2:30 High-Sensitivity Laser-Based Detection for Capillary Zone Electrophoresis. S. Wu, Y. F. Cheng, M. Yu, C. Earle, **N. J. Dovichi**
3:15 Electrospray Ionization–MS Detection of Protonated Organic Bases in LC Effluent. M. G. Ikonomou, A. T. Blades, **P. Kebarle**
3:45 Photodetachment-Modulated Electron Capture Detection. R. S. Mock, **E. P. Grimsrud**
4:15 Selective Detection for SFC. **D. J. Bornhop,** J. G. Wangsgaard, B. E. Richter
4:45 HPLC–ICP/MS Speciation Studies of Gold/Zinc/Copper Complexes in Biological Fluids. **R. C. Elder,** M. L. Tarver, W. B. Jones, Y. L. Zhang, K. Tepperman

TUESDAY MORNING

SECTION A

Division of Analytical Chemistry Award in Electrochemistry Symposium—II

R. L. McCreery, *Presiding*

9:00 Introductory Remarks. **T. Kuwana**
9:05 Presentation of the Division of Analytical Chemistry Award in Electrochemistry to Ralph N. Adams
9:10 Award Address: Properties of Pretreated Carbon Fiber Electrodes Pertinent to In Vivo Electrochemical Applications. **R. N. Adams**
9:40 Dynamics of Dopamine and Oxygen in the Brain Detected with Voltammetry. **R. M. Wightman,** J. L. Brown
10:25 Electrochemical Approaches to Understanding Brain Chemistry. **J. B. Justice, Jr.**
10:55 Neurochemical Analysis at the Single-Cell Level. **A. G. Ewing**
11:30 Chromatographic and Amperometric Approaches to Signal Enhancement for LC/EC: Studies on Brain Epinephrine Metabolism. **I. N. Mefford,** M. I. Massana, J. K. Hsiao

SECTION B

Division of Analytical Chemistry Award in Chemical Instrumentation Symposium—II

R. B. Bilhorn, *Presiding*

9:00 Photodiode Array Spectrometer Systems for ICP Emission Spectrometry. **G. Horlick**
9:30 Electronic Imaging Systems in Analytical Spectrometry. **G. M. Hieftje**
10:00 New Approach to Detection at Low Light Levels. **J. D. Winefordner**
10:45 Spatial Interferometry for the UV to Near-IR. **J. V. Sweedler,** M. B. Denton
11:15 Hadamard Transform Spectrometry. A. P. Bohlke, J. White, J. D. Tate, R. M. Hammaker, **W. G. Fateley**

SECTION C

Symposium on Capillary Chromatography: The Applications—III

J. Nikelly, *Presiding*

9:00 Particle Beam LC/MS, SFC/MS of Environmental and Pharmaceutical Compounds. **P. E. Sanders,** R. Willoughby, J. Buchner
9:30 Derivatization and Separation of Amphetamines by Capillary GC. **H. D. Rood,** J. A. Knitter
10:00 Capillary GC Analysis of Trichothecene Microbial Biotransformation Products. **S. P. Swanson**
10:40 RPLC Analysis of Monocyclic Peptide Hepatotoxins from Cyanobacteria (Blue–Green Algae). **A. M. Dahlem**
11:15 Radioisotope Detection for Capillary Electrophoresis. **S. L. Pentoney, Jr.,** R. N. Zare, J. Quint

SECTION D

Symposium on Two-Dimensional NMR Spectroscopy—I

D. L. Rabenstein, *Presiding*

8:30 Structural Studies of Complex Carbohydrates by Multinuclear Two-Dimensional NMR. **R. A. Byrd**
9:05 Complete Relaxation Matrix Analysis of 2D NOE Spectra for Refinement of DNA and Protein Structures in Solution. D. Kerwood, M. Gochin, B. A. Borgias, **T. L. James**
9:40 NMR Structure Refinement of the Taq I DNA Restriction Site. **P. A. Mirau**
10:30 Protein Structure Determination by Two- and Three-Dimensional NMR. **A. M. Gronenborn,** G. M. Clore
11:05 Use of Isotopes in Two- and Three-Dimensional NMR Studies of Enzyme/Inhibitor Complexes. **S. W. Fesik,** R. T. Gampe, Jr., E.R.P. Zuiderweg, E. T. Olejniczask, H. L. Eaton

TUESDAY AFTERNOON

SECTION A

Division of Analytical Chemistry Award in Electrochemistry Symposium—III

R. M. Wightman, *Presiding*

2:00 Electroanalytical Investigations of Neuropharmacological Mechanisms: Dopaminergic Antagonism. **J. O. Schenk**
2:25 High-Speed In Vivo Electrochemical Studies of Monoamine-Containing Brain Grafts. **G. A. Gerhardt**
2:50 Electrochemical Studies of Iron–Sulfur Proteins: Ferredoxin and Corrinoid/Iron–Sulfur Protein. **B. A. Feinberg,** E. T. Smith, S. R. Harder, W-P. Lu, S. W. Ragsdale
3:30 Multielectrode, Multicolumn LC with Electrochemical Detection. **C. L. Blank**
3:55 Electrochemically Controlled Binding of Ethidium to Calf Thymus DNA at a Carbon Paste/Ethidium Tetracyanoquinodimethane Electrode. **J. Q. Chambers,** R. D. Mounts, M. A. Lange, B. A. Swaile
4:20 Silver(I)–"Cross-Linked" Cyanometallates as Novel Materials for Modification of Electrode Surfaces. **P. J. Kulesza,** Z. Galus

SECTION B

Division of Analytical Chemistry Award in Spectrochemical Analysis Symposium—I

J. W. Olesik, *Presiding*

1:55 Presentation of the Division of Analytical Chemistry Award in Spectrochemical Analysis to Gary M. Hieftje
2:05 Award Address: Analytical Atomic Spectrometry—Is the End Near? **G. M. Hieftje**
2:50 Looking for Single Molecules in Small Droplets. **J. M. Ramsey,** W. B. Whitten
3:15 Giga-Atom Detection Limits in DCP-AES. **C. B. Boss,** B. T. Buckley

3:55 Ionization Probe for Laser-Generated Plumes. **E. S. Yeung,** H-M. Pang
4:20 2D Hadamard Transform Imaging Spectrometry. A. P. Bohlke, J. S. White, J. D. Tate, J. M. Jarvis, J. V. Paukstelis, R. M. Hammaker, **W. G. Fateley**
4:45 Molecular Photofragmentation–Fluorescence Spectrometry. **E. L. Wehry**

SECTION C

Chromatography

G. Vigh, *Presiding*

2:20 Recent Progress in the Displacement Chromatography of Enantiomers on Cyclodextrin–Silica Columns. G. Quintero, J. C. Jaszberenyi, A. Bartha, G. Farkas, **G. Vigh**
2:40 Influence of Eluent Ionic Strength upon Solute Retention on Cyclodextrin–Silica Columns. **G. Quintero,** G. Vigh
3:00 Recent Developments in the Preparative Separation of Enantiomers on Pirkle-Type Columns Using Displacement Chromatography. P. L. Camacho, E. Geiger, J. C. Jaszberenyi, G. Farkas, A. Bartha, **G. Vigh**
3:35 Anion and Cation Effects on the Polarity and Selectivity of Liquid Organic Salt Stationary Phases Used in GC. **K. G. Furton,** R. Morales
3:55 Thermal Modulation Injection Device for SFC. **S. Mitra,** N. K. Wilson
4:15 Reverse-Phase Alumina for Lipophilicity Determination by HPLC. **J. E. Haky,** S. Vemulapalli

SECTION D

Symposium on Two-Dimensional NMR Spectroscopy—II

C. L. Wilkins, *Presiding*

2:00 Applications of Various Two-Dimensional NMR Techniques to Problems in Chemistry. **J. N. Shoolery**
2:35 Two-Dimensional NMR of Nucleic Acid Oligomers. G. C. Levy, K. D. Bishop, S. R. LaPlante, S. S. Wang, **P. N. Borer**
3:25 Two-Dimensional NMR for Organic Chemists: Automation in 2D Data Collection, Processing, and Plotting. **L. F. Johnson**
4:00 Two-Dimensional NMR of Aqueous Solution with Water Elimination by Transverse Relaxation. C. Larive, **D. L. Rabenstein**

SECTION E

Emerging Technologies in Analytical Chemistry
Cosponsored with the Younger Chemists Committee

2:00 Introductory Remarks. **S. Daunert**
2:05 Emerging Analytical Chromatographic Technologies Using Supercritical Fluids. **M. Lee**
2:40 Peptide Interactions with Metals Probed by SERS. **R. Garrell**
3:15 Analysis of Three-Way Data Arrays in Multifrequency Phase-Resolved Fluorescence Spectroscopy. **L. McGown,** D. W. Millican, M. S. Cooter, D. S. Burdick, X. M. Tu
3:50 Biosensors Using Vitamin B_{12} Derivatives. **L. G. Bachas**

WEDNESDAY MORNING SECTION A

Symposium on Analytical Measurements Based on Piezoelectric Crystal Responses—I

D. A. Buttry, *Presiding*

8:55 Introductory Remarks. **S. Bruckenstein**
9:00 New Description for the Viscoelastically Loaded Quartz Resonator. **K. K. Kanazawa,** C. E. Reed
9:30 Transport Phenomena Accompanying Redox Switching in Polythionine Films Immersed in Strong and Weak Acid Solutions. **S. Bruckenstein,** C. P. Wilde, M. Shay, A. R. Hillman
10:00 Quartz Crystal Microbalance Measurements of Redox-Induced Changes in Solvent and Ion Content in Disulfide Anchored Redox Monolayers on Gold Electrodes. **H. DeLong,** D. A. Buttry
10:30 Electrochemical Quartz Crystal Microbalance Studies of Polyheterocycles. **J. R. Reynolds,** Y-J. Qiu, C. K. Baker
10:50 Application of Quartz Crystal Microbalance to Monitor the Electropolymerization and Ion–Solvent Transport of Conductive Polymer Films. **R. Borjas,** D. A. Buttry
11:10 Measurement of Solvent Swelling in Poly(vinylchloride)/Crown Ether Ion-Selective Electrode Films During K^+ Transport. **H. Meyer,** D. A. Buttry
11:30 Probing Mixed Monolayer Films and Formation of Conductive Organic Films by the Electrochemical Quartz Crystal Microbalance Technique. **M. Hepel**

SECTION B

Division of Analytical Chemistry Award in Spectrochemical Analysis Symposium—II

J. E. Freeman, *Presiding*

9:00 Capacitively Coupled Plasma Sources—From AE to GC. **M. W. Blades,** D. C. Liang, D. Huang
9:25 ICP Signal Fluctuations Due to Individual Aerosol Droplets. **J. W. Olesik,** L. J. Smith
9:50 Trace Elements in Uranium by ICP/FT Spectrometry. **L. R. Layman,** G. B. Bentley, B. A. Palmer
10:30 Reduction of Interferences in Secondary Ion MS by Resonance Ionization. **S. W. Downey**
10:55 Nonthermal Features and Fundamental Parameters in the ICP. **M. Huang,** D. S. Hanselman, G. M. Hieftje
11:20 Furnaces and Plasmas: Investigations of Chemical Processes in High-Temperature Sources. **G. D. Rayson,** Y. Shen, M. R. Fresquez, D. Lenhoff

SECTION C

Symposium on Chromatography of Biopolymers—I
Cosponsored with the Division of Polymer Chemistry

R. M. Riggin, *Presiding*

8:50 Introductory Remarks.
9:00 Plenary Lecture: Recent Developments in Chromatography of Biopolymers. **F. E. Regnier**
9:45 Correlation of Salt Effects on Protein Retention in High-Performance Anion- and Cation-Exchange Chromatography. **K. M. Gooding,** M. N. Schmuck, M. P. Nowlan
10:30 Displacement Chromatography of Biopolymers on Group-Specific Affinity Supports. **G. Subramanian,** G. Jayaraman, S. M. Cramer
11:00 HPAE-PAD Analysis of Carbohydrates: Theory and Applications. **J. D. Olechno,** S. R. Carter, M. R. Hardy, J. Statler
11:30 Methods for the Determination of Oligosaccharide Groups in Therapeutic Proteins. **P. M. Kovach,** D. K. Clodfelter, R. M. Riggin

SECTION D

Symposium on Expert Systems in Analytical Chemistry

S. D. Brown, *Presiding*

8:00 Opportunities for Using Expert Systems in Design, Monitoring, and Control of Advanced Life Support Missions on Manned Space Stations. **C. M. Wong,** R. A. Yost, M. R. Rudokas, R. S. Upadhye
8:40 Expert Systems in Method Development of Graphite Furnace AAS. **J. Smeyers-Verbeke,** P. Vankeerberghen, D. L. Massart

PHOTO COURTESY OF GREATER MIAMI CONVENTION & VISITORS BUREAU

Historic Cap Florida lighthouse on Key Biscayne

9:20 Expert Systems for Evaluation of Chemical Sensor Data. **A. M. Harper**
10:10 Expert System for Classification and Identification of Mass Spectra of Toxic Compounds. **D. R. Scott**
10:50 Expert Systems for Evaluating Analytical Chemical Data. **S. R. Heller,** D. Bigwood
11:30 Use of PC-Based Expert Systems in Analytical Chemistry. **F. A. Settle, Jr.,** M. A. Pleva

WEDNESDAY AFTERNOON

SECTION A

Symposium on Analytical Measurements Based on Piezoelectric Crystal Responses—II

M. Hepel, *Presiding*

1:30 Thin-Film Dissolution Kinetics Using a Quartz Crystal Microbalance. **W. Hinsberg,** K. K. Kanazawa, C. G. Willson
2:00 Monitoring Corrosion Processes in Solution with the Quartz Crystal Microbalance. **M. R. Deakin**
2:25 Mechanism for Multilayer Oxide Formation at a Gold Electrode. **M. Shay,** S. Bruckenstein
2:55 Quartz Microbalance Studies of CO Oxidation at Pt Electrodes. **C. P. Wilde,** S. Bruckenstein
3:30 Quartz Crystal Microbalance Thermal Analysis Combined with MS. **J. W. Garrett,** A.P.M. Glassford
4:05 Quartz Crystal Microbalance Biosensor for Glucose Detection Using Immobilized Hexokinase. **S. J. Lasky,** D. A. Buttry
4:25 Application of the Quartz Crystal Microbalance to the Study of Plasma/Surface Chemistry and Physics. **J. F. Evans**

SECTION B

Division of Analytical Chemistry Award in Spectrochemical Analysis Symposium—III

J. Mitchell, *Presiding*

2:00 Spectroscopic Imaging. **R. M. Miller**
2:25 Acoustic Waveguide Sensors: A Theoretical and Experimental Study of Wave Mode Selection. **G. J. Bastiaans**
2:50 On-Column Detection for Microcolumn Separations. **C. A. Monnig,** J. W. Jorgenson
3:30 Long-Pulse Laser Vaporization for Deposition of Thin-Film High-Temperature Superconductors. **R. E. Russo,** M. Balooch, D. R. Olander
3:55 Evaluation of Pharmaceutical Metered-Dose Inhalers. **A. G. Childers**
4:15 Elucidation of Supercritical Fluid Solvodynamics Using Time-Resolved Fluorescence Spectroscopy. **F. V. Bright,** T. A. Betts

SECTION C

Symposium on Chromatography of Biopolymers—II

Cosponsored with the Division of Polymer Chemistry

R. M. Riggin, *Presiding*

2:00 Prediction of Gel Filtration Separations. **L. Hagel**
2:30 Towards a Mechanism of SEC. **M. Potschka**

PHOTO COURTESY OF GREATER MIAMI CONVENTION & VISITORS BUREAU

Bayside Marketplace and downtown Miami skyline

3:00 SEC of Rods, Spheres, and Coils. **P. L. Dubin**
3:40 Chromatographic Partition as a Tool for the Physicochemical Characterization of Macromolecules. **H. Waldmann-Meyer**
4:10 SEC of Charged and Stiff Polysaccharides. **M. Rinaudo**

SECTION D

General—II

R. E. Synovec, *Presiding*

2:00 Absorbance Spectrophotometry by Double-Beam Position-Sensitive Detection. **R. E. Synovec**
2:20 Quantitative Resonance Raman Spectroscopy. **T. J. Vickers,** C. K. Mann, C. K. Chong, J. Zhu
2:40 Ion-Sieving Effects in Polyaniline Matrices. **W. E. Rudzinski,** L. Lozano
3:10 Improving Electrochemical Response in Flow-Injection Analysis by Cross-Correlation. **D. J. Curran,** R. E. McKean
3:30 Electrochemical Detection of Underivatized Amino Acids and Oxalyl Thiolesters in Capillary Electrophoresis. **C. E. Engstrom,** A. G. Ewing
3:50 Unavoidable Flow Rate Errors in HPLC. **J. P. Foley,** J. E. Crow, B. A. Thomas, M. Zamora

THURSDAY MORNING

SECTION A

Symposium on Analytical Measurements Based on Piezoelectric Crystal Responses—III

S. Rose-Pehrsson, *Presiding*

9:00 Gaseous HCl Detection with a Zn-Coated Piezoelectric Resonator. **G. G. Neuberger**
9:20 Atmospheric Aerosol Analysis with the Quartz Crystal Cascade Impactor. **R. L. Chuan**
9:55 Quartz Crystal Microbalance as a Detector for Nucleic Acid Hybridization. **N. C. Fawcett,** J. A. Evans
10:15 Acoustic Membrane Multisensors for Chemical, Biological, and Physical Variables. **R. M. White**
11:00 Sensing Mechanisms in Acoustic Wave Sensors. **S. J. Martin,** A. J. Ricco, C. G. Frye, R. C. Hughes
11:30 Selection of Sorbent Coating Materials for SAW Chemical Sensors and Arrays. **J. W. Grate**

SECTION B

Symposium on Solid-State Luminescence—I

T. D. Harris, *Presiding*

8:40 Introductory Remarks. **P. W. Bohn**
8:45 New Laser Methods for Studying Solid-State Defect Dynamics. K. M. Cirillo, **J. C. Wright**
9:30 Quantitative Determination of Impurities in Gallium Arsenide by Low-Temperature Luminescence and Electronic Raman Scattering. **T. D. Harris,** M. L. Schnoes
10:30 Emission and Resonance Raman Spectroscopic Determinations of Excited-State Distortions. K-S. Shin, L. Larson, **J. I. Zink**
11:15 Luminescence as a Probe of Adduct Formation at Semiconductor-Derived Interfaces. **A. B. Ellis,** L. K. Leung, E.R.M. Luebker, G. J. Meyer, C. J. Murphy, G. C. Lisensky

SECTION C

Symposium on Chromatography of Biopolymers—III

Cosponsored with the Division of Polymer Chemistry

P. L. Dubin, *Presiding*

9:00 Effect of Polypeptide Chain Length on Retention Behavior in Reversed-Phase and Ion-Exchange HPLC. **R. S. Hodges,** T.W.L. Burke, N. E. Zhou, C. T. Mant
9:30 Use of Protein Conformation in the Design of HPLC Separations. **M. Kunitani**
10:00 High-Performance Polymeric Sorbents for Separations of Biopolymers. **J. Coupek,** O. Mikes
10:45 Hydrophobic Interaction Chromatography of Biopolymers. **S-L. Wu,** W. S. Hancock

11:15 Surfactant-Mediated Hydrophobic Interaction Chromatography of Proteins. **D. B. Wetlaufer,** J. J. Buckley, J. Gehas

11:40 Multimodal HPLC: Salt-Induced Hydrophobic Interaction Chromatography on Charged Stationary Phases. **J. B. Wheatley,** D. E. Schmidt, Jr.

SECTION D

General—III

J. K. Swadesh, *Presiding*

9:00 Methods Development for Sampling and Analysis of Trace Environmental Pollutants. **S. Kaneko,** K. Hatanaka, R. Oshio

9:20 Applications of an On-Line Detector of Optical Activity. **J. K. Swadesh,** T. A. Perfetti

9:40 Prototropic Dissociation Kinetics of Photoexcited Hydroxyaromatics in Aqueous–Ethanol Solutions. **S. G. Shulman,** R. Townsend, R. N. Kelly, S. Chen

10:10 Capillary GC/MS Quantitation of a New Organophosphate Insecticide in Animal Feeds. **N. L. Freshour,** P. W. Langvardt

10:30 Analysis of Model Titan Atmospheric Components Using Ion Mobility Spectrometry. **D. R. Kojiro,** M. J. Cohen, D. H. Humphry, N. Takeuchi, R. F. Wernlund, R. M. Stimac

10:50 Detoxification and Disposal of Halogenated Organic Compounds. **S. S. Shukla,** T. Nguyen

11:10 Polarographic and Voltammetric Study of Indium(III) Complexes in Aqueous and Mixed Solvent Media. **M. C. Eshwar,** M. S. Qureshi

THURSDAY AFTERNOON SECTION A

Symposium on Analytical Measurements Based on Piezoelectric Crystal Responses—IV

S. Bruckenstein, *Presiding*

1:45 Pattern Recognition Analysis of Responses from Surface Acoustic Wave Devices for the Detection of Hazardous Vapors Including Mixtures. **S. Rose-Pehrsson,** J. W. Grate, D. S. Ballantine

2:10 Coating Selection Strategies for Chemical Sensors. **D. S. Ballantine**

2:35 Surface Acoustic Wave Piezoelectric Crystal Aerosol Mass Microbalance. **W. D. Bowers,** R. L. Chuan

3:10 Industrial Hygiene Applications of Coated Surface Acoustic Wave and Lamb Wave Chemical Sensors. **E. T. Zellers**

3:30 Acoustic Waveguide Sensors: The Importance of Surface Chemistry. **G. J. Bastiaans**

4:00 UV Laser-Induced Etching of the First-Row Transition Metals. **G. W. Tyndall,** C. R. Moylan

4:35 Materials Characterization Using Surface Acoustic Wave Devices. **G. C. Frye,** A. J. Ricco, S. J. Martin

SECTION B

Symposium on Solid-State Luminescence—II

P. W. Bohn, *Presiding*

2:00 Fluorescence Photobleaching Recovery Investigations of Transport in Self-Assembling Structures. **B. R. Ware**

2:45 Fluorescence Characterization of the Wettability Gradient on Modified Silica Surfaces. **V. Hlady,** Y. S. Lin, J. D. Andrade
3:45 Time-Resolved Fluorescence as a Probe for Molecular Transport at Liquid–Solid Interfaces. **A. L. Wong,** M. L. Hunnicutt, J. M. Harris
4:30 Surface Molecular Orientations by Optical Waveguide Fluorescence Mediated Linear Dichroism. **P. W. Bohn,** D. M. Cropek

SECTION C

Symposium on SFE and SFC—I

M. E. McNally, *Presiding*

2:00 Multidimensional SFC. **J. Levy**
2:30 Simplex Optimization Separations in SFC. J. A. Crow, **J. P. Foley**
3:00 Microcolumns in SFC: Packed and Open Tubular. **M. L. Lee,** K. M. Payne, K. E. Markides
3:45 Evaluation of Trace Organic Impurities in Various Industrial Liquid Carbon Dioxides. **R. Denyszyn,** K. Maquire
4:15 Optimization of the Analysis of Additives in Polymers Using Coupled SFE/SFC. **T. W. Ryan,** S. G. Yocklovich, E. J. Levy

FRIDAY MORNING

SECTION A

Symposium on Solid-State Luminescence—III

W. M. Reichert, *Presiding*

8:45 Laser-Based Studies of Cellular Macromolecular Damage and Chemical Carcinogenesis. R. Jankowiak, P. Lu, **G. J. Small**
9:30 Total Internal Reflection Fluorescence Video Microscopy of Cell–Surface Contacts. **W. M. Reichert,** G. A. Truskey, E. Winakur
10:30 Electronic Excitation Transport and Its Relation to Polymer Chain Statistics. **C. W. Frank**
11:15 Luminescence of Degraded Poly(vinylchloride). **E. D. Owen**

SECTION B

Symposium on SFE and SFC—II

M. E. McNally, *Presiding*

9:00 Enhancing Chromatographic Analysis in GC or SFC Using SFE as an Injection Technique. **M. R. Andersen,** J. T. Swanson, B. E. Richter
9:30 SFE and Coupled SFE/GC: Recovery and Analysis of Trace Organics Collected on Sorbent Resins. **S. B. Hawthorne,** D. J. Miller, M. S. Krieger
10:00 Column Technologies for Sensitive and Quantitative SFC. **M. L. Kumar,** A. Rosselli, D. B. Boyer, R. K. Houck
10:45 On-Line Supercritical Sample Preparation Accessory for Chromatography. **J. B. Nair,** J. W. Huber, III
11:15 Combined Supercritical Fluid Extraction and Chromatography with FT-IR Detection. **P. M. Griffiths,** K. L. Norton, A. J. Lange

Conferences

■ **Micro '89 Conference and Exhibition.** Sept. 13–15. London, U.K. *Contact: Royal Microscopical Society, 37/38 St. Clements, Oxford 0X4 1AJ, U.K.*

■ **Dioxin '89: 9th International Symposium on Chlorinated Dioxins and Related Compounds.** Sept. 17–22. Toronto, Ontario, Canada. *Contact: Congress Canada, Conference Management, 73 Richmond St. W., Suite 300, Toronto, Ontario, Canada M5H 1Z4 (416-860-1772)*

■ **Biosensors '89.** Sept. 28–29. Cambridge, U.K. *Contact: Renata Duke, IBC Technical Services Ltd., Bath House, 56, Holborn Viaduct, London EC1A 2EX, U.K.*

■ **31st Conference on Analytical Chemistry in Energy Technology.** Oct. 10–12. Gatlinburg, TN. *Contact: W. R. Laing, Oak Ridge National Laboratory, P.O. Box 2008, MS 6127, Oak Ridge, TN 37831 (615-574-4852)*

■ **7th Annual Membrane Technology/Planning Conference.** Oct. 17–19. Cambridge, MA. *Contact: BCC, 25 Van Zant St., Norwalk, CT 06855 (203-853-4266)*

■ **Instrument Society of America International Conference and Exhibition on Instrumentation.** Oct. 22–27. Philadelphia, PA. *Contact: ISA, 67 Alexander Dr., P.O. Box 12277, Research Triangle Park, NC 27709*

■ **4th Annual San Diego Conference on Nucleic Acid Applications.** San Diego, CA. Oct. 25–27. *Contact: San Diego Conference, P.O. Box 12785, La Jolla, CA 92037-0675 (619-943-1541)*

Short Courses and Workshops

■ **Short Course on Mathematical and Computer Methods in X-ray Spectrometry.** Aug. 21–25. Albany, NY. *Contact: Henry Chessin, Dept. of Physics, State University of New York—Albany, 1400 Washington Ave., Albany, NY 12222*

■ **Short Course on Quantitative Thin-Layer Chromatography.** Sept. 13–14. Blacksburg, VA. *Contact: Camag Scientific, P.O. Box 563, Wrightsville Beach, NC 28480 (800-334-3909)*

■ **Course on Flame AA.** Sept. 18–22. Houston, TX. *Contact: Rose Ann Cochran, NUS Analytical Updating Services, Park West Two, Pittsburgh, PA 15275 (412-788-1080)*

■ **Course on Experimental Design for Productivity and Quality in Research, Development, and Manufacturing.** Sept. 18–22 and Dec. 11–15. Houston, TX. *Contact: Statistical Designs, 9941 Rowlett, Suite 6, Houston, TX 77075 (713-947-1551)*

■ **Short Courses on Mass and IR Spectrometry and Spectral Interpretation.** Oct. 5–7, Chicago, IL; Nov. 1–3, Pittsburgh, PA. *Contact: Barbara Nowicki, PACS, 409 Meade Dr., Coraopolis, PA 15108 (412-262-4222)*

■ **Short Course on Quality Assurance of Chemical Measurements.** Nov. 9–10. Pittsburgh, PA. *Contact: Barbara Nowicki, PACS, 409 Meade Dr., Coraopolis, PA 15108 (412-262-4222)*

ACS Courses

The following courses are offered in conjunction with the 198th ACS National Meeting in Miami Beach, Sept. 10–15.

■ **On-Line Process Analyzers: The Key to Maximizing Industrial Process Efficiency.** Sept. 8–10. Kenneth Clevett

■ **Experimental Design for Productivity and Quality in R&D.** Sept. 8–10. Stanley Deming and Stephen Morgan

■ **Effective Management of Chemical Analysis Laboratories.** Sept. 9–10. John H. Taylor, Jr., and Mary Routson

■ **Analytical Laboratory Operations: Analysis of Water and Waste Samples.** Sept. 9–10. Marcus Cooke

■ **Analytical Laboratory Operations: Analysis of Air Toxics.** Sept. 9–10. Marcus Cooke, Robert Lewis, and William Winberry

■ **Fundamentals of High-Performance Liquid Chromatography.** Sept. 9–10. Harold McNair

■ **Capillary Gas Chromatography.** Sept. 9–10. Stuart Cram and Milos Novotny

■ **Quality Assurance of Chemical Measurements.** Sept. 9–10. John K. Taylor

■ **Environmental Laboratory QA/QC Data Validation.** Sept. 9–10. Henry Nowicki and William Purves

■ **Laboratory Applications of Lotus 1-2-3 and Other Software: Beyond the Basics.** Sept. 9–10. Glenn Ouchi

■ **Size-Exclusion Chromatography.** Sept. 9–10. Alfred Rudin

For information on these and other ACS courses, contact the Department of Continuing Education, American Chemical Society, 1155 16th St., N.W., Washington, DC 20036 (202-872-4508).

Call for Papers

■ **2nd International Symposium on High-Performance Capillary Electrophoresis.** San Francisco, CA. Jan. 29–31, 1990. The meeting will feature oral and poster presentations on topics that include zone electrophoresis, isoelectric focusing, micellar separations, CE/MS, gel columns, isotachophoresis, detector design, instrumentation, and analytical and micropreparative applications for pharmaceuticals, peptides, proteins, carbohydrates, oligonucleotides, subcellular structures, and whole cells. Prospective authors should request abstract forms from Shirley Schlessinger, HPCE '90, 400 East Randolph Dr., Chicago, IL 60601 (312-527-2011). Deadline for submission of abstracts is Sept. 1.

■ **4th Symposium on the Analysis of Steroids.** Pécs, Hungary. April 24–26, 1990. The symposium will focus on industrial and pharmaceutical steroid analysis and the determination of steroids in biological samples. Topics include clinical steroid analysis, analytical methodology for studying the biosynthesis and metabolism of steroids, pharmacokinetic studies of steroid drugs, determination of steroids in samples of plant and animal origin, analysis of pharmaceutical dosage forms, and structure elucidation of steroids. Abstracts of 200 words or less should be submitted by Sept. 15 to S. Görög, c/o Chemical Works of Gedeon Richter Ltd., P.O.B. 27, H-1475 Budapest, Hungary. Authors should indicate if their contributions are for oral or poster presentation.

■ **14th International Symposium on Column Liquid Chromatography.** Boston, MA. May 20–25, 1990. The symposium will feature general and invited lectures, posters, and informal discussion sessions devoted to recent advances in HPLC and related techniques, with particular emphasis on bioanalytical chemistry. Sessions will address advances in separation methods, mechanisms, detection, sample preparation, automation, derivatization, preparative LC, biopolymer separation, chiral recognition, capillary and conventional electrophoresis, SFC, and field-flow fractionation. Prospective authors should submit 150-word abstracts by Oct. 1 to Shirley Schlessinger, Symposium Manager, HPLC '90, 400 East Randolph Dr., Chicago, IL 60601 (312-527-2011).

These events are newly listed in the JOURNAL. See back issues for other events of interest.

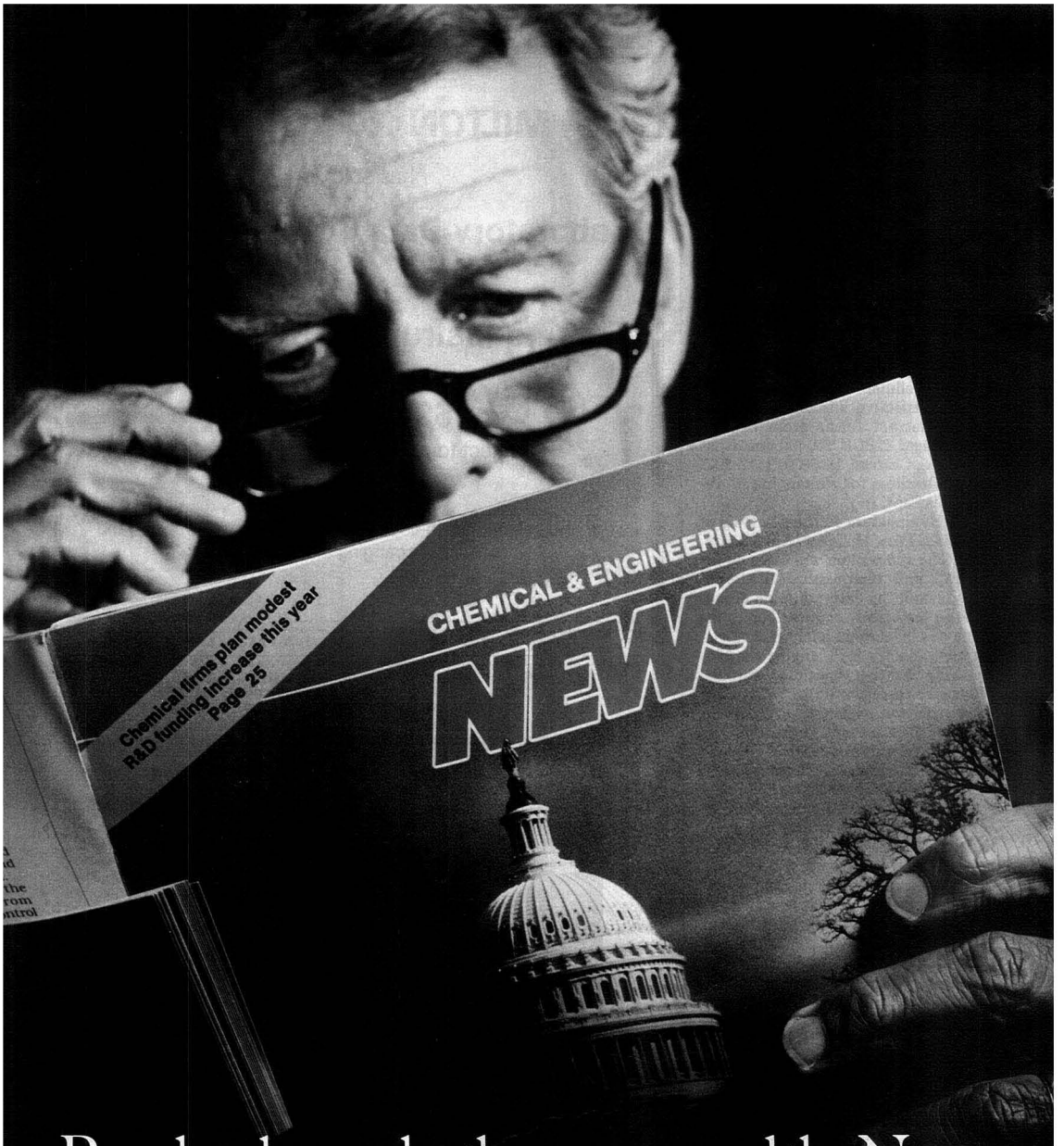

People who make the news, read the News.

When you're sitting at the top, you need to get to the bottom of news that affects your business. That's why senior executives throughout industry read Chemical & Engineering News each week.

It's the only weekly chemical magazine that covers the news from three angles. Not just science. Not just technology. Not just business. But all three. So you not only know what's happening in chemistry, you know how it's going to affect your business.

Read the weekly the newsmakers read. Read Chemical & Engineering News.

Call 800-227-5558

American Chemical Society, 1155 Sixteenth Street, N.W., Washington, D.C. 20036.

CHEMICAL & ENGINEERING NEWS

BUSINESS
SCIENCE
TECHNOLOGY

A Historic Collaboration

July marked the 25th anniversary of the publication in ANALYTICAL CHEMISTRY *of Abraham Savitzky and Marcel Golay's landmark paper describing a smoothing algorithm for the reduction of random noise from measured spectra* (Anal. Chem. *1964,* 36, *1627–39). The digital smoothing filters they described have been used extensively in data analysis because they are versatile and easy to implement.*

When the paper was published, both scientists were employed by the Perkin-Elmer Corporation; Savitzky as an instrumentation specialist in the research department of the Instrument Division and Golay as a senior research scientist. Golay, an electrical engineer, retired in 1955 from the U.S. Signal Corps Engineering Laboratories (Fort Monmouth, NJ) and began a second career as a consultant to P-E. This 34-year association lasted until his death (see p. 922 A).

GOLAY

SAVITZKY

Savitzky met Golay when he was a graduate student at Columbia University working on the development of a double-beam spectrophotometer that used a Golay IR detector. After receiving his Ph.D. in physical chemistry in 1949, Savitzky was employed by P-E as an engineer developing IR process control instrumentation. Later he was involved in P-E's initial GC research and in building P-E's earliest prototype GC instrument. In 1960 he became involved in the emerging field of computer-assisted instruments and, as a principal scientist, led programming teams in the development of P-E's IR software for the microcomputer. Savitzky retired in 1985 to form his own consulting firm for software development and information services (Silvermine Resources, Inc.). On the occasion of the 25th anniversary of this classic work, Savitzky looks back at the genesis of the publication.

Abraham Savitzky
Silvermine Resources, Inc.
3 Mail Coach Court
Wilton, CT 06897

In late 1959 or early 1960, John Atwood, then director of research for the Perkin-Elmer Instrument Division, Norman Adams, Marcel Golay, and I discussed the analysis and interpretation of IR spectra untouched by human hands. Our first problem was the recognition of spectral characteristics such as peaks, valleys, and shoulders. It appeared that these features could be determined from changes in sign in the first and second derivatives.

We asked Golay to look into a simple and fast method for calculating the derivatives. My notebooks show that in September and October 1960 he provided me with sets of first- and second-derivative convoluting integers for parabolas. We used those on synthetic spectra to prove our ability to find spectral features. This method worked well enough for spectra without noise but worked poorly when we added synthetic noise.

A summary of this work, with a table of the criteria for recognition of spectral features, was published in ANALYTICAL CHEMISTRY in December 1961 (Vol. 33, No. 13, p. 25 A). This article discussed averaging of adjacent points for noise reduction but still did not recognize the smoothing algorithm. (This paper, incidentally, also mentioned determination by multiple instruments, one of the key methods of today's chemometrics.)

FOCUS

By early 1962 we had efficient routines for first and second derivatives, but a notebook entry for March 1962 reads: "I need a general purpose convolution program" and defines its characteristics.

Earlier, I had committed to presenting a paper titled "Some Numerical Operations on Analytical Data" at the 15th annual summer symposium of the Division of Analytical Chemistry. The symposium was held in June 1962 at the University of Maryland. In January I wrote to Golay, who was at the Technische Hogeschool in Eindhoven, The Netherlands:

> It would be very helpful if you could join me as co-author. I would plan to call on you primarily for the development and elegant explanation of the derivative functions as well as for some guidance on the type of filtering functions to study.

> I am not as concerned about the oral presentation as I am about the material which will be published in *Analytical Chemistry*. There are some very few references to the method in the literature, but it is apparently not well enough known, especially by analytical chemists.

At about this time, my reading and work with the generalized program and real data prompted me to look more closely at smoothing as well as derivatives. In April 1962 I wrote to Golay:

> The objective of this paper is to extend the application of the methods you suggested for determination of the first and second derivatives into other areas.

The class of methods which should be discussed is characterized by a convolution of the experimental data with a set of integers, followed by normalization. The importance of these methods is that for the smoothing functions and for the derivative functions, the computer program is essentially the same. Thus a single general purpose program which provides for entry of the set of convolution integers and the normalizing factor can handle a very broad class of problems.

One of the basic differences

Marcel Golay—A Memorial

Marcel Jules Edouard Golay, inventor of the open-tubular (capillary) column, died suddenly on April 27, shortly before his 87th birthday. The entire chromatographic community mourns the passing of this active and vital member. At the time of his death, Golay was preparing a plenary lecture on chromatography under turbulent flow conditions for the May meeting of the International Symposium on Capillary Chromatography in Riva del Garda, Italy. This work described how chromatographic measurements can provide information on the properties of the turbulent flow that is otherwise inaccessible. He was also conducting a very difficult experiment on the design of improved open columns and was advising scientists at the Perkin-Elmer Corporation in various high-technology areas.

Marcel Golay was born on May 3, 1902, in Neuchâtel, Switzerland. He graduated in 1924 as an electrical engineer from the Eidgenössische Technische Hochschule (ETH), the Swiss Technical University in Zürich, and joined Bell Telephone Laboratories in the United States. He left Bell in 1928 to pursue graduate studies at the University of Chicago, where he received a Ph.D. in physics in 1931. After graduation he joined the U.S. Signal Corps Engineering Laboratories in Fort Monmouth, NJ. He retired in 1955 as chief scientist of the Components Division and became a consultant to Philco (Philadelphia, PA) in network and information theory and to the Perkin-Elmer Corporation (Norwalk, CT) in scientific instrumentation. During 1961–1962 he was a professor at the University of Technology in Eindhoven (The Netherlands), and from 1963 until his death he was a senior research scientist at P-E.

Although the invention of the open-tubular column was Golay's best-known achievement in the field of chromatography, it was only one of his many contributions to science. Indeed, the immense scientific and technical knowledge of the man was fascinating. His accomplishments span a variety of areas that at first glance appear unrelated but that all include the acquisition, transfer, and processing of information.

In radio communications he is well known for the invention of the dispersionless Golay delay line, a device for detecting the presence of a certain pattern of information in a signal that is passing through a delay line. In information theory and pattern recognition he invented the perfect binary and ternary codes, the only two multierror correction codes ever found. He created the concept of complementary codes that are used worldwide in the Loran C precision radio navigation system and that are still broadcast constantly by countless radio beacons throughout the world. He also developed a number of image signal-processing analysis algorithms. One of these is a complete image-processing language used in an instrument that can successfully identify 17 different normal and abnormal human white blood cells.

In the field of instrumentation Golay made many landmark contributions. In IR spectroscopy the Golay detector is the most sensitive room-temperature detector available and performs essentially to theoretical limits over a wide spectral range. This is a pneumatic detector in which the IR signal heats a small gas volume whose expansion is detected by the motion of a flexible mirror membrane. In NMR spectroscopy, he invented a very elegant system to tune the spectrometer and rapidly achieve the minimum bandwidth. This system decomposes the nonuniform magnetic field in the sample space into its orthogonal spherical harmonics; it is then possible to cancel each function independently. Together with Abraham Savitzky (see p. 921 A of this issue), he developed a smoothing algorithm that permits the reduction of random noise from measured spectra. In chromatography, besides the invention of open-tubu-

between using the digital computer rather than an analog device for performing the function is that a symmetrical set of data around the central point allows the use of functions which are a reasonable fit to the experimental function.

What I would like to have is a "cookbook" procedure (for mathematically unsophisticated chemists like myself, rather than for mathematicians) for generating the set of integers for any desired function and for derivatives of any degree from zero on up. The useful thing, for the paper, would be to have a simple set of rules for obtaining the integers and normalizing function, plus a simple, elegant proof in the appendix.

Golay's reply to this letter became the basis for the appendix. The paper was submitted to ANALYTICAL CHEMISTRY in February 1964 and received a quick review. Of the two reviewers, one said essentially, "nothing new, don't publish" and the other said, "interesting, publish." My reply was that the previously published work had discussed applications in statistical analysis of small numbers of observations. No one, apparently, had applied the techniques to the large numbers of sampled data points that we saw with the newly computerized instruments. Fortunately the Editor, Lawrence Hallett, agreed.

In thinking about why the technique has been so widely used, I've come to the following conclusions. First, it solves a common problem—the reduction of random noise by the well-recognized least-squares technique. Second, the method was spelled out in detail in the paper, including tables and a sample computer subroutine. Third, the mathematical basis for the technique, although explicitly and rigorously stated in the article, was separated from a completely nonmathematical explanation and justification. Finally, the technique itself is simple and easy to use, and it works.

PHOTO COURTESY OF THE PERKIN-ELMER CORPORATION

lar columns, Golay contributed to the investigation of high-speed GC and LC, the influence of instrumental contributions to column performance, and the development of sampling methods.

It is remarkable that this scientist, an electrical engineer by training, received two major awards of the American Chemical Society: the ACS Award in Chemical Instrumentation (1961) and the ACS Award in Chromatography (1981). He was also the recipient of the Distinguished Award of the Instrument Society of America, the Tswett Chromatography Award of the International Symposium on Advances in Chromatography, the Chromatography Anniversary Medal of the Academy of Sciences of the USSR, and the Dal Nogare Award in Chromatography of the Chromatography Forum of the Delaware Valley, as well as many other awards. In 1977 Golay received an honorary doctorate from the Ecole Polytechnique Fédérale of Lausanne, Switzerland. He was the author of more than 90 scientific papers, and he obtained 41 patents. Golay's legacy in high-resolution chromatography will be maintained by the newly established Marcel Golay Medal. The first recipients of this award, presented at the recent International Symposium on Capillary Chromatography, were R. E. Kaiser, R. D. Dandeneau, and E. H. Zerenner.

Discussions with Golay were unusual and exciting experiences. He always went right to the center of the problem, analyzing it at the most profound level, drawing on the necessary contributions of physical chemistry and information theory. Using the required mathematics, he was able to clearly state a model and to derive the consequences of the abstraction in a straightforward manner. The conclusion was a beautiful description of the experiment that had to be performed. Making the device work was rarely easy, but it was always worthwhile. The early papers of Golay on the open-tubular column give an excellent idea of this process and the results.

Few major contributions that can be traced to a single man have, at the same time, had such a profound influence on so many people. How many thousands of chemists have used a capillary column? (It is estimated that in 1987 60% of all GC analyses were carried out on open-tubular columns.) How many have been saved by a diagnosis based on the results of GC/MS analysis? What is the impact on our society of the environmental regulations based on information collected by capillary GC/MS analyses? These contributions reflect the enduring and immeasurable scientific and technical legacy of Marcel Golay.

Georges Guiochon
Leslie Ettre

NEW PRODUCTS

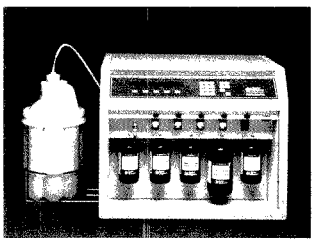

PCR-Mate DNA synthesizer, designed for work involving the polymerase chain reaction (PCR) process, accommodates various scales of synthesis and eliminates the need for HPLC or gel purification. Applied Biosystems **401**

LC. K-Prime 400 series automated process chromatographs consist of a microprocessor-based control unit, software, process chromatograph, and personal computer and user interfaces. The systems accommodate columns from 70 mm to 2 m in diameter. Amicon Division, W. R. Grace & Co. **404**

FT-IR. Model 205 FT-IR spectrometer incorporates a sealed, desiccated optical bench; a computer with high-resolution graphics displayed on an integral monitor; a touch-sensitive, push-button control panel; and a sample mounting system that permits the use of plug-in, prealigned sampling accessories. Nicolet **405**

Electrophoresis. P/ACE System 2000 is a high-performance capillary electrophoresis system with IBM-based computer control. Each capillary is housed in a temperature-controlled cartridge, and buffer and sample vials are sealed to eliminate the risk of evaporation. Beckman **406**

Viscosity. OctaVisc automatic viscosity measuring system, which handles up to eight samples at a time, includes a temperature-controlled sample-handling unit, an optical/electric computer interface unit, and user-friendly software. Design Scientific **407**

Workstation. Omega-4 System 4C chromatography workstation is capable of acquiring data from up to four channels. The system, which is compatible with all major LC and GC instruments, features full-color graphics, screen windows, and drop-down menus. Perkin-Elmer **408**

Spectrometer. Model 300 fiber-optic spectrophotometer is designed for remote near-IR and UV–vis process monitoring and method development. Fiber multiplexing capability for monitoring multiple sample points is available. Guided Wave **409**

GC. Model 69-770P microprocessor-controlled, single-column gas chromatograph features a thermal ionization detector, a precision pressure regulator designed for control of low capillary flow rates, and a choice of five injection modes. Gow-Mac **410**

Detector. SPD-M6A diode array detector for HPLC compensates for array noise and dark current via a temperature-controlled polychromator with two temperature selections. Spectrum and chromatogram files are stored on disk in ASCII format for import into other software packages. Shimadzu **411**

Pump. Model 060 is a 60 L/s turbomolecular pump designed for the production of hydrocarbon-free high and ultrahigh vacuum with low sound levels. The pump is suitable for use in leak detectors and in systems based on MS. Balzers **412**

Pyrolysis. Pyroprobe 1000 allows uninterrupted sequential runs on the same sample at different thermal conditions without removing the sample probe. Computer control of the filament temperature provides for sample processing at a variety of heating rates and final temperatures up to 1400 °C. Chemical Data Systems **413**

Software

Kinetics. Gas kinetics database, available on floppy disk for use on personal computers, contains data on the rates of approximately 2000 chemical reactions. The database can be searched by chemical reactants or by bibliographic reference. National Institute of Standards and Technology **415**

LIMS. ASTRAL features sample management, automated decision making, and report generation capabilities plus a security guard to prevent tampering with data. The system is compatible with most laboratory instruments. Applied Research Laboratories/Fisons Instruments **416**

Manufacturers' Literature

Process analysis. Brochure describes the process diode array spectrophotometer, which uses UV–vis light to determine components in a gas or liquid stream in < 1 s. Du Pont **423**

HPLC newsletter. *Chromatogram,* Vol. 10, No. 1, includes articles on determination of debrisoquine and its 4-hydroxy metabolites in human urine and on separation of catecholamines and indoleamines. 12 pp. Beckman **418**

Fluorescence. Brochure highlights the Model F-2000 fluorescence spectrophotometer, which features scan speeds of 1200 nm/min, slew rates of 200 nm/s, and an intracellular cation measurement option. 8 pp. Hitachi **419**

Monoclonal antibodies. Wall chart and guide provide media recommendations and a general discussion of antibody purification problems. A number of applications are discussed. Amicon Division, W. R. Grace & Co. **420**

LC. Guide discusses instruments for liquid chromatography and sample preparation, including pumps, detectors, fraction collectors, and liquid-handling instruments. 14 pp. Gilson Medical Electronics **421**

Spectrophotometer. Brochure highlights the Spectronic 3000 Array spectrophotometer, which features a sample positioning platform that allows for automated measurement of up to eight samples at one time. Milton Roy **424**

For more information on listed items, circle the appropriate numbers on one of our Readers' Service Cards

Don't inject variables into your chromatography. Use Millex® filter units.

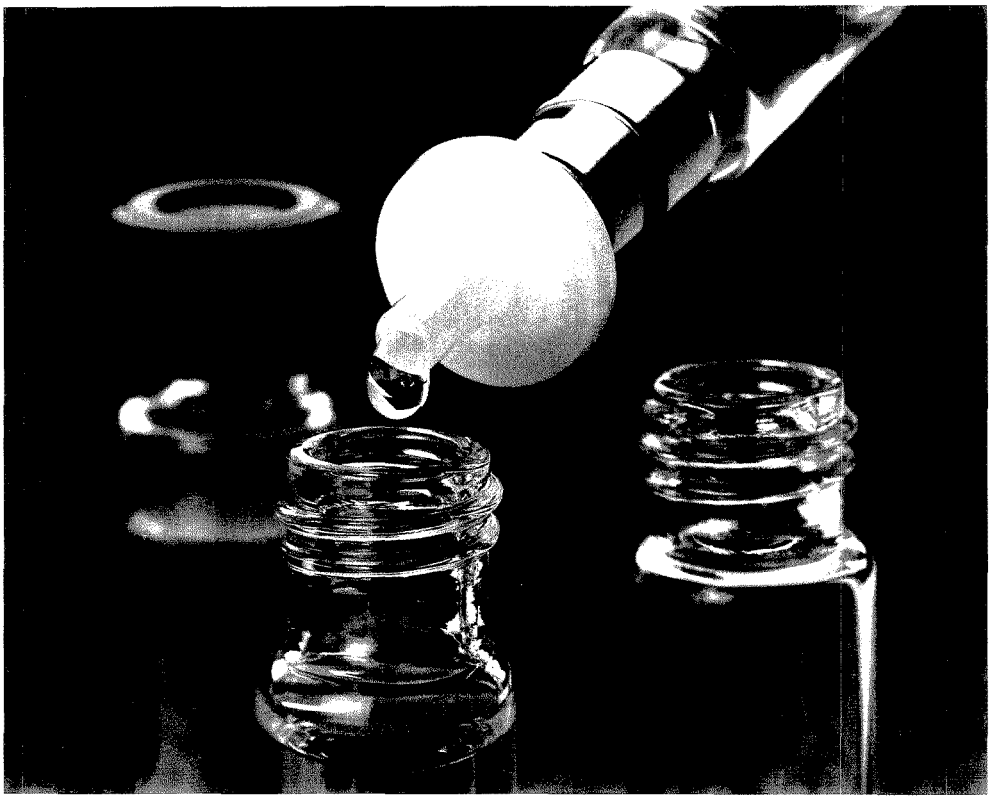

Use Millex HPLC filters, and put an end to particle contamination problems. Maximize column life while improving the consistency of your chromatographic results.

Designed for fast, reliable sample clarification, Millex units remove all particulate contaminants down to the rated pore size. Devices are available in 4 mm, 13 mm, and 25 mm configurations, for sample volumes ranging from less than 1 ml up to 100 ml, and offer these advantages:

Maximum sample recovery. Hold-up volume of 4 mm Millex units is less than 10 µl after air purge. For 13 mm units, less than 50 µl. For 25 mm units, less than 0.1 ml.

Ultraclean design. Membranes are incorporated into solvent-resistant housings. There are no glues, binders, or dyes to add unwelcome extractables to your analyses.

Wide chemical compatibility. Millipore's unique Durapore® membrane is non protein-binding, and compatible with most organic, aqueous, or isocratic solutions. Other membrane types are available to clarify a broad range of samples and solvents.

CIRCLE 96 ON READER SERVICE CARD

Try Millex HPLC filters in your lab—free. We'll send you a free prep kit and a brochure on sample management and reagent purification. Call (800) 225-1380. In Massachusetts, (617) 275-9200. Or write Millipore Corporation, 80 Ashby Rd., Bedford, MA 01730.

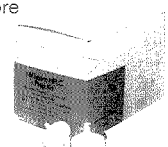

HPLC applications. *Food and Beverage Notes* contains articles on the determination of amino acids in animal blood and tissue, pet food, and animal feeds and on determination of carbamates in foods. 12 pp. Waters Chromatography Division of Millipore 422

Homogenizers. Brochure highlights Models PT 3000 and PT 6000 homogenizers for biomedical and industrial applications. The instruments provide particle sizes down to 1 μm in sample volumes ranging from 0.3 mL to 30 L. Brinkman 430

Electrochemistry. Guide describes electrochemical instruments and systems for LC detection, voltammetric analysis, corrosion measurements, and electrochemical research. EG&G Princeton Applied Research 431

Chlorine. Bulletin discusses total residual chlorine analyzers for field, laboratory, and on-line measurement of residual chlorine in water. Specifications, principles of operation, and applications are presented. Ionics 432

LC. Brochure discusses PRP-X300 ion exclusion LC columns for organic acid and alcohol separations. Chromatograms illustrating a variety of applications are included. Hamilton Co. 433

Catalogs

Spectrometry. Catalog features air-path, vacuum, ultra-high-vacuum, and grazing incidence spectrometers. Also included are stepping motor scan drives, light sources, and detectors. 32 pp. Acton Research Corp. 425

Electrodes. Catalog features pH, metal, ion-selective, reference, and carbon electrodes. Conductivity measuring cells and resistance thermometers are also listed. 48 pp. Metrohm 427

Safety. Catalog includes products for personal protection; liquid storage; spill protection; lab organization; and radioactive handling, storage, and decontamination. 30 pp. Whatman Lab-Sales 428

Radiochemicals. Catalog includes carbon-14 labeled amino acids, carbohydrates, methylated proteins, and dicarboxylic acids. Photographic equipment and supplies for autoradiography are included. 52 pp. Sigma Chemical Co. 426

LC. Catalog features packed and empty columns, tubing, frits, fittings, accessories, and tools. Chromatograms for a variety of applications are included. 136 pp. Anspec 429

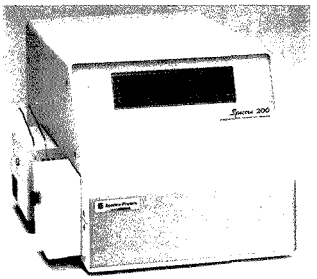

Spectra 200 is a variable-wavelength UV–vis detector that can be programmed for timed wavelength changes, spectral scanning, and gradient baseline correction. Spectra-Physics 402

INDEX TO ADVERTISERS IN THIS ISSUE

CIRCLE INQUIRY NO.	ADVERTISERS	PAGE NO.
22	**Balston, Inc.** Gillett Brown & Associates	883A
20	**Beckman Instruments, Inc.**	896A
24, 25	**Beckman Instruments, Inc.** Cochrane, Chase, Livingston & Company	875A
27	**Beckman Instruments, Inc.** Techmarketing	905A
16	**Bio-Rad Chemical Division** Pan & Associates	888A
18	***Burdick & Jackson Division/Baxter** Nordtrom/Cox Marketing	877A
30	**Fred S. Carver Inc.** Scott Inc. Advertising	919A
32	***Dionex Corporation** Rainoldi, Kerzner & Radcliffe	886A
58	**Galileo Electro-Optics Corp.** Legasse Associates Advertising Inc.	899A
60	***Gilson Medical Electronics, Inc.**	893A
61	****Gilson Medical Electronics SA**	893A
63	**Hamamatsu Corporation** Ketchum/Mandabach & Simms	895A
65	***Hewlett-Packard Company** Brooks Communications	871A
–	**International Marketing Ventures**	919A
75	**ITT Electro-Optical Products Division** Colburn Advertising & Associates, Inc.	914A
92	**Laser Precision Analytical**	881A
90	**Leco Corporation**	OBC
94	**Mattson Instruments, Inc.** Cunningham & Welch Design Group	872A
98	**E. Merck**	882A
96	***Millipore Corporation** Mintz & Hoke, Inc.	925A
110	***Nicolet Analytical Instruments**	884A
120	***Omega Engineering, Inc.** Media Business House	IFC
122	**On-Site Instruments**	882A
125	***Parr Instrument Company** FBA Marketing Communications	892A
127	****Philips Analytical**	902B
140	**Rheodyne, Inc.** Bonfield Associates	901A
154	**Siemens Analytical X-Ray Instruments, Inc.**	879A
152	***Swagelok Company** Falls Advertising Company	917A
156	***Techne, Inc.** Brunswick Advertising	913A
158	***Tekmar Company** Kenyon Hoag Associates	880A
175	***Wheaton** The Wheaton Agency	903A

** See ad in ACS Laboratory Guide.*
*** Company so marked has advertisement in Foreign Regional edition only.*
Advertising Management for the American Chemical Society Publications

CENTCOM, LTD

President
Thomas N. J. Koerwer
Executive Vice President *Senior Vice President*
James A. Byrne **Benjamin W. Jones**
Clay S. Holden, *Vice President*
Robert L. Voepel, *Vice President*
Joseph P. Stenza, *Production Director*

500 Post Road East
P.O. Box 231
Westport, Connecticut 06880
(Area Code 203) 226-7131
Telex No. 643310
FAX No. 203-454-9939

ADVERTISING SALES MANAGER
Bruce E. Poorman

ADVERTISING PRODUCTION MANAGER
Jane F. Gatenby

SALES REPRESENTATIVES

Philadelphia, PA . . . Patricia O'Donnell, CENTCOM, LTD., GSB Building, Suite 405, 1 Belmont Avenue, Bala Cynwyd, Pa. 19004. Telephone: 215-667-9666, FAX: 215-667-9353

New York, NY . . . John F. Raftery, CENTCOM, LTD., 60 East 42nd St., New York, N.Y. 10165. Telephone: 212-972-9660

Westport, CT . . . Edward M. Black, CENTCOM, LTD., 500 Post Road East, P.O. Box 231, Westport, Ct. 06880. Telephone: 203-226-7131, Telex 643310, FAX: 203-454-9939

Cleveland, OH . . . Bruce E. Poorman, John C. Guyot, CENTCOM, LTD., 325 Front St., Suite 2, Berea, Ohio 44017. Telephone: 216-234-1333, FAX: 216-234-3425

Chicago, IL . . . Michael J. Pak, CENTCOM, LTD., 540 Frontage Rd., Northfield, Ill. 60093. Telephone: 312-441-6383, FAX: 312-441-6382

Houston, TX . . . Michael J. Pak, CENTCOM, LTD., Telephone: 312-441-6383

San Francisco, CA . . . Paul M. Butts, CENTCOM, LTD., Suite 1070, 2672 Bayshore Frontage Road, Mountain View, CA 94043. Telephone: 415-969-4604

Los Angeles, CA . . . Clay S. Holden, CENTCOM, LTD., Newton Pacific Center, 3142 Pacific Coast Highway, Suite 200, Torrance, CA 90505. Telephone: 213-325-1903

Boston, MA . . . Edward M. Black, CENTCOM, LTD., Telephone: 203-226-7131

Atlanta, GA . . . John F. Raftery, CENTCOM, LTD., Telephone: 212-972-9660

Denver, CO . . . Paul M. Butts, CENTCOM, LTD., Telephone: 415-969-4604

United Kingdom
Reading, England . . . Malcolm Thiele, Technomedia Ltd., Wood Cottage, Shurlock Row, Reading RG10 OQE, Berkshire, England. Telephone: 073-434-3302, Telex #848800, FAX: 073-434-3848
Lancashire, England . . . Technomedia Ltd., c/o Meconomics Ltd., Meconomics House, 31 Old Street, Ashton Under Lyne, Lancashire, England. Telephone: 061-308-3025

Continental Europe . . . Andre Jamar, International Communications, Inc., Rue Mallar 1, 4800 Verviers, Belgium. Telephone: (087) 22-53-85, Telex #49263, FAX: (087) 23-03-29

Tokyo, Japan . . . Sumio Oka, International Media Representatives Ltd., 2-29 Toranomon, 1-Chome Minato-ku Tokyo 105 Japan. Telephone: 502-0656, Telex #22633, FAX: 591-2530

If your job involves process measurement, here's an opportunity to make an investment in your career....

PROCESS MEASUREMENT AND CONTROL

A New Audio Course from the American Chemical Society

Special 30-day free examination offer for ACS members!

Process Measurement and Control offers you a complete background in every aspect of this area—from understanding the principles fundamental to making these measurements. . .deciding on your application. . .to selecting the equipment to best do it. . .to running your application. Here's what you'll be able to do after taking this course:

- Choose the right equipment for your application
- Obtain better on-line process control
- Optimize the selection of equipment and controller
- Understand process and engineering instrument drawings
- Comprehend manufacturers' literature, including accuracy and sensitivity specifications
- Know how to obtain the proper accuracy of your instrument to meet requirements

In addition, you'll learn about the practical side of equipment selection.....how to:

- Speak the language you need to communicate with equipment vendors
- Protect yourself from over-enthusiastic vendor claims
- Look for the right components when selecting equipment

All in all, this course gives you a complete overview of the theories, instrumentation, and applications of process measurement and control.

Who Should Take This Course

You should, if you are a:

- Scientist or engineer who has just been assigned to do process measurement—to get the background you need
- Manager that has just been given responsibility for a process measurement area—to direct, understand, and communicate with your staff who perform this function
- Manager responsible for training new personnel to perform process measurement—for use in group or self-paced individual learning
- Salesperson for an instrumentation company—to see how your product fits in with the competition and to learn the vocabulary to communicate with your customers

Brief Course Outline

- Introduction
- Measurement—Instrumentation
- Pressure Measurement
- Temperature Measurement
- Flow Measurement
- Control Valves
- Level Measurement
- On-Line Physical Property Measurement
- Analysis Instrumentation—On-Line Chemical Composition Measurement
- Control Instrumentation

The Instructor

Marvin D. Weiss is retired after thirty years of experience in a variety of areas: development for a major instrument company, instrument applications in major chemical companies, academic teaching and consulting, and management of instrument divisions of major design and construction companies.

The Unit

Process Measurement and Control consists of four cassettes (five hours of taped instruction) and a 280-page manual. It comes in one compact package, so that you can keep it with you to study when you want—at work, at home, or even while traveling.

Order your course today! Use the coupon below or call 1-800-227-5558.

Order Form

Please send me **Process Measurement and Control** (Catalog No. A8):

	Qty.	US & Canada	Export	Total
Complete Course	_____	$435	$522	_____
Additional Manuals	_____	$42	$50	_____
			Total order	_____

Payment Options:

1. Payment enclosed (make check payable to American Chemical Society).
2. Purchase order enclosed. P.O. # _____
3. Charge my ☐ MasterCard/VISA ☐ AMEX ☐ Diners Club/Carte Blanche.

Account No. _____

Name of cardholder _____

Expires _____

Signature _____

4. Send me my course to examine free for 30 days. I am an ACS member. ACS membership no. (above your name on your C&EN mailing label): _____

Signature _____

Ship to:

Name _____

Address _____

City, _____

State, ZIP _____

Phone _____

Please allow 3-4 weeks for delivery. Prices quoted in U.S. dollars. Foreign payment must be in U.S. currency by international money order, UNESCO coupons, or U.S. bank draft.

Mail this order form to **American Chemical Society, Distribution Office Dept. 17, P.O. Box 57136, West End Station, Washington, DC 20037.** 17

Analytical CHEMISTRY

EDITOR: **GEORGE H. MORRISON**

ASSOCIATE EDITORS: **Klaus Biemann, Georges Guiochon, Walter C. Herlihy, Robert A. Osteryoung, Edward S. Yeung**

Editorial Headquarters
1155 Sixteenth St., N.W.
Washington, DC 20036
Phone: 202-872-4570
Telefax: 202-872-6325

Managing Editor: Sharon G. Boots

Associate Editors: Louise Voress, Mary Warner

Assistant Editors: Grace K. Lee, Alan R. Newman

Editorial Assistant: Felicia Wach

Director, Operational Support: C. Michael Phillippe

Production Manager: Leroy L. Corcoran

Art Director: Alan Kahan

Designer: Amy Meyer Phifer

Production Editor: Elizabeth E. Wood

Circulation: Claud Robinson

Editorial Assistant, LabGuide: Joanne Mullican

Journals Dept., Columbus, Ohio

Associate Head: Marianne Brogan

Journals Editing Manager: Joseph E. Yurvati

Associate Editor: Rodney L. Temos

Staff Editor: Sharon K. Hatfield

Advisory Board: Bernard J. Bulkin, Michael S. Epstein, Renaat Gijbels, Peter R. Griffiths, Thomas L. Isenhour, Nobuhiko Ishibashi, James W. Jorgenson, Peter C. Jurs, Mary A. Kaiser, David L. Nelson, Lawrence A. Pachla, Ralph E. Sturgeon, George S. Wilson, Mary J. Wirth, Andrew T. Zander, Richard N. Zare *Ex Officio:* Sam P. Perone

Instrumentation Advisory Panel: James B. Callis, Bruce Chase, R. Graham Cooks, L. J. Cline Love, Sanford P. Markey, Ronald E. Majors, Linda B. McGown, Gary W. Small, R. Mark Wightman

Published by the
AMERICAN CHEMICAL SOCIETY
1155 16th Street, N.W.
Washington, DC 20036

Publications Division

Director: Robert H. Marks

Journals: Charles R. Bertsch

Special Publications: Randall E. Wedin

Manuscript requirements are published in the January 1, 1989 issue, page 91. Manuscripts for publication (4 copies) should be submitted to ANALYTICAL CHEMISTRY at the ACS Washington address.

AUTHOR INDEX

Angel, S. M., 1648

Bachas, L. G., 1728
Bartsch, R. A., 1618
Bello, J. M., 1779
Bodor, N., 1723
Bolshov, M. A., 1758
Boutron, C. F., 1758
Brajter-Toth, A., 1709
Bright, F. V., 1768
Brumby, S., 1783
Buck, R. P., 1624

Campiglia, A. D., 1697
Carey, W. P., 1667, 1674
Carroll, M. K., 1768
Chen, J.-Y. T., 1678
Chiari, M., 1602
Chicz, R. M., 1742
Christian, G. D., 1773
Clark, G. D., 1773
Coles, B. A., 1787
Compton, R. G., 1787

DeGrandpre, M. D., 1674
Dyke, J. T., 1667

Ellerbe, P., 1718
Eyring, E. M., 1786

Farag, H., 1723
Fay, M. J., 1686
Fenn, J. B., 1702
Franko, M., 1660
Freiser, H., 1621
Frolow, F., 1618

Garland, W. A., 1732
Gelfi, C., 1602
Gianazza, E., 1602
Glick, M. R., 1694
Gough, D. S., 1652

Hampp, R., 1755
Hannaford, P., 1652
Heben, M. J., 1630
Heo, G.-S., 1618
Hercules, D. M., 1686
Hernández Méndez, J., 1789
Hieftje, G. M., 1768
Hoffmann, D. P., 1686
Hsu, B.-H., 1723
Huber, D. M., 1656
Hughes, K. D., 1656

Iglehart, M. L., 1624
Isidro Agudo, R. M., 1789

Jones, B. T., 1670, 1694
Jorgensen, B. S., 1674

Keil, R., 1755
Kjellström, T. L., 1728

Laserna, J. J., 1697
Leone, J. A., 1791
Lewis, N. S., 1630
Liberato, D. J., 1732
Lowe, R. M., 1652
Lytle, F. E., 1656

Mann, M., 1702
Marinenko, R. B., 1612
McCreery, R. L., 1637
Meiselman, S., 1718
Meng, C. K., 1702
Mikkelsen, S. R., 1737
Moreno Cordero, B., 1789
Morita, K.-i., 1763
Mossoba, M. M., 1678
Myklebust, R. L., 1612
Myrick, M. L., 1648

Nadeau, R. W., 1732
Newbury, D. E., 1612
Niemann, R. A., 1678

Oldfield, N. F., 1732
Olsher, U., 1618
Oquendo, J. N., 1791

Penner, R. M., 1630
Pentoney, S. L., Jr., 1642
Pérez Pavón, J. L., 1789
Phillips, G. R., 1786
Pilkington, M. B. G., 1787
Proctor, A., 1686
Prókai, L., 1723

Quint, J. F., 1642

Rechnitz, G. A., 1737
Regnier, F. E., 1742
Rice, R. J., 1637
Righetti, P. G., 1602
Ruzicka, J., 1773

Sander, L. C., 1749
Sandifer, J. R., 1624
Shimizu, Y., 1763
Shoham, G., 1618
Sinha, P. K., 1602
Smith, B. W., 1670, 1694
Sniegoski, L. T., 1718
Stokes, D. L., 1779

Tokuda, K., 1763
Tran, C. D., 1660

Vo-Dinh, T., 1779
Volk, K. J., 1709

Wangen, L. E., 1667
Welch, M. J., 1718
White, E., V, 1718
Winefordner, J. D., 1670, 1694, 1697
Wise, S. A., 1749

Yost, R. A., 1709
Yu, W.-h., 1621

Zare, R. N., 1642
Ziegler, H., 1755
Zybin, A. V., 1758

PERSPECTIVE: ANALYTICAL BIOTECHNOLOGY

Isoelectric Focusing in Immobilized pH Gradients

Pier Giorgio Righetti,* Elisabetta Gianazza, Cecilia Gelfi, and Marcella Chiari

Chair of Biochemistry, Faculty of Pharmacy and Department of Biomedical Sciences and Technologies, University of Milan, Via Celoria 2, Milan 20133, Italy

Pranav K. Sinha

Institute of Clinical Chemistry and Biochemistry, Universitätsklinikum Rudolf Virchow, Spandauer Damm 130, D-1000 Berlin 19, FRG

Immobilized pH gradients (IPG), introduced as early as 1982, have been plagued by several problems that have hampered their use over the years. We review here recent technical advances that have led to the solution of these problems and to the development of a successful and trouble-free IPG technique. In particular, it was discovered that the buffers used (acrylamido weak acids and bases) were prone to two major degradation pathways, hydrolysis at the amido bond and autopolymerization. A new generation of these buffers is described, in which both degradation routes are completely inhibited. In addition, the formulas and physicochemical properties of these acrylamido buffers are described for the first time. These buffers consist of a set of eight weak acrylamido acids and bases, with pK values evenly distributed in the 3.1–10.3 pH range, and two strong titrants: 2-acrylamido-2-methylpropanesulfonic acid (pK = 1) and QAE-acrylamide (pK > 12). The advantage and limitations of the IPG technique are evaluated. In particular, examples of difficult separations at very acidic and alkaline pH values, where conventional isoelectric focusing would fail, are described. Applications of the IPG technique to the fields of human and animal genetics, for the resolution of "neutral or electrophoretically silent" mutants, are discussed.

INTRODUCTION

Isoelectric focusing (IEF) is now well into its third decade, if we consider it beginning with the early work of Kolin in 1954–1955 on "artificial pH gradients" (i.e., pH gradients generated by diffusion of nonamphoteric buffers titrated to two limiting pH values and then subjected to a quick electrophoretic step). "First generation" IEF (*1*, *2*) was on shaky ground and did not find wide-spread use. "Second generation" IEF, described in 1961–1962 by Svensson (*3*, *4*), was the technique that was used until the early 1980s and became a routine method used in biochemical research. Considering that IEF was proposed before disc electrophoresis (*5*, *6*), the leading technique of the late 1960s and 1970s, and considering the relatively easier manipulations and higher resolving power of IEF, IEF could have immediately overtaken disc electrophoresis had it been better publicized. It should be remembered that disc electrophoresis is seldom used today, whereas the use of discontinuous buffers is routine (e.g., sodium dodecyl sulfate electrophoresis in polyacrylamide gels for mass discrimination of polypeptides).

Table I Problems with CA-IEF Focusing

(A) medium of very low and unknown ionic strength
(B) uneven buffering capacity
(C) uneven conductivity
(D) unknown chemical environment
(E) nonamenable to pH gradient engineering
(F) cathodic drift (pH gradient instability)
(G) low sample load ability

By 1980, it was apparent to many IEF users that there were some inherent problems with the technique that had not been solved in the more than 20 years of use (see Table I). In particular, a most troublesome phenomenon was the near-isoelectric precipitation of samples of low solubility at the isoelectric point (pI) or of components present in large amounts in heterogeneous samples. The inability to reach stable steady-state conditions (resulting in a slow pH gradient loss at the cathodic gel end) and to obtain narrow and ultranarrow pH gradients, aggravated matters. Perhaps, most troublesome was the nonreproducibility and nonlinearity of pH gradients produced by the amphoteric buffers, the so-called "carrier ampholytes" (CA). CA buffers are a class of oligoamino oligocarboxylic acids produced according to, or as a variant of, the classical Vesterberg (*7*) synthesis, in which substances containing an oligoamino backbone are allowed to react with acrylic acid. The quality of these compounds (sold as Ampholine by LKB, Pharmalyte by Pharmacia, Servalyte by Serva, Biolyte by Bio Rad, Resolyte by BDH, etc.) can be demonstrated by focusing carbamylation trains (*8*). Here, protein markers are boiled in urea to produce a series of spots of constant decrements of −1 positive charge because the free $-NH_2$ groups react with cyanate to form substituted ureas. Only Pharmalyte attains a nearly ideal pH profile, as seen by the fairly regular distribution of spots along the pH scale. All other chemicals exhibit quite irregular pH courses (see Figure 1). This is disastrous not only in conventional IEF runs because of the nonreproducibility but also in two-dimensional maps, where constancy of spot position is essential for comparing different runs.

Thus, in 1982 Bjellqvist et al. (*9*) proposed the revolutionary concept of immobilized pH gradients (IPG) obtaining for the first time indefinitely stable and highly reproducible pH gradients by using a set of only seven nonamphoteric weak acids and bases, copolymerized into the fibers of a polyacrylamide gel. This technique ("third generation" IEF) also

0003-2700/89/0361-1602$01.50/0

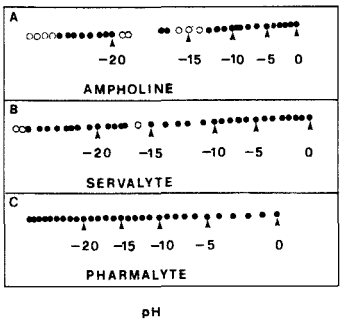

Figure 1. IEF of creatine kinase carbamylation train standards, followed by Coomassie Blue staining: (A) LKB Ampholine pH 3.5–10; (B) Servalyte ISO-DALT grade pH 3–10; (C) Pharmalyte pH 3–10. "Zero" represents the unmodified protein; the negative numbers refer to progressively blocked $-NH_2$ residues, originating new spots in the carbamylation train. Solid circles represent well-stained protein spots; open circles represent fading spots. Modified from figure in ref 8, Tollaksen et al.

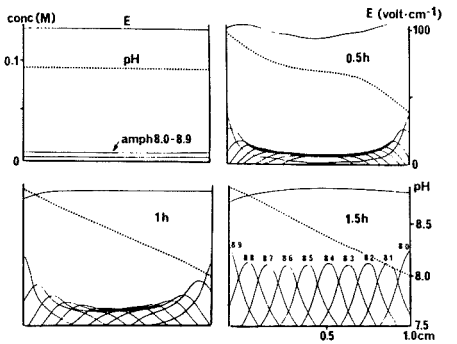

Figure 2. Calculated time development of an isoelectric focusing process involving 10 ampholytes in a closed vessel. The isoionic points of the ampholytes are evenly distributed in the pH 8.0–8.9 range. The initial distribution of the amphoteric buffers is indicated in the upper left diagram. The calculation was performed assuming a constant voltage (100 V/cm) across the system. The anode is positioned to the right in the diagrams. Each x axis represents the distance from the cathode on the same scale as the bottom right figure. Reprinted with permission from C. Schaefer-Nielsen (*50*). Copyright 1986 John Wright & Sons, Inc.

allowed substantial pH gradient engineering, with the concomitant benefit, in ultranarrow pH gradients, of a much increased resolving power (1 order of magnitude greater than that obtained in conventional IEF). Even IPGs, however, over the years, developed some problems, so that in 1985 a "fourth generation" IEF was proposed (*10–12*) consisting of a mixed-bed gel, containing a primary immobilized pH gradient admixed with a secondary pH gradient produced by soluble CA buffers.

A survey of these "four generations" of IEF is beyond the scope of this review. For conventional carrier ampholyte isoelectric focusing (CA-IEF) the reader is referred to a standard text book on IEF (*13*). A historical overview has just appeared (*14*). The main focus of this review will be on newly developing areas, in which IPGs have proven to be far superior than standard IEF techniques. The fields of biochemical (including animal and plant) genetics and of forensic medicine have at present benefited most from the IPG method, since new silent mutants have been detected and unambiguous phenotyping has been made possible. For the most recent developments, the reader is urged to consult a special issue of *Journal of Biochemical and Biophysical Methods* (June/July, vol. 16, No. 2/3, 1988) and the September 1988 issue of *Electrophoresis*, both entirely dedicated to IPGs. The basic technology of IPGs has been amply reviewed (*15–20*).

Nevertheless, as an introduction to the IPG technology, we will give here a brief review on CA-IEF, just to emphasize the major differences between the two techniques.

CONVENTIONAL ISOELECTRIC FOCUSING (CA-IEF)

Briefly, IEF is an electrophoretic technique by which amphoteric compounds are fractionated according to their pI values along a continuous pH gradient. Contrary to zone electrophoresis, where the constant pH of the separation medium establishes a constant charge density at the surface of the molecule, and causes it to migrate with constant mobility (in the absence of sieving), the surface charge of an amphoteric compound in IEF keeps changing, and decreasing, according to its titration curve, as it moves along the pH gradient approaching its equilibrium position (i.e. the region where the pH equals its pI). There, its mobility equals zero and the molecule comes to a stop.

The gradient is created, and maintained, by the passage of current through a solution of amphoteric compounds with closely spaced pI values, encompassing a given pH range. The electrophoretic transport causes these buffers (CA) to stack according to their pIs, and a pH gradient, increasing from anode to cathode, is established. This process is shown in the computer simulation of Figure 2. At the beginning of the run, the medium has a uniform pH, which equals the average pI of the CAs, and uniform CA concentration throughout (Figure 2, upper left panel). At t = 0.5 h, the most acidic (pI 8.0) and the most alkaline (pI 8.9) species have collected close to the anode and cathode, respectively, so that portions of the pH gradient begin to develop. At t = 1 h, the ampholytes have separated further and at this point an almost linear pH gradient has been established, that spans the pH range defined by the pIs of the ampholytes (in the simulation, a system of 10 ampholytes, in equimolar ratios, having pIs spaced at 0.1 pH unit increments in the pH 8.0–8.9 range). At t = 1.5 h, the ampholytes have separated into symmetrical zones having overlapping Gaussian profiles, as predicted by Svensson (*3*, *4*). At this point the system has achieved a steady state maintained by the electric field and no further mass transport is expected, except from symmetric, to and fro micromovements of each species about its pI, generated by the action of two opposite forces, diffusion and voltage gradient, acting on each focused component (this pendulum movement, diffusion ↔ electrophoresis, is the primary cause of the residual current under isoelectric steady-state conditions).

APPPLICATIONS AND LIMITATIONS OF CA-IEF

The technique only applies to amphoteric compounds and more precisely to good ampholytes with small pI–pK_1, i.e. with a steep titration curve around their pI, conditio sine qua non for any compound to focus in a narrow band. This is very seldom a problem with proteins but it may be so for short peptides, that need to contain at least one acidic, or basic, amino acid residue, besides the $-NH_2$ and –COOH terminus (which would make them isoelectric between ca. pH 4 and pH 9 and prevent them from focusing). Another limitation with short peptides is encountered at the level of the detection methods: CAs are reactive to most peptide stains. This problem may be circumvented by using specific stains, when appropriate, or by resorting to immobilized pH gradients (IPG), which do not give background reactivity to nihydrin and other common stains for primary amino groups (e.g., dansyl chloride, fluorescamine).

Table II. Properties of Carrier Ampholytes

1. Fundamental "classical" properties
   (a) buffering ion has a mobility of zero at pH
   (b) good conductance
   (c) good buffering capacity
2. Performance properties
   (a) good solubility
   (b) no influence on detection systems
   (c) no influence on sample
   (d) separable from sample
3. "Phenomena" properties
   (a) "plateau" effect, drift of the pH gradient
   (b) chemical change in sample
   (c) complex formation

In practice, notwithstanding the availability of CAs covering the pH 2.5–11 range, the limit of CA-IEF is in the pH 3.5–10 interval. On statistical grounds, this poses a minor problem, as most protein pI values cluster between pH 4 and 6; it might well be a major problem, however, for specific applications. When a restrictive support like polyacrylamide (PAA) is used, a limit exists also for the size of the largest molecules which retain an acceptable mobility through the gel. A conservative evaluation sets an upper limit around 750 000 daltons when using standard techniques. The molecular form in which the proteins are separated strongly depends upon the presence of additives, like urea and/or detergents. Moreover, supramolecular aggregates or complexes with charged ligands can be focused only if their K_d is lower than 1 μM and if the complex is stable at pH = pI. Aggregates with higher K_d are easily split by the pulling force of the current, whereas most chromatographic procedures are unable to modify the native molecular form.

THE CARRIER AMPHOLYTE CHEMICALS

Table II lists the general properties of the carrier ampholytes, i.e. of the amphoteric buffers used to generate and stabilize the pH gradient in IEF. The fundamental and performance properties are required for a well-behaved IEF system, whereas the "phenomena" properties are the drawbacks or failures inherent to the technique. For instance, the "plateau effect" or "cathodic drift" is a slow decay of the pH gradient with time, whereby, upon prolonged focusing, at high voltages, the pH gradient with the focused proteins is lost in the cathodic compartment. There seems to be no remedy for it (except abandoning CA-IEF in favor of the IPG technique), because there are complex physicochemical causes underlying it, including a strong electrosmotic flow generated by the covalently affixed negative charges in the matrix (carboxyls and sulfate in both polyacrylamide and agarose). In addition, it appears that basic CAs could stick to membranes and, in general, hydrophobic proteins by hydrophobic interaction (which cannot be cured during the electrophoretic run, whereas ionic CA–protein complexes are easily split by the voltage gradient).

In chemical terms, CAs are oligoamino, oligocarboxylic acids, available from different suppliers under different trade names (Ampholine from LKB Produkter AB, Pharmalyte from Pharmacia Fine Chemicals, Biolyte from Bio Rad, Servalyte from Serva GmbH, Resolyte from BDH). There are two basic synthetic approaches: (a) the Vesterberg's approach, consisting in reacting different oligoamines (tetra-, penta-, and hexaamines) with acrylic acid (*21*) and (b) the Pharmacia synthetic process, which involves the copolymerization of amines, amino acids, and dipeptides with epichlorohydrin (*3*). The wide-range synthetic mixture (pH 3–10) seems to contain hundreds, possibly thousands, of different amphoteric chemicals having pIs evenly distributed along the pH scale. Since they are obtained by different synthetic approaches, CAs from different manufacturers are

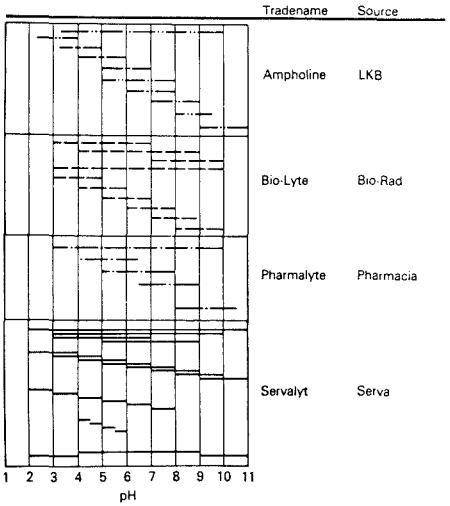

Figure 3. pH ranges of the most common commercially available carrier ampholytes. Reprinted with permission from A. Chrambach and B. An der Lan. Copyright 1981 IRL Press, Ltd.

bound to have somewhat different pIs: thus, if a higher resolution is needed, or for two-dimensional maps of complex samples, we suggest use of blends of the different chemicals (a useful one: 50% Pharmalyte, 30% Ampholine, and 20% Bio Lyte (v/v/v)).

CAs, from any source, should have an average molecular mass around 750 daltons (size interval 600–900 daltons, the higher M_r referring to the more acidic CA species) thus they should easily be separable (unless they are hydrophobically complexed to proteins) from macromolecules by gel filtration. Dialysis is not recommended, due to the tendency of CAs to aggregate, while salting out of proteins with ammonium sulfate seems to completely eliminate any contaminant CAs. A further complication arises from the chelating effect of acidic CAs, especially toward Cu^{2+} ions, which could inactivate metalloenzymes. In addition, focused CAs represent a medium of very low ionic strength (less than 1 mequiv/L at the steady state); since the isoelectric state involves a minimum of solvation, and thus of solubility, for the protein macroion, there could be a tendency, for some proteins (e.g. globulins) to precipitate during the IEF run in the pI proximity. This is a severe problem in preparative runs whereas in analytical procedures it can be lessened by reducing the total amount of sample applied.

Figure 3 gives the pH intervals of the various brands of commercial CAs: narrow cuts encompass from 1 to 3 pH units, whereas wide ranges cover intervals from 7 (pH 3–10) to 9 (pH 2–11) pH units. One pH unit spans, formerly available only from Serva, are now produced also by Pharmacia. There are also a few, 1/2 pH unit spans (from Serva) but in general they afford poor resolution due to the very few buffering species available in these narrow intervals. It is often best to focus in a wider range (1–2 pH units) and locally adjust the pH with the aid of "separators".

IMMOBILIZED pH GRADIENTS. THE CHEMICALS

IPGs are based on the principle that the pH gradient, which exists prior to the IEF run itself, is copolymerized, and thus insolubilized, within the fibers of a polyacrylamide matrix. This is achieved by using, as buffers, a set of six chemicals

Table III. Acidic Acrylamido Buffers

pK[d]	formula	name	M_r	source
1.0	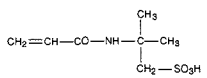	2-acrylamido-2-methylpropanesulfonic acid	207	*a*
3.1	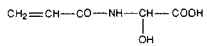	2-acrylamidoglycolic acid	145	*b*
3.6	CH_2=CH-CO-NH-CH_2-COOH	*N*-acryloylglycine	129	*c*
4.6	CH_2=CH-CO-NH-$(CH_2)_3$-COOH	4-acrylamidobutyric acid	157	*c*

[a] Polysciences, Inc., Warrington, PA. [b] Righetti, P. G.; Chiari, M.; Sinha, P. K.; Santaniello, E. *J. Biochem. Biophys. Methods* **1988**, *16*, 185–192. [c] Pharmacia-LKB Biotechnology, Uppsala, Sweden. [d] The pK values for the three Immobilines and for 2-acrylamidoglycolic acid are given at 25 °C; for AMPS (pK 1.0) the temperature of the pK measurement is not reported.

Table IV. Basic Acrylamido Buffers

pK[e]	formula	name	M_r	source
6.2	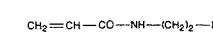	(2-morpholinoethyl)acrylamide	184	*a*
7.0	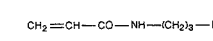	(3-morpholinopropyl)acrylamide	198	*a*
8.5	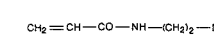	[(*N*,*N*-dimethylamino)ethyl]acrylamide	142	*a*
9.3	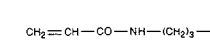	[(*N*,*N*-dimethylamino)propyl]acrylamide	156	*a*
10.3	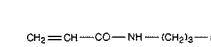	[(*N*,*N*-diethylamino)propyl]acrylamide	184	*b*
>12[d]	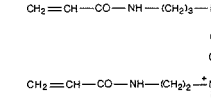	[(*N*,*N*,*N*-triethylamino)ethyl]acrylamide	198	*c*

[a] Pharmacia-LKB Biotechnology, Uppsala, Sweden. [b] Sinha, P. K.; Righetti, P. G. *J. Biochem. Biophys. Methods* **1987**, *15*, 199–206. [c] IBF, Villeneuve La Garenne, France. [d] QAE-acrylamide. [e] All pK values (except for pK 10.3) measured at 25 °C. The value of pK 10.3 refers to 10 °C.

(called Immobiline, by analogy with Ampholine; originally they were seven, but the production of the pK 4.4 buffer has been discontinued, due to its close proximity with the pK 4.6 species) having pK values distributed in the pH 3.6–9.3 range. Until now, not much was known about the Immobiline chemicals, except that they are acrylamido derivatives, with the general formula: CH_2=CHCONHR, where R denotes a set of two weak carboxyls, with pK values 3.6 and 4.6, for the acidic compounds, and a set of four tertiary amino groups, with pK values 6.2, 7.0, 8.5, and 9.3, for the basic buffers. We recently described the characterization of these structures, their synthetic routes, and purification protocol (*21*, *22*). Tables III and IV list all the compounds available today, their chemical names, formulas, and physicochemical data. It can be appreciated that there are a few more than the six commercially available from Pharmacia-LKB (*16*). In fact, we list a total of 10 such buffers. Eight of them are weak acids and bases, with pKs covering the pH 3.1–10.3 range, whereas the other two are strongly acidic (pK 1.0) and a strongly basic (pK > 12) titrants, which were introduced in 1984 by Gianazza et al. (*23*) for producing linear pH gradients covering the entire pH 3–10 range. Computer simulations had shown that, in the absence of these two titrants, extended pH intervals would exhibit strong deviations from linearity at the two extremes, as the most acidic and most basic of the commercial Immobiline would act simultaneously as buffers and titrants (*24*). The synthesis of 2-acrylamidoglycolic acid (pK 3.1) was recently described (*25*) and its use in the separation of strongly acidic proteins proposed (because the pH gradient could be extended to as low as pH 2.5). Also [(*N*,*N*-diethylamino)propyl]acrylamide (pK 10.3) was recently utilized for analysis of strongly alkaline proteins (*26*, *27*). Given the fairly evenly spaced pK values along the pH scale, it is clear that the set of 10 chemicals proposed here (eight buffers, two titrants) are quite adequate to ensure linear pH gradients along the pH 2.5–11 axis (the ideal ΔpK for linearity would be 1 pH unit between two adjacent buffers). The rule ΔpK = 1 is fairly well respected except for two "gaps" (between the pK 4.6 and 6.2 and the pK 7.0 and 8.5 species). Even though we can arrange for highly satisfactory pH gradients, we are still searching for two suitable acrylamido buffers able to close these two gaps.

PROBLEMS WITH THE IMMOBILINE CHEMICALS

Given such a sophisticated and highly reproducible methodology (the first example of true "pH gradient engineering") it is important to know how to handle the Immobiline chemicals to obtain optimum performance run after run. Unfortunately, in the first few years after the introduction of the IPG methodology, not much work was devoted to studying the shelf life of the Immobiline species. As problems begun to be reported by users, we started a long overdue study on the stability of Immobiline buffers (*28*). Given their structure, it was apparent that these chemicals could degrade through two major pathways: (1) autopolymerization (a simple check for it is that the solution becomes slightly opalescent) and (2) hydrolysis at the amide bond, thus splitting the acrylamide moiety from the buffering group at the other extremity of the molecule (producing free acrylic acid and an amino acid in the case of the acidic immobilines and free acrylic acid and a diamine in the case of the basic immobilines). In both cases

the results of an IPG experiment would fail. Our studies led us to conclude that the best way to store the Immobiline chemicals would be to titrate their solutions (0.2 M in water) to ca. pH 4 (this ensuring absence of hydrolysis, autopolymerization and inhibiting also CO_2 absorption in the case of the basic buffers). Although recommended, this procedure was seldom used because it made any attempt at checking the pH of the limiting solutions when preparing any desired pH range difficult. Thus, we proposed the most simple alternative, that of dispensing the stock immobiline solutions (reconstituted to 25 mL) into 5-mL aliquots, which would be kept frozen at −20 °C.

Hydrolysis of Immobiline. However, it was later discovered that even in the frozen state some of the alkaline Immobilines (notably the pK 9.3 species) would degrade, notwithstanding the low temperature value (*29*). The apparent degradation of the pK 9.3 chemical was as high as 20% per year, indeed much too high for reproducible results, as expected from the Immobiline technology. It appears strange that hydrolysis should occur in the frozen state, yet reactions in frozen solutions are not uncommon; e.g., Kiovsky and Pincock (*30*) have reported the spontaneous mutarotation of glucose. In our case, since the Immobiline pK 9.3 is a liquid, it could be hypothesized that, during freezing, the aqueous solvent and the liquid immobiline would separate into two distinct phases. Traces of humidity in the pure Immobiline phase (which would have a rather high pH, since a 0.2 M solution already exhibits an apparent pH value of 11.5) would thus favor a spontaneous hydrolytic process.

Autopolymerization. We were dismayed to discover the instability of the Immobiline chemicals; however, soon a new, more devastating phenomenon was uncovered, that of autopolymerization. This was also quite harmful and affected the reproducibility of IPGs. Like hydrolysis, autopolymerization occurs particularly in the four alkaline Immobilines, is purely autocatalytic, and is greatly accelerated by deprotonated amino groups (*31*). By this process, oligomers and n-mers are formed, which stay in solution and can even be incorporated into the IPG gel, because (in principle) they still contain an olefinic bond at one extremity (unless they anneal to form a ring). These autopolymerization products range in size from simple dimers and trimers to molecules having the same elution volume of a 64 000-dalton protein, like hemoglobin. Analysis of the pK 9.3 Immobiline stored frozen revealed, after more than 6 months of storage, the presence of ca. 20% polymer (Figure 4). These products of autopolymerization, when added to proteins in solution, are able to bridge them via two unlike binding surfaces (ionic on one side, hydrophobic in the opposite surface); a lattice is formed and the proteins (especially larger ones, like ferritin, α_2-macroglobulin, thyroglobulin) are precipitated out of solution. This precipitation power is quite strong and begins already at the level of short oligomers (>decamer). As a short-term remedy, we have described an easy method for oligomer removal, based on adsorption onto hydrophobic polymer phases (e.g., the XAD-2 polymer or a C_{18}-bonded phase) (*32–34*) at alkaline pH values, where the n-mers of alkaline Immobiline species would exhibit a marked hydrophobic character. It turned out that this problem of autopolymerization, long neglected or simply ignored by all of us, had in fact plagued most of the users of the IPG technique up to the year 1988. For scientists trying to apply the IPG method as a first dimension in 2-D maps, the results were disastrous. As an example, Hochstrasser et al. (*35*) described substantial losses of all polypeptide chains, in 2-D maps of human sera, larger that 100 000 daltons, no doubt due to their precipitation out of solution by oligomers and n-mers present in alkaline Immobilines. In addition, soluble homo- and hetero-Immobiline polymers, prepared ad hoc, are able to precipitate out of solution also some smaller proteins having a peculiar amino acid composition (e.g., histones and the "high-mobility group" chromatin proteins) (*36, 37*).

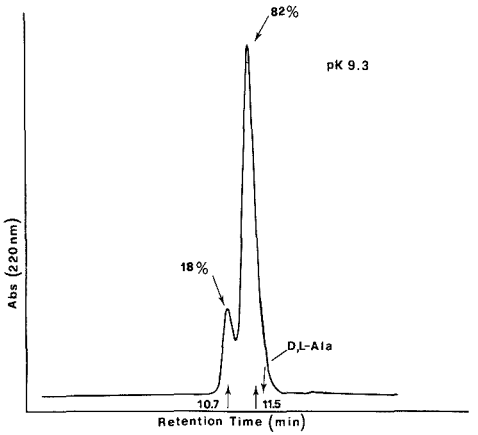

Figure 4. Control of the degree of autopolymerization of Immobiline chemicals. Analysis performed by HPLC in a Bio-Gel TSK column. Samples and column were buffered at pH 6.8 with 20 mM phosphate. Ten microliters of 50 mM, pK 9.3, Immobiline was injected and eluted at 1 mL/min flow rate. The eluate was monitored at 220 nm and automatically integrated. Note the large amount of polymeric material (18%) present in the sample. D,L-Ala: elution position of alanine, marker of the column total volume. Reprinted with permission from ref 31. Copyright 1987 VCH Verlagsgesellschaft mbH.

A New Generation of Immobiline. Given the above findings, it was clear to all IPG users that the technique needed a new foundation if it was to survive and gain widespread acceptance. Gåveby et al. (*38*) recently described a solution where the Immobiline chemicals are used in a solvent where neither degradation occurs. (1-propanol seemed to possess these special requirements). During the summer of 1988 of new generation, called Immobiline II, was launched. The chemicals are supplied directly as 0.2 M aqueous solutions, (laced with inhibitor) for the acidic species, and in 1-propanol for the basic compounds. Before, all immobilines were supplied as free powders or liquids in brown bottles to which it was necessary to add 25 g of water to produce a 0.2 M solution.

There were several reasons for adopting 1-propanol as solvent for alkaline Immobiline. First of all, the vapor pressure and boiling point of 1-propanol are about the same as those of water. In addition, 1-propanol is fully miscible with water. However, there are some minor drawbacks in using 1-propanol, which the users of IPGs should be aware of. At the maximum concentration of 1-propanol (ca. 10%, in formulations utilizing all four alkaline Immobilines) IPG gels may not polymerize satisfactorily and may become gluey (it is known that alcohols have in general an inhibitory power on polymerization). In such cases, we suggest increasing the amount of catalysts until proper polymerization is achieved (in general, at least 20% more of both catalysts, TEMED and persulfate, should be adopted). The second effect is simply due to the decrease of the dielectric constant in the presence of 1-propanol. At the maximum added level (10%) there is a nonnegligible effect on the pK values of Immobiline, a positive shift (+0.07 pH units) for the acidic and a negative shift (−0.12 pH units) for the alkaline species. However, because the Immobiline gels are routinely washed, the 1-propanol will only be present during polymerization but not during the IPG run, so no detrimental effects should be observed.

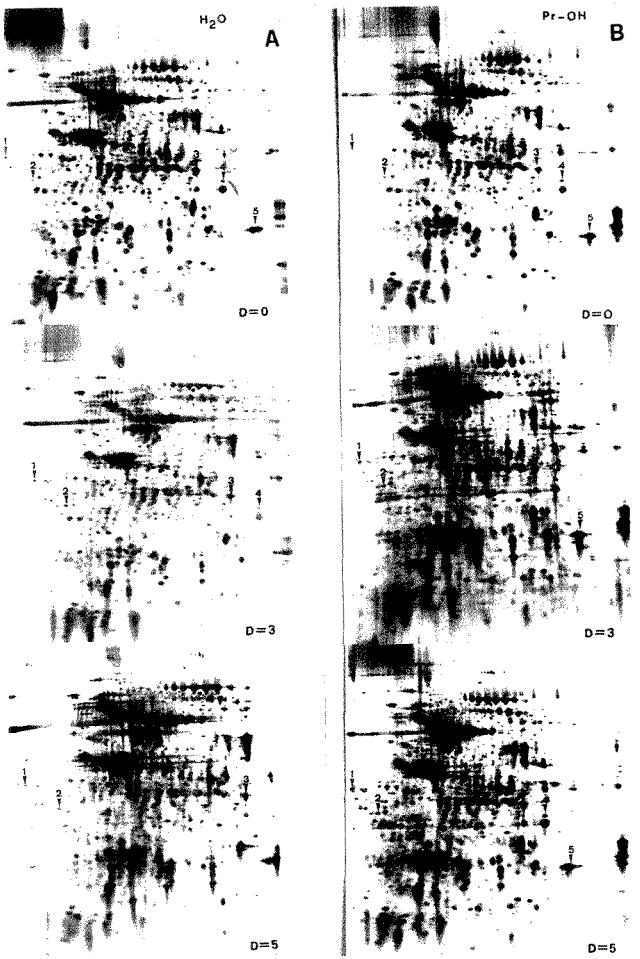

Figure 5. Comparison of 2-D maps with the four alkaline immobilines aged in water (H_2O; A) or in 1-propanol (Pr-OH; B). First dimension: IPG pH 4-8 interval, 4% T ([grams of acrylamide + grams of bis(acrylamide)]/100 mL solution), 4% C ((grams of acrylamide)/%T) gel in presence of 8 M urea and 0.5 M Nonidet P-40 (NP-40). Second dimension: horizontal sodium dodecyl sulfate electrophoresis (SDS-PAGE); stacking gel 6% T, in 125 mM Tris–HCl, pH 6.8 and 0.1% SDS; running gel 12–15% T gradient in 375 mM Tris–HCl, pH 8.8 and 0.1% SDS. Sample: *Vicia faba*, cv. Kristall. Ground bean seeds extracted in a lysis buffer containing 9 M urea, 2% NP-40, 2% 2-mercaptoethanol, and 0.8% Ampholine pH 3.5–10. Two acidic (no. 2 and 3) and three basic (no. 3–5) spots are numbered in the map. In A, the basic Immobilines have been dissolved in water and incubated at 60 °C for zero time ($D = 0$), 3 days ($D = 3$), or 5 days ($D = 5$). The same applies to B, except that the basic Immobilines were dissolved in 1-propanol. Reprinted with permission from ref 38. Copyright 1988 Elsevier Science Publishers B.V.

In forced aging experiments, the pK 7.0 Immobiline, kept in 1-propanol for 5 days at 60 °C, failed to reveal any trace of acrylic acid (the detection limit being 0.03 mol %) whereas, when dissolved in water, and stored at 25 °C, after 40 days had hydrolyzed to an extent of 6%. If we accept 1% acrylic acid as the maximum tolerable level of degradation in the Immobiline II generation, we can ask how long a storage time would be required to reach this cut-off limit. In an Arrhenius plot, by extrapolation, it appears that to reach this guard level (1% acrylic acid), the pK 3.6 immobiline should be stored 1200 days and the pK 4.6 Immobiline as long as 4800 days (both at a temperature of 8 °C).

At the beginning, it was though that, in order to guarantee this much extended stability, the alkaline Immobilines should be stored in totally anhydrous 1-propanol. We then realized that, upon prolonged use, simply by opening and closing the bottles, these solutions would quickly absorb substantial moisture from the air; thus, we decided that the solvent should contain 1% water. Any doubts about the validity of this approach were readily dispelled. In Figure 5 (2-D maps of seed proteins), the multitude of spots remain remarkably constant when using propanol-dissolved alkaline Immobilines, even upon aging, whereas, when the same species are dissolved in water, as was previously done, and subjected to forced aging, all the train of alkaline spots are quickly lost at the cathodic end (take as reference spots no. 3 to 5).

LIMITS OF IPGs: HOW TO BREAK BARRIERS

When trying to formulate IPG recipes outside the pH 4–10 range, e.g., a more acidic (pH 3–4) or more alkaline (pH 10–11)

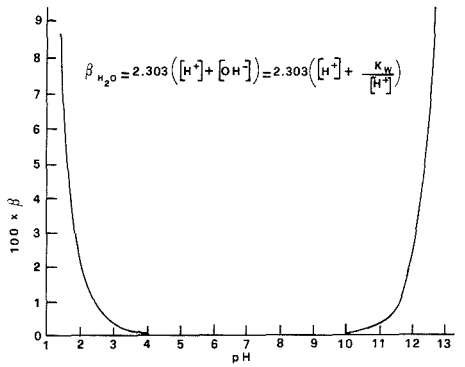

Figure 6. Buffering power (β) of water along the pH axis. For calculations, we have taken as pK of the base H^+ the value of −1.74 and as pK of the conjugated acid OH^- the value of 15.74 (the molarity of water being 55.56). K_w is the ionic product of water. It is seen that water does not have any appreciable buffering power in the pH 4–10 interval. Calculations and simulations are according to the computer program in ref 23 and 24.

IPG interval, one is faced with severe problems, as two new "Immobilines" become operative, a weak base with a pK = −1.74 and a weak acid with a pK = 15.74. They are the H^+ and OH^- ions in equilibrium with undissociated water. It might be argued that their pK values are so remote from the extremes of even the most extended IPG intervals (pH 2.5–11) that they should not alter these pH values. They do, in fact, as there are constantly 55.56 mol of water present throughout the systen (hence the provocative concept of water as an Immobiline) vs ca. 3–10 mM of each buffering Immobiline, as adopted in most IPG formulations. The effects of water on the system can be appreciated in Figure 6: it is seen that already at pH 3 and pH 11 the buffering power (β) of water is not negligible, whereas outside these limits it rises so sharply as to nullify any attempt at using IPGs in these regions. In addition to the problems of the buffering power of water, there is another serious drawback to using IPGs at these pH extremes: the matrix acquires a net charge, negative at lower pH, positive at high pH (e.g., at pH 3 the Immobiline matrix must contain 1 mM extra carboxyls to neutralize the 1 mM protons defining this pH value in bulk water; at pH 11 it will bear an extra 1 mM positively charged amino groups for balancing the 1 mM hydroxyls in solution). These excess bound charges will produce, during the electrophoretic run, a strong electrosmotic flow (proportional to the applied voltage gradient) which will eventually dry out the cathodic and anodic extremes, with consequent burning of the gel matrix. There is an additional problem, moreover. At very low and high pH values, the background conductivity becomes prominent, much higher than the conductivity of the IPG gel. As a result of this, ampholytes will focus at these pH extremes with distribution profiles exhibiting both skewness and curtosis (in other words, they should produce strongly asymmetric and broad peaks), due to the fact that the voltage gradient across the gel will be strongly uneven (i.e. quite low in the region of high conductivity and quite high in regions of low conductivity). Thus, it might event be doubtful that focusing at these pH extremes could be feasible at all. On the contrary, we have obtained excellent separations in the pH 3–4 and pH 10–11 ranges by resorting to viscosity gradients (which act as quenchers of conductivity and electrosmosis) incorporated in the gel matrix. These viscosity gradients (in general sucrose or sorbitol, up to 30%) will be oriented so as to have the denser part in the most conducting region of the gel (*39*, *40*). Figure 7 shows the effect of incorporating these viscosity gradients

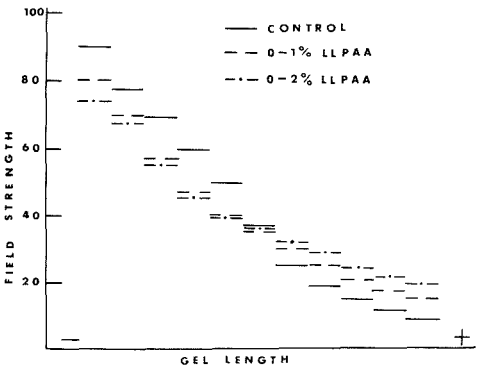

Figure 7. Use of "conductivity and electrosmosis quenchers" at extreme pH values in IPGs. Voltage gradients across an Immobiline pH 3–4 gel. Three gels were made, a control and two additional ones containing a 0–1% and a 0–2% gradient of liquid linear polyacrylamide (LLPAA). All gels were prerun overnight at 800 V/cm, then, while under a total voltage drop of 500 V (over a 9.5 cm electrode distance), segmental voltage gradients were measured at 6.5 mm increments from cathode to anode by moving manually the voltage probe across the pH gradient. In the graph, each horizontal bar represents a 6.5 mm gel distance. The gel polarity is marked by minus and plus signs. The ordinate units are V/cm. Reprinted with permission from ref 40. Copyright 1986 VCH Verlagsgesellschaft mbH.

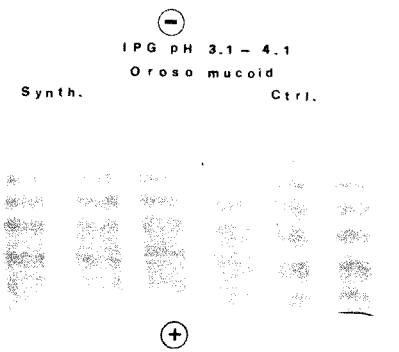

Figure 8. Isoelectric focusing of orosomucoid in an IPG pH 3.1–4.1 gradient. The gel was a 5% T, 4% C matrix, containing 20 mM of pK 3.6 Immobiline as buffering ion. The gel was washed, dried, and reswollen in a cassette in 0–30% sorbitol gradient (dense part at the anode) containing 0.8% Ampholine pH 3.5–5.0. Twenty microliters of orosomucoid purified from human serum (30 μg of total protein) was added in pockets precast at the cathode. Focusing was at 700 V for 5 h at 10 °C. Staining was with Coomassie Blue R-250. Two gels were run: one containing a synthetic (Synth.) pK 3.6 acrylamido buffer (as given in Table III; lanes 1–4 from left), and a control (Ctrl.) gel made with commercial Immobiline (right panel; lanes 5–7 from left). The samples in the seven lanes are identical. Reprinted with permission from ref 21. Copyright 1989 MacMillan.

in the gel (in this particular case, a gradient of linear liquid polyacrylamide, LLPAA, had been polymerized within the gel fibers; however, a sorbitol density gradient will be easier to prepare): as the viscosity is increased toward the most conducting gel regions (pH 3 at acidic, pH 11 at alkaline values) the voltage gradient over the gel length (which drops exponentially following the increments of conductivity) tends to be smoothed. As a result of a more even voltage profile, good focusing is thus ensured even under the most adverse conditions (*25–27*).

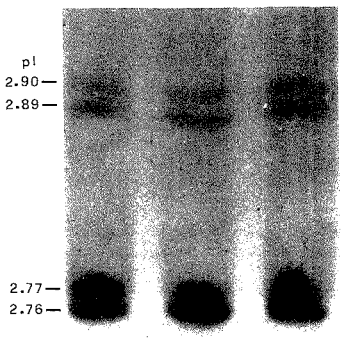

Figure 9. IEF of pepsin. A 4% T, 4% C IPG matrix in the pH 2.5–3.5 interval was made, containing 20 mM 2-(acrylamido)glycolic acid as buffering ion and the p*K* 9.3 Immobiline as titrant. The gel was polymerized in the presence of 0.5% Ampholine pH 2.5–4 and was 0.5 mm thick and 18 cm long. Thirty microliters of pepsin from pig stomach mucosa was loaded in pockets precast at the cathode. The gel was not prefocused. Running conditions: 2 h at 300 V followed by 5 h at 800 V, 10 °C. Staining with Coomassie Brilliant Blue R-250 in copper sulfate. The pIs were derived by linear interpolation from the gradient slope estimated by computer simulations. The picture is a closeup of the four focused pepsin bands, encompassing 6 cm of the entire gel length. The samples in the three lanes are identical. Reprinted with permission from ref 25. Copyright 1988 Elsevier Science Publishers B.V.

It is of interest to see some applications of focusing at pH extremes. Figure 8 gives an example of an IPG separation of orosomucoid purified from human serum and analyzed in a pH 3.1–4.1 range. The protein is resolved into six zones, isoelectric in the pH 3.2–3.7 region. The same number of bands can be observed in conventional IEF, but with reduced resolution and zone distortion (*41*). By use of the new p*K* 3.1 Immobiline, an even more acidic, pH 2.5–3.5, IPG gradient could be created. At such extreme pH conditions, pepsin is resolved into four isozymes, two major, with pI values 2.76 and 2.78, and two minor, with pI values 2.89 and 2.90 (Figure 9). All four forms possessed enzyme activity as demonstrated by in situ zymogramming with a casein–agar overlay (*25*). There are no known examples of focusing in gels phases in CA-IEF at such low pH values, and with such remarkable resolution. In sucrose density gradients, Stenman (*42*) attempted to create low pH gradients by resorting to mixtures of free acids of different strengths. However, nothing below pI 3.1 could be focused and steady-state patterns could never be obtained. In addition, the pH profile was quite irregular. At the opposite pH extreme, a comparison is made of focusing oligoclonal immunoglobulin bands of sera from myeloma patients in CA-IEF vs IPG gels (Figure 10). In some sera, there is a clear indication in CA-IEF of one major band focusing in proximity of pH 10 (Figure 10A, tracks with arrow). When the same samples are analyzed in an IPG spanning a pH range of 6–10.5, this major immunoglobulin band is seen to be resolved into different components (Figure 10B). In a narrower pH range (8–10.5), the same sample is seen to be resolved into three major zones with traces of lower pI components (Figure 10C). In conventional IEF, there is no way to properly control the pH at alkaline values and, notwithstanding the existence of a pH 9–11 CA interval, rarely such gradients can be extended above pH 10, if they can reach this pH value at all. In IPGs, immobilization of the buffers and proper gel shielding from atmospheric CO_2 allow reproducible separations up to pH 11 (*26*, *27*). It should be remembered that, even at such pH extremes, IPG matrices are remarkably

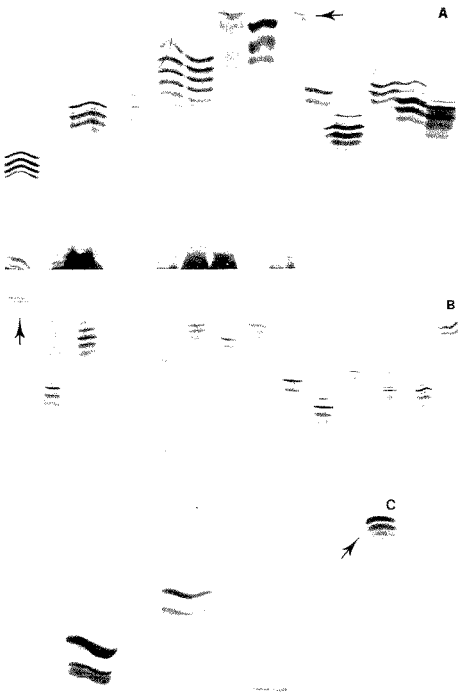

Figure 10. Focusing of oligoclonal immunoglobulin bands from sera of patients with myeloma: (A) CA-IEF in a pH 6–10 Ampholine range; (B) IPG in a pH 6–10.5 interval; (C) IPG in a pH 8–10.5 range. All gels were stained with Coomassie Blue (100 μg of total serum protein applied per track). The arrow indicates a sample with a high pI (ca. 10) immunoglobulin band (A), split into three major components in the two IPG gels (B and C). The reduced stain intensity of this band in A is probably due to its loss in the cathodic compartment.

stable, but the proteins may not be stable, so that separations should be quite rapid. In fact, due to the marked increase in conductivity at very low and high pH values, runs can be terminated in only a few hours, even in 1 pH unit ranges, which in general require an overnight run.

EFFECT OF SALTS ON PROTEIN PATTERNS IN IPG GELS

Since its inception, the IPG technique was recognized as being quite tolerant of the salt levels in the sample. This was publicized as one of the biggest advantages of the IPG technique when compared with CA-IEF, which was known to be quite sensitive to even low salt levels in the sample. Thus biological samples (containing high salt and dilute proteins) could be run in IPGs without prior dialysis or concentration. This is only partially true. It is true with regard to the IPG matrix which, in principle, tolerates large amounts of salt; but it is not true with regard to the protein sample. Righetti et al. (*43*) recently demonstrated that salts formed from strong acids and bases (e.g., NaCl, Na_2SO_4, Na_2HPO_4), present in a protein sample applied to an IPG gel, induce protein

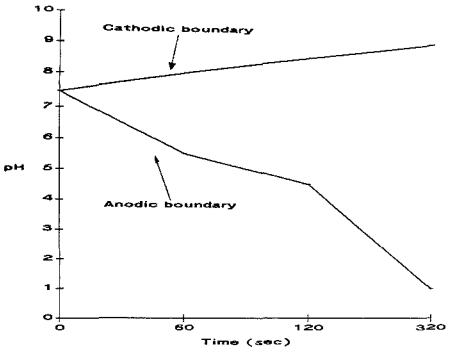

Figure 11. Assessment of pH of salt ion boundaries in the sample zone as a function of time. Pockets cast in the gel middle (pH 7.5) were filled with 20 μL of 100 mM NaCl. The cathodic and anodic edges were covered with strips of alkaline and acidic pH indicators, respectively. The pH in the two boundaries was assessed by visual inspection of color changes at the given time intervals at constant 2000 V. Reprinted with permission from ref 43. Copyright 1988 VCH Verlagsgesellschaft mbH.

Table V The "Pentalogue" of IPGs

1 avoid high salt levels in your sample (>40 mM)
2 avoid salts formed by strong acids and bases (e.g., NaCl, Na_2SO_4, Na_2HpO_4)
3 in presence of high salt levels, add high levels of CA (e.g., 10% CA to 100 mM salt)
4 if salt is needed for sample solubility, use salts formed from weak acids and bases (e.g., Tris–acetate, Tris–glycinate, any of the Good's buffers (e.g., ACES, ADA, MOPS, etc.) titrated around the p*K* of their amino groups
5 in presence of high salt levels, run your sample at low voltage for several hours (e.g., 500 V for 4 h) so as to prevent formation of strongly acidic and alkaline boundaries

modification (e.g., oxidation of the iron moiety in hemoglobin) (Hb) even at low levels (5 mM) and irreversible denaturation (precipitation) at higher levels (>50 mM). This effect is due to production of strongly alkaline cationic and strongly acidic anionic boundaries formed by the splitting of the salt's ion constituents, as the protein zone *is not and cannot be buffered by the surrounding gel until it physically migrates into the IPG matrix*. In order to explain the phenomenon in more detail, Figure 11 shows what happens in the sample liquid droplet, containing high salt levels (in this case, 100 mM NaCl), as soon as the voltage is applied. Within a few minutes, at an applied voltage drop of 200 V/cm, the anodic end of the sample layer reaches a pH as low as 1, with an apparently more modest pH increment in the rear (cathodic) boundary. These extreme pH values generated in the two boundaries are also a function of the initial applied voltage (Figure 12). At moderate voltage gradients (e.g., 50 V/cm) no adverse pH boundaries are generated, whereas at progressively higher voltages, strong pH zones are generated, which cause the denaturation and precipitation of the protein macroions present in the sample layer. Substitution of "strong" salts in the sample zone with salts formed by weak acids and bases, e.g., Tris–acetate, Tris–glycinate, Good's buffers, essentially abolishes both phenomena, oxidation and irreversible denaturation. Suppression of strong salt effects is also achieved by adding, to the sample zone, carrier ampholytes in amounts proportional to the salt present (e.g., by maintaining a salt:CA molar ratio of ca. 1:1). Low-voltage runs for extended initial periods (e.g., 4 h at 500 V) are also beneficial. Table V summarizes all these recommendations. With these latest findings, we feel that the IPG technique is now trouble-free and can

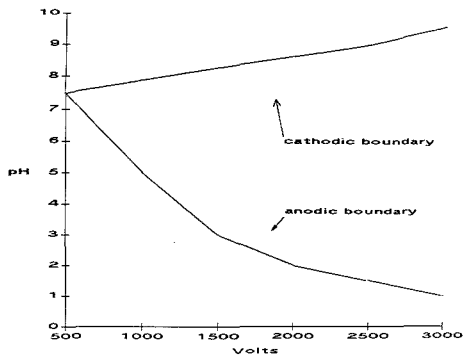

Figure 12. Assessment of pH of salt ion boundaries in the sample zone as a function of applied voltage. The same experiment as in Figure 11 was repeated, except that pH estimations were made as a function of different voltage gradients applied (from 500 to 3000 V) after 10 min from application of the electric field. Note that here and in Figure 11 the alkaline pH estimate must be regarded as highly approximate, since the pH indicators, being negatively charged, move against the Na^+ boundary toward lower pH values. Conversely, the pH of the anodic boundary is a much better estimate, since the pH indicator, when it starts leaching out of the filter paper strip, moves with the Cl^- boundary. Reprinted with permission from ref 43. Copyright Verlagsgesellschaft mbH.

be safely replicated in any laboratory where high-resolution is needed.

ANALYSIS OF NEUTRAL MUTANTS

With conventional IEF it is very difficult to engineer pH gradients narrower than 1 pH unit (in fact most CA ranges commercially available encompass 2 to 3 pH units). As a result of this, the resolving power of CA-IEF rarely exceeds 0.01–0.02, while in IPGs a limit of ΔpI = 0.001 pH unit has been achieved (ΔpI, or resolving power, is the difference in isoelectric points between a protein and the nearest resolved contaminant, given in pH units) (*9*). With a ΔpI like that, it should be possible to resolve even neutral mutants, i.e. those carrying a spot mutation involving amino acids with no ionizable side chains (thus called) "electrophoretically silent"), undistinguishable by standard electrophoretic analysis. A case in point is given in Figure 13: when analyzing a sample of fetal hemoglobin (Hb F, from a heterozygous for Hb Sardinia, AγγT, carrying a Ile-75 → Thr mutation in the γ chains) this mutant was hardly resolved from the "wild-type" HbF by conventional CA-IEF (upper panel) even though the IEF pattern gave a clear hint of sample heterogeneity. When the same separation was repeated in an IPG interval of 0.25 pH units (central panel) adequate separation was obtained between these two species. In reality the situation is more complex than that. Even normal newborns contain in their cord blood two HbF tetramers, called Aγ and Gγ (in a ratio of ca. 1:4) produced by two genes carrying an Ala-136 → Gly substitution in the γ chains. The latter species have not been resolved by any chromatographic (including HPLC) or electrophoretic technique but now, in a 0.1 pH unit interval IPG run, they could be fractionated into single components (lower panel). The identity of these two bands was confirmed by eluting the two zones from the IPG gel, preparing heme-free chains (acid–acetone powder) and direct analysis of the gamma chains by conventional IEF in 8 M urea and 2% neutral detergent (Nonidet P-40). It was shown that the higher pI band contained only the Aγ fetal chain, whereas the lower pI species essentially comprised only Gγ chains. In addition, the ratio between the two bands was 1:4, as expected from genetic expression of these two Hb's (*44*). Note that the difference

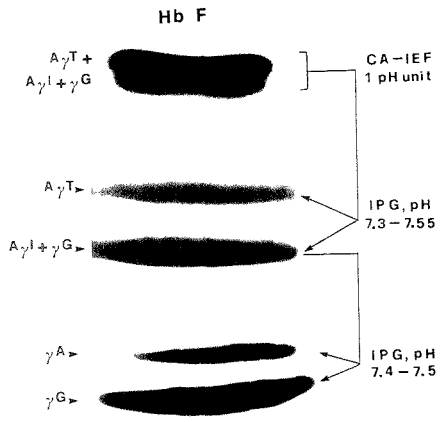

Figure 13. Focusing of umbilical cord lysates from an individual heterozygous for HbF Sardinia (for simplicity, only the HbF bands are shown, and not the two other major components of cord blood, i.e. Hb A and HbF_{ac}): (upper) focusing performed in a 1 pH unit span in CA-IEF, note that broadening of the HbF zone occurs, but not splitting into well-defined zones; (central) same sample, but focused over an IPG range spanning 0.25 pH units, (bottom) focusing of the lower band in central panel, but in an IPG gel spanning 0.1 pH unit. The resolved Aγ/Gγ bands are in a 20:80 ratio, as theoretically predicted from gene expression. Their identity was ascertained by eluting the two zones and fingerprinting the γ chains.

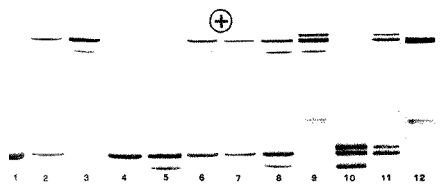

Figure 14. Immobiline gel, pH range 6.7–7.7, showing selected Hb phenotypes in short tail land race sheep. Samples: (1) $B\alpha^{Le}$; (2) $AB\alpha^{Le}$; (3) $A\alpha^{Le}\alpha^{Hi}$; (4) $B\alpha^{Le}\alpha^{Hi}$ (α^{Hi} weak); (5) $B\alpha^{Le}\alpha^{Hi}$; (6 & 7) $AB\alpha^{Le}\alpha^{Hi}$ (α^{Hi} weak); (8) $AB\alpha^{Le}\alpha^{Hi}$; (9) $A\alpha^{A1Le}\alpha^{Hi}\alpha^{Le}$; (10) $B\alpha^{A1Le}\alpha^{Hi}\alpha^{Le}\alpha^{Hi}$; (11) $AB\alpha^{A1Le}\alpha^{Hi}\alpha^{Le}$ (α^{Hi} weak); (12) $A\alpha^{Le}$. Reprinted with permission from Braend et al. Copyright 1987 Danske Dyrlaegeforening.

in isoelectric points between the two species is barely 0.003 of a pH unit (pI 7.450 for Gγ vs. 7.453 for Aγ), which means that our system can attain a resolution of $\Delta pI = 0.001$ pH unit, as predicted (*9*).

Hemoglobins (Hb) have also been used as a model to study genetic polymorphism in animals, like sheep (*45*), cattle (*46*), domestic dogs (*47*) and mice (*48*). In sheep, the extensive Hb polymorphism detected by the IPG technique (16 different Hb phenotypes observed in 61 English Saanen goats) has allowed Braend and Tucker (*49*) to propose a genetic theory of five β-globin genes (A_4, A_6, A_8, E, and D) and two closely linked α-globin loci ('α and "α) of which the "α has a variant allele, called "α^x. It should be noted that previous electrophoretic and chromatographic analysis had disclosed only five different types of goat Hb's (called HbA, HbB, HbD, HbD Malta, and HbE). The extensive HbA phenotype polymorphism described in ref 49 is a typical "bonus" of the IPG technique. An example of IPG analysis of short tail race sheep is given in Figure 14: the bands are razor-sharp and the different haplotypes are recognized at a glance.

CONCLUSIONS

In spite of their extensive development (*15–20*), we feel that IPGs are only now becoming widely recognized even though 6 years has elapsed since their official introduction (*9*). As described here, it appears that IPGs are now trouble-free. Given the exquisite resolution afforded, and the many advantages over CA-IEF, we look forward to the rapid diffusion of this technique, clearly the leading electrophoretic methodology of this decade. With the improved reliability, pH range, and resolution afforded, IPGs should find widespread application for the analysis of the microheterogeneity of proteins produced by recombinant organisms, particularly those intended for human therapeutic use.

ACKNOWLEDGMENT

Supported in part by a grant from Progetto Finalizzato Biotecnologie e Biosensori, Consiglio Nazionale delle Ricerche (CNR, Roma). Parts of this work were presented at the Third Annual Seminar on Analytical Biotechnology, Baltimore, MD, May 22–25, 1989.

LITERATURE CITED

(1) Kolin, Alexander *J. Chem. Phys.* **1954**, *22*, 1628–1629.
(2) Kolin, Alexander *J. Chem. Phys.* **1955**, *23*, 407–410.
(3) Svensson, Harry *Acta Chem. Scand.* **1961**, *15*, 325–341.
(4) Svensson, Harry *Acta Chem. Scand.* **1962**, *16*, 456–466.
(5) Ornstein, Leonard *Ann. N.Y. Acad. Sci.* **1964**, *121*, 321–349.
(6) Davis, Baruch J. *Ann N.Y. Acad. Sci.* **1964**, *121*, 404–427.
(7) Vesterberg, Olof *Acta Chem. Scand.* **1969**, *23*, 2653–2666.
(8) Tollaksen, Sandra L.; Edwards, Jesse J.; Anderson, Norman G. *Electrophoresis* **1981**, *2*, 155–160.
(9) Bjellqvist, Bengt; Ek, Kristina; Righetti, Pier G.; Gianazza, Elisabetta; Görg, Angelika; Postel, Wilhelm; Westermeier, Reiner *J. Biochem. Biophys. Methods* **1982**, *6*, 317–339.
(10) Rimpilainen, Maria; Righetti, Pier G. *Electrophoresis* **1985**, *6*, 419–422.
(11) Altland, Klaus; Rossmann, Ute *Electrophoresis* **1985**, *6*, 314–325.
(12) Fawcett, John S.; Chrambach, Andreas *Electrophoresis* **1986**, *7*, 266–272.
(13) Righetti, Pier G. *Isoelectric Focusing*: Theory, *Methodology and Applications*; Elsevier: Amsterdam, 1983.
(14) Righetti, Pier G. *J. Biochem. Biophys. Methods* **1988**, *16*, 99–108.
(15) Righetti, Pier G. *J. Chromatogr.* **1984**, *300*, 165–223.
(16) Righetti, Pier, G.; Gianazza, Elisabetta In *Methods of Biochemical Analysis*; Glick, David, Ed.; Wiley: New York, 1987; pp 215–278.
(17) Righetti, Pier G.; Gianazza, Elisabetta; Gelfi, Cecilia *Sep. Purif. Methods* **1987**, *16*, 105–169.
(18) Righetti, Pier G. *Trends Anal. Chem.* **1986**, *5*, 16–20.
(19) Righetti, Pier G; Gelfi, Cecilia; Gianazza, Elisabetta In *Analytical Gel Electrophoresis of Proteins*; Dunn, Michael, J., Ed.; Wright: Bristol, 1986; pp 141–202.
(20) Righetti, Pier G.; Gelfi, Cecilia; Gianazza, Elisabetta In *New Directions in Electrophoretic Methods*; Jorgenson, James, W., Phillips, Marshall, Eds.; ACS Symposium Series 335; American Chemical Society: Washington, DC, 1987; pp 33–53.
(21) Chiari, Marcella; Casale, Elena; Santaniello, Enzo; Righetti, Pier G. *Appl. Theor. Electr.* **1989**, *1*, 99–102.
(22) Chiari, Marcella; Casale, Elena; Santaniello, Enzo; Righetti, Pier G. *Appl. Theor. Electr.* **1989**, *1*, 103–107.
(23) Gianazza, Elisabetta; Celentano, Fabrizio; Dossi, Giulio; Bjellqvist, Bengt; Righetti, Pier G. *Electrophoresis* **1984**, *5*, 88–97.
(24) Dossi, Giulio; Celentano, Fabrizio; Gianazza, Elisabetta; Righetti, Pier G. *J. Biochem. Biophys. Methods* **1983**, *7*, 123–142.
(25) Righetti, Pier, G.; Chiari, Marcella; Sinha, Pranav K.; Santaniello, Enzo *J. Biochem. Biophys. Methods* **1988**, *16*, 185–192.
(26) Gelfi, Cecilia; Bossi, Maria L.; Bjellqvist, Bengt; Righetti, Pier G. *J. Biochem. Biophys. Methods* **1987**, *15*, 41–48.
(27) Sinha, Pranav K.; Righetti, Pier G. *J. Biochem. Biophys. Methods* **1987**, *15*, 199–206.
(28) Pietta, Pier G.; Pocaterra, Elena; Fiorino, Antonio; Gianazza, Elisabetta; Righetti, Pier G. *Electrophoresis* **1985**, *6*, 162–170.
(29) Astrua-Testori, Silvia; Pernelle, Jean J.; Wahrmann, Juan P.; Righetti, Pier G. *Electrophoresis* **1986**, *7*, 527–529.
(30) Kiovsky, Thomas E.; Pincock, Robert E. *J. Am. Chem. Soc.* **1966**, *88*, 4704–4710.
(31) Rabilloud, Thierry; Gelfi, Cecilia; Bossi, Maria L.; Righetti, Pier G. *Electrophoresis* **1987**, *8*, 305–312.
(32) Righetti, Pier G.; Gelfi, Cecilia; Bossi, Maria L.; Boschetti, Egisto, *Electrophoresis* **1987**, *8*, 62–70.
(33) Righetti, Pier G.; Gelfi, Cecilia; Bossi, Maria L. *J. Chromatogr.* **1987**, *392*, 123–132.
(34) Rabilloud, Thierry; Pernelle, Jean J.; Wahrmann, Juan P.; Gelfi, Cecilia; Righetti, Pier G. *J. Chromatogr.* **1987**, *402*, 105–113.
(35) Hochstrasser, Denis, F.; Augsburger, Valérie; Funk, Matthieu; Appel, Ron; Pellegrini, Christian; Muller, Alex, F. In *Electrophoresis '86*; Dunn,

Michael J., Ed.; VCH: Weinheim, 1986; pp 566-568.
(36) Righetti, Pier G.; Delpech, Marc; Moisand, Françoise; Kruh, Jacques; Labie, Dominique *Electrophoresis* **1983**, *4*, 393-398.
(37) Righetti, Pier G. In *Protein Structure. A Practical Approach*; Creighton, T. E., Ed.; IRL Press: Oxford, 1989; pp 23-63.
(38) Gåveby, Britt M.; Pettersson, Per; Andrasko, Jan; Ineva-Flygare, Lourdes; Johannesson, Ulrika; Görg, Angelika; Postel, Wilhelm; Domscheit, Albert; Mauri, Pier L.; Pietta, Pier G.; Gianazza, Elisabetta; Righetti, Pier G. *J. Biochem. Biophys. Methods* **1988**, *16*, 141-164.
(39) Bianchi-Bosisio, Adriana; Righetti, Pier G.; Egen, Ned; Bier, Milan *Electrophoresis* **1986**, *7*, 128-133.
(40) Mosher, Richard, A.; Bier, Milan; Righetti, Pier G. *Electrophoresis* **1986**, *7*, 59-66.
(41) Montiel, Maria D.; Carracedo, Angel; Lopez-Rodriguez, Isidro; Rodriguez-Calvo, Maria S.; Cocheiro, Luis; Huguet, Emilio; Genê, Manuel *Electrophoresis* **1988**, *8*, 268-272.
(42) Stenman, Ulf H. In *Progress in Isoelectric Focusing and Isotachophoresis*; Righetti, Pier G. Ed.; Elsevier: Amsterdam; 1975; pp 39-49.
(43) Righetti, Pier G.; Chiari, Marcella; Gelfi, Cecilia *Electrophoresis* **1988**, *9*, 65-73.
(44) Cossu, Gianfranco; Righetti, Pier G. *J. Chromatogr.* **1987**, *398*, 211-216.
(45) Braend, Mikael; Aursjo, John; Austbo, Olof *Acta Vet. Scand.* **1987**, *28*, 121-123.
(46) Braend, Mikael *Animal Genet.* **1988**, *19*, 59-62.
(47) Braend, Mikael *J. Hered.* **1988**, *11*, 211-212.
(48) Whitney, Barry J., III; Cobb, Ronald R.; Popp, Raymond A.; O'Rourke, Thomas W. *Proc. Natl. Acad. Sci. U.S.A.* **1985**, *82*, 7646-7650.
(49) Braend, Mikael; Tucker, Elisabeth M. *Biochem. Genet.* **1988**, *26*, 511-518.
(50) Schaefer-Nielsen, Claus In *Gel Electrophoresis of Proteins*; Dunn, M. J., Ed.; Wright: Bristol, 1986; pp 1-36.

ARTICLES

Strategies for Background Subtraction in Electron Probe Microanalysis/X-ray Compositional Mapping

Robert L. Myklebust,* Dale E. Newbury, and Ryna B. Marinenko

Room A121, Chemistry Building, National Institute of Standards and Technology, Gaithersburg, Maryland 20899

The calculation of quantitative electron microprobe compositional maps requires accurate correction for the background that arises from the X-ray bremsstrahlung. Different strategies are appropriate for wavelength-dispersive X-ray spectroscopy (WDS) and energy-dispersive X-ray spectrometry (EDS). For WDS mapping, the dependence of the bremsstrahlung on average atomic number can be used to make an indirect calculation of the background appropriate to each location in the map from the background measured on a known pure element standard. For EDS mapping, the background can be measured directly at each map location. For complex specimens, a combined WDS-EDS measurement/background correction strategy can be applied.

I. INTRODUCTION

Compositional mapping with the electron microprobe is the technique of creating quantitative images by carrying out complete quantitative analysis procedures at every point of a scan matrix (*1*). In addition to performing the matrix correction procedures that compensate for interelement effects on the measured X-ray intensities (correction factors for atomic number Z, absorption A, and fluorescence F; or "ZAF") (*2*), a careful correction must be made for the spectral background, which arises principally from the X-ray bremsstrahlung, if accurate quantitation is to be achieved for minor and trace constituents. The intensity of the bremsstrahlung depends strongly on the composition, varying at a particular X-ray energy approximately with the atomic number. Kramers (*3*) described the functional dependence of the bremsstrahlung intensity:

$$I_\nu = kZ\left(\frac{E_0 - E_\nu}{E_\nu}\right) \quad (1)$$

where E_0 is the incident electron beam energy, E_ν is the bremsstrahlung energy, and Z is the atomic number of the target.

For mixed targets, the bremsstrahlung varies approximately with the weight concentration average of the atomic numbers of the elemental constituents, which is denoted as $\bar{Z}$. In conventional fixed-beam location (single point) analysis, background correction is normally accomplished by one of several different approaches that depend on the type of spectrometer employed. For wavelength-dispersive spectrometers (WDS) these are as follows:

(1) The spectrometer(s) can be detuned from the characteristic peak to measure the background on either side of the peak while the beam continues to excite the same region of unknown composition that is being analyzed.

(2) On a system with multiple spectrometers, the background can be measured on one spectrometer while the other spectrometers are tuned to characteristic X-ray peaks. A correction for efficiency is then used to adjust the measured background to the values appropriate to these other spectrometers.

(3) From an initial calculation of the composition of the unknown, the average atomic number can be calculated based on major constituents. The background can then be measured on a pure element with approximately this same atomic number, providing no characteristic peaks of this element occur at the wavelengths of interest. Alternately, a substantially different atomic number can be used for the background measurement with appropriate scaling based on the average atomic number and Kramers' equation.

For energy-dispersive spectrometers (EDS), the entire X-ray spectrum is measured, and background can be removed directly from the measured spectrum by either of two techniques:

(1) Mathematically filtering the spectrum with a digital filter as proposed by Schamber (*4*). The digital filter is a

high-pass transformation that preserves the high-frequency components of the spectrum. The filter includes the peaks, while discriminating against the background, which is the slowly varying spectral component.

(2) Modeling the X-ray bremsstrahlung intensity beneath the X-ray peaks and subtracting this from the integrated peaks as proposed by Fiori et al. (*5*). For this method, at least two background points at widely separated energies must be measured on each spectrum. The bremsstrahlung is then fitted with an equation containing Kramers' expression for the generation of bremsstrahlung, the absorption of the bremsstrahlung in the specimen, and the absorption in the window and inactive portions of the detector. Since the absorption in the specimen depends on the composition, this method must be iterated within the matrix correction routine.

For the analysis procedures of compositional mapping, the background problem is exacerbated by the sheer number of analytical data points involved, namely the $n \times n$ product of the matrix of picture elements (pixels), where the background may differ significantly from one pixel to another. Clearly, method 1 for WDS compositional mapping will greatly increase the time required to measure a map since three measurements, one on-peak and two off-peak values, are needed at each pixel of the map. Moreover, when little or none of the element is present in the specimen, performing an accurate background subtraction by this method often requires one to count the background and the peak for equivalent time periods to obtain good statistical precision. Since only one measurement per pixel may require several hours to complete the image scan, tripling the time is not an effective method.

In WDS compositional mapping, Swyt and Fiori (*6*), Marinenko et al. (*1*), and Myklebust et al. (*7*) have described instrumental methods for background correction that make use of scanning a background matrix map in a manner analogous to the WDS procedure 2 described above. The difficulty with such methods is the time-intensive nature of such a process. Since most instruments have a small number of wavelength-dispersive spectrometers, e.g., three or fewer, the necessity of devoting a spectrometer to a background channel means losing the opportunity to measure an element of interest, which may increase the time spent in completing a compositional map.

Although the peak-to-background ratios in EDS are smaller than in WDS, the background corrections are handled much more easily since the entire spectrum is always collected and background information is obtained for each image location at the same time as the peak information is acquired. However, because the peak-to-background ratios in EDS are smaller, the background correction is larger and therefore more important than in WDS.

II. THEORY

A. WDS Case. *1. Defocusing Artifacts.* For compositional mapping measurements using WDS, a major instrumental artifact arises in the measurement of characteristic X-ray intensities because of the effect of spectrometer defocusing. In the case of characteristic X-rays, the X-ray intensity at any point in the scan matrix on a flat specimen can vary for either of two reasons: The composition of the specimen may vary or the spectrometer may defocus because the beam has been scanned sufficiently far off the optic axis of the spectrometer as is shown in Figure 1. For example, in a scan at 200 diameters magnification, which corresponds to a 500 μm wide deflection on the specimen, the characteristic X-ray intensity falls by 50% at the extremity of the scan field relative to the center. Several methods have been devised to correct for spectrometer defocusing, including stage scanning with a fixed electron beam (*8*, *9*), crystal rocking (Swyt and Fiori (*6*)), standard mapping (Marinenko et al (*10*)), and standard modeling (Myklebust et al. (*11*), Marinenko et al. (*1*)).

An important question to consider in making an accurate background correction is whether the background is similarly affected by wavelength spectrometer defocusing. Myklebust et al. (*12*) have observed that the background measured on

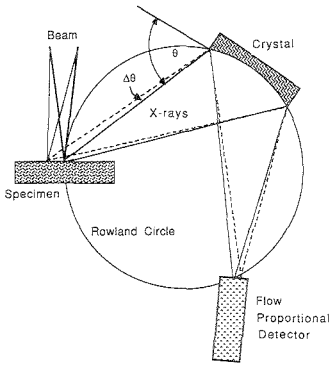

Figure 1. Diagram of a focusing wavelength-dispersive spectrometer. If the X-ray source does not fall on the focusing circle of the spectrometer, the Bragg angle (q) will diffract a different wavelength of X-ray into the detector.

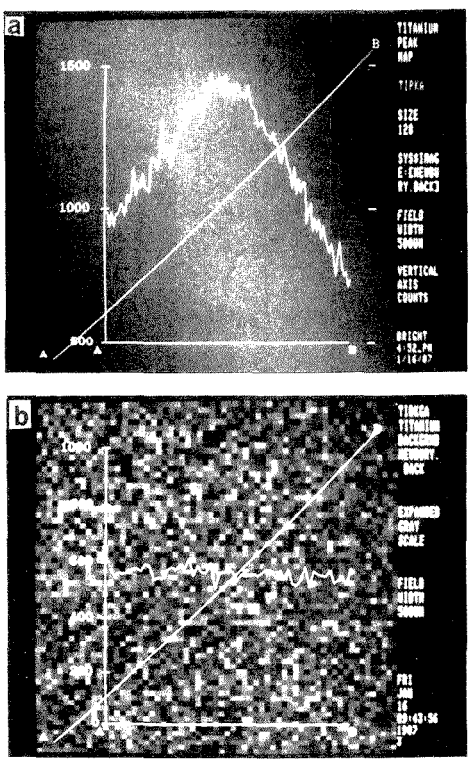

Figure 2. Defocusing effects for a scan field of 0.5 mm × 0.5 mm on (a) a characteristic peak and (b) a nearby background channel. The line traces along the vector **A–B** are shown for each intensity map. The vertical scale is in X-ray counts.

a homogeneous specimen by WDS does not noticeably change from point to point on an image. When the situation is examined in detail, we conclude that it is not in fact necessary to scan a background map for WDS analyses. The spectral background, which consists mostly of the X-ray bremsstrahlung, is a slowly varying function with wavelength, except in the region of an absorption edge. The strong defocusing effect observed for sharply peaked characteristic X-rays thus becomes negligible for the background. This observation is demonstrated in Figure 2, which compares a standard map recorded with a scanned field of 0.5 mm by 0.5 mm (200×) for a characteristic peak (Figure 2a) and a background region obtained by detuning the peak (Figure 2b). To be sure that sufficient background counts were recorded in the background map to observe any defocusing effects, the beam current and the pixel dwell time were increased to accumulate a total of approximately 500 counts/pixel. A line trace across this background map, which has been strongly enhanced by image processing to increase visual sensitivity to small intensity changes, reveals that the defocusing effect is less than 2% across the image, compared to the peak map, where the defocusing results in a drop of more than 50% in the intensity.

2. WDS Background Correction Method Based on Average Atomic Number. Although spectrometer defocusing is not a significant problem when one is correcting an image for the background, there remains the very important problem of correcting for the variation in the background with the average atomic number of the unknown. We propose that a suitable background correction for compositional images can be developed as follows:

(1) The spectrometers (A, B, C, etc.) are first tuned on a standard to the characteristic peaks of interest for the analysis. For example, consider the analysis of an Al–Cu alloy with trace Zn, for which the spectrometers could be assigned as follows: A = Al, B = Cu, and C = Zn.

(2) A background reading is taken for each wavelength spectrometer on another element with atomic number Z. In the Al–Cu–Zn example, this element could be Ti.

(3) The characteristic peak maps are then recorded for the unknown, with correction for defocusing by any of the four possible methods: stage scanning, crystal rocking, standard mapping, or peak modeling.

(4) Quantitative analysis is performed at each pixel with *ZAF* matrix corrections (corrections for X-ray generation, specimen self-absorption of X-rays, and secondary X-ray fluorescence) or α coefficients. In this first quantitative calculation stage, the measured background on element Z (Ti) is used for background subtraction.

(5) Based upon the weight concentrations of the major constituents determined in this analysis, e.g., Al and Cu, the average atomic number ($\bar{Z}$) is calculated at each pixel (forming a "$\bar{Z}$ map").

(6) This $\bar{Z}$ map is used to calculate a background map appropriate to each spectrometer, assuming the Z-dependence of Kramers' equation and using the calculation

$$I_{BG} = \frac{\bar{Z}}{Z}(BG)_{Z_i} \qquad (2)$$

where $(BG)_{Z_i}$ is the background measured with that spectrometer, A, B, or C, on element Z (Ti). For the major constituents Al and Cu, this background correction will be insignificant, but for the minor constituent, Zn, the background correction will significantly decrease the intensity.

(7) The quantitation procedure is now repeated with the background at each pixel taken from the background maps. If necessary, the background computation could be repeated inside the quantitative procedure's iteration loop, but the initial estimate of the average atomic number from the quantitative analysis of the major constituents is sufficiently accurate to give an accurate background correction on the first calculation.

B. EDS Case. Since the EDS system is not a focused spectrometer, there is no defocusing of the spectrometer for either the peaks or the background when a compositional map is measured. We have chosen to model the continuum at each pixel as an integral part of the matrix correction procedure employed in FRAME C (*2*). In this method, two background regions are integrated along with the integrations of each peak. The two coefficients A and B in eq 3 are then computed from the background measurements

$$I_{BG} = \{A(E_0 - E)^2 + B(E_0 - E)\}(P_E f(\chi)/E) \qquad (3)$$

where I_{BG} is the continuum intensity at energy E, E_0 is the beam voltage, P_E is the detector efficiency, and $f(\chi)$ is the absorption factor for the X-rays of energy E. The integrated background beneath each peak can then be computed by using eq 3 at the energy of each peak. Since this background computation depends on the specimen composition, it must be included in the matrix correction iteration procedure. Alternatively, the spectrum could have been digitally filtered to remove the background prior to integrating the peak areas. No additional background corrections need be applied to these images since the background subtraction and the composition are determined at the same time. Digital filtering for background removal does, however, suffer possible inaccuracies when peaks are closely spaced and partially overlapping so that no distinct background regions bound the peaks, a situation that one often encounters when analyzing complex specimens.

C. Background Strategy with Combined EDS/WDS Systems. Many modern electron probe microanalyzers and analytical scanning electron microscopes have combined EDS and WDS capabilities. With both spectrometries available, a powerful mapping strategy can be devised that combines the useful features of both. The complementary nature of the features of EDS and WDS has been discussed at length (*13*). To summarize briefly:

(*1*) *Spectrum Coverage.* EDS effectively provides parallel detection of the complete X-ray spectrum over the energy range of interest so that, in principle, many elements can be mapped simultaneously. WDS provides only single-channel coverage.

(*2*) *Resolution.* EDS resolution in terms of the peak full width at half-maximum is approximately 150 eV at Mn K α, while WDS resolution is less than 10 eV. EDS is subject to frequent peak overlap problems, while most peaks closely spaced in energy are well resolved by WDS.

(*3*) *Sensitivity.* The poorer resolution of EDS leads to a lower peak-to-background ratio and therefore poorer sensitivity, typically 0.1 wt % (1000 ppm). The higher resolution of WDS gives an improved peak-to-background ratio and a detection limit approximately 10 times lower, or 0.01 wt % (100 ppm). A related point is the count rate capability. The pulse processing time of EDS is at least a factor of 20 longer than that for WDS, leading to significant differences in limiting count rates. EDS is typically limited to 20 000 counts/s, while WDS can count in excess of 100 000 counts/s. Moreover, for EDS, the limiting count rate is integrated over the entire spectrum and not just the peak of interest, while for WDS, the entire limiting count rate can be applied to a single peak.

The comparison of these characteristics suggests the following characteristics for mapping with combined EDS/WDS systems:

(1) If the number of constituents to be mapped does not exceed the number of wavelength spectrometers available, WDS is preferred for data collection, because of the greater count rate capability, particularly for minor and trace constituents.

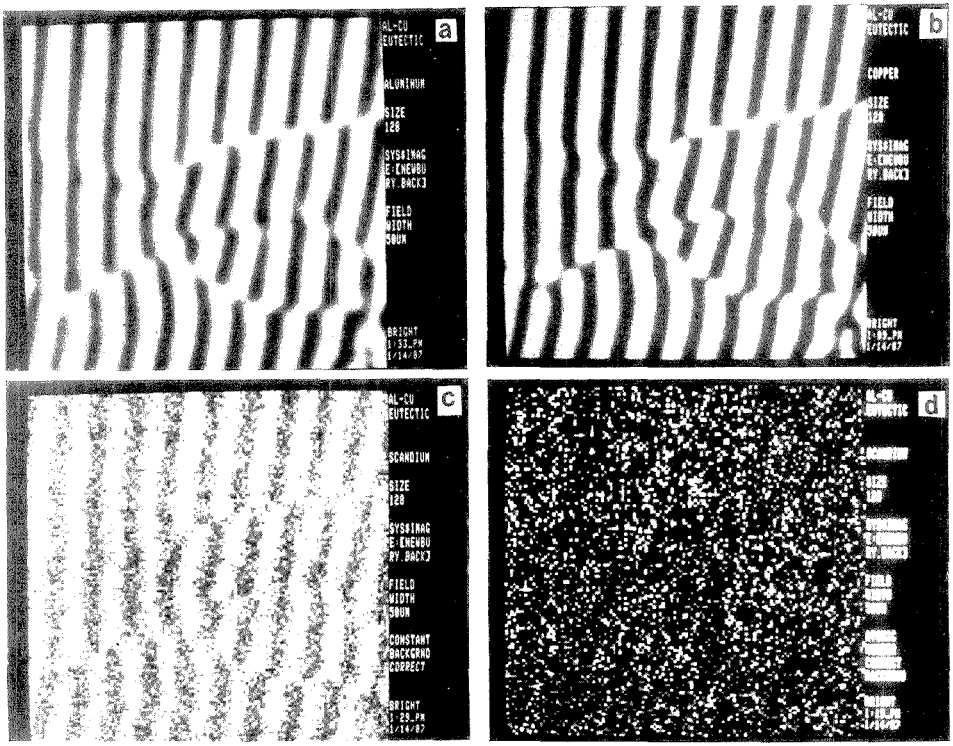

Figure 3. Compositional maps for aluminum–copper eutectic alloy: (a) aluminum; (b) copper; (c) scandium, with constant background correction based on measurements on carbon; (d) scandium, with variable background correction based on the average atomic number calculated from the principal constituents.

(2) If the number of constituents exceeds the number of wavelength spectrometers, then a combined EDS/WDS strategy is preferred:

(a) Major constituents (greater than 10 wt %) are measured with EDS, except in those cases where bad overlaps occur, in which cases WDS must be used.

(b) Minor constituents that are well resolved may be measured by EDS, but the counting statistics will be poor. WDS is preferred for minor constituents whenever available.

(c) Trace and minor constituents that suffer interferences must be measured by WDS.

(d) Background correction proceeds in two stages. First, major elements that are measured by EDS are quantified with the EDS background procedure. Any major elements measured by WDS must also be simultaneously quantified, with a simple fixed value WDS background correction. WDS major element concentrations must also be provided as information to the EDS background correction procedure if background modeling, which is concentration dependent, is used. Second, the concentrations for the major constituents are used to calculate the $\bar{Z}$ map for the WDS background mapping procedure, and WDS minor and trace elements are calculated. With this combined EDS/WDS procedure, it is often possible to simultaneously map 10 or more constituents, depending on the number of wavelength spectrometers available and the particular interference situation for EDS spectrometry. When multiple spectrometers are employed, each with a different azimuthal angle relative to the specimen, attention must be paid to the possible problem of absorption effects at interfaces where the material composition changes. The absorption path length within each absorbing material may depend on the exact orientation of the interface relative to each spectrometer. Corrections appropriate to the local geometry of the interface will be the subject of future development.

III. RESULTS

In the following examples, in order to enhance the visibility of structures regardless of their absolute concentration level, the gray scale has been applied by assigning the brightest level to the highest concentration or intensity value for that particular image. This method of presentation was necessary because of the wide range in concentrations to be depicted. Thus, in these presentations, the intensities in images of different constituents from the same field of view are not directly comparable.

A. WDS Case. *1. Test of the Method.* As a test of the accuracy of this method, images were prepared for a eutectic alloy of aluminum and copper, which was characterized by a fine lamellar structure. Two spectrometers were assigned to the Al and Cu characteristic peaks, while the third spectrometer recorded the signal at the wavelength for scandium, which is not present in the specimen. Background readings were taken for all three spectrometers on carbon. The initial quantitation was performed with the carbon background readings for the measured Al and Cu intensities. The quantitative compositional maps for Al and Cu are shown in parts a and b of Figure 3. (In all the images in this paper, higher concentrations are indicated by gray levels on the white end of the scale.) Despite the lack of scandium in the specimen,

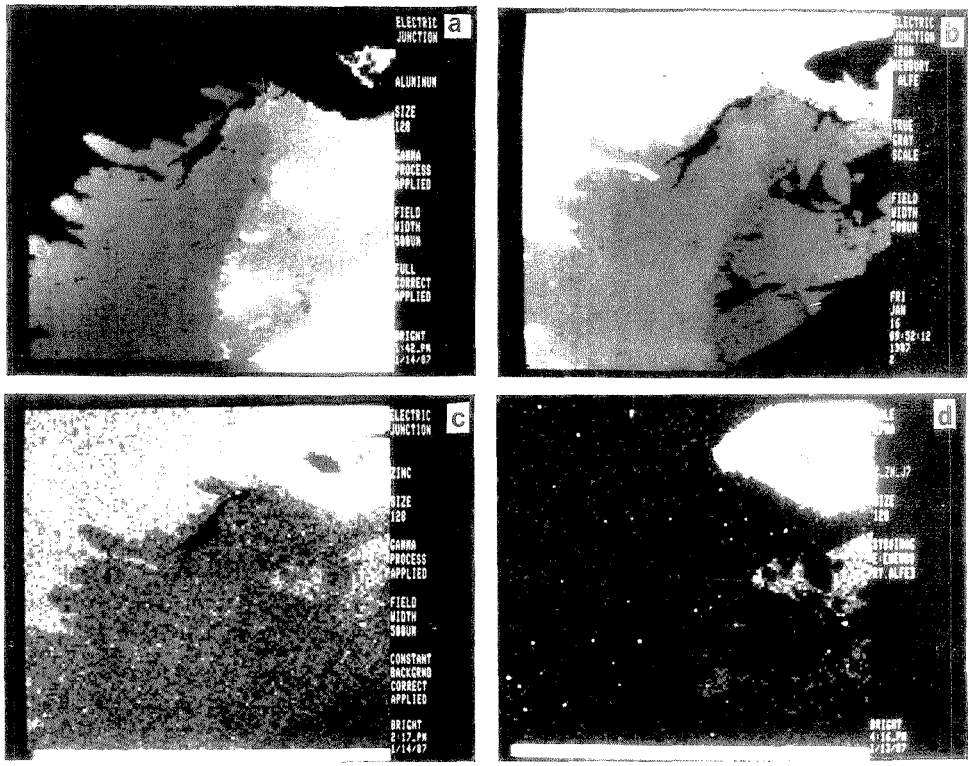

Figure 4. Compositional maps for a failed electrical junction between an aluminum wire and a steel screw: (a) aluminum; (b) iron; (c) zinc with constant background correction based on measurements on carbon, the constrast having been artificially enhanced to make low concentration levels visible; (d) zinc with variable background correction based on the average atomic number calculated from the principal constituents, the contrast having been artificially enhanced.

the calculated scandium map, Figure 3c, shows an apparent segregation of scandium in the copper-rich phase. A $\bar{Z}$ map was then calculated from the concentrations for Al and Cu. From this $\bar{Z}$ map, background maps were calculated for all three spectrometers. The calculated background map for the scandium spectrometer was then subtracted from the scandium signal map, and the quantitation was repeated, with the result shown in Figure 3d. The apparent compositional structure that is visible in the scandium map corrected with a constant background, Figure 3c, is completely eliminated in the scandium map corrected with an individual pixel background calculated from the average atomic number, Figure 3d. The maximum concentration represented in Figure 3d is 0.08%, which represents the limit of detection for scandium under the conditions used for this compositional map (20 keV, 17 nA, 2-s integration time, 128 × 128 scan matrix, 2000 diameters magnification).

2. Example of an Application. As an example of an application of the method to a practical problem, consider the compositional mapping of an aluminum wire–iron screw electrical junction that has undergone failure while in service (*14*). Figure 4a,b shows the distribution of iron and aluminum at the reaction zone associated with the failure. A map for zinc with a constant background correction is shown in Figure 4c, with a high degree of contrast expansion applied. In addition to the zinc-rich region in the upper right of this image, there is apparently more zinc in the iron-rich region of the specimen than in the aluminum-rich region. The apparent zinc concentration in the iron-rich region is 0.45 wt % and in the aluminum-rich region is 0.35 wt %. However, after correction with the variable background based upon average atomic number (Figure 4d), the true situation is found to be reversed, with zinc at a level of 0.30 wt % in the aluminum-rich constituent and a level of 0.05 wt % zinc in the iron-rich region, which is at the detection limit.

For calculation of compositional maps, the correction of background by the average atomic number method gives significantly improved performance and efficiency over the methods previously utilized. Further testing is needed to describe more accurately practical detection limits. Additional improvements in accuracy can be expected by incorporating a more accurate background equation, that of Small et al. (*15*), to model the atomic number dependence of the background more closely:

$$\ln (I_n) = M \ln [Z(U - 1)] + B \qquad (4)$$

where I_n is the generated continuum intensity, U is the overvoltage (E_0/E_n), E_0 is the beam voltage, E_n is the excitation potential, $M = 0.00599E_0 + 1.05$, and $B = 0.322E_0 + 5.80$.

B. EDS Case. *1. Test of the Method.* The importance of the atomic number dependence of the background for EDS analyses can be seen in Figure 5. The images are of the same Al–Cu material as shown in Figure 3 except that the maps were made with EDS instead of WDS analyses. Figure 5a is the aluminum map, and Figure 5b is the copper map. A separate window was set up to measure scandium as was done

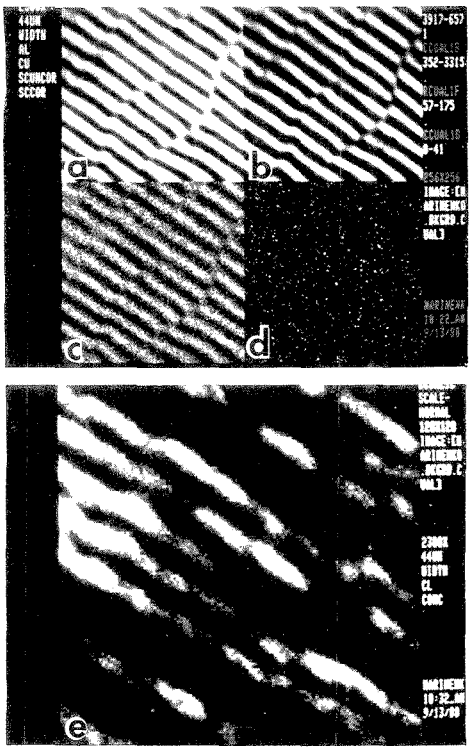

Figure 5. EDS compositional maps for an aluminum–copper eutectic alloy: (a) aluminum; (b) copper; (c) uncorrected scandium map; (d) scandium with variable background correction built into the EDS quantitative analysis procedure; (e) chlorine.

Figure 6. EDS compositional maps for a complex ceramic: (a) magnesium; (b) vanadium; (c) aluminum; (d) iron. (Sample courtesy of J. Blendell and C. Handwerker, Institute for Materials Science and Engineering).

in the WDS analyses. Figure 5c shows the uncorrected scandium image that exactly matches the copper image. Since there is a large difference in atomic number between the two phases in this material, it is easy to see that the background increases directly with average atomic number. In the case of EDS maps, this average atomic number correction to the background is taken into account when the background is modeled for each pixel. Figure 5d shows the scandium map after the background has been modeled in the EDS quantitative analysis program. If a digital filter is used instead of modeling the continuum, the results are just as satisfactory except that the background map cannot be displayed after the spectra have been filtered. The method does not miss elements that are present in small quantities such as the chlorine that was found as a contaminant in the Al–Cu specimen. Figure 5e is the quantitative chlorine map, showing chlorine to be present (up to a maximum of 4.5 wt %) in some of the aluminum areas of the specimen.

2. *Example of an Application.* Figure 6 presents an example of an application of the background-corrected EDS mapping technique to the analysis of a complex microstructure. The sample is a ceramic containing magnesium, vanadium, cobalt, and oxygen as major constituents. EDS composition mapping of this structure was simultaneously performed for the major constituents, with oxygen calculated by assumed stoichiometry, and for two minor constituents, iron and aluminum, which were detected during quantitative analysis. Figure 6 shows the compositional maps for two of the major constituents, magnesium and vanadium, and for aluminum and iron. The maximum concentrations for the minor constituents detected in these maps were 7% for iron and 19% for aluminum.

CONCLUSIONS

The images presented demonstrate that poor background subtraction methods can definitely lead to analysis errors not only in compositional maps but also in individual point analyses in the electron microprobe. It is especially important for EDS quantitative analysis mapping programs to determine the background correctly since the bremsstrahlung background in an EDS spectrum is much more significant than the background measured with WDS. Large errors can occur in WDS analyses of minor or trace constituents in a specimen if the background is not handled properly. For example, if a constant background from an element of higher atomic number than the specimen is used, the resulting background will be too high and the concentration of a minor element in the specimen will be too low, or may even be apparently negative.

The $\bar{Z}$ map background correction method for WDS described in this paper offers the advantage of speed, greater statistical precision, and accuracy in background subtraction and eliminates the need to devote a valuable spectrometer to the measurement of background during mapping, thus freeing a spectrometer for the much more valuable task of measuring an elemental constituent of interest.

For complex, multielement systems, a combined EDS/WDS strategy can be developed to permit simultaneous mapping of 10 or more constituents.

ACKNOWLEDGMENT

We thank J. Blendell and C. Handwerker of the Institute for Materials Science and Engineering for providing the specimen of magnesium–vanadium–cobalt oxide ceramic.

LITERATURE CITED

(1) Marinenko, R. B.; Myklebust, R. L.; Bright, D. S.; Newbury, D. E.; *J. Microsc.* **1987**, *145*, 207.
(2) Myklebust, R. L.; Thorne, B. B. *NBS Tech. Note (U.S.)* **1984**, No. 1200.
(3) Kramers, H. A. *Phil. Mag.* **1923**, *48*, 836.
(4) Schamber, F. H.; *Proceedings of the 8th National Conference on Electron Probe Analysis*; New Orleans, 1973, paper 85.
(5) Fiori, C. E.; Myklebust, R. L.; Heinrich, K. F. J.; Yakowitz, H. *Anal. Chem.* **1976**, *48*, 172.

(6) Swyt, C. R. Fiori, C. E. *Microbeam Analysis—1986*; San Francisco Press: San Francisco, CA, 1986; p 482.
(7) Myklebust, R. L.; Marinenko, R. B.; Newbury, D. E.; Bright, D. S. *Microbeam Analysis—1985*; San Francisco Press: San Francisco, CA, 1985; p 101.
(8) Mayr, M.; Angelli, J. *X-Ray Spectrom.* **1985**, *14*, 89.
(9) Ono, Y.; Nielsen, C. H.; Tagata, S.; Seo, Y. *Microbeam Analysis—1985*; San Francisco Press: *San Francisco, CA*, 1985; p 145.
(10) Marinenko, R. B.; Myklebust, R. L.; Bright, D. S.; Newbury, D. E. *Microbeam Analysis—1985*; San Francisco Press: San Francisco, CA, 1985; p 159.
(11) Myklebust, R. L.; Newbury, D. E.; Marinenko, R. B.; Bright, D. S. *Microbeam Analysis—1986*; San Francisco Press: San Francisco, CA, 1986; p 495.
(12) Myklebust, R. L.; Newbury, D. E.; Marinenko, R. B.; Bright, D. S. *Microbeam Analysis—1987*; San Francisco Press: San Francisco, CA, 1987; p 25.
(13) Goldstein, J. I.; Newbury, D. E.; Echlin, P.; Joy, D. C.; Fiori, C. E.; Lifshin, E. *Scanning Electron Microscopy and X-ray Microanalysis*; Plenum: New York, 1981; p 205.
(14) Newbury, D.; Greenwald, S. *J. Res. Natl. Bur. Stand. (U.S.)* **1980**, *85*, 429.
(15) Small, J. A.; Leigh, S. D.; Newbury, D. E.; Myklebust, R. L. *J. Appl. Phys.* **1987**, *61*, 459.

RECEIVED for review January 31, 1989. Accepted April 21, 1989.

Alkali-Metal and Alkaline-Earth Cation and Proton Selectivities of Dibenzo-14-crown-4 and Its Derivatives in Polymeric Membranes

Uriel Olsher* and Felix Frolow

Department of Chemical Services, The Weizmann Institute of Science, Rehovot 76100, Israel

Gil Shoham*

Department of Analytical and Inorganic Chemistry, The Hebrew University of Jerusalem, Jerusalem, Israel

Gwi-Suk Heo and Richard A. Bartsch*

Department of Chemistry and Biochemistry, Texas Tech University, Lubbock, Texas 79409-1061

The influence of attaching pendant groups with additional coordinating sites to dibenzo-14-crown-4 upon the response of solvent–polymeric membranes to alkali-metal and alkaline-earth cations and protons has been determined. Marked variation in cation selectivity is noted when –OH, $-OCH_2CH_2OCH_3$, and $-OCH_2CO_2H$ groups are attached to the central carbon of the three-carbon bridge in the ionophore.

Electrically neutral macrocyclic polyethers (crown ethers) function as ionophores for alkali-metal and alkaline-earth cations. The metal ions are bound by the ethereal oxygens and the resulting complexes are usually highly stable and often significantly selective. These properties have been utilized in the development of cation-selective synthetic membranes (*1–8*). When incorporated into the matrix of solvent–polymeric membranes, lipophilic crown ethers act as ionophores and exhibit rather selective transport properties for alkali-metal and alkaline-earth metal cations (*1–4*, *6*). One of the common methods used to determine the selectivity of the membrane toward a specific cation and, in turn, one of the potential uses of these membranes is emf measurement with an "ion-selective electrode" assembly (*5*, *7*, *8*). The selectivity of the membrane, which is estimated by K_{ij}^{pot}, has been shown to be highly dependent on the selectivity of the incorporated ligands, as expressed by the complex stability constants of the ionophores with the cations.

Previously it was shown that the crown ether dibenzo-14-crown-4 (DB14C4, **1**) is a selective complexing agent for Li^+ (*6*) and is therefore a candidate for use in solvent extraction and membrane transport of Li^+. To probe the effect of attaching pendant functions which have additional coordination sites upon the cation selectivity of DB14C4 compounds, a series of DB14C4 derivatives has been synthesized. This study is focused upon DB14C4 rather than 14-crown-4, which is also a selective ionophore for Li^+ (*9*, *10*). The DB14C4 system provides a rigid and well-defined macrocyclic conformation which is an ideal "base" for the square-pyramidal coordination that favors Li^+ complexation (*6*, *11*, *12*). Hence with the DB14C4 system, conformational changes of the macrocyclic skeleton are minimized, which should enhance and sharpen the effects of pendant functional groups.

The cation selectivities of DB14C4 compounds toward alkali-metal and alkaline-earth cations and protons have been determined by the Δemf method, using an ion-selective cell assembly (*4*, *6*, *8*). We now report the results of cation selectivity measurements which have been performed on DB14C4 (**1**) and DB14C4 derivatives **2**, **3**, and **4**.

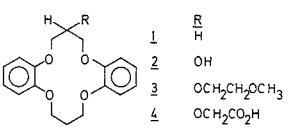

	R
1	H
2	OH
3	$OCH_2CH_2OCH_3$
4	OCH_2CO_2H

EXPERIMENTAL SECTION

Synthesis. Synthetic routes for **1–4** are summarized in Figure 1, whereas complete details for the preparation of **1**, **2**, and **4** are presented elsewhere (*11*, *13*, *14*).

sym-Dibenzo-14-crown-4-oxyethyl methyl ether (**3**) was synthesized by the following procedure. After removal of the protecting mineral oil from sodium hydride (0.45 g, 19 mmol) by washing with pentane under nitrogen, dry tetrahydrofuran (200 mL) and **2** (2.0 g, 6.0 mmol) were added. The reaction mixture was stirred for 30 min at room temperature and 2-methoxyethyl bromide (1.8 g, 13 mmol) in 30 mL of THF was added dropwise during 1 h, after which the mixture was stirred 2 h at room temperature, refluxed for 2 h, and filtered. The filtrate was

0003-2700/89/0361-1618$01.50/0

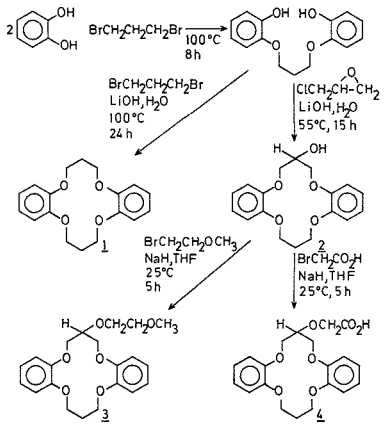

Figure 1. Synthetic routes to dibenzo-14-crown-4 and its derivatives.

Table I. Sensitivies of Crown-Based Polymeric Membrane Electrodes Containing Ionophores 1–4 for Ammonium Ion Standards

ionophore	range of linearity for aqueous NH_4Cl solutions, M	slope[a]
1	10^{-1}–10^{-4}	41.7 ± 0.9
2	10^{-1}–10^{-4}	43.2 ± 1.1
3	10^{-1}–10^{-4}	42.8 ± 1.2
4	10^{-1}–10^{-3}	45.6 ± 1.4

[a] For plots of emf in mV vs log $[NH_4^+]$, M.

evaporated in vacuo and the residue was dissolved in methylene chloride. The solution was washed with 1 N sodium hydroxide and water, dried over magnesium sulfate, and evaporated in vacuo. The residual oil was subjected to high vacuum at 100 °C to remove unreacted 2-methoxyethyl bromide, refluxed in pentane overnight, and placed in a refrigerator overnight. Crown ether **3** (2.20 g, 92% yield) was obtained as a white solid with mp 55–57 °C. IR (deposited film on sodium chloride plate): 1240, 1220, and 1110 cm^{-1} (aryl and/or alkyl C–O). ^1H NMR ($CDCl_3$): δ 2.23 (q, 2 H), 3.37 (s, 3 H), 3.50–3.72 (m, 2 H), 3.72–4.00 (m, 9 H), 4.47 (m, 1 H), 6.91 (m, 8 H). Anal. Calcd for $C_{21}H_{26}O_6$: C, 67.38; H, 6.95. Found: C, 67.61; H, 6.82.

Membrane Preparation and emf Measurement. The solvent–polymeric membranes were prepared with 2 wt % of the crown ether, 33 wt % of poly(vinyl chloride) (PVC), and 65 wt % of the membrane solvent dioctyl sebacate (DOS). In a second set of experiments, the polymeric membranes were prepared in similar fashion but with the addition of 30 mol % of KTpClPB relative to the weight of crown ether. The membrane preparation and the emf measurement technique have been described in detail elsewhere (*3*, *4*, *6*). Cells of the type Hg;HgCl, KCl(satd)|electrolyte bridge|sample solution||membrane||internal filling solution, AgCl;Ag with double junction reference electrodes and Philips IS-560 electrode bodies for mounting the membranes were used. The internal filling solution was aqueous 0.010 M NH_4Cl. The separate solution technique (*3*, *4*) and 0.10 M sample solutions were used to determine the selectivity factors, which are given by

$$\log K_{NM}^{Pot} = \frac{(emf_N - emf_M)Z_nF}{2.303RT} - \log a_m^{Z_N - Z_M} + \log a_N \qquad (1)$$

where Z_N is the charge of reference ion, Z_M is the charge of interfering ion, emf_N is the emf of the cell assembly when the sample is a solution of the chloride of the interfering cation, and emf_M is the emf of the cell assembly when the sample is a solution of the chloride of the reference cation (NH_4^+). The emf measurements were performed at 25 °C by using 0.10 M aqueous solutions of the respective chlorides (*4*) and had a standard deviation of <0.1 mV for single determinations. Sensitivies of the crown-based electrodes containing ionophores 1–4 for lithium ion standards are given in Table I.

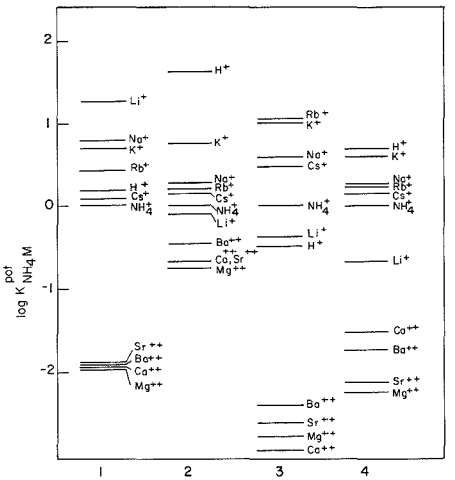

Figure 2. Selectivity factors log $K_{M1,M2}^{pot}$ for solvent polymeric membranes containing ionophores **1**, **2**, **3**, and **4**: reference, NH_4^+ (M1); membrane composition, 2 wt % ionophore, 33 wt % PVC, 65 wt % DOS.

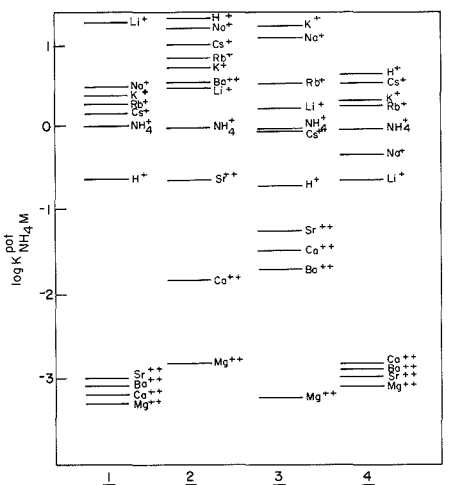

Figure 3. Selectivity factors log $K_{M1,M2}^{pot}$ for solvent polymeric membranes containing ionophores **1**, **2**, **3**, and **4**; [reference, NH_4^+ (M1); membrane composition, 2 wt % ionophore, 33 wt % PVC, 65 wt % DOS + incorporated lipophilic anionic sites (KTpClPB).

RESULTS

The potentiometrically determined selectivity factors induced in solvent–polymeric membranes by the four DB14C4 compounds are presented in Figures 2 and 3. The selectivity factors, given as log $K_{M1,M2}^{pot}$ values, represent the membrane preference for cation M2 relative to cation M1, the reference cation. In this study, the reference cation was NH_4^+ and the membrane solvent was dioctyl sebacate (DOS). In a second set of experiments, a similar system was used in which lipo-

philic anionic sites [potassium tetrakis(*p*-chlorophenyl)borate, KTpClPB] were incorporated into the synthetic membrane (Figure 3).

The results presented in Figures 2 and 3 can be summarized briefly as follows: [1] For the metal cations, the membrane containing 1 is selective for Li^+, the membrane containing **2** prefers K^+ or Na^+ (depending on the conditions), the membrane containing **3** prefers Rb^+ or K^+, and the membrane containing **4** prefers Cs^+ or K^+. [2] The membrane containing **1** prefers Li^+ over all the other alkali-metal and alkaline-earth cations regardless of the membrane composition or the measurement conditions, whereas the selectivities of membranes containing **2**, **3**, or **4** are sensitive to both factors. [3] For membranes containing any of the four DB14C4 compounds, there is strong preference for monovalent cations over the divalent cations although to a lesser extent for membranes containing **2**. [4] Proton uptake is significant for membranes containing compounds **2** or **4** (which possesses an ionizable group) and is much lower for membranes containing compounds **1** or **3**. [5] Incorporation of lipophilic anionic sites (KTpClPB) in membranes containing **1** improves the selectivity toward Li^+. However for membranes containing **2–4**, this type of membrane modification does not exhibit any clear effect on selectivity other than changing the apparent preferred cation.

DISCUSSION

To be used as an ionophore, a compound should meet the following requirements: [1] The carrier molecule is composed of polar and nonpolar groups. [2] The carrier molecule is able to assume a stable conformation that provides a polar cavity, suitable for the uptake of a cation, and a nonpolar lipophilic exterior. [3] The polar groups in the cavity can be any polar atom that is capable of coordinating directly to the metal cation. Oxygen atoms are preferred for the alkali-metal and alkaline-earth cations and may be ether, hydroxyl, carbonyl, or carboxylate units. [4] The number of binding sites in the cavity is 4–12 with a lower coordination number for the smaller cations (e.g. Li^+) and a higher coordination number for the larger cations (e.g. Cs^+). [5] The molecular structure of the molecule and hence the geometry of the cavity binding sites are of central importance. High selectivities are achieved by locking the coordinating sites into a rigid arrangement around the cavity. The cation that best fits into the offered cavity is preferred. [6] Although relatively rigid (point 5 above), the ligand should be flexible enough to allow for a sufficiently rapid ion exchange. [7] To allow adequate stability and mobility in the membrane, the overall dimensions of the carrier molecule should be rather small but still compatible with high lipid solubility.

Compounds 1–4 appear to meet all these general requirements but differ considerably among themselves in the number of potential binding sites (point 4), in the arrangement and geometry of the "apparent cavity" (point 5), and in the overall polar character of the molecule (point 7). It is therefore not surprising that although all four derivatives are potentially good ionophores, they exhibit different selectivities toward the alkali-metal and alkaline-earth cations. Moreover, although the basic unit is DB14C4, the additional functional groups change completely the binding characteristic of the ligands. The crystal structure of the lithium complexes of **1** (*12*) and **4** (*11*) and the monohydrate complex of **2** (*15*) indicate that the DB14C4 units assume nearly identical conformations upon complexation with H_2O or Li^+. This suggests that the structure of the DB14C4 unit is identical in the complexes of all four compounds and is independent of environmental conditions and is also probably independent of the metal cation to be bound. This evidence for similar rigid and stable macrocyclic conformations in the DB14C4 unit indicates that the macrocyclic ethereal oxygens form an identical geometrical arrangement in all four compounds and it is only the side arm functional groups that change the overall three-dimensional arrangement of the binding site (*15*).

The results of the membrane selectivity factor measurements for compounds **1–4** for the alkali-metal and alkaline-earth cations clearly demonstrate that compound **1** is a good and selective complexing agent for Li^+, whereas the derivatives **2–4** are poor complexing agents for Li^+ relative to the other alkali-metal cations. Considering the crystal structures of the lithium complexes of **1** and **4** (*11*, *12*) and the monohydrate complex of **2** (*15*) and on the basis of the examination of molecular models of all four compounds, we interpret the expermental selectivity results for compounds **1–4** as follows: [1] In stable complexes of Li^+ with small macrocyclic polyether compounds, Li^+ prefers pentacoordination, and especially the square-pyramidal geometry. [2] The DB14C4 macrocycle provides an ideal "base" for the square-pyramidal coordination, in which a direct interaction of the lithium cation and the four ethereal oxygens occurs. [3] The fifth (apical) coordination site in the DB14C4/Li^+ complex is occupied by the counterion or a solvent molecule. [4] In derivative **2**, the –OH group gives rise to proton binding probably because a monohydrate complex is formed which should strongly bind a proton. Also the encapsulated water molecule would hinder coordination of metal cations which explains the poor selectivity. [5] In derivatives **3** and **4**, the additional side arm is too short to bring the functional group into a proper apical position for the preferred Li^+ coordination. Moreover, these side arms are flexible enough to allow an "open" conformation in which the functional groups (the side arm etheral oxygens and the carboxylate group) could participate in six- to eight-coordination binding of larger cations (Na^+, K^+, Rb^+ or Cs^+). In these higher coordination complexes, the remaining binding sites are probably filled by counterions and/or solvent molecules. [6] The similar selectivities observed for crown ether alcohol **2** and crown ether carboxylic acid **4** indicate that the latter is functioning in its nonionized forms. [7] The reduced selectivities of compounds **2–4** toward any particular cation in certain conditions and the dependence of this selectivity on the membrane composition could be associated with the more "open" coordination assumed by these derivatives and the greater anion and solvent molecule participation in the coordination sphere. The macrocycle contribution (four binding sites) to the stability of the complex is reduced as the coordination number increases and when a monohydrate complex is formed. [8] The divalent cations are generally strongly rejected by all four compounds because of the special structural property of the DB14C4 frame whose "V"-shaped conformation allows direct or close contact with the counterion(s) only at one side of the complex (*12*). Divalent cations are disfavored, therefore, because of the lack of room for the charge balancing counterion(s) (especially if the counterions are monovalent (*12*)).

CONCLUSIONS

For the design of more selective ionophores for Li^+ to be incorporated in solvent–polymeric membranes, the following points are noted: [1] The DB14C4 frame (compound **1**) appears to be a good starting structure. [2] To improve the selectivity of **1** toward Li^+, an internal fifth ligand should be added. [3] The side arms consisting of –OH, $-OCH_2CH_2OCH_3$, or $-OCH_2COOH$ are too short and the latter two are probably too flexible, which allows coordination of larger cations. [4] To eliminate competitive reactions with protons and formation of stable hydrate complexes, the ionophore should not contain functional groups which can participate in hydrogen bonding and in acid–base reactions (e.g. –OH and –COOH). [5] From points 3 and 4, it appears that a longer and more rigid side

arm, carrying an etheral functionality, would be best for the lithium fifth coordination role.

ACKNOWLEDGMENT

Preparation of the solvent–polymeric membranes and the emf measurements were conducted in the laboratories of Professor Dr. W. Simon at ETH-Zentrum in Zürich, Switzerland.

LITERATURE CITED

(1) Rechnitz, G. A.; Eyal, E. *Anal. Chem.* **1972**, *44*, 370.
(2) Petranek, J.; Ryba, O. *Anal. Chim. Acta* **1974**, *72*, 375.
(3) Ammann, D.; Pretsch, E.; Simon, W. *Anal. Lett.* **1972**, *5*, 843.
(4) Erne, D.; Morf, W. E.; Arvanitis, S.; Cimerman, Z.; Ammann, D.; Simon, W. *Helv. Chim. Acta* **1979**, *62*, 994.
(5) Morf, W. E.; Ammann, D.; Bissig, R.; Pretsch, E.; Simon, W. In *Progress in Macrocyclic Chemistry*; Izatt, R. M., Christensen, J. J., Eds.; Wiley: New York, 1979; pp 1–61.
(6) Olsher, U. *J. Am. Chem. Soc.* **1982**, *104*, 4006.
(7) Amann, D.; Morf, W. E.; Anker, P.; Meier, P. C.; Pretsch, E.; Simon, W. *Ion-Sel. Electrode Rev.* **1983**, *5*, 3.
(8) Simon, W.; Morf, W. E.; Meier, P. C. *Struct. Bond.* **1973**, *16*, 113.
(9) Kimura, K.; Yano, H.; Kitazawa, S.; Shono, T. *J. Chem. Soc., Perkin Trans. 2* **1986**, 1945.
(10) Kimura, K.; Oishi, H.; Miura, T.; Shono, T. *Anal. Chem.* **1987**, *59*, 2331.
(11) Shoham, G.; Christianson, D. W.; Bartsch, R. A.; Heo, G. S.; Olsher, U.; Lipscomb, W. N. *J. Am. Chem. Soc.* **1984**, *106*, 1280.
(12) Shoham, G.; Lipscomb, W. N.; Olsher, U. *J. Chem. Soc., Chem. Commun.* **1983**, 208.
(13) Heo, G. S.; Bartsch, R. A.; Schlobohm, L. L.; Lee, J. G. *J. Org. Chem.* **1981**, *46*, 3574.
(14) Bartsch, R. A.; Heo, G. S.; Kang, S. I.; Liu, Y.; Strzelbicki, J. *J. Org. Chem.* **1982**, *47*, 457.
(15) Olsher, U.; Frolow, F.; Bartsch, R. A.; Pugia, M. J.; Shoham, G. *J. Am. Chem. Soc.*, in press.

RECEIVED for review December 23, 1988. Accepted May 1, 1989. G.S. thanks the Bat-Sheva Foundation of Israel for financial support. Research conducted at Texas Tech University was supported by a grant from the Robert A. Welch Foundation.

Electrochemical Study of the Mechanism of Cadmium Extraction with Dithizone

Wei-hua Yu and H. Freiser*

Strategic Metals Recovery Research Facility, Department of Chemistry, University of Arizona, Tucson, Arizona 85721

A current-scanning polarographic study of extraction processes involving dithizone and its metal chelates using the ascending water electrode (AWE) has been conducted. Of the metals examined, Cd(II) gives a wave that arises from the transfer of an unusual, charged, mixed ligand complex species, $Cd(OAc)Dz_2^-$. Other metal ions that form extractable dithizonates could be indirectly determined by their effect on the dithizonate wave.

INTRODUCTION

This represents a continuation of our electrochemical studies of the transfer processes associated with metal ion extractions utilizing the ascending water electrode (AWE) (*1–7*), which has proven to be a useful approach to the elucidation of the details of the chemistry of solvent extraction.

In this report, the behavior of diphenylthiocarbazone (dithizone), a weak monobasic acid with an aqueous pK_a of 4.7 (*8*), a widely used extractant whose sulfur atom bonding site results in a fair degree of selectivity, is examined, and its mechanism of extraction of cadmium is elucidated in this paper.

EXPERIMENTAL SECTION

The apparatus and procedures for current scan polarography at the AWE have been described earlier (*2–8*). The electrolytic cell used earlier was slightly modified in order to improve the stability of the organic reference electrode. The elimination of tetramethylammonium chloride, TMA^+,Cl^-, from both aqueous and organic reference solutions (which contain 1 M LiCl and 0.01 M tetraheptylammonium tetraphenylborate, THA^+,TPB^-, respectively) of the electrode resulted in stable readings for at least a month, whereas the earlier organic reference had to be replaced at least weekly. With the new arrangement, the potential of the organic reference electrode is largely determined by the charge of the double layer, inasmuch as there is not a common ion transferring across the aqueous/organic interface. As no charge flows through the electrode, i.e., no charging or discharging occurs, the potential is reproducible. The net effect is a shift in the $\Phi_0{}^aE$ of 106 ± 7 mV in the positive direction, compared to the electrode containing TMA^+Cl.

The electrolyte used in the 1,2-dichloroethane (DCE) phase was 0.01 M THA^+,TPB^-, prepared by mixing THA^+,Br^- dissolved in DCE and aqueous Na^+,TPB^- in stoichiometric proportions. Dithizone (Eastman Kodak Co.) was purified by recrystallization. 1,2-Dichloroethane (DCE) (Aldrich Chemical Co.) was used as received. All other reagents were analytical reagent grade.

RESULTS AND DISCUSSION

When current scan polarography is carried out on a HDz–DCE solution containing 0.01 M THA^+,TPB^- as supporting electrolyte in contact with 0.2 M sodium acetate aqueous solution, a well-defined cathodic wave is obtained (Figure 1). The features of this wave are as follows:

1. The limiting current of the cathodic wave is proportional to the initial concentration of HDz in DCE.
2. The limiting current is proportional to the square root of the height of the head of the aqueous reservoir.
3. The half wave potential shifts 49.5 mV ± 2.0 more positive per unit increase in pH in the range 6.4 to 10.7.
4. The logarithmic analysis shows the slope of 59.3 mV ± 3.0.

These characteristics suggest that the diffusion-controlled cathodic wave represents the transfer of the dithizonate anion from aqueous to organic phase. This is quite analogous to the behavior of other acidic extractants (*1–4*).

When Cd ion is present in the aqueous solution, another cathodic wave having a more positive half-wave potential, which is completely distinct from the deprotonated wave, appears (Figure 2). The minimum pH of the appearance of the new wave is 5.4, which is lower than that for the depro-

0003-2700/89/0361-1621$01.50/0

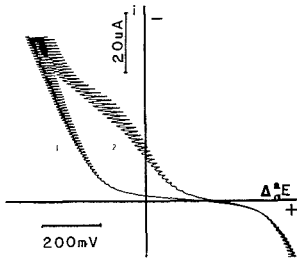

Figure 1. Polarography of dithizone: aqueous phase, 0.2 M sodium acetate of pH 8.0 ± 0.1; DCE solution, 0.01 M THA·TPB, HDz (mM) (1) 0 and (2) 0.4.

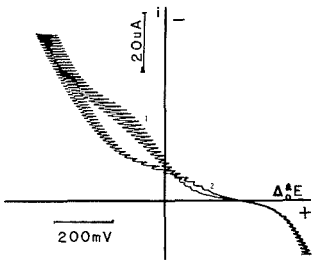

Figure 2. Polarography of dithizone in the presence of cadmium: aqueous phase, 0.2 M sodium acetate, cadmium sulfate (mM) (1) 0 and (2) 0.8; DCE solution, 0.01 M THA·TPB, 0.4 mM HDz.

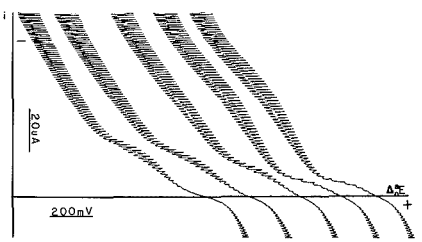

Figure 3. Effect of cadmium concentration: aqueous phase, 0.2 M sodium acetate of pH 7.5 ± 0.1, cadmium sulfate (mM) (1) 0.08, (2) 0.1, (3) 0.2, (4) 0.4, and (5) 1; DCE solution, 0.01 M THA·TPB, 0.8 mM HDz.

tonated wave. No wave is observed in the absence of acetate in aqueous phase. The new wave must result from the electrochemical transfer of a hitherto unobserved chelate anion of Cd, in which both dithizone and acetate must be involved.

Effect of HDz. The two separate cathodic waves can be observed when HDz is in excess (Figure 3). At constant $[Cd^{2+}]$, increasing $[HDz]_0$ has no effect on the chelate anion wave, but the dithizonate wave grows, since the former depends on Cd and the latter is related to the fre HDz. The relation between the limiting current of the chelating wave and the height of the aqueous reservoir demonstrates that this wave also is diffusion-controlled when HDz is in large excess.

Effect of Cd. When Cd is in mild excess ($[HDz]_0$ = 0.6 mM, [Cd] > 0.4 mM), the half-wave potential of the chelating wave becomes more negative while the limiting current remains constant, as might be expected by its control by the concentration of HDz. The limiting current is independent of the column height of the aqueous reservoir, characteristic of a kinetically controlled wave. Unless both HDz and acetate are in excess, the kinetically controlled wave will be observed.

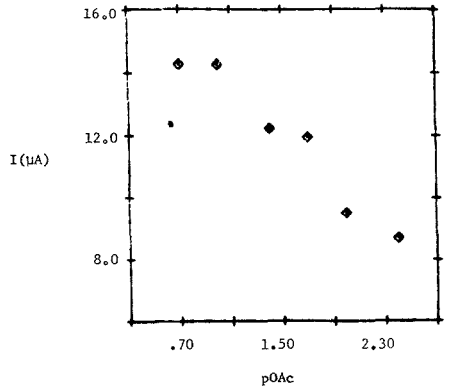

Figure 4. Effect of acetate on the limiting current of the complex wave: aqueous phase, 0.5 M magnesium sulfate, 0.2 mM cadmium sulfate; DCE solution: 0.01 M THA·TPB, 1.5 mM HDz.

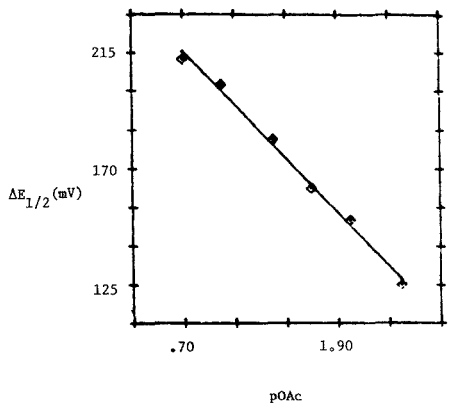

Figure 5. Effect of acetate on the half-wave potential of the complex wave: aqueous phase, 0.5 M magnesium sulfate, 0.2 mM cadmium sulfate; DCE solution, 0.01 M THA·TPB, 1.5 mM HDz.

Effect of Acetate. When $[Cd^{2+}]$ is 0.2 mM and [HDz] is 1.5 mM, no chelate anion wave appears until the $[OAc^-]$ is at least 2 mM. The limiting current of the wave rises with increasing concentration of acetate, reaching a plateau at $[OAc^-]$ = 0.2 M (Figure 4). The half-wave potential shifts 50 mV more positive per decade increase of $[OAc^-]$ (Figure 5), indicating that one acetate is present in the transferring anion.

Logarithmic analysis of the diffusion-controlled chelate wave (when both $[HDz]_0$ and $[OAc^-]$ in aqueous solution are in large excess over $[Cd^{2+}]$) gives a slope of 61 mV ± 5.7, signifying that the transferring species causing the chelate anion wave is monovalent. Taken together with the evidence that one OAc^- is present, as deduced above, $Cd(Dz)_2OAc^-$ must be the transferring anionic species. The limiting current reaches half the plateau value, a point at which half the cadmium is in the anionic acetate complex from, at pOAc = 1.9, which suggests a stepwise formation constant of this species from the neutral $CdDz_2$ of $10^{1.9}$.

The result of the following experiment supports the assumption of a chelate anion having a 1:2 Cd:Dz ratio: A series of polarograms is run, increasing the concentration of cadmium from 0.02 to 0.2 mM, while keeping the amount of HDz constant and in excess, e.g., 0.8 mM. The limiting current

Table I[a]

[Cd], mM	i_a, μA	i_c, μA
0.04	64.6	
0.08	57.12	5.44
0.1	54.4	6.8
0.2	38.08	12.24

[a] i_a and i_c stand for the currents of the deprotonated wave and chelate wave, respectively.

Scheme I

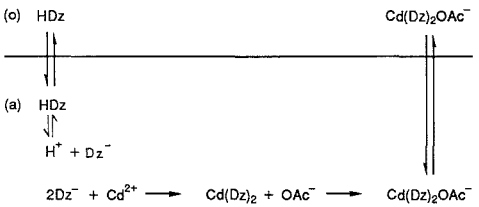

of the dithizonate wave decreases, and the chelate anion wave appears and increases with increasing [Cd] (Table I).

The effect of the cadmium on the size of the dithizonate wave can be derived with the help of the following equations:

$$i_1 = K(C - nM_2) \quad (1)$$

$$i_2 = K(C - nM_2) \quad (2)$$

where C, M_i, and i_i are the initial concentration of HDz, the concentration of Cd, and the limiting current of the dithizonate wave, respectively, and n is the number of dithizonates in the chelate. Taking the ratio i_1/i_2, the value of n can be readily obtained

$$\frac{i_1}{i_2} = \frac{C - nM_1}{C - nM_2} \quad (3)$$

From the data in Table I, n is found to be 2, proving that the transferring complex ion is $Cd(Dz)_2OAc^-$, a five-coordinated cadmium complex (9).

The process can be depicted as shown in Scheme I. The half-wave potential for the diffusion controlled wave can be calculated from the following equation:

$$\Delta_0{}^aE_{Cd(Dz)_2OAc_c} = \Delta_0{}^aE^\circ_{Cd(Dz)_2OAc} - \frac{RT}{2F}\ln\frac{D_{[Cd(Dz)_2]_1}}{D_{[Cd(Dz)_2OAc]_0}} - \frac{RT}{F}\ln\frac{K_D}{k_2[OAc]} \quad (4)$$

When formate is substituted for acetate, it behaves similarly, but because it is a weaker ligand than acetate, the cathodic wave begins to appear at higher formate concentrations and higher pH, with a more negative half-wave potential than when acetate is present.

Although no other metal ion that forms extractable chelates with dithizone gives rise to a characteristic wave, either anodic or cathodic, the presence of the metal ion in the aqueous phase can be detected by its effect on reducing the limiting current of the dithizonate wave. For example, when lead(II) is present instead of Cd(II), no additional wave appears, but the size of the dithizonate wave decreases. This signifies that only Cd forms the unusual anionic mixed ligand under our experimental conditions. Instead, the simple neutral extractable complex is formed, consuming dithizone and transferring without electrochemical trace into the DCE phase. Further, the effect on the dithizonate wave could form the basis for an indirect determination of those metals that form dithizonate complexes.

ACKNOWLEDGMENT

The authors gratefully acknowledge the helpful discussions with S. Muralidharan.

Registry No. Cd, 7440-43-9; dithizone, 60-10-6; acetic acid, 64-19-7.

LITERATURE CITED

(1) Yoshida, Z.; Freiser, H. *Electroanal. Chem.* **1984**, *162*, 307.
(2) Yoshida, Z.; Freiser, H. *Inorg. Chem.* **1984**, *23*, 3931.
(3) Yoshida, Z.; Freiser, H. *J. Electroanal. Chem.* **1984**, *179*, 31.
(4) Lin, S.; Freiser, H. *J. Electroanal. Chem.* **1985**, *191*, 437.
(5) Lin, S.; Zhao, Z.; Freiser, H. *J. Electroanal. Chem.* **1986**, *210*, 137.
(6) Lin, S.; Freiser, H. *Anal. Chem.* **1987**, *59*, 2834.
(7) Yu, W.; Freiser, H. *Anal. Sci.* **1987**, *3*, 401.
(8) Morrison, G. H.; Freiser, H. *Solvent Extraction in Analytical Chemistry*; John Wiley and Sons: New York, 1957.
(9) Cotton, F. A.; Wilkinson, G. *Advanced Inorganic Chemistry*; 3rd ed.; pp. 515 (1972).

RECEIVED for review January 3, 1989. Accepted April 21, 1989. The research was supported by a grant from the National Science Foundation.

Anal. Chem. 1989, 61, 1624–1630

Analysis of Transient Currents and Interfacial Kinetics for Neutral Carrier Membranes

James R. Sandifer*

Corporate Research Laboratories, Eastman Kodak Company, Rochester, New York 14650

Michael L. Iglehart and Richard P. Buck

Department of Chemistry, University of North Carolina, Chapel Hill, North Carolina 27514

General and simplified digital simulation schemes are used to generate current–time and component potential–time curves and carrier concentration profiles. For reversible interfaces, the analytical transient is a good representation. However, experimental $I-t$ curves require introduction of potential-dependent interfacial ion-transfer kinetics to reproduce short-time parts of the transients. Attempts to fit whole transients globally, with independently determined parameters (e.g., concentrations and the dc diffusion coefficient), are partially successful. Very good fits can be made by adjusting membrane concentrations and interfacial kinetic parameters, which are experimentally uncertain. A striking new result is that best fits require ion transfer coefficients far from 0.5 (asymmetric barriers). This effect is not unexpected since the applied voltage appears asymmetrically across back-to-back diffusion layers, with most potential drop in the membrane phase.

INTRODUCTION

In a series of paper (*1–7*), the mechanism of ion transport through neutral carrier ion-selective membranes has been studied by several authors. Neutral carriers (ionophores) are uncharged, hydrophobic complexing agents that selectively extract ions into inert, passive, fixed-site or mobile-site membranes. Preferred compositions of "normal" membranes are 33 wt % PVC [poly(vinyl chloride)], 66 wt % plasticizer, and 1 wt % neutral carrier. The plasticizer is typically a low dielectric constant, oil soluble ester such as DOS (dioctyl sebacate) or DNA (dinonyl adipate). The extraction reaction can be an ion-dipole outer sphere or adduct formation inner sphere reaction. Normal PVC membranes contain fixed negative sites at low concentrations, (0.05–0.5 mM), typically 0.1 mM in our system. The normal valinomycin loading in potassium-selective membranes is ≈10 mM, and the concentration of $Kval^+$ (the potassium/valinomycin complex) equals that of the negative sites, while the free K^+ concentration is negligibly small.

Perturbations of equilibrium or steady-state systems, with or without carriers, are required to measure interfacial and bulk ion transport rates. Establishment of mechanism requires consistency from different electrochemical and radiochemical techniques. Many prior studies of potentiometric responses of carrier-based ion selective electrodes demonstrate permselectivity but only infer possible transport mechanisms. In this paper, new results on carrier-induced ion transport, using transient current–time responses, are analyzed. The technique is supplementary to impedance measurements, current–voltage measurements, potentiometric measurements, and chemical analyses already reported (*1–7*). The complete current–time ($I-t$) analysis reported here requires digital simulation solutions of the nonlinear transport equations. A recent experimental study was incomplete because only the short and long time responses could be analyzed by using appropriate approximations (*6*) and concentration profiles were inferred from an approximate theory using a simplified model.

CLOSED-CIRCUIT SHUTTLE CARRIER MECHANISM AND NORMAL BEHAVIOR

The Ideal Reversible Interface Model. The K^+–valinomycin permselective membrane provides a standard system for describing normal current–voltage (*4*) and current–time (*6*) responses of the "closed circuit shuttle" carrier mechanism (*8*). The principal concepts are found in our work and that of Simon (*9–11*) and Armstrong (*12–14*). An ideal, homogeneous, fixed-uninegative site or mobile-site membrane (*1, 2, 5*) is assumed to contain site-equivalent or excess carrier with a complex formation constant of about 10^6 L/mol so that nearly all counterions are $Kval^+$. The membrane is plasticized and counterions are substantially ionized, i.e., $Kval^+$ is only partially ion-paired with sites S^-, so that current is carried only by $Kval^+$. Donnan exclusion is obeyed (*3*), and virtually no anions from the electrolyte are present in the membrane. It follows that the membranes are ideally permselective for cations, and surface ion exchange reactions are ideally rapid and reversible. Potentiometric responses are Nernstian or, in the presence of interferences, expressed by the Nicolsky–Eisenman equation.

Under an applied electrical perturbation, current is carried by $Kval^+$ moving from site-to-site without dissociation (*13*). Carrier is released at the interface where K^+ exits the membrane, but remains trapped in the membrane and is subject to back diffusion across the membrane according to Fick's laws. The model system, shown in Figure 1, is basically a simple concentration polarization of carrier such that the carrier, under dc current, has a high concentration at the exiting interface and a much lower concentration at the K^+-entering interface. For fixed-site membranes, the ac resistance is determined by the charge-carrier complex concentration (equal to fixed-site concentration) and charge-carrier mobility. At large dc voltages, there is a constant, limiting current. The apparent differential resistance (dV/dI) becomes infinite, but the integral resistance for ion motion remains finite.

Electrochemical Expectations from the Model. The anticipated behavior of the closed-circuit shuttle mechanism can be deduced and compared with data from impedance measurements (*1, 2*), Donnan failure potentiometry (*3*), steady-state current–voltage measurements (*4*), current–time transients at constant applied voltage (*6*), and voltage–time transients at constant forced current (*15*). Current–voltage curves are expected to be ohmic at low applied voltages, with resistances independent of excess carrier, to deviate negatively from ohmic responses at moderate applied voltages, and to show a transition region followed by a limiting current at high

0003-2700/89/0361-1624$01.50/0

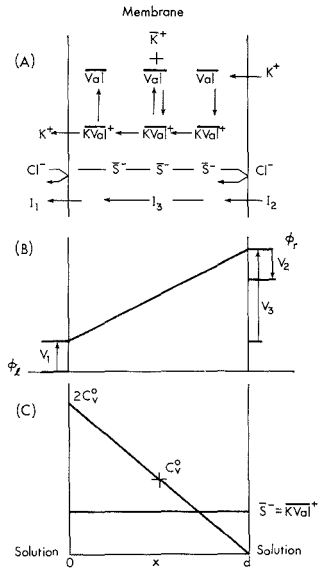

Figure 1. Model membrane with disposition of carrier, ion carrier complex and free ion. (A) Sites are $\bar{S}^-$; solution anion, Cl^-, is excluded from the membrane. Bulk and interfacial currents are individually identified. (B) Components of the potential profile, V_1, V_2, V_3, and the potentials of the bathing phases, ϕ_r and ϕ_l. (C) Idealized composition of the membrane for fully polarized carrier, on the limiting current plateau, assuming fixed sites at concentration S^-. C_V° is total concentration of valinomycin.

applied voltages. The limiting currents should be *independent* of bathing electrolyte concentrations (assuming Donnan exclusion), since ion-carrier complex concentration cannot exceed the site concentration. Limiting currents should be *dependent* on excess carrier concentration since concentration polarization of carrier determines the limiting current value. These points have been verified experimentally within limits (*1–7*).

Shapes of current–time transients depend upon the applied voltages. They can be constant at low applied voltages (in the ohmic range) or initially constant followed by a rapid decay to the steady-state limiting currents at higher applied voltages (but below Donnan exclusion breakdown).

The distribution of applied voltage across the membrane requires further comment. When a constant voltage is applied and current decays to the steady-state value, the voltage appears in three distinct segments: two interfacial segments and an internal or bulk phase segment. At steady state, with high applied voltages, most of the potential drop is at the interface where cations enter, because the carrier concentration is low there. The bulk potential is simply IR_∞, where the resistance is a constant calculated from the uniform site concentration and the mobility of $Kval^+$, provided sites are immobile. This potential becomes *constant* for high applied voltages on the ideal, constant limiting current plateau. The rest of the applied voltage appears at the interface where cations exit the membrane and the carrier concentration is twice the average bulk value, according to this reversible-interface, fixed-site, diffusion-controlled model.

Omissions from Available Transport Theory. Three major omissions from this ideal theory are slow interfacial ion exchange kinetics (or presence of a resistive surface layer), breakdown of Donnan exclusion so that anions enter the membrane at high applied voltages or at high bathing concentrations, membrane instability, including loss of plasticizer, carrier, or mobile sites, or uptake of water. The issue of slow interfacial kinetics is treated here, within the context of the Butler–Volmer equation. However, interpretations based upon the possible existence of a highly resistive film on the surface may be required in the future in order to account for certain anomalies to be described later. Alternative forms of the charge transfer equations might also be required. Most recently, Armstrong and Todd have commented on instabilities (*16*). Instability is difficult to treat theoretically, and it is hoped that this problem does not compromise the experiments too severely. However, fresh membranes were used throughout this study and only one membrane was used for each measurement in order to avoid the consequences of instability. Effects of Donnan failure on limiting currents and a simplified theory have been discussed (*17*). Breakdown of Donnan exclusion was avoided in this work by keeping applied voltages below values at which it might occur. Information obtained at higher voltages would probably be too difficult to interpret to make such measurements worth while.

Interfacial ion transfer described by Butler–Volmer kinetics has been stressed consistently by Cammann (*18, 19*). However, slow interfacial kinetics have always been difficult to prove when the interface is bathed in a high resistance medium or when the underlying phase is highly resistive. Nevertheless, evidence of measurably slow interfacial ion transfer rates in polymers and ionic conductors continues to accumulate (*20*) and may reflect either true surface kinetics or a resistive surface layer. "Measurably slow" means heterogeneous rate constants with values of $\simeq 10^{-3}$ to 10^{-5} cm/s. Larger values contribute immeasurably small surface resistances, and smaller values would be inconsistent with rapid, nearly reversible responses of membrane potentials to step changes in the activities of bathing solutions.

Application of Butler–Volmer kinetics to ion exchange, using four-position, quasi-thermodynamic methods, was mentioned in 1975 (*21*) and elaborated and corrected in two later publications (*22, 23*). Digital simulations of membrane transport with surface kinetics were introduced (*24*) as a means of finding cases and conditions suitable for determining surface rates. Impedance methods appeared to offer the most promise (*25*). Koryta (*26–28*) used a simplified version with two back-to-back diffuse layers but without a compact layer. The two models were subsequently compared (*29*) to show how the apparent transfer coefficient would depend on applied voltage across the interface for constant bulk concentrations. Interest in surface kinetic effects has increased through the work of Armstrong (*30–32*). Kinetic data were already obtained for the reaction of K^+ with surface carrier on (or in) lipid bilayers (*33, 34*).

SURFACE KINETICS AND SIMULATION SCHEMES

In agreement with the older work (*29*) and recent usage (*19, 30*), Table I summarizes the constant bulk concentration surface–kinetic equations in two forms

$$K^+ = \bar{K}^+; \text{ rate constant } k_s' \quad (1)$$

and

$$K^+ + \overline{val} = \overline{Kval}^+; \text{ rate constant } k_{s'} \quad (2)$$

where bar values are membrane quantities. The assumed complex formation constant is written

$$\beta = (\overline{Kval}^+)/(\bar{K}^+)(\overline{val}) = \sim 10^6 \text{ L/(mol s)} \quad (3)$$

The complexation constant is large enough to obviate consideration of free K^+ in the membrane, but not large enough to render the dissociation kinetics so small as to eliminate current flow by dissociation of complex at the exiting side of

Table I. Fixed Concentration Kinetic Equations for Two Interfacial Models

Model I

$$K^+ \rightleftharpoons \bar{K}^+$$

$\pm I/F = k_s'\{(\bar{K}^+)\exp[(1-\alpha)f(V-V_0')] - (K^+)\exp[-\alpha f(V-V_0')]\}$
At $I = 0$, $V(\text{eq}) = V_0' + (1/f)\ln(K^+)/(\bar{K}^+)$
$V_0' = (1/f)\ln k_{K^+} = (1/F)(\mu^\circ_{K^+} - \mu^\circ_{\bar{K}^+})$
V_0' follows from equality of the electrochemical potentials: $\bar{\mu}_{K^+} = \bar{\mu}_{\bar{K}^+}$
In terms of $(V - V_0) - (V_{eq} - V_0) = \eta$, $I = I_0\{\exp[(1-\alpha)f\eta] - \exp[-\alpha f\eta]\}$
$I_0 = Fk_s'(K^+)^\alpha(K^+)^{1-\alpha}$

Model II

$$K^+ + \overline{\text{val}} \rightleftharpoons \overline{\text{Kval}}^+$$

$\pm I/F = k_s\{(\overline{\text{Kval}}^+)\exp[(1-\alpha)f(V-V_0)] - [(K^+)(\overline{\text{val}})/C_0]\exp[-\alpha f(V-V_0)]\}$
At $I = 0$, $V(\text{eq}) = V_0 + (1/f)\ln[(K^+)(\overline{\text{val}})/(\overline{\text{Kval}}^+)C_0]$
$V_0 = (1/f)\ln k_{K^+}\beta = (1/F)(\mu^\circ_{K^+} - \mu^\circ_{\bar{K}^+}) + (1/F)\mu^\circ_{K^+}\ \mu^\circ_{\overline{\text{val}}} - \mu^\circ_{\overline{\text{Kval}}^+}$
V_0 follows from equality of the electrochemical potentials: $\bar{\mu}_{K^+} = \bar{\mu}_{\overline{\text{Kval}}^+} - \bar{\mu}_{\overline{\text{val}}}$
$I = I_0\{\exp[(1-\alpha)f\eta] - \exp[-\alpha f\eta]\}$
$I_0 = Fk_S(\overline{\text{Kval}}^+)^\alpha[(K^+)(\overline{\text{val}})/C_0]^{1-\alpha}$
$k_S/k_S' = \beta^{-\alpha}C_0^{1-\alpha}/(\overline{\text{val}})$; $f = F/RT$; C_0 is a normalizing concentration, typically 1 M; $\beta = (\overline{\text{Kval}}^+)/(\bar{K}^+)(\overline{\text{val}})$; $k_{K^+} = \bar{K}^+/K^+$

the membrane. The standard partition coefficient for reaction 1, k_i, is related to standard-state free energies according to

$$RT\ln k_i = \mu_0 - \bar{\mu}_0 \tag{4}$$

R and T are the gas constant and temperature, respectively. The system is shown in Figure 1. Positive currents flow in the direction of positive x. Currents in Figure 1 would be negative because positive applied voltage is on the right-hand side of the membrane. The applied voltage V_{Appl} is composed of three segments

$$V_{Appl}(\text{right–left}) = (\phi - \bar{\phi})_{right} + (\bar{\phi}_r - \bar{\phi}_l) + (\bar{\phi} - \phi)_{left} = V_2 + V_3 + V_1 \tag{5}$$

Because this is a two-interface problem, and current is continuous

$$I_1 = Fk_s\{[(K^+)(\overline{\text{val}})/(C_0)]\exp[-\alpha f(V_1 - V_0)] - (\overline{\text{Kval}}^+)\exp[(1-\alpha)f(V_1 - V_0)]\} \tag{6}$$

$$I_2 = -Fk_s\{[(K^+)(\overline{\text{val}})/(C_0)]\exp[-\alpha f(V_2 - V_0)] - (\overline{\text{Kval}}^+)\exp[(1-\alpha)f(V_2 - V_0)]\} \tag{7}$$

In eq 6 and 7, C_0 is a scaling concentration to make the units work out, and V_0 is the standard transfer potential difference, as defined by Koryta (*26*, *28*). Also, $f = F/RT$ where F is the Faraday constant.

$$I_3 = V_3/R_m \tag{8}$$

and

$$I = I_1 = I_2 = I_3 \tag{9}$$

R_m is the ordinary high-frequency resistance, R_∞

$$R_m = R_\infty = (dRT/AF^2)\Sigma(z_i^2D_iC_i)^{-1} \tag{10}$$

where d and A are membrane thickness and area and z_i, D_i, and C_i are charges, diffusion coefficients, and concentrations, respectively.

Simulation Scheme. Digital simulation of Fick's second law, the continuity equation for carrier, was done by an explicit method. The variable sequential simplex algorithm (*35*) provided a simple and reliable way to solve eq 6–10 for I, V_1, V_2, and V_3. Beginning with a known set of concentration profiles for all species, a set of guesses for the values of V_1 and V_2 is used to calculate a corresponding set of Y values, defined as

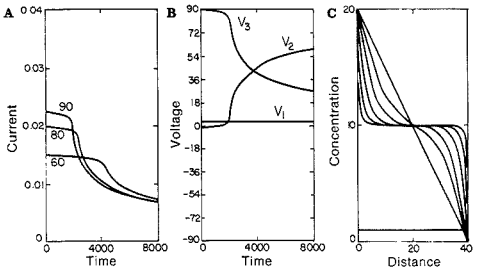

Figure 2. Responses calculated from general simulation theory: (A) current transients for three applied voltages in units of RT/F; (B) voltage transients for 90 RT/F volts, applied; (C) valinomycin concentration profiles at different times following polarization with 90 RT/F volts. Outer to inner curves correspond to 10, 400, 1000, 2000, and 4000 dt units. The steady-state profile is also shown.

$$Y = (I - I_n)^2 \tag{11}$$

where I is the average of the I_n values (I_1, I_2, I_3). The simplex algorithm is then used to generate the unique set of V_n values corresponding to a minimum value of Y (zero), which occurs only when $I_1 = I_2 = I_3 = I$. A net set of concentration profiles are generated by using a digital simulation technique, described previously (*36*). Although convergence is good, calculations are accurate, and simulations are stable within known limits, the method is slow because of the simplex steps. Results using this algorithm are illustrated in Figures 2 and 3 for hypothetical membranes containing 1 unit of $\overline{\text{Kval}}^+$, 1 unit of fixed negative sites, and 10 units of valinomycin. It should be noted that the algorithm is general, and it is not necessary to assume immobile sites. However, as will be shown below, this assumption allows very good fits of experimental results. In Figure 2 the diffusion coefficients of $\overline{\text{val}}$ and $\overline{\text{Kval}}^+$ are 0.01 $(dx)^2/dt$ units, where dx is the thickness of a volume element (40 were used) and dt is the time interval between iterations. α was fixed at 0.5, k_s was fixed at 0.2 dx/dt units, and V_0 was assigned a value of zero ($k_i = 1$).

In Figure 2A, the applied voltage was assigned values of 60, 80, and 90 RT/F units (1.536, 2.048, and 2.304 V, respectively) proceeding from the lower to the upper curve. The current is given in units of $FC_0\,dx/dt$. Each current transient consists of superimposed plots of I_1, I_2, and I_3 using the simplex algorithm (*23*). High convergence is indicated. Figure 2B shows the potential distributions of V_1, V_2, and V_3 as functions of time for 90 RT/F volts applied. Figure 2c shows concentration profiles at different times during polarization. In parts A and B of Figure 3, the dimensionless diffusion coefficient has been increased to 0.4 and α has been assigned values 0.05, 0.1, 0.2, 0.5, 0.8, 0.9, and 0.95, increasing in the direction of the arrows. Figure 3A shows the current transients, and Figure 3B shows the corresponding voltage transients. Note that V_1 is constant, and equal to its equilibrium value, when α is less than or equal to 0.5. In Figure 3C the dimensionless diffusion coefficient is 0.10, α is 0.5, and k_s has been assigned values 0.01, 0.02, 0.04, and 0.10 dx/dt units, proceeding from the lower to upper curves.

A simplified algorithm can be devised by noting that the nonpolarized interface does not always control current. For example, when the applied voltages are large and positive, the exiting interface is virtually reversible. Thus V_1 in Figure 1 takes on its reversible value as illustrated in Figures 2 and 3. These results will be discussed later. The applied voltage appears mainly across V_2 and V_3. The left interface serves

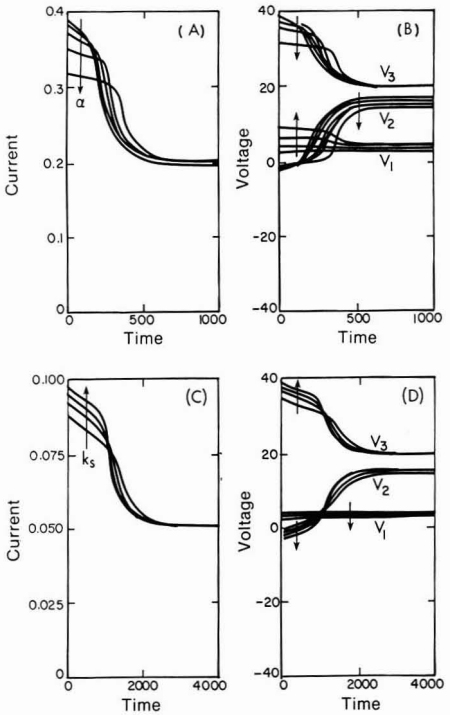

Figure 3. Responses calculated from general simulation theory. (A) Current transients using α = 0.05, 0.1, 0.2, 0.5, 0.8, 0.9, and 0.95 from upper to lower curves. Other parameters are in the text. (B) Voltage transients corresponding to Figure 3a. Arrows show directions of increasing α. (C) Current transients assuming k_s = 0.01, 0.02, 0.04, and 0.10 from lower to upper curves. (D) Voltage transients corresponding to Figure 3C. Arrows show directions of increasing k_s.

as a "reference" electrode with a nearly fixed potential, while the right side polarizes as valinomycin is consumed. The bulk membrane resistance acts like a large constant solution resistance in series with the interface, since it has been assumed that the sites are fixed. Thus, the $\overline{\text{Kval}}^+$ concentration profile is also flat and time-invariant. The entire membrane acts like a thin layer cell in which carrier is being "oxidized" on the left and "reduced" on the right with loss and gain of potassium ion rather than electrons.

One can view the current at the entering (reducing) interface as described by eq 7. Adding $-V_{2,\text{equil}} - V_0$ into the exponential, and factoring out the same term, expressed as concentrations, eq 7 is rewritten as

$$I_2 = -i_0\{\exp(-\alpha f\eta_2) - \exp[(1-\alpha)f\eta_2]\} \quad (12)$$

with

$$i_0 = Fk_s(\overline{\text{Kval}}^+)^\alpha[(\text{K}^+)(\overline{\text{val}})/C_0]^{1-\alpha} \quad (13)$$

$$\eta_2 = -(V_2 - V_{\text{equil}}) \quad (14)$$

Simultaneously

$$I_1 = i_0\{\exp(-\alpha f\eta_1) - \exp[(1-\alpha)f\eta_1]\} \quad (15)$$

with

$$\eta_1 = V_1 - V_{\text{equil}} \quad (16)$$

Because the cell is symmetric, $V_{\text{equil}} = V_{1,\text{equil}} = V_{2,\text{equil}}$. The potential difference at the left interface is given approximately by

$$\eta_1 \cong [(1-\alpha)/\alpha]\eta_2 + (RT/F)\ln[(\overline{\text{val}}_2)/(\overline{\text{val}}_1)] \quad (17)$$

which results from setting I_1 and I_2 equal, assuming a high voltage limit, and rearranging. The bulk potential drop, $V_3 = V_{\text{Appl}} - \eta_1 - \eta_2$, moves in opposition to η_2 because η_1 is never more than about 10% of η_2. Total current, I, through the interface at d and through the bulk of the membrane is given approximately by

$$I = C_p\,d\eta_2/dt + I_2 = (V_{\text{Appl}} - \eta_2)/R_m \quad (18)$$

where C_p is an estimate of the pseudocapacitance at d. It allows current flow parallel to ion transport defined in eq 12 and must be included in the simulation to ensure stability. Calculations are independent of the value of C_p, provided it is less than about 10 μF/cm^2. Virtually all of the current is then defined by I_2, and the estimate becomes better at longer times.

The simplified algorithm is as follows. i_0 is calculated from the last concentration profile and I_2 is calculated from this value of i_0 and the last value of η_2. Equation 18 is then solved numerically to proceed a dt unit to a new value of I and η_2. The latter is used in Feldberg's algorithm (*37*) to calculate a new concentration profile, and the algorithm cycles back to the i_0 calculation.

EXPERIMENTAL SECTION

Experimental details have been fully described in ref 6. Membrane compositions are 1% valinomycin, 33% poly(vinyl chloride), and 66% plasticizer: DNA (dinonyl adipate) or DOS (dioctyl sebacate). Because of possible changes in membrane properties following polarization, only one experiment was performed on each membrane. All calculations were performed on an IBM 3090 mainframe computer used in time-sharing mode.

RESULTS

Simulations of Reversible and Irreversible Interface Membranes. The major features of analytical transport theory for ideal, reversible interfaces have been reported (*3*, *6*, *8*). At high applied voltages on the carrier-transport-limited plateau, the current–time trace begins at the ohmic value and declines, rather abruptly after a "transition" time, to the free carrier transport-limited value.

The shapes of these curves, simulated with the general algorithm, are shown in Figure 2. Increased voltages decrease the transition times. The membrane resistance of this example is 4000 $(RT/F)/(FC_0\,dx/dt)$ units and the initial current is given by the applied voltage divided by the membrane resistance. The voltage distribution is shown in Figure 2B for interfacial (V_1 and V_2) and bulk (V_3) components, corresponding to 90 RT/F volts applied. The exiting interfacial potential difference V_1 is virtually at equilibrium. Figure 2C shows the carrier concentration profiles at different times during polarization. These are remarkably similar to the published schematic profiles (*6*). V_2 rises abruptly when the carrier concentration at the right side reaches zero. Although a constant voltage is applied to the cell, the response actually resembles constant current situations because V_{Appl}/R_m is virtually constant until the "transition" time.

Irreversible, kinetically limited interfaces are simulated in Figure 3. α has been varied in parts A and B of Figure 3, holding k_s constant at 0.2 dx/dt units. Note that V_1 approaches its equilibrium value as α approaches zero. D is 0.4 $(dx)^2/dt$ units in these simulations so that the dimensionless resistance would be 100 $(RT/F)/(FC_0\,dx/dt)$ units. The initial current should then be 0.4, with V_{Appl} = 40 RT/F units. The dimensionless resistance in parts C and D of Figure 3 is 400 units, so the initial current should be 0.10 if it were not limited by interfacial kinetics. This limit is approached as k_s increases, holding α constant at 0.5. V_1 decreases toward its equilibrium value as k_s increases.

These observations justify use of the simplified algorithm, illustrated by calculations shown in Figure 4. Responses are

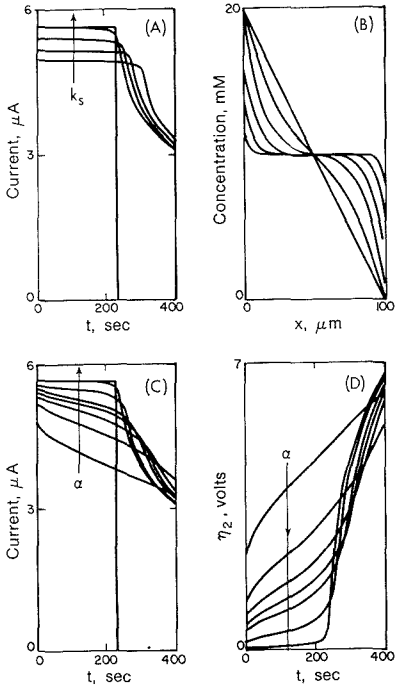

Figure 4. Responses calculated from the simplified theory. (A) Current transients using V_{Appl} = 15 V, D_{val} = 10^{-8} cm²/s, $Kval^+$ = 0.1 mM, C_V° = 10 mM, bathing K^+ = 1 mM (both sides), d = 100 μm, and α = 0.5. k_s was varied from 10^{-12} to 10^{-3} cm/s in 10^3 cm/s increments, from lower to upper curves. (B) Concentration profiles for k_s = 2 × 10^{-3} cm/s and α = 0.3 at 10, 40, 100, 200, 400, and 1000 s. (C) Current transients calculated with values of α = 0.01, 0.02, 0.03, 0.04, 0.05, 0.01, and 0.3 (bottom to top curves) with k_s = 2 × 10^{-3} cm/s. (D) Corresponding over voltage (η_2) transients.

in dimensional form, and model parameters are assigned that are close to those required for experimental data fits. Current transients are shown in Figure 4A, for a range of k_s values. Figure 4B shows profiles of carrier at different times during polarization. Figure 4C shows current transients for various *apparent* values of α. Figure 4D is the computed potential difference, η_2, for the current-controlling interface when V_{Appl} is positive and current is negative, e.g., flowing from right to left.

A particularly interesting result of the simulations in parts A and C of Figure 4 is the comparison and agreement of the simulated current and the approximate short-time solution of the transport problem (6). The aproximate solution is the curve with precipitous drop at $t = \tau$.

Simulation Fitting of Experimental Current–Time Curves. Responses of a series of seven membranes were analyzed to obtain overall simulation fits. Parameters are given in Table II for DOS membranes and Table III for DNA membranes. The membrane resistance was calculated from the applied voltage and the initial current. The diffusion coefficient for valinomycin was calculated from the measured concentration and the limiting current at long times. The site ($\overline{Kval^+}$) concentration was calculated from the diffusion coefficient and the initial current. "Best fit" values were assumed for k_s and α. The exchange current and charge transfer resistances were calculated from the other parameters in the tables.

Table II. DOS Membrane Parameters (Figure 5)

membrane	A	B	C
KCl, mM	1.00	1.00	10.0
Val, mM	9.72	9.62	9.43
V_{Appl}, V	13.82	16.50	10.87
d, μm	129.0	120.0	128.0
Rm, MΩ cm²	2.41	2.59	2.12
D_{val} × 10^8 cm²/s	1.75	1.77	1.75
$Kval^+$, μM	81.3	69.4	91.6
k_S × 10^3 cm/s	5.0	5.0	2.0
α	0.05	0.05	0.05
i_0, μA/cm²	7.37	7.24	25.67
R_{ct}, kΩ cm²	3.48	3.54	0.997
A = 0.785 cm²			

Table III. DNA Membrane Parameters (Figure 6)

membrane	A	B	C	D
KCl, mM	1.00	1.00	1.00	1.00
Val, mM	9.93	9.58	9.60	2.53
V_{Appl}, V	14.3	17.14	14.78	4.24
d, μm	120.0	114.0	120.0	124.0
Rm, MΩ cm²	2.90	3.32	2.44	2.95
D_{val} × 10^8 cm²/s	1.46	1.48	1.07	1.64
$Kval^+$, μM	75.1	61.5	122.0	67.9
k_s × 10^3 cm/s	5.0	5.0	5.0	10.0
α	0.05	0.05	0.05	0.05
i_0, μA/cm²	7.49	5.57	7.43	2.03
R_{ct}, kΩ cm²	3.42	4.60	3.45	12.59
A = 0.785 cm²				

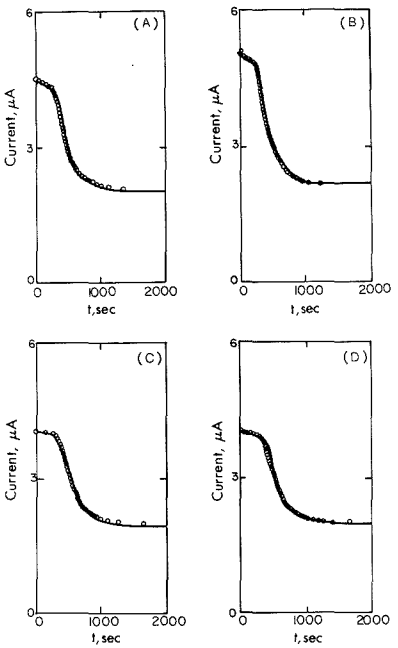

Figure 5. Simulated current–time curves and experimental points for DOS membranes. Simulations used the simplified theory. Parameters are shown in Table II. D is a second attempt to fit the data in C, except k_s = 5 × 10^{-3} cm/s and α = 0.08.

Figures 5 and 6 show how well the theoretical curves fit the experimental data points. Parts A and B of Figure 5 are essentially repeats of the same experiment using DOS membranes. Figure 5C shows what happens when the KCl con-

Table IV. Comparison of Resistances Measured before and after Polarization

membrane	DOS A	DOS B	DNA A	DNA B	DNA C	DNA D
applied polarization voltage, V	13.82	16.50	14.30	17.14	14.78	4.24
time resistance measd after polarization, h	9.5	264	0.5	12	9	12
resistance before polarization, MΩ	3.53	3.23	3.73	4.3	2.89	3.85
resistance after polarization, MΩ	2.07	1.03	2.98	2.12	1.72	2.61
ratio of resistance after and before polarization	0.59	0.32	0.80	0.49	0.60	0.68

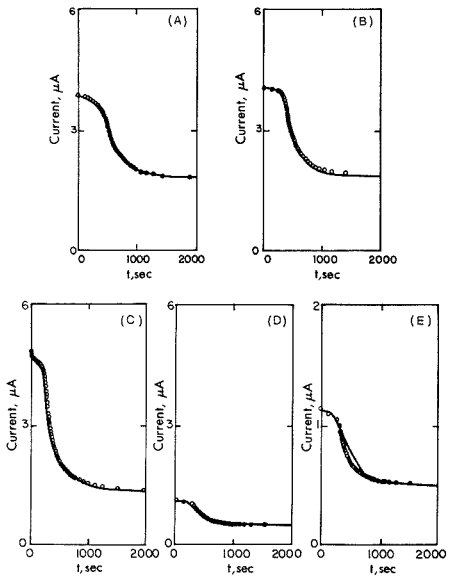

Figure 6. Simulated current–time curves and experimental points for DNA membranes. Simulations used the simplified theory. Parameters are shown in Table III. E is a replot of D with expanded scale.

centration is increased from 1 to 10 mM. Figure 5D shows a second attempt to fit the data shown in Figure 5C with $k_s = 5.0 \times 10^{-3}$ and $\alpha = 0.08$. Acceptable fits can obviously be obtained within this range of values. Since α is only an apparent value, its concentration dependence may not be too surprising.

Figure 6A–C shows essentially repeats of the same experiment using DNA membranes. Figure 6D shows what happens when the valinomycin concentration in the membrane is decreased by a factor of 3.8. The charge transfer resistance increases by a factor of 3.3, implying an α value of 0.05, consistent with the theory. Notice, however, that a replot of Figure 6D with an expanded scale, Figure 6E, shows a less-than-perfect fit of the data.

Table IV shows a comparison of resistances measured before and after polarization of each of the membranes except DOS C.

DISCUSSION

The model appears to be quite good, but not perfect. The Butler–Volmer equation is inadequate to fully describe the charge transfer process under all conditions of concentration (DOS results, Figure 5). Notice that an order-of magnitude increase in KCl concentration resulted in only about a factor of 3.5 decrease in the charge transfer resistance, implying an α value of 0.45. Unfortunately, this value provides a vastly inferior fit of the data.

The model agrees more nearly with the DNA data, but these results are not internally consistent. Notice in Table III that the diffusion coefficients, calculated directly from the limiting currents, are not the same for all four membranes. Differences are obvious even when looking at the raw data. Major problems may arise because the measurement of current–voltage curves requires many hours and the membranes may be severely perturbed.

Resistances are still quite high, however (Table IV), and the membranes calibrate Nernstianly even long after polarization. It is therefore reasonable to believe that the results reflect an accurate approximation of the true nature of the processes occurring in the membranes. It is interesting that a statistical analysis of the data shown in Table IV, and a wealth of experimental observations not reported here, reveals a stronger dependence of the ratio of resistances upon time-after-polarization than upon the applied polarization voltage. Furthermore, resistances generally rise with time-of-soaking (in 0.1 M KCl) by as much as a factor of 4 (over a period of about 5 days) prior to polarization. Polarization initiates a steady *decline* in resistance.

The calculated exchange current densities and charge transfer resistances, R_{ct}, are similar to those reported before. Armstrong and Todd (*32*) report >30 $\mu A/cm^2$ for bis(2-ethylhexyl) sebacate membranes containing 1 wt % valinomycin and potassium tetraphenylborate, bathed in 10 mM KCl. Xie and Cammann (*18*) report about 18 $\mu A/cm^2$ for dibutyl phthalate with 1 wt % valinomycin.

The surprising new result of this work is the uniform requirement that *apparent* α be small, $\simeq$0.05. From prior analysis (*30*), apparent α can be calculated to be from 0.02 to 0.07, depending on the bathing concentration, over a range of potential differences (including the pzc) when the concentration of K^+ is fixed by convection. The conventional theory does not allow for current-dependent concentration polarization. The space charge region in the membrane is dilute, with correspondingly low capacitance, by virtue of the low dielectric constant and low concentration of sites. Then, nearly all applied overvoltage appears inside the membrane at the side where K^+ enters, and no applied voltage assists the ion jump over the barrier set by the energy to remove K^+ from water and insert it into the carrier. The single inconsistent data are the exchange current densities that should be almost linearly dependent on K^+. However, this discrepancy may arise from failure of the algorithm to converge at short times when responses are too fast. Of course, it is also possible that the theoretical model requires further refinements, such as inclusion of a resistive film on the surface or an alternative form for the charge transfer equations.

Our data suggest that the K^+ interfacial process is almost exactly equivalent to electron transport (by usual thermionic emission) from a metal to an n-type semiconductor in a Schottky diode. In both cases most applied voltage appears on the dilute side of the interface, where the potential modifies the space charge profile by bending the bands in the semiconductor or the exactly equivalent bend of the ion's chemical potential in the membrane.

LITERATURE CITED

(1) Horvai, G.; Graf, E.; Toth, K.; Pungor, E.; Buck, R. P. *Anal. Chem.* **1986**, *58*, 2735.
(2) Toth, K.; Graf, E.; Horvai, G.; Pungor, E.; Buck, R. P. *Anal. Chem.* **1986**, *58*, 2741.

(3) Buck, R. P.; Toth, K.; Graf, E.; Horvai, G.; Pungor, E. *J. Electroanal. Chem.* **1987**, *223*, 51.
(4) Iglehart, M. L.; Buck, R. P.; Pungor, E. *Anal. Chem.* **1988**, *60*, 290.
(5) Lindner, E.; Graf, E.; Niegreisz, Z.; Toth, K.; Pungor, E.; Buck, R. P. *Anal. Chem.* **1988**, *60*, 295.
(6) Iglehart, M. L.; Buck, R. P.; Pungor, E. *Anal. Chem.* **1988**, *60*, 1018.
(7) Linder, E.; Niegreisz, Z.; Toth, K.; Pungor, E.; Berube, T. R.; Buck, R. P. *J. Electroanal. Chem.* **1989**, *259*, 67.
(8) Morf, W. E.; Wuhrmann, P.; Simon, W. *Anal. Chem.* **1976**, *48*, 1031.
(9) Morf, W. E.; Simon, W. *Helv. Chim. Acta* **1986**, *69*, 1120.
(10) Thoma, A. P.; Viviani-Nauer, A.; Arvanitis, S.; Morf, W. E.; Simon, W. *Anal. Chem.* **1977**, *49*, 1567.
(11) Thoma, A. P. Dissertation, Swiss Federal Institute of Technology, Zurich, 1977.
(12) Armstrong, R. D. *Electrochim. Acta* **1987**, *32*, 1549.
(13) Armstrong, R. D.; Nikitas, P. *Electochim. Acta* **1985**, *30*, 1627.
(14) Armstrong, R. D.; Todd, M. *Electrochim. Acta* **1987**, *32*, 155.
(15) Horvai, G.; Toth, K.; Pungor, E.; Iglehart, M.; Buck, R. P. "Impedance and Polarization Studies on Neutral Carrier Ion-selective Electrode Membrane", Euroanalysis VI (Fed. Europ. Chem. Socs.), Paris, September 1987.
(16) Armstrong, R. D.; Todd, M. *Electrochim. Acta* **1987**, *32*, 1403.
(17) Iglehart, M. L.; Buck, R. P. *Talanta* (Kolthoff Honor Issue), in press.
(18) Xie, S.-L.; Cammann, K. *J. Electroanal. Chem.* **1987**, *229*, 249.
(19) Xie, S.-L.; Cammann, K. *J. Electroanal. Chem.* **1988**, *245*, 117.
(20) Linder, E.; Pungor, E.; Buck, R. P. *Evidence for Ionic Electrokinetics at Pure Ionic Interfaces*; Extended Abstracts; The Electrochemical Society: Princeton, NJ, 1987; Vol. 87-1, p 402.
(21) Buck, R. P. *CRC Crit. Rev. Anal. Chem.* **1976**, *5*, 323.
(22) Buck, R. P. *Ion Exchange: Interfacial and Transport Properties*; The Electrochemical Society, Princeton, N.J. (1981).
(23) Melroy, O. R.; Buck, R. P. *J. Electroanal. Chem.* **1982**, *136*, 19.
(24) Brumleve, T. R.; Buck, R. P. *J. Electroanal. Chem.* **1978**, *90*, 1–31.
(25) Stover, F. S.; Brumleve, T. R.; Buck, R. P. *Anal. Chim. Acta* **1979**, *109*, 259–273.
(26) Koryta, J. Electrochim. *Acta* **1979**, *24*, 293.
(27) Koryta, J. *Ion-Sel. Electrode Rev.* **1983**, *5*, 131.
(28) Koryta, J. *Electrochim. Acta* **1984**, *29*, 445.
(29) Buck, R. P.; Bronner, W. E. *J. Electroanal. Chem.* **1986**, *197*, 179.
(30) Armstrong, R. D. *J. Electroanal. Chem.* **1988**, *245*, 113.
(31) Armstrong, R. D.; Lockart, J. C.; Todd, M. *Electrochim. Acta* **1986**, *31*, 591.
(32) Armstrong, R. D.; Todd, M. *Electrochim. Acta* **1986**, *31*, 1413.
(33) Stark, G.; Ketterer, B.; Benz, R.; Lauger, P. *Biophys. J.* **1971**, *11*, 981.
(34) Laprade, R.; Ciani, S.; Eisenman, G.; Szabo, G. *Membranes*; Eisenman, G., Ed.; Marcel Dekker: New York, 1975; Vol. 3, Chapter 3.
(35) Leggett, D. J. *J. Chem. Educ.* **1983**, *60*, 707.
(36) Sandifer, J. R.; Buck, R. P. *J. Phys. Chem.* **1975**, *79*, 384.
(37) Feldberg, S. W. *Electroanalytical Chemistry*; Bard, A. J., Ed.; Marcel Dekker: New York, 1969; Vol. 3.

RECEIVED for review October 26, 1988. Accepted April 18, 1989.

Preparation and Electrochemical Characterization of Conical and Hemispherical Ultramicroelectrodes

Reginald M. Penner, Michael J. Heben, and Nathan S. Lewis*

Division of Chemistry and Chemical Engineering, California Institute of Technology, Pasadena, California 91125

We describe a new ultramicroelectrode fabrication technique that has allowed the preparation of conical Pt–Ir ultramicroelectrodes with radii of 0.5–10 μm. These electrodes have been characterized by scanning electron microscopy, cyclic voltammetry, and chronoamperometry. The smallest radii electrodes ($r < 2$ μm) exhibited diffusional behavior at times longer than 70 μs in accord with a hemispherical geometry, while larger radii electrodes exhibited diffusional behavior consistent with a conical geometry. A first-order mathematical approach to diffusion at conical surfaces has been developed to explain these results.

INTRODUCTION

The construction of Pt, Au, and graphite ultramicrodisk electrodes with element radii as small as 0.1 μm has become routine in many electrochemical laboratories (*1*). The inherently small time constants of ultramicroelectrodes (UMEs) allow fast, transient electrochemical experiments to be performed (*2–10*), and the low total current allows voltammetry to be performed in highly resistive media (*2*, *11–15*). Additionally, mass transport to a UME is extremely rapid, and this permits the determination of fast heterogeneous rate constants using steady-state voltammetry (*16–22*). However, the interpretation of steady-state electrochemical results for the disk geometry is complicated by the fact that the steady-state current density near the edge of a microdisk can be much greater than at the center (*23–33*). Consequently, the mathematical analysis of cyclic voltammetry and chronoamperometry at microdisks is difficult and frequently involves approximations (e.g. ref 27–33).

UMEs possessing a hemispherical geometry would circumvent this problem, since the steady-state current density at a hemispherical surface is uniform. Consequently, simplified mathematical treatments are available for this electrode geometry (*34*). Unfortunately, conventional UME construction techniques are not well suited to preparing hemispherical ultramicroelectrodes (*1*). Thus, experimental results for this UME geometry, despite its obvious theoretical advantages, are notably absent from the literature.

We report here a new procedure for preparing both glass- and polymer-insulated Pt–Ir alloy UMEs. These UMEs have cone (or hemisphere) radii in the range 0.5–10 μm. We also present data for the electrochemical characterization of these electrodes by cyclic voltammetry and chronoamperometry. The chronoamperometry data for the conical UMEs has been analyzed in terms of an expression that combines linear diffusion and radial diffusion terms. These measurements have yielded the first experimental information on the diffusional properties of cone-shaped microelectrodes.

EXPERIMENTAL SECTION

I. Chemicals. Reagent grade $K_4Fe(CN)_6$, KCl, KOH, and Na_2SO_4 (all from J. T. Baker) and NaCN (Mallinckrodt) were used as received. Aqueous solutions were prepared with 18 MΩ cm deionized water obtained from a Barnstead Nanopure system. Poly(α-methylstyrene) (Aldrich Chemical Co., MW = 60 000) was used as received. Pt(70%)–Ir(30%) wire (diameter = 0.020 in.) was obtained from Engelhard Industries.

II. Apparatus. *A. Electrochemistry.* Chronoamperometry and cyclic voltammetry were performed by using a Princeton

*Author to whom correspondence should be addressed.

0003-2700/89/0361-1630$01.50/0

Applied Research (PAR) Model 173 potentiostat in conjunction with a PAR Model 175 voltage programmer. Cyclic voltammograms at scan rates below 500 mV/s were recorded on a Houston Instruments Model 2000 X-Y recorder. Data from faster voltammetric sweeps, or from current–time transients, were recorded on a Nicolet Model 2090 III digital storage oscilloscope. Direct currents (dc) were measured with a Keithley Model 427 current amplifier, and alternating currents (ac) were measured with a Keithley Model 177 voltmeter. Etching characteristics were recorded by using a Linear Co. strip chart recorder.

Electrochemical cells were of a conventional one-compartment design. All microelectrode experiments were performed by using a conventional three-electrode configuration and a saturated calomel reference electrode (SCE).

B. Scanning Electron Microscopy. Scanning electron microscopy (SEM) and energy dispersive X-ray (EDX) elemental analysis were performed with a CamScan SEM equipped with a Tracor-Northern X-ray analyzer and data station. A typical accelerating voltage for these measurements was 20 kV. Prior to SEM examination, all electrodes were coated with ca. 200 Å of gold by using a plasma coater. The spatial profile analysis of Pt using EDX methods was not impeded by the presence of this Au coating.

III. Tip Etching. The electrochemical etching bath consisted of an unstirred solution of 2 M NaOH and 6 M KCN. The cyanide facilitated the complexation and dissolution of metal from the immersed wire, and the NaOH inhibited the formation of HCN. All etching was performed in a fume hood.

The apparatus used for tip etching and coating has been described previously (*35*). An ac voltage of 25 V root mean square was applied between an immersed Pt–Ir wire and a graphite counter electrode, and the depth of immersion was adjusted until the average current was 1.25 A root mean square. Etching was terminated when the desired conical geometry and aspect ratio were obtained (see Results, section I).

IV. Tip Coating. *A. Glass Coating Procedures.* A coating apparatus was used to apply controllable, uniform coatings of nonporous glass insulation to the etched Pt–Ir tips (*35*). Soda-lime glass (Corning Glass No. 0080) was cleaned with *i*-C_3H_7OH and deionized water and was then used for coating the Pt(70%)–Ir(30%) wire. Procedures used for degassing the glass bead and for manipulation of the Pt–Ir wire have been described previously (*35*). Tip translation speeds in the range 0.3–0.5 mm/min and glass temperatures of 1350 ± 20 °C were used to form the UMEs studied in this work.

B. Polymer Coating Procedures. After a survey of a number of other polymers, poly(α-methylstyrene) (PαMS) was selected as the preferred polymer coating material. The other materials investigated yielded either erratic coating qualities (e.g. poly(vinyl chloride)) or a brittle coating that shattered during hardening (e.g., polystyrene). PαMS has similar mechanical properties to those of polystyrene, but it has a lower melting temperature (*36*), which apparently makes it more suitable for the tip coating process. The PαMS (Aldrich) consisted of small polymer beads (weight = ca. 20 mg), each of which was approximately the correct size for coating a single Pt–Ir tip.

The procedure used for polymer coating was qualitatively similar to that for glass coating. Because of the lower temperatures involved in the polymer coating process, and the lack of the need to remove bubbles from the PαMS melt, a simpler procedure utilizing a soldering iron (Ungar, 22W) with an "omega" shaped wire (diameter = 4 mm) was often employed. The polymer bead was supported by this wire and was heated by the soldering iron. Tip coating was accomplished by translating the wire (by hand) through the polymer melt. A typical tip translation speed was approximately 0.5 mm/s, although qualitatively similar UME tip behavior was observed for tip speeds between 0.25 and 1.0 mm/s. In contrast to the glass coating process, the rate of tip translation during the polymer coating step did not appear to be an important variable in determining the final coating morphology.

The quantity of exposed metal at the coated tip was found to vary reproducibly with the polymer melt temperature. The polymer temperature was monitored by immersion of an iron–constantan thermocouple wire directly into the melt. During coating, the polymer melt was adjusted to a temperature of 190–205 °C. Within this temperature range, the cone/hemisphere radius decreased from 10 to 0.5 μm as the temperature was increased.

Figure 1. Scanning electron micrograph (SEM) of the tip of a Pt–Ir wire after electrochemical etching.

V. Electrochemical Pretreatment and Surface Conductivity. Following glass or polymer coating, reversible steady-state voltammograms in the $Fe(CN)_6^{4-}$ test solution were not always observed initially. Instead, for approximately 10% of the UMEs with either type of insulation, the cyclic voltammetry appeared to be quasi-reversible, with plots of log $[(i_l - i)/i]$ vs $E - E_{1/2}$ yielding reciprocal slopes of 80–90 mV (*21*). However, when such electrodes were potentiostated at −0.6 V vs SCE for several minutes, the apparent reversibility of the $Fe(CN)_6^{4-/3-}$ wave usually improved. Slopes of log $[(i_l - i)/i]$ vs $E - E_{1/2}$ were then close to 60 mV, as expected for reversible electron-transfer processes (*21*). This observation suggests that a surface oxide layer was initially present at the exposed Pt–Ir surface and was possibly introduced during the preceding electrochemical etch. Electrochemical reduction of this oxide then enabled routine voltammetry to be performed with these UMEs.

An additional complication was sometimes observed with glass-coated UMEs. In some cases, the cyclic voltammetry of $Fe(CN)_6^{4-/3-}$ was superimposed on a steeply sloping background current. This observation suggested the presence of a parallel resistance in the electrochemical equivalent circuit. This current was found to result from a surface conductivity effect. Insulating the exposed metal shaft of such electrodes with epoxy was found to remove the sloping background component from these voltammograms and resulted in normal, reversible electrochemical behavior.

RESULTS

I. Properties of Etched Pt–Ir Tips. The coating of Pt–Ir metal tips by glass and polymer layers was found to be a function of the sharpness, surface roughness, and cone angle of the etched tips. Extremely sharp metal tips (tip radius <1 μm) facilitated the polymer and glass coating processes, and these tips resulted in the conical UME geometries of interest in this study. Details of the tip etching procedures have been described previously (*35*), and these procedures readily yielded tip radii in the range 0.5–1.0 μm.

An SEM image of a typical etched (but uncoated) Pt–Ir tip is shown in Figure 1. The geometry of this tip was close to conical, with an aspect ratio (height/base diameter) $\alpha = 1.3$ and a radius of curvature at the tip apex of approximately 1.0 μm. Typical aspect ratios were found to be 1.2–1.3. The surface of the hemispherical tip in Figure 1 was observed to be smooth to the limiting resolution of the SEM. This indicates that the metal underwent an effective electropolishing process during etching (*37*). For this reason, further polishing of the metal surface, even after insulating with glass or polymer coatings, was not necessary. Also, the longitudinal grooves revealed by the SEM images of the tip shaft were not de-

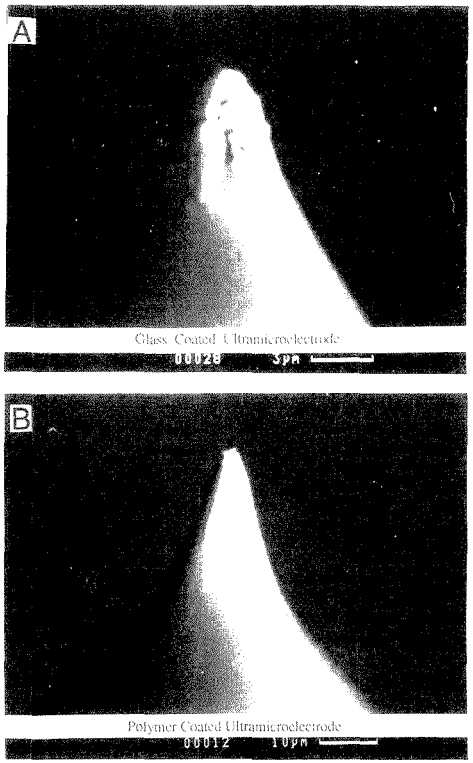

Figure 2. A. SEM image of the glass-coated UME used to obtain the cyclic voltammetry data shown in Figure 3A. B. SEM image of the polymer-coated UME used to obtain the cyclic voltammetry data shown in Figure 3B.

trimental to the final UME performance characteristics, because this area was insulated from contact with the electrolyte by the glass/polymer coating process.

Over a variety of runs, we observed that etched tips varied widely in geometry and morphology as a result of changes in etching voltage, etching time, or the age of the etching solution. Fortunately, the current vs time relationships of etching tips provided a bath-independent means by which the etching process could be monitored (*35*). Such curves reliably described the evolution of the tip structure for most experiments, and the etching procedure was found to be quite satisfactory for producing the desired tip features. Additionally, varying the termination time of the etching process yielded "sharp" tips possessing aspect ratios from 0.5 to 10. Although we have found that an aspect ratio of 1.2–1.4 is optimal for polymer and glass coated UMEs, the etching procedure is thus capable of producing other types of tips for use in other applications.

II. Characterization of Insulated UME Tips. *A. Scanning Electron Microscopy.* Figure 2 displays SEM images of representative etched and coated Pr–Ir microelectrodes. For the glass-coated UME shown in Figure 2A, the interface between the glass insulator and the exposed metal surface is clearly visible. Notably, although this interface is not geometrically uniform, no cracks or other defects in the glass/metal seal are evident. In SEM images of polymer coated UMEs, such as that shown in Figure 2B, a well-defined interface was not apparent between the polymer insulator and the exposed metal surface. The difficulty in resolving this interface implies that there was an intimate seal between these two components of the UME. Defects, cracks, and other mechanical deformations were similarly absent in SEM images of other glass-coated and polymer-coated UMEs. Thus, it appears that both the glass and polymer coatings adhere extremely well to the etched Pt–Ir surface. This feature is critical for making well-defined microelectrodes by any tip insulation process.

The exact location of the insulator–metal boundary for polymer-coated tips was determined by using both SEM imaging and EDX spectroscopy. The increased brightness near the apex of the polymer-coated tip in the SEM image of Figure 2B is consistent with the expected increase in electron backscattering efficiency at exposed Pt–Ir regions. This conclusion was corroborated by obtaining EDX spectra as a function of position along the tip axis. Selected spots (0.05 μm × 0.05 μm) at a series of distances from the tip apex were analyzed for the presence of Pt. Pt absorption lines were clearly evident at the areas near the tip apex. However, the intensity of these absorptions decreased as the electron beam traversed the interface between the bright and dark regions of the SEM image (Figure 2B). At distances greater than 0.5 μm beyond this interface, Pt absorption lines were no longer discernible, supporting the conclusion that the dark regions in the SEM image corresponded to coated areas of the metal wire.

The exposed metal surface of the polymer-coated UME (Figure 2B) closely approximated a conical geometry, with an aspect ratio (α = 1.2) similar to that of the etched, uncoated Pt–Ir tips (Figure 1). In addition, no significant texture of the metal surface is apparent in the SEM image of Figure 2B, indicating that the surface was smooth on a scale of 0.1 μm. Greater roughness is visible at the exposed metal tip of the glass-coated UME (Figure 2A). This indicates that the characteristic conical tip geometry produced by the etching procedure described above is not retained after exposure of the metal to the high temperatures inherent to the glass coating procedure.

B. Cyclic Voltammetry. Cyclic voltammograms for the glass-coated and polymer-coated UMEs shown in Figure 2, obtained in aqueous 4.34 mM $Fe(CN)_6^{4-}$, 1.0 M KCl solutions, are shown in Figure 3A and Figure 3B, respectively. At the two slowest scan rates (2 and 10 mV/s) in this figure, the shape of the voltammograms is sigmoidal, and no cathodic wave was observed. The combination of these two features indicates that radial diffusion was established and that steady-state mass transport conditions were present for both types of tips (*38*). At faster scan rates (50, 200, and 1000 mV/s), significant forward and reverse peak currents were observed, indicating the presence of diffusional mass transport limitations on these time scales (*38*).

These data can be used to estimate the critical (or smallest) dimension of the exposed metal at the UME tip. As a qualitative first approximation, the apparent hemispherical radii, r_{app}, of these UMEs (Figure 2) can be estimated from the limiting current, i_l, by using the equation describing hemispherical diffusion: $i_l = 2\pi nFDCr_{app}$ (*34*). The limiting currents obtained from the 2 mV/s scans in Figure 3 are $i_{l,glass}$ = 7.1 nA and $i_{l,polm}$ = 16.4 nA. These values yield apparent hemispherical radii of r_{app} = 3.4 μm and r_{app} = 7.85 μm for the glass- and polymer-coated UMEs, respectively.

An independent estimate of the small dimension of the exposed metal surface is available from the change in the shape of the cyclic voltammogram as a function of scan rate. The appearance of peaks (both cathodic and anodic) in the voltammogram signals the onset of linear diffusion. This condition occurs when the diffusion layer thickness becomes

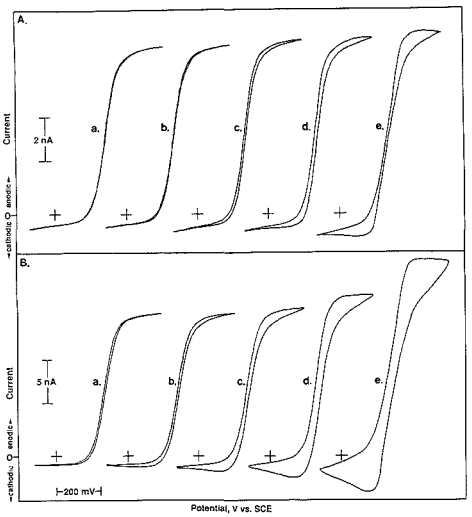

Figure 3. A. Cyclic voltammograms for the glass-coated UME of Figure 2A immersed in 4.34 mM $Fe(CN)_6^{4-}$, 1 M KCl(aq) at potential scan rates of (a) 2, (b) 10, (c) 50, (d) 200, and (e) 1000 mV/s. B. Cyclic voltammograms for the polymer-coated UME of Figure 2B in the same solution. Scan rates are the same as in Figure 3A.

Table I. Comparison of UME Radii Determined from SEM Data and Cyclic Voltammetric Data for Typical Glass- and Polymer-Coated UMEs

electrode	$r_{c,SEM}$,[a] μm	r_{app},[b] μm	r_{CV},[c] μm
glass	2.8	3.40	2
polymer	8.2	7.85	6

[a] Radius at the base of the exposed metal surface as estimated from SEMs shown in Figure 2. [b] Radius calculated from the voltammetric limiting current at ν = 2 mV/s by using the expression for steady-state hemispherical diffusion, $i_l = 2\pi FDCr_{app}$ (*34*). [c] Radius estimated from the ratio i_p/i_l at ν = 1 V/s according to a microdisk voltammetric model (*32*).

less than the smallest dimension of the electrode (*38*). Thus, an analysis of the voltammetry in the transition region between linear and spherical diffusion yields an estimate of the UME radius that is independent of that calculated by using the value of the limiting current. A quantitative treatment of linear scan voltammetry at microdisk electrodes by Aoki et al. (*32*) has shown that a unique relationship exists between the dimensionless parameter $p = (nFr^2\nu/RTD)^{1/2}$ (where r is electrode radius and ν is voltage scan rate) and the ratio between the voltammetric peak current and the steady-state limiting current, i_p/i_l. The values of this ratio for the 1 V/s scans shown in parts A and B of Figure 3 are 1.1 and 1.2, respectively. These values yield apparent microdisk radii of 2 μm for the glass-coated UME (Figure 3A) and 6 μm for the polymer-coated UME (Figure 3B) (*32*). These calculated values are in reasonable agreement with the apparent radii calculated from the limiting current formula for hemispherical diffusion to these UMEs.

Analysis of SEM images and EDX spectra allowed the cone base radius, r_c, of the polymer-coated and glass-coated UMEs of Figure 3 to be established as 8.2 and 2.8 μm, respectively. These values are compared in Table I with those obtained from cyclic voltammetry. Since the apparent voltammetric radius values, r_{app}, were calculated by using the hemispherical limiting current equation (vide supra), the agreement shown

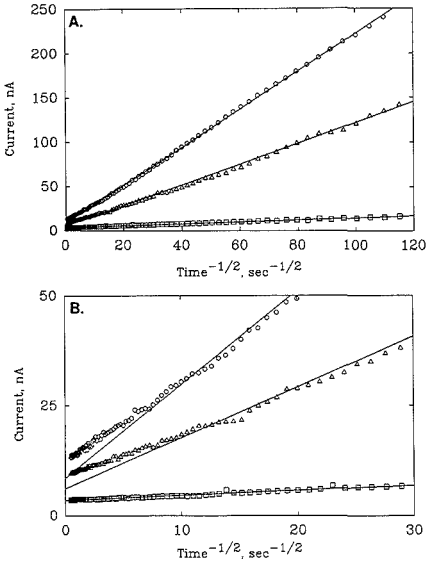

Figure 4. Current vs time$^{-1/2}$ plots for potential steps at three polymer-coated, Pt–Ir UMEs. Potential steps were applied from 0.0 to 0.5 V vs SCE in 4.21 mM $Fe(CN)_6^{4-}$, 0.5 M Na_2SO_4(aq). Key: (○) r_{app} = 6.5 μm (r_{app} is the apparent hemispherical radius of the UME); (△) r_{app} = 4.8 μm; (□) r_{app} = 1.7 μm. Panel A shows plot of data for time interval from 70 μs to 3 s; B, data for time interval from 1 ms to 3 s.

in Table I between the SEM data and the apparent electrochemical radius data suggests that this equation is an acceptable approximation to the steady-state electrochemical behavior of these cone-shaped UMEs. Of course, a more quantitative treatment (necessary for time-dependent processes, vide infra) would account for differences in the areas of cones, disks, and hemisphere with identical radii. However, the close agreement evident in Table I between qualitative electrochemical radii and actual geometric radii did prove to be a satisfactory guide for the selection of polymer-coated UMEs of various metal areas.

C. Chronoamperometry. A quantitative evaluation of the electrochemical behavior of these ultramicroelectrodes is possible using chronoamperometry (*39*, *40*). Figure 4A shows typical i vs $t^{-1/2}$ data in aqueous 0.5 M Na_2SO_4–4.21 mM $Fe(CN)_6^{4-}$ solutions for polymer-coated UMEs possessing apparent hemispherical radii of r_{app} = 1.7, 4.8, and 6.5 μm (as estimated from the observed i_l values for these electrodes). In these experiments, the potential was stepped from 0.0 to 0.5 V vs SCE. Note that the linearity of these plots is excellent (correlation coefficient >0.99) for times between 70 μs and 0.01 s.

Because the concentration of ferrocyanide in this solution and its diffusion coefficient (7.94×10^{-6} cm^2/s (*39*)) are known, the slopes of these plots can be used in the Cottrell equation to calculate an apparent electrode area. These areas are listed in Table II.

The i vs $t^{-1/2}$ data at long times (t > 1 ms) are shown in greater detail in Figure 4B. Positive deviations of the experimental data from the Cottrell line are particularly evident for the r_{app} = 4.8 μm and r_{app} = 6.5 μm radii UMEs. These positive deviations are expected in the time interval where a transition from linear diffusion to hemispherical diffusion occurs (*39*). This change in the mode of diffusion will occur when the diffusion layer increases in thickness and assumes dimensions greater than those of the conical metal surface (*38*).

Table II. Summary of Geometric Data for Polymer-Coated UMEs Obtained from Chronoamperometry Experiments and SEM Investigations

A_{Cott},[a] cm^2	r, μm	a	A_{Cott}/A_{hemi}[f]	α[g]
3.46×10^{-6}	6.51[b]	2.000π[d]	1.29	1.19
1.91×10^{-6}	4.84[b]	2.002π[d]	1.30	1.20
1.81×10^{-7}	1.70[c]	2.000π[e]	1.00	

[a] Areas calculated from the slopes of the i vs $t^{-1/2}$ plots (Figure 4A) by using the Cottrell equation (eq 2). [b] Base radius of the right circular cone with aspect ratio, $\alpha = 1.2$, which possesses the Cottrell area listed in column 1 (calculated from the equation $A = \pi r_c(r_c^2 + h^2)^{1/2}$). [c] Radius of the hemisphere which possesses the Cottrell area listed in column 1. [d] Value of the a coefficient obtained by fitting the experimental log i vs log t data (Figure 5). The radius listed in column 2 was obtained from the short time (Cottrell region) current by using eq 2 with $A = \pi r_c(h^2 + r_c^2)^{1/2}$ and $\alpha = h/2r_c = 1.2$. A value for a was then obtained by fitting the steady-state time regime to eq 3 with $r = r_c$. [e] Value of the a coefficient used to fit the experimental log i vs log t data (Figure 5). [f] Ratio between the experimentally determined Cottrell areas for each UME listed in column 1 and the surface area of a hemisphere possessing the radius listed in column 2. [g] Aspect ratio (α = cone height/cone diameter) of a right circular cone calculated as described in Results, section IIC.

Thus, a quantitative analysis of the i vs t data spanning this transition region should yield information regarding the size and the geometry of the exposed metal at the UME tip.

A first-order mathematical description of the chronoamperometric transients for a general electrode geometry can be obtained by writing the total diffusion-limited current as a sum of the planar flux and radial flux diffusion components (*26*, *34*):

$$i_{total} = i_{planar} + i_{radial} \quad (1)$$

The form of the planar component of this expression is given by the well-known Cottrell equation (*34*):

$$i_{planar} = nFAD^{1/2}C/(\pi^{1/2}t^{1/2}) \quad (2)$$

This portion of the total current can be calculated for any electrode geometry and will provide an excellent approximation to the total diffusion-limited current at sufficiently short electrolysis times. For the particular UME geometries of interest in this work, the hemispherical area is given simply by $A_{hemi} = 2\pi r^2_{hemi}$, while the conical area, A_{cone}, equals $\pi r_c(h^2 + r_c^2)^{1/2}$, where h and r_c are equal to the height and base radius of a right circular cone.

The geometric information of interest is contained in the radial diffusion term of eq 1. For spherical, hemispherical, and disk UME geometries, a general expression for the radial component in eq 1 has been found to be (*26*)

$$i_{radial} = arnFDC \quad (3)$$

where r is the electrode radius and a is a function of the electrode geometry (*26*). For spheres $a = 4\pi$, for hemispheres $a = 2\pi$, and for disks, the apparent a is time dependent but approaches $a = 4$ as $t \rightarrow \infty$. To date, the applicability of this treatment and the appropriate value of a are unknown for conical electrodes, because the conical UME geometry has not been available for investigation.

Thus, if eq 1 provides a correct description of the diffusion-limited current response of a conical UME, the only adjustable parameter in the fitting of the chronoamperometric data in Figure 4 is the value of a. To apply eq 1 to this UME geometry, the Cottrell area of the UME was obtained from the slopes of the i vs $t^{-1/2}$ data at times <0.01 s ($t^{-1/2} > 10$ s$^{-1/2}$) by using eq 2. The measured Cottrell area was then used in conjunction with the observed cone aspect ratio of 1.2 (Figure 2B) to calculate a value for r_c, the base radius of the cone. Fitting the long time regions of the chronoamperogram to eq 1–3 with $r = r_c$ then yielded a best value for a.

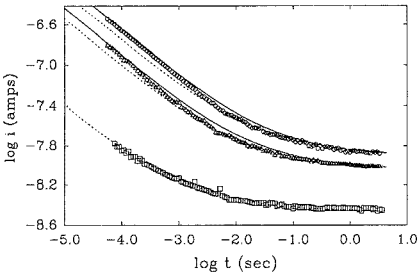

Figure 5. Comparison of experimental log i vs log t data for the plots in Figure 4 with the theoretical behavior expected for both the conical electrode geometry (solid line) and the hemispherical electrode geometry (broken line). The calculations were done by using eq 1–3, as described in the text. Key: (○) $r_{app} = 6.5$ μm UME; (△) $r_{app} = 4.8$ μm; (□) $r_{app} = 1.7$ μm.

Figure 5 displays experimental and theoretical log i vs log t plots for the three UMEs used in the chronoamperometry of Figure 4. Only the UMEs with the two largest r_{app} values yielded chronoamperometry that deviated from hemispherical diffusion predictions; thus, only these electrodes yielded values for r_c and a (Table II) with use of the conical diffusion treatment described above. For these two conical UMEs, the agreement between the two values for a is excellent. Furthermore, measurement of numerous other conical UMEs in this radius range yielded a values of 1.9π–2.2π. Thus, the apparent a value for these types of conical electrodes, obtained from the steady-state portion of the chronoamperogram, was close to that expected for a hemispherical electrode geometry, $a_{hemi} = 2\pi$ (*34*, *41*). Of course, the value of a also depends on the geometry and extent of the insulating region of the electrode assembly; thus, the values for conical electrodes obtained in this work are probably fortuitously close to the $a = 2\pi$ value for a hemisphere on an infinite insulating planar support.

Another method for determining the value of a is to utilize the relationship between the steady-state limiting current in the cyclic voltammetry (Figure 3) and the conical base radius, r_c, as determined by SEM. For steady-state diffusion, eq 3 should describe the relationship between r_c and the total observed current at the UME. For the polymer-coated conical UME of Figure 2B, using the value for r_c determined by SEM analysis (8.2 μm) and the observed i_l value at 2 mV/s (i_l = 16.4 nA), eq 3 yields a value for a of 1.9π. This value is in excellent agreement with those determined by analysis of the chronoamperometry data using eq 1. This implies that the semiquantitative approach of eq 1 is a quite satisfactory description of the diffusional behavior of these conical UMEs over a range of radii and time regimes.

Also shown in Figure 5 are log i vs log t calculations for these UMEs based on a hemispherical electrode geometry. These data are presented merely to illustrate the deviation from pure hemispherical diffusion displayed by these conical UMEs. To obtain these fits, a value for r_{app} was obtained from the steady-state limiting current by using eq 3 with $a = 2\pi$, as expected for a hemisphere. The entire theoretical chronoamperogram was then calculated by using this value for r with $a = 2\pi$ and $A = 2\pi r_{app}^2$ in eq 1–3, as would hold if the UME were indeed a hemisphere. Note that for the $r_{app} = 4.8$ μm and $r_{app} = 6.5$ μm UMEs, the currents calculated by using this method underestimate the actual values in the short time (Cottrell) regime. For example, the $r_{app} = 6.5$ μm UME has a response in the Cottrell region that is displaced by 0.1 = log 1.25 from the hemispherical calculation. The discrepancy

indicates that the actual electroactive surface area of the UME is 25% greater than that expected on the basis of the erroneous assumption that the UME is indeed a hemisphere.

The correction in area necessary to achieve agreement between the hemispherical UME model and actual Cottrell area is further evidence for a conical UME geometry. An aspect ratio of 1.20 is required for a right circular cone of base radius r_c = 6.5 μm to yield a 29% increase in exposed area relative to a hemisphere with r_{app} = 6.5 μm. Similarly, the aspect ratio required for a 29% increase in area of the r_{app} = 4.8 μm UME is α = 1.19. These values, summarized in Table II, agree well with the geometric α values of 1.2–1.3 obtained by direct SEM measurements on these electrodes.

The electrochemical behavior of the r_{app} = 1.7 μm radius UME (□ in Figure 5) is distinctly different from that of the larger radii UMEs discussed above. Note that the experimental data is overlaid by calculated log i vs log t data for the hemispherical model over the entire time regime investigated. Thus, the electrochemical behavior of this electrode during chronoamperometry is essentially indistinguishable from that of a hemispherical UME over the full range of experimental times (*34*, *39*, *40*). Significantly, UMEs that exhibited hemispherical diffusion behavior always possessed $r_{app} < 2$ μm.

For both the r_{app} = 4.8 μm and the r_{app} = 6.5 μm UMEs of Figure 5, the current calculated from eq 1 is in good (but not perfect) agreement with the data over the entire experimental time interval. The slight overestimate of the actual current in the transition region indicates that the apparent value for a is too large in this time interval. This observation is evidence for an apparent a coefficient that is weakly time dependent over this time regime. A similar situation has been observed for chronoamperometry at microdisk electrode surfaces (*26*, *39*, *40*). Observation of a time-dependent apparent a is equivalent to stating that the first-order treatment given by eq 1 is not a rigorously correct solution to the diffusion equations in this time regime. However, a rigorous solution to the diffusion equation for a cone is expected to be quite complicated, and the semiquantitative approach embodied by eq 1–3 is apparently quite satisfactory for describing the behavior of our UMEs over the time regimes of usual experimental interest.

DISCUSSION

The combination of SEM images, cyclic voltammetry, and chronoamperometry data indicates that the tip etching/coating process is capable of producing well-defined conical and apparent hemispherical ultramicroelectrode tip geometries. The larger radii UMEs ($r_{app} > 2$ μm) exhibited electrochemical behavior in accord with diffusion to a cone, and the aspect ratio and base cone radius of these electrodes given by the SEM analysis were consistent with the electrochemical behavior of these tips. In contrast, for smaller radii UMEs ($r_{app} < 2$ μm), chronoamperometric data for $t > 70$ μs was consistent with hemispherical diffusion. Although hemispherical mercury microelectrodes have been reported previously (*42–46*), the fabrication procedure reported here is the first to our knowledge to yield solid metal electrodes in this theoretically advantageous geometry (*1*).

Assuming that the UMEs share a common etched tip geometry, a unified picture, Figure 6, can be obtained for the effects of the tip coating process. When the radius of the exposed metal approaches the ultimate etched tip radius ($r \approx 1$ μm), the apparent electrochemical geometry of the exposed metal should approximate that of a hemisphere for most experimentally accessible times. Greater UME diameters should display greater amounts of surface area on the conical tip surface. As shown in Table II, this behavior is in accord with the data for the UMEs examined in this work. The r_{app} = 1.7 μm electrode exhibited a chronoamperometric response in accord with that expected for a hemispherical electrode over the entire experimental time range, while significant deviations from hemispherical behavior were observed for the r_{app} = 4.8 μm and r_{app} = 6.5 μm UMEs.

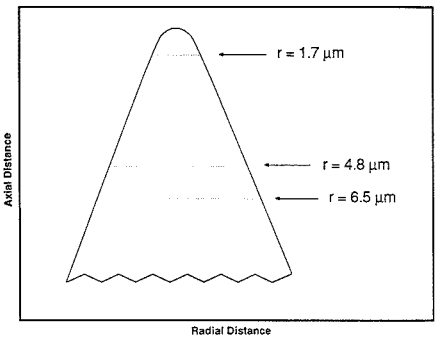

Figure 6. Representation of the etched tip geometry showing the approximate location of the insulator–metal interface (broken lines) for the r_{app} = 1.7, 4.8, and 6.5 μm polymer-coated UMEs examined in the chronoamperometry section.

Our two-step fabrication procedure is conceptually simple and is similar to procedures used previously to prepare glass-insulated Pt–Ir electrodes for in vivo potentiometry in neurophysiology applications (*47*, *48*). However, both the etching and coating steps of the procedure have undergone significant refinement, in order that geometrically well-defined and microscopically smooth metal surfaces remain exposed after insulator coating. Previous workers have found it necessary to subject the coated and etched metal wire to an intentional "exposure step", in which the insulating material is apparently removed from the coated assembly to expose bare metal (*47*, *48*). We have found that this step is unnecessary, because exposed metal areas with the desired geometries, and intimate insulator–metal seals, are present in coated wires prepared by our etching/coating process.

UMEs with radii both larger and smaller than those described above could be obtained by manipulating the coating conditions as described in the Experimental Section above. The smallest UME radius obtained by using the fabrication methods described here was r_{app} = 0.05 μm (estimated from the voltammetric limiting current). We have found that it is routinely possible to prepare UMEs with somewhat larger radii (r_{app} = 0.2–0.5 μm) by using either the glass or polymer coating procedures. These values are comparable to the smallest electrode radii accessible when conventional microdisk construction techniques are used (*1*).

This new UME design possesses a number of other significant features: (1) No mechanical pretreatment (i.e., polishing) of the UME is required (because the etched metal surface is microscopically smooth); (2) the metal–insulator seals of these electrodes are reproducible and abrupt; and (3) the procedure does not require the handling of micrometer size wire that is commonly used in conventional microdisk fabrication processes. Polymer-coated versions of these UMEs can be prepared with a minimum of equipment in any electrochemical laboratory.

A possible disadvantage of this design is the fact that the metal surface of the UMEs described here cannot be renewed by polishing. This problem is inherent to the protruding hemispherical geometry, but is partially offset by the ease with which new UMEs can be prepared with our procedure.

An obvious application of our UME tips is in scanning tunneling microscopy (STM). This application requires sharp,

geometrically well-defined tips fabricated from chemically inert conductors. Our insulated Pt–Ir tips would seem to be especially well suited to in situ STM applications, where faradaic currents from the body of the metal wire normally preclude effective feedback control of the tunneling current (*49–51*). Additionally, the resolution of scanning electrochemical microscopy is critically dependent on the tip radius. Our tips are the smallest reported to date and should be capable of producing far higher resolution than that currently obtained with 5–10 μm radius wires (*52–54*). These tips could also be used in high-speed electroanalytical methods, where the advantageous geometry and low total exposed surface area can be exploited, and in neurophysiological studies that require easily prepared, chemically inert, implantable microelectrodes. Application of this tip fabrication procedure to these problems is currently being explored and will be described in future publications.

Registry No. IrPt, 11110-72-8; NaOH, 1310-73-2; KCN, 151-50-8; $Fe(CN)_6^{4-}$, 13408-63-4; poly(α-methylstyrene), 25014-31-7.

LITERATURE CITED

(1) Fleischmann, M.; Pons, S.; Rolison, D. R.; Schmidt, P. P. *Ultramicroelectrodes*; Datatech Systems, Inc.: Morganton, NC, 1987; Chapter 3.
(2) Howell, J. O.; Wightman, R. M. *Anal. Chem.* **1984**, *56*, 524–529.
(3) Howell, J. O.; Wightman, R. M. *J. Phys. Chem.* **1984**, *88*, 3915–3918.
(4) Montenegro, M. I.; Pletcher, D. *J. Electroanal. Chem. Interfacial Electrochem.* **1986**, *200*, 371–374.
(5) Fitch, A.; Evans, D. H. *J. Electroanal. Chem. Interfacial Electrochem.* **1986**, *202*, 83–92.
(6) Amatore, C. A.; Jutand, A.; Pfuger, F. *J. Electroanal. Chem. Interfacial Electrochem.* **1987**, *218*, 361–365.
(7) Andrieux, P.; Garreau, D.; Hapiot, P.; Pinson, J.; Saveant, J. M. *J. Electroanal. Chem. Interfacial Electrochem.* **1988**, *243*, 321–335.
(8) Wipf, D. O.; Kristensen, E. W.; Deakin, M. R.; Wightman, R. M. *Anal. Chem.* **1988**, *60*, 306–310.
(9) Andrieux, C. P.; Garreau, D.; Hapiot, P.; Saveant, J. M. *J. Electroanal. Chem. Interfacial Electrochem.* **1988**, *248*, 447–449.
(10) Wipf, D. O.; Wightman, R. M. *Anal. Chem.* **1988**, *60*, 2460–2464.
(11) Bond, A. M.; Fleischmann, M.; Robinson, J. *J. Electroanal. Chem. Interfacial Electrochem.* **1984**, *168*, 299–312.
(12) Bond, A. M.; Fleischmann, M.; Robinson, J. *J. Electroanal. Chem. Interfacial Electrochem.* **1984**, *180*, 257–263.
(13) Cassidy, J.; Khoo, S. B.; Pons, S.; Fleischmann, M. *J. Phys. Chem.* **1985**, *89*, 3933.
(14) Dribble, T.; Bandyopadhyay, S.; Ghoroghchian, J.; Smith, J. J.; Sarfarazi, F.; Fleischmann, M.; Pons, S. *J. Phys. Chem.* **1986**, *90*, 5275–5277.
(15) Bruckenstein, S. *Anal. Chem.* **1987**, *59*, 2098–2101.
(16) Dayton, M. A.; Ewing, A. G.; Wightman, R. M. *Anal. Chem.* **1980**, *52*, 2392–2396.
(17) Scharifker, B.; Hills, G. *J. Electroanal. Chem. Interfacial Electrochem.* **1981**, *130*, 81–97.
(18) Russell, A.; Repka, K.; Dibble, T.; Ghoroghchian, J.; Smith, J. J.; Fleischmann, M.; Pitt, C. H.; Pons, S. *Anal. Chem.* **1986**, *58*, 2961–2964.
(19) Bond, A. M., Oldham, K. B.; Zoski, C. G. *J. Electroanal. Chem. Interfacial Electrochem.* **1988**, *245*, 71–104.
(20) Oldham, K. B.; Zoski, C. G.; Bond, A. M.; Sweigart, D. A. *J. Electroanal. Chem. Interfacial Electrochem.* **1988**, *248*, 467–473.
(21) Galus, Z.; Golas, J.; Osteryoung, J. *J. Phys. Chem.* **1988**, *92*, 1103–1107.
(22) Bond, A. M.; Henderson, T. L. E.; Mann, D. R.; Mann, T. F.; Thormann, W.; Zoski, C. G. *Anal. Chem.* **1988**, *60*, 1878–1882.
(23) Soos, Z. G.; Lingane, P. J. *J. Phys. Chem.* **1964**, *68*, 3821–3828.
(24) Newman, J. *J. Electrochem. Soc.* **1966**, *113*, 501–502.
(25) Flanagan, J. B.; Marcoux, L. *J. Phys. Chem.* **1973**, *77*, 1051–1055.
(26) Dayton, M. A.; Brown, J. C.; Stutts, K. J.; Wightman, R. M. *Anal. Chem.* **1980**, *52*, 946–950.
(27) Oldham, K. B. *J. Electroanal. Chem. Interfacial Electrochem.* **1981**, *122*, 1–17.
(28) Galus, Z.; Schenk, J. O.; Adams, R. N. *J. Electroanal. Chem. Interfacial Electrochem.* **1982**, *135*, 1–11.
(29) Aoki, K.; Osteryoung, J. *J. Electroanal. Chem. Interfacial Electrochem.* **1981**, *122*, 19–35.
(30) Aoki, K.; Osteryoung, J. *J. Electroanal. Chem. Interfacial Electrochem.* **1981**, *125*, 315–320.
(31) Shoup, D.; Szabo, A. *J. Electroanal. Chem. Interfacial Electrochem.* **1982**, *140*, 237–245.
(32) Aoki, K.; Akimoto, K.; Tokuda, H.; Osteryoung, J. *J. Electroanal. Chem. Interfacial Electrochem.* **1984**, *171*, 219–230.
(33) Pons, S.; Fleischmann, M. *Anal. Chem.* **1987**, *59*, 1391A–1399A.
(34) Galus, Z. *Fundamentals of Electrochemical Analysis*; Halsted Press: New York, 1976; Chapter 4.
(35) Heben, M. J.; Dovek, M. M.; Lewis, N. S.; Penner, R. M.; Quate, C. F. *J. Microsc.*, in press.
(36) *Polymer Handbook*, Interscience: New York, 1966.
(37) Petzow, G. *Metallographic Etching*; American Society for Metals: Metals Park, OH, 1978; Chapter 1.
(38) Wightman, R. M. *Anal. Chem.* **1981**, *53*, 1125A–1134A.
(39) Hepel, T.; Osteryoung, J. *J. Phys. Chem.* **1982**, *86*, 1406–1411.
(40) Hepel, T.; Plot, W.; Osteryoung, J. *J. Phys. Chem.* **1983**, *87*, 1278.
(41) Delahay, P. *New Instrumental Methods in Electrochemistry*; Interscience: New York, 1954; p 54.
(42) Lines, R.; Parker, V. D. *Acta Chem. Scand.* **1977**, *B31*, 369.
(43) Wehrmeyer, R. K.; Wightman, R. M. *Anal. Chem.* **1985**, *57*, 1989–1993.
(44) Golas, J.; Osteryoung, J. *Anal. Chim. Acta* **1986**, *186*, 1–9.
(45) Golas, J.; Osteryoung, J. *Anal. Chim. Acta* **1986**, *181*, 211–218.
(46) Golas, J.; Galus, Z.; Osteryoung, J. *Anal. Chem.* **1987**, *59*, 389–392.
(47) Wolbarsht, M. L.; MacNichol, E. F., Jr.; Wagner, H. G. *Science* **1960**, *132*, 1309–1310.
(48) Guld, C. *Med. Electron. Biol. Eng.* **1964**, *2*, 317–327.
(49) Sonnenfeld, R.; Hansma, P. K. *Science* **1986**, *232*, 211–213.
(50) Itaya, K.; Sugawara, S. *Chem. Lett.* **1987**, 1927–1930.
(51) Dovek, M. M.; Heben, M. J.; Lewis, N. S.; Penner, R. M.; Quate, C. F. *Molecular Phenomena at Electrode Surfaces*; Soriaga, M. P., Ed.; ACS Symposium Series 378; American Chemical Society: Washington, DC, 1988; pp 174–201.
(52) Lin, C. W.; Fan, F.-R. F.; Bard, A. J. *J. Electrochem. Soc.* **1987**, *134*, 1038–1039.
(53) Craston, D. H.; Lin, S. W.; Bard, A. J. *J. Electrochem. Soc.* **1988**, *135*, 785–786.
(54) Bard, A. J.; Fan, F.-R. F.; Kwak, J.; Lev, O. *Anal. Chem.* **1989**, *61*, 132–138.

RECEIVED for review September 27, 1988. Accepted April 18, 1989. The authors acknowledge the Office of Naval Research, Grant No. N00014-88-K-0482, for support of the research, and N.S.L. acknowledges additional support from the Camille and Henry Dreyfus Foundation Teacher-Scholar Program. This is Contribution No. 7861 from the Division of Chemistry and Chemical Engineering at Caltech.

Quantitative Relationship between Electron Transfer Rate and Surface Microstructure of Laser-Modified Graphite Electrodes

Ronald J. Rice and Richard L. McCreery*

Department of Chemistry, The Ohio State University, 120 West 18th Avenue, Columbus, Ohio 43210

Previous investigations demonstrate that increases in electron transfer rate constant, k°, on highly ordered pyrolytic graphite (HOPG) basal plane correlate with the appearance of edge plane defects and that such defects may be created with laser or electrochemical pretreatment. In the current work both capacitance (C°_{obs}) and k°_{obs} for $Fe(CN)_6^{3-/4-}$ on HOPG were measured as functions of power density of the activating laser. Over a power density range from 0 to 130 MW cm^{-2}, k°_{obs} increased by more than 5 orders of magnitude while C°_{obs} increased by a factor of 8. Both k°_{obs} and C°_{obs} may be expressed as linear combinations of the basal and edge plane k° and C° values, weighted by the fractional coverage of edge plane on the electrode surface (f_e). Determinations of f_e from both k°_{obs} and C°_{obs} are quantitatively consistent and in both cases increase with power density above a threshold of 45 MW cm^{-2}. Although effects of surface roughness may also be involved, the results indicate that the electron transfer activity of laser-modified HOPG is predominantly dependent on edge plane density.

INTRODUCTION

The wide variation of heterogeneous electron transfer rate constants (k°) on carbon electrodes has attracted a variety of investigations into the influence of surface chemistry on charge transfer kinetics. The many factors which may affect k° on carbon have been discussed many times in the primary literature (*1–16*) and in a recent monograph (*17*). The overall motivation of these research efforts is an understanding of what aspects of the carbon surface determine k° for simple systems such as $Fe(CN)_6^{3-/4-}$ and more complex cases like O_2 reduction and many organic redox systems.

Our laboratory's approach to the problem has involved laser activation (*12, 13, 16*) of both glassy carbon (GC) and highly ordered pyrolytic graphite (HOPG) combined with Raman spectroscopy as a probe of carbon microstructure (*18, 19*). HOPG is a structurally well-characterized material whose basal plane is atomically clean when freshly cleaved. HOPG can serve as a simple model of more complicated materials such as GC, to permit insights into the structural changes which promote electron transfer. For the case of laser activation of basal plane HOPG, we showed that k° for $Fe(CN)_6^{3-/4-}$ changes suddenly with increasing laser power density, with a rate increase of approximately 5 orders of magnitude occurring after 50 MW/cm^{-2} laser treatment (*18*). This activation correlates with the formation of graphite edge plane on the original HOPG basal plane. The correlation of edge plane density and high k° was also observed for electrochemical activation of HOPG and for laser activation of edge plane HOPG and GC-20.

The 1360-cm^{-1} Raman band of carbon materials is a good marker for edge plane, with greater 1360-cm^{-1} intensity indicating smaller graphitic microcrystallites (*18, 20, 21*). The correlation is based on spectra of carbons with different basal plane lattice parameter, L_a, determined from X-ray diffraction (*20*). While the 1360-cm^{-1}/1582-cm^{-1} Raman intensity ratio is directly proportional to the reciprocal of L_a in carbon powders, it is not obvious how this quantitative proportionality applies to laser-activated HOPG. There is no reason to expect an even or narrow distribution of L_a over the activated basal plane surface or into the bulk HOPG. Although the 1360/1582 ratio will increase with edge plane density (and decreasing microcrystalline size), the relationship should be considered semiquantitative, and it would be risky to attempt to calculate edge plane density from the Raman data with useful accuracy. The objective of the work reported here was a quantitative correlation of edge plane density with electron transfer rate for laser-activated HOPG. If the qualitative conclusion that electron transfer occurs at edge plane defects is correct, then the observed rate constant should quantitatively track the edge plane density.

The approach we used to quantitatively evaluate edge plane density was originally suggested by Yeager et al. (*22–24*) and is based on capacitance measurements. Edge plane carbon has much higher capacitance per unit area, C°, than basal plane, so capacitance can serve as a measure of edge plane density in the absence of other effects. By correlating capacitance changes with k° changes caused by laser activation, we will establish a more quantitative relationship between observed k° and surface edge plane density.

EXPERIMENTAL SECTION

All solutions were prepared daily by using distilled water which was then purified with a Nanopure water purification system. Potassium ferrocyanide was used as received from Mallinckrodt Inc. for the preparation of 1 mM potassium ferrocyanide in 1 M KCl, which was then degassed for approximately 20 min with purified argon. The HOPG was a gift from Arthur Moore at Union Carbide, Parma, OH. Basal plane HOPG was mounted as described previously (*18*), with the electrode being defined by a Viton O-ring with 1 mm inside diameter. Although HOPG was cleaved in the conventional way with adhesive tape, it was noted that special care was required to avoid forming defects on the freshly cleaved surface. As will be discussed below, a small number of defects can yield a large error in the observed basal plane rate constant. Carefully cleaved and handled basal plane HOPG exhibited a ΔE_p for $Fe(CN)_6^{3-/4-}$ in 1 *M* KCl of at least 700 mV at 0.2 V/s, and smaller ΔE_p values indicated a defective surface. If localized mechanical damage occurred on the surface during cell assembly, it was possible to observe two voltammetric couples with different ΔE_p for $Fe(CN)_6^{3-/4-}$, indicating a damaged region larger than $(Dt)^{1/2}$. As a routine practice, any fresh basal HOPG surfaces exhibiting two voltammetric peaks or a single couple with $\Delta E_p < 700$ mV for $Fe(CN)_6^{3-/4-}$ were rejected and cleaved again.

Edge plane HOPG surfaces are difficult to prepare due to irregularities in how the edges are cut. It is likely that rough edges can be folded over during polishing or cleaning, leading to partial basal plane exposure. For measurements on edge plane HOPG, the sample was embedded in Torr-seal (Varian) with the edge exposed and then sanded with 600-grit silicon carbide sandpaper and polished successively with 1.0-, 0.3-, and 0.05-μm alumina before rinsing with Nanopure water.

Cyclic voltammetry experiments were performed with a Tecmar Labmaster analog interface board in a PC compatible computer which controlled an Advanced Idea Mechanics (Columbus, OH) Model 8709 potentiostat. A BAS Model RE-1 Ag/AgCl reference electrode (3 M NaCl) was used for all electrochemical experiments.

* Author to whom correspondence should be addressed.

0003-2700/89/0361-1637$01.50/0

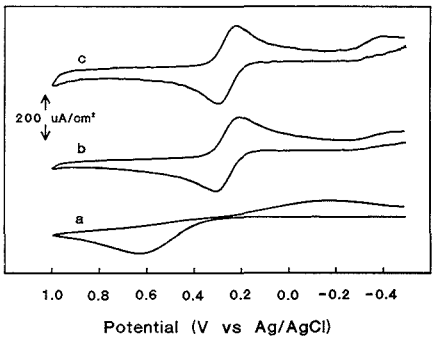

Figure 1. Cyclic voltammograms (0.2 V s^{-1}) of 1 mM $Fe(CN)_6^{3-/4-}$ in 1 M KCl on HOPG basal plane: (a) freshly cleaved; (b) after three 50 MW cm^{-2} laser pulses in air; (c) freshly cleaved surface after three 90 MW cm^{-2} laser pulses in air. Reduction at ca. −0.4 V is apparently due to dioxygen.

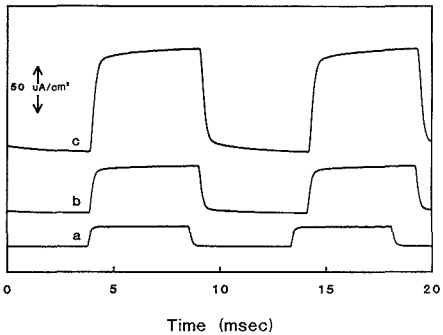

Figure 2. Raw current density waveforms for HOPG basal plane in 1 M KCl, in response to a ca. 100 Hz, 20 mV p–p triangle wave applied potential. dc potential was 0.00 V vs Ag/AgCl, electrolyte was 1 M KCl. The three E_{app} waveforms differed slightly in frequency and amplitude, but in all cases had the same value of dE/dt. Curve a is fresh HOPG, curve b is after three 50 MW cm^{-2} laser pulses, and curve c is a fresh surface after three 90 MW cm^{-2} pulses in air.

All cyclic voltammetry experiments used a scan rate of 0.2 V/s unless otherwise indicated. A platinum wire was used as an auxiliary electrode for all electrochemical experiments. A diffusion coefficient for $Fe(CN)_6^{3-}$ of 6.3×10^{-6} cm^2/s was used for analysis of all electrochemical data.

Differential capacitance measurements were made by applying a 100-Hz, 20-mV peak to peak triangle wave centered on 0.0 vs Ag/AgCl from an Exac Model 128 function generator to the electrochemical cell and recording the current response on a Tektronix Model 7854 digital oscilloscope. This method has been described and characterized by Gileadi et al. (*25, 26*). The area of the electrode used for capacitance calculations was determined by chronoamperometry and had a typical value of 0.06 cm^2. Semiintegral analysis of voltammograms was performed by using the G1 algorithm of Oldham as described elsewhere (*27*), and $k°$ values were determined conventionally from ΔE_p by the method of Nicholson (*28*). Due to the need for extrapolation of Nicholson's working curves for $\Delta E_p > 200$ mV, $k°$ values below 10^{-4} cm s^{-1} are less accurate than those in the range of 10^{-1} to 10^{-3} cm s^{-1}.

Laser pretreatment was performed in ambient air with three 9-ns laser pulses from the beam center of a Nd:YAG laser operating at 1064 nm. Due to variations in beam quality and pulse-to-pulse variability, cited power densities are ±20%. The measured power density was found to be sensitive to laser alignment and aging, and power densities reported in a preliminary communication (*19*) were found to be erroneously low. The cell was assembled immediately after electrode activation. In situ activation in the electrochemical cell was not employed due to power density variations induced by Fresnel diffraction of laser light from the O-ring. This effect is of interest in itself but was avoided here by activating in ambient air without the O-ring present.

Electrochemical activation was conducted with a procedure similar to that of Engstrom (*5, 6*) with a controlled potential anodization at various potentials followed by a cathodic step to −0.1 V vs Ag/AgCl for 30 s. Raman spectra were obtained with a 515-nm laser and Spex 1403 spectrometer as described previously ("gross" spectra, ref 18).

RESULTS AND DISCUSSION

The qualitative effects of laser irradiation on HOPG electron transfer kinetics, capacitance, and Raman spectra were examined initially, over a wider range of power densities than reported previously (*18*). Figure 1 shows voltammograms for $Fe(CN)_6^{3-/4-}$ on the initial HOPG basal plane and after 50 and 90 MW cm^{-2} laser irradiations. There is a large decrease in ΔE_p after the 50 MW cm^{-2} pulses and a further, but smaller, decrease at higher power density. Figure 2 shows the current waveforms resulting from a 20-mV peak-to-peak 100-Hz triangle wave potential to a blank electrolyte solution. Before laser irradiation, the waveform is a square wave, indicating a nearly ideal capacitance of 1.9 μF cm^{-2}. After 50 MW cm^{-2} laser treatment the current increases slightly, with a minor increase in slope of the square wave response. At higher laser power densities (curve C), the current continues to increase, as does the slope. Raman spectra following treatment at the power densities in Figures 1 and 2 are shown in Figure 3. As noted previously (*18, 19*), the 50 MW cm^{-2} pretreatment produces a 1360-cm^{-1} band indicating fracturing of the HOPG lattice. At high power densities, the first-order Raman bands broaden and coalesce, indicating severe disorder of the carbon lattice (*20, 21, 29, 30*). Quantitative changes in $k°$ upon laser activation are indicated in Figure 4. The initial $k°$ before activation was very low on basal plane HOPG, with values below 1×10^{-7} cm s^{-1}. Significant variation in this initial rate constant was observed, probably due to adventitious defects, but it was always less than 6×10^{-7} cm s^{-1}. Laser irradiation at power densities below 45 MW cm^{-2} had no effect on the observed ΔE_p. Above 45 MW cm^{-2}, the laser treatment caused an abrupt increase in $k°$ from $<10^{-7}$ to $>10^{-3}$ cm s^{-1}. With

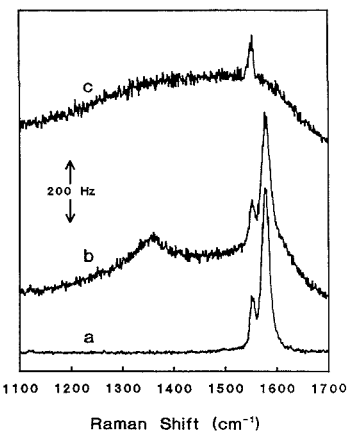

Figure 3. Raman spectra of HOPG basal plane before and after laser treatment. Raman laser was 515 nm, ca. 75 mW at sample. Laser pretreatment was the same as in Figures 1 and 2, with spectra a–c corresponding to 0, 50, and 90 MW cm^{-2} pretreatment. The small peak at 1565 cm^{-1} is due to atmospheric dioxygen and is irrelevant to the carbon results.

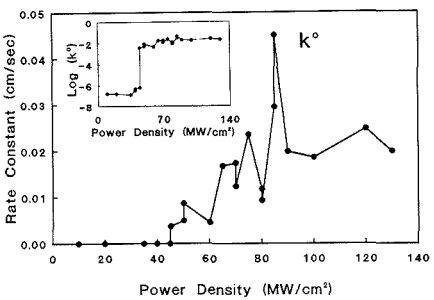

Figure 4. Observed electron transfer rate constant, $k°_{obs}$ for $Fe(CN)_6^{3-/4-}$, calculated from voltammograms similar to those in Figure 1, as a function of laser activation power density. Each voltammogram was preceded by cleavage of the HOPG basal plane and three laser pulses in air. Inset shows same data with a logarithmic ordinate.

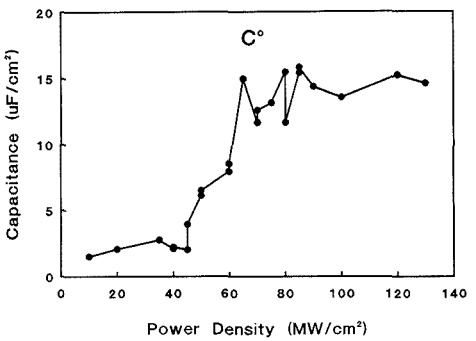

Figure 5. Observed capacitance, $C°_{obs}$, for HOPG as a function of laser power density. Surfaces prepared were as in Figure 4; electrolyte was 1 M KCl.

increasing power density, $k°$ continued to increase, reaching a plateau of about 0.02 cm s^{-1} at high power density. The significant variability in $k°$ apparent in Figure 4 probably results from variation in surface cleanliness occurring when activation is carried out in air and has been noted previously on glassy carbon (*16*). While this variation is quite large, it is small considering the 5+ order of magnitude range in $k°_{obs}$ (see inset of Figure 4). Semiintegration over the entire power range showed sigmoidal curves, indicating no observable adsorption or other unexpected effects (*27*).

The capacitance of HOPG basal plane was measured as a function of laser power density with the results shown in Figure 5. Untreated basal plane has an anomalously low capacitance of 2–3 $\mu F\ cm^{-2}$, which has been attributed to its partial semiconductor character (*14, 23, 24*). This capacitance is independent of the triangle wave frequency over a range from 10 to 1000 Hz, implying a negligible Faradaic component. Above 45 MW cm^{-2}, $C°$ increases with power density up to a plateau of ca. 15 $\mu F\ cm^{-2}$. Note that $C°$ increased by a factor of about 8 over a power density range where $k°$ increased by a factor of 10^5.

Edge plane HOPG exhibited a $C°$ of 60 $\mu F\ cm^{-2}$ and $k°$ for $Fe(CN)_6^{3-/4-}$ of 0.06 cm s^{-1} after conventional polishing and rinsing in Nanopure water. Laser activation at high power (100 MW cm^{-2}) increased $C°$ slightly to 70 $\mu F\ cm^{-2}$ and $k°$ to 0.10 cm s^{-1}. It is likely that the laser removed polishing debris and mechanical effects of polishing to yield slightly higher values of $C°$ and $k°$. While literature values for $C°$ on edge plane HOPG vary significantly, the value of 70 $\mu F\ cm^{-2}$ is within the commonly cited range (*23, 31*). Despite the variation in reported values, it is clear that edge plane HOPG has a $C°$ ca. 30 times that of basal plane. Furthermore, the edge plane $k°$ is at least 10^5 times as large as properly prepared basal plane.

The effects of electrochemical pretreatment (ECP) of basal plane HOPG on $k°$ and $C°$ were also examined, although in less detail. The apparent capacitance of the ECP surface was much higher than laser pretreated surfaces, with values of 80–150 $\mu F\ cm^{-2}$ being observed for ECP potentials of 2.1–2.5 V (2 min anodization followed by 30 s at −0.10 V). $k°$ values for these same surfaces ranged from 0.01 to 0.22 cm s^{-1}. The slopes of the nominally flat "square waves" shown in Figure 2 were much larger for ECP surfaces, consistent with a large Faradaic component of the observed capacitance. ECP has no effect on $k°$ or $C°$ at pretreatment potentials of 1.8 V or below.

It is clear from the results reported here and in the literature that the basal and edge planes of HOPG differ greatly in their electrochemical properties. It is well-known that HOPG is an anisotropic material, with the "a" (in plane) and "c" (perpendicular to plane) axes differing greatly in electrical and thermal conductivity, thermal expansion coefficient, optical properties, and tensile strength (*32, 33*). Thus it is not surprising that the $k°$ and $C°$ values reflect this anisotropy.

The qualitative changes in the HOPG surface upon laser treatment are not unexpected, based on previous work. The large decrease in ΔE_p for $Fe(CN)_6^{3-/4-}$ accompanies the appearance of the 1360-cm^{-1} Raman band and is attributable to creation of graphitic edge plane. The severe broadening of Raman bands at high power density is consistent with severe disorder of the graphitic lattice. The spectrum of Figure 3C is similar to that of amorphous carbon and certain carbon blacks, which have small L_a and L_c lattice parameters and relatively large interplanar spacing (*20, 21, 29, 30*). On the basis of the voltammetry of Figure 1, such surfaces have good electron transfer activity but have been severely altered structurally from HOPG. The increased slopes of the capacitance waveforms upon activation may be due to surface Faradaic reactions or nonideal capacitance. The increase upon 50 MW cm^{-2} treatment is slight and is much smaller than that for glassy carbon, electrochemically pretreated HOPG, or severely disordered surfaces. Such behavior has been attributed to surface redox reactions (*4, 34*), capacitance with a variety of RC time constants (*25, 26*), or incorporation of nonelectroactive cations into surface films (*35*). For the initial and 50 MW cm^{-2} surfaces, the slope is a minor contribution to the observed capacitance but does serve as an indication of nonideal capacitive behavior.

On a more quantitative basis, the large difference in $k°$ for basal vs edge plane is consistent with previous reports from our lab and others but is much larger than that reported in the 1970s. Morcos and Yeager (*15*) report a basal to edge plane ratio of $k°$ for $Fe(CN)_6^{3-/4-}$ of about 3, whereas our lab (*18, 19*) and others (*3*) observe a ratio of more than 10^5. This discrepancy is attributable to the extreme care required to avoid defects on the freshly cleaved basal plane surface. Even a small density of surface defects yields a large rate increase on basal plane, resulting in an erroneously small ratio of edge to basal plane $k°$ values. In addition, it is difficult to prepare clean edge plane surfaces, resulting in low $k°$ values and an apparent decrease in the edge/basal $k°$ ratio. It is possible that the basal plane $k°$ reported here (<10^{-7} cm s^{-1}) is actually smaller, and the low observed activity is due entirely to defects.

The capacitance we observe for untreated basal plane (~2.0 $\mu F\ cm^{-2}$) is also smaller than reported values (ca. 3 $\mu F\ cm^{-2}$) (*24*). Since the ratio of edge to basal plane $C°$ is much smaller than the $k°$ ratio, the observed capacitance will be less sen-

sitive to adventitious defects. As will be shown below, an edge plane defect density of 1.6% would increase the observed basal C° from 2 to 3 $\mu F\ cm^{-2}$, so it is possible the discrepancy is caused by variations in the density of unavoidable edge plane defects. Alternatively, the difference may result from the use of a different electrolyte. In either case, the discrepancy is not important to the conclusions drawn here.

The effects of laser pretreatment on basal plane C°_{obs} and k°_{obs} can be divided into three regions, depending on power density. Below 45 MW cm^{-2}, no effect on k° is observed, and C° varies slightly. Between 45 and 90 MW cm^{-2} both k° and C° increase, by factors of ca. 10^5 and 8, respectively. The Raman spectrum of HOPG following laser activation in this power range exhibits a 1360-cm^{-1} band indicating the formation of edge plane. Thus k° and C° increases correlate with the spectroscopic marker for edge plane. At power densities from 90 to 130 MW cm^{-2}, k° and C° have reached plateaus, showing no apparent trend with increasing power density. The Raman spectrum in this high power density region corresponds to very disordered carbon lacking a well-defined 1360/1582 intensity ratio.

It was concluded from the spectroscopic results that the mechanism of HOPG basal plane activation by laser irradiation involved the formation of edge plane on the basal plane surface (*18*). While the mechanism of edge plane formation is currently unclear, increased edge plane always produces increased k°. As a first approximation, it is useful to hypothesize that k° is solely a function of edge plane density on HOPG, and that the observed rate constant, k°_{obs}, is a weighted sum of the basal and edge plane k° values, as indicated by

$$k^\circ_{obs} = k^\circ_e f_e + k^\circ_b(1 - f_e) \quad (1)$$

where $k^\circ_e = k^\circ$ for pure edge plane, $k^\circ_b = k^\circ$ for pure basal plane, and f_e is the fraction of electrode area which is edge plane. Equation 1 does not address the issue of why edge plane has a higher rate constant but merely states that the observed rate constant depends on f_e. Equation 1 should hold for the case where $(Dt)^{1/2}$ is large relative to both the edge plane defects and the distance between them. It is similar to the expressions derived by Amatore, Saveant, and Tessier (*36*) for partially blocked electrodes with surface coverage not too close to 1. Making the same hypothesis about observed capacitance yields

$$C^\circ_{obs} = C^\circ_e f_e + C^\circ_b(1 - f_e) \quad (2)$$

where C°_e is the capacitance per unit area of pure edge plane and C°_b is the capacitance per unit area of pure basal plane. C°_e may include a component due to surface Faradaic processes or nonideal capacitance, but the contribution of this component is assumed to be equal for any edge plane, regardless of its origin. Provided C°_e, C°_b, k°_e, and k°_b are known, eq 1 and 2 may be used to calculate f_e for a given surface from k°_{obs} and C°_{obs}. This approach provides two independent measurements of f_e based on both electron transfer kinetics and capacitance.

k°_b is less than 10^{-7} cm s^{-1}, probably in the region of 10^{-9} cm s^{-1}. Since k°_e is much larger than k°_b, the contribution of k°_b to k°_{obs} in eq 1 is negligible on laser-treated surfaces and the accuracy of k°_b is unimportant for determining f_e from eq 1. The average of several k° values for laser-activated edge plane HOPG yielded a value of 0.10 cm s^{-1} for k°_e. This result is lower than laser-treated GC by a factor of 2 but is higher than for activated basal plane. Using 10^{-7} cm s^{-1} for k°_b and 0.10 for k°_e, f_e was calculated from eq 1 and the data of Figure 4, as a function of power density. The plot of f_e vs power density determined from k°_{obs} is shown in Figure 6. Since k°_b contributes negligibly to k°_{obs}, f_e is proportional to k°_{obs}. Thus the observed k° is determined solely by the edge plane

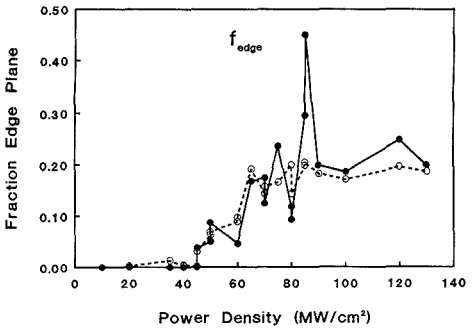

Figure 6. Plots of f_e vs power density calculated from k°_{obs}, C°_{obs}, and eq 1 and 2: closed circles, f_e calculated from data of Figure 4 and eq 1, with $k^\circ_e = 0.10$ cm s^{-1} and $k^\circ_b = 1 \times 10^{-7}$; open circles, f_e calculated from data of Figure 5 with $C^\circ_b = 1.9\ \mu F\ cm^{-2}$ and $C^\circ_e = 70\ \mu F\ cm^{-2}$.

contribution for k°_{obs} greater than about 10^{-6} cm s^{-1}.

Equation 2 may be used to calculate f_e from C°_{obs} as a function of power density, using values of 1.9 $\mu F\ cm^{-2}$ for C°_b and 70 $\mu F\ cm^{-2}$ for C°_e. The results are plotted in Figure 6 on the same scale as f_e values determined from k°_{obs}. f_e values determined from either k° or C° show simiar trends with power density and agree within experimental variation. There are plateaus below 45 MW cm^{-2} and above 90 MW cm^{-2}, and there is an increase with power density in between.

The agreement among f_e values determined from independent measurements of capacitance and k° is significant in light of the wide range of k°_{obs} values covered and the relatively small variation in C°_{obs}. For example, generation of 1% edge plane on initially perfect basal plane would increase k°_{obs} by a factor of at least 10^4, while C°_{obs} would increase by only 37%. The quantitative correlation of C°_{obs} and k°_{obs} implied by the similar f_e values supports the validity of eq 1 and 2. In mechanistic terms, the results of Figure 6 imply that both capacitance and charge transfer rate are controlled by the fractional density of edge plane on the electrode surface. Thus the laser treatment of HOPG basal plane serves to increase edge plane density, as shown qualitatively in previous work, and the current results demonstrate a quantitative relationship.

A proportionality between k°_{obs} and f_e, as in eq 1, permits the conclusion that electron transfer is localized on edge plane for HOPG, with the possible exception of very low k°_{obs} ($<10^{-7}$ cm s^{-1}). While the association of electron transfer sites with edge plane is itself significant, it does not reveal the chemical nature of the site. There are likely to be oxygen-containing functional groups on edge plane, but several strong arguments are available against their involvement in electron transfer to $Fe(CN)_6^{3-/4-}$ or ascorbic acid, and similar common test systems (*16*, *37*). Surface oxides may be involved in more complicated redox processes such as O_2 reduction, hydrazine oxidation, and binding of large or small biological molecules, but large k° values for small, presumably outer sphere electron transfers appear possible without oxygen functional groups.

The observation of a single voltammetric couple over a wide range of k° values is significant with regard to the nature of the surface. The voltammograms used to calculate k° values for Figure 4 had the classical shape expected for a planar electrode, implying that any surface heterogeneity occurs on a dimension that is small relative to $(Dt)^{1/2}$ (*36*). Thus the distance between exposed edge plane regions on the laser-treated surfaces must be less than a few micrometers, and the diffusion fields to these regions must overlap heavily on the voltammetric time scale. Provided $(Dt)^{1/2}$ is large compared

to the distance between edge plane sites, the voltammogram will be governed by the Nicholson–Shain treatment and eq 1 will apply. Raman results presented elsewhere (*18*) indicate an approximate average microcrystallite size on laser-treated HOPG of several hundred angstroms (*20*), indicating a spacing between edge plane sites of much less than 1 μm. Thus the activated surface is behaving like an array of small active sites closely packed in an inert plane, with an observed k° governed by eq 1. While the inert plane is very unreactive toward electron transfer, it does have capacitance, leading to the minimum observed C° for basal plane of ~ 2 μF cm^2.

It can be argued that rate and capacitance increases upon laser activation may be due to increases in microscopic surface area, since HOPG basal plane is initially very flat. Surface roughness is insufficient to explain the current results because both k°_{obs} and C°_{obs} should be proportional to roughness factor if roughness were the only variable involved. If roughness were responsible for the 10^4 increase in k°_{obs} with laser activation, there would be a 10^4 increase in capacitance, contrary to the observed results. Because some roughening is likely to accompany edge plane formation, there may be a contribution of microscopic area increases to k°_{obs} enhancement. The extent of this contribution is difficult to assess without independent measurement of microscopic surface area.

Application of these results to more commonly used carbon materials such as glassy carbon is complicated by uncertainties in the measurement of k° and C°. HOPG basal plane is clean and has a well-defined capacitance with very low contribution from surface Faradaic reactions. However, glassy carbon (GC) exhibits a large variation of C° and k° with pretreatment (*1*), in part because of surface cleanliness and the presence of surface oxides. As noted earlier, such oxides can undergo Faradaic reactions which contribute to observed "capacitance", leading to an erroneously high capacitance. The best GC surface for comparison to the present results is vacuum heat treated (VHT) GC-20, which has a capacitance of 10 μF cm^2 and appears to be free of surface redox groups (*4*). Equation 2 results in an f_e of 15% for a capacitance of 10 μF cm^2 and predicted k° of about 0.04 cm s^{-1} for $Fe(CN)_6^{3-/4-}$. The observed rate constant on VHT GC-20 is about 0.15 cm s^{-1} (*4*). It may be an oversimplification to apply the HOPG results to the microstructurally distinct GC-20 surface, but it appears that edge plane density affects C°_{obs} and k°_{obs} in similar ways on both HOPG an GC-20 surfaces.

Several recent reports from our laboratory (*12*, *16*, *37*) and from others (*3*, *4*, *38*) have noted an inverse correlation of capacitance and k° for GC-20 and pyrolytic graphite, in apparent contradiction to current results. For example, polished GC-20 may have a capacitance in the 60–100 μF cm^2 range, but this value decreases to 10 μF cm^2 upon VHT (*4*). However, the k° may increase significantly upon VHT, in contradiction to eq 1 and 2. This apparent discrepancy is very likely attributable to the involvement of surface oxides on polished GC surfaces. Such oxides may make a large (even dominant) contribution to C°_{obs}, but have minor or negative effects on k° for simple systems (*16*). Thus removal of oxides by VHT or laser treatment may greatly reduce C°_{obs} while having minor or positive effects on k°_{obs}. Similar arguments can be made about surface impurities, since they may have a larger effect on k°_{obs} than C°_{obs}. Equations 1 and 2 will be valid when edge plane density is the major variable determining C°_{obs} and k°_{obs}, and the main point of this paper is the effect of laser treatment and carbon microstructure on f_e. If other variables such as surface cleanliness or oxides are important, such as on most glassy carbon surfaces, eq 1 and 2 would not be expected to apply. In particular, it is possible to increase k°_{obs} while reducing C°_{obs} on GC-20 by removing impurities and surface oxides. In the case of HOPG, the initial surface is oxide free, and the base-line C°_{obs} is free of Faradaic contributions.

ACKNOWLEDGMENT

The authors thank Robert Bowling for assistance with Raman spectra and Arthur Moore of Union Carbide for providing HOPG samples.

LITERATURE CITED

(1) Hu, I. F.; Karweik, D. H.; Kuwana, T. *J. Electroanal. Chem.* **1985**, *188*, 59.
(2) Hu, I-F.; Kuwana, T. *Anal. Chem.* **1986**, *58*, 3235.
(3) Wightman, R. M.; Deakin, M. R.; Kovach, P. M.; Kuhr, W. G.; Stutts, K. J. *J. Electrochem. Soc.* **1984**, *131*, 1578.
(4) Fagan, D. T.; Hu, I. F.; Kuwana, T.; *Anal. Chem.* **1985**, *57*, 2759.
(5) Engstrom, R. C.; Strasser, V. A. *Anal. Chem.* **1985**, *56*, 136.
(6) Engstrom, R. C. *Anal. Chem.* **1982**, *54*, 2310.
(7) Cabaniss, G. E.; Diamantis, A. A.; Murphy, W. R., Jr.; Linton, R. W.; and Meyer, T. J. *J. Am. Chem. Soc.* **1985**, *107*, 1845.
(8) Wang, J.; Hutchins, L. O. *Anal. Chim. Acta* **1985**, *167*, 325.
(9) Gonon, F. G.; Fombarlet, C. M.; Buda, M. J.; Pujol, J. F. *Anal. Chem.* **1981**, *53*, 1386.
(10) Wightman, R. A.; Paik, E. C.; Borman, S.; Dayton, M. A. *Anal. Chem.* **1978**, *50*, 1410.
(11) Kepley, L. J.; Bard, A. J. *Anal. Chem.* **1988**, *60*, 1459.
(12) Poon, M.; McCreery, R. L. *Anal. Chem.* **1986**, *58*, 2745.
(13) Poon, M.; McCreery, R. L. *Anal. Chem.* **1987**, *59*, 1615.
(14) Randin, J.-P. In *Encyclopedia of Electrochemistry of the Elements*, Bard, A. J., Ed.; Dekker: New York, 1976; Vol. 7, pp 12–21, 238–239.
(15) Morcos, I.; Yeager, E. *Electrochim. Acta* **1970**, *15*, 953.
(16) Poon, M.; McCreery, Richard L.; Engstrom, R. *Anal. Chem.* **1988**, *60*, 1725.
(17) Kinoshita, K. *Carbon: Electrochemical and Physical Properties*, Wiley: New York, 1988; Chapter 5.
(18) Bowling, R. J.; Packard, R. T.; McCreery, R. L. *J. Am. Chem. Soc.* **1989**, *111*, 1217.
(19) Bowling, R. J.; Packard, R. T.; McCreery, R. L. *J. Electrochem. Soc.* **1988**, *135*, 1605.
(20) Tuinstra, F.; Koenig, J. L. *J. Chem. Phys.* **1970**, *53*, 1126.
(21) Dresselhaas, M. S.; Dresselhaas, G. *Adv. Phys.* **1981**, *30*, 139.
(22) Randin, J. P.; Yeager, E. *J. Electroanal. Chem.* **1972**, *36*, 257.
(23) Randin, J. P.; Yeager, E. *J. Electrochem. Soc.* **1971**, *118*(15), 711.
(24) Randin, J. P.; Yeager, E. *J. Electroanal. Chem.* **1975**, *58*, 313.
(25) Gileadi, E.; Tshernikovski, N. *Electrochim. Acta* **1971**, *16*, 579.
(26) Gileadi, E.; Tshernikovski, N.; Babai, M. *J. Electrochem. Soc.* **1972**, *119*(8), 1018.
(27) Bowling, R.; McCreery, R. L. *Anal. Chem.* **1988**, *60*, 605.
(28) Nicholson, R. S. *Anal. Chem.* **1965**, *37*, 1351.
(29) Vidano, R.; Fischbach, D. B. *J. Am. Ceram. Soc.* **1978**, *61*, 13.
(30) Nakamizo, M.; Kammereck, R.; Walker, P. L. *Carbon* **1974**, *12*, 259.
(31) Reference 17, p 294.
(32) Autio, G. W.; Scala, E. *Carbon* **1968**, *6*, 41.
(33) Macia, G. *Carbon* **1987**, *25*, 837.
(34) Oren, Y.; Soffer, A. *J. Electroanal. Chem.* **1985**, *186*, 63.
(35) Nagaoka, et al. *Anal. Chem.* **1988**, *60*, 2766.
(36) Amatore, C.; Saveant, J.; Tessier, D. *J. Electroanal. Chem.* **1983**, *147*, 39.
(37) Bowling, R. J.; Packard, R. T.; McCreery, R. L. *Langmuir* **1989**, *5*, 683.
(38) Bodalbhai, L.; Brajter-Toth, A. *Anal. Chem.* **1988**, *60*, 2557.

RECEIVED for review January 4, 1989. Accepted May 1, 1989. This work was supported by the Air Force Office of Scientific Research and by the donors of the Petroleum Research Fund, administered by the American Chemical Society. Raman instrumentation was developed under the support of The Chemical Analysis Division of the National Science Foundation.

Anal. Chem. 1989, 61, 1642–1647

On-Line Radioisotope Detection for Capillary Electrophoresis

Stephen L. Pentoney, Jr., and Richard N. Zare*

Department of Chemistry, Stanford University, Stanford, California 94305

Jeff F. Quint

Beckman Instruments, Inc., Scientific Instruments Division, Fullerton, California 92634

Two simple, on-line radioactivity detectors for capillary electrophoresis are described. The first capillary electrophoresis/radioisotope detector system utilizes a commercially available semiconductor device, which is positioned external to the separation channel and which responds directly to impinging γ or high-energy β radiation. The second capillary electrophoresis/radioisotope detector utilizes a commercially available plastic scintillator material that completely surrounds (360°) the separation channel, thereby improving the efficiency of detection. The system performance is evaluated for both detection schemes by using synthetic mixtures of ^{32}P-labeled sample molecules. The efficiency of the semiconductor detector (planar geometry) is determined to be approximately 26%, whereas that of the plastic scintillator is found to be approximately 65%. The detection limits are determined to be in the low-nanocurie range for separations performed under standard conditions (an injected sample quantity of 1 nCi corresponds to 110×10^{-18} mol of ^{32}P). The lower limit of detection is extended to the subnanocurie level by use of flow (voltage) programming to increase the residence time of labeled sample components in the detection volume.

The highly efficient separations afforded by capillary electrophoresis (CE) are a direct result of employing extremely narrow separation channels. Effective dissipation of heat generated by the passage of electrical current through the separation medium occurs only when the capillary inner surface area to internal volume ratio is sufficiently large (typically 10^4 to 10^5 m^{-1}). For this reason capillary tubes with internal diameters ranging from 200 μm to as small as 10 μm (*1*) have been selected for CE separations.

Early in the development of capillary electrophoresis, it was noted that the successful detection of separated sample components present within the narrow confines of these capillary tubes posed a major challenge (*2*). In response to this challenge, much research has been directed toward the development of sensitive and selective detectors for capillary electrophoresis. The reported CE detector technology has been largely borrowed from the field of high-performance liquid chromatography (HPLC), especially from microcolumn HPLC. Successful extension of the various HPLC detection schemes to capillary electrophoresis has generally involved miniaturizing existing technology while at the same time striving for improved sensitivity.

One detection scheme that is used widely in HPLC but has received little attention in capillary electrophoresis applications is radioisotope detection (*3–6*). The availability of an on-line radioisotope detector for CE would be especially appealing for several reasons. First, state-of-the-art radiation detection technology can offer extremely high sensitivity. Second, radioisotope detection affords unrivaled selectivity because only those sample components that have been radiolabeled yield a response at the detector. Third, the radiolabeled molecule possesses the same chemical properties as the unlabeled molecule, thereby permitting tracer studies to be conducted. Fourth, radioisotope detection can be directly calibrated to provide a measurement of absolute concentration of the labeled species. Finally, a capillary electrophoresis system in which radioactivity detection is coupled with more conventional detectors would add extra versatility to this new separation technique.

Radioisotope detection of ^{32}P, ^{14}C, and ^{99}Tc has previously been reported by Kaniansky et al. for isotachophoresis (*7, 20*). In their work, isotachophoretic separations were performed by using 300 μm internal diameter fluorinated ethylene–propylene copolymer capillary tubing and either a Geiger–Mueller tube or a plastic scintillator/photomultiplier tube combination to detect emitted β particles. One of their reported detection schemes involved passing the radiolabeled sample components directly through a plastic scintillator. Detector efficiency for ^{14}C-labeled molecules was reported to be 13–15%, and a minimum detection limit of 0.44 nCi was reported for a 212 nL cell volume.

Altria et al. reported the CE separation and detection of radiopharmaceuticals containing ^{99m}Tc, a γ emitter with a 6-h half-life (*8*; see also ref 9). Their design involved passing a capillary tube ($\simeq$2 cm long) through a solid block of scintillator material and detecting the light emitted as technetium-labeled sample zones traversed the detection volume. Unfortunately, detection limits and detector efficiency have not been reported.

We report here the design and characterization of two simple on-line radioisotope detectors for capillary electrophoresis. The first detector utilizes a commercially available semiconductor device that responds directly to emitted β particles that pass through the walls of the fused silica separation channel. A similar semiconductor detector for γ-emitting radiopharmaceuticals separated by high-performance liquid chromatography has previously been reported by Needham and Delaney (*10*). Alternatively, a second detector utilizes a commercially available plastic scintillator material that completely surrounds (360°) the detection region of the separation channel. Light emitted by the plastic scintillator is collected and focused onto the photocathode of a single, cooled photomultiplier tube. The detectors described in the present work are applicable to both high-energy β emitters and γ emitters. We report here on their application to the detection of ^{32}P-labeled molecules separated by capillary electrophoresis.

EXPERIMENTAL SECTION

On-Line Radioactivity Detectors. The first on-line radioactivity detector (see Figure 1) consisted of a Model S103.1/P4 spectroscopic grade cadmium telluride semiconductor detector and a Model CTC-4B radiation counting system (Radiation Monitoring Devices, Inc., Watertown, MA). The cadmium tel-

* Author to whom correspondence should be addressed.

0003-2700/89/0361-1642$01.50/0

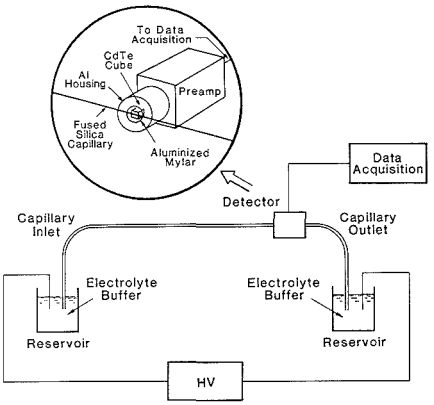

Figure 1. Experimental setup of the capillary electrophoresis/semiconductor radioisotope detector system. The inset shows the positioning of the CdTe probe with respect to the capillary tubing. The 2-mm Pb aperture is not shown in this illustration.

luride detector probe consisted of a 2-mm cube of CdTe, which was set in a thermoplastic and positioned behind a thin film of aluminized Mylar at a distance of approximately 1.5 mm from the face of an aluminum housing (see Figure 1). A 2 mm wide Pb aperture (0.008 in. thick) was used to shield the CdTe detector element from radiation originating from regions of the capillary adjacent to the detection volume. The aluminum housing incorporated a BNC-type connector that facilitated both physical and electrical connection to a miniature charge-sensitive preamplifier. The CdTe probe and preamplifier assembly were mounted on an x-y translation stage, and the face of the aluminum housing was brought into direct contract with the polyimide-clad fused capillary/Pb aperture assembly. The CdTe detector was operated at the manufacturer's suggested bias voltage of 60 V, and the detector signal (the creation of electron-hole pairs produced as β particles were decelerated within the semiconductor material) was amplified by the charge-sensitive preamplifier and sent through a 6-ft. cable to the counting a display electronics of the CTC-4B counting unit. Although the CTC-4B is capable of room-temperature energy discrimination, all experiments reported here were performed with a relatively large energy window. The upper energy discriminator setting was 1 MeV (the maximum setting for the CTC-4B), and the low energy setting was 0.01 MeV.

The CdTe radioactivity detector was computer-interfaced to a laboratory personal computer by using the open collector output of the CTC-4B counting unit. The open collector output was tied high by way of a 1-KΩ pull-up resistor so that the unit provided a negative going transistor-transistor logic (TTL) pulse for each count measured. This TTL signal was sent to a photon counter (Model 1109, EG&G Princeton Applied Research), and counting intervals (typically 1 s) for run-time data acquisition were preselected by way of front panel thumbwheel switches on the photon counter. The binary coded decimal (BCD) output of the photon counter was read at the end of a preset counting interval (strobe sent by the 1109 counter) by a laboratory computer (IBM PC-XT) using a 32-bit digital I/O board (Model DT2817, Data Translation, Inc., Marlboro, MA). Data acquisition and storage were accomplished with software that was written in-house (BASIC). Migration times and peak widths reported here were determined manually from scale-expanded portions of the recorded electropherograms.

The second on-line radioactivity detector consisted of a plastic scintillator material (BC-400, Bicron Corp., Newbury, OH), which was machined from 1 in. diameter rod stock into a $^5/_8$ in. diameter (front face) solid parabola (see Figure 2). A special rotating holder was constructed for the plastic scintillator, and the curved outer surfaces were coated by vaccum deposition with a thin film of aluminum in order to reflect the emitted light toward the front face of the scintillator. A 2-mm detection length was defined

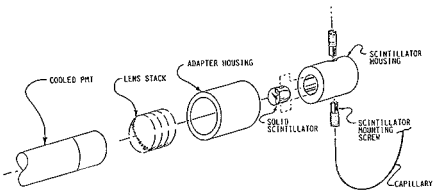

Figure 2. Exploded diagram of the plastic scintillator radioisotope detector. The fused silica capillary is exposed to a 2-mm section of the plastic scintillator that is located in between the press-fit aluminum mounting rods.

within the parabola by 0.250 in. outer diameter aluminum mounting rods, which were press-fit (coaxial to the separation capillary) in the sides of the scintillator as illustrated in Figure 2.

The light emitted by the scintillator as radiolabeled sample passed through the detection region was collected and focused onto the photocathode of the cooled photomultiplier tube (Centronic No. 4283) by a condenser lens combination (Physitec, No. 06-3010, focal length 16 mm). Photon counting was accomplished with a Model 1121A discriminator control unit and a Model 1109 photon counter (EG&G Princeton Applied Research, Princeton, NJ). The background count rate observed under typical operating conditions for this system was approximately 12 counts/s. This detector system was observed to yield a large response (at the onset and completion of each separation), which was associated with the application or termination of high voltage. Although the cause of this response is not yet fully understood, the signal was observed to damp out within the first 1–2 min of a run and therefore posed no interference to the separations reported here.

Apparatus. The experimental setup of the capillary electrophoresis system was similar to that described previously (*11*, *12*) and is illustrated in Figure 1. For the semiconductor detector, a 2-mm section of a 100 μm internal diameter, 100 cm long, fused silica capillary tube (TSP 100/365 Polymicro Technologies, Inc.) was exposed to the CdTe semiconductor by placing the Pb foil aperture directly in between the face of the detector housing and the fused silica capillary at a distance of 75 cm from the inlet end of the capillary tube. For the plastic scintillator detector, a 2-mm section of a 100 μm internal diameter, 140 cm long, fused silica capillary was exposed to the scintillator by passing the capillary through a 400-μm hole that was drilled through the aluminum mounting rods and the central 2-mm portion of the parabola at a distance of 75 cm from the capillary inlet. This resulted in a detection volume of approximately 15 nL for both detectors.

Each end of the capillary tubing was dipped into a 4-mL glass vial containing approximately 3 mL of electrolyte–buffer solution. Connection to high voltage was provided by a strip of Pt foil submersed in each of the buffer reservoirs. The injection end of the capillary was connected to ground while the detection end was held at a high negative potential, typically –20 kV. Plexiglass shielding (0.25 in. thick) was placed around the ground buffer reservoir because the top of this vial was quickly contaminated by sample solution carried on the outside of the capillary tube during the sample injection procedure. This contamination, if unshielded, leads to unnecessary operator exposure to radiation.

The current through the system was monitored as a potential drop across a 1-KΩ resistor in the ground side of the circuit. The capillary system and detector were enclosed in a Plexiglass box to prevent operator exposure to high voltage. Electroosmotic flow rates reported here were measured in a manner similar to that described by Huang et al. (*13*). The capillary tube was filled with running buffer diluted by 10%, the buffer reservoirs were filled with running buffer, and the current was monitored as one tubing volume was displaced by supporting buffer under the influence of the applied potential. Sample introduction was accomplished in all experiments reported here by using hydrostatic pressure.

The high-voltage power supply (Model MG30N100, Glassmann High Voltage, Whitehouse Station, NJ) was continuously programmable from 0 to –30 kV by means of an external 0–10-V direct current (dc) signal voltage. The flow programming experiments reported here were accomplished by manually reducing the

program voltage to the high-voltage supply.

Reagents. Aqueous ethanol solutions of the triethylammonium salts of adenosine 5′-[α-^{32}P]triphosphate (ATP), thymidine 5′-[α-^{32}P]triphosphate (TTP), and cytidine 5′-[α-^{32}P]triphosphate (CTP) were purchased from Amersham (Arlington Heights, IL). Radioactive sample concentrations reported for detector efficiency determination were adjusted from the manufacturer's specifications after subjecting several diluted aliquots of the stock solution to liquid scintillation counting. The concentration was further corrected for radiochemical purity according to the manufacturer's specifications because liquid scintillation counting measures the total sample activity and does not account for the presence of radiolabeled impurities. Stock solutions were stored at −15 °C in order to minimize sample loss due to hydrolysis. Injected sample solutions were prepared in 0.25-mL plastic vials by diluting stock solutions with buffer and were also stored at −15 °C.

Water used to prepare solutions was freshly deionized and distilled with a water purifier (Model LD-2A coupled with a Mega-Pure Automatic Distiller, Corning Glassworks). The supporting electrolyte for all experiments reported here was a borate buffer (pH 8.1, 0.20 M) prepared from reagent-grade sodium borate decahydrate and boric acid (J. T. Baker).

RESULTS AND DISCUSSION

Successful detection of ^{32}P-labeled molecules separated by capillary electrophoresis using the above detection schemes in which a sensor is positioned external to the separation channel is made possible by several factors. These include (1) the large energy associated with β decay of ^{32}P (1.7 MeV), (2) the high sensitivity and small size of commercially available semiconductor detectors, (3) the availability of efficient solid scintillator materials and sensitive photomultiplier tubes, (4) the short lengths of fused silica (capillary wall thickness) and aqueous electrolyte through which the radiation must pass before striking the detector, and (5) the relatively short half-life of ^{32}P (14.3 days).

The process of β decay for ^{32}P may be written as (*14*)

$$^{32}_{15}\mathrm{P} \rightarrow {}^{32}_{16}\mathrm{S} + \beta^- + \bar{\nu} \qquad (1)$$

where β^- represents the negatively charged β particle and $\bar{\nu}$ is the antineutrino. ^{32}P is an example of a "pure β emitter" that populates only the ground state of the product nucleus. Each β decay transition is characterized by a fixed decay energy that is shared between the β particle and the antineutrino. As a result, the β particle is emitted with an energy that varies from decay to decay and ranges from zero to the "β end-point energy", which is numerically equal to the transition decay energy. A β energy spectrum for ^{32}P shows a maximum particle energy of 1.7 MeV and an average particle energy of approximately 0.57 MeV. The penetrating ability of β particles through various media may be obtained from literature range–energy plots in which the product of particle range and medium density ("mass thickness") is plotted against particle energy. Such plots are especially useful because they may be used to predict the penetration length at a given particle energy in media other than that used to obtain the original plot (*14*). From such plots, one would predict that the average β particle energy (≃0.57 MeV) produced by decay of ^{32}P would correspond to a range of approximately 2000 μm in water and approximately 950 μm in fused silica. Thus, ^{32}P decay would be detectable by a sensitive device positioned external to the fused silica capillary tubing (of the dimensions normally selected for capillary electrophoresis separations).

Because the CdTe detector was not visible through the aluminized Mylar film, it was necessary to check for proper alignment of the capillary tube with respect to the CdTe cube. This was accomplished by filling the detection volume with radioactive material and monitoring the signal level as the detector was translated with respect to the capillary. The observed signal was not very sensitive to positioning when the capillary was offset over a range of ±1.5 mm for the center of the aluminum housing but dropped off rapidly at greater distances. All experiments reported here were performed with the capillary positioned at the center of the aluminum housing, as indicated in Figure 1.

Table I. Injection Data for CdTe Radioisotope Detector CE System

injection no.	DPM
1	101 885
2	110 449
3	101 884
4	111 375
5	103 512
6	113 018
7	109 432
8	104 581
9	106 740
10	107 357
av	107 023
std dev	3996
% RSD	3.7
injection vol	84 nL

Table II. Injection Data for Plastic Scintillator Radioisotope Detector CE System

injection no.	DPM
1	89 732
2	95 220
3	90 353
4	94 939
5	90 564
6	90 039
7	94 648
8	96 628
9	95 212
10	93 150
av	93 049
std dev	2621
% RSD	2.8
injection vol	72 nL

Detector Efficiency. In order to calculate the efficiency of the on-line radioactivity detectors for ^{32}P, it was necessary to determine the volume of sample that was injected onto the capillary tube by the gravity flow technique. The volume of sample introduced by hydrostatic pressure was determined as follows: A plug of ^{32}P-labeled ATP was introduced onto the capillary by raising the sample vial 6.5 cm above the high-voltage reservoir for 30 s. The end of the capillary was then returned to the anode reservoir, and electrophoresis was performed for 5 min at high voltage. This 5-min high-voltage period served to transfer the sample plug toward the detector and away from the injection end of the capillary as if an actual separation were being performed. At the end of the 5-min period the voltage was switched off and the electrolyte within the capillary tube was driven, via syringe, into a liquid scintillation vial located beneath the capillary outlet. This rinsing process was continued until approximately eight capillary volumes of electrolyte were collected. The collected sample plugs were mixed with scintillation cocktail and subjected to liquid scintillation counting. The injection volumes were determined by relating the activity of the sample plugs to that of the injected sample solution. The injection volumes and repeatability of the manually performed hydrostatic injections for the two detector efficiency determinations are shown in Tables I and II.

The results from replicate capillary electrophoresis runs in which a standard solution of adenosine 5′-[α-^{32}P]triphosphate was injected into the capillary are shown in Tables III and IV. The tables list the migration time, peak width, peak area, and detector efficiency. Representative electropherograms

Table III. CdTe Radioisotope Detector Efficiency Data

run no.	elution time, min	peak area, counts	residence time, min	efficiency
1	18.33	1519	0.049	27.6%
2	17.96	1372	0.048	25.4%
3	18.30	1461	0.049	26.5%
4	18.07	1511	0.048	28.0%
5	17.98	1407	0.048	26.1%
6	17.48	1601	0.047	30.3%
7	17.76	1197	0.047	22.7%
8	17.32	1195	0.046	23.1%
9	17.91	1392	0.048	25.8%
10	17.37	1266	0.046	24.5%
11	17.77	1359	0.047	25.7%
av	17.84	1389		26.0%
std dev	0.34	132		2.2%
% RSD	1.9	9.5		8.4%

Table IV. Plastic Scintillator Radioisotope Detector Efficiency Data

run no.	elution time, min	peak area, counts	residence time, min	efficiency
1	20.65	3375	0.055	72.7%
2	20.62	3088	0.055	66.5%
3	20.55	3119	0.055	67.2%
4	20.54	3091	0.055	66.5%
5	20.69	2953	0.055	63.6%
6	20.84	2881	0.056	60.9%
7	21.22	2883	0.057	59.9%
8	21.00	2952	0.056	62.4%
9	20.84	3213	0.056	67.9%
10	20.88	3122	0.056	66.0%
av	20.78	3068		65.4%
std dev	0.22	156		3.8%
% RSD	1.06	5.07		5.8%

corresponding to the two detector efficiency determinations and the conditions under which the separations were performed are shown in Figures 3 and 4. The efficiencies reported in the tables were calculated by using the following equation:

$$\begin{aligned} \text{NOC} &= \{\text{DPM}_{\text{peak}}\}\{\text{residence time}\}\{\text{efficiency}\} \\ &= \{\text{DPM}_{\text{peak}}\}\{\text{detector length/zone velocity}\}\{\text{efficiency}\} \end{aligned} \quad (2)$$

where NOC represents the number of observed counts integrated over a peak, DPM_{peak} represents the number of radioactive transformations occurring each minute in the injected sample plug, the residence time is the amount of time (in minutes) a radioactive molecule within a given sample zone spends in the detection volume, and the efficiency is the fractional number of events sensed by the detector. The efficiencies for the on-line detectors described here are a function of detector collection geometry, i.e., positioning of the CdTe probe or plastic scintillator with respect to the capillary, as well as particle flux attenuation by the capillary wall (a fraction of the emitted β particles are of sufficiently low energy to be stopped by the capillary wall material). Note that the residence time within the detector must be determined for each component in a mixture because separated sample zones travel with different velocities according to their individual electrophoretic mobilities. This is in sharp contrast with radio HPLC detection in which the residence time for each sample component is the same and is given by the ratio of the detector cell volume to the mobile phase flow rate. The residence time for a particular sample component separated by capillary electrophoresis is easily obtained from its migration time and from the length of capillary to which the detector is exposed.

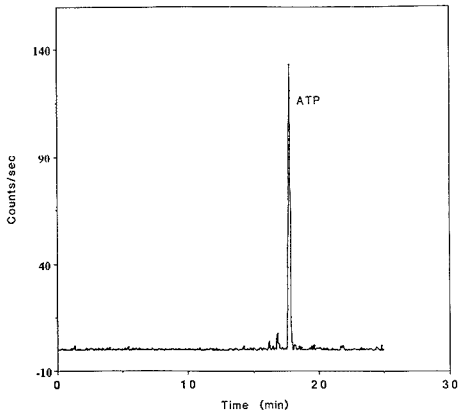

Figure 3. Capillary electropherogram of adenosine 5′-[α-^{32}P]triphosphate obtained by injecting approximately 51 nCi (7×10^{-8} M solution) onto the capillary and applying a constant potential of −20 kV. The separation was continuously monitored with the CdTe semiconductor radioisotope detector. Data was subjected to a 5-point sliding smooth. Electrolyte was 0.2 M borate buffer, pH = 8.1.

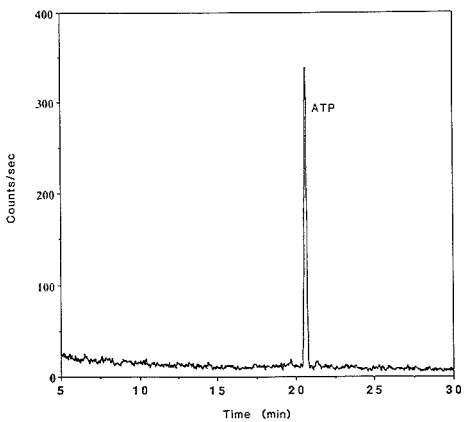

Figure 4. Capillary electropherogram of adenosine 5′-[α-^{32}P]triphosphate obtained by injecting approximately 38 nCi (6×10^{-8} M solution) onto the capillary and applying a constant potential of −25 kV. The separation was monitored with the plastic scintillator radioisotope detector. Data was subjected to a 5-point sliding smooth. The electrolyte was the same as in Figure 3.

Results obtained for the replicate runs shown in Tables III and IV indicate that the efficiency of ^{32}P detection for the on-line CdTe radioactivity detector is approximately 26%, while the efficiency of the plastic scintillator radioactivity detector is approximately 65%, reflecting the improved geometry of the latter device. The background noise level of the CdTe detector system is a function of the low energy discriminator setting. The value of 0.01 MeV selected for all experiments reported here gave a background count rate of approximately 10 counts/min while leaving a wide energy window open for detection. Comparison of signal-to-noise ratios in the two electropherograms indicates that the two detectors exhibit quite similar sensitivities despite the fact that the efficiency of the plastic scintillator detector is a factor

Table V. Capillary Electrophoresis Separations Performed under Standard (Runs 1–6) and Flow Programmed (Runs 7–12) Conditions[a]

run no.	peak width, min	peak area, counts	voltage program
1	0.38	985	20 kV constant
2	0.34	1098	
3	0.43	1236	
4	0.38	1016	
5	0.48	1078	
6	0.35	968	
av	0.39	1064	
7	0.87	2404	20 kV initial,
8	0.79	2705	10 kV during
9	0.71	2081	detection period
10	0.81	2448	
11	1.12	2695	
12	0.80	2673	
av	0.85	2501	

[a] Peak area ratio, 2.4; current ratio, 2.4; voltage ratio, 2.0.

of 2.5 times greater than that of the semiconductor detector. This is caused by the extremely low background noise level of the CdTe device compared to that of the cooled photomultiplier tube used in this work.

Flow Programming. Equation 2 suggests that the number of counts measured (the detector sensitivity) over a sample peak may be increased by lengthening the residence time of the sample in the detection volume. This is equivalent to increasing the counting time on a liquid scintillation counter and this concept has been recognized in both radio HPLC applications (see, for example, ref 15) and radioisotope detection in isotachophoresis (*7, 20*). In capillary electrophoresis, the velocity of a sample zone may be reduced and its residence time increased by simply reducing the applied potential as the zone passes through the detection volume. The most efficient implementation of this flow programming concept would involve reducing the zone velocities only while the sample was present within the detection volume and operating at a relatively high potential at all other times. To our knowledge, this type of flow programming has not previously been explored in capillary electrophoresis. Although it is demonstrated only for radioisotope detection here, this methodology should be applicable to other modes of sample detection in CE.

The flow programming concept is demonstrated in Table V, which lists the peak width and peak area for five capillary electrophoresis separations performed with and without flow programming. Separations 1–5 were performed at a constant potential of −20 kV using the CeTe radioisotope detector, while in runs 6–10 the potential was reduced to −10 kV as soon as signal was detected above the detector background level. Because the zone velocity is directly proportional to the applied field strength, the average temporal peak width and area (number of counts observed) for the five flow programmed runs were approximately doubled. This improvement in sensitivity is, however, accompanied by an increase in analysis time as well as a small loss in resolution due to zone broadening. The magnitude of the resolution losses incurred during flow programming will be strongly dependent upon the amount of sample injected and the additional run time associated with the flow programming process. For injected sample plug lengths that are several times larger than the length associated with diffusional broadening (typical operating conditions), the resolution loss will not be significant. In the limit of injected sample plugs with no initial width (δ function), the additional peak variance increases linearly with programming time (ignoring analyte–wall interactions) and the resolution loss will become significant.

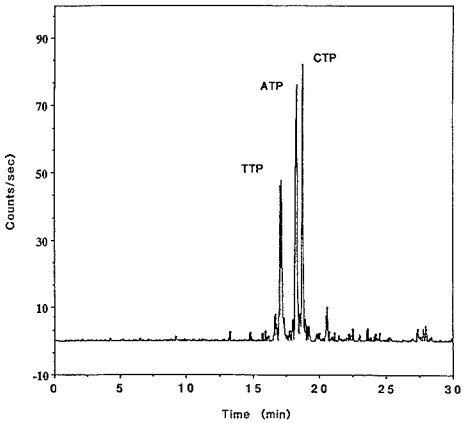

Figure 5. Capillary electropherogram of thymidine 5′-[α-^{32}P]triphosphate, cytidine 5′-[α-^{32}P]triphosphate, and adenosine 5′-[α-^{32}P]triphosphate obtained by injecting approximately 19 nCi (2×10^{-8} M solution) of each component onto the capillary and applying a constant potential of −20 kV.

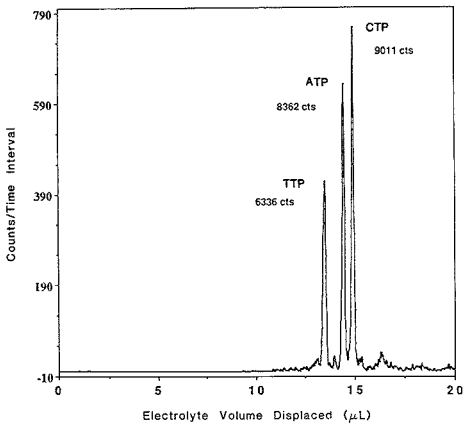

Figure 6. Flow programmed capillary electropherogram of thymidine 5′-[α-^{32}P]triphosphate, cytidine 5′-[α-^{32}P]triphosphate, and adenosine 5′-[α-^{32}P]triphosphate obtained by injecting approximately 19 nCi (2×10^{-8} M solution) of each component onto the capillary. The separation was flow programmed by applying a constant potential of −20 kV until radiolabeled sample approached the detection volume and then reducing the potential to −2 kV as the sample zones traversed the detection region. Note that the detector signal has been plotted as a function of electrolyte volume displaced, resulting in a time-compressed abscissa over the flow programmed region of the electropherogram. The operating current was 38 μA at −20 kV and 3.8 μA at −2 kV. The data was subjected to a 5-point sliding smooth.

A striking example of increased sensitivity gained through the application of flow programming is illustrated in Figures 5 and 6. In Figure 5, a synthetic mixture of thymidine 5′-[α-^{32}P]triphosphate (^{32}P-TTP), cytidine 5′-[α-^{32}P]triphosphate (^{32}P-CTP), and adenosine 5′-[α-^{32}P]triphosphate (^{32}P-ATP) was injected with each component present at a concentration of approximately 2×10^{-8} M ($\simeq$19 nCi injected) by using hydrostatic pressure and separated under the influence of a constant −20-kV applied potential. In Figure 6 the sample solution and injection volume were the same as in Figure 5, but the residence time of each component was increased by

reducing the applied potential from −20 to −2 kV as radioactive sample was passing through the detection volume. At the same time, the counting interval was increased proportionately (from 1 to 10 s) and the detector signal was plotted as a function of electrolyte volume displaced through the capillary tube. Note that this results in a time-compressed abscissa over the flow programmed period of the electropherogram (the entire separation required about 70 min in this case). It is important to point out that the lower limit of detection for radioisotope detection refers to the lowest sample activity contained within a peak that may be detected and accurately quantified. From the data presented in Table V and Figures 3–6 it is apparent that the lower limit of detection for this system is greatly dependent upon the conditions under which the analysis is performed and that detector sensitivity may be extended by an order of magnitude or more by using flow programming.

The sensitivity gain afforded by this flow programming methodology will ultimately be limited by practical considerations of analysis time and resolution losses caused by diffusional broadening of the sample zones. Simplicity and consideration of analysis time, however, still make flow counting detection for capillary electrophoresis an attractive alternative to the quantitatively superior batch counting approach in which fractions are collected and subjected to conventional counting techniques (*15*). The batch counting approach, provided that sufficiently small fractions may be collected, does offer the advantage of decoupling separation considerations from measurement time. Considering only the limitation imposed by diffusional spreading of sample zones during the flow programmed portion of a run, it is possible to predict the extent to which detector sensitivity may be improved by flow programming. For an injection volume of 84 nL, as used in this work, and a maximum allowable increase in zone variance defined to be 10%, approximately 84 min of flow programming would be permitted (this calculation assumes a rectangular injection profile and a solute diffusion coefficient of 10^{-6} cm^2/s and neglects both diffusional broadening prior to flow programming and velocity-dependent analyte–wall interactions). This 10% increase in variance would be accompanied by a 250-fold increase in the number of counts observed over a peak. Because the sensitivity of radioisotope detection is governed by counting statistics, a 16-fold increase in the signal-to-noise ratio $(NOC/(NOC)^{1/2})$ would result. Thus, a lower limit of detection of about 10^{-11} M would seem to be a conservative extrapolation. Obviously, the limitations imposed by diffusional broadening would become more severe if the initial injection volume were reduced.

In an automated implementation of the flow programming methodology, that is, with the high-voltage power supply under computer control, there is a further limitation imposed upon achievable sensitivity gains. There must be enough sample present to generate a signal that is sufficiently large to exceed the detector background level under standard (non-flow-programmed) conditions in order to initiate the flow programming procedure. In certain instances, however, prior knowledge of migration times for the compounds of interest would permit this limitation to be overcome.

CONCLUSION

Two simple on-line radioisotope detectors for capillary electrophoresis have been described and characterized for the analysis of ^{32}P-labeled analytes. The minimum limit of detection for these systems was shown to be strongly dependent upon the conditions under which the analysis is performed. For standard CE separations that are performed at a relatively high (constant) voltage, the minimum limit of detection was found to be in the low-nanocurie (injected sample quantity) range, corresponding to an analyte concentration of about 10^{-9} M. The lower limit of detection for this type of detection system was extended to the sub-nanocurie level ($\simeq 10^{-10}$ M) by application of flow programming methodology, which served to increase the residence time of labeled sample components within the detection volume. Thus radioisotope detection, when applicable, has a sensitivity which is superior to that of most other detection schemes and which is comparable to that of electrochemical detection (*16*, *17*) and laser-induced fluorescence detection (*11*, *18*, *19*).

One improvement to the current systems would involve automation of the flow programming methodology, and such efforts are currently under way in this laboratory. A second improvement over the current semiconductor system would involve optimizing the detector geometry by capturing a larger solid angle with the CdTe detector. The performance of the plastic scintillator radioisotope detection scheme would be greatly improved by reducing the background noise level through the use of a quieter photomultiplier tube or two photomultiplier tubes operated in the coincidence mode. In certain instances it would be desirable to reduce the effective detection volume of these systems in order to increase resolution. This could be accomplished by installing a narrower aperture in the semiconductor detector or machining a smaller detection region in the plastic scintillator detector. In either case, detector sensitivity will be reduced because the detection volume and effective residence time will be decreased. Hence, there is once again a practical trade-off between detector sensitivity and resolution.

ACKNOWLEDGMENT

S.L.P. thanks David J. Rakestraw, Patrick H. Vacarro, and W. Howard Whitted for many helpful conversations pertaining to this work.

LITERATURE CITED

(1) Nickerson, B.; Jorgenson, J. W. *HRC CC, J. High Resolut. Chromatogr. Chromatogr. Commun.* **1988**, *11*(7), 533–534.
(2) Jorgenson, J. W.; Lukacs, K. D. *Science* **1983**, *222*, 266–272.
(3) Kessler, M. J. *Analytical and Chromatographic Techniques in Radiopharmaceutical Chemistry*; Wieland, D. M., Tobes, M. C., Mangner, T. J., Eds.; Springer-Verlag: New York, 1987; Chapters 5–7.
(4) Roberts, T. R. *Radiochromatography*; Journal of Chromatography Library; Elsevier: Amsterdam, 1978; Chapter 6.
(5) Kessler, M. J. *Am. Lab.* **1988**, *20*(6), 86–95.
(6) Kessler, M. J. *Am. Lab.* **1988**, *20*(8), 76–81.
(7) Kaniansky, D.; Rajec, P.; Švec, A.; Havaši, P.; Macášek, F. *J. Chromatogr.* **1983**, *258*, 238–243.
(8) Altria, K. D.; Simpson, C. F.; Bharij, A.; Theobald, A. E. Paper presented at the 1988 Pittsburgh Conference and Exposition, New Orleans, February, 1988; Abstr. No. 642.
(9) Berry, V. *LC/GC* **1988**, *6*, 484–491.
(10) Needham, R. E.; Delaney, M. F. *Anal. Chem.* **1983**, *55*, 148–150.
(11) Gassmann, E.; Kuo, J. E.; Zare, R. N. *Science* **1985**, *230*, 813–814.
(12) Gordon, M. J.; Huang, X.; Pentoney, S. L., Jr.; Zare, R. N. *Science* **1988**, *242*, 224–228.
(13) Huang, X.; Gordon, M. J.; Zare, R. N. *Anal.* Chem. **1988**, *60*, 1837–1838.
(14) Knoll, G. F. *Radiation Detection and Measurement*; John Wiley and Sons, Inc.: New York, 1979.
(15) Markl, P. Radiometric Detectors. In *Instrumentation for High Performance Liquid Chromatography*; Journal of Chromatography Library, Volume 13; Elsevier: Amsterdam, Oxford, New York, 1978; pp 151–161.
(16) Wallingford, R. A.; Ewing, A. G. *Anal. Chem.* **1988**, *60*, 258–263.
(17) Wallingford, R. A.; Ewing, A. G. *Anal. Chem.* **1987**, *59*, 1762–1766.
(18) Gozel, P.; Gassmann, E.; Michelsen, H.; Zare, R. N. *Anal. Chem.* **1987**, *59*, 44–49.
(19) Dovichi, N. J. Paper presented at the 41st ACS Summer Symposium on Analytical Chemistry, Stanford University, June 26–29, 1988.
(20) Kaniansky, D.; Rajec, P.; Švec, A.; Marák, J.; Koval, M.; Lúčka, M.; Franko, Š.; Sabanoš, G. *J. Radioanal. Nucl. Chem.* **1989**, *129*(2), 305–325.

RECEIVED for review November 22, 1988. Accepted April 17, 1989. Support for this work by Beckman Instruments, Inc., is gratefully acknowledged.

Near-Infrared Surface-Enhanced Raman Spectroscopy Using a Diode Laser

Stanley M. Angel* and Michael L. Myrick

Environmental Sciences Division, Lawrence Livermore National Laboratory, Livermore, California 94550

Near-infrared (near-IR) surface-enhanced Raman spectra (SERS) were measured for a highly luminescent compound, tris(2,2'-bipyridyl)ruthenium(II) ($[Ru(bpy)_3]^{2+}$), with a 785-nm diode laser using Cu and Ag metal electrodes. No luminescent interference was encountered and spectra were measured with high sensitivity. SER spectra were measured for 6 mM solutions of this compound using only 4.3 mW of power from the diode laser. In addition, SER spectra were measured for pyridine on Ag and Cu electrodes. Relative SER enhancements for pyridine were compared for both metals using 785-nm-wavelength and 632-nm-wavelength excitation.

INTRODUCTION

Surface-enhanced Raman spectroscopy (SERS) has been a focus for much study since it was first reported by Fleischmann and co-workers in 1974 (*1*). Thus far, a considerable amount of this study has aimed at understanding the physical origin of the phenomenon (*1–4*), but recently there have been many investigations of potential analytical uses for SERS (*5–9*). Although it has not yet come into general use, SERS is an attractive analytical technique. This is partly because for certain types of molecules it can be very sensitive. Furthermore, because SERS is a vibrational spectroscopy, a SER spectrum contains considerable molecular information. At Lawrence Livermore National Laboratory, we are investigating the possibility of making analytical SER measurements over fiber optics for remote monitoring of groundwater contaminants. For this purpose, small powerful laser sources are needed.

With the introduction of Fourier transform (FT) Raman instruments (*10*, *11*), near-infrared (near-IR) Raman spectroscopy has become an excellent technique for eliminating sample fluorescence and photochemistry in Raman measurements. Recently, the range of near-IR Raman techniques was extended to include near-IR SERS (*12–14*). Most SER studies to date have been performed by use of visible excitation sources such as Ar-ion lasers, and sample luminescence complicates the measurement in this, as in any, Raman technique. While luminescence from adsorbed species is generally quenched by the metal, luminescence may originate from analyte in solution or from other species in complex samples (e.g. natural waters). Though methods exist for removing small Raman signals from a large fluorescence background (*15–21*), these do not eliminate fluorescence, but rather take advantage of the different time scales or the different polarization properties of Raman scattering and luminescence. Near-IR SERS reduces the magnitude of the fluorescence problem (*12–14*) because near-IR excitation eliminates most sources of luminescence (*10*).

Potential applications of near-IR SERS are numerous. A principal interest in this laboratory has been remote monitoring of groundwater contaminants over optical fibers. Near-IR SERS offers many advantages for this application. In addition to eliminating fluorescence problems from the optical fiber and sampling region, near-IR excitation should significantly reduce the intensity of fiber-optic Raman bands due to the n^{-4} dependency of the Raman intensity, while the SERS intensity does not decrease monotonically with excitation wavelength. Also, the absorption losses of many optical fibers are very low for near-IR radiation.

Near-IR SERS is also applicable to monitoring highly luminescent molecules. As an example, resonance Raman studies have been performed on tris(1,10-phenanthroline)ruthenium(II), $[Ru(phen)_3]^{2+}$, bound to DNA to determine the stereoselectivity of binding (*22*). The use of near-IR SERS for the same purpose, while introducing possible surface effects, would avoid problems associated with luminescence of the complex or the biological molecules to which the complex binds, as well as possible changes in binding due to electronic excitation of the molecules. Any spurious results due to photoreaction products could also be eliminated.

Near-IR SERS also has physical significance, in that this wavelength range is significantly different from the visible wavelength range used in most SER studies. The calculation of near-IR SER enhancement factors might be useful for verification of models currently used to explain the SERS phenomenon (*1–4*).

For SERS to become a widely accepted analytical technique, a number of obstacles must be surmounted, not the least of which is a convenient laser source. Most SER studies have been performed with visible-excitation sources such as Ar-ion lasers. Ion lasers have the disadvantage of being expensive to purchase and maintain, large and usually water cooled, and not applicable for general laboratory analytical measurements. Semiconductor lasers do not suffer from these problems. These solid-state devices are inexpensive, small, easy to use, and long-lived and require little maintenance. The problem with semiconductor lasers is that powerful single-mode lasers are only available at near-IR wavelengths, though this is likely to change in the near future. Semiconductor lasers have already been demonstrated to be remarkably versatile and useful in a number of spectroscopic applications, as indicated by Ishibashi and co-workers (*23*, *24*). To date, however, no report has been made of the use of laser diodes for SERS.

The ability to perform SERS with a small, inexpensive, and highly portable excitation source could increase the number of laboratories capable of effectively using this technique by providing a relatively easy entry to SERS research. Also, the development of semiconductor-laser excitation would expand the number of potential applications of SERS for nonlaboratory uses such as in situ environmental monitoring. Thus, the purpose of the present work is to demonstrate that near-IR SERS can be performed with laser-diode excitation sources and to describe the characteristics of this technique. The observation of SERS for pyridine and $[Ru(bpy)_3]^{2+}$ on Ag and Cu electrodes using 785-nm excitation from a laser diode is reported. These two analytes were chosen because their SER spectra are well documented in the literature (*25*, *26*).

EXPERIMENTAL SECTION

SER spectra were measured on the surface of the working electrode of a standard three-electrode electrochemical cell.

0003-2700/89/0361-1648$01.50/0

Electrodes were prepared from 1-mm-diameter Ag or Cu wire that was sealed in a glass capillary tube with Norland brand optical epoxy (type NOA-61) and polished flat to expose only the front 1-mm-diameter face of the wire to solution. Electrodes were polished with 3M-brand Imperial lapping film, using a 1-μm grade for final polishing. Electrodes were repolished and rinsed after each analysis.

Measurements are reported in aqueous solution. Electrode potentials were controlled with a PAR Model 362 scanning potentiostat and are listed relative to the saturated calomel electrode (SCE). The supporting electrolyte was 0.1 M KCl in all cases. Solutions were prepared in distilled water. Pyridine was obtained from J. T. Baker Chemical Co. and was used without further purification. $[Ru(bpy)_3]Cl_2$ was obtained from Alfa Chemical Co. and contained 6.31% water.

Roughening of the electrode surface was performed by repeated in situ oxidation–reduction cycles (ORCs). ORCs either were performed manually, oxidizing for approximately 20–30 s at +400 mV followed by reduction at −400 mV for $[Ru(bpy)_3]^{2+}$ and −700 mV for pyridine, or were performed automatically, allowing the potentiostat to cycle between these potentials for approximately 10 min at a scan rate of 50 mV/s. ORCs were performed in situ since the ultimate goal of this work is to develop portable remote in situ environmental monitoring technology. Part of this research involves determining whether in situ SERS is possible for identifying contaminants.

The spectrometer used for these studies consisted of an $f/4$ scanning double monochromator (SPEX Model 1681B) with 1200 grooves/mm holographic gratings and an $f/1$ collection lens. The detection system was a GaAs photomultiplier (RCA Model 31034) operated at −1800 V with a photon counting system (EG&G Model 1121A amplifier discriminator with Model 1112 counting system). All SER spectra were recorded with a 2-s integration time and a nominal spectral resolution for a 1000 cm^{-1} Raman band of 16 cm^{-1} using the 632-nm laser line and 10 cm^{-1} using the 785-nm laser line. Scans typically required about 10 min.

The 514.5-nm line of an Ar-ion laser was used for measuring fluorescence spectra, while SER spectra were measured by using the 632-nm line of a helium–neon (HeNe) laser (PMS Model LSTP-0050) or the 785-nm line from a GaAlAs diode laser (D.O. Industries, Model GALA-078-16-8). A very strong broad-band emission from the diode laser was removed by using an 830-nm band-pass interference filter that was tilted at a large angle to allow maximum transmission of the 785-nm laser line. This filter significantly attenuated the output power of the diode laser and was only used because a 785-nm band-pass filter was not available.

Instability of the laser diode was noted. It was found that the exact wavelength of lasing depended upon length of operating time (a thermal effect) and applied power. When the diode was allowed to thermally equilibrate at full power for several minutes prior to use, the output of the diode appeared to be stable.

Measurements with a United Detector Technologies power-meter indicated that the 632-nm line of the HeNe laser produced approximately 8.5 mW of power. The laser diode, when unfiltered, produced 10 mW of power; however, use of the 830-nm interference filter reduced the maximum usable intensity to 4.3 mW at 785 nm.

SERS was performed with electrodes immersed in the analyte solution. With 632-nm and 785-nm excitation, little sample absorbance of the excitation light by the $[Ru(bpy)_3]^{2+}$ solution was noted, even though there was about a 10-mm thickness of aqueous solution between the SERS electrode and the cell window that faced the laser-focusing lens and also between the electrode and the cell window that faced the spectrometer-collection lens. However, when 514.5-nm excitation was used, this sample strongly attenuated the incident radiation and resulted in intense $[Ru(bpy)_3]^{2+}$ luminescence from unadsorbed molecules in the analyte solution. When focused to a tight spot, the intense 514.5-nm radiation appeared to be totally attenuated within 4 to 5 mm of entering the analyte solution so that the electrode had to be placed very close to the walls of the sample cell.

A 90° scattering geometry was used to collect the SER spectra. The electrode normal was at about a 60° angle with respect to the incident laser beam. ORCs were performed while the SERS electrodes were illuminated with the laser at the power used to make subsequent measurements.

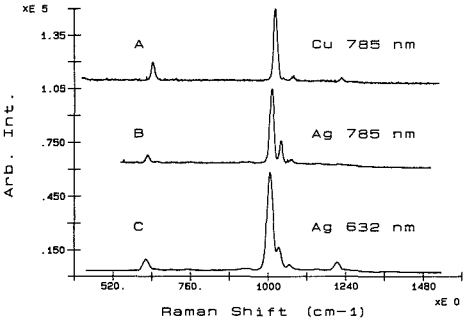

Figure 1. SERS of 0.1 M pyridine in 0.1 M KCl(aq) at −0.7 V vs SCE. Curve A shows SERS for 785-nm excitation with a diode laser on a Cu electrode. Curves B and C are for Ag electrodes. The spectrum for 785-nm excitation is shown by B, and for 632-nm excitation by C.

RESULTS AND DISCUSSION

SERS of Pyridine. The SER spectra of pyridine are well documented in the literature, and this molecule has been used as a model in many SERS studies. Recent reports from this laboratory (*13*, *14*) and Chase and Parkinson (*12*) have indicated that pyridine displays a large SER effect when excited in the near-IR region by a Nd-YAG laser. For this reason, pyridine is used as a model in the present study.

Figure 1 shows SER spectra for 0.1 M pyridine in 0.1 M KCl(aq) solution. Curve A gives data for pyridine adsorbed on an ORC-roughened Cu electrode when excited by 785-nm radiation from a GaAlAs diode laser filtered to prevent interference from the broad-band emission of the laser. This spectrum is similar to that obtained on a roughened Ag electrode using 785-nm excitation (curve B), except for the relative intensities of a few bands. Differences between pyridine bands on Cu and Ag electrodes using visible-wavelength excitation have been described in the literature (*25*) and will not be elaborated on here. Curve C shows the spectrum of pyridine adsorbed on a roughened Ag electrode using 632-nm excitation. This spectrum is very similar to the 785-nm excited spectra, the exceptions being the higher-energy part of the SER spectrum. There is significant attenuation of the intensity of the pyridine bands above about 1500 cm^{-1} when 785-nm excitation is used, and this is due to the reduced sensitivity of the photomultiplier-tube detection system in the near-IR region.

Relative SER enhancements were measured for pyridine on the Cu and Ag electrodes by comparing the intensity of the SER band measured at 1008-cm^{-1} using each excitation wavelength to the intensity of the corresponding band using each excitation wavelength of the regular Raman spectra of neat pyridine. The intensity of the band measured at 1008-cm^{-1} for the neat pyridine spectrum was used to normalized differences in the system response and laser power at the two wavelengths. For Ag, the SER enhancement for pyridine at 785 nm is about the same magnitude as the enhancement at 632 nm within a factor of about 2. However, for Cu, the enhancement at 785 nm is a factor of about 6 larger than at 632 nm. Both of these values are in agreement with published enhancements at 632 nm and 780 nm (*27*).

It seems apparent that a properly filtered and stabilized semiconductor laser can yield useful near-IR-SER spectra for compounds like pyridine. In succeeding experiments, we have attempted to make use of the properties of near-IR excitation to record the SER spectrum of a more interesting and strongly luminescent metal complex, $[Ru(bpy)_3]^{2+}$, in a lower concentration range.

SERS of $[Ru(bpy)_3]^{2+}$. $[Ru(bpy)_3]^{2+}$ and similar com-

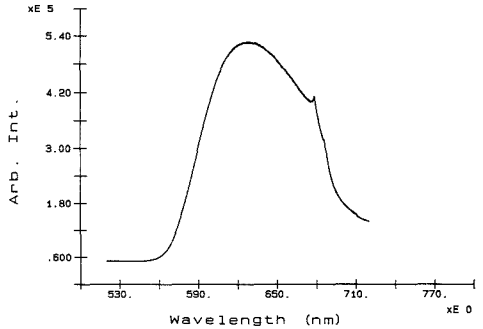

Figure 2. Luminescence of 6 mM $[Ru(bpy)_3]^{2+}$ in 0.1 M KCl(aq). Excitation is from the 514.5-nm line of an Ar-ion laser. Data are for solutions at room temperature.

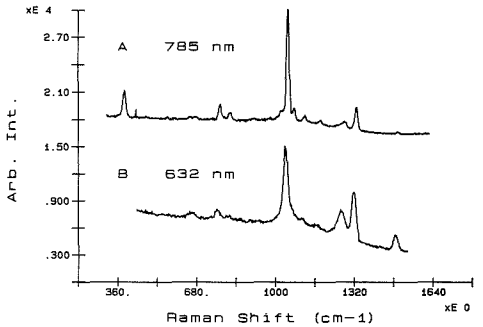

Figure 3. SER spectrum of 6 mM $[Ru(bpy)_3]^{2+}$ in 0.1 M KCl(aq) on an Ag electrode at −0.4 V vs SCE. Curve A gives data for 785-nm excitation from a diode laser, while B gives data for 632-nm excitation.

plexes, such as $[Ru(phen)_3]^{2+}$, may have important biological applications; recent work indicates they may be intercalated into DNA and sensitize the photocatalytic cleavage of the DNA strands (*28*). Vibrational studies of this phenomenon would be difficult to perform with resonance-enhanced Raman spectroscopy because kinetic phenomena would be occurring as the molecules absorbed light. Normal Raman spectroscopy would be insufficiently sensitive to the small quantities of complex involved, and thus near-IR SERS would appear to have potential applicability to this system.

Shown in Figure 2 is the luminescence of 6 mM $[Ru(bpy)_3]^{2+}$ in 0.1 M KCl(aq) at room temperature. This emission was obtained with 514.5-nm excitation from an Ar-ion laser. The unusual band shape of the luminescence shown here is due to instrument response variations of our spectrometer over the large energy range covered. As shown, the luminescence covers a large energy range extending from approximately 540 to 900 nm. This very bright luminescence, when measured under the same conditions as the SER spectra, is much more intense than the Raman signal over most of this range when excitation is in the visible region. As will be shown below, even low-energy visible excitation results in significant luminescence, which interferes with the SER signal. Luminescence following high-energy excitation is frequently a significant problem even for "nonluminescent" molecules (*29*), the residual luminescent impurities contributing to this difficulty.

Figure 3 shows the SER spectra of 6 mM $[Ru(bpy)_3]^{2+}$ in 0.1 M KCl(aq) solution on an Ag electrode roughened by several ORCs. Curve A of Figure 3 gives the SER spectrum of $[Ru(bpy)_3]^{2+}$ on an Ag electrode when the molecule is excited at 785 nm. What is remarkable about this spectrum is

Table I. Positions and Relative Intensities of SER Bands for $[Ru(bpy)_3]^{2+}$ on Cu and Ag Electrodes at −0.4 V vs SCE Using 785-nm Excitation from a Laser Diode (All Values in cm^{-1})[a]

Cu electrode	Ag electrode	Ag electrode[b]
288 vw	287 w	284 w
		334 w
		369 sh
358 s	379 s	378 s
422 w	425 vw	425 vw
550 w	552 vw	550 w
652 m	646 m	644 m
	666 w	665 m
772 s	769 s	765 s
809 vw	809 m	802 vw
	1023 sh	1025 m
1018 vvs	1044 vvs	1039 vvs
1063 w	1069 m	1063 m
1108 w	1110 w	1107 w
1178 s	1174 w	1170 s
1281 w	1273 m	1271 s
1311 s	1323 vs	1315 vs
1485 w	1490 w	1486 vs

[a] Relative intensities for high-energy bands are much reduced due to low near-IR PMT response. The spectral resolution is nominally 10 cm^{-1}. Key: s, strong; m, medium; w, weak; v, very; sh, shoulder. [b] Taken from ref 26, excitation wavelength is 647.1 nm; some very weak bands are not listed.

that it was obtained in the analyte solution with no evidence of luminescence from or attenuation of the laser beam by analyte in solution, even though there was 1 cm of solution on the excitation and collection sides of the electrode. SER spectra could not be obtained by using 514.5-nm excitation under these same conditions because of intense $[Ru(bpy)_3]^{2+}$ luminescence and attenuation of the laser line. These spectra (summarized in Table I) agree with data previously published for this complex (*26*) within the experimental error. By comparison, the spectrum shown in curve B, obtained by excitation at 632 nm with a more intense HeNe laser, is complicated by background luminescence despite the fact that the peak absorbance of the complex is at 455 nm in room-temperature aqueous solution and decreases rapidly at lower energy. This 632-nm-excited luminescence is visible to the eye when an appropriate filter is used and interferes with the measurement of the SER spectra.

An additional point to be made concerning the spectra of Figure 3 concerns the relative enhancements obtained at the two wavelengths for $[Ru(bpy)_3]^{2+}$. Using the same electrode and solution, we found that the absolute magnitude (in counts per second) of 785-nm-excited SERS is slightly larger than that of the 632-nm-excited spectrum. Relative enhancements are difficult to obtain quantitatively due to differences in detector response, optical alignment, and excitation intensity. However, the relative enhancement obtained for the near-IR-excited spectrum is qualitatively larger than for the visible-excited spectrum. Optics were aligned for maximum signal in both cases. However, detector response falls rapidly in the near-IR region, and the excitation power available from the near-IR diode was only 51% that of the 632-nm line.

In Figure 4 is shown the SERS of 6 mM $[Ru(bpy)_3]^{2+}$ on a Cu electrode. Enhancements for this compound on the Cu electrodes appeared smaller than on Ag electrodes, though of the same general magnitude, which is consistent with reported wavelength-dependent SER enhancements of pyridine on Cu and Ag electrodes (*27*).

Curve A of Figure 4 gives the SER spectrum on Cu for excitation at 785 nm with the semiconductor laser. Again, a reasonably clear spectrum is obtained with this source. In contrast, the data of curve B, showing SERS using 632-nm

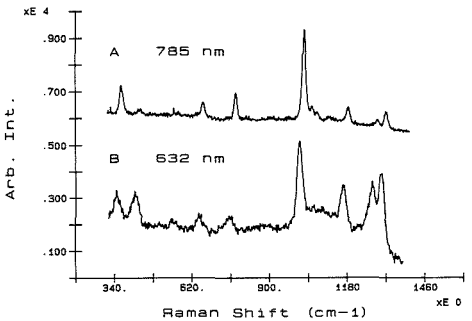

Figure 4. SER spectrum of 6 mM $[Ru(bpy)_3]^{2+}$ in 0.1 M KCl(aq) on a Cu electrode at −0.4 V vs SCE. Curve A gives data for 785-nm excitation from a diode laser, while B gives data for 632-nm excitation.

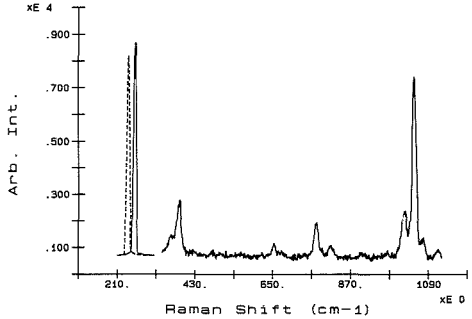

Figure 5. Mode hopping of diode laser. To the left are measurements of the laser line for two different applied power levels (the laser line positions are offset by about 250 cm^{-1} for clarity). To the right is a SER spectrum of $[Ru(bpy)_3]^{2+}$ on an Ag electrode using an intermediate power of the diode laser. Illustrated are effects of mode hopping: splitting of SER bands due to multiple simultaneous discrete modes of the solid-state excitation source.

excitation, reveal a large amount of background luminescence from the bulk analyte solution. These data also indicate that enhancements for $[Ru(bpy)_3]^{2+}$ on the Cu electrode are greater for 785-nm excitation than for 632-nm excitation.

Characteristics of Laser Diode Excitation. It is especially important for Raman applications that the laser be "single-mode"; i.e., it possess a narrow, well-defined frequency. For other applications such as photoacoustic spectroscopy, spectrophotometry, or fluorescence, this requirement is relaxed because molecular absorption bands are usually broad compared to the laser line width, even for multimode diode lasers. However, Raman bands are usually narrow, and the Raman band positions are measured relative to the laser line. Accurate calculation of vibrational frequencies therefore relies upon precise knowledge of the laser frequency. A principal difficulty with the use of the laser diode for Raman studies is its tendency to "mode hop", or change frequencies by discrete amounts, depending upon operational temperature and applied power. However, this difficulty may be easily overcome by taking appropriate precautions before use of the diode.

Shown in Figure 5 is a SER spectrum of 2 mM $[Ru(bpy)_3]^{2+}$ complicated by mode hopping. On the left-hand side of the figure, two distinct wavelengths of laser activity are shown, measured with the diode laser at two different power levels. The intensities of the narrow laser lines are scaled arbitrarily for easier comparison; however, the higher-energy line was obtained by reducing power to the laser.

Also shown in Figure 5 is a SER spectrum of 2 mM $[Ru(bpy)_3]^{2+}$ on an Ag electrode. Evident in this spectrum is the result of "mode hopping" of the diode laser; the two largest SER bands appear as doublets with pronounced side bands. In effect, this gives rise to a superposition of SER spectra with an energy offset of about 25 cm^{-1}, which corresponds to the energy separation of the two modes of the diode laser. This spectrum was obtained by operating the diode laser at a power level intermediate between those required to obtain the laser lines shown on the left of Figure 5.

To overcome this potential problem, we found it necessary to allow the device to come to thermal equilibrium before beginning an experiment. This required approximately 15–20 min. In addition, best results were obtained with the laser operating at the full recommended power of the device.

Although some spectra were obtained that had the general appearance of Figure 5, it was more commonly observed that the positions of the peaks in the SER spectra appeared to shift slightly in a random fashion. This appeared not to be due to misalignment of the monochromator but rather to variation of the lasing mode. Thus, for this particular diode laser, it was determined that the position of the laser line should be determined for each new experiment. The position of the laser line, after equilibration at full power, did not appear to vary significantly over extended periods of time. For this reason, and because of the long life of the laser device (on the order of 10 000 h or greater at full power), it is reasonable for some applications to leave the diode laser at full power continuously.

The diode laser used for this work was of moderately low power compared to other diode lasers that are commercially available. It seems likely that much greater sensitivity will be possible as more powerful single-mode diode lasers become available. The use of a more powerful diode laser coupled with the proper detection system might provide a relatively low-cost alternative to an FT Raman system for measuring SER (or normal Raman) spectra of highly fluorescent compounds.

LITERATURE CITED

(1) Fleischmann, M.; Hendra, P.; Mcquillan, A. *Chem. Phys. Lett.* **1974**, *26*, 163.
(2) Furtak, T. In *Advances in Laser Spectroscopy*; Garetz, B., Lombardi, J., Eds.; Wiley: New York, 1983; Vol. 2, p 175.
(3) *Surface Enhanced Raman Scattering*; Chang, R., Furtak, T., Eds.; Plenum Press: New York, 1982.
(4) Jeanmarie, D.; van Duyne, R. *J. Electroanal. Chem. Interfacial Electrochem.* **1977**, *84*, 1.
(5) Vo-Dinh, T.; Hiromoto, M.; Begun, G.; Moody, R. *Anal. Chem.* **1984**, *56*, 1667.
(6) Enlow, P.; Buncick, M.; Warmack, R.; Vo-Dinh, T. *Anal. Chem.* **1986**, *58*, 1119.
(7) Alak, A.; Vo-Dinh, T. *Anal. Chem.* **1987**, *59*, 2149.
(8) Torres, E.; Winefordner, J. *Anal. Chem.* **1987**, *56*, 1626.
(9) Carrabba, M.; Edmonds, R.; Rauh, R. *Anal. Chem.* **1987**, *59*, 2559.
(10) Hirschfeld, T.; Chase, B. *Appl. Spectrosc.* **1986**, *40*, 133.
(11) Chase, D. B. *J. Am. Chem. Soc.* **1986**, *108*, 7485.
(12) Chase, D.; Parkinson, B. *Appl. Spectrosc.* **1988**, *42*, 1186.
(13) Angel, S.; Katz, L.; Archibald, L.; Lin, L.; Honigs, D. *Appl. Spectrosc.* **1988**, *42*, 1327.
(14) Angel, S.; Katz, L.; Archibald, D.; Honigs, D. *Appl. Spectrosc.* **1989**, *43*, 367.
(15) Yaney, P. *J. Opt. Soc. Am.* **1972**, *62*, 1297.
(16) van Duyne, R.; Jeanmaire, D.; Shriver, D. *Anal. Chem.* **1974**, *46*, 213.
(17) Morhange, J.; Hirlimann, C. *App. Opt.* **1976**, *15*, 2969.
(18) Angel, S.; DeArmond, K.; Hanck, K.; Wertz, D. *Anal. Chem.* **1984**, *56*, 3000.
(19) Mann, C.; Vickers, T. *Appl. Spectrosc.* **1987**, *41*, 427.
(20) Hamaguchi, H.; Tahara, T.; Tasumi, M. *Appl. Spectrosc.* **1987**, *41*, 1265.
(21) Bright, F.; Heiftje, G. *Appl. Spectrosc.* **1988**, *40*, 583.
(22) Barton, J.; Danishefshy, A.; Goldberg, J. *J. Am. Chem. Soc.* **1984**, *106*, 2172.
(23) Nakanishi, K.; Imasaka, T.; Ishibashi, N. *Anal. Chem.* **1985**, *57*, 1219.
(24) Imasaka, T.; Yoshitake, A.; Ishibashi, N. *Anal. Chem.* **1984**, *56*, 1077.
(25) Pettinger, B.; Wenning, U.; Wetzel, H. *Surf. Sci.* **1980**, *101*, 409.
(26) Virdee, H.; Hester, R. *J. Phys. Chem.* **1984**, *88*, 451.
(27) Pettinger, B.; Wetzel, H. *Ber. Bunsen-Ges. Phys. Chem.* **1981**, *85*, 473.

(28) Kelly, J.; McConnel, D.; Ohlligin, C.; Tossi, A.; Kirsh-De Mesmaeker, A.; Nasielshi, J. J. Chem. Soc., Chem. Commun. 1987, 1821.
(29) Hirschfeld, T. Appl. Spectrosc. 1977, 31, 328.

RECEIVED for review February 7, 1989. Accepted April 14, 1989. The work at Lawrence Livermore National Laboratory was performed under the auspices of the U.S. Department of Energy under Contract W-7405-Eng-48. The authors express thanks to Paul Duhamel of the Office of Health and Environmental Research for supporting their research under Contract No. RPIS-003906.

Studies of Sputtering Atomizers for Atomic Absorption Spectroscopy

David S. Gough,* Peter Hannaford, and R. Martin Lowe

CSIRO Division of Materials Science and Technology, Locked Bag 33, Clayton, Victoria 3168, Australia

Factors influencing absorption sensitivity and reproducibility have been investigated for several sputtering atomizers, including the Analyte Corporation Atomsource and a similar system reported previously. The enhancement in sensitivity (factor of 3) of the Atomsource over that of the earlier system for given sputtering conditions is shown to result mainly from the longer absorption path in the Atomsource. The reproducibility is found to be comparable for the various atomizers studied, e.g. about 0.5–1% relative standard deviation for the case of chromium in low-alloy steel. The presence of water vapor in the argon sputtering gas at levels greater than about 10 ppm is found to have a deleterious effect on the sputtering efficiency and reproducibility.

INTRODUCTION

The use of cathodic sputtering as a means of atomizing samples for atomic absorption spectroscopy was proposed by Russell and Walsh (*1*) in 1959, soon after the introduction of the atomic absorption technique. With the sputtering method the sample to be analyzed is made the cathode of a low-pressure rare-gas discharge and subjected to bombardment by energetic rare-gas ions formed in the discharge. Under the action of the ion bombardment, atoms are ejected from the cathode surface, thereby creating an atomic vapor of the cathode material. The first reported sputtering atomizer, that of Gatehouse and Walsh (*2*), required the samples to be in the form of a hollow cathode and to be mounted inside the sputtering chamber. An improved sputtering atomizer described by Gough et al. (*3*) allowed solid samples with a flat face to be mounted onto the outside of a glass chamber against an insulating disk (called the discharge arrester) and O-ring. The disk had a central hole to confine the discharge to a constant area and a narrow recessed step adjacent to the sample to prevent sputtered material from establishing electrical contact between the sample and inner walls of the chamber. The system utilized a flowing stream of argon to help remove gaseous impurities from within the chamber, but was not satisfactory for the analysis of readily oxidized metals such as aluminum or zinc. An important advance in the development of sputtering atomizers was to introduce the flowing argon gas as closely as possible to the sample surface. In the system described by Gough (*4*), which is shown in Figure 1, the gas is admitted into the chamber through a narrow (0.1 mm) annular gap located just below the cathode surface (Figure 1b). The pressure developed behind the narrow gap forces the gas to enter the sputtering chamber at high speed. This arrangement has two distinct advantages: (i) the fast gas flow entrains sputtered atoms, greatly reducing lateral and back diffusion, and sweeps them into the light path, resulting in an increased absorption sensitivity of typically an order of magnitude. (ii) The rapid flow of gas at the cathode surface sweeps away gaseous impurities and thus allows metals such as aluminum to be analyzed without difficulty.

A newly developed commercial sputtering atomizer, called the Atomsource (Analyte Corp., Grants Pass, OR), also incorporates the principle of high-speed flow of argon at the cathode surface. In this device six jets of argon are directed at the cathode surface to produce a balanced flow of gas that sweeps the sputtered atoms orthogonally away from the surface and into the center of the chamber (see Figure 2). An advantage of the Atomsource is the use of a T-shaped absorption chamber in which the gas flow, with entrained sample atoms, is directed along the light path to increase the absorption sensitivity. The robust design of the Atomsource arrester allows it to be operated at higher powers (factor of about 4) than those of the earlier atomizers, thus increasing the rate of sputtering from the surface of a sample. Applications of the Atomsource have been discussed in a number of recent publications. Ohls (*5*) has reported a preliminary study of the use of the Atomsource in the analysis of metals and of solutions deposited on metallic cathodes. Kim and Piepmeier (*6*) have recently reported detailed studies of sample loss rates and discharge conditions in the Atomsource and also in a simple, single-jet atomizer. These authors also carried out scanning electron microscopy studies of the surface profiles produced under various discharge and flow conditions. Chakrabarti et al. (*7*) have recently reported studies of the transient atomization of solutions deposited on metallic cathodes, and Winchester and Marcus (*8*) have used the Atomsource to atomize nonconducting powders.

In this paper we report investigations into the physical principles underlying differences in absorption sensitivity and reproducibility of various sputtering atomizers that utilize a high-speed flow of gas at the cathode surface.

EXPERIMENTAL SECTION

Sputtering Atomizers. A number of glass sputtering chambers were constructed with the three basic configurations shown in Figure 3. The sample mounting arrangement and gas inlet system for these cells is the same as in Figure 1b. It consists of a hollow ceramic disk that is sealed by an O-ring between the sample and the main body of the chamber. The argon sputtering gas enters the chamber through the 0.1-mm gap in the arrester and, because of the pressure differential across this gap, is forced into the cell at high speed ($\sim 10^4$ cm/s at the orifice). The rapid

0003-2700/89/0361-1652$01.50/0

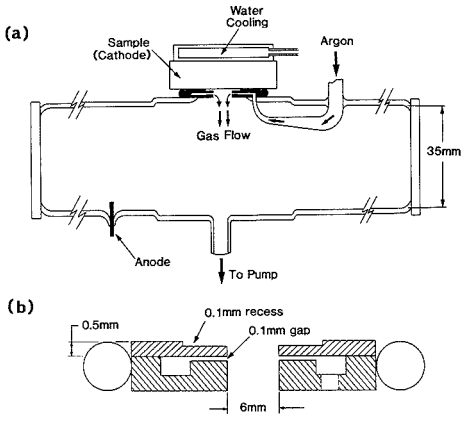

Figure 1. (a) Glass sputtering atomizer as used in ref 4. (b) Details of arrester used with this atomizer and also with atomizers described in Figure 3.

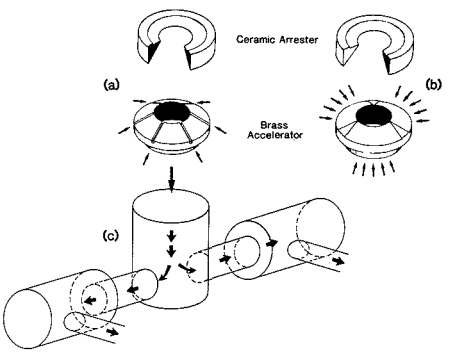

Figure 2. (a) Exploded drawing of the Atomsource six-jet pneumatic accelerator/arrester system. (b) Exploded drawing of modified accelerator/arrester system. (c) Internal shape of the Atomsource sputtering chamber. Arrows indicate gas flow.

flow of gas close to the cathode surface sweeps sputtered atoms away from the sample and into the light path at speeds that, for a given pressure, depend on the diameter of the tube forming the sputtering chamber. For most of the work described here tubes of 13 mm i.d. were used with argon flow rates of 0.3–0.4 L/min (at atmospheric pressure), which results in a gas speed through the tube of about 800 cm/s at a pressure of 4 Torr. Absorption measurements were made (a) along the axis of the tubes to determine absorption sensitivities and (b) across the tubes at various distances downstream from the cathode to determine the atom distributions within the various types of atomizer. The absorption measurements were made using the strong Cr resonance line at 357.9 nm because this wavelength is readily transmitted through the glass walls of the cells.

Other Equipment. The atomic absorption measurements were carried out with the sputtering atomizers replacing the flame in a Varian-Techtron AA6 spectrometer. The discharge current, argon gas pressure, and timing sequences for the sputtering atomizers were regulated by using the control box and associated microprocessor supplied with the Atomsource. The pumping lines from the cells to the Atomsource control box were identical for all of the sputtering cells used in this work. Cell pressures quoted in this text, except for those in Table II, are the pressures indicated on the Atomsource control box, but because the pressure sensor is situated inside the control box downstream from the cell, the actual pressure in the cell will be slightly different. An accurate,

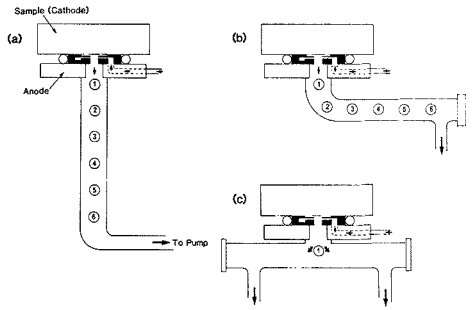

Figure 3. Glass sputtering atomizers used in this work: (a) straight-tube atomizer, (b) 90° curved-tube atomizer, (c) T-shaped atomizer. Numbers indicate approximately the positions at which absorbance measurements were made (see Figure 4).

absolute pressure gauge, MKS Baratron type 122A, placed at the pumping port of the sputtering chamber indicated that the pressure reading at the control box was high by typically 10%. The control box can be set for a high-current "preburn" sputtering period to clean the sample surface prior to switching to the desired operating current for the "burn" period. A 200 L/min rotary vacuum pump was used with the control box. Water vapor measurements were made with a Dupont Model 303 moisture analyzer.

Procedure for Reproducibility Measurements. Reproducibility tests were carried out using Cr determinations on a British Chemical Standards low-alloy steel (BSS 402) as a typical test case. Absorption measurements were made at 357.9 nm, with a hollow-cathode current of 3.5 mA and a monochromator band-pass of 0.3 nm. For these measurements the control box was set for a pressure of 4 Torr, a preburn of 20 s at a current of 40 mA, and a burn of 60 s at a current of 25 mA. A 60-s burn time was chosen because experience with the various atomizers showed that even after a high-current preburn the absorption can take around 30 s to reach a steady value. Each set of reproducibility measurements consisted of a series of 10 consecutive readings. Between each reading the sample was removed from the atomizer and rubbed with 400-grit emery paper until all traces of the previous burn had been removed. Relative standard deviations were calculated from the 10 individual measurements.

RESULTS AND DISCUSSION

Atom Distributions. An important feature in the design of sputtering atomizers of the type used in this work is the ability of the fast-flowing argon stream to entrain the sputtered atoms and sweep them away from the cathode and into the region of observation. Atom distributions for both straight and 90° curved cells (Figure 3a,b) have been determined by measuring absorptions across the cells at various distances downstream from the cathode. The results are shown in Figure 4, where the encircled numbers correspond to the positions shown in Figure 3. The close similarity of the shapes and absorbance values for curve A (straight tube, 12 mm i.d.) and curve B (90° curved tube, 13 mm i.d.) indicates that for these diameters and gas conditions (0.4 L/min, 5 Torr) the gas flow very efficiently sweeps the sputtered atoms around the 90° bend of the curved tube. The slightly lower absorbance values for curve A relative to curve B are attributed to the slightly smaller diameter of the straight tube. The results for the 90° curved tubes of varying diameters (curves B–E) indicate that for the flow conditions used here the optimum diameter is around 13 mm i.d. In wider tubes (curve D) the overall gas speed through the cell is reduced and atoms are less efficiently swept around the bend. In narrower tubes (curves C and E), although the gas speed is higher, the proximity of the walls of the tube results in a larger number of atoms being deposited on the walls. The enhancement in

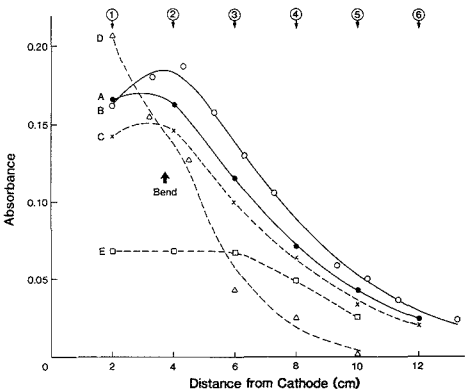

Figure 4. Comparison of atom distributions for straight-tube atomizer with 90° curved-tube atomizers of various sizes: (A) straight tube, 12 mm i.d.; (B) 90° curved tube, 13 mm i.d.; (C) 90° curved tube, 10 mm i.d.; (D) 90° curved tube, 18 mm i.d.; (E) 90° curved tube 6 mm i.d. The sample was 3.0% Cr in low-alloy steel. Sputtering conditions: 40 mA, ~600 V, 5 Torr of argon, flow rate 0.4 L/min.

Table I. Comparison of Absorbances Measured across and along Glass Atomizers[a]

atomizer type	measured absorbance across tube (position 1)	measured absorbance along tube
90° curved tube (Figure 3b)		
6 mm i.d.	0.07	0.26
13 mm i.d.	0.16	0.65
18 mm i.d.	0.21	0.49
T-piece tube[b] (Figure 3c)		
13 mm i.d.	0.26	0.86

[a] Conditions: 3% Cr in low-alloy steel; burn current 40 mA; discharge voltage ~500 V; gas flow rate 0.3 L/min. [b] Discharge voltage ~600 V for this atomizer.

absorption sensitivity gained by directing the gas flow along the light path can be determined by comparing absorptions measured *along* the axis of the glass cells with absorptions measured *across* the cells at position 1. For both the T-piece and 90° curved tube (Figure 3c and Figure 3b), the absorbance measured along the tube is about 4 times greater than that measured across the cell (see Table I). The results shown in Table I confirm that the atoms are most efficiently swept around the bend for diameters of around 13 mm.

In order to compare the absorption sensitivity of the glass cells with that of other cells such as the Atomsource, it is necessary to define some standard conditions for measuring the absorptions. All of the sputtering chambers tested in this work were used in conjunction with the Atomsource gas control box and power supply. In this system the pressure is monitored in the control box some distance downstream from the sputtering chamber and is not necessarily the same as the pressure at the sample surface. The pressure at the surface will be influenced to some degree by the localized high pressures that develop at the gas inlet orifice and are dependent on the orifice dimensions. For example, we find that when a glass cell with the arrester system shown in Figure 1b is operated at the same indicated pressure and discharge current as that of the Atomsource, the discharge voltages in the two cases are considerably different. In order to compare absorption sensitivities of different sputtering atomizers, we have in each case adjusted the pressure until the discharge voltages are the same for a given discharge current. We also

Table II. Comparison of Measured Absorbances in Various Sputtering Atomizers[a]

atomizer type	absorbance	pressure,[b] Torr
Atomsource (normal six-jet arrester)	0.111	4.3
Atomsource (modified continuous slit arrester)	0.103	5.1
T-piece glass cell	0.133	5.9
previous glass cell (ref 4)	0.036	4.6

[a] Conditions: 0.55% Cr in low-alloy steel; burn current 25 mA; discharge voltage 430 V; gas flow rate 0.3 L/min. [b] Measured at outlet of cell.

maintained a constant gas flow rate for all of the cells used by adjusting a valve mounted on the pumping line to the vacuum pump. Using this constant power, constant gas flow rate criterion, we find that the absorbances measured with the Atomsource and the T-piece glass sputtering cell (Figure 3c) are essentially the same (see Table II).

The above results indicate that the enhanced absorption sensitivity of the Atomsource over that of the earlier glass atomizer (*4*), when the instruments are operated under similar discharge and gas flow rate conditions, results mainly from the increased absorption path length due to efficient sweeping of sputtered atoms along the light beam. The similarity of absorption readings for the Atomsource and T-piece glass cell indicates that the gas inlet and arrester system for the glass sputtering atomizers used in this work (Figure 1b) and previously (*4*) is, under similar sputtering conditions, equally as efficient as the six-jet accelerator/arrester system of the Atomsource in producing a high concentration of sputtered atoms in the absorption chamber. This point has been further demonstrated by incorporating in the Atomsource sputtering chamber a modified accelerator/arrester system (shown in Figure 2b) that admits argon through a continuous slit, as in the ceramic discharge arrester shown in Figure 1b. For the same voltage, current, and gas flow rate, absorbances measured with this modified arrester were similar to those recorded for the Atomsource six-jet system in the same sputtering chamber (see Table II).

It is possible to operate the Atomsource at powers of 3–4 times higher than for the glass systems used here, and this can lead to a further 3–4-fold increase in atom density in the chamber. However, at the higher discharge powers increased background emission from the discharge can affect the signal to noise ratio.

An advantage of arrester systems that admit argon through a continuous slit is that the sputtering produces a single, uniform crater at the surface of the sample and thus should be suitable for depth profile studies.

Background Nonatomic Absorption. In the sputtering atomizer described previously (*4*), a small amount of background absorption was detected from particles formed by agglomeration of sputtered atoms in the discharge. This background absorption is not detectable (i.e., <0.1%) in the Atomsource under the operating conditions used here or in the glass cells used in this work. However, when the gas flow rate is reduced by about one-half (for pressures around 4–5 Torr), background absorption (e.g. 0.4% for the extreme case of pure silver samples) can be detected in both the Atomsource and glass atomizers. The slower gas speed in the large glass atomizer described earlier (*4*) is apparently less efficient at sweeping atoms away from the high-atom-density region adjacent to the cathode surface where agglomeration is most likely to occur.

Effect of Water Vapor. It is known from previous work (*4*) that water vapor in sputtering systems can have a deleterious effect on sputtering efficiency and should be kept to

Table III. Effect of Water Vapor on Sputtering in the Atomsource[a]

	run 1 dry argon[b]	run 2 moist argon[c]	run 3 dry argon[b]
mean absorbance	0.103	0.096	0.102
% RSD[d]	0.8	1.4	0.5
discharge, V	523	548	526

[a] Conditions: 0.42% Cr in low-alloy steel; burn current 25 mA; gas flow rate 0.3 L/min. [b] 3 ppm water. [c] 17 ppm water. [d] Based on 10 measurements with the sample removed, ground, and replaced between each measurement.

a minimum, particularly when reactive elements such as aluminum are being sputtered. Quantitative measurements of the effect of water vapor in the argon supply on the measured absorbance have been carried out using the Du Pont moisture analyzer to monitor the *input* argon supply to the Atomsource sputtering chamber. Two cylinders of high-purity argon were used, one containing 3 ppm water and the other 17 ppm. Absorbance measurements were made (at 25 mA, 0.3 L/min) for the case of Cr in a low-alloy steel sample. A series of 10 absorption readings was taken using the dry argon (3 ppm water), 10 readings with "moist" argon (17 ppm water), and a further 10 readings with dry argon. The results presented in Table III show that, even at levels of around 20 ppm, water vapor has a significant effect on the sputtering: The absorption has decreased for the higher water content argon, and the precision of the measurements is noticeably worse. The voltages shown in this table also reflect the changed sputtering conditions. Thus to obtain the best results with sputtering atomizers, it is important to use argon that is free from water, i.e., at levels less than about 10 ppm.

Water may also be absorbed on the surface of materials used in the construction of the sputtering chamber and gas lines. Once such materials have been exposed to the atmosphere, any absorbed moisture will outgas under vacuum at rates dependent on the nature of the material. The body of the Atomsource sputtering chamber is made from Delrin, which is a potential source of contamination by water (*9*), and tests have been made to check for water retention in this system. The Atomsource head was flushed for 24 h with dry argon, by which time the gas passing through the system was dry. It was left sealed for a further 24 h under an atmosphere of dry argon, and then with dry argon flowing through the head (at a flow rate of 0.3 L/min) the water content in the gas *leaving* the Atomsource head was measured. The water content of the gas was initially greater than 1000 ppm and fell to 40 ppm after 6 h. In the same test carried out on an all-glass atomizer of similar dimensions the water content was again over 1000 ppm initially, but fell to 40 ppm after only 10 min of flushing. Absorption measurements showed that this outgassed water can affect the stability of sputtering. It was found that after standing for 24 h in dry argon the Atomsource chamber required 4 h of flushing combined with occasional sputtering "burns" before stable, reproducible absorption readings were obtained.

The above results show the importance of excluding water vapor from the sputtering discharge and that particular care must be taken with the purity of the inlet argon supply to the atomizer. Although water vapor is expected to be the major contaminant in sputtering atomizers, it is of course important that the sputtering gas be free from other contaminants such as oxygen and carbon dioxide.

Reproducibility Studies. Studies of the long-term reproducibility of analyses have been made for the Atomsource and the glass sputtering chambers. Details of the method are given in the Experimental Section. Briefly, the procedure consisted of taking 10 consecutive readings on fresh surfaces of the same sample, flushing with argon for a period, taking a further set of readings, flushing again, and so on. The analysis used for these measurements was Cr in low-alloy steel. Before commencing, the system was flushed for 4 h and then sealed overnight at a positive pressure of argon. Next day the system was first flushed with dry argon for 30 min, after which time the reproducibility of measurements in the Atomsource was around 2% relative standard deviation (RSD). However, this value will be influenced by residual water vapor (see previous section) and should not be considered typical. Following a further 4 h of flushing, the reproducibility had improved to around 1% RSD, which is essentially the same as found for the earlier sputtering atomizer (*4*) for chromium in low-alloy steel. The reproducibility remained approximately constant at this level over a number of additional flushing periods lasting a total of 3 days. However, although the RSD for each set of readings remained constant over this period, the measured absorbance showed a small steady increase during each set of readings and also to some extent between sets, e.g. after 4 h of flushing, mean absorbance 0.097, RSD 1.1%; after 6 h of flushing, mean absorbance 0.100, RSD 0.9%; after 22 h of flushing, mean absorbance 0.103, RSD 0.8%, and so on. Similar measurements using the glass atomizer also showed a small increase of measured absorbance with time.

Investigations showed that the small increase of absorbance with time was related to the deposition of sputtered material around the arrester and accelerator. If the arrester/accelerator are brushed in situ between each reading with a small bottle brush, the drift in absorption does not occur, and it would appear that the effect may be caused by a reduction in the sputtered area (and hence an increase in the current density at the sample surface) or by small changes in the local pressure and flow conditions caused by changes in the geometry of the gas inlets. However, although the drift in the results can be eliminated by brushing, the act of brushing introduces gaseous impurities to the chamber, and the reproducibility is reduced to around 1.5–2% RSD. In order to remove these impurities and recover the original reproducibility, it is necessary to flush the system for a few minutes after each brushing. Thus to obtain high precision from the Atomsource or glass sputtering chambers, we find it is necessary to lightly brush the accelerator/arrester and then to flush with dry argon for a few minutes before taking a reading. By adoption of this procedure a constant absorbance could be maintained over several hours with a reproducibility of typically 0.8% RSD.

ACKNOWLEDGMENT

We are grateful to Varian-Techtron Pty. Ltd., Australia, for their cooperation and generous loan of the Atomsource sputtering unit. We also thank A. Walsh and P. L. Larkins for helpful discussions and A. E. Bernhard of Analyte Corp. for his comments on the manuscript.

Registry No. Water, 7732-18-5; argon, 7440-37-1.

LITERATURE CITED

(1) Russell, B. J.; Walsh, A. *Spectrochim. Acta* **1959**, *15*, 883–885.
(2) Gatehouse, B. M.; Walsh, A. *Spectrochim. Acta* **1960**, *16*, 602–604.
(3) Gough, D. S.; Hannaford, P.; Walsh, A. *Spectrochim. Acta* **1973**, *B28*, 197–210.
(4) Gough, D. S. *Anal. Chem.* **1976**, *48*, 1926–1931.
(5) Ohls, K. *Fresenius' Z. Anal. Chem.* **1987**, *327*, 111–118.
(6) Kim, H. J.; Piepmeier, E. H. *Anal. Chem.* **1988**, *60*, 2040–2046.
(7) Chakrabarti, C. L.; Headrick, K. L.; Bertels, P. C. *J. Anal. At. Spectrosc.* **1988**, *3*, 713–723.
(8) Winchester, M. R.; Marcus, R. K. *Appl. Spectrosc.* **1988**, *42*, 941–944.
(9) *Machine Design* **1982** (April), *54*, 108.

RECEIVED for review December 28, 1988. Accepted April 19, 1989.

Identification of Immobilized Bacteria by Aminopeptidase Profiling

K. D. Hughes and F. E. Lytle*

Department of Chemistry, Purdue University, West Lafayette, Indiana 47907

D. M. Huber*

Department of Botany and Plant Pathology, Purdue University, West Lafayette, Indiana 47907

Conventional aminopeptidase methods require cell concentrations of approximately 10^8 to 10^{10} cells/mL and an incubation period in the labeled substrates of 20 h. In order to obtain the large number of cells required to perform this assay, a 36–48-h growth period must precede the assay. An improved procedure is described that combines time-resolved fluorometry and a nondestructive whole cell immobilization procedure. This method has reduced cell concentrations 80 000-fold from that required for the standard assay, has reduced the room-temperature incubation period from 20 h to 3 min, and has shortened the total turnaround time for the assay from 2.5 days to approximately 3–7 h.

At present a major goal of "improved" microbial identification techniques is to reduce the time required for identification. The turnaround time can be broken into two specific elements. The first is the growth period required to isolate and obtain enough sample to analyze, and the second is the time required to process the sample, including measurement and data reduction steps. The objectives of this research have thus been 2-fold: first, to reduce the total number of cells required to perform the assay and then to reduce the required incubation time of the microbial cells in the labeled substrates. Decreasing the number of cells and the incubation time period will decrease the total turnaround time for pathogen identification, and aminopeptidase profiling thus will become a much more practical method for bacterial and fungal identification.

Identification methods that utilize inherent enzyme reactions in the organism can provide a "measurement advantage" due to the chemical amplification that is present with such systems. It is apparent then that bacterial identification schemes based on such measurements may have the most success in reducing the "total" analysis time. One such technique is aminopeptidase profiling, which has been employed since the early 1970's to elucidate the metabolic characteristics of bacterial pathogens (*1*). The method is based upon microbial metabolism of nonfluorescent L-amino acid β-naphthylamide substrates to produce the highly fluorescent tag, β-naphthylamine (βNA). Histograms that plot the normalized hydrolysis of these substrates provide a distinct aminopeptidase profile pattern that reveals various metabolic characteristics of that microbial species. This metabolic "fingerprint" can be utilized as a means for identification and differentiation of pathogen species (*2*).

Conventional aminopeptidase techniques utilize a filter fluorometer and as a result require cell concentrations of 10^8 to 10^{10} cells/mL and a 20-h incubation period to produce a significant βNA fluorescent signal. These high cell concentrations and lengthy incubation periods are due to the poor detection limit of the instrumentation and the large background emission associated with the assay. The lower limit of detection with the filter fluorometer is approximately 10^{-7} M βNA, and the assay has a blank equivalent to 3×10^{-6} M βNA (*3*) (Table I). The linear dynamic range of the assay is 1.5 orders of magnitude, and thus differentiation of closely related species is impossible even with the significant concentration of the bacterial cells employed. In order to improve the assay to current standards, many modifications had to be implemented with respect to the instrumentation and the chemical procedures. The instrumental modification consisted of replacing the filter fluorometer with a time-resolved laser fluorometer. Typically, increases in source intensity without a simultaneous decrease in the blank have little effect on detection limits. Because of this, a detailed examination into reducing the magnitude of the interference from each component of the blank was investigated. The results of this study have been published by Coburn et al. (*2*, *3*).

By application of laser-based instrumentation to the assay, the detection limit for βNA has been reduced to nanomolar concentrations and the linear dynamic range of the assay is increased to 3 orders of magnitude. This improvement in measured signal to noise ratio has allowed for a decrease in the incubation period from 20 to 4 h when the same concentration of sample is used. Even with this five-fold reduction in the incubation period, there is a significant contribution to the blank from the autohydrolysis of the labeled substrates (*2*, *3*). In addition, as a result of each substrate decomposing at a different rate and each microbial sample having a different inherent luminescence, a series of blank measurements are also required to calculate the amount of enzymatic hydrolysis. The ability to reduce cell concentrations for the assay hinges upon the extent of enzymatic hydrolysis observed for a particular cell concentration and the actual identification procedure. The standard aminopeptidase procedure consists of incubating a series of test tubes containing a suspension of cells and one of the amino acid substrates. The total number of cells required to produced an aminopeptidase profile is dependent on the concentration of cells and the number of substrates included in the profile. For example, in order to produce a 20-nutrient profile with one repetition, 40 5-mL tubes, each containing 5×10^7 cells, or a total of 2×10^9 bacterial cells would be required.

In an attempt to reduce the total number of cells required and eliminate many of the cumbersome procedural steps in the method, the possibility of immobilizing the sample was explored. There have been many applications in the literature in which whole cells have been immobilized to allow for repeated use. Immobilization is completed by either chemical or physical processes, which include confinement by hydrophobic gels and adsorption to polymers (*4*, *5*). Gel confinement techniques have diffusional limitations and thus are not suitable for a rapid aminopeptidase profiling technique. Physical adsorption to ion-exchange resins was attempted, and absorption of *Pseudomonas phaseolicola* cells was successfully completed. The anion-exchange resin, however, also absorbed the amino acid substrates and the fluorophore tag βNA. As a result, these investigations were terminated. Alternatively,

0003-2700/89/0361-1656$01.50/0

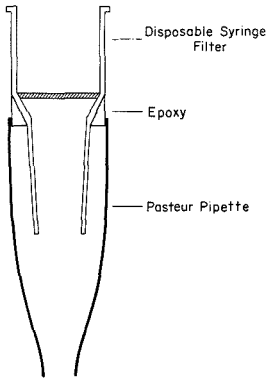

Figure 1. Miniature immobilization apparatus.

the use of micropore filters to remove bacteria from incubation solutions has appeared frequently in the literature as a simple and clean method of terminating enzymatic reactions and/or collecting fermentation products (*6*, *7*). The primary practical problem in pursuing this possibility was finding a membrane system convenient to use and one that adds little fluorescence to the blank through solvent-extractable contaminants. The system that evolved is a cell collection device housing a replaceable 25-mm membrane.

The method developed is nondestructive to the sample and has the ability to differentiate between viable and nonviable cultures. Sample preparation is extremely simple when compared to other techniques, as there is no complicated procedure for cell lysis, biomarker extraction, or derivatization. The current methodology also has the capability of easily being automated compared to the original profiling procedure. Along with these characteristics, the modified procedures have reduced cell concentrations for the standard assay over 800 000-fold and 800-fold from previously reported work (*2*), has reduced the room-temperature incubation period from 20 h to 3 min, and has shortened the total turnaround time for the assay from 2.5 days to approximately 3–7 h.

EXPERIMENTAL SECTION

Instrumentation. A detailed description of the time-resolved laser fluorometer has been published previously by Coburn et al. (*2*). The excitation source is a PAR Model 2100 nitrogen laser. The sample is excited from the bottom in order to reduce scattered radiation, and the fluorescent signal is collected at 90° and focused into a JY single monochromater. The detector is an RCA 931A photomultiplier tube, and temporal resolution is obtained with a PAR Model 162/165 boxcar integrator. The integrated signal is subsequently analog to digital (A/D) converted and stored in an IBM XT.

Immobilization Apparatus. A "large" immobilization apparatus was constructed from a cell collection device obtained from Ace Scientific (East Brunswick, NJ) and a Teflon insert obtained from a Millipore syringe filter holder. The sintered glass membrane filter support originally in the cell collection device was removed and replaced with the Teflon insert. This modification increased the flow rate of the filtration step and decreased the carryover between substrate incubations. Immobilization is achieved with a replaceable Durapore (HVLP) membrane filter with a pore diameter of 0.45 μm. This system required an incubation solution of approximately 1 mL and a wash solution, which was used to rinse the sample and dilute the incubation solution to measurement volume, of 4 mL.

A miniature immobilization apparatus was prepared by cementing a small disposable high-performance liquid chromatography (HPLC) nylon syringe filter (Micron Separations, Inc.) onto a cut Pasteur pipet (Figure 1). The cement used was Duco cement manufactured by Du Pont. The syringe filter had a 3-mm diameter and 0.45-μm pore size, and contained a membrane made of nylon. Each of these was used for one bacterial sample and then discarded. The incubation solution has been reduced to 100 μL while the wash and dilution volume has been reduced to 700 μL.

Table I. Blank Contributions in Equivalent Concentrations of βNA

blank contribn	conventional[a] assay	time-resolved only	immobilized and time-resolved
buffer	1.1×10^{-7} M	2.4×10^{-10} M	2.4×10^{-10} M
autohydrolysis[b]	2.5×10^{-8}	5×10^{-9}	5×10^{-9}
cell emission	3.0×10^{-6}	3×10^{-8}	
membrane apparatus			5×10^{-10}
total	3×10^{-6}	3.5×10^{-8}	5×10^{-9}

[a] Data taken from ref 3. [b] Conventional and time-resolved substrate concentration is 1×10^{-5} M. Immobilized substrate concentration is 1×10^{-4} M.

Physical Immobilization. Quaternary ammonium exchange resin was incubated in 1 M NaOH for 24 h and then rinsed to pH 7 with distilled water. Physical adsorption of *Pseudomonas phaseolicola* cells was completed by incubating, at room temperature, 1 g of the prepared resin and a 30% transmission (540 nm) suspension of the bacterial cells. Approximately 10^9 cells were adsorbed at the end of 90 min. This value corresponds well with published literature (*4*).

Chemicals. Water was purified by distillation and stored in glass. The buffer consisted of 0.005 M Tham standard grade obtained from Fisher and 0.005 M NaCl analytical reagent grade obtained from Mallinckrodt. The buffer was acidified to pH 8 with concentrated HCl and stored in glass. The anion-exchange resin, Amberlite IRA-400, was obtained from Mallinckrodt. The amino acid β-naphthylamide substrates were obtained from Sigma and stored as solids below 0 °C. The β-naphthylamides used were L-alanyl (ALA), L-arginyl (ARG), L-cystinyl-di- (CYS), L-glycyl (GLY), L-histidyl (HIS), L-hydroxyprolyl (HPRO), L-leucyl (LEU), and L-lysyl (LYS). Stock solutions were prepared with Burdick and Jackson methanol at a concentration of 0.001 M. These solutions were stored at 4 °C and were stable for months. Working solutions were prepared just prior to use at a 1:10 dilution.

Biological Samples. Unless otherwise stated, cells were removed from 15 h old nutrient agar cultures and diluted in buffer. Microliters of this cell suspension were subsequently applied to the membrane immediately before analysis. All cells were trapped, but the fraction of viable cells in the original sample was not determined.

RESULTS AND DISCUSSION

The assay blank consists of Raman and Rayleigh scatter, emission from the buffer, a contamination of free βNA produced form the autohydrolysis of the substrates, and an intrinsic luminescence due to the biological matrix. Table I outlines the improvements afforded by the new measurement protocol. A change in buffer from Tris to Tham (same molecule, different name and purity) resulted in the fluorescence impurities being reduced 2 orders of magnitude. Preparing substrate stock solutions in methanol instead of water reduced the autohydrolysis by an order of magnitude (*3*). The introduction of temporal resolution reduced the interferences from scatter and the biological matrix, and this, combined with the above-mentioned fluorescent impurity reductions, allowed for a net decrease in the conventional aminopeptidase assay blank of 2 orders of magnitude.

The methodology utilizing these procedural modifications was used to differentiate between races of *P. megasperma sojae* (*3*). Further improvement in the linear dynamic range of the measurement is theoretically available by reducing the cell concentration. This was attempted for cultures of *Pseudomonas phaseolicola* and *Xanthomonas phaseoli* at

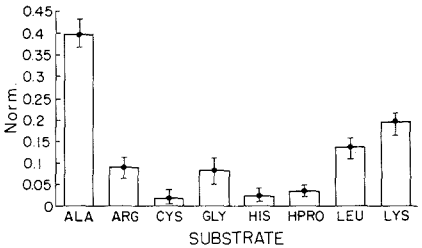

Figure 2. Average profile of *Pseudomonas phaseolicola* obtained with repeated use of 5×10^6 cells and a 3-min incubation. Forty separate incubations were produced over an 8-h period.

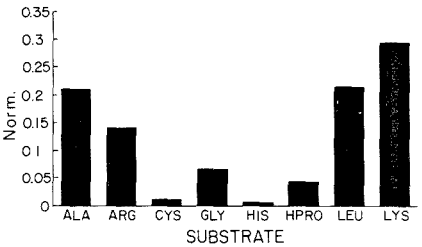

Figure 3. Aminopeptidase profile of *Pseudomonas phaseolicola* obtained with a filter fluorometer. A concentration of 10^8 cells/mL and a 20-h incubation period were utilized.

50 000 cells/mL by using sophisticated pattern recognition techniques (*8*). The difficulty was due to the rate of autohydrolysis nearly equaling the rate of enzymatic hydrolysis. Thus the full dynamic range was not attainable at the anticipated signal to noise ratio. In order to have the lowest blank possible as well as an insignificant rate of autohydrolysis, a whole cell immobilization scheme was investigated.

Immobilization Procedure. Many of the time-consuming and cumbersome procedural steps of the conventional assay have been eliminated with the incorporation of cell immobilization, resulting in a very simple and straightforward method. The procedure now consists of the following steps: A small aliquot of a cell suspension is added to the membrane, and the buffer solution is subsequently removed by suction. The fluorophore-labeled substrate solution is applied to the membrane, and the incubation is allowed to proceed. After incubation the solution is removed and analyzed for the fluorescent tag while the sample of cells is still retained on top of the membrane. The trapped cells are washed with buffer, and then the next substrate solution is applied and incubation is started again. By conversion of the standard homogeneous aminopeptidase assay into a heterogeneous type the magnitude of the blank decreases, as it is no longer dominated by the biological matrix, which varies with cell concentration and microbial species. In fact, the background associated with the measurement is reduced an additional order of magnitude (Table I). This is a net reduction of 3 orders of magnitude from that of the original filter fluorometer method. It is worth noting that the biological matrix suppresses the signal expected for a given level of βNA; thus the measurement is aided twice by removing the cell matrix. Indeed, the signal to noise ratio is increased enough to allow the incubation period to be reduced from 4 h to 3 min. The autohydrolysis of the substrates is controlled by an equilibrium process that can be related to the initial substrate concentration and the final dilution volume. The magnitude of the autohydrolysis term was not affected by the increase in substrate concentration. This was unexpected but obviously advantageous.

This immobilization procedure was used to obtain replicate aminopeptidase profiles of the plant pathogen *Pseudomonas phaseolicola* (Figure 2). This histogram is the average of five complete eight-substrate aminopeptidase profiles. Each separate profile was produced by sequentially adding 1×10^{-4} M substrate solutions to the same 5×10^6 cells trapped on the membrane and incubating for 3 min. The same cells therefore underwent 40 separate, 3-min incubations, which spanned an 8-h period. This reuse of sample permits a further reduction in the number of cells required for the assay by a factor equivalent to the number of substrates used to create the profile by the conventional method. The order of substrate incubations has not been observed to affect the profile obtained, but this should not be assumed for all microbial species, as a number of aminopeptidase enzymes have the capability of hydrolyzing different amino acids. The stimulation of certain aminopeptidase enzymes early on in the profile could in theory alter substrates appearing later in the profile. The identity of the substrates and the order in which they were used in this investigation were chosen at random.

The precision of the technique is illustrated with error bars in Figure 2, and since pattern recognition algorithms are used to match profiles, a pooled standard deviation for the substrates is calculated. The pooled standard deviation for the replicate profiles shown in Figure 2 is 2.4%. The reproducibility of the technique was examined further by comparing profiles produced on the same day from the same cells and profiles produced on different days with different cells. The mean character difference (*9*), which is similar to a Euclidean distance, was 1% for the same-day profiles. The mean character difference for profiles produced on different days is approximately 3%.

Reproducibility of filter fluorometer profiles is slightly less, as the standard deviation per substrate is approximately 4%. An aminopeptidase profile for *Pseudomonas phaseolicola*, obtained with a filter fluorometer, is presented in Figure 3 for comparison. This profile is produced with cell concentrations of 10^8 cells/mL and a 20-h incubation period. This profile compares well with that shown in Figure 2 when kinetic variations due to cell concentration and incubation time are taken into account. The aminopeptidase technique is self-leveling, and thus substrates showing weak activity initially, such as leucine and lysine, tend to overtake other substrates when the incubation period is increased. This effect can be observed when the magnitude of hydrolysis for these two substrates is compared after 3 min and 20 h. There is greater lysine and leucine activity after 20 h, but the ratio between the two substrates remains the same for both incubation periods. It should also be noted that two of the major limitations to obtaining reproducible profiles with the standard technique are the variations in cell concentrations between each substrate incubation and percentage of viable cells present during the incubation. By utilization of the same sample of cells for each substrate incubation, much of the variation observed in the substrate hydrolysis within a profile and with replicate profiles can be eliminated.

Nondestructive analysis of a sample can also be of great benefit when one is investigating long-term sample behavior. It is well-known that the composition of the growth media used to culture the bacterial populations affects both the identity and quantity of different cellular components. The adaptive behavior of *Pseudomonas phaseolicola* cells retained on the immobilization membrane was investigated (Figure 4). Each profile was produced with the same 5×10^6 cells and a 3-min incubation. The introduction of a different culture medium (Pseudomonas Agar-F (PAG)) from that utilized in Figure 2 produces an aminopeptidase profile that lacks hydroxyproline activity (see Figure 4A). The incubation of these same cells 1 h later reveals that the cells have adapted to the substrates

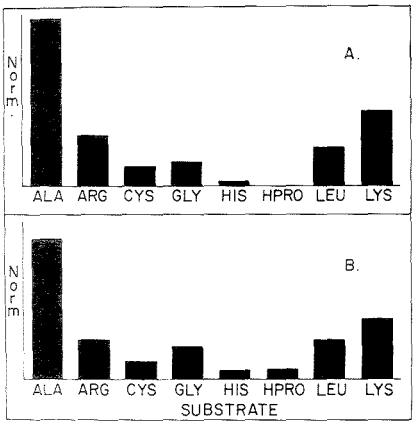

Figure 4. Aminopeptidase profiles of *Pseudomonas phaseolicola* showing adaptive behavior to the substrates used in the analysis: (A) initial and (B) 1 h later.

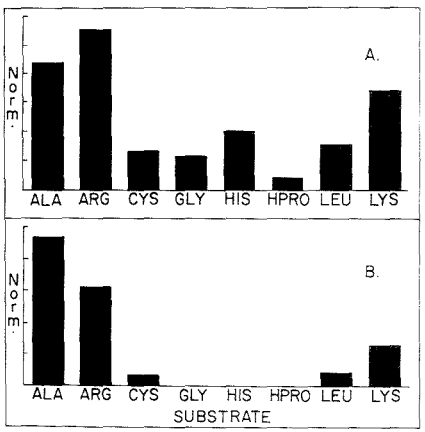

Figure 5. Aminopeptidase profiles obtained from 5×10^5 cells and a 3-min incubation: (A) *Pseudomonas phaseolicola* and (B) *Pseudomonas aureofaciens*.

that were introduced in the first profile run. The hydroxyproline activity has increased, as seen in Figure 4B. The question of which profile is correct (Figure 4A or 4B) is of critical importance since pattern recognition algorithms are utilized for identification. At present, all identification techniques that rely on "fingerprints" of microbial organisms must obey strict guidelines with respect to culture media composition. The correct profile will correspond directly to the identity of the "standard" growth media. This observation is under further investigation as it may produce a method of eliminating the restrictions on growth media just discussed. A number of different growth media are being investigated to examine the aminopeptidase activity that results after an initial incubation with all the substrates. The ramifications of this investigation could be of major importance to microbial identification methods.

Immobilization Apparatus Miniaturization. The drive to increase sensitivity and produce an assay capable of automation requires not only a further reduction in cell numbers but a reduction in reagent and measurement volumes. The immobilization system used in the investigations that produced Figures 2 and 4 utilized a 25-mm replaceable membrane. This system required an incubation solution of approximately 1 mL and a wash solution, which was used to rinse the sample and dilute the incubation solution to measurement volume, of 4 mL. In order to reduce the solution volumes, a miniature immobilization system was created. This immobilization system employs a 3-mm membrane with a 0.45-μm pore size (Figure 1). The incubation solution can now be reduced to 100 μL while the wash and dilution volume has been reduced to 700 μL. This system was used to differentiate clearly both qualitatively and quantitatively between samples of *Pseudomonas phaseolicola* and *Pseudomonas aureofaciens*, two related species (Figure 5). Each profile was produced with 5×10^5 cells and a 3-min incubation period. It should be noted that the profile obtained from the *Pseudomonas phaseolicola* sample deviates with respect to the weaker hydrolyzed substrates from the profiles shown in Figure 2. This deviation is due to the decrease in cell concentration from that used in Figure 2. This situation can be corrected by increasing the number of viable cells immobilized or by increasing the incubation time period. The need for the presence of these substrates showing weaker activity must be appraised with respect to the ability of pattern recognition algorithms to identify the organism and the turnaround time for the identificaiton. If identification can be completed without the presence of the weaker activity substrates, then further reductions in cell concentrations can be achieved. These considerations are being investigated further.

Table II. Comparison of Methods for an Eight-Nutrient Profile

parameter	conventional assay	time-resolved only[a]	immobilized and time-resolved
cell growth	36–48 h	2–6 h	2–6 h
no. cells req	4×10^9	50×10^6	500×10^3
tot incubn time	20 h	4 h	24 min
no. of measmts	16	16	8
total time	2.5 days	6–10 h	3–7 h

[a] Data taken from ref 2.

Present and Predicted Performance. The conventional technique and the technique described in this paper are compared in Table II. The growth period that precedes the assay has been reduced from 36–48 to 2–6 as a direct result of the total number of cells required to perform the assay being reduced from 4×10^9 to 5×10^5. The autohydrolysis values represent the contribution to the blank that occurs during the full incubation period cited. The incubation time of each substrate has been reduced from 20 h to 3 min due to the large increase in signal to noise ratio facilitated by utilizing an immobilized cell technique. For an eight-nutrient profile, the total incubation time is 24 min since each substrate is sequentially instead of the conventional simultaneous incubation of each substrate. It is obvious, though, that all eight substrates are not needed to differentiate between these two species; thus, the analysis time could be reduced accordingly. One other important outcome of the immobilization procedure is that the number of sample measurements required to perform the assay has been reduced by a factor of 2. This is a consequence of the assay having a constant blank reading for each substrate that does not change with bacteria type or concentration. The end result of these instrumental and methodological improvements can be seen by the decrease in total turnaround time for identification from 2.5 days to approximately 3–7 h.

Research is under way to increase the sensitivity of the technique and lower the cell numbers still further. The av-

enues being explored consist of decreasing reagent and dilution volumes and improving the instrumental sensitivity and selectivity by incorporating improved optics and a nanosecond transient recorder. Analysis is also under way that will unveil the experimental trades present between the cell concentration, the substrate concentration, and the incubation time period. Optimization of the procedure will undoubtedly allow for a decrease in cell concentrations with a minimal increase in incubation time. The end goal of these improvements is total elimination of the cell growth period.

Registry No. Ala-β-naphthylamide, 720-82-1; Arg-β-naphthylamide, 7182-70-9; di-Cys-β-naphthylamide, 1259-69-4; Gly-β-naphthylamide, 716-94-9; His-β-naphthylamide, 7424-15-9; Hpro-β-naphthylamide, 3326-64-5; Leu-β-naphthylamide, 732-85-4; Lys-β-naphthylamide, 4420-88-6; aminopeptidase, 9031-94-1.

LITERATURE CITED

(1) Huber, D. M.; Mulanax, M. W. *Phytopathology* **1969**, *59*, 1032.
(2) Coburn, J. T.; Lytle, F. E.; Huber, D. M. *Anal. Chem.* **1985**, *57*, 1669.
(3) Coburn, J. T.; Lytle, F. E.; Huber, D. M. *Anal. Biochem.* **1986**, *154*, 305.
(4) Vieth, W. R.; Venkatsubramanian, V. In *Immobilized Microbial Cells*; Venkatsubramanian, V., Ed.; ACS Symposium Series 106; American Chemical Society: Washington, DC, 1979; Chapter 1.
(5) Rossomando, E. F. *High Performance Liquid Chromatography in Enzymatic Analysis*; John Wiley & Sons: New York, 1987.
(6) Pau, C.; Patonay, G.; Moss, C. W.; Hollis, D.; Carlone, G. M.; Plikaytis, B. D.; Warner, I. M. *Clin. Chem.* **1987**, *33*, 337.
(7) Gabler, R.; Ryan, M. In *Purification of Fermentation Products*; LeRoith, D., Ed.; ACS Symposium Series 271; American Chemical Society: Washington, DC, 1985; Chapter 1.
(8) Coburn, J. T.; Forbes, R. A.; Freiser, B. S.; Becter, L.; Lytle, F. E.; Huber, D. M. *Anal. Chim. Acta* **1986**, *184*, 65–76.
(9) Jurs, P. C.; Isenhour, T. L. *Chemical Applications of Pattern Recognition*; Wiley: New York, 1975.

RECEIVED for review February 15, 1989. Accepted May 3, 1989. This research has been supported by the National Science Foundation Grant CHE-8320158 and the Showalter Foundation. K.D.H. is also grateful to the Purdue Research Foundation for a David Ross Fellowship.

Water as a Unique Medium for Thermal Lens Measurements

Mladen Franko[1] and Chieu D. Tran*

Department of Chemistry, Marquette University, Milwaukee, Wisconsin 53233

The temperature effect on thermal lens measurements in water has been investigated. The magnitude and sign of the thermal lens signal intensity were found to be strongly dependent on the temperature of the aqueous solution. Depending on whether the measurements are performed at temperatures lower or higher than −0.01 °C, the photoinduced thermal lens can have either a positive (converging) or negative (diverging) focal length. At precisely −0.01 ± 0.04 °C, no thermal lens signal could be observed. This is because the dn/dT values of water are positive at $T < -0.01$ °C, negative at $T > -0.01$ °C, and equal to zero (i.e., maximum refractive index) at $T = -0.01$ °C. This unique characteristic was exploited to enhance the sensitivity of thermal lens measurements in water. For instance, the thermal lens signal of an aqueous solution was enhanced up to 2.4 times when the temperature of the solution was increased from +20.0 to +90.0 °C. For thermally unstable compounds, the sensitivity enhancement was achieved by synergistic use of the bimodal characteristic of the thermal lens technique and the temperature effect on the thermooptical properties of water. Typically, two sample cells, one at −7.9 °C and the other at +12.0 °C, were placed on both sides and symmetrically about the beam waist. The sensitivity of this two-cell system was 1.80 or (1 + T) times that of the single cell (T is the transmittance of the first cell).

Thermal lens techniques have been demonstrated to be a sensitive method for low-absorbance measurements (*1–12*). Absorptivities as low as 10^{-7} have been measured by using these techniques. The technique is based on the nonuniform temperature rise that is produced in an illuminated sample by nonradiative relaxation of the energy absorbed from a TEM_{00} laser beam (*1–12*). For weak absorbing species, the thermal lens signal, which is measured as the relative change in the laser beam center intensity in the far field, $\Delta I_{bc}/I_{bc}$, is related to the excitation laser power P and sample absorbance A by

$$\frac{\Delta I_{bc}}{I_{bc}} = \frac{1.21P(dn/dT)A}{\lambda k} \quad (1)$$

where λ is the wavelength, and dn/dT and k are the temperature coefficient of the refractive index and thermal conductivity of the solvent, respectively (*1, 2*). It is thus clear that in addition to the sample absorbance and excitation laser power, the thermal lens signal intensity is directly proportional to dn/dT and inversely proportional to the k value of the solvent. Generally, nonpolar solvents provide good media for thermal lens measurements owing to their high dn/dT and low k values (*1, 2, 10, 12*). Conversely, water, which is the most powerful and widely used solvent in spectrochemical analysis, specifically for metal ions and biological compounds, is considered to be the worst medium for thermooptical techniques because it has very low dn/dT and high k values (*1, 2, 10, 12*). This is very unfortunate because it severely limits the scope of these techniques. As a consequence, considerable efforts have been made in the last few years to ameliorate the thermal physical properties of water. Most notable methods include the use of micelles or reversed micelles to enhance the sensitivity of thermal lens measurements in water (*10, 12*). Unfortunately, in spite of the success, these methods involve the addition of surfactants into the aqueous solution, which sometimes may produce some unwanted effects (*13–15*). It is thus particularly important that a new method which can improve the thermal physical properties of water without the use of any additive be developed.

The extensive hydrogen-bonding network and multiple structural characteristics enable water to be unique among solvents. For instance, its density increases as temperature

* To whom correspondence should be addressed.
[1] Permanent address: Nuclear Chemistry Section, J. Stefan Institute, Ljubljana, Yugoslavia.

0003-2700/89/0361-1660$01.50/0

is lowered and reaches a maximum value at about 4 °C (*16, 17*). Based on the relationship between density and refractive index, it is expected that water possesses negative dn/dT values at room temperature and positive values at subzero temperatures. There will be a certain temperature at which $dn/dT = 0$ (or the refractive index is maximum). As a consequence, it is fully expected that the sensitivity of thermal lens measurements depends on the temperature of the aqueous solution. A change in the solution temperature not only can enhance the signal intensity but also can eliminate it completely. Therefore, it is of extreme importance that a relationship between the temperature of aqueous solution and the thermal lens signal intensity be carefully studied. Knowledge gained from this study not only guides the selection of an appropriate measurement temperature at which maximum sensitivity can be achieved but also provides fundamentals for the development of a sensitivity enhancement method utilizing the bimodal characteristic of the thermal lens technique.

Such considerations prompted this study, which aims to investigate the effect of temperature on the thermal lens signal intensity of aqueous solution. It will be demonstrated for the first time in the communication that either a positive (converging) or a negative (diverging) photoinduced thermal lens can be formed in water by simply varying the temperature of the aqueous solution. Based on the relationship between the thermal lens signal intensity and temperature, a novel method will be developed that aims to enhance the sensitivity of the technique.

EXPERIMENTAL SECTION

The effect of temperature on the thermal lens signals was investigated by using the dual-wavelength pump/probe configuration thermal lens spectrometer that was developed recently in our laboratory (*11*). Unless otherwise stated, the sample was excited by either a 514.5- or 457.9-nm excitation beam (20 mW; 1-Hz modulation), and the photoinduced thermal lens was measured by a He–Ne probe laser (632.8 nm). Sample solution was placed in a standard 1-cm^2 quartz cell whose temperature was controlled by means of a water jacket cell holder. A Neslab thermostated bath (Model RTE-19 with temperature stability of ±0.01 °C) was used to circulate the ethylene glycol–water mixture through the cell holder to control the cell temperature. A thermistor (Fenwall Electronics UUA-33J1) was connected to the cell holder to monitor the cell temperature. The resistances of the thermistor were related to the temperatures of the sample solution at the laser beams by a calibration curve that was constructed by inserting a precision standard thermometer equipped with 0.01 °C divisions into the sample cell and recording its temperatures and the corresponding resistances of the thermistor over a temperature range of −8 to 80 °C.

A single-laser, single-beam thermal lens apparatus was used to study the dependency of the thermal lens signal on the position of the cell relative to the beam waist and to develop a two-cell system to enhance the sensitivity. As shown in Figure 1, the laser used in this apparatus was a 35-mW He–Ne laser (Spectra-Physics Model 127) whose output was focused by a 10 cm focal length lens (for the single-cell experiment) or a 30 cm focal length lens (for the two-cell experiment) and modulated by an electronic Uniblitz shutter (Vincent Associates Model 214). A water jacket cell holder placed on a translation stage provided the variation in the distance between the sample cell and the laser beam waist. The laser intensity was detected by a pin photodiode (PD) placed behind a pinhole (Ph) and 3 m from the sample. The output of the photodiode was amplified and fed into a digital memory oscilloscope (Heath Model 4850). The output of the scope was connected to an AT&T personal computer (Model PC 6300) to accumulate and average the signals. Typically, the thermal lens was recorded as the time-dependent change in the far field beam center intensity after the onset of laser illumination.

$$I_{bc}(t) = I_{bc}(0)\left[1 + \left(\frac{\theta}{1 + t_c/t}\right) + \tfrac{1}{2}\left(\frac{\theta}{1 + t_c/t}\right)^2\right]^{-1} \quad (2)$$

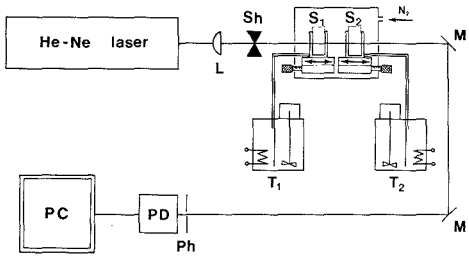

Figure 1. Schematic diagram of the single-laser, single-beam thermal lens spectrometer: L, lens; Sh, electronic shutter; S_1, sample cell 1 at −7.9 °C; S_2, sample cell 2 at +12.0 °C; M, mirror; Ph, pinhole; PD, pin photodiode; PC, personal computer.

where t_c, the time constant, depends on the spot size, ω, of the beam in the sample, the density, ρ, specific heat capacity, C_p, and thermal conductivity, k, of the solvent and is given by

$$t_c = (\omega^2 \rho C_p)/4k \quad (3)$$

The strength of the thermal lens, θ, was calculated from [intercept]$^{-1}$ of the plots of $I_{bc}(t)/I_{bc}(0) - I_{bc}(t)$ vs $1/t$.

Alignment for the two-cell system was performed by initially placing cell 1, which contained sample (5.0×10^{-7} M nickel phthalocyanine), before the beam waist and cell 2, which contained water, after the beam waist. The two cells were kept at room temperature, and the position of cell 1 relative to the beam waist was adjusted so as to provide maximum thermal lens signal. Subsequently, the sample (cell 1) and blank (cell 2) were interchanged, and the position of cell 2 relative to the beam waist was adjusted to provide maximum thermal lens signal. The system was now aligned, and measurements were then performed by filling both cells with the 5.0×10^{-7} M nickel phthalocyanine aqueous solution and cooling cell 1 to −7.9 °C and cell 2 to +12 °C. In order to eliminate condensation problems associated with low-temperature measurements, a majority of the thermal lens apparatus including the cell holders was placed inside a drybox containing nitrogen gas.

RESULTS AND DISCUSSION

Thermal lens signals of 1.0×10^{-6} M ferroin aqueous solution at different temperatures, which were measured with a pump/probe thermal lens apparatus, are shown in Figure 2. The signals, as explained earlier, were recorded as the probe laser beam center intensity. The signal for the sample at +20.00 °C is shown in Figure 2a. In this case, the intensity of the probe beam decreased gradually when the 514.5-nm excitation beam was allowed to excite the sample. This was because the refractive index gradient that was produced by the heat generated from the sample absorption of the pump beam acted as a thermal lens to modify the beam center intensity of the probe beam. The thermal lens formed in this case was a diverging lens because it defocused the probe beam and, hence, decreased the beam center intensity. It is of particular interest to observe the dependency of the sign and the strength of the thermal lens on the temperature of the aqueous solution. As shown in Figure 2a–f, five different thermal lens signals were obtained from the same sample solution, which was excited with the same laser intensity and modulated at the same frequency. The only difference between these signals is the solution temperature. Lowering the temperature from 20.00 to 7.58 °C resulted in a 2.19-fold decrease in the thermal lens signal intensity (2b). At +3.26 °C, the signal intensity is only about $^1/_{20}$ of that at 20.00 °C (2c). It is fascinating to see the complete lack of thermal lens effect at +0.02 °C: At this temperature, the heat generated by the sample absorption of the pump beam had no observable effect on the intensity of the probe beam (Figure 2d). It is important to add that the water was still in the liquid phase

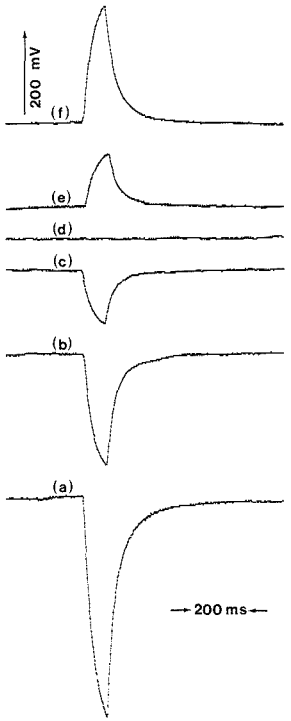

Figure 2. Thermal lens signal of aqueous solution at different temperatures: (a) +20.00, (b) +7.58, (c) +3.26, (d) +0.02, (e) −2.80, and (f) −5.87 °C.

at this temperature. In fact, in this study using the 1-cm^2 quartz cell, the aqueous solution remained in the supercooled liquid state at temperatures as low as −8 °C. This is hardly surprising, considering the small volume of the sample cell (*16*, *17*). The state of the sample can be accurately evaluated by using thermal lens signal because under the present experimental conditions, which include the use of a 60 mm focal length lens to focus the excitation beam and a 10 mm path length cell, no thermal lens effect is expected to be observed for a solid 10 mm thick inside a cell. Photothermal signal which is presumably generated from such effect as thermal lens and photothermal deformation may be observed for a thin slide of solid without the cell (*18*, *19*). In addition, based on the thermooptical properties of ice ($dn/dT = -3.8 \times 10^{-5}$ K^{-1} and k = 22 mW cm^{-1} K^{-1}) (*20*), it is expected that instead of a positive signal as in the case of supercooled water, a negative signal of about −23 mV (for 514.5-nm excitation) would have been obtained for a 5-mm slice of ice (without the cell).

The magnitudes of the thermal lens signals in supercooled water at −2.80 and −5.87 °C are the same, within experimental error, as those at +3.26 and +7.58 °C, respectively (Figure 2e,f and Figure 2c,b). The sign of the thermal lens signals in supercooled water is, however, opposite to those in the normal liquid water. The beam center intensity of the probe beam was increased by the induced thermal lens in supercooled water. Apparently, the heat produced as a consequence of the sample absorption formed a converging lens. The positive focal length thermal lens focused the probe beam and led to an increase in the beam center intensity. Because the thermal conductivity of water is always a positive number, the results obtained seem to suggest that the divergent thermal lens

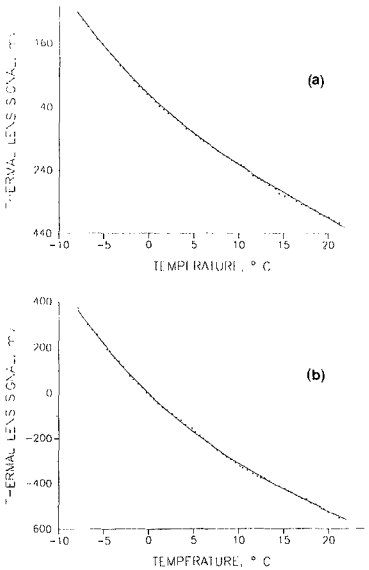

Figure 3. Plot of thermal lens signal of aqueous solution excited at 457.9 (a) and 514.5 nm (b) against temperature. Points are experimental values, and the solid line is the best fit.

formed at $T > 0$ °C is due to the negative dn/dT values while the positive dn/dT values at $T < 0$ °C led to the convergent thermal lens. The transition temperature at which $dn/dT = 0$ is about 0.02 °C. It is thus clear that the thermal lens signal intensity is strongly affected by the temperature of the aqueous solution. This dependency is expected to provide excellent means for the determination of thermal physical properties of water as well as for the enhancement in the sensitivity of the thermal lens technique. In this study three principal applications based on this dependency were investigated. They include (a) the precise and accurate determination of the temperature at which the refractive index of water is maximum, (b) the derivation of a general equation to enable the calculation of the relative thermal lens signal intensity at any given temperature, and (c) the development of a novel method to enhance the sensitivity of the thermal lens technique.

Precise knowledge of the temperature at which the refractive index of water is maximum is of scientific as well as technological importance because it would help not only to derive a more appropriate theoretical model to explain the multiple structures of water but also to improve the performance of dye lasers. The thermal lens technique is particularly suited for the determination of this temperature because the signal intensity is directly proportional to the dn/dT value of the solvent (eq 1). Thermal lens measurements were, therefore, performed on the same 1.0×10^{-6} M ferroin aqueous solution from −8 to +22 °C at 0.5 °C increments in order to determine accurately the temperature at which $dn/dT = 0$ or the refractive index is maximum. The thermal lens signal intensities, which were obtained with the 457.9-nm excitation wavelength, are plotted in Figure 3a as data points against the temperatures of the aqueous solution. It is reasonable to express the thermal lens signal intensity in a polynominal formula of the third order because the signal is known to be dependent on the dn/dT and k values of the solvent (eq 1) and these two thermooptical values have been experimentally found to follow polynomial formulas (*21*, *22*).

$$S = a_0 + a_1 t + a_2 t^2 + a_3 t^3 \quad (4)$$

where S is the change in the probe beam intensity in millivolts and t is the solution temperature in degrees Celsius. A least-squares method was used to perform iterations to obtain the best fit. The a_0, a_1, a_2 and a_3 coefficients for the best fit, which is illustrated as a solid line in Figure 3, were found to be −0.1854, −27.1800, 0.6106, and -1.1330×10^{-2}, respectively. From these coefficients, the temperature at which the thermal lens signal intensity equals zero (and thus $dn/dT = 0$) is calculated to be −0.01 ± 0.04 °C. The accuracy of the technique was further investigated by measuring and calculating the temperature at which the thermal lens signal produced by the 514.5-nm excitation wavelength equals zero. The results are shown as data points in Figure 3b. From curve fitting, the temperature was found to be −0.01 ± 0.04 °C, which is the same as the value obtained for the 457.9-nm excitation wavelength. This is hardly surprising, considering the fact that the thermal lens signals produced by either 457.9- or 514.5-nm excitation were monitored by the same He–Ne probe laser. Therefore the zero thermal lens signal in both cases corresponds to the temperature at which the dn/dT at the probe laser wavelength, i.e., 632.8 nm, equals zero. In fact, this observation lends credence to the accuracy of the technique.

It is interesting to note that the refractive index goes through the maximum value at −0.01 °C whereas the density is maximum at 4 °C (*16*, *17*). As described earlier in the Experimental Section, the reported temperature is the value measured inside the sample cell and at the laser beams so that this difference is not due to any experimental inaccuracy or error but rather due to the unique properties of water. It can be explained on the basis of the Lorentz–Lorentz equation (*23*)

$$\frac{n^2 - 1}{n^2 + 2} = \rho P_{LL} \quad (5)$$

where n is the refractive index, ρ is the density, and P_{LL} is the specific refraction. For most liquids, P_{LL} is generally assumed to be constant and independent of pressure and temperature. However, this assumption is not valid for water and D_2O, as it was theoretically (*23*) and experimentally (*24*) proven that P_{LL} does vary slightly with both of these variables. Differentiating eq 5 under this condition, at constant pressure, gives

$$\frac{6n}{(n^2 + 2)^2} \frac{\partial n}{\partial T} = \frac{\partial P_{LL}}{\partial T} \rho + \frac{\partial \rho}{\partial T} P_{LL} \quad (6)$$

It is thus clear that for water and D_2O, the refractive index and density do not go through maxima at the same temperature. Furthermore, because P_{LL} and ρ are positive and $\partial P_{LL}/\partial T$ is negative (*25*), $\partial n/\partial T$ is expected to go through zero at the temperature where $\partial \rho/\partial T$ is positive, i.e., at the temperature lower than 4 °C. This prediction is in very good agreement with the observation of the present work that the refractive index of water undergoes a maximum at −0.01 °C whereas its maximum density is at 4 °C. A variety of explanations has been proposed to explain the variation of P_{LL} with temperature and pressure. They include the change with temperature of either the concentration of "icelike" structures or the average polarizability of water molecules (*23*, *25*).

The temperature value determined in this study is not only more accurate but also more precise than other values reported previously (*23–32*). This is due to the ultrasensitivity and unique characteristics of the thermal lens technique. In fact, the results obtained from the large number of previous studies are scattered and sometimes controversial (*23–32*). For instance, with the sodium D line (589 nm) used as the measurement wavelength, the temperature has been reported to be as low as −3.3 °C and as high as +0.19 °C (*23–30*). For the 632.8-nm wavelength, values of +1.4 and +2.0 °C have been reported (*31*, *32*). The discrepancy may be due to the fact that these studies are based on the measurements of refractive index at different temperatures and the determination of the temperature at which the refractive index is maximum (*26–31*). In addition to the relatively low sensitivity of the techniques used, i.e., refractometers, there are large uncertainties associated with the determined temperature. The latter deduction is based on the fact that the change in the refractive index with temperature decreases as it approaches the maximum value. This can be seen by the relatively smaller thermal lens signals at the temperatures close to −0.01 °C. As a consequence, a refractometer that is capable of detecting a 1×10^{-6} difference in the refractive index would produce uncertainties as high as ±0.5 °C in the determined temperature (*27*). Furthermore, the refractive indices determined in these studies are relative to those of air, i.e., relative refractive indices. Therefore, any fluctuation in the air temperature or density will produce uncertainty in the n values and thus the determined temperature. In fact, it has been estimated that a 0.77 °C fluctuation in air temperature will produce a 1×10^{-6} change in the refractive index, which corresponds to a ±0.5 °C error in the determined temperature. Conversely, in the thermal lens method the air temperature had no effect on the determined value. This is because the technique is based on the measurement of the strength of the photoinduced thermal lens in the sample. Nonuniform heating by nonradiative relaxation of the sample subsequent to its absorption of the excitation beam produced the thermal lens. The position of the lens was the place where the excitation beam was focused. In this case, it was the center of the sample cell. Therefore, the thermal lens measurement is immune to any changes in the environment outside the sample cell. As a consequence, the temperature determined by this method corresponds to the value at which the absolute refractive index of water is maximum.

The temperature determined by the thermal lens technique is more precise than other values because, different from other techniques used in previous studies, the signal obtained by the thermal lens technique is directly proportional to the dn/dT value of water. Lack of thermal lens signal is a clear indication of the case where $dn/dT = 0$ or when the refractive index of water is maximum. Because it is easier to determine the zero signal than the maximum signal from a group of signals having very close intensities, the temperature determined by the thermal lens method is inherently more precise than those obtained by other methods. In fact, based on the ±1.6 mV standard deviations of the blank signal, the uncertainty associated with the temperature at which $dn/dT = 0$ is estimated to be ±0.04 °C. This error is about 12 times smaller than those for the other methods.

It is evident from Figure 3 that the sensitivity of the thermal lens technique depends on the temperature of the aqueous solution. Higher signal intensity is to be expected for solution at higher temperature. This possibility was investigated by measuring the thermal lens signal intensity of the same sample solution from −8 to 80 °C. The results obtained are plotted as data points against the solution temperature (Figure 4). For comparison, these signal intensity values were plotted as the relative intensity to that at +20.0 °C, RI, which is defined as

$$RI = S_t/S_{20} \quad (7)$$

where S_t and S_{20} are the thermal lens signals of the same sample solution at t °C and +20.0 °C, respectively. As illustrated in Figure 4, the sensitivity of the technique can be appreciably improved by simply increasing the temperature

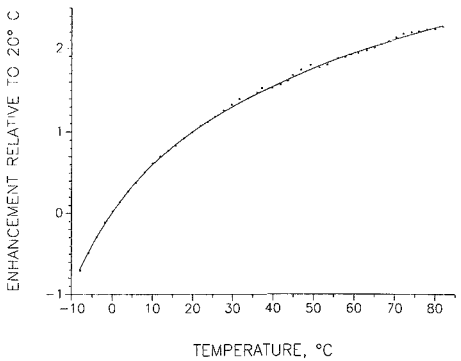

Figure 4. Plots of relative thermal lens signal of aqueous solution against temperature. Points are experimental values, and the solid line is the best fit.

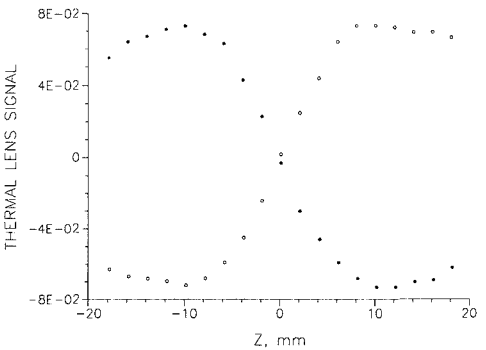

Figure 5. Plots of thermal lens signal of aqueous solution at −7.9 and +12.0 °C against the distance between the sample cell and the beam waist: ●, sample at −7.9 °C; ○, sample at +12.0 °C.

of the aqueous solution. For instance, a 1.93-fold increase in the sensitivity was achieved by increasing the solution temperature from +20.0 to 59.3 °C. At 80.3 °C, the thermal lens signal intensity was found to be 2.24 times that at 20.0 °C. To facilitate the calculation of a relative signal intensity at any given temperature, the results are assumed to be of a polynomial formula of the fifth order:

$$\mathrm{RI} = a_0 + a_1 t + a_2 t^2 + a_3 t^3 + a_4 t^4 + a_5 t^5 \qquad (8)$$

where RI is the relative signal intensity and t is the solution temperature in degrees Celsius. A least-squares method was then used to perform iterations to obtain the best fit. The a_0, a_1, a_2, a_3, a_4, and a_5 coefficients for the best fit, which is illustrated as a solid line in Figure 4, were found to be 1.29 × 10^{-3}, 0.0727, −1.563 × 10^{-3}, 2.604 × 10^{-5}, −2.395 × 10^{-7}, and 8.891 × 10^{-10}, respectively. From these coefficients, the thermal lens signal of an aqueous solution at +90.0 °C is calculated to be 2.4 times higher than that at +20.0 °C. Therefore, the sensitivity of thermal lens measurements for thermally stable compounds can be substantially enhanced by performing the measurement at elevated temperatures.

The sensitivity enhancement can also be achieved by the synergistic use of the bimodal characteristic of the thermal lens technique and the temperature effect of water. This is because thermal lens is measured as the relative change in the beam center intensity, $\Delta I_{bc}/I_{bc}$, or in the spot size in the far field, $\Delta\omega^2/\omega^2$, and the change in $\Delta I_{bc}/I_{bc}$ or $\Delta\omega^2/\omega^2$ is known to be strongly affected by the position of the sample relative to the waist of the laser beam. It has been shown that (*33*)

$$\frac{\Delta I_{bc}}{I_{bc}} = \frac{I_{bc}(t=0) - I_{bc}(t=\infty)}{I_{bc}(t=\infty)} = \frac{\omega^2(t=\infty) - \omega^2(t=0)}{\omega^2(t=0)} = \frac{\Delta\omega^2}{\omega^2}$$
$$= \frac{2.303P(\mathrm{d}n/\mathrm{d}T)A}{\lambda k}\left[\frac{2Z_1Z_c}{Z_1^2 + Z_c^2}\right] \qquad (9)$$

where A is absorbance of the sample, P is excitation laser power, λ is the excitation wavelength, k and $\mathrm{d}n/\mathrm{d}T$ are thermal conductivity and temperature coefficient of refractive index of solvent, Z_1 is distance from sample to the beam waist, and Z_c is the confocal distance, which is defined as $Z_c = \pi\omega_0^2/\lambda$ where ω_0 is the spot size at the beam waist. The equation predicts that the plot of $\Delta I_{bc}/I_{bc}$ will be an antisymmetric curve with $\Delta I_{bc}/I_{bc} = 0$ at $Z_1 = 0$ and maximum and minimum values at $Z_1 = +Z_c$ and $-Z_c$, respectively. The physical implication of the equation is as follows: Placement of a diverging (thermal) lens after the waist of the beam increases the far field spot size while placement of the lens before the waist decreases the spot size. Conversely, a converging lens placed after the waist of the beam decreases the spot size, and an increased spot size will be produced when the lens is before the beam waist. The validity of eq 9 was investigated by measuring thermal lens signal as a function of the sample position for sample at −7.9 and at +12.0 °C. These two particular temperatures were selected because, as shown in Figure 3, the strengths of the photoinduced thermal lenses at these two temperatures are exactly equal but have opposite sign; i.e., the sample at −7.9 °C produces a converging lens whereas a diverging lens is formed at +12.0 °C. The results obtained are shown in Figure 5. It is pleasing to see very good agreement between experimental results and theory. At 12.0 °C, aqueous solution produced a diverging thermal lens upon absorption of a laser beam because it has a negative $\mathrm{d}n/\mathrm{d}T$ value. As predicted by the theory, the strength and sign of the thermal lens strongly depended on the position of the sample relative to the beam waist. As shown in the figure, no observable thermal lens was seen when the sample was placed at the beam waist. Placing the sample after the beam waist produced divergence in the laser beam, which led to the decrease in the beam center intensity. As a consequence, positive thermal lens signals were observed. Conversely, placing the sample before the beam waist produced a focusing effect on the laser beam, which as a consequence led to negative thermal lens signals. Cooling the sample down from +12.0 to −7.9 °C produced a reversed effect. This is as expected because, having a positive $\mathrm{d}n/\mathrm{d}T$ value, the −7.9 °C aqueous solution formed a converging thermal lens upon absorption of the laser beam. The effect of this converging lens is exactly opposite to that of the diverging lens; i.e., it focused the beam when placed after the beam waist (negative thermal lens signals) and defocused the beam when it was before the beam waist (positive thermal lens signals). It is pleasing to see the equality in the absolute thermal lens signal intensities produced by the sample at +12.0 and at −7.9 °C when they are placed at the same position. Applications of this interesting antisymmetric behavior of the thermal lens and unique properties of water include the possibility of enhancing the sensitivity of the thermal lens technique. It is anticipated that the sensitivity of the technique can be substantially enhanced when the measurement is made on two identical cells whose temperatures are set at −7.9 and +12.0 °C and that are placed symmetrically on either side of the beam waist. The sensitivity enhancement stems from the additive characteristic of the thermal lens technique. That is, the total signal is the sum of two signals: the positive signal of the −7.9 °C cell (or the negative signal of the +12.0 °C cell), which is placed before

the beam waist, and the similar positive signal of the +12.0 °C cell (or the negative signal of the −7.9 °C cell), which is placed after the beam waist. The total thermal lens signal of the system can be written as (*33*)

$$\frac{\Delta I_{bc}}{I_{bc}} = -2\left[\frac{Z_1}{f_1^{\infty}} + \frac{Z_2}{f_2^{\infty}}\right] \tag{10}$$

where Z_1 and Z_2 are the distance from the beam waist to cell 1 (at −7.9 °C) and cell 2 (at 12 °C) whose steady-state focal lengths f_1^{∞} and f_2^{∞} are given by

$$f_1^{\infty} = \frac{\pi k_1 \omega_1^2}{2.303P(dn/dT)_1 A_1} \tag{11}$$

$$f_2^{\infty} = \frac{\pi k_2 \omega_2^2}{2.303P(dn/dT)_2 A_2} \tag{12}$$

where P is the laser power, A is absorbance, k is the thermal conductivity, dn/dT is the temperature coefficient of the refractive index of the solvent, and ω is the beam spot size in the sample cell, which can be calculated from

$$\omega^2 = \omega_0^2(1 + (Z/Z_c)^2) \tag{13}$$

and

$$Z_c = \pi\omega_0^2/\lambda \tag{14}$$

Assuming that the beam spot size in cell 1 and cell 2 are equal, eq 10 can be written as

$$\frac{\Delta I_{bc}}{I_{bc}} = 4.606\left[\frac{Z_1 E_1 A_1}{Z_c(1 + (Z_1/Z_c)^2)} + \frac{Z_2 E_2 A_2}{Z_c(1 + (Z_2/Z_c)^2)}\right] \tag{15}$$

where

$$E_1 = \frac{-P_1(dn/dT)_1}{\lambda k_1} \tag{16}$$

and

$$E_2 = \frac{-P_2(dn/dT)_2}{\lambda k_2} \tag{17}$$

In this case, $A_1 = A_2$ because the sample in cell 1 and cell 2 had the same chemical composition and concentration. The temperature of cell 1 is at −7.9 °C whereas cell 2 is at +12.0 °C, which according to the aforementioned results gives

$$\frac{(dn/dT)_1}{k_1} = -\frac{(dn/dT)_2}{k_2}$$

There are some losses in the laser power at cell 2 as compared to that at cell 1 because of the reflection from windows of cell 1. Therefore, $E_2 = -E_1 T$ where T is the transmittance of cell 1. In order to achieve maximum thermal lens signals and hence enhancement, cell 1 and 2 are placed at the confocal distance symmetrically on either side of the beam waist. Therefore, $Z_2 = -Z_1 = Z_c$; substituting this condition into eq 11 gives

$$(\Delta I_{bc}/I_{bc}) = -2.303A(E_1 + E_1 T) \tag{18}$$

The relative enhancement (RE) of the present two-cell system in relation to that of the one-cell system is therefore

$$RE = 1 + T \tag{19}$$

Experimental results are shown in Figure 6. Three different experiments were performed in order to clearly demonstrate the method. In the first experiment, the sample cell (cell 1) whose temperature was set constant at −7.9 °C was placed before the beam waist and a second cell (cell 2) that

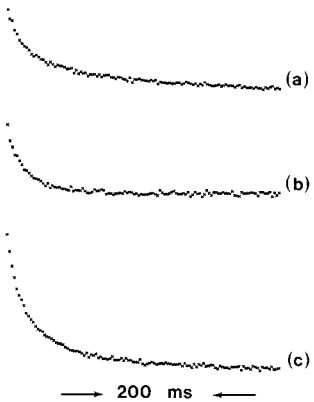

Figure 6. Thermal lens responses measured on a single-beam apparatus of aqueous solutions at different temperatures and distances relative to the beam waist: (a) sample at −7.9 °C placed before the beam waist (cell 1); (b) sample at +12.0 °C placed after the beam waist (cell 2); (c) cell 1 and cell 2 together.

contained water was placed after the beam waist and symmetrically to cell 1. The relative distance of cell 1 to the beam waist was adjusted to give maximum thermal lens signal. As expected from the theory, due to the positive dn/dT value, this aqueous solution formed a converging lens, and because it was placed before the beam waist, the photoinduced thermal lens signal is positive (Figure 6a). The thermal lens signal intensity for this case was calculated to be 0.084 ± 0.001. In the second set of experiments, cell 1, which was placed before the beam waist, contained water and cell 2 contained sample at +12 °C. The relative position of cell 2 to the beam waist was adjusted to give maximum signal. As shown in Figure 6b, the diverging lens placed after the beam waist produced a positive thermal lens signal. The thermal lens signal intensity for this case was calculated to be 0.078 ± 0.001, which is only about 93% of the signal intensity found for the first case. The 7% discrepancy can be attributed to the loss in the laser power by reflection at the windows of cell 1, as it was found that the transmittance of the quartz cell used in this study was 94%. Figure 6c shows the thermal lens signal taken with a system in which both cell 1 and cell 2 contained sample solution. The thermal lens signal intensity of this system was found to be 0.151 ± 0.002, which is not exactly the sum of 6a and 6b but only 1.80 ± 0.02 times that of 6a. This is as expected because, according to the theory described above, the reflection at two windows of cell 1 and the absorption of the sample solution in this cell made the excitation power at cell 2 less than that at cell 1. In fact, in this work the transmittance of cell 1, which contained 5.0×10^{-7} M nickel phthalocyanine aqueous solution, was only 0.88. Therefore, the relative enhancement calculated on the basis of eq 19 is 1.88, which is relatively higher than the experimental value of 1.80. The discrepancy is probably due to the invalidity in assuming that the beam spot sizes in cell 1 and cell 2 are the same. The thermal lens produced by cell 1 led to a divergence in the laser beam. Therefore, the beam spot size in cell 2 became relatively larger as compared to the case where cell 1 is absent. As a consequence, cell 2 produced a relatively smaller thermal lens signal because the signal is known to be inversely proportional to the spot size in the sample. It may be possible to eliminate the mismatch in the beam spot sizes of cell 1 and cell 2 and to produce the maximum thermal lens signal for the two-cell system by moving cell 2 closer to cell 1. However, such alignment is impractical because it would

require different alignments for different samples and/or concentrations.

It is important to point out that one of the unique characteristics of the thermal lens technique is the fact that its signals do not increase linearly with the cell length. This is because in this technique, the signal depends on the power density in the excitation laser beam. As a consequence, the signal intensity would not be doubled with the use of a cell with twice the path length (*34*, *35*) because in a long path length cell, the spot size of the laser beam will be enlarged as it propagates through the cell (*34*, *35*). The consequence of this spot size enlargement is the decrease in the laser power density and in the thermal lens signal because these two terms are known to be inversely proportional to the beam spot size. In addition, the time constant t_c also becomes longer. A longer measurement time is necessary, which as a consequence worsens the detection limit because the fluctuation in the laser intensity increases with time (*34*). Conversely, the beam spot size within each cell and the time constant remain the same with the use of the two-cell method developed in this work. In fact, the two-cell method may be the only way to provide a thermal lens signal that is the sum of the two individual signals produced by each cell while keeping the background noise the same.

CONCLUSION

Water has been demonstrated to be a unique medium for thermal lens measurements. Depending on whether the measurements are performed at temperatures lower or higher than −0.01 °C, the photoinduced thermal lens in water can have either a positive (converging) or negative (diverging) focal length. At precisely −0.01 ± 0.04 °C, no thermal lens signal could be observed. This is because the dn/dT values of water are positive at temperatures less than −0.01 °C, negative at temperatures higher than −0.01 °C, and equal to zero (i.e., maximum refractive index) at −0.01 °C. One possible application of this unique property is the development of a highly efficient dye laser that operates at −0.01 °C, the temperature at which losses due to the photoinduced heating effect is zero.

The unique characteristic of water was exploited in this work to enhance the sensitivity of thermal lens measurements in water. For instance, the thermal lens signal intensity of an aqueous solution can be enhanced up to 2.4 times by simply increasing the solution temperature from +20 to +90 °C. For thermally unstable compounds, the sensitivity enhancement can be achieved by synergistic use of the bimodal characteristic of the thermal lens technique and the temperature effect on the thermooptical properties of water. Typically, two sample cells, one at −7.9 °C and the other at +12.0 °C, were placed on both sides and symmetrically about the laser beam waist. The sensitivity of this two-cell system was found to be 1.80 or $(1 + T)$ times that of the single cell (T is the transmittance of the first cell). While it is true that the enhancement obtained by these methods is relatively lower than the values obtained by performing the measurements in nonpolar solvent (*10*, *12*), they are of particular importance for certain classes of compounds such as biological molecules, which are not soluble in nonpolar solvents and cannot be extracted into these media. Experiments are now in progress to explore this possibility and to apply the developed enhancement methods to the area of general trace chemical analysis.

LITERATURE CITED

(1) Harris, J. M.; Dovichi, N. J. *Anal. Chem.* **1980**, *52*, 695A.
(2) Dovichi, N. J. *CRC Crit. Rev. Anal. Chem.* **1987**, *17*, 357.
(3) Teramae, N.; Voigtman, E.; Lanauze, J.; Winefordner, J. D. *Anal. Chem.* **1986**, *58*, 761–765.
(4) Teramae, N.; Winefordner, J. D. *Appl. Spectrosc.* **1987**, *41*, 164, 165.
(5) Ramos, G. R.; Alvarez-Coques, M. C. G.; Smith, B. W.; Omenetto, N.; Winefordner, J. D. *Appl. Spectrosc.* **1988**, *42*, 341–346.
(6) Tran, Chieu D. *Anal. Chem.* **1986**, *58*, 1714–1716.
(7) Tran, Chieu D. *Appl. Spectrosc.* **1986**, *40*, 1108–1110.
(8) Tran, Chieu D. *Appl. Spectrosc.* **1987**, *41*, 512–516.
(9) Tran, Chieu D. *Analyst* **1987**, *112*, 1417.
(10) Tran, Chieu D. *Anal. Chem.* **1988**, *60*, 182.
(11) Franko, M.; Tran, C. D. *Anal. Chem.* **1988**, *60*, 1925.
(12) Tran, C. D.; Van Fleet, T. A. *Anal. Chem.* **1988**, *60*, 2478.
(13) Fendler, J. H. *Membrane Mimetic Chemistry*; Wiley: New York, 1982.
(14) *Ordered Media in Chemical Separations*; Hinze, W. L., Armstrong, D. W., Eds.; American Chemical Society: Washington, DC, 1987.
(15) Hinze, W. L. *Solution Chemistry of Surfactants*; Mittal, K. L., Ed.; Plenum: New York, 1979; Vol. 1, pp 79–127.
(16) Angell, C. A. *Water, a Comprehensive Treatise*; Plenum: New York, 1982; Vol. 7, Chapter 1.
(17) Angell, C. A. *Ann. Rev. Phys. Chem.* **1983**, *34*, 593.
(18) Burgi, D. S.; Nolan, T. G.; Risfelt, J. A.; Dovichi, N. J. *Opt. Eng.* **1984**, *23*, 756.
(19) Olmstead, M. A.; Amer, N. M.; Kohn, S.; Fournier, D.; Boccara, A. C. *Appl. Phys. A* **1983**, *32*, 141.
(20) Hobbs, P. V. *Ice Physics*; Clarendon Press: Oxford, U.K., 1974.
(21) Saubade, Ch. *J. Phys. C.* **1984**, *17*, 3493.
(22) Powell, R. W.; Ho, C. Y.; Liley, P. E. *Natl. Std. Ref. Data Series—NBS 8* **1966**, 118.
(23) Eisenberg, H. J. *J. Chem. Phys.* **1965**, *43*, 3887.
(24) Thormahlen, I.; Straub, J.; Grigull, U. J. *Phys. Chem. Ref. Data* **1933**, *14*, 933.
(25) Eisenberg, D.; Kauzmann, W. *The Structure and Properties of Water*; Oxford University Press: Oxford, U.K., 1969.
(26) Tilton, L. W. Taylor, J. K. *J. Res. Natl. Bur. Std.* **1938**, *20*, 419.
(27) Saubade, Ch. *J. Phys.* **1981**, *42*, 359.
(28) Jamin, J. *C. R. Hebd. Seances Acad. Sci. Paris* **1856**, *143*, 1191.
(29) Duclaux, J.; Bricout, V. *J. Phys. Radium* **1947**, *8*, 185.
(30) Hawkes, J. B.; Astheimer, R. W. *J. Opt. Soc. Am.* **1948**, *38*, 804.
(31) Grange, B. W.; Stevenson, W. H.; Viskanta, R. *Appl. Opt.* **1976**, *15*, 858.
(32) Abbate, G.; Bernini, U.; Ragozzino, E.; Somma, F. J. *J. Phys. D* **1978**, *11*, 1167.
(33) Dovichi, N. J.; Harris, J. M. *Anal. Chem.* **1980**, *52*, 2338.
(34) Carter, C. A.; Harris, J. M. *Appl. Spectrosc.* **1983**, *37*, 166.
(35) Morris, M. D. In *Detectors for Liquid Chromatography*; Yeung, E. S., Ed.; John Wiley: New York, 1986; pp 105–147.

RECEIVED February 6, 1989. Accepted April 19, 1989. Acknowledgment is made to the donors of the Petroleum Research Fund, administered by the American Chemical Society, for financial support of this research.

Spectrophotometric Method for the Analysis of Plutonium and Nitric Acid Using Partial Least-Squares Regression

W. Patrick Carey and Lawrence E. Wangen

Chemical and Laser Science Division, G740, Los Alamos National Laboratory, Los Alamos, New Mexico 87545

James T. Dyke*

Material Science and Technology Division, E501, Los Alamos National Laboratory, Los Alamos, New Mexico 87545

A method for the determination of Pu(III) and nitric acid concentrations using the multivariate calibration technique of partial least-squares (PLS) regression coupled with visible absorption spectra (500–880 nm) is presented. Quantitation of plutonium using its visible spectrum is straightforward; however, the effects of nitric acid on the Pu(III) absorption spectra are subtle and nitric acid quantitation from the absorbance spectrum is more difficult. In this study PLS regression is successfully applied to quantitate both plutonium and nitric acid using the information contained in the absorption spectra of appropriate solutions. The calibration set, covering a range of Pu(III) from 1.99 to 29.9 g/L was modeled with a standard error of 0.20 g/L. Similarly, nitric acid ranging from 0.44 to 3.08 M was successfully modeled with a standard error of 0.18 M. Evaluation of the calibration models, using test samples that span the range of the calibration concentrations, gave predictions on the order of the standard error of the calibration models.

INTRODUCTION

Plutonium can be precipitated from acidic solutions by forming an insoluble oxalate salt of Pu(III). It has been shown that the concentrations of both nitric acid and oxalic acid affect the solubility of the Pu(III) oxalate product (*1*, *2*). The solubility of the plutonium(III) oxalate is minimized under the conditions of 0.5–1.0 M nitric acid and 0.05–0.1 M excess oxalic acid. These concentrations result in a solubility of Pu(III) between 2 and 20 mg/L. If the nitric acid is more concentrated, the solubility of Pu(III) increases, i.e. in 2.0 M nitric acid the Pu(III) concentration increases 10-fold. There are also indications that increasing the oxalic acid concentration above 0.2 M will lead to increased solubility of the plutonium. To assist in the study of the precipitation reaction of plutonium(III) oxalate, it would be beneficial to have a rapid analytical method for examining the initial solution to determine the concentrations of plutonium and nitric acid.

In this study, a method for predicting both Pu(III) and nitric acid from visible absorption spectra of solutions containing the species of interest using partial least-squares (PLS) regression was evaluated. Several techniques for estimating Pu(III) based on visible absorption spectroscopy have been developed, and quantitation is fairly straightforward (*3–6*). The difficulty remains in the determination of the nitric acid concentration from the visible absorption spectra. In this paper we demonstrate the use of PLS for extracting the small signal of the nitric acid effect in the presence of a much larger signal due to the Pu(III) absorption. This information provides a measure of nitric acid concentration that can be used in studying the precipitation reaction.

The fundamental theory and applications of PLS have been investigated by several researchers (*7–11*). This technique, which uses the full spectrum of data, correlates latent variables in the spectral responses to the analyte concentration vector. The latent variables, which are orthogonal vectors, account for the variance present in the spectral response data block or matrix. The PLS 2-block modeling used is based on the algorithm in which the scores are orthogonal. This method is similar to principal component regression in that the spectral responses are factor analyzed by orthogonal vectors, but it proceeds one step further and uses information from the analyte concentration vector in the construction of PLS latent variables. The correlation built by PLS between the spectral latent variables and the concentration variable discriminates between multiple analytes if their effects on the spectra are not fully collinear. By use of PLS in this study, two separate models were built, one each for Pu(III) and nitric acid. Predictions of analyte concentrations in several unknown sample solutions were performed by using the models developed during calibration.

EXPERIMENTAL SECTION

All chemicals used were reagent grade, except for the plutonium nitrate stock solutions. Plutonium nitrate stock solutions were obtained by dissolving PuO_2 in HNO_3/HF followed by the removal of fluoride through ion exchange. The concentrations of these stock solutions were determined by standard radiochemical methods based on γ-ray spectroscopy with a relative standard deviation of 0.5% (*12*). A calibration set, Figure 1, and a test sample set were prepared by performing volumetric dilutions of the stock solutions. During these dilutions, various amounts of nitric acid were added such that the calibration and test sets span the acid range encountered in the precipitation studies.

Spectra between 500 and 880 nm were obtained on each sample by using a 0.2 cm path length flow cell. The spectrometer used for these experiments was an LT Industries Quantum 1200. This instrument allows for the remote placement of sample cell and detector in an isolated glovebox with a fiber optic bundle transporting the light. Resolution of this instrument is on the order of 1 nm with the scan for the visible region requiring 200 ms. For each sample, 10 scans were acquired and averaged.

Data analysis was performed by using a PLS 2-block routine developed at the University of Washington (*13*). This code was implemented on a VAX 11-780 where all the calibration models were constructed.

Nitric Acid Determination. The nitric acid concentration of each sample was determined by a standard addition method (*14*) designed to avoid the formation of hydronium ion from hydrolysis of plutonium in the sample. One hundred microliters of sample was mixed with 10.0 mL of 1.0 M potassium thiocyanate used to complex plutonium. Then 100-μL standard additions of 0.092 M nitric acid were made, and the resulting pH was measured with a Ross combination semimicro-pH electrode (Orion) and a portable pH meter (SA250, Orion). The inclusion of an estimate of the hydronium ion activity coefficient was necessary for the acid range used in this study. Using the standard equation for the Debye-Hückel activity coefficient, a value of approximately 0.75 was estimated as the activity coefficient for hydronium ion. However, when this value was used to determine hydronium ion activity of 10 prepared acid samples whose total acidity had

0003-2700/89/0361-1667$01.50/0

Table I. Variance Described by PLS Models for Plutonium(III) and Nitric Acid

	spectral response		Pu(III)		nitric acid	
latent variable	each, %	total, %	each, %	total, %	each, %	total, %
1	94.53	94.53	98.80	98.80		
2	3.61	98.14	1.16	99.96		
1	94.35	94.35			5.78	5.78
2	1.81	96.17			29.55	35.34
3	3.51	99.68			1.17	36.51
4	0.14	99.82			28.12	64.63
5	0.05	99.87			16.91	81.55
6	0.02	99.90			11.52	93.07

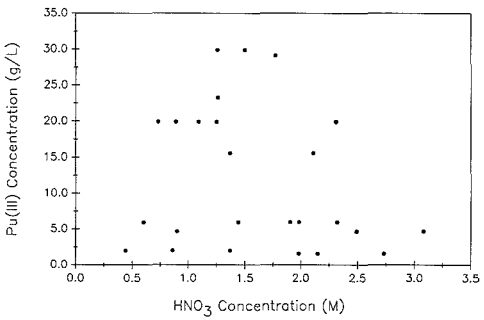

Figure 1. Plot of nitric acid concentration versus Pu(III) concentration in the calibration set.

previously been measured by sodium hydroxide titration, the known value was constantly underestimated. (Four of these samples contained a hydrolyzable metal, thorium nitrate.) We resorted to estimating the activity coefficient experimentally since the ionic strength and hydronium ion concentrations were not consistent with the Debye–Hückel theory. This procedure involves determining the activity coefficient by the following expression:

$$\gamma_{H_3O^+} = \frac{10^{-pH}}{[H_3O^+]} \quad (1)$$

where the pH is the measured quantity of hydronium ion activity during the standard addition experiment and $[H_3O^+]$ is the known concentration of added nitric acid after dilution. This procedure assumes complete dissociation of nitric acid. The mean value of this estimated activity coefficient, $\gamma_{H_3O^+}$, for the 10 standards was 0.93 ± 0.01. By use of this estimated activity coefficient in the following equation, the initial acid concentration, $[H_3O^+]_i$, in each calibration and test set sample can be estimated.

$$V_i[H_3O^+]_i\gamma_{H_3O^+} + V_a[H_3O^+]_{STD}\gamma_{H_3O^+} = (V_i + V_a)10^{-pH} \quad (2)$$

V_i and V_a are the volumes of the initial sample and added standard respectively, and $[H_3O^+]_{STD}$ is the concentration of the standard. The estimation of nitric acid using the above method has a relative error of 2.4%.

RESULTS AND DISCUSSION

Visible spectra of the plutonium species are presented in Figures 2 and 3. Figure 2 shows the sensitivity of several Pu(III) absorption bands in solutions containing 2.0 to 29.9 g/L Pu(III). The nitric acid concentration in these four samples is approximately 1.3 M. In high-precision analytical measurements, the bands at 565 and 601 nm are commonly used to quantitate Pu(III). The effect of nitric acid on plutonium(III) nitrate complex absorption is presented in Figure 3. At a constant level of 6.0 g/L Pu(III), nitric acid was varied from 0.6 to 2.3 M. This effect is most readily observed at 565 nm, where the absorption peak tends to narrow or become more symmetrical with increasing nitric acid concentration, and between 750 and 825 nm, where a change in one or more

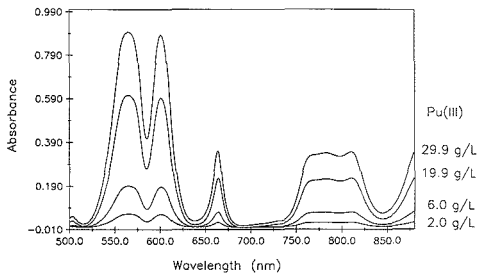

Figure 2. Absorbance spectra of Pu(III) from 2.0 to 29.9 g/L.

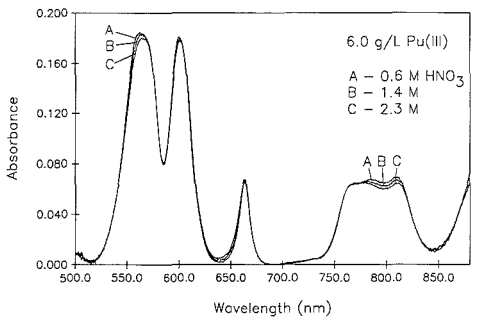

Figure 3. Effect of nitric acid on Pu(III) absorbance spectra. Nitric acid varies from 0.6 to 2.3 M with a constant 6.0 g/L Pu(III) concentration.

underlying absorbance bands causes shifts in the spectra.

Two separate models, one each for Pu(III) and nitric acid, were built using PLS regression. For each regression model, the spectral responses from the 25-sample calibration set formed the X block (independent variables) and the concentrations of Pu(III) or nitric acid formed the Y block (dependent variable). All variables were mean centered and scaled by their standard deviation as part of the model. For both models, the optimum number of latent variables to include in the calibration was determined by cross validation (alternating one sample removed method), and the models include all 25 samples. Table I shows the variance described by the PLS model for both Pu(III) and nitric acid and the correlations of spectral responses to the Y-block information. The first latent variable of the X block corresponds to 94.35% of the variance in the spectral responses, which is primarily due to the large signal of changing Pu(III) concentration as seen in Figure 1. This first latent variable in Table I describes 99.80% of the information in the Y block containing Pu(III). Therefore, Pu(III) has a large signal-to-noise ratio, which is to be expected, and its modeling should be straightforward. Nitric acid, however, has only 5.78% of its variance described

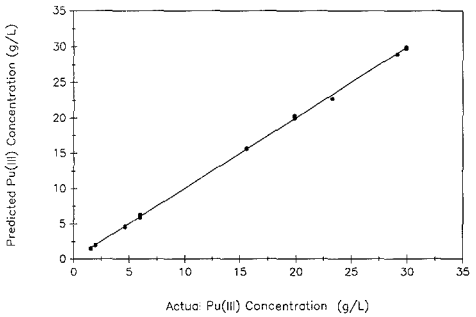

Figure 4. Actual Pu(III) concentration versus predicted Pu(III) concentration based on a two latent variable PLS model.

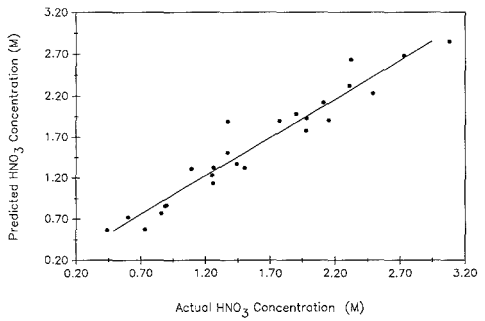

Figure 5. Actual nitric acid concentration versus predicted nitric acid concentration from a six latent variable PLS model.

by the first latent variable. In subsequent latent variables, more of the nitric acid information is being correlated with spectral responses orthogonal to latent variable 1. Since very little spectral variance is being used to model nitric acid, one would expect a small signal-to-noise ratio and a model with a higher degree of error than the Pu(III) model.

The accuracy of a multivariate model can be visually examined by plotting the actual calibration concentrations versus the predicted values for each sample. For Pu(III), the 25 sample concentrations are plotted versus their estimated concentrations using a two latent variable model in Figure 4. As expected, Pu(III) is easily modeled with an r^2 statistic of 1.00 and a standard error of 0.20 g/L. Figure 5 provides a similar plot of actual versus predicted concentrations for nitric acid using a six latent variable model. In this case, the model describes the overall nitric acid effect on the spectra but with a greater degree of error than the Pu(III) model. The r^2 statistic for the nitric acid model was 0.93 with a standard error of 0.18 M.

The best test for the validity of a calibration model is to examine the prediction capability of the model on samples not included in the calibration sample set. To validate the constructed models, a test set containing six samples with known Pu(III) and nitric acid concentrations were analyzed in the same manner as the calibration set samples. Table II compares the resulting predictions with known values. The calibration model is proven to be valid if the predicted value of an unknown is within the standard error range of the model, which is a calculation of the standard deviation of the model residuals. For example approximately 95% of future samples

Table II. Prediction Results for Test Set Samples

	Pu(III), g/L			nitric acid, M		
sample	true	estimated	difference	true	estimated	difference
1	1.99	2.00	0.01	1.98	1.96	0.02
2	5.97	5.99	0.02	1.15	1.47	0.32
3	29.9	30.3	0.4	1.07	0.92	0.15
4	19.9	19.7	0.2	2.13	2.47	0.34
5	4.67	4.62	0.05	2.08	1.97	0.11
6	15.6	15.2	0.4	0.94	1.16	0.22
			0.25[a]			0.23[a]

[a] Standard error of prediction.

should fall within twice the standard error if the unknowns come from the same population as the standards. For Pu(III), with a standard error of 0.20 g/L, all of the predictions were within two standard errors with four of the six predictions within one standard error. For nitric acid all predicted values are within the two standard error limit (0.18 M HNO_3) estimated by the model, and half of these samples are within one standard error. The actual standard error of prediction was 0.25 g/L and 0.23 M for Pu(III) and nitric acid, respectively, which is larger than the error for the calibration sets for both analytes. Although the number of samples was limited in both calibration and test sets, there was no statistical difference between the standard errors based on a F-test comparison. The results of this test set provide confidence that both the Pu(III) and nitric acid models are valid over the range of concentrations normally encountered in the precipitation studies.

We have demonstrated the use of the plutonium(III) nitrate absorbance spectra coupled with PLS regression for the determination of Pu(III) and nitric acid concentrations over the analyte ranges of 1.99 to 29.9 g of plutonium and 0.44 and 3.08 M nitric acid. The precision of these predictions is suitable for studying the effects of oxalic acid and nitric acid concentrations during the precipitation of plutonium oxalate. Although greater precision could be obtained from other analysis methods, the information gained from these spectral measurements is well suited for rapid analytical measurement. The coupling of multivariate regression techniques with absorbance spectroscopy provides quantitation of both Pu(III) and nitric acid from a single spectral measurement, thereby simplifying the instrumentation used in studying the precipitation reaction.

Registry No. Pu, 7440-07-5; nitric acid, 7697-37-2.

LITERATURE CITED

(1) Burney, G. A.; Porter, J. A. *Nucl. Chem. Lett.* **1967**, *3*, 79–85.
(2) Cleveland, J. M. *The Chemistry of Plutonium*; American Nuclear Society: La Grange Park, IL, 1979; pp 401–403.
(3) Wangen, L. E.; Phillips, M. V.; Walker, L. F. U.S. Department of Energy Report LA-11297, 1988.
(4) Hagan, P. G.; Miner, F. J. Atomic Energy Report, RFP-1391, 1969.
(5) Van Hare D. R. U.S. Department of Energy Report, DP-1713.
(6) Baldwin, D. L.; Stromatt, R. W. U.S. Department of Energy Report PNL-SA-15318, 1987.
(7) Lorber, A.; Wangen, L. E.; Kowalski, B. R. *J. Chemom.* **1987**, *1*, 19–31.
(8) Geladi, P.; Kowalski, B. R. *Anal. Chim. Acta* **1986**, *185*, 1 and 19.
(9) Haaland, D. M.; Thomas, E. V. *Anal. Chem.* **1988**, *60*, 1193–1208.
(10) Otto, M.; Wegscheider, W. *Anal. Chem.* **1985**, *57*, 63.
(11) Martens, M.; Martens, H. *Appl. Spectrosc.* **1986**, *40*, 303.
(12) Parker, J. L. U.S. Department of Energy Report LA-8146-MS, 1980.
(13) Veltkamp, D.; Kowalski, B. R. Center for Process Analytical Chemistry, BG-10, University of Washington, Seattle, WA, PLS 2-Block Modeling, Version 3.0, 1988.
(14) Baumann, E. W.; Torrey, B. H. *Anal. Chem.* **1984**, *56*, 682–685.

RECEIVED for review January 23, 1989. Accepted May 1, 1989.

Anal. Chem. 1989, 61, 1670–1674

Continuum Source Atomic Absorption Spectrometry in a Graphite Furnace with Photodiode Array Detection

Bradley T. Jones, Ben W. Smith, and James D. Winefordner*

Department of Chemistry, University of Florida, Gainesville, Florida 32611

A graphite furnace continuum source atomic absorption spectrometer using a photodiode array detector is described that provides high-resolution wavelength versus absorbance spectra over a 2.5-nm range for a single atomization step. The multiwavelength detection power allows the simultaneous determination of several elements, reduces problems caused by spectral interferences, and automatically corrects for nonzero background absorbance. Each spectrum is acquired in 0.33 s, and several successive specra can be obtained during a single run. Three-dimensional wavelength–absorbance–furnace temperature spectra can be obtained by using ramped heating steps to provide a rough separation of elements in a mixture. Limits of detection calculated for 19 elements range from 0.1 pg for magnesium to 700 pg for arsenic. The sampling precision was found to be better than 10% relative standard deviation in all cases, with the precision for a single atomization being greatly increased when multiple absorption lines for a single element are observed in the spectrum. The error found for the measurement of the iron concentration in an NBS standard bronze was 8.5%, with the calculated concentration agreeing with the certified concentration within 95% confidence limits.

INTRODUCTION

Continuum source atomic absorption spectrometry (CSAAS) has enjoyed a period of steady growth over the last 25 years. In 1966, Fassel and co-workers presented a lengthy evaluation of continuum sources in AAS (*1*). That work employed a 150-W xenon arc lamp as the light source, an oxyacetylene burner as the atomizer, and a 0.5 m focal length monochromator with a photomultiplier tube for detection. They found that this arrangement produced limits of detection (LOD) within 1 order of magnitude of those observed with line sources, except for those elements whose most sensitive absorption lines fall below 250 nm, where the source intensity and detector sensitivity were greatly reduced. Since that time, well over 50 papers on the subject have been published, including several excellent review articles (*2–5*). A particularly interesting historical perspective is given in one of these reviews showing that CSAAS dates back as far as 1875 (*3*).

The recent combination of CSAAS with graphite furnace atomization has produced detection limits for many elements that are better than or comparable to those obtained by inductively coupled plasma (ICP) emission spectrometry (*6*). Furthermore, graphite furnace CSAAS has "far better absolute detection limits, smaller sample size requirements, more accurate analysis of liquids containing suspended particles bigger than a few micrometers, and the possibility of performing direct solids measurements" (*5*). The optimization of electrothermal atomization parameters including measurement mode, atomizer type, and atomization temperature has been thoroughly investigated (*6, 7*). The technique has been applied to the simultaneous determination of seven metals, all at the microgram-per-liter level, in blood serum (*8*).

The advantages of graphite furnace CSAAS are many: simple optical configurations, simultaneous multielement detection, background correction, and low detection limits (above 250 nm). The biggest disadvantage today is the same one observed in 1966: poor source intensity below 250 nm. Some other disadvantages include the need for a high-resolution monochromator, usually an echelle monochromator, to fully resolve the absorption line; the need for multiple detectors, usually photomultiplier tubes, for simultaneous multielement analysis; and the need for wavelength modulation to overcome the instability of the continuum source and broad-band background absorption. The latter two requirements impose the restraint of complex computer programs to achieve high-speed data acquisition and processing. These problems seem to have prevented the commercial production of a CSAAS instrument at the present time.

This work presents a graphite furnace CSAAS system with photodiode array detection. The diode array allows wavelength versus absorbance spectra to be obtained directly with the use of a high-resolution monochromator. Broad-band background absorption and spectral interferences can be observed and corrected for directly in the acquired spectrum without the need for wavelength modulation. This eliminates the need for complex computer programs, other than those readily supplied by the diode array manufacturer. This system further simplifies the optical arrangement typically used in CSAAS by eliminating the need for rotating quartz modulation plates or other background correction schemes such as double beam paths, deuterium lamp background correction, and Zeeman splitting background correction.

EXPERIMENTAL SECTION

Instrumentation. Figure 1 is a schematic diagram of the optical arrangement used in this work. The light source is a 300-W Cermax xenon arc lamp (ILC Technology, Sunnyvale, CA). The spectral and noise characteristics of this lamp (formerly the Eimac lamp from Varian) are well-known, and it has been recommended for use in CSAAS experiments (*9, 10*). The collimated radiation from the lamp was focused through the center of the graphite furnace atomizer (Shimadzu Model GFA-4A, Koyoto, Japan) by using a 12.7 cm focal length quartz lens. The graphite tube was 30 mm long with a 4.2-mm inner diameter and 6.15-mm outer diameter. A second quartz lens recollimated the light at the exit end of the furnace. The collimated beam was then folded 90° by a 45°–45°–90° quartz prism due to space restrictions and focused onto the entrance slit of a J-Y H10 0.1-m monochromator acting as a predisperser (Instruments SA, Inc., Metuchen, NJ). The 16-nm bandpass of radiant flux at the exit slit of the H10 was focused by a fourth lens onto the entrance slit of an HR1000 1.0-m monochromator (ISA). The HR1000 was found to give the lowest minimum detectable signal in a previously reported comparison of 11 monochromators evaluated for CSAAS (*11*). The radiant flux at the exit plane of the HR1000 was detected by an optical spectrometric multichannel analyzer (OSMA, Model IRY-1024, Princeton Instruments, Princeton, NJ). The spectral and noise characteristics of the 1024-element self-scanned intensified photodiode array are reported elsewhere (*12*). The spectral bandpass of the HR1000 was determined by the resolution of the diode array, which is given in the manufacturer's literature as three to four elements on the array corresponding to 0.075–0.100 mm in length. This effective "slit width" corresponds to about a 0.05-nm spectral bandpass in first order given that the measured reciprocal linear dispersion for the monochromator was 0.5 nm/mm. This resolution is not sufficient to fully resolve most

0003-2700/89/0361-1670$01.50/0

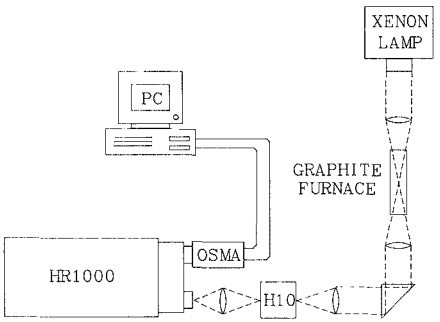

Figure 1. Schematic diagram of the optical arrangement used for CSAAS measurements.

atomic absorption lines since the values for the full width at half-maximum (fwhm) for such lines are typically 0.01 nm or less. A spectral bandpass in this range was obtained by making measurements with the HR1000 in fourth or fifth order. In fifth order the observed spectral bandpass was 0.01 nm and the length of the diode array (25.4 mm) corresponded to 2.54 nm. The entrance slit of the monochromator was set at 0.1 mm to match the width of the four-diode resolution on the array. The J-Y H10 served as a filtering device to eliminate source radiation that would have appeared due to lower orders reaching the diode array.

Sample Preparation. Stock solutions (1000 mg/L in 2% HNO_3) were obtained from Inorganic Ventures, Inc. (Brock, NJ) for the 19 elements tested. A mixture of these elements (each element 10 mg/L) was prepared, and dilutions were made as necessary to obtain analytical calibration curves. Two complex real samples were analyzed. A seawater sample collected at Dennis, MA, was atomized without pretreatment. An NBS standard bronze sample (SRM No. 52) dissolved in 10% nitric acid (3.02 g in 250 mL) was also directly injected into the furnace.

Procedure. Table I lists the heating conditions recommended by Shimadzu and used in this study for the 19 elements investigated. The heating parameters for barium were not listed by Shimadzu so they were taken from a literature reference (*13*). The drying step for each sample consisted of a temperature ramp lasting for 30 s to a final temperature of 110 °C. Following the drying step, the time required to reach the appropriate charring temperature was less than 1 s with stepwise heating. The charring temperature was maintained for the duration given in Table I, followed by stepwise atomization at the given temperature and duration. Each atomization step was immediately followed by a cleaning step of 5 s at 2800 °C. A cooling period of 30 s was allowed between atomizations. When simultaneous multielement analysis was desired, a compromise charring temperature was chosen as the lowest charring temperature recommended for the elements in question. Similarly, a compromise atomization temperature was chosen as the highest atomization temperature recommended.

Atomic absorbance spectra were acquired as follows. The wavelength of maximum absorption of the element in question was positioned on the H10 monochromator. The fifth order of the wavelength was then selected on the HR1000. Since the upper limit on the HR1000 was 1500 nm, the fourth order was chosen for elements whose absorption maxima occurred above 300 nm. A spectrum of the incidence radiation (I_0) at this wavelength was then acquired with the OSMA and stored. Ten 33-ms exposures were averaged for each spectrum. The total acquisition time for each spectrum was therefore 330 ms. The signal-to-noise ratio (S/N) for this method of data acquisition was found to be much higher than that for a single 330-ms exposure. A dark spectrum at the analytical wavelength was taken in a similar method with the source radiation blocked at the entrance slit of the predispersing monochromator. Next, a 10-μL aliquot of the sample was injected into the furnace, and the atomization program was started. During the atomization step, 10–15 spectra were stored depending on the atomization duration. The absorbance spectrum was calculated for each spectrum by using the software supplied with the OSMA and the I_0 and dark spectra recorded earlier. The spectrum during the atomization showing the highest absorbance for the element in question was then used to prepare analytical calibration curves of peak height versus concentration. The detection limit was calculated as that amount of analyte giving rise to an absorbance signal equal to 3 times the standard deviation observed in the blank spectrum.

Table I. Atomization Parameters Used for CSAAS Measurements[a]

element	charring step temp, °C	charring step time,[b] s	atomization step temp, °C	atomization step time,[b] s
Ag	400	20	1300	3
Al	800	20	2600	3
As	300	20	2100	4
Ba[c]	900	20	2800	7
Ca	700	20	2300	4
Cd	300	20	1100	3
Co	500	20	2300	5
Cr	500	20	2500	4
Cu	500	20	2300	4
Fe	500	20	2300	4
Li	500	20	2400	5
Mg	500	20	1900	4
Mn	500	20	2200	4
Na	500	20	1800	3
Ni	500	20	2400	4
Pb	300	20	1300	3
Sb	300	20	1800	4
Sr	500	20	2200	4
Zn	300	20	1300	3

[a] Parameters taken from Shimadzu manufacturer's literature unless otherwise noted. [b] Time reported is the total time that the graphite furnace remained at the given temperature following a stepwise heating period that lasted less than 1 s. [c] Parameters for barium taken from ref 13.

RESULTS AND DISCUSSION

Absorption Spectra. Absorbance spectra for several elements have been previously reported for a graphite furnace CSAAS experiment using a diode array for a detector (*14*, *15*). These works focused on simultaneous molecular and atomic absorption measurements; the resolution of the atomic lines was poor. Nevertheless, lead, copper, manganese, zinc, cadmium, vanadium, and nickel were determined in various crude oils and pigments (*14*), and matrix chloride interferences were characterized in the determination of copper and manganese (*15*).

High-resolution atomic absorption spectra were acquired in this work as stated above and are presented as plots of absorbance versus wavelength. The length of the diode array limits each spectrum to a 2.5-nm region. Even with this limitation, a judiciously chosen region of the spectrum may encompass lines from several different elements. Figure 2 is an absorption spectrum obtained during the atomization of 10 μL of the 19-element stock mixture (each element 10 mg/L). The strongest absorption line for antimony and a very strong line for lead are present. Four other elements have much stronger lines elsewhere, but even in this limited spectra window, each can be detected at sub-milligram-per-liter levels. Figure 3 is also an absorption spectrum obtained for the same mixture, but over a different wavelength region. The richness of the nickel spectrum demonstrates the greater informing power of this technique compared to that of single-wavelength conventional AAS. Figure 4 is an absorption spectrum of the same mixture showing the major chromium absorption line. Since the wavelength is above 300 nm, the spectrum was acquired by using the HR1000 monochromator in the fourth order. The fwhm of the absorption lines in this spectrum are quite similar to those in the other two spectra, showing that the resolution is not significantly degraded upon changing

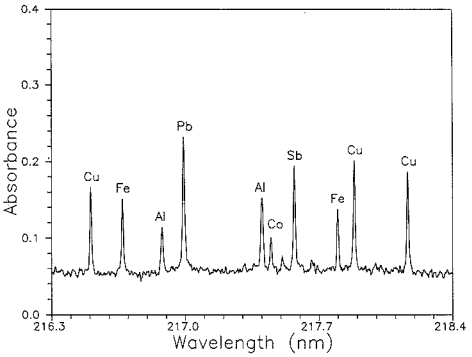

Figure 2. CSAAS spectrum of the 19-component mixture in the region of the major absorption line of antimony. Each element is present at 10 mg/L.

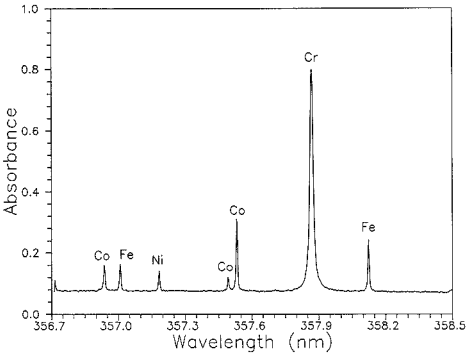

Figure 4. CSAAS spectrum of the 19-component mixture in the region of the major absorption line of chromium. Each element is present at 10 mg/L.

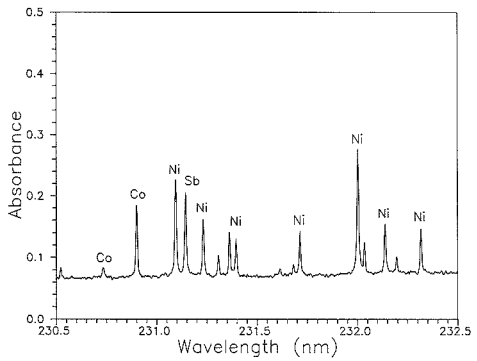

Figure 3. CSAAS spectrum of the 19-component mixture in the region of the major absorption line of nickel. Each element is present at 10 mg/L.

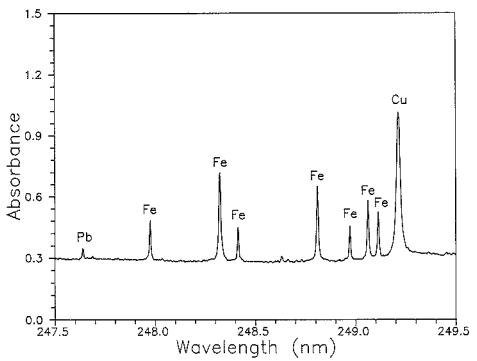

Figure 5. CSAAS spectrum of the NBS SRM No. 52 standard bronze dissolved in 10% nitric acid. The major absorption line of iron is shown at 248.3 nm.

from fifth to fourth order. The widening of the chromium line is due to collisional broadening rather than losses in spectral resolution.

Background Correction and Spectral Interferences. Background correction had long been a significant problem in graphite furnace CSAAS. The errors created by nonzero background absorbance are especially great in samples containing a large amount of solid particulates (*16*), or in complicated sample matrices such as urine (*17*). Wavelength modulation, a rapid, repetitive scanning procedure, seems to be the preferred method for automatic background correction in CSAAS (*18*). Unfortunately, this form of correction requires high-speed data acquisition and processing. A microcomputer-controlled system works nicely for this approach (*19*), and errors originating from nonsimultaneous measurement of analyte and reference signals have been evaluated theoretically (*20*).

In this work, the multiwavelength capabilities of the diode array are implemented to achieve background-corrected spectra without the need for wavelength modulation. Each absorption spectrum in Figures 2–4 is automatically background-corrected. The base line in each case is not positioned at 0.00 absorbance unit, but rather in the range of 0.06–0.08 absorbance unit. This apparent absorbance may arise from several sources. Small particles may be present in the furnace during atomization, causing a small fraction of the incident radiation to be scattered. Some molecular species may also be present, actually absorbing part of the radiation in a broad band. Also, slow downward drifts in the lamp intensity may occur between the measurement of I_0 and the absorption spectrum. Whatever the origin of this broad-band background may be, it is easily corrected for in the final spectrum. When the peak height is measured, the base line is automatically subtracted by use of the supplied software. Background absorption due to narrow-band sources such as molecular fine structure may still present problems due to the half-widths of the absorbing lines relative to the resolution inherent in the spectrometer.

A more pronounced example of the need for background correction can be seen in Figure 5. The absorption spectrum obtained for 10 μL of the NBS bronze solution has a base-line absorbance of 0.3 absorbance unit. Also, the large absorption line for copper (the major constituent in bronze) has wings that appear to extend underneath some of the iron lines. In both situations, the background is easily corrected. Figure 6 shows a case where a broad-band absorption covers the range of the spectrum. The spectrum was acquired during the atomization of 10 μL of seawater. The sloping base line in Figure 6 changed drastically during the atomization period. The iron peaks are easily detected upon the changing background.

Spectral interferences, though rare, have been directly observed in CSAAS (*21*). These interferences have also been corrected with the use of wavelength modulation (*22*). Such corrections are easily made with the diode array system without wavelength modulation.

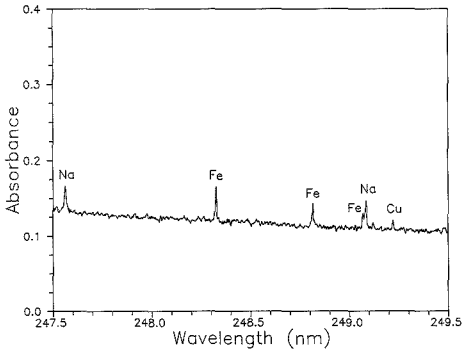

Figure 6. CSAAS spectrum of a seawater sample showing the major absorption line of iron.

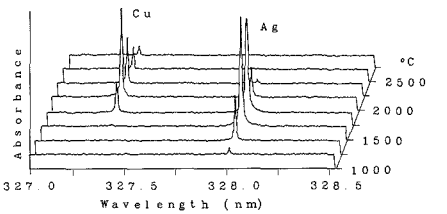

Figure 7. Three-dimensional plot of absorbance versus furnace temperature for a mixture containing silver and copper, each at 10 mg/L.

Figure 6 shows a good example of spectral interference. The sodium line just below 249.1 nm, although it is an extremely weak transition, interferes with an iron line due to the high concentration of sodium in seawater. The easiest solution to this problem is obvious; since several iron lines are present in the spectrum, another may be used for quantitation. Another approach for avoiding spectral overlap is demonstrated in Figure 7. The three-dimensional spectrum was acquired during a furnace heating ramp between 1000 and 2750 °C with a heating time of 3 s. Time-resolved graphite furnace CSAAS spectra are usually acquired without the added dimension of wavelength (*23*). In Figure 7, the silver is atomized prior to the copper. A similar heating ramp could separate absorption lines of elements that spectrally interfere on the basis of differences in their atomization temperatures; three-dimensional plots have other useful applications. The absorbance versus temperature profile adds identification power to an already powerful technique. Also, such a spectrum can be obtained for an unknown sample to determine the optimum atomization temperature.

Analytical Figures of Merit. Detection limits for the 19 elements tested are reported in Table II. Those detection limits found for this work compare well with the best previously reported detection limits for graphite furnace CSAAS. The best detection limits reported for commercially available line source graphite furnace AAS instruments are still 1–2 orders of magnitude lower than the best CSAAS results, especially below 250 nm. Again, this is a result of poor source intensity in this region. The xenon arc lamp has a sharp drop in intensity below 250 nm, as can be seen by the increase in background noise in Figure 2 at 217 nm compared to that in Figure 3 at 231 nm. As a result, the minimum detectable signal for arsenic at 193.7 nm is 0.011 absorbance unit, while that for nickel at 232.0 nm is 0.004 absorbance unit. The linear dynamic range for each element was between 1 and 2 orders of magnitude, with the calibration curves deviating significantly from linearity above 0.1 absorbance unit. This range can be greatly increased, however, by selecting less sensitive absorption lines when the major lines reach absorbance greater than 0.1. The nickel line at 232.2 nm for example is about 10 times less intense than the one at 232.0 (Figure 3), so the linear dynamic range could be extended an order of magnitude greater in concentration.

Table II. Absolute Limits of Detection Observed for Graphite Furnace CSAAS

element	wavelength, nm	limit of detection, pg: this work	limit of detection, pg: literature Val	line source[a]
Ag	328.1	10		0.1
Al	309.3	80	20[b]	1
As	193.7	700		8
Ba	553.5	300		4
Ca	422.7	60	2[c]	1
Cd	228.8	50		0.02
Co	240.7	10	20[c]	0.8
Cr	357.9	30	6[c]	0.4
Cu	324.7	3	2[c]	0.5
Fe	248.3	4	10[d]	1
Li	670.8	7		1
Mg	285.2	0.1	0.6[c]	0.02
Mn	279.5	10	2[c]	0.05
Na	589.0	0.9	10[c]	0.4
Ni	232.0	80	30[b]	5
Pb	283.3	80		0.7
Sb	217.6	500		8
Sr	460.7	50		1
Zn	213.9	100	8[c]	0.1

[a] Detection limits reported in manufacturer's literature for Thermo Jarrell Ash spectrometers, 1988. [b] Taken from ref 8. [c] Taken from ref 6. [d] Taken from ref 7.

The sampling precision for several elements was checked by performing 16 successive atomizations. In each case the relative standard deviation was below 10%. The precision for a single atomization can be greatly increased if several absorption lines for one element occur within the spectral window. The 11 nickel lines in Figure 3, for example, could each be used to make quantitative measurements for a sample of unknown nickel concentration. In this case, the precision of the technique would be better than that of a single-line method by a factor of $(11)^{1/2}$. The accuracy of the method was tested by comparing the iron concentration found in the NBS bronze standard to its certified value. The calculated value was 0.107 ± 0.009% (in the metal) with 95% confidence limits. The NBS certified value for SRM No. 52 is 0.117 ± 0.012%.

CONCLUSIONS

Graphite furnace CSAAS with diode array detection offers several advantages over normal CSAAS measurements. The unique wavelength versus absorbance spectra make background correction easier, and spectral interferences are less important. Similar spectra could be obtained by using a mechanically scanned monochromator and a single detector, but to have the same signal-to-noise ratio for such a spectrum, an increase in analysis time of a factor of 1024 would be incurred. Since each photodiode views the sample for 0.33 s per spectrum, a scanned spectrum would have to reside on each resolution element for 0.33 s, making the total analysis time 338 s. The short residence time of the atomic vapor during the atomization step prevents such a long analysis time. The increased informing power of the diode array system improves the confidence level of unknown measurements, while increasing the precision of the technique. The limited spectral range of a single measurement imposed by the diode array can be overcome by making repetitive atomizations. By

judiciously choosing the region for each spectral measurement, one can minimize the number of necessary atomization steps.

Registry No. Ag, 7440-22-4; Al, 7429-90-5; As, 7440-38-2; Ba, 7440-39-3; Ca, 7440-70-2; Cd, 7440-43-9; Co, 7440-48-4; Cr, 7440-47-3; Cu, 7440-50-8; Fe, 7439-89-6; Li, 7439-93-2; Mg, 7439-95-4; Mn, 7439-96-5; Na, 7440-23-5; Ni, 7440-02-0; Pb, 7439-92-1; Sb, 7440-36-0; Sr, 7440-24-6; Zn, 7440-66-6; bronze, 12597-70-5; water, 7732-18-5.

LITERATURE CITED

(1) Fassel, V. A.; Mossotti, v. G.; Grossman, W. E. L.; Kniseley, R. N. *Spectrochim. Acta* **1966**, *22*, 347–357.
(2) O'Haver, T. C. *Analyst* **1984**, *109*, 211–217.
(3) Marshall, J.; Ottaway, B. J.; Ottaway, J. M.; Littlejohn, D. *Anal. Chim. Acta* **1986**, *180*, 357–371.
(4) Harnly, J. M. *Anal. Chem.* **1986**, *58*, 933A–943A.
(5) O'Haver, T. C.; Messman, J. D. *Prog. Anal. Spectrosc.* **1986**, *9*, 483–503.
(6) Harnly, J. M.; Miller-Ihli, N. J.; O'Haver, T. C. *Spectrochim. Acta* **1984**, *39B*, 305–320.
(7) Harnly, J. M.; Kane, J. S. *Anal. Chem.* **1984**, *56*, 48–54.
(8) Lewis, S. A.; O'Haver, T. C.; Harnly, J. M. *Anal. Chem.* **1985**, *57*, 2–5.
(9) Cochran, R. L.; Hieftje, G. M. *Anal. Chem.* **1977**, *49*, 2040–2043.
(10) O'Haver, T. C.; Harnly, J. M.; Zander, A. T. *Anal. Chem.* **1978**, *50*, 1218–1221.
(11) Harnly, J. M. *Anal. Chem.* **1984**, *56*, 895–899.
(12) Talmi, Y.; Simpson, R. W. *Appl. Opt.* **1980**, *19*, 1401–1414.
(13) Epstein, M. S.; Zander, A. T. *Anal. Chem.* **1979**, *51*, 915–918.
(14) Tittarelli, P.; Lancia, R.; Zerlia, T. *Anal. Chem.* **1985**, *57*, 2002–2005.
(15) Shekiro, J. M., Jr.; Skogerboe, R. K.; Taylor, H. E. *Anal. Chem.* **1988**, *60*, 2578–2582.
(16) Harnly, J. M.; O'Haver, T. C. *Anal. Chem.* **1977**, *49*, 2187–2193.
(17) Guthrie, B. E.; Wolf, W. R.; Veillon, C. *Anal. Chem.* **1978**, *50*, 1900–1902.
(18) O'Haver, T. C. *Anal. Chem.* **1979**, *51*, 91A–100A.
(19) O'Haver, T. C.; Harnly, J. M.; Marshall, J.; Carroll, J.; Littlejohn, D.; Ottaway, J. M. *Analyst* **1985**, *110*, 451–458.
(20) Harnly, J. M.; Holcombe, J. A. *Anal. Chem.* **1985**, *57*, 1983–1986.
(21) Miller-Ihli, N. J.; O'Haver, T. C.; Harnly, J. M. *Anal. Chem.* **1982**, *54*, 799–803.
(22) Zander, A. T.; O'Haver, T. C.; Keliher, P. N. *Anal. Chem.* **1977**, *49*, 838–842.
(23) Miller-Ihli, N. J.; O'Haver, T. C.; Harnly, J. M. *Appl. Spectrosc.* **1983**, *37*, 429–432.

RECEIVED for review January 30, 1989. Accepted May 1, 1989. This research was supported by NIH 5 R01 GM38434-02.

Polymer-Coated Cylindrical Waveguide Absorption Sensor for High Acidities

W. Patrick Carey* and Michael D. DeGrandpre[1]

Chemical and Laser Science Division, G740, Los Alamos National Laboratory, Los Alamos, New Mexico 87545

Betty S. Jorgensen

Material Science and Technology Division, E549, Los Alamos National Laboratory, Los Alamos, New Mexico 87545

The development of a chemical sensing scheme for the detection and quantitation of greater than 1 M concentration of acids, particularly nitric acid, is presented with the overall goal of using this chemistry to create optical sensors. The detection chemistry is based on the physical entrapment of Hammett indicators in a polymer blend of polybenzimidazole and polyimide, which is silane-coupled to optical elements. The polymer coating protects the optical element from chemical attack, and its hydrophilic nature and low porosity make the sensor more selective. By use of the indicator chromazurol-S, nitric and hydrochloric acid concentrations ranging from 2 to 10 M can be measured with a precision of 0.05 M. Indicators that cover a range of 0.5–10.0 M acid concentrations have also been investigated. Cylindrical waveguide sensors, using both a fiber optic and a sapphire rod with the immobilized polymer chemistry, were constructed based on the absorption of light by the acid indicator, chromazurol-S. Because of the difference in the refractive index of the optical elements and the polymer material, separate detection techniques for the two sensors are presented. The fiber-optic sensor uses an absorption measurement of a thin film, and for the sapphire rod, an evanescent field absorption process occurs.

INTRODUCTION

A variety of fiber-optic sensors have been developed for measuring pH through the immobilization of common colorimetric indicators (*1–3*). Most of these were constructed to operate in the physiological pH region. However, there are many chemical processes where the acidity is below pH 0 and outside the normal range of measurement for both fiber-optic sensors and pH electrodes. One example of a high-acid process is the separation of rare-earth metals, where optimal operating conditions require maintaining a level of 7.5 M nitric acid. An on-line sensor to monitor the acidity would greatly increase the efficiency of the process and minimize operating costs. Therefore, a high-acidity in situ sensor needs to be developed for these applications.

In the early 1930s, Hammett and Deyrup conceived the Hammett (H_0) acidity function as a measure of hydrogen ion concentration in molar levels of acids. This system is based on optical absorption changes caused by the protonation of weak bases such as substituted anilines (*4–6*). The basicity of the amine lone pair can be adjusted with the addition of electron-donating or -withdrawing groups on the benzene ring. For example, acid ranges from 0.1–10.0 M can be measured with a combination of several nitro and chloronitroaniline derivatives. Similarly, more complex compounds with multiple benzene rings and amine or other weak base functionalities also exhibit characteristics of Hammett indicators.

In this study, various Hammett indicator analogues such as chromazurol-S, methyl violet B, victoria blue, rhodamine B, and methyl green $ZnCl_2$ were examined for their response to acid conditions between 1 and 10 M. These indicators were tested in a polybenzimidazole (PBI) and polyimide (PI) matrix that was silane-coupled to a glass microscope slide. Dynamic range and reproducibility studies were performed to choose an indicator with a response in the 4–10 M range. The next step was to immobilize the selected indicator system to a

[1] Current address: Department of Chemistry, BG-10, University of Washington, Seattle, WA 98195.

0003-2700/89/0361-1674$01.50/0

cylindrical waveguide and to use the evanescent field penetration of visible light to monitor the absorption changes of the indicator with various acid concentrations.

Evanescent field spectroscopy was developed for chemical analysis by Harrick (7) and Fahrenfort. Their technique, attenuated total reflection spectroscopy (ATR), uses planar optical waveguides with precise control of the launch angle and polarization. Using evanescent field sensing through fiber optics or cylindrical rods is a relatively recent advancement of the technique (8–10). Although the launch angle and polarization are not sustained in multimode cylindrical waveguides, they offer greater sensitivity than do conventional ATR methods because of the longer path length and increased number of reflections. In this sense, evanescent field spectroscopy is changed from a characterization tool to a practical approach for quantitative chemical analysis.

The same virtues of other fiber-optic chemical sensors such as optrodes (11) apply to cylindrical waveguide sensors. These advantages include immunity to electrical interferences, remote and in situ operation, broad spectral coverage (0.3–2.0 μm for fused silica, 0.2–5.0 μm for sapphire), and the ability to be multiplexed to a single instrument. An evanescent field sensor can be made more sensitive than a reflectance type optrode, at the expense of sensor size. Moreover, the sensor can be designed to accommodate the sensitivity required for a specific application by selection of appropriate fiber length and diameter, core and cladding (polymer coating) refractive indices, and fiber bend radius if a coiled sensor is used (10).

Long lengths (>1 cm) of modified commercial fiber optics for evanescent field spectroscopy are difficult to implement because of the extremely fragile and polar nature of the exposed core (typically glass or fused silica). In this work, the PBI/PI polymer coating protected the modified portion of the fiber optic from chemical attack, chemical interferences, and stresses. Indicators were incorporated into the polymer as a transducer for nitric and hydrochloric acid, neither of which have intrinsic absorbances in the wavelength region used for the analysis.

EXPERIMENTAL SECTION

Polymer/Indicator Immobilization. The polymers PBI (Celanese Corp.) and polyisoimide (Thermid IP 630, National Starch and Chemical Corp.) were dissolved in *N,N*-dimethylacetamide (DMAC) (Aldrich) to make a 10% solution and were blended in a 1:1 mixture. Approximately 0.5 g of the indicator was dissolved per 100 mL of polymer solution. The polymer solution was silane-coupled to the optical elements in order to provide adhesion when exposed to highly acidic solutions. (This procedure extended the adhesion of the polymer from 5 min to at least 12 weeks.) A glass slide, a fiber-optic core of a stripped fiber (200 μm core PCS, Fiberguide Industries), and a sapphire rod (1 mm diameter, Saphikon) were treated with a 2% aqueous solution of (chloropropyl)trimethoxysilane for 15 min, washed with distilled water, and heated in air (110 °C) for 30 min. The substrates were then dip-coated with the polymer mixture and allowed to cure at 175 °C for 24 h. Film thickness was dependent on the withdrawal speed of the optical materials from the polymer solution and the concentration of the polymer/indicator mixture. Film thicknesses on the order of 1–3 μm were obtainable by this method, as estimated by using the method of interference patterns from weakly absorbing materials (12) and by scanning electron microscope cross sections of the coated fiber.

Evaluation. Preliminary studies of the indicator response characteristics were performed with coated glass slides using a Hewlett-Packard 8451A diode array spectrophotometer. Standardized nitric and hydrochloric acid solutions from 0.5 to 10.5 M were used throughout the study. The fiber-optic and sapphire rod sensors were constructed in a single beam arrangement, shown in Figure 1. For the fiber-optic sensor, 15 cm of the jacket and cladding was stripped from one end and coated with the above procedure up to the unstripped cladding. The coated portion of the fiber was inserted into a flow cell consisting of low dead volume

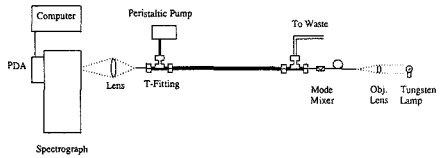

Figure 1. Diagram of instrumental setup involving the polymer-coated cylindrical waveguides.

Table I. Immobilized Indicator Evaluation in Nitric Acid

indicator	response range, AU	acid range, M	λ_{max}, nm
rhodamine B	0.5	0.5–8	522
methyl green ZnCl	0.25	0.5–4	590
victoria blue	0.3	0.5–5	600
methyl violet B	1.0	0.5–8.5	630
chromazurol-S	1.4	2–10	546

T-fittings with Teflon ferrules connected to Teflon tubing and a peristaltic pump. The flow cell arrangement for the sapphire rod consisted of larger tubing and T-fittings and had an overall length of 19 cm for the 25 cm long rod.

Light from a tungsten lamp was focused into the fiber optic with a 10× objective lens (numerical aperature (NA) = 0.25) completely filling the light acceptance cone of the 0.24-NA fiber. A mode scrambler (Newport FM-1) was inserted before the sensor section to ensure that the response was independent of launch conditions. Illumination for the sapphire rod sensor used a 0.24-NA optical fiber butted to the sapphire rod endface near the entrance of the flow cell, underfilling the 0.56-NA sapphire rod.

The sensor output (both fiber optic and sapphire rod) was focused into a single grating spectrograph (*f*/3.8, Aries Monospec 27) fitted with a photodiode array detector (Tracor-Northern 6500). A 150-groove/mm grating dispersed light from 300 to 720 nm across the active elements of the diode array. The resolution of the instrument is approximately 4 nm.

All solution refractive index measurements were performed with an Abbe refractometer.

RESULTS AND DISCUSSION

Polymer/Indicator Selection. The polymer system used to immobilize the organic indicators on the optical elements was characterized on glass slides before the experimentation with cylindrical waveguide sensors. When the original Hammett indicators, such as *o*-nitroaniline, were used, bleeding of the organic dye from the PBI polymer occurred. Polymer blends, such as PBI mixed with PI, change the pore size of the structure, allowing transport rates and properties to be varied. A ratio of 1:1 PBI/PI was determined to be optimum for both fast response time and elimination of indicator bleeding.

Absorbance spectra of the polymer/indicator coatings immobilized on glass slides were taken in various acid (nitric or hydrochloric) concentrations. The PBI/PI blend has a broad-band UV absorption from 300 to 415 nm in acidic media. The absorbance of the PBI/PI mixture is sensitive to changing acid concentrations because of protonation of the secondary amine present in the structure, but this feature is not well characterized due to the high optical density of the polymer. The classical Hammett indicators absorb from 350 to 450 nm, overlapping this polymer absorbance spectrum. Because the polymer absorption ends at 415 nm, the Hammett indicators that absorb in the visible region of the spectrum can be monitored easily.

The sensitivity and the wavelength of maximum absorption of various indicators that have been tested for their responses in nitric acid are listed in Table I. The indicator chromazurol-S was the most promising for monitoring a process where

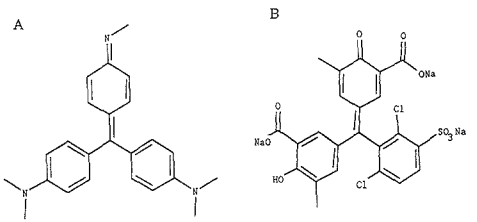

Figure 2. Molecular structures of Hammett indicators (A) methyl violet B and (B) chromazurol-S.

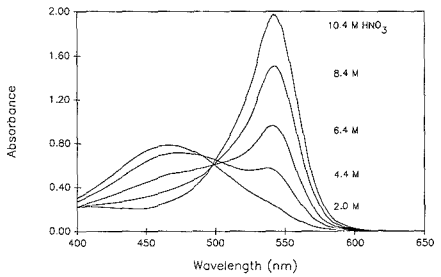

Figure 3. Absorbance spectra of chromazurol-S immobilized onto glass slide with PBI/PI in nitric acid solutions.

acid conditions in the 4–10 M range are frequently encountered. This indicator has the highest sensitivity and covers the concentration region needed for our application. All of the other indicators, such as methyl violet B in Figure 2, are amine derivatives that respond in the 1–6 M acid range. Chromazurol-S responds in the 4–10 M acid region because of its weakly basic carbonyl functionality, and the structure was more stable in the acidic environment than that of the amines.

The absorbance spectra of chromazurol-S in the PBI/PI polymer mixture at different levels of nitric acid are presented in Figure 3. The indicator has absorbance maxima at 470 and 546 nm and an isosbestic point at 500 nm. The 470-nm band (base form) decreases with increasing acid concentration, and the 546-nm band (acid form) simultaneously increases. This type of response aids in calibration because acid concentrations can be based on pattern identification or peak intensity ratios only, without the need for intensity reproducibility over long periods of time.

The longevity of the coated slides with immobilized chromazurol-S and methyl violet B was tested. They withstood nitric acid for an average period of 8 weeks with partial functionality intact. When the slides were soaked in 8.8 M nitric acid, the signal intensity of the 546-nm band of chromazurol-S degraded approximately 9% after 1 week, whereas the 630-nm band of methyl violet B degraded 51% in the same period of time in 4.4 M nitric acid. These results were similar for hydrochloric acid at the same concentrations.

The responses of chromazurol-S and methyl violet B were tested for possible interferences from the nitrate salts of sodium, calcium, and thorium. No interferences were detected from salt concentrations ranging from 0.1 to 1.5 M in 4 M nitric acid. Whether the aqueous metal complexes can penetrate the porous polymer is unknown, but no interaction would be expected to take place between the metal ions and the indicators at these acid concentrations.

The sensitivity and reproducibility of the polymer-immobilized chromazurol-S, to both nitric and hydrochloric acid, are presented in Figure 4. The sensitivity to hydrochloric acid is much greater than to nitric acid for this indicator

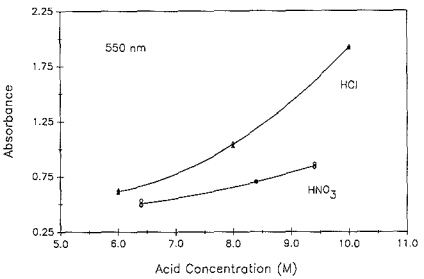

Figure 4. Signal response at 550 nm for chromazurol-S for hydrochloric and nitric acids.

because of the relative degree of dissociation of the two acids. The degree of dissociation of nitric acid drops off rapidly at approximately 4 M concentration (*13*). The random error of the spectrophotometer response at all acid levels for chromazurol-S in each acid is approximately the same at 0.012 AU. For the indicator chromazurol-S, the relative error in the signal at the mean of the response curves in Figure 4 is 1.2% for hydrochloric acid and 1.9% for nitric acid.

Fiber-Optic Absorption Sensor. Because the refractive index (RI) of the PBI/PI coating (RI = 1.67 in distilled water) was greater than that of the fused silica fiber optic (RI = 1.46), it was possible to operate the fiber-optic sensor in two different ways, depending on polymer coating thickness. If the coating thickness is on the order of the wavelength propagated, the guided light will be refracted into the polymer coating and either be totally guided in the polymer or traverse the core and polymer. This inverted waveguide structure has been used by other researchers as a gas-phase chemical sensor (*14*). There are disadvantages to using the inverted waveguide sensor in liquid media. Penetration of the thin polymer film by the liquid phase will often change the optical properties and dimensions (swelling) of the coating, which can result in the appearance of intensity maxima and minima during ratio calculations in a broad-band transmission. This effect was evident with PBI/PI coatings of 0.5–3 μm, which exhibited spectral shifts and intensity changes that completely masked the indicator response. A study of the PBI/PI films on glass slides (no indicator), using the interference fringe method described in ref 12, indicated that the polymer blend swelled nearly 8% when transferred from an environment of distilled water to 8 M nitric acid.

These unwanted effects may be circumvented by making the coating much thinner than 1 μm (nearly a monolayer). Under these conditions, no interference can be observed and total internal reflection occurs at the solution/polymer interface (*15*). Since the polymer film is much thinner than the wavelength of light being propagated, light at the polymer/fused silca interface is only being refracted and not reflected back into the polymer in the same manner as an inverted waveguide.

The results of a fiber-optic sensor operating by an absorption interaction are shown in Figure 5. The reference spectrum was taken from transmission through the coated fiber when it was in 2.0 M nitric acid. The absorbance band of the protonated form of chromazurol-S appears at about 550 nm. The large offsets at the nonabsorbing wavelengths (beyond 600 nm) are due to the RI changes of the nitric acid solutions, indicating that the waveguide is evanescently coupled to the sensing medium. Figure 6 shows that the nitric acid solutions fall on the same curve as variable RI sucrose solutions measured by this sensor at 700 nm. This result supports the assumption that the polymer film is thin enough to avoid interferences from swelling in the acid solution.

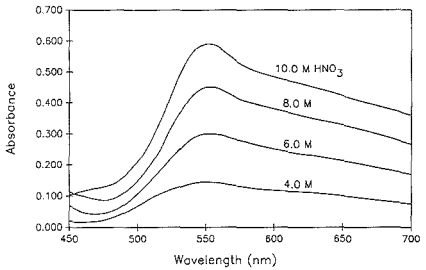

Figure 5. Absorption spectra of chromazurol-S in PBI/PI immobilized onto a silica core fiber referenced to 2.0 M nitric acid.

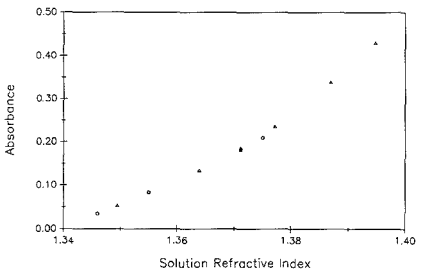

Figure 6. Signal response of fused silica sensor at 700 nm to varying refractive index solutions of sucrose (O) and nitric acid (Δ).

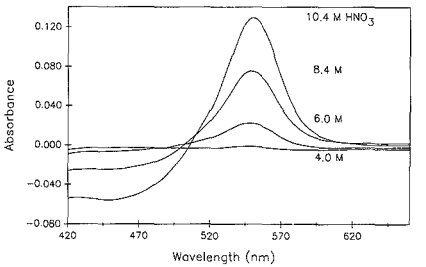

Figure 7. Evanescent field absorption spectra of immobilized chromazurol-S in PBI/PI on a sapphire rod referenced to 3.0 M nitric acid.

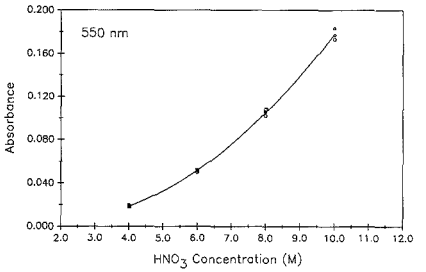

Figure 8. Response curve of the 550-nm absorbance band of chromazurol-S on sapphire rod to nitric acid.

Although the response is still dependent on RI, it is a broad band offset with a slight slope most probably due to wavelength RI dispersion. The base form of the indicator absorbs at 470 nm (Figure 3). The decreasing absorbance in this region is offset by the attenuation caused by the increase in RI around the sensor. Below 450 nm, the polymer interferences begin to appear.

In a study of the response characteristics of the coated silica fiber, noise and reproducibility measurements were taken. Peak-to-peak noise measurements indicated a detection limit of 5×10^{-4} AU (3 × root mean square noise) for the coated fiber-optic sensor (100 scans, 5-s acquisition time). Seven replicate samples at three acid levels were monitored, resulting in an overall 1.65% relative error in the absorbance signal. This error closely matches the 1.9% relative error obtained on the microscope slides for nitric acid. A linear regression line was fitted to the absorbance values at 550 nm, showing evidence that the solution refractive index offset has some effect on the signal since the absorbance of the 546-nm band of the indicator has a nonlinear relationship (see Figure 4) to acid concentration. (Subtraction of the 700-nm band from the 550-nm signal was not conducted since there is a wavelength dependence upon refractive index attenuation.) Predictions of unknown samples using this calibration line at 7.0 M nitric acid yielded a standard error of prediction of 0.06 M.

Sapphire Rod Evanescent Field Sensor. By use of an optical material such as sapphire (RI = 1.76) with a refractive index greater than that of the PBI/PI polymer mixture, evanescent field sensing can take place without the refractive index effects of the solution as seen above. Figure 7 shows the absorbance spectra taken from a coated sapphire rod with 3.0 M nitric acid used as a reference. The two absorbing bands of chromazurol-S follow the same trend as that shown in Figure 3. The 470-nm band decreases in absorbance with increasing acid concentration, thus providing a negative absorbance in these spectra. At 550 nm, the band is increasing in absorbance similar to the one in Figure 3 with increasing acid concentration. At the lower wavelengths near 420 nm, the effects of the polymer absorption are evident by the nonreturning base line. Base-line shifts due to RI changes are evident beyond 600 nm, but are substantially less than that of the fused silica sensor (Figure 5). This supports previous results that indicated insensitivity to RI changes when the core RI is much higher than the surrounding matrix RI (*10*).

Noise measurements to estimate the detection limit for the sapphire rod evanescent field sensor were tested and calculated to be approximately 8×10^{-4} AU (3 × root mean square noise with 150 scans and 7.5-s acquisition time). The sensor response to nitric acid for the 550-nm absorbance band is presented in Figure 8. A second-order regression curve is fitted through the data points representing a sensitivity similar to that obtained in Figure 4 for chromazurol-S immobilized on a microscope slide. As a measure of sensor reproducibility, the absorbance signals had a relative error of 2.8%. This error is larger than for both the microscope slide and silica fiber sensor, primarily because of the larger dead volume in the flow cell for the sapphire rod. The corresponding standard error of prediction from this calibration curve is 0.05 M nitric acid with an unknown sample at 7.0 M. Although the sensitivity of the sapphire rod sensor is more than adequate for our application, it may be further improved by launching light nearer to the critical angle (*7*). This may be accomplished by using a high NA input fiber or by launching the light into the sapphire rod off axis.

This paper has demonstrated two techniques in the application of optical sensors for high-acidity processes. The first is a unique immobilization method for optical acid indicators in porous polymers. This technique proved to be rugged and reliable in the hostile conditions of the system under study. The second important technique is the application of evanescent field spectroscopy using cylindrical waveguides. Although there have been previous studies using

evanescent field sensing, this work has shown its usefulness in remote in situ process monitoring when specific chemistries are applied to the waveguide. The sensors provide an adequate signal-to-noise ratio and reproducibility with a fast response time (2 min after encountering the sample) for in situ measurements.

ACKNOWLEDGMENT

We thank Lloyd Burgess for many helpful discussions during the course of this work.

LITERATURE CITED

(1) Jones, T. P.; Porter, M. D. *Anal. Chem.* **1988**, *60*, 404–406.
(2) Kirkbright, G. F.; Narayanaswamy, R.; Welti, N. A. *Analyst* **1984**, *109*, 1025–1028.
(3) Munkholm, C.; Walt, D. R.; Milanovich, F. P.; Klainer, S. M. *Anal. Chem.* **1986**, *58*, 1427–1430.
(4) Dawber, J. G.; Wyatt, P. A. H. *J. Chem. Soc.* **1960**, 3589–3593.
(5) Paul, M. A.; Long, F. A. *Chem. Rev.* **1957**, *56*, 1–45.
(6) Rochester, C. H. *Acidity Functions*; Academic Press: New York, 1970.
(7) Harrick, N. J. Internal Reflection Spectroscopy; Interscience: New York, 1967.
(8) Simhony, S.; Kosower, E. M.; Katzir, A. *Appl. Phys. Lett.* **1986**, *49*, 253–254.
(9) Paul, P. H.; Kychakoff, G. *Appl. Phys. Lett.* **1987**, *51*, 12–14.
(10) DeGrandpre, M. D.; Burgess, L. W. *Anal. Chem.* **1988**, *60*, 2582–2586.
(11) Seitz, W. R. *Anal. Chem.* **1984**, *56*, 16A–34A.
(12) Manifacier, J. C.; Gasiot, J.; Fillard, J. P. *J. Phys. E.* **1976**, *9*, 1002–1004.
(13) Chedin, M. J. *J. Chim. Phys.* **1952**, *49*, 109–125.
(14) Smock, P. L.; Orofino, T. A.; Wooten, G. W.; Spencer, W. S. *Anal. Chem.* **1979**, *51*, 505–508.
(15) Russell, A. P.; Fletcher, K. S. *Anal. Chim. Acta* **1985**, *170*, 209–216.

RECEIVED for review March 14, 1989. Accepted May 1, 1989.

Picogram Level Quantitation of 2,3,7,8-Tetrachlorodibenzo-*p*-dioxin in Fish Extracts by Capillary Gas Chromatography/Matrix Isolation/Fourier Transform Infrared Spectrometry

Magdi M. Mossoba,* Richard A. Niemann, and Jo-Yun T. Chen

Division of Contaminants Chemistry, Food and Drug Administration, 200 C St., S.W., Washington, D.C. 20204

For the first time, gas chromatography/matrix isolation/Fourier transform infrared spectrometry (GC/MI/FTIR) has been reported to confirm the identity of 2,3,7,8-tetrachlorodibenzo-*p*-dioxin (2378-TCDD) and to quantify its level in fish extracts in the 170–220 pg range "on disk". When expressed on a fish tissue basis, analyte levels ranged from 15 to 45 pg/g. Spectroscopic identification was based on the position and relative intensity of seven absorption bands. Optical alignment as well as performance evaluation and optimization of the GC/MI/FTIR system are described. The use of [$^{13}C_{12}$]2378-TCDD as an internal standard was essential for quantitation, and quality assurance controls were used to verify system performance. GC/MI/FTIR quantitation of 2378-TCDD was compared with that independently found by GC with electron capture detection. Recovery of 2378-TCDD averaged 52% (n = 8, 30% relative standard deviation) for fish extracts.

2,3,7,8-Tetrachlorodibenzo-*p*-dioxin (2378-TCDD) (*1*) is an environmental contaminant that has received considerable attention. Concern over its extreme toxicity to laboratory test animals has required application of analytical methods at the pg/g (parts per trillion, pptr) level. Capillary gas chromatography/mass spectrometry (GC/MS) in the selected ion mode has been the preferred technique for measuring dioxins because of high sensitivity and structure specificity, but dioxin isomers generally cannot be distinguished by electron impact GC/MS. Capillary GC/Fourier transform infrared spectrometry (GC/FTIR) logically complements GC/MS by providing information on isomer identity (*2*). However, on-the-fly GC/FTIR has inadequate sensitivity for 2378-TCDD residue application. The GC/matrix isolation/FTIR technique (GC/MI/FTIR) (*3*, *4*) has greater sensitivity, since the chromatographically separated components are trapped at 12 K in a microscopic argon matrix, thus allowing an increase in the FTIR spectral acquisition time. Because each analyte molecule is isolated in a cryogenic solid matrix of IR-transparent argon atoms, a decrease in the absorption bandwidths may be observed, leading to an increase in band absorbances. GC/MI/FTIR instrumentation has been used to obtain spectra of the 22 TCDD isomers (*5*, *6*), the $^{13}C_{12}$-labeled and the unlabeled (^{12}C) 2378-TCDD (*7*), but these studies were limited to standards and/or to analyte levels one or more orders of magnitude greater than would normally be isolated from a biological matrix such as fish.

Unequivocal spectroscopic identification of compounds at subnanogram levels has already been achieved by GC/MI/FTIR (*4*, *7*, *8*). The observed positions and relative intensities of FTIR bands allowed spectral interpretation at these levels.

We have used GC/MI/FTIR to confirm the identity of 2378-TCDD in fish extracts and to quantitate it at the picogram level. In this paper we describe procedures for optimization of detectability and calibration and the use of an isotopically labeled [$^{13}C_{12}$] 2378-TCDD as an internal standard. We have also identified several extract components that are potential interferences.

EXPERIMENTAL SECTION

Gas Chromatography and Cryolect Interface. Gas chromatographic separations were performed on a Hewlett-Packard Model 5890 equipped with a ^{63}Ni electron capture (EC) detector and connected to a Hewlett-Packard 3392A integrator. A 25 m × 0.20 mm i.d. cross-linked methyl silicone capillary column, 0.33 μm stationary phase (Hewlett-Packard), was used throughout this study. Helium containing 1.5% argon (Matheson Gas Products)

at approximately 27 cm/s linear velocity was used as carrier gas, and nitrogen (99.999%) at 45 mL/min was used as the make-up gas to the EC detector. The injector and detector temperatures were 250 and 350 °C, respectively. The carrier and make-up gases were passed through filters which removed traces of moisture (Alltech Associates Hydro-Purge II) and oxygen (Supelco Gas Purifier and MG Scientific Gases Oxisorb, for He/Ar and N_2, respectively). Splitless injections of 1–3 μL of isooctane solutions were made over 10–15 s, and the injector was purged at 2.75 min. The initial column oven temperature was 75 °C with a 2-min hold, followed by a 20 °C/min increase to 270 °C, and the column oven was held at this temperature until the separation was complete.

The Cryolect interface (*9*) as supplied (Mattson Instruments, Madison, WI) required some modification and considerable optimization. The end of the capillary column exited through the top of the oven and was connected to one end of a union (SGE, Austin, TX) attached to a small, cartridge-heated block placed on the top oven wall insulation. At the other end of the union the effluent was split. Two splitter unions were tested. The first was Model VSOS (SGE), a stock item, which had exposed stainless steel at the conical end where the effluent is split. The second was a specially fabricated all-glass-lined (silanized deactivated) union (SGE) which was found to be more satisfactory in preserving TCDD peak shape. The column effluent was split to two pieces of fused silica tubing, each 0.7 m long: a 0.17 mm i.d. piece went back into the column oven and was inserted into the EC detector, while a 0.20 mm i.d. piece was connected to an open-split interface (Valco cross) located on top of the heated block. Connected to the opposite port of the cross was the 0.17 mm i.d. × 1 m heated (270 °C) fused silica transfer line to the evacuated chamber (10^{-6} Torr) in which the cryogenic (11–12 K) collection disk was located. The remaining two perpendicular cross ports served as a pneumatic switch.

Whenever deposition on disk was not required, purified helium swept across these two other ports at 60 mL/min to vent the column effluent away from the transfer line going to the collection disk. During the deposition cycle, the helium flow was cut back to 0.1 mL/min, which allowed carrier gas from a line that is T-connected to the vent line to flow into the cross as a make-up between the total flow through the collection disk transfer line (1 mL/min) and the column flow into the cross (0.9 mL/min). Since column flow rate was nearly equal to the maximum flow through the transfer line, loss of analyte was avoided by setting the carrier gas make-up flow rate to half its recommended value, i.e., to 2.5 mL/min. Peak absorbance measured on disk then increased 20%. The splitter union, splitter lines, and open-split interface were all covered with insulation, and the block was heated to 270 °C. The column effluent split ratio was calculated from EC response factors (area counts per nanogram injected) obtained with 10-ng injections of 1234-TCDD made with the column attached to the splitter union, and again with the column outlet directly inserted into the EC detector. A ratio of 99.5:0.5 was so determined, with the smaller portion going to the EC detector.

MI/FTIR Instrumentation. A Mattson Instruments Sirius 100 FT-IR spectrometer equipped with a Cryolect matrix isolation unit was used. The Cryolect system has been described in detail (*3*, *4*, *9*), except for the optical bench alignment procedure, which will be discussed here. The IR beam from the spectrometer is focused onto the frozen argon matrix by the first mirror of an independently adjustable double parabolic mirror assembly. The gold-plated mirror surface of the collection disk reflects the transmitted light back through the matrix to the second mirror of the assembly. The light then travels to a third parabolic mirror which focuses the beam onto the element surface area, 760 × 760 μm^2, of a narrow band (750 cm^{-1} cutoff), high sensitivity mercury cadmium telluride (MCT) detector cooled to liquid nitrogen temperature. The IR beam must be focused on the cryogenic disk as a microscopic circular dot which samples the analyte preserved in frozen argon. Otherwise, an optically distorted beam will degrade the spectroscopic signal and the IR-reconstructed chromatographic peak shape.

The Cryolect optical bench alignment used an external helium–neon gas laser mounted along the spectrometer output light scribe line. To align the spectrometer and the Cryolect optical benches, a flat mirror was placed on the Cryolect bench and its position adjusted between the second and third parabolic mirrors along the light path until the reflected laser light fell on the laser source aperture. Next the position of each of the two mirrors of the double parabolic mirror assembly was independently adjusted so that the incident and reflected laser beams were visible at only one spot on the gold-plated collection disk. The external laser was then removed, and a quartz beam splitter was substituted for the KBr beam splitter. By use of two alignment stands placed on the spectrometer output beam scribe line, the position of the flat mirror that diverts the beam toward the Cryolect bench was optimized. With the iris set at its smallest aperture, the focus of each of the two parabolic mirrors of the assembly was further adjusted so that the incident circular image of the source visually overlaid the reflected image on the collection disk. After the KBr beam splitter was reinstalled and the flat mirror on the Cryolect bench was removed, the second and third parabolic mirrors were successively adjusted until the interferogram centerburst was maximized. The vacuum chamber was pumped down and the disk cooled to 11 K. By use of a quartz beam splitter again, the height of the double parabolic mirrors assembly unit was visually adjusted such that the beam is focused onto a 343-μm diameter reference notch drilled (number 80 drill bit, 0.0135 in. (0.343 mm)) into the collection disk; the height of the deposition tip of the transfer line had also been adjusted to that of the reference notch. The KBr beam splitter was reinstalled and the interferogram was remaximized, giving 12.7 V at 5% iris aperture. Fine tuning adjustments were made to the double parabolic mirror assembly by monitoring the major band absorbance of 8–10 ng of 1234-TCDD on disk. It was observed that a 5% iris yielded a slightly higher absorbance value than did other apertures, which implied that the source image at the disk was probably optimally matching the size of the frozen analyte.

Standards and Quality Assurance Solutions. All solutions were prepared in isooctane (Burdick & Jackson, distilled in glass). A 7.9 ng/μL solution of 1234-TCDD was used to optimize instrument performance. A 500 pg/μL working stock solution of 2378-TCDD was prepared from a concentrated standard (KOR Isotopes, Cambridge, MA). An aliquot of the working stock solution was used to prepare a 4.0 pg/μL fortification standard. A 15.0 pg/μL $^{13}C_{12}$-labeled 2378-TCDD (National Institute of Standards and Technology SRM 1614) internal standard was prepared in a 5-mL volumetric flask by transferring and diluting the contents of a weighed ampule containing 96.6 ng of internal standard per gram of solution. The contents of a second weighed ampule of [$^{13}C_{12}$]2378-TCDD were transferred to a concentrator tube, the lower 1-mL portion of which was calibrated in 100-μL increments, and concentrated to 100 μL under a stream of purified nitrogen. Aliquots (25 or 63 μL; digital Micro/pettors, SMI, Emeryville, CA) from this tube were mixed with aliquots (40 or 100 μL) from the unlabeled working stock solution in two other tubes and were diluted to 200 μL to prepare two GC/MI/FTIR calibration standards. These two 2378-TCDD calibration standards contained ^{12}C at 100 pg/μL + ^{13}C at 93 pg/μL, and ^{12}C at 250 pg/μL + ^{13}C at 234 pg/μL, respectively. The quality assurance (QA) solutions were prepared at various concentrations from aliquots of the unlabeled fortification standards and the internal standard.

Test Sample Preparation. The edible portion of ground fish was analyzed by the method of Niemann et al. (*10*) which includes base/acid treatment and off-line size exclusion, C-8, and C-18 HPLC cleanup to isolate the analyte 2378-TCDD. The chosen fish had a bioincurred analyte level that had previously been determined by GC/MS with multiple ion detection. Although major contaminants in the cleaned-up extracts, which were materials bleeding off the C-18 columns, had not interfered with the MS-monitored ions, they did interfere severely with infrared identification of analyte. However, these components were completely removed by a Hamilton PRP-1 column (polystyrene gel, 5 μm in diameter, 4.6 mm i.d. × 15 cm, 100% AN at 1.0 mL/min, 45 °C) added as another stage of HPLC cleanup after that of the C-18 column. The collected dioxin fraction eluted shortly after the interfering material which came off at or near the void volume. After evaporation to dryness and residue uptake into 100 μL of isooctane, the analyte level was quantitated by fused silica capillary GC/EC under the following conditions: 0.2 mm i.d. × 50 m ULTRA No. 1 (bonded phase methyl silicone, Hewlett-Packard); temperature programmed at 20 °C/min from 75

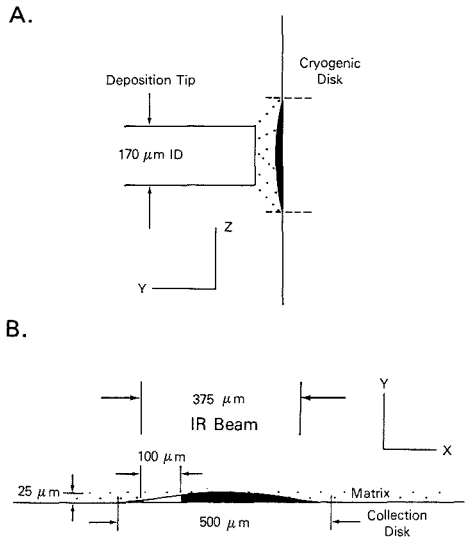

Figure 1. (A) During effluent trapping, the heated (270 °C) GC transfer line tip is about 100 μm from the slowly rotating cryogenic (12 K) collection disk located in a vacuum chamber. The solid surface in the y–z plane is the cross sectional area of the frozen analyte in the argon matrix. (B) After the GC separation is complete, FTIR measurement begins. The shape of the cross section of the solid analyte in the x–y plane is given as absorbance (y axis) vs GC retention time (x axis) in Figure 2 (see text).

°C (2 min) to 250 °C (hold); hydrogen carrier gas at 40 cm/s (linear velocity measured at 250 °C); 300 °C injector; 350 °C detector; splitless injections of 1-μL solutions. Next, [^{13}C]2378-TCDD internal standard was added at 1–1.5 times the unlabeled level as screened by GC/EC, and the extract was submitted along with QA solutions for GC/MI/FTIR analysis.

GC/MI/FTIR Analysis. The prepared extract was transferred to a sample tube (bottom part graduated in 10 μL; Kontes, Vineland, NJ) with two 0.1-mL isooctane rinses and concentrated under a stream of nitrogen while the tube was warmed in a water bath. When the volume reached about 20 μL, the tube walls were rinsed with 25 μL of isooctane and concentration was continued to about 3 μL. The solution was never allowed to go to dryness and was analyzed within a few hours. The entire volume (equivalent to 15 ± 0.5 g of fish in the test portion), or as much as could be taken up into the syringe (1–3 μL), was injected. A typical day's run included two calibration standards, one or more QA solutions, and a fish extract.

Calibration plots of absorbance (in units of 10^{-3} A; strongest band) vs picograms injected were made for native and labeled analytes generated over 9 days of injecting calibration standards. The amount of 2378-TCDD present in test solutions (extracts or QA) was calculated from the observed milliabsorbance values, the ^{12}C and ^{13}C regression line equations describing the calibration plots, and the picogram amounts of internal standard added. QA solution measurements were used to verify that the calibration curves had not shifted.

At the start of a GC/MI/FTIR run, the Cryolect collection disk begins to rotate slowly at a predetermined speed (50 μm/s) and the effluent is directed toward the outer rim of this cryogenic collection disk, thus freezing instantly into a solid matrix (Figure 1). A cross section of the frozen analyte in the IR-transparent argon matrix, defined as being in the x–y plane, is shown in Figure 1B. By this definition, the disk moves along the x direction during effluent collection, while the thickness of the frozen analyte varies along the y axis. Since the disk rotation and GC separation occur simultaneously during analyte collection, the distance along the x axis is indexed by the GC retention time. Thus, the position of a separated component trapped on disk is denoted by the

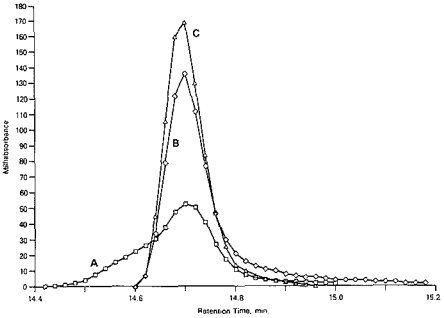

Figure 2. IR-reconstructed GC peak shapes of 1234-TCDD standard on cryogenic disk obtained by monitoring the most intense band at 1433 cm^{-1} and using a VSOS SGE splitter union: (A) before optical alignment; (B) after optical alignment; and (C) using a specially fabricated all-glass-lined union (SGE) after optical alignment (intensity normalized to 8.0 ng injection; retention time normalized to 14.7 min). Less tailing was found in (C) and the observed peak height, which served as a reference, exhibited increased intensity.

retention time of its corresponding GC peak. The shape of the cross section of the frozen analyte in the x–y plane, as measured by FTIR, is the IR-reconstructed chromatographic peak shape. Hence, the independent variable (x axis) is GC retention time and the dependent variable (y axis) is absorbance (Figure 2; see Results and Discussion). The chromatographic retention time was used only to index the position on the collection disk of a component in the argon matrix to within a few seconds (up to several hundred micrometers). However, a rigorous Cryolect disk-scanning protocol was followed in order to *reproducibily* pinpoint the location of a peak maximum. For several consecutive measurements, when the computer-controlled stepper motor, which rotates the collection disk, positioned a component (of known retention time) trapped in the argon matrix in the path of the IR beam, the observed absorbance for that component was different (up to 20%) each time. A backlash of at least 338 steps or 50 μm (1 s on the retention time scale) in the collection disk drive train appeared to prevent reproducible disk positioning under normal operating procedures. To overcome this problem, at 1.2-s intervals we sampled a narrow window of about 5 s where we expected to find the maximum amount of analyte (top of GC peak). In this case the observed absorbance increased to its maximum value and then declined. The spectrum with the maximum absorbance is the one that corresponds to the configuration in which the focused IR beam optimally falls within the analyte area. Using this protocol, 1000 analyte interferograms were coadded (9 min 5 s at 4-cm^{-1} resolution) at each sampling interval. The background was usually collected (1000 scans) before or after the analyte peak.

RESULTS AND DISCUSSION

The matrix isolation FTIR spectrum of 2378-TCDD (Figure 3A) exhibited about a dozen bands, with a maximum absorbance at 1471 cm^{-1}. Figure 3B shows the spectrum of [$^{13}C_{12}$]2378-TCDD. Because the level of the 2378-TCDD isomer was in the subnanogram range, we first had to document and optimize the performance of the GC/MI/FTIR system to be able to confirm spectroscopically the identity of this relatively weak infrared absorber and quantitate its level in the various matrices.

GC/MI/FTIR System Optimization. The IR-reconstructed chromatographic peak shape of the analyte on the Cryolect disk is a useful diagnostic tool which was used to monitor and improve the performance of both the GC interface and the Cryolect. The most intense band at 1433 cm^{-1} of the standard 1234-TCDD was monitored for this purpose. The retention time of the IR-reconstructed chromatographic peak was always slightly shorter than the retention time observed by EC, since after the effluent is split, it follows two

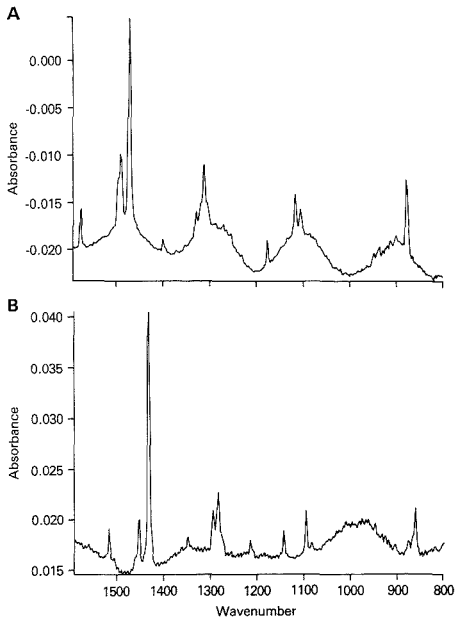

Figure 3. Observed MI/FTIR spectra in the 1600–800-cm^{-1} region acquired at 4-cm^{-1} resolution by coadding 1000 scans (9 min 5 s) of (A) about 1.3 ng of 2378-TCDD standard injected and (B) about 1.1 ng of [^{13}C]2378-TCDD standard injected.

unequal pathways. The EC line is under pressure, whereas the Cryolect line flow is determined by the Cryolect chamber vacuum. This difference, which could be minimized, also depends on the nature of the GC interface (e.g., transfer lines lengths and internal diameters).

Effects of Independently Adjustable Parabolic Mirrors and Laser Optical Alignment. The observed shape of the IR-reconstructed chromatographic peak (Figure 2) depended not only on the efficiency of the GC separation and the transfer process but also on the alignment and focus of the IR beam. When the mirrors of the parabolic mirror assembly were mounted in one fixed position, a distorted peak shape was obtained (Figure 2A). The cross-sectional area of such a beam appeared as a small circular area of condensed light as well as a less intense elongated coma when visible light was used. The shoulder on the leading edge of the IR-reconstructed peak was eliminated by replacing the fixed-position parabolic mirror assembly with one in which each mirror of the parabolic mirrors pair was replaced with an independently adjustable mirror that allowed proper alignment of the IR beam. This resulted in sharper peaks (Figure 2B,C).

Effect of Splitter Union. The effect of splitter unions on the shape of the IR-reconstructed GC peak could then be determined and the peaks compared to those found by EC. When the original VSOS SGE splitter union was used, the IR-reconstructed GC peak height (Figure 2B) was less intense and showed more tailing (full width at half maximum, fwhm 5.4 s) than when a specially fabricated all-glass-lined SGE union was used, fwhm 5.2 s (Figure 2C), which justified our decision to use the all-glass-lined union. In the absence of any union, when the column was directly inserted into the EC detector, the chromatographic efficiency was good and a symmetrical peak shape was observed, fwhm 4.0 s (Figure 4A). The effect of using the original VSOS SGE splitter union is

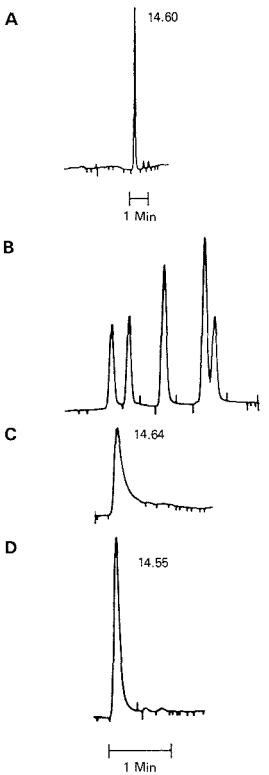

Figure 4. Partial GC/EC chromatograms. (A) 1234-TCDD standard, 7.9 ng injected, observed with the capillary column directly connected to EC, shows a symmetrical peak, fwhm 4.0 s; retention time 14.60 min; chart speed 0.6 cm/min. (B) A chlorinated pesticide standard mix shows no tailing with the original VSOS SGE union installed, fwhm 5.1 s for the middle peak (divert-to-vent mode). Mix contains dieldrin, heptachlor, heptachlor epoxide, DDE, and chlorpyrofos; elution order undetermined; levels range from 4 to 7 ng/component; chart speed 2.0 cm/min. (C) 1234-TCDD standard, 0.79 ng injected shows tailing and reduced peak height with the original VSOS SGE union installed; chart speed 2.0 cm/min. (D) Same as (C) using the specially fabricated all-glass-lined SGE union, fwhm 5.7 s (divert-to-vent mode). The same EC response factor was found for both (C) and (D).

shown in Figure 4B,C. It is noted that pesticides (Figure 4B), but not TCDD (Figure 4C), produced symmetric GC peaks with no tailing. The GC/EC fwhm values observed with the special all-glass-lined SGE union were 5.7 s, when the flow was diverted to the vent port (Figure 4D), and 7.5 s, when the effluent was deposited onto the cryogenic disk. These results indicate that the extent of postcolumn broadening is smaller in the Cryolect (fwhm 5.2 s) than in the EC line (fwhm 5.7 s), and that the efficiency is only slightly worse than in the absence of unions (fwhm 4.0 s). Bourne and Croasmun (*9*) recently reported a larger fwhm value, 6.8 s, observed by FTIR under similar Cryolect conditions.

Collection Disk Rotation Parameter. The IR-reconstructed GC peak shape also depends on the rotation speed of the collection disk, which is another independent factor that determines the physical length in micrometers over which an eluting compound will be spread. In general, this speed should be set so that an eluting component will not be deposited over a previously eluting component as long as their adjacent GC

peaks are chromatographically resolved at the base line. The only available disk rotation speed value, 50 μm/s, was satisfactory. The distance along the collection disk surface that corresponds to the fwhm of the IR-reconstructed GC peak (5.2 s) is 260 μm, whereas the peak base width is close to 500 μm, excluding the tail. This is actually the length along the x axis of the cross section of the frozen analyte in the x–y plane (Figure 1B). The dimension along the z direction of the cross section of the solid analyte in the y–z plane (Figure 1A) could not be documented. Reedy et al. (*4*) pointed out that absorbance is inversely proportional to the square of the diameter of the area over which analytes are condensed and that the focused IR beam must fall within the surface area on which the analyte is collected.

IR Beam Size on Disk. When the focused IR beam was allowed to fall onto the 343 μm i.d. reference notch located on the collection disk surface, the interferogram centerburst voltage was at a minimum of 2.1 V, which is about 17% of its maximum value of 12.7 V obtained with the beam focused on the disk mirror surface. This result indicated that the diameter of the focused IR beam cross-sectional surface area on the collector disk (d_{IR}) is slightly (9.3%) over 343 μm. It is not known how d_{IR}, which is 375 μm, compares with the width of the argon matrix, which is also the dimension of the cross section of the frozen analyte along the z direction of the deposition surface (Figure 1A). If such distance were smaller than 375 μm, an FTIR microscope would be needed for the IR beam to fall within the surface area of a deposited analyte. The use of a matching MCT detector element surface area is also a requirement.

FTIR Characterization of Standards. Several characteristic FTIR bands have been observed for the symmetrical and planar 2378-TCDD isomer (Figures 3A and 5B). Identification was based on the most intense seven bands: the 1575, 1489, and 1471 cm^{-1} absorbances arising from the C=C skeletal in-plane vibrations of the aromatic ring, the C—O—C asymmetric stretch at 1312 cm^{-1}, the aromatic ring trigonal bending at 1176 cm^{-1}, the aromatic ring breathing at 1117 cm^{-1}, and the C—H out-of-plane bending at 879 cm^{-1}. In general, these absorption band positions are in agreement with those found for 2378-TCDD in KBr by Chen (*11*); however, band intensities are diminished, relative to the most intense 1471-cm^{-1} band, in the argon matrix spectrum. Variations in band intensities for small planar molecules in matrix environments have been explained in terms of molecular orientation effects (*12*). With the exception of the C–O–C asymmetric stretch vibration, which appeared at the same frequency by both KBr and matrix isolation techniques, the other bands are found to have shifted to higher frequencies by 3–9 cm^{-1} in the argon matrix. The bands observed by matrix isolation for the ^{13}C-labeled 2378-TCDD (Figures 3B and 5B) are shifted with respect to the unlabeled compound to lower frequencies by about 20–50 cm^{-1}, and the separation between the two most intense bands used for quantitation (1471 cm^{-1}, ^{12}C, and 1432 cm^{-1}, ^{13}C) was 39 cm^{-1}. Because the overlap between the spectra of the unlabeled and the labeled compounds was small, the [$^{13}C_{12}$]2378-TCDD was used as an internal standard which was added to the prepared extract before GC/MI/FTIR analysis. The unlabeled and labeled 2378-TCDD isomers coelute, and thus are sprayed and condensed on the cryogenic collection disk at the same microscopic spot.

The effect of signal averaging can be seen in the spectra of a standard solution containing 190 pg (^{12}C) and 176 pg (^{13}C) obtained after coadding 32-scan (Figure 5A) and 1000-scan (Figure 5B) interferograms of analyte and background. The seven bands used for the identification of the 2378-TCDD isomer could be observed satisfactorily, and signal averaging

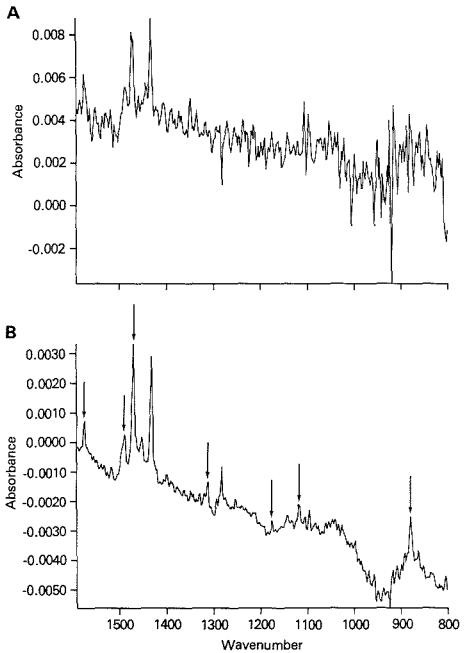

Figure 5. MI/FTIR spectra (4 cm^{-1}) observed for a standard solution containing 190 and 176 pg of [^{12}C]- and [^{13}C]2378-TCDD, respectively, acquired by coadding (A) 32 scans (17 s) and (B) 1000 scans (9 min 5 s). Arrows indicate monitored bands for confirming the presence of 2378-TCDD (frequencies (cm^{-1}): 1575, 1489, 1471, 1312, 1176, 1117, 879).

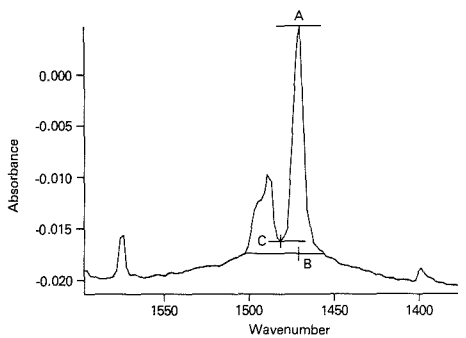

Figure 6. MI/FTIR spectrum of 2378-TCDD standard showing a small range around the most intense 1471-cm^{-1} band; see text.

for times longer than 9 min 5 s (1000 scans) was not necessary. The band intensities were obtained from the band heights measured on the plotted spectra. The heights of bands that overlapped with adjacent bands, such as the most intense two bands at 1471 and 1432 cm^{-1}, were determined indirectly. From the spectrum obtained for either the ^{12}C or ^{13}C alone (Figure 3), the constant ratio (AC/AB) could be found (Figure 6). For ^{12}C and ^{13}C mixtures, the distance AC could still be observed, and AB was calculated as the observed AC value divided by the known ratio (AC/AB). Fringes in the base line were often found in such low-level spectra and were probably due to multiple reflections of the IR beam between the col-

Table I. Confirming the Identity of 2378-TCDD by Normalizing the Absorbance of Six Selected Characteristic IR Bands to the Absorbance of the Strongest Band at 1471 cm^{-1}

	absorbance ratio, %, at					
test material	1575 cm^{-1}	1489 cm^{-1}	1312 cm^{-1}	1176 cm^{-1}	1117 cm^{-1}	879 cm^{-1}
^{12}C standard (1.3 ng)	18	31	29	13	18	33
carp 1,[a] extract 224	20	38	24	14	21	34
carp 1,[a] extract 226	15	28	33	15	17	33
carp 1, extract 55	15	35	22	–[b]	17	33
carp 1, extract 65	16	30	22	15	19	37
catfish, extract 146	15	31	24	13	18	31
carp 1, extract 68[b]	–	–	–	–	–	–
carp 2, extract 77	16	25	23	12	16	32
carnivores composite, extract 69	–[b]	34	–[b]	–[b]	–[b]	–[b]
acceptable absorbance ratio range,[c] %	16–21	24–36	19–31	7.6–18	14–20	29–38

[a] Fortified with [^{12}C]2378-TCDD. [b] Noisy. [c] Range = range of average ratios of absorbance at specified wavenumbers to that at 1471 cm^{-1}, as determined from five injections of calibration standards at amounts between 200 and 400 pg (1471 cm^{-1} = 100%).

lection disk mirror surface and the outer surface of the argon matrix. The background was usually collected close to the peak of interest, specifically about 12 s before or after the 14.77-min retention time of 2378-TCDD, in order to minimize the effects of the interference fringes.

Analysis of Fish Extracts. Prepared fish extracts contained interferences in the IR measurements which were undetected by EC. These materials gave very intense FTIR bands consistent with a siloxane structure at 2969 and 2935 cm^{-1} (C–H stretch), 1021 cm^{-1} (Si–O stretch), 1262 cm^{-1} (CH_3 in-plane bend), and 808 cm^{-1} (CH_3 rock), and obscured any TCDD bands that were present at levels that were about 2 orders of magnitude lower than those of the contaminants. From earlier mass spectrometry work (*10*) we know that these interfering materials bled from the Du Pont C-18 HPLC columns used in the last step of extract cleanup. The structure of one component was recently identified (*13*) as bleeding from a Waters C-18 column. Fortunately, the bleed material was completely removed with a PRP-1 (Hamilton) column and the spectra of 2378-TCDD in fish extracts could be observed (Figure 7).

The spectra of fish extracts (Figure 7) show the monitored analyte bands riding on patterns attributed to fringes. For extracts 226 and 55 derived from the same test portion, the fact that equivalent amounts of analyte were measured on disk even though one extract was prepared from fortified tissue, illustrates the highly variable efficiency of analyte removal from these tubes. The peak-to-peak noise level found for extract 226, containing 212 pg of 2378-TCDD "on disk", was 0.27 mAbs in the range 1600–1300 cm^{-1} where the most intense band (1471 cm^{-1}, 4.6 mAbs) was found, yielding a signal-to-noise ratio (SNR) of 17:1. The MI/FTIR absorption bands can be sharp; however, this is evident only at resolutions that are high enough (e.g., 2 cm^{-1} or 1 cm^{-1}) to match the natural bandwidths of the absorption bands. While sharp bands can improve detectability and quantitation, data acquisition at a higher resolution would require a measurement time that is much longer than the one used, 9 min 5 s, in order to recover the same SNR, 17:1, obtained at 4 cm^{-1}.

Identification of 2378-TCDD required satisfying the following criteria. The ^{12}C and ^{13}C spectra were coincident at the expected retention time on disk. The monitored seven characteristic bands of [^{12}C]2378-TCDD and the major band of [^{13}C]2378-TCDD occurred at the correct wavenumbers. The ratios of absorbances of the six weaker bands to the strongest one at 1471 cm^{-1} (referenced as 100%) for a nanogram-level [^{12}C]2378-TCDD standard (Table I) were similar to those respective ratios observed for calibration standards at equivalent or bracketing amounts expected from test analyses. Ratios were deemed similar if they fell within the range determined by the average ±2 standard deviations as defined

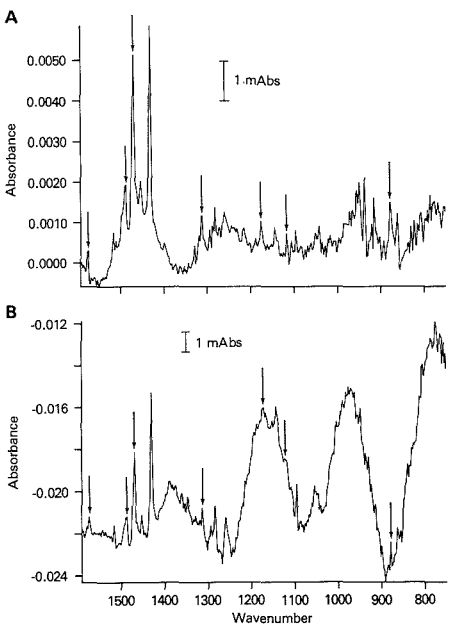

Figure 7. MI/FTIR spectra (1000 scans, 4 cm^{-1}) obtained at 2378-TCDD retention time on disk for fish extracts: (A) extract number 226, a test portion of carp fortified at 55 pg/g (unlabeled), 212 pg "on disk" at 27% internal standard (IS) recovery; (B) extract number 55, same test portion of carp as (A) but unfortified, 221 pg "on disk" at 63% IS recovery. Arrows indicate monitored bands for confirming the presence of 2378-TCDD (frequencies (cm^{-1}): 1575, 1489, 1471, 1312, 1176, 1117, 879).

by standards. When all band ratios were outside the acceptable range, quantitation based upon the 1471-cm^{-1} band was unreliable, and the presence of 2378-TCDD would not be considered as confirmed. When only one or two bands were outside the range by 1–2%, analyst judgment was exercised and the identity of 2378-TCDD might be confirmed. Table I presents the absorbance ratios and acceptable ranges for judging confirmation. The identity of 2378-TCDD could not be confirmed for fish extract 68, one of triplicate analyses of carp 1, because the spectrum was inexplicably noisy, and for extract 69, the lowest level extract (<100 pg "on disk"; 10 pg/g tissue basis by GC/EC), because of poor SNR; the major band absorbance at 1471 cm^{-1} was still detectable at SNR better

Table II. Quantitation of 2378-TCDD in Fish Extracts by GC/MI/FTIR and Comparison with GC/EC Results

test material[a]	extract no.	mAbs[b] ^{12}C	mAbs[b] ^{13}C	GC/MI/FTIR quantitation, pg ^{12}C	GC/MI/FTIR quantitation, pg ^{13}C	^{13}C recovery, %	total [^{12}C]2378-TCDD, pg GC/MI/FTIR	total [^{12}C]2378-TCDD, pg GC/EC	IR as % of EC
carp 1[c]	224	4.6	5.4	212	229	30.6	692	658	105
carp 1[c]	226	4.6	4.8	212	203	27.1	782	645	121
carp 1	55	4.8	6.0	221	256	68.2	324	332	98
carp 1	65	4.8	10.4	221	449	59.8	370	279	132
catfish	146	4.7	4.8	216	203	54.1	400	304	131
carp 1	68	2.5	4.4	–[d]	186	49.5		309	
carp 2	77	3.4	3.9	173	172	67.3	257	214	120
carnivores composite	69	2.2	2.9	–[d]	120	61.5		145	
N						8			6
average						52.3			118.0
RSD, %						30.2			11.9

[a] The catfish and the two carps were caught in Saginaw Bay, MI, and the carnivores were composited from fish caught in the Arkansas River, AR. [b] Milliabsorbance at 1471 cm^{-1} for ^{12}C and 1432 cm^{-1} for ^{13}C. [c] Fortified with [^{12}C]2378-TCDD. [d] Not confirmed by seven-band monitoring; see text.

Table III. Quantitation of 2378-TCDD in QA Standard by GC/MI/FTIR

QA std	mAbs[a] ^{12}C	mAbs[a] ^{13}C	GC/MI/FTIR quantitation, pg ^{12}C	GC/MI/FTIR quantitation, pg ^{13}C	^{13}C recovery, %	total [^{12}C]2378-TCDD, pg GC/MI/FTIR	total [^{12}C]2378-TCDD, pg TRUE	IR as % of TRUE
63	4.0	8.8	183	379	50.5	363	320	114
71	3.5	7.6	160	326	43.4	368	320	115
225	3.1	3.3	141	137	36.6	385	320	120
215	3.6	4.1	165	172	57.4	286	280	102
66	3.0	3.5	152	151	59.2	257	240	107
108	1.8	3.0	89	125	64.2	139	180	77[b]
102	1.9	2.3	95	89	39.6	239	200	119
102A	2.6	3.5	–[c]	151	33.5		240	
218	4.8	5.6	246	259	69.1	355	320	111
223	7.3	8.8	376	424	94.2	399	400	100
78	3.3	5.6	168	259	69.1	242	240	101
103	2.8	4.1	142	182	48.5	292	320	91
N					12			11
average					55.5			105.3
RSD, %					31.1			12.3

[a] Milliabsorbance at 1471 cm^{-1} for ^{12}C, and 1432 cm^{-1} for ^{13}C. [b] QA108 was not a Dixon outlier at 95% confidence. [c] Measurement subject to an interference.

than 3:1. In the remaining six extracts the identity of 2378-TCDD was confirmed.

Other Components in Fish Extracts. Several other compounds were commonly found in different extracts (Figure 8). For example, an alkyl phthalate was present in extracts 146, 68, 77, and 69 (retention time, t_R 16.06 min) exhibiting several characteristic bands at 2971 and 2943 cm^{-1} (aliphatic hydrocarbon), 1737 cm^{-1} (ester carbonyl), 1292 cm^{-1} (C–O–C asym. stretch), and 1128 cm^{-1} (C–O–C symmetrical stretch). Another phthalate was also found in extracts 146, 77, and 69 (t_R 14.26 min). A compound with a long aliphatic chain was found at t_R 14.00 min for extract 68, and a ketone-containing species eluted at 15.11 min for extracts 146, 77, and 68.

FTIR Quantitation. 2378-TCDD calibration plots of absorbance (1471 and 1432 cm^{-1} bands for ^{12}C and ^{13}C, respectively) vs picograms injected have been generated in the 93–500 pg range (less than 1 order of magnitude). The data for each of the two calibration sets used were accumulated over a 9-day period during which fish extracts and QA standards were analyzed. The regression line equations for the two sets with eight and six observations, respectively, are as follows: ^{12}C, $y = 0.021x + 0.11$; ^{13}C, $y = 0.023x + 0.17$; and ^{12}C, $y = 0.019x + 0.08$; ^{13}C, $y = 0.019x + 0.57$. The instrumentation, despite its complexity, appeared remarkably stable during this work. The 95% confidence bounds of the regression lines encompassed the origin, thus indicating the absence of bias.

Quantitative results for fish extracts are summarized in Table II. Satisfactory repeatability was achieved in quantitation of the pair of duplicate extracts prepared from carp 1. Total 2378-TCDD varied by 13% for the fortified and 14% for the unfortified extracts. In general, GC/MI/FTIR quantitation of total 2378-TCDD compared favorably to the independent GC/EC results, but on the average results tended to have an 18% high bias relative to EC. Since the GC/EC quantitation of extracts prepared by this method had been validated by mass spectrometry (*10*), the source(s) of error may partly be due to the GC/MI/FTIR measurements. When expressed on a fish tissue basis, extract levels ranged from 10 (extract number 69) to 45 pg/g (pptr) (extract number 224) with most at 15–20 pg/g (pptr).

Analytical results obtained for the QA standards, and presented in Table III, typically exhibit high accuracy in the range 200–400 pg. At worst, accuracy was +20% and averaged 5% high bias. The spread in results of the standards was similar to that found for fish extracts analyzed by this technique and was comparable to that found by GC/EC. Since test extract recoveries averaged 52–56% with very high variability, the use of an isotopically labeled internal standard was required to achieve accurate results.

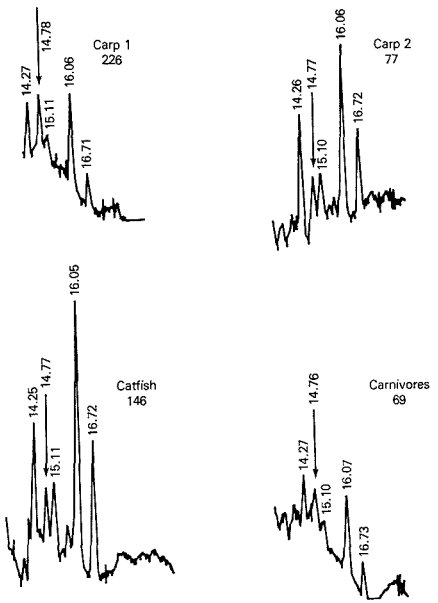

Figure 8. Partial GC/EC chromatograms observed for different fish extracts during cryogenic sample deposition. 2378-TCDD retention time was 14.77 (±0.01) min. Information is restricted to monitoring only; deposition (divert-to-cryogenic disk mode) conditions broadened peaks within the transfer line to EC detector. Quantitation by GC/EC was performed previously by using another capillary chromatograph independent of GC/MI/FTIR instrumentation.

CONCLUSIONS

GC/MI/FTIR was used to identify and quantitate the 2378-TCDD isomer in fish extracts in the range 170–220 pg "on disk". An internal standard was required. Results agreed with those independently obtained by GC/EC, showing that quantitation at such levels (15–45 pg/g, pptr) is possible by GC/MI/FTIR. Quantitation performance suggests that the instrumentation is remarkably stable.

Recovery efficiency remains to be improved. A minimum identification extract level requirement of about 170 pg "on disk" may have been partially dictated by the presence of fringes in the spectra.

ACKNOWLEDGMENT

The authors thank S. W. Page for extensive discussions during the course of this work, D. Wright of SGE for generously supplying the all-glass-lined splitter union, C. Kopral for statistical analysis, F. Fry for computer graphics, J. Easterling for precision machining work, and E. A. Hanson for technical assistance.

LITERATURE CITED

(1) Chlorinated Dioxins and Related Compounds 1986. Proceedings of the 6th International Symposium held at Fukuoka, Japan, 16–19 September 1986. *Chemosphere* **1987**, *16*(8-9), 1599–2210.
(2) Grainger, J.; Gelbaum, L. T. *Appl. Spectrosc.* **1987**, *41*, 809–820.
(3) Bourne, S.; Reedy, G. T.; Coffey, P. J.; Mattson, D. *Am. Lab.* (*Fairfield, Conn.*) **1984**, *16*, 90–101.
(4) Reedy, G. T.; Ettinger, D. G.; Schneider, J. F.; Bourne, S. *Anal. Chem.* **1985**, *57*, 1602–1609.
(5) Gurka, D. F.; Brasch, J. W.; Barnes, R. H.; Riggle, C. J.; Bourne, S. *Appl. Spectrosc.* **1986**, *40*, 978–991.
(6) Grainger, J.; Barnhart, E.; Patterson, D. G., Jr.; Presser, D. *Appl. Spectrosc.* **1988**, *42*, 321–326.
(7) Holloway, T. T.; Fairless, B. J.; Freidline, C. E.; Kimball, H. E.; Kloepfer, R. D.; Wurrey, C. J.; Jonooby, L. A.; Palmer, H. G. *Appl. Spectrosc.* **1988**, *42*, 359–369.
(8) Mossoba, M. M.; Chen, J. T.; Brumley, W. C.; Page, S. W. *Anal. Chem.* **1988**, *60*, 945–948.
(9) Bourne, S.; Croasmun, W. R. *Anal. Chem.* **1988**, *60*, 2172–2174.
(10) Niemann, R. A.; Brumley, W. C.; Firestone, D.; Sphon, J. A. *Anal. Chem.* **1983**, *55*, 1497–1504.
(11) Chen, J. T. *J. Assoc. Off. Anal. Chem.* **1973**, *56*, 962–972.
(12) *Vibrational Spectroscopy of Trapped Species*; Hallam, H. E., Ed.; Wiley: New York, 1973.
(13) Anthoni, U.; Larsen, C.; Nielsen, P. H.; Christophersen, C. *Anal. Chem.* **1987**, *59*, 2436–2438.

RECEIVED for review February 3, 1989. Accepted May 1, 1989. This work was presented at the 14th Annual Meeting of the Federation of Analytical Chemistry and Spectroscopy Societies in Detroit, MI, on October 5, 1987, and in part at the 3rd Annual Cryolect Users Meeting in Research Triangle Park, NC, on May 11, 1988.

Anal. Chem. 1989, 61, 1686-1693

Application of Cross-Correlation to Quantitative Analysis of Binary Mixtures Using Extended X-ray Absorption Fine Structure

Douglas P. Hoffmann, Andrew Proctor, Martin J. Fay, and David M. Hercules*

Department of Chemistry, University of Pittsburgh, Pittsburgh, Pennsylvania 15260

Quantitative information can be obtained from extended X-ray absorption fine structure (EXAFS) spectra by cross-correlation analysis. The cross-correlations of normalized spectra from a binary mixture with standard compound spectra yield correlation parameters that are proportional to the respective amount of each standard present. A calibration series can be made by creating composite spectra from two standard spectra. The cross-correlation parameters obtained from the correlation of the standards with the composite spectra generate a calibration curve. The calibration curve allows the correlation parameters obtained for the binary mixtures to be converted into their respective mole fractions. Without suitable standards the method still yields semiquantitative trend information. Although this method is not suggested as a direct substitute for standard EXAFS analysis, it does provide a relatively fast and easy route to obtain initial information about coordination numbers. This information could then be used as a starting point for more complicated curve-fitting analysis.

1. INTRODUCTION

Over recent years utilization of EXAFS (extended X-ray adsorption fine structure) spectroscopy has grown tremendously, mostly due to the number of synchrotron sources that have become available to the general scientific community. The results of this growth are that EXAFS applications can be found in almost every scientific field. In addition, improvement in computer hardware and software means that data analysis upon which EXAFS is critically dependent, is playing an increasingly important role. Although in principle, and for the most part in practice, obtaining high-quality EXAFS data is relatively easy, data analysis has always been somewhat intimidating. The analysis is complicated by the number of variables involved and the number of steps required for data reduction to obtain the pseudo radial distribution function, PRDF (vide infra). When a series of spectra have been analyzed by standard methods, using reliable reference materials, comparisons of coordination numbers (N), radial distances (RD), relative Debye–Waller ($\Delta\sigma^2$) factors, and edge shifts (ΔE_0) are possible. This is a long and involved procedure.

One problem that hinders the standard EXAFS analysis is the overlap of signal from more than one chemical or structural phase of the probed element. This situation often results in radial peaks which are derived from any combination of backscatters, coordinations, and phases of the sample. Thus when attempting to perform standard EXAFS analysis, a multiple shell fit of a single radial peak may be required. While fitting multiple shells from a single peak is possible, it significantly increases the number of variables involved in the fitting procedure. This in turn leads to an increase in the number of combinations that can yield a reasonable fit and so reduces the reliability of the result. Therefore, this type of analysis increases the amount of time and effort required to obtain meaningful answers.

The purpose of the present work is to demonstrate a method of obtaining quantitative analytical information from EXAFS by means of cross-correlation analysis. Cross-correlation is a powerful data analytical tool in which two spectra are compared to determine the degree of their similarity (*1–5*). Using normalized spectra allows the resultant correlation parameters to yield both quantitative and semiquantitative or qualitative information. The $\chi(E)$ spectra, representative of the EXAFS oscillations, were found to be the most useful form of the EXAFS data. However the use of $\chi(k)$ and derivatives was also examined. The resultant concentration information is directly related to the coordination number normally extracted via the standard EXAFS method. If the coordination number is the sole piece of information required, then the correlation approach may be all that is required. If so, the savings in data analysis time will be considerable. If information about RD, $\Delta\sigma^2$, and ΔE_0 is also required, then initial correlation analysis can provide a firmer foundation from which to attempt the more complicated curve fitting analysis.

Physical mixtures of Co_3O_4 and $CoAl_2O_4$ were chosen as a series of "unknown" samples so that the major variables (N, RD, $\Delta\sigma^2$) would be known exactly. Therefore the physical mixtures represent a set of ideal samples, so problems normally associated with highly dispersed or amorphous materials (variations in dispersion, disorder, phase segregation) do not need be accounted for in this case. In future publications we will show the application of the present method to well dispersed transition metal oxide catalysts.

2. EXPERIMENTAL SECTION

Sample Preparation. Mixtures of Co_3O_4 and $CoAl_2O_4$ were prepared from pure (99.9%) standard compounds. The two standard samples were treated in a similar manner to ensure that no artifacts were introduced by the preparation method. The two compounds were weighed out in the desired stoichiometric ratios, combined, and ground to finer than 100 mesh. A standard IR wiggle-bug mixer was used for approximately 15 min to ensure complete mixing. The samples were then diluted to approximately 3–5 wt % cobalt with graphite. The diluted samples were ground again and then wiggle bugged for approximately 15 min. The following mole ratios of $Co_3O_4/CoAl_2O_4$ were used: 10/1, 5/1, 1/1, 1/5, 1/10. The nomenclature used for the samples is OX# where # refers to the mole percent of Co_3O_4. The above mole ratios correspond to samples OX91, OX83, OX50, OX17, and OX9. The purity and accuracy of the preparation procedure could not be verified by standard XRD techniques. XRD could not be used since both Co_3O_4 and $CoAl_2O_4$ have similar crystal structure and hence yield XRD powder diffraction patterns which were identical given the peak widths obtained.

EXAFS Measurements. Room temperature K-edge (7709.0 eV) cobalt X-ray absorption spectra were measured on line X18B at the National Synchrotron Light Source (NSLS) located at Brookhaven National Laboratory. Normal beam operating characteristics were 2.5 GeV and 50–120 mA. The X-ray absorption coefficient was measured simultaneously by transmission and fluorescence using standard ionization chambers. Powder samples were mounted between Kapton tape in the void of a $^1/_{16}$

0003-2700/89/0361-1686$01.50/0

in. aluminum sample plate; sample density was controlled by dilution with graphite. No background interference was seen as a result of these mounting procedures. Data reduction was carried out either on a VAX mainframe cluster or on an IBM PC/AT Clone (80286/80287, 8 MHz) microcomputer.

Standard EXAFS Data Reduction. It is not necessary to present a comprehensive review of standard EXAFS data analysis, but a brief outline of the standard methods of data reduction is appropriate. There are several in-depth reviews of the various data analysis procedures that can provide a more detailed explanation of the data reduction steps (*6–9*).

EXAFS data reduction can be arbitrarily separated into primary and secondary data reduction procedures (*6*). The goal of the primary data reduction step is to obtain a correctly normalized and calibrated pseudo radial distribution function (PRDF) from the raw experimental data. The first step of the primary data reduction is to separate the desired EXAFS oscillations from the rest of the X-ray absorption spectrum to produce a normalized $\chi(E)$ spectrum. The second step converts the energy scale, E, to the wave vector scale, k, where $k = [(8\pi^2 m/h^2)(E)]^{1/2}$; m is the rest mass of the electron, h is Plank's constant, and E, the kinetic energy of the emitted photoelectron, is approximately equal to $(E_{h\nu} - E_0)$. $E_{h\nu}$ is the photon excitation energy and E_0 is the edge energy. Thus it can be seen that k is nonlinear with respect to the energy scale. The importance of this nonlinearity will be discussed below. Next the $\chi(k)$ spectrum is weighted by k^n (where $n = 1, 2, 3$) to help offset damping effects at high k, whereupon it is Fourier transformed to produce the PRDF. The last part of the primary data analysis consists of isolating a desired radial peak in the PRDF and back transforming it to obtain the $\chi(k)$ from (hopefully) a single radial shell. The secondary data reduction involves analysis of this back transformed $\chi(k)$. One method of analysis is to curve fit $\chi(k)$ by an iterative nonlinear least-squares (NLLS) procedure to determine the desired structural parameters (N, RD, $\Delta\sigma^2$, ΔE_0). It should be noted that this can be a very time-consuming (and frustrating) procedure. The entire data analysis pathway requires a great deal of care to ensure that the many steps involved are handled consistently so that meaningful results can be derived from the curve-fitting procedure. The use of suitable standard spectra or theoretical parameters further restricts such analysis.

Preprocessing $\chi(E)$ for Correlation Analysis. The data analysis method being proposed here uses the $\chi(E)$ spectrum, but the $\chi(k)$ spectrum was also tested for comparison. The steps involved in obtaining a properly normalized $\chi(E)$ spectrum have been briefly outlined above. However several more simple steps are necessary before the $\chi(E)$ spectrum can be used for correlation analysis. First, the spectrum must be interpolated onto a uniform X axis grid with constant resolution (0.25 eV was chosen here). This ensures a constant increment and allows for greater accuracy in determining energy values. The next step requires selecting a common energy range for all spectra to be correlated. The spectra in this study were extracted by using a range of 25–750 eV beyond the edge jump. The extracted spectrum was again interpolated to give a spectrum with 512 points. This number of points, NU, is necessary to satisfy the relation, $NU = 2^n$ (n is an integer), which is a restriction placed on the analysis by the FFT algorithm (*10*). If the $\chi(k)$ spectrum was to be used for comparative purposes, then the spectrum was converted to k space. The $\chi(E)$ or $\chi(k)$ spectra were then filtered with a 5% Hanning window. The Hanning window filter is unity at all points except in the end regions where it falls to zero smoothly following a half period cosine wave. This allows the two ends of the spectrum also to smoothly approach zero.

Discrete Correlation. Fourier transform based correlation has proven to be a powerful numerical tool for comparing two data sets. Several authors have shown that correlation based analysis may yield qualitative and quantitative information from spectra of multicomponent mixtures, including spectra of low signal to noise (S/N), as well as providing a basis for spectral library searching (*1–4, 11–14*). Several reviews and books have been written on the subject; therefore only a brief overview of correlation analysis will be presented here (*5, 15*).

Use of digital spectral data requires consideration of the digital or discrete form of correlation. For two discrete functions $a(k)$ and $b(k)$ containing NU points each ($k = 0$, NU − 1), the correlation of $a(k)$ by $b(k)$ is defined as (*15*)

$$c(\tau) = \sum_{k=0}^{NU-1} a(k)b(\tau + k) \tag{1}$$

where τ is the displacement of $b(k)$ with respect to $a(k)$ for each point of the correlation ($\tau = 0$, NU − 1). What is not explicitly obvious from eq 1 is that the functions (i.e. spectra) $a(k)$ and $b(k)$ are assumed to be periodic; a given period ($k = 0$, NU − 1) is represented by the total spectrum. As a result the end regions of the spectrum should join smoothly to avoid spurious effects in the Fourier transformation which is required later in the analysis. At each displacement of $b(k)$ from $a(k)$ the products of all common or overlapping points are summed to give a single point in the correlation function. Evaluation at all possible displacements yields the full correlation function. Because of the periodic nature it follows that displacements where $\tau > NU/2$ are effectively negative.

When there is no displacement of the two spectra along their X axes, $\tau = 0$, the response of the correlation function, $c(0)$, shall be termed R_0. If there is no uncertainty in the X axis calibration, R_0 will represent the true extent of correlation between the two spectra. If there is an offset or error in the X axis calibration, then the true correlation response will be slightly offset from $\tau = 0$. The response at this point is termed R_{MAX}. The displacement of R_{MAX} due to uncertainty in X axis calibration will be discussed in detail below. For the magnitude of the correlation (R_0 or R_{MAX}) to be a direct measure of the degree of similarity, the spectra first need to be normalized. With eq 1 as the basis for correlation, it can be seen that if the sum of squares of all ordinate values equals unity for a given spectrum, then the magnitude of the correlation (R_0) of a spectrum with itself (autocorrelation) would also be unity. Thus, for spectra which are correctly normalized, the range over which R_0 may vary is $-1.0 \le R_0 \le 1.0$.

Calculating the full correlation function from eq 1 requires NU multiplications for every correlation point obtained and thus NU^2 multiplications for the complete correlation of two spectra. This can be a very time-consuming set of computations. The burden of this mathematical task can be reduced by using the fast Fourier transform (FFT) (*10*). The Fourier transformation of eq 1 yields (*15*)

$$C_{CORR}(n) = A(n)\, B^*(n) \tag{2}$$

where $C_{corr}(n)$, $A(n)$, and $B(n)$ are the Fourier transforms (FT) of $c_{corr}(\tau)$, $a(k)$, and $b(k)$, respectively, for the range of $n = 0$ to NU − 1; $B^*(n)$ is the complex conjugate of $B(n)$. The index n represents the pseudo frequency domain, where $n = 0$ is the zeroth frequency or DC level and $n = NU/2$ is the Nyquist or maximum frequency (*15*). Thus the series of summation and multiplication operations which were required in the pseudo time domain (eq 1) can be carried out in the pseudo frequency or Fourier domain simply by one set of multiplications. The total correlation function can then be retrieved by inverse Fourier transformation. Because of the FFT, the forward and inverse Fourier transformation route represents a significant saving in computation time.

It should be noted that the FFT route only saves computation time in calculating the full correlation function. Examination of eq 1 shows that extraction of R_0 alone is a trivial operation requiring just NU multiplications (after suitable normalization). However it is more useful to obtain the full correlation function rather than just one point since the R_{MAX} can be easily found. In addition, any filtering operation (such as smoothing or differentiation) can easily be carried out in Fourier space prior to normalization and correlation multiplication.

Since $A = (\boldsymbol{R}_A + i\boldsymbol{I}_A)$ and $B^* = (\boldsymbol{R}_B - i\boldsymbol{I}_B)$, where $\boldsymbol{R}$ and $\boldsymbol{I}$ are the real and imaginary parts of the complex functions A and B, expansion of eq 2 leads to

$$C_{CORR} = (\boldsymbol{R}_A\boldsymbol{R}_B + \boldsymbol{I}_A\boldsymbol{I}_B) + i(\boldsymbol{I}_A\boldsymbol{R}_B - \boldsymbol{I}_B\boldsymbol{R}_A) = \boldsymbol{R}_{CORR} + i\boldsymbol{I}_{CORR} \tag{3}$$

For spectra where the S/N is high, there is probably no need to carry out any prior data smoothing. However with really noisy data the impact of the noise will eventually make itself felt by artificially depressing the value of R_0 from unity. We have previously considered the effect of noise on cross-correlation R_0 values elsewhere (*11*). While noise does tend to depress R_0, the overall shape of the correlation function remains fairly constant.

The symmetry of the whole cross-correlation function is another measure of the smilarity of the two spectra along with R_0. Spectral symmetry can be gauged effectively by autoconvoluting the correlation function. However for quantitative purposes, using spectra of high S/N, the efficacy of this measure is still under investigation and this route will not be considered in the present work since we are not dealing with noisy data.

Even though the spectra used in this study are of high spectral quality, and no smoothing of the data was carried out, it is important to consider the possibility of filtering (smoothing and differentiation) in general since some of the presented results concern the effect of differentiating the EXAFS data. If $y(k)$ has a Fourier transform $Y(n)$ then the mth derivative of $y(k)$, $d^m y/dk^m$ is related to its Fourier transform as follows:

$$d^m y/dk^m \leftarrow \mathrm{FT} \rightarrow (i2\pi n)^m Y(n) \tag{4}$$

Thus derivatization is carried out in Fourier space simply by multiplying $Y(n)$ by a suitable weighting or filter function defined by $(i2\pi n)^m$. The effect of i $(=-1^{1/2})$ is simply to flip the real and imaginary parts depending on the value of m. Generally a derivative filter can be written in the form $F_m = cn^m$ where c is a constant.

Prefiltering two spectra which are then correlated essentially means multiplying the real and imaginary parts of both spectra by the filter F. This reduces to multiplying the final correlation real and imaginary parts by F^2. If the original filter is a first derivative filter of form $F_1 = cn$ then $F_1^2 = c^2n^2 = F_2$. F_2 is clearly a second derivative filter (see eq 4). Thus in general, correlation of mth spectral derivatives gives the $(2m)$th derivative of the correlation function. However it is essential to carry out this prefiltering before correlation multiplication because then the filtered FT's of the original spectra can be correctly normalized.

Normalization. The cross-correlation of a spectrum with itself is termed autocorrelation. Substituting $A = B = X$ in eq 3 produces the result that the FT of the autocorrelation of X is $(\boldsymbol{R}_X^2 + \boldsymbol{I}_X^2)$, which is totally real. By application of the inverse discrete FT (*15*) it follows that R_0 for autocorrelation is simply the weighted sum of these real coefficients. Thus

$$R_0 = \frac{1}{\mathrm{NU}} \sum_{n=0}^{N-1} (\boldsymbol{R}_X^2 + \boldsymbol{I}_X^2) \tag{5}$$

Therefore if both the real $(\boldsymbol{R}_X)$ and imaginary $(\boldsymbol{I}_X)$ Fourier coefficients of any spectrum X are first normalized by NORM where

$$\mathrm{NORM}^2 = \frac{\mathrm{NU}}{\sum_{n=0}^{N-1} (\boldsymbol{R}_X^2 + \boldsymbol{I}_X^2)} \tag{6}$$

then clearly R_0 will equal unity for an autocorrelation. This will be the maximum value which R_0 can have and will arise only when the cross-correlation is an autocorrelation; i.e. $A = B = X$. Thus the range of R_0 lies between +1 and −1. This normalization procedure then allows the correlation of two spectra in Fourier space to be prefiltered, if required, and produce meaningful qualitative and quantitative information.

In addition, the mean value of the original spectrum should generally be subtracted from each point prior to the transform step. This enhances the range of R_0 values in the final correlation. For EXAFS spectra this step can be bypassed because the nature of $\chi(E)$ is such that this is already the case.

Obtaining Quantitative Information. It will be shown below that the correlation parameter obtained from the $\chi(E)$ spectra can be used for quantitative analysis. But first it is necessary to consider some problems associated with quantification of the R_0 parameter and the choice of $\chi(E)$ for quantitative analysis compared to $\chi(k)$ or their respective first derivatives.

Figure 1 shows the correlation functions obtained from the autocorrelation of $\chi(E)_{Co_3O_4}$ (Figure 1A), autocorrelation of $\chi(E)_{CoAl_2O_4}$ (Figure 1C), and the cross-correlation of $\chi(E)_{Co_3O_4}$ and $\chi(E)_{CoAl_2O_4}$ (Figure 1B). The dashed horizontal lines indicate the zero level for each spectrum. There are both positive and negative values for the correlation functions depending on the relative displacement of the two spectra. It is also evident that there are several positive peak maxima. For autocorrelations (Figure 1A,C), the largest peak maximum is centered at $\tau = 0$ and has a magnitude of $R_0 = 1.0$. For the cross-correlation (Figure 1B) the peak

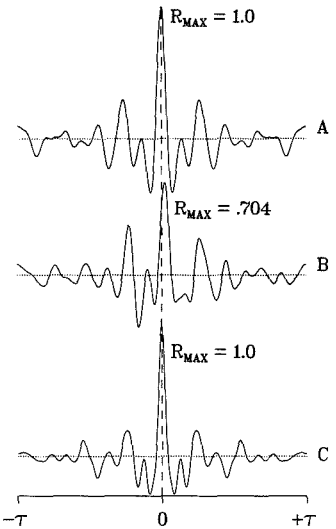

Figure 1. Correlation functions: (A) autocorrelation of Co_3O_4, (B) cross-correlation of Co_3O_4 and $CoAl_2O_4$, (C) autocorrelation of $CoAl_2O_4$.

maximum occurs displaced from $\tau = 0$ and its magnitude, R_{MAX}, is less than 1.0. Clearly for this cross-correlation R_{MAX} is greater than R_0. The problem of which of these two values, R_0 or R_{MAX}, represents the true correlation between the two different spectra now arises. The multiple positive maxima indicate that there are several displacements at which the two spectra have some degree of positive correlation. To determine which maximum represents the true degree of correlation between two dissimilar spectra and which R parameter should be used as the basis for the quantitative analysis, two questions must be considered. First, if the X axes are offset with respect to one another, how should the correct correlation parameter be determined? Second, if the X axes are perfectly aligned, will the maximum correlation parameter be found at $\tau = 0$ for any two given spectra?

The first question requires some degree of certainty that calibration of the X axis is as accurate as possible. In EXAFS, defining the X axis is sometimes difficult but the difference between the experimentally determined X axis and the absolute X axis can be reproduced within a few electronvolts from sample to sample. The autocorrelation in Figure 1A is a special case because the spectrum is correlated with itself allowing no possible chance of X axis misalignment. Thus the maximum correlation parameter is always $R_{MAX} = R_0 = 1.0$. Parts A and B of Figure 2 show the cross-correlation functions obtained from the correlation of $\chi(E)_{Co_3O_4}$ with identical spectra which differ only by having had their edge calibrations offset by 5 and 10 eV, respectively. As would be expected, one can see that the peak maxima are offset from $\tau = 0$ for both cross-correlations. In addition the magnitude of the R_{MAX} parameter has decreased from the autocorrelation value of unity. This decrease in the R parameter is expected since the two spectra are no longer identical. In order to observe the effect of X axis offset on the value of the correlation parameter, EXAFS data for the Co_3O_4 standard were analyzed by introduction of both positive and negative edge shifts of 1, 3, 5, 10, 15, and, 20 eV. Figure 3 shows representative spectra which were correlated with the central spectrum at $\Delta E_0 = 0$. The edge shift is listed with each spectrum. In Figure 3 the $\Delta E_0 = 0$ spectrum does not actually represent a properly calibrated X axis. The $\Delta E_0 = 0$ displacement was chosen so that a large energy excursion (±20 eV) could be obtained without including the absorption edge features. It should be noted that in EXAFS altering the energy calibration and then extracting $\chi(E)$ does not simply mean that the whole spectrum is shifted along the X axis. For displacement of the edge energy in the positive direction, the first, and largest, EXAFS oscillation becomes more and more attenu-

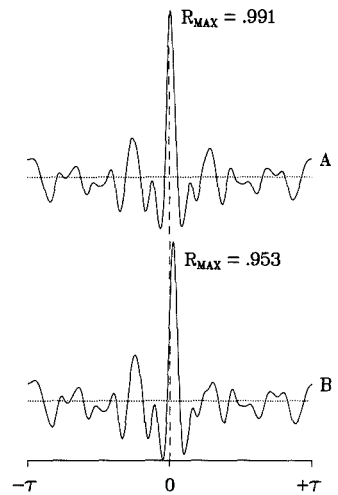

Figure 2. Correlation functions: (A) cross-correlation of Co_3O_4 (ΔE_0 = 0 eV) with Co_3O_4 (ΔE_0 = 5 eV), (B) cross-correlation of Co_3O_4 (ΔE_0 = 0 eV) with Co_3O_4 (ΔE_0 = 10 eV).

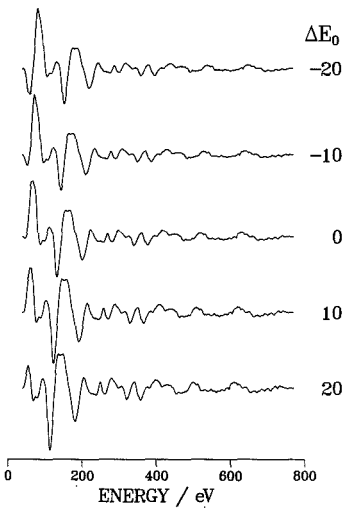

Figure 3. $\chi(E)$ spectra representing a shift of ±20 eV with respect to the ΔE_0 = 0 eV spectrum. Shifts (ΔE_0) given in electronvolts.

ated until it is no longer fully represented for the ΔE_0 = 20 eV spectrum. It has already been stated that it is necessary to window the $\chi(E)$ spectrum prior to the FT to ensure a smooth transition to zero at the extreme ends of the spectrum. This windowing operation is responsible for the decrease in intensity of the main peak as the energy shift increases. For the shift in the edge energy in the negative direction there is no attenuation of the major spectral features which are present in the Δ = 0 eV spectrum but additional low-energy features are included within the chosen energy window. Thus it is expected that when correlations between the ΔE_0 = 0 eV spectra and the other spectra are performed, only the autocorrelation of the ΔE_0 = 0 eV spectra will have a correlation parameter, $R_{MAX} = R_0 = 1.0$. For the other correlations the parameter which best represents the true correlation is R_{MAX} rather than R_0.

Figure 4 shows the difference in R_{MAX} from autocorrelation of

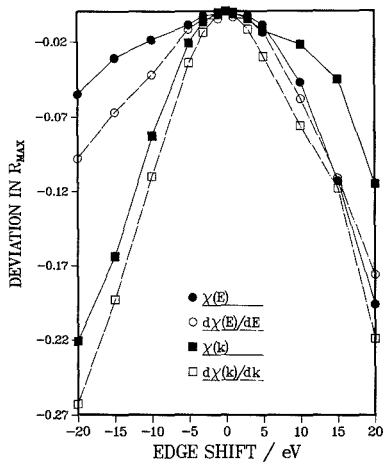

Figure 4. Change in the value of the R_{MAX} parameter as a function of edge shift for the spectra shown in Figure 3. Correlations were performed by using spectra of $\chi(E)$, $d\chi(E)/dE$, $\chi(k)$, $d\chi(k)/dk$.

the ΔE_0 = 0 eV shifted spectrum with the R_{MAX} value from the cross-correlation of the corresponding $\chi(E)$, $d\chi(E)/dE$, $\chi(k)$, and $d\chi(k)/dk$ edge shifted spectra. It can be seen in Figure 4 that R_{MAX} for $\chi(E)$ decreases more rapidly when the edge shift is moved in the positive direction than in the negative direction. Thus it seems clear that positive excursions of $\chi(E)$ which tend to attenuate the signal more than negative shifts also tend to depress R_{MAX} to a greater extent. However the results indicate that these differences in R_{MAX} will introduce a relatively minor error for spectra with axes not displaced more than ±5.0 eV. The results for $d\chi(E)/dE$ produce similar changes in R_{MAX} for positive edge shifts but increased deviations for negative edge shifts. It is evident from the results for $d\chi(k)/dk$ which give the most pronounced deviations of all that the derivative correlation parameters are more sensitive to misalignment than their unfiltered counterparts. The FT domain weighting scheme employed by taking the derivative emphasizes the high-frequency content of the signal. This may be useful in some situations where large changes in R_{MAX} would be advantageous, (e.g. in helping to find optimal alignment) but here it is desirous that R_{MAX} change minimally as a function of misalignment. The negative shift results from $\chi(k)$ in Figure 4 show larger R_{MAX} deviation than those for $\chi(E)$. On the positive shift side this trend is reversed. On this basis there is not much difference between the use of $\chi(E)$ and $\chi(k)$ since they both show a fairly small deviation over the ±5 eV range. However since the wave vector axis, k, depends on $E^{1/2}$, any change in E_0 in the calibration step will cause a nonlinear modification in the k scale. This means that two identical spectra which differ slightly in calibration can never completely overlap at all possible k values at any one displacement τ. Because of this and the very nature of cross-correlation it would seem much more natural to utilize $\chi(E)$ data than $\chi(k)$ data, to minimize errors due to misalignment.

The second question, while related to the previous discussion, requires some additional considerations. Along with the possible differences in the X axis, the possibility of two spectra having a maximum correlation not in the vicinity of τ = 0 when their X axes are perfectly aligned merits discussion. A spurious R_{MAX} is more likely to occur when the spectral features are of similar magnitude over the entire range of the spectra. Thus a (major) positive correlation may occur at a large offset ($\pm\tau$) of the two spectra due to fortuitous alignment of several totally unrelated spectral regions. This is an undesired artifact since only the correlation of similar spectral regions should be used to obtain quantitative information. Figure 5 shows the $\chi(E)$ spectra of Co_3O_4 and $CoAl_2O_4$ standards along with the $\chi(E)$ spectra of the physical mixtures. There is a common sinusoidal pattern in the Co_3O_4 and $CoAl_2O_4$ spectra. It can also be seen that the magnitude

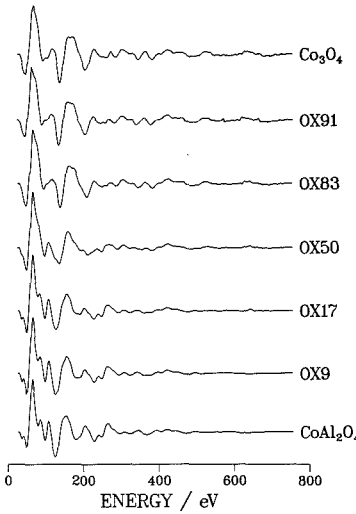

Figure 5. $\chi(E)$ spectra of the Co_3O_4 and $CoAl_2O_4$ standards and the physical mixtures. Spectra are labeled on the figure.

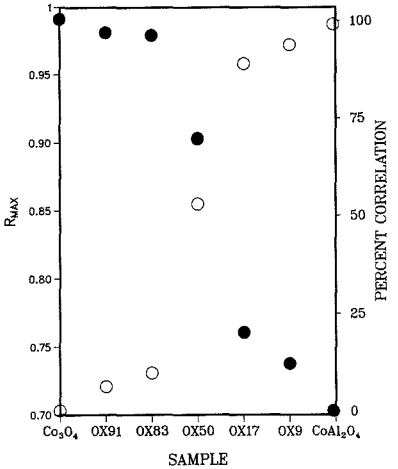

Figure 6. R_{MAX} parameters for each sample with respect Co_3O_4 (●) and $CoAl_2O_4$ (○).

of the signal is attenuated as the energy increases. It is this decay in signal as a function of increasing energy that decreases the probability of a spurious R_{MAX} occurring in this case and for EXAFS data in general. Once the spectra are offset beyond the overlap of the first major EXAFS oscillation, positive correlations may occur but they will be smaller in magnitude than the τ = 0 peak because of large differences in the magnitudes of the correlating regions.

Thus if two different $\chi(E)$ spectra are correlated, the central peak, which is representative of their maximum correlation, may or may not be located at τ = 0. For two different spectra (e.g. $\chi(E)_{Co_3O_4}$ and $\chi(E)_{CoAl_2O_4}$) the displacement of the main correlation peak, R_{MAX} in Figure 1b, may be due either to misalignment of their X axes or to the slight offset in their spectral features. The exact cause is not easily determined, but no matter what the reason the magnitude obtained for R_{MAX} within a window of $\pm 10\tau$ around R_0 will be the correlation parameter most representative of the similarity between the two spectra. Positive correlations outside of this range can be rejected and are not considered as the basis for quantitative analysis.

An additional correction to increase the accuracy of R_{MAX} for slight X axis misalignment is to use the average value of R_{MAX} over the range of $\pm$ 1τ. This obviously lowers the value of R_{MAX} for an autocorrelation from 1.0 but as long as this same average range is used for all correlations, then no artifacts should be introduced. Once a value for R_{MAX} has been obtained, it can then be used to gain insight into the similarity with the spectrum or spectra with which it has been correlated. In the application of this method of data analysis to EXAFS, the main objective is to obtain quantitative analytical information from a series of samples that are representative of at least two phases. The following description of data analysis will concentrate on the analysis of a known binary mixture.

Binary Mixtures. The first step in obtaining quantitative information from a series of samples with two major constituents is to select standards that best represent the two extremes of the series. Just as caution must be exercised in choosing standards for normal EXAFS data analysis, care must be taken to ensure that the standards chosen possess properties that are common to all of the samples. Thus if a bulk crystalline standard is used to analyze a well-dispersed, disordered amorphous material, which may be chemically similar, the correlation would give insight into the relative dispersions (particle size) but may not yield chemical information. Thus the two standards used for the correlation should have similar physical and chemical characteristics with respect to the two components that are to be quantified. If proper standards are not easily found, then using the two end point samples from the series as correlation standards allows relative quantitative measurements within the series.

Once the two standards have been chosen, cross-correlation is performed between each sample and each standard separately. This yields two R_{MAX} values for each sample. The two standards also have two R_{MAX} values, one obtained from their autocorrelation (R_0 = 1.0) and the other obtained from the cross-correlation with each other. The R_{MAX} value for the cross-correlation of the two standards will be the same for both standards since the correlation of spectrum A with B will yield a R_{MAX} equal to the correlation of B with A. Thus the R_{MAX} value obtained for the cross-correlation of the standards should represent the lowest value of R_{MAX} = R_{LOWER}. The maximum value is obviously that obtained from the auto-correlation of either standard, R_{MAX} = R_{UPPER}. The values obtained from the cross-correlation of the samples with either standard should fall in the range between R_{LOWER} and R_{UPPER}. If the values fall outside of this range, then either there is another component present that has not been accounted for in one or both of the standards, or the samples that fall outside of the correlation range better represent the extremes of the series. If this is the case, then the choice of standards need to be reconsidered and the components involved in the series reconsidered.

Figure 6 shows the R_{MAX} vaues obtained for the correlation of spectra from the physical mixtures derived from the Co_3O_4 and $CoAl_2O_4$ standards. The right-hand side of Figure 6 shows the ordinate given in terms of percent correlation. This allows a first approximation of how the samples in the series compare with the standards to be determined. This point in the analysis should not be overlooked since it yields useful semiquantitative information concerning relative trends within the series. In this instance it is not so critical that the ranges of R_{MAX} values from R_{UPPER} to R_{LOWER} actually give large absolute deviations since we are only concerned with relative changes.

To convert the changes in R_{MAX} into percent composition, a calibration curve needs to be constructed. If an experimentally measured set of standard mixtures is not available, then the calibration series can be computer generated. The calibration curve spectra are obtained by making computer composites from the two standard spectra. It is known that the total $\chi(E)$ spectrum is simply the sum of all of the individual $\chi(E)$ spectra from each contributing phase weighted by its appropriate mole fraction (7). The composite spectra are formed by addition of the two standard spectra, weighted by their percent contribution to the final composite spectrum. These calibration spectra are cross-correlated with each standard to obtain a R_{MAX} value with respect to that standard. Obtaining quantitative data from correlation analysis of a binary mixture is based on the assumption that the two phases

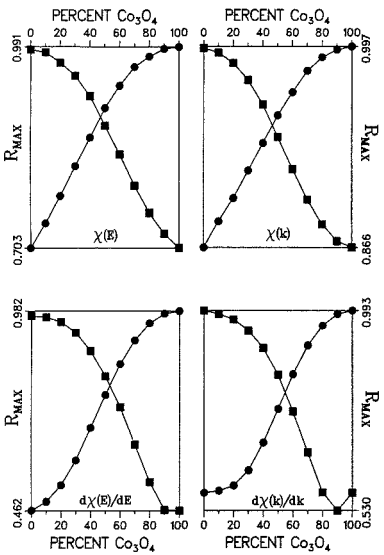

Figure 7. Calibration curves with respect to Co_3O_4 (●) and $CoAl_2O_4$ (■) for computer composite spectra: $\chi(E)$, $d\chi(E)/dE$, $\chi(k)$, and $d\chi(k)/dk$.

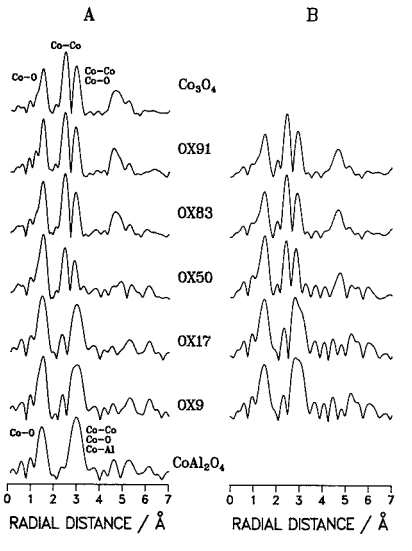

Figure 8. (A) PRDF for the Co_3O_4 and $CoAl_2O_4$ standards and physical mixtures. The bond types responsible for the radial peaks are shown for the standards. (B) Computer composite PRDFs with the same mole percents as the physical mixtures. Mole percents are given in the figure.

of the mixture have enough spectral uniqueness that their presence is detectable in the final spectrum. Thus oscillations caused by the local environment around the different phase(s) of the element probed are used as a fingerprint for the identification and quantification of the phase(s) present. The best quantitative results will be obtained by those spectra which have sufficient unique spectral features that a constant change in R_{MAX} is obtained as a function of sample composition.

Figure 7 shows the variations of R_{MAX} as a result of correlating $\chi(E)$, $d\chi(E)/dE$, $\chi(k)$, and $d\chi(k)/dk$ spectra with the Co_3O_4 and $CoAl_2O_4$ standards for computer-generated composite spectra. Note that the R_{MAX} ranges for the derivative correlations ($d\chi(E)/dE$ and $d\chi(k)/dk$) are both greater than those for the unfiltered correlations. While it is desirable to have a large R_{MAX} range, the most important requirement of the calibration curves is that they be as linear as possible. It can be seen that for all four calibration curves the variation in R_{MAX} is nonlinear particularly for correlations that represent greater than 70% of the same phase as the standard. Thus once a spectrum is composed of a major (>70%) and minor phase, the major phase, tends to saturate the R_{MAX} response. Since the change in composition results in a smaller change in R_{MAX} for the saturated region, there will be some loss of quantitative accuracy and precision. The calibration curves for the first derivatives of both the $\chi(E)$ and $\chi(k)$ spectra show discontinuities with respect to the $CoAl_2O_4$ standard and are more nonlinear with respect to Co_3O_4 than their normal χ spectra. This suggests that the derivative χ will not yield as reliable quantitative data as the unfiltered χ.

Thus the problems associated with the nonlinearity of k space misalignment and the nonlinearity of the calibration curves for the derivative spectra indicate that the derivative and $\chi(k)$ spectra should not be used to obtain reproducible quantitative results. The $\chi(E)$ spectra are therefore expected to yield the most accurate and reproducible quantitative results. Quantitative analysis is additionally aided by use of the two calibration lines. Measuring a given mixture with respect to both standards permits an average concentration to be obtained from the two calibration lines. This will help to minimize any error introduced from the nonlinear sections of the calibration curves.

3. RESULTS AND DISCUSSION

Visual Inspection. Figure 5 shows the $\chi(E)$ spectra for the Co_3O_4 and $CoAl_2O_4$ standards and for the series of physical mixtures. It is evident that there is similarity between the spectra of Co_3O_4 and $CoAl_2O_4$. It can also be seen that the OX91 and OX83 samples closely resemble Co_3O_4 and the OX17 and OX9 samples closely resemble $CoAl_2O_4$. The OX50 sample does not strongly favor one standard over the other.

Figure 8A shows the PRDFs for Co_3O_4 and $CoAl_2O_4$ and the series of physical mixtures obtained from the FT of the $\chi(k)k^3$ spectra. The bond types for the individual radial peaks for the standards are also shown. It appears that the PRDFs for samples OX91 and OX83 are very similar to that of Co_3O_4. The first radial peak at approximately 1.9 Å increases slightly relative to the other radial peaks as the amount of Co_3O_4 in the sample decreases. For the OX50 sample the first radial peak has become the dominant peak and the longest radial peak of Co_3O_4 (~4.7 Å) has essentially disappeared into the noise. However the PRDF of OX50 is visually still more representative of Co_3O_4 than of $CoAl_2O_4$. For samples OX17 and OX9 the PRDF closely resembles that of $CoAl_2O_4$. It can be seen that the first radial peak (~1.9 Å) for OX17 and OX9 is the dominant peak which differs from the $CoAl_2O_4$ standard. The Co_3O_4 Co–Co radial peak (~2.5 Å) is also evident in OX17 and OX9, indicating that the Co_3O_4 contribution is greater as a minor component than for $CoAl_2O_4$ in the OX83 and OX91 samples. It is interesting to note that the loss of the longest radial peak from Co_3O_4 and the increase in the contribution from the lower radial peaks, normally associated with a decrease in long range order, is seen for the OX50 sample. This is the only real evidence for the presence of the $CoAl_2O_4$ phase in the OX50 sample.

Figure 8B shows the PRDF calculated from the computer generated calibration spectra derived by mixing the $\chi(E)$ spectra of Co_3O_4 and $CoAl_2O_4$. The composites are shown for those PRDFs of the same mole fractions as the samples. There are many similarities between the composite PRDFs and the PRDFs obtained experimentally for the series of physical mixtures (Figure 8A). The features which represent the Co_3O_4 phase are most dominant for the OX91, OX83, and OX50

samples whereas the OX17 and OX9 samples most closely resemble the $CoAl_2O_4$ standard. These spectra (trends) are very similar to those obtained experimentally.

EXAFS Curve Fitting. It should be noted that for the set of samples studied here it is very fortunate to have one radial peak (RD ~ 1.9 Å) which is common to both Co_3O_4 and $CoAl_2O_4$ and representative of backscattering from a common Co–O bond, and a second radial peak which is unique to only one phase (Co_3O_4) but also representative of only a single interaction (RD ~ 2.85 Å, Co–Co). Therefore the information obtained from the single shell fit of the Co–Co peak can be used to determine some of the parameters necessary to perform a double shell fit of the common (Co–O) peak such as the percent Co_3O_4. An additional advantage of calibrating with physical mixtures is having a high degree of certainty of the values for the parameters used in the fit. For this reason it should be remembered that the results obtained from EXAFS curve fitting will be obtained with a higher degree of precision than is normally possible for unknown compounds. For curve fitting analysis the radial distances were held constant at their theoretical values and the relative Debye–Waller factor ($\Delta\sigma^2$) was fixed at zero since it was assumed that there was no difference in the degree of disorder for the standards and the samples. The theoretical values for the peak parameters of the samples and the Co_3O_4 and $CoAl_2O_4$ standards are listed in Table I. The coordination number for the first radial peak of Co_3O_4 (Co–O, $N = 5.33$) is due to the combination of tetrahedral cobalt (33.3%, $N = 4.0$) and octahedral cobalt (66.7%, $N = 6.0$) and the coordination number for the first radial peak of $CoAl_2O_4$ (Co–O, $N = 4.0$) is from tetrahedrally coordinated cobalt. The coordination numbers for the samples are determined by weighting the coordination of the pure compound by the mole fraction of that phase in the mixture.

Table II lists the results obtained for standard EXAFS curve fitting of the first (~1.9 Å) and second (~2.8 Å) radial peaks of the samples using the Co_3O_4 and $CoAl_2O_4$ standards. The first radial peak was fit using two shells where only the coordination numbers for Co_3O_4 and $CoAl_2O_4$ along with the edge shift were allowed to float. From the coordination number the mole fraction, x%, can be obtained by

$$x\% = (N_{\text{theory}}/N_{\text{calc}})100 \quad (7)$$

where N_{theory} is the known coordination number of the standard and N_{calc} is the coordination number obtained from the NLLS fit of the EXAFS data. It can be seen in Table II that for the two ends of the series (OX91 and OX9) the fit is much worse than for the other samples. For the OX91 sample the curve fit does not appear to acknowledge the presence of $CoAl_2O_4$ (negative coordination). This would suggest that when one phase is a minor component (<10%) there is difficulty in obtaining accurate quantitative information.

When the second radial shell, representative of only the Co_3O_4 phase, was fit, only $N_{Co_3O_4}$ and E_0 were allowed to float. In Table II the values obtained for the mole fraction of the Co_3O_4 are closer than those obtained for the two-shell fit. Note that the largest error associated with these measurements is for the samples where Co_3O_4 is a minor phase as would be expected. Some of the error associated with the OX17 and OX9 samples could be from the small lobe which can be seen to the low side of the second radial peak of $CoAl_2O_4$ (RD ~ 3.0 Å). This small lobe may partially be due to Fourier ringing from the second $CoAl_2O_4$ radial peak or due to some contamination in the $CoAl_2O_4$ standard. Thus the quantitative capabilities for EXAFS, even for ideal systems of an isolated single shell radial peak, may be somewhat limited by interference from the major phase.

Correlation Analysis. Quantitative analysis was performed by using Co_3O_4 and $CoAl_2O_4$ as the standard spectra for correlation analysis. Figure 6 illustrates the R_{MAX} values obtained for the $\chi(E)$ spectra. These results yield semiquantitative information about the species relative to the two standards. For example, OX91 and OX83 show greater similarity to Co_3O_4 and each other than to OX17 and OX9. This is true for the cross-correlation with respect to either the Co_3O_4 or $CoAl_2O_4$ standards. The OX50 sample shows a slightly higher correlation with respect to Co_3O_4 than to $CoAl_2O_4$ but does not show a major allegiance to either standard. Thus without a calibration curve the relative nature and trend within the series with respect to the Co_3O_4 and $CoAl_2O_4$ standards can be obtained.

By use of the calibration curves in Figure 7, quantitative results were obtained for the series of physical mixtures using $\chi(E)$, $d\chi(E)/dE$, $\chi(k)$, and $d\chi(k)/dk$ spectra. Table III lists these results, measured relative to the Co_3O_4 and $CoAl_2O_4$ standards, along with their average values. The results obtained for the $d\chi(E)/de$, $\chi(k)$, and $d\chi(k)/dk$ spectra all have some results that do not fall within the limits of the calibration curve, mainly for samples that have a high concentration of the same phase as the standard. While the average for these three spectral types falls within 10% of their actual values, the average is not reliable since the values are based on the erroneous boundary condition that any values which fall outside of the concentration limits are equal to that limit. As was predicted from the previous discussion the $\chi(E)$ values yield the most reliable quantitative results. Their average values are all within 5% of the actual concentrations. It is also evident that the values obtained for the same sample from the two different calibration curves never differ by more than 10%. Although these results are obtained for an idealized system, it seems fair to assume that if the spectra are properly calibrated and the standards are representative of the phases or variables which are changing throughout the series, then the calibration should be good within ±10% for "real" samples. This compares favorably with standard EXAFS curve fitting analysis.

Although the time required to perform the correlation analysis can be measured with relative ease, the amount of time required to perform the standard EXAFS analysis is not estimated as easily. Correlation analysis required extraction of 7 spectra, the creation of 9 composite spectra, and a total of 32 cross-correlations. This analysis was performed on a SPERRY PC/IT microcomputer; the total time needed to obtain the R_{MAX} values was less than 30 min. The EXAFS analysis is not so straightforward since once the individual $\chi(k)k^3$ spectra are obtained, the curve fitting may require several attempts allowing different combinations of the variables to either "float" or remain fixed. Thus the number of radial peaks and the number of attempts needed to obtain an acceptable standard deviation for the curve fit can vary. Note that for these samples the relative Debye–Waller factors ($\Delta\sigma^2$) and the radial distances (RD) were held constant. The EXAFS analysis was performed on a VAX mainframe and the analysis took approximately 2 h. But as the complexity of the samples increase, the time required to perform the standard EXAFS analysis will also increase whereas the time required for the correlation analysis will remain virtually the same. Therefore the results obtained from correlation analysis could then be used as a starting point for the standard EXAFS curve fitting analysis. This should help to decrease the time required for the standard data analysis and also yield another set of data concerning the quantitative trends within the series of samples.

4. CONCLUSIONS

A method of obtaining quantitative (concentration hence coordination number) information from EXAFS spectroscopy

Table I. Theoretical Mole Percents, Mole Ratios, and Coordination Numbers for the Standards and Physical Mixtures

sample	Co_3O_4	OX91	OX83	OX50	OX17	OX9	$CoAl_2O_4$
			Mole Percent				
$X_{Co_3O_4}$	100	91	83	50	17	9	0
$X_{CoAl_2O_4}$	0	9	17	50	83	91	100
			Mole Ratio				
(Co_3O_4:$CoAl_2O_4$)		10:1	5:1	1:1	1:5	1:10	
			Coordination Number RD ~ 1.92 Å (Co–O)				
$N_{Co_3O_4}$	5.33	4.84	4.44	2.67	0.89	0.48	0.00
$N_{CoAl_2O_4}$	0.00	0.36	0.66	2.00	3.33	3.64	4.00
			RD ~ 2.85 Å (Co–Co)				
$N_{Co_3O_4}$	6.00	5.45	5.00	3.00	1.00	0.55	0.00

Table II. Results of Standard EXAFS Curve Fitting for the First and Second Radial Shells[a]

sample	OX91	OX83	OX50	OX17	OX9
Results of Curve Fitting of 1st Radial Peak (RD ~ 1.95 Å)					
$N_{Co_3O_4}$	5.63	4.61	2.50	0.89	0.78
$N_{CoAl_2O_4}$	−0.27	0.70	2.41	3.35	3.36
$X_{Co_3O_4}$	106	86	47	17	15
$X_{CoAl_2O_4}$	−7	18	60	84	84
Results of Curve Fitting of 2nd Radial Peak (RD ~ 2.85 Å)					
$N_{Co_3O_4}$	5.55	5.02	2.99	1.23	0.84
$X_{Co_3O_4}$	93	84	50	21	14

[a] The radial distances were held constant at their known values and the Debye–Waller factor was held constant at zero. The edge shift was ±3.0 eV for the series.

Table III. Results of Correlation Analysis As Determined from the Calibration Curves for the $\chi(E)$, $\chi(E)/dE$, $\chi(k)$, $\chi(k)/dk$ Spectra

sample	$\chi(E)$	$d\chi(E)/dE$	$\chi(k)$	$d\chi(k)/dk$
Correlation Standard Co_3O_4				
OX9	10	<0	<0	<0
OX17	16	11	6	<0
OX50	50	50	46	46
OX83	82	84	84	87
OX91	86	87	78	87
Correlation Standard $CoAl_2O_4$				
OX9	17	21	21	21
OX17	25	26	24	22
OX50	56	53	57	53
OX83	87	>100	95	>100
OX91	91	>100	>100	>100
Average Percent Co_3O_4 from Both Calibration Lines				
OX9	14	11[a]	11[a]	11[a]
OX17	21	19	15	11[a]
OX50	53	52	52	50
OX83	85	92[a]	90	94[a]
OX91	89	94[a]	89[a]	94[a]

[a] Average based on restrained percentages.

has been demonstrated for binary systems. The method is based on the cross-correlation response of normalized $\chi(E)$ spectra with spectra of two suitable standards. If the standards truly represent the known composition extremes, then composite spectral profiles can be constructed in order to create a calibration curve. Thus the unknown cross-correlation responses, R_{MAX}, can then be converted in percent composition and hence coordination number N. If N is the only information required, then the analysis can stop at this point. Because the extraction of the correlation information is quite straightforward compared to the standard EXAFS curve fitting approach, considerable time savings can be achieved. In cases where standard spectra are unavailable or impossible to obtain, then the extreme members in a given series can be used as standards. In this case the results cannot be calibrated exactly in order to extract percent composition or N but approximate relative trends can be observed. In either case the correlation-based information can be used as a starting point in the standard curve fitting analysis. However it should be noted that use of adequate standards is also a severe limitation of curve-fitting EXAFS data as well.

EXAFS spectra seem particularly suited to correlation analysis. The natural damping at higher energies ensures that R_{MAX} can be found close to R_0. This results in giving more weight to the lower energy oscillations which, in this case, is most suitable since the higher energy data is most likely to have poorer S/N. In addition, because χ is related to the PRDF via the Fourier transform, the PRDF or some similar function derived from $\chi(E)$ also appears in the correlation analysis because correlation is simply complex multiplication in Fourier space (eq 2).

The materials chosen to demonstrate the analysis technique presented above also serve to highlight a specific analytical point with regard to EXAFS. The problems that can arise in X-ray diffraction (XRD) from analysis of materials with similar crystal structure are alleviated in EXAFS because of the elemental backscattering specificity. Thus EXAFS can easily distinguish Co_3O_4 and $CoAl_2O_4$ whereas XRD cannot do so readily.

In future publications the authors will demonstrate the application of this technique to the analysis of heterogeneous catalysts.

ACKNOWLEDGMENT

We thank Professor Pedro Montano, Mohan Ramanathan, and Mark Engbretson at Beamline X18B, NSLS, for their guidance in collecting our EXAFS data.

LITERATURE CITED

(1) Horlick, G. *Anal. Chem.* **1973**, *45*(2), 319–324.
(2) Lam, R. B.; Sparks, D. T.; Isenhour, T. L. *Anal. Chem.* **1982**, *54*(12), 1927–1931.
(3) Lam, R. B. *Appl. Spectrosc.* **1983**, *37*(6), 567–569.
(4) Mann, C. K.; Goleniewski, J. R.; Sismanidis, C. A. *Appl. Spectrosc.* **1982**, *36*(3), 223–227.
(5) Horlick, G.; Hieftje, G. M. Correlation Methods in Chemical Data Measurement. In *Contemporary Topics in Analytical and Clinical Chemistry*; Hercules, D. M., Hieftje, G. M., Snyder, L. R., Evenson, M. A., Eds.; Plenum Press: New York, 1978; pp 153–216.
(6) Fay, M. F.; Proctor, A.; Hoffmann, D. P.; Hercules, D. M. *Anal. Chem.* **1988**, *60*(21), 1225A–1243A.
(7) Teo, B. K. *EXAFS: Basic Principles and Data Analysis*; Springer-Verlag: New York, 1986.
(8) Lee, P. A.; Citrin, P. H.; Eisenberger, P.; Kincaid, B. M. *Rev. Mod. Phys.* **1981**, *53*(4), 769–806.
(9) Sayers, D. E.; Bunker, B. A. *Data Analysis*; John Wiley & Sons: New York, 1988.
(10) Cooley, J. W.; Tukey, J. W. *Math. Comput.* **1965**, *19*(90), 297.
(11) Hoffmann, D. P.; Proctor, A.; Hercules, D. M. *Anal. Chem.* **1989**, *61*, 898–904.
(12) Ng, R. C. L.; Horlick, G. *Appl. Spectrosc.* **1985**, *39*(12), 834–840.
(13) Hallowell, J. R., Jr.; Delaney, M. F. *Anal. Chem.* **1987**, *56*(22), 1544–1549.
(14) Rossi, T. M.; Warner, I. H.; *Appl. Spectrosc.* **1986**, *40*(1), 44–52.
(15) Brigham, E. O. *The Fast Fourier Transform*; Prentice-Hall: New York, 1974.

RECEIVED for review November 21, 1988. Accepted May 8, 1989. The authors acknowledge financial support for this work from the National Science Foundation, Grant CHE-8411835. D.P.H. acknowledges BP America for a graduate fellowship.

Fourier Transform Atomic Absorption Flame Spectrometry with Continuum Source Excitation

Mark R. Glick, Bradley T. Jones, Benjamin W. Smith, and James D. Winefordner*

Department of Chemistry, University of Florida, Gainesville, Florida 32611

The design and performance of a Fourier transform atomic absorption flame spectrometer (FT-AAS) is presented. A 300-W xenon arc continuum source and a Michelson interferometer are used. A signal to noise disadvantage arising from the multiplex feature of FT-AAS is demonstrated by varying the photon flux at the detector without changing the exciting radiation. A grating is used for dispersion of the radiation before the interferometer to reduce the spectral window at the photomultiplier tube. Detection limits for several elements are generally an order of magnitude poorer than those obtained by continuum atomic absorption methods using echelle-grating spectrometers. Line profiles and absorption spectra, within the region of the spectral window selected by the grating, can be obtained with this method. Standard curves for sodium were constructed to extend the linear calibration range, by using absorbances measured at the absorption maximum and 0.022 nm off-line.

INTRODUCTION

Atomic absorption spectrometers (AAS), although commercially available only with line sources, have been constructed with continuum sources since their first analytical use. Because the sensitivity of the absorption method is dependent on the effective spectral bandwidth of the spectrometer (*1–3*), the use of continuum sources has been limited. When line sources are used, the effective bandwidth is determined by the width of the atomic emission line in the source. When continuum sources are used, the monochromator determines the effective bandwidth; only when the effective bandwidth approaches that of the analyte absorption line can the sensitivity of continuum source AAS equal that of line source AAS. For this reason, much work on continuum source AAS dwells on the development of high-resolution spectrometers.

To achieve the resolution needed for AAS, several different approaches have been taken. High-resolution Fabry–Perot interferometers have been demonstrated with continuum source AAS (*4, 5*) and, the more practical, echelle-grating spectrometers (*6–8*). Modulation to achieve resolution of the analytical line has been illustrated, including spectral line modulation (*9*) and sample modulation (*10, 11*). Resonance monochromators have been used to decrease the effective spectral bandwidth (*12–14*). Of all these methods, the use of echelle-grating monochromators has been the most successful and is the subject of several reviews (*15–17*).

Other interferometers have been suggested as possible components in an atomic absorption spectrometer (*18, 19*). Fourier transform spectrometry (FTS) has the advantages of high spectral resolution capability, wavelength accuracy, and high throughput. The disadvantages expected of FTS in the visible and ultraviolet regions have also been well documented (*18, 20, 21*). In the photon shot noise limited cases, a multiplex advantage is not realized. For dense spectra, such as molecular fluorescence and absorption spectra, a multiplex disadvantage can even appear (*22, 23*).

To continue our investigation of Fourier transform spectrometry in the visible and ultraviolet regions, we have used a commercially available Michelson interferometer for atomic absorption measurements in a flame. Absorption spectra can be obtained with the Fourier transform atomic absorption spectrometer (FT/AAS), and multielement determinations can be performed for elements within the selected spectral window. Detection limits for several elements with analytical lines in the visible and ultraviolet regions are given. The advantages of continuum source AAS that have been realized in other systems—automatic background correction, multielement analysis, single source, extended calibration curves—can also be found in this system. The detection limits are at least 1 order of magnitude poorer than other continuum source, atomic absorption spectrometers.

EXPERIMENTAL SECTION

A diagram of the Fourier transform atomic absorption spectrometer is shown in Figure 1. Radiation from the continuum source was passed through the flame without any spectral dispersion. A lens was used to focus the radiation from the lamp on an iris diaphragm, where it was apertured and collimated by a second lens. A second iris diaphragm allowed only a portion of the collimated radiation from the less turbulent region of the lamp image to pass through the flame (*24*). After the flame, a grating was used to disperse the radiation before the interferometer. A quartz lens focused a portion of the dispersed radiation onto the entrance aperture of the interferometer.

The Michelson interferometer (DA3.02, Bomem, Vanier, Quebec) in this system was commercially available and used without modification. A photomultiplier tube (R647, Hamamatsu, Bridgewater, NJ) was used for detection of the interferogram. The source of radiation was an unfiltered, 300-W xenon arc lamp (Cermax, ILC Technologies, Sunnyvale, CA). Predispersion of the radiation was accomplished by a 2400 groove/mm, plane-ruled grating, blazed at 300 nm (SLM-Aminco, Urbana, IL). The grating could be rotated to select the radiation window of interest, which was focused onto the entrance aperture of the interferometer. The spectral half-width of the source radiation entering the interferometer was approximately 5 nm.

The fuel-lean air/acetylene flame was produced by a 10-cm slot burner (Perkin-Elmer, Norwalk, CT). Collimated white light, apertured to 1 cm diameter, passed through the flame to the grating. A second aperture was used to reduce the collection of flame emission. Even at concentrations as high as 10 mg/mL, no analyte emission could be detected with the optical configuration shown in Figure 1.

Each absorption measurement was made by recording a reference spectrum with 1.00-cm^{-1} resolution, unless indicated otherwise. One hundred interferograms were coadded for both reference and absorption spectra. The scan rate of the interferometer was 0.15 cm/s, for an average time of spectrum acquisition of 10 min.

RESULTS AND DISCUSSION

A grating was used for predispersion of the radiation entering the interferometer to limit the window of radiation striking the detector (*25*). In the photon shot noise limited

* Author to whom correspondence should be sent.

0003-2700/89/0361-1694$01.50/0

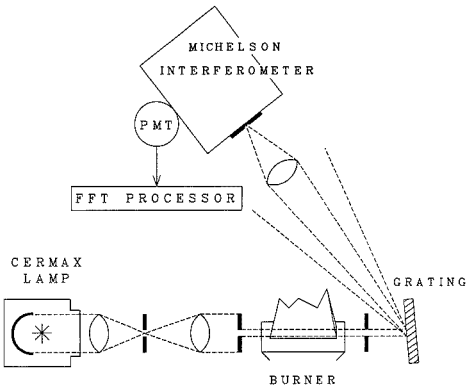

Figure 1. Schematic diagram of the Fourier transform atomic absorption spectrometer using a continuum source.

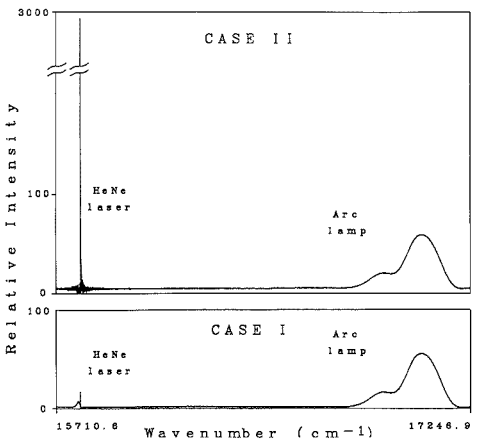

Figure 2. Relative intensities of HeNe laser radiation and excitation radiation from the xenon arc lamp. In case II the laser radiation reaching the photomultiplier tube was approximately 200 times that in case I.

region, predispersion resulted in an increase in the signal to noise ratio (S/N), because the photon flux at the detector is reduced. This limits the spectral region that can be used for multielement analysis to 5 nm. The entire absorption spectrum in that window can be obtained by the spectrometer, but unlike echelle-grating systems, multiple lines at discontinuous spectral regions cannot be simultaneously measured.

Gratings with poorer dispersion could be used to obtain a larger spectral window, which would permit the acquisition of absorption spectra over an even wider range. The larger spectral window, however, would also increase the radiation at the detector and degrade S/N.

To clearly demonstrate the multiplex disadvantage, the effect of photon flux at the detector on the S/N of sodium absorption lines was qualitatively investigated. The Bomem interferometer uses an internal HeNe laser for alignment, which unavoidably strikes the photomultiplier tube. To attain a spectrum with high S/N, the HeNe laser radiation was spatially blocked at the exit port of the interferometer. In Figure 2, case I shows the relative intensity of the HeNe laser radiation that could not be blocked, in comparison to the excitation radiation from the continuum source. For case II,

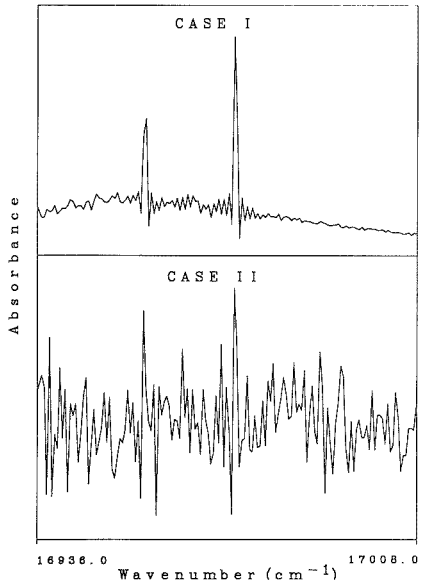

Figure 3. Comparison of signal to noise of the sodium doublet for case I and case II. Instrumental bandwidth was 1.00 cm^{-1}.

Table I

element	wavelength, nm	detection limit, μg/mL FT/continuum	detection limit, μg/mL continuum[a]
Ag	328.068	0.2	0.007
Cu	324.754	0.1	0.01
Mn	279.482	0.2	0.01
Na	588.995	0.02	0.003

[a] Reference 17.

the internal laser radiation was not blocked, and an external HeNe laser was also used to increase the photon flux striking the detector. In case II of Figure 2, the laser radiation has a peak intensity almost 200 times that of case I. The excitation radiation was not changed.

The effect on S/N of the absorption spectrum of the sodium doublet is shown in Figure 3. The poorest signal to noise is obtained in case II, when the HeNe laser radiation is much more intense than the excitation radiation. The noise from the HeNe is distributed to the analytical lines. Unfortunately, the radiation from the internal laser cannot be blocked entirely, and inevitably it reaches the photomultiplier tube. In the shot noise limited region, this contributes to a multiplex disadvantage. A solar-blind photomultiplier tube would avoid this particular problem.

Detection limits for several elements with lines in the ultraviolet and visible region are shown in Table I. Generally, the detection limits are at least an order of magnitude poorer than those that have been obtained by an echelle-grating spectrometer and continuum source. The same trend of poorer detection limits as the analytical line moves to shorter wavelengths that is observed in other continuum source AAS methods was observed here.

In an effort to determine the cause of the poorer detection limits, the sensitivity and noise of the system were investigated. The sensitivity is related to the effective spectral resolution and in this system is determined by the mirr

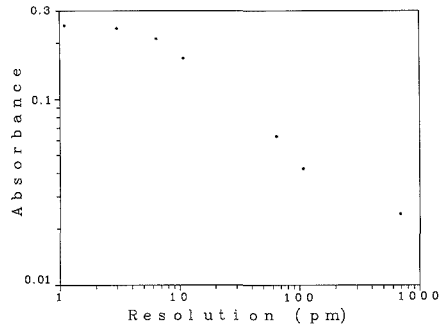

Figure 4. Dependence of observed absorbance on instrumental bandwidth. Copper absorbance was measured at 327.396 nm.

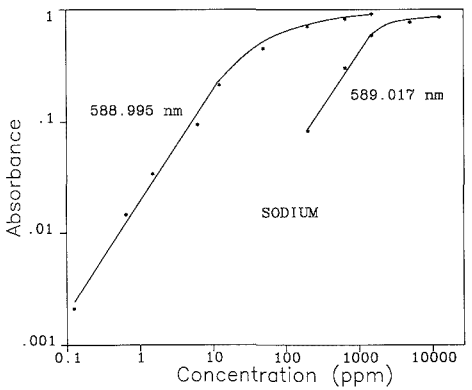

Figure 5. Calibration curves for sodium, using absorbance measurements at the peak, 588.995 nm, and 0.022 nm off the peak, 589.017 nm: 1.00 cm^{-1} resolution and 10-min acquisition time.

movement of the interferometer. Figure 4 shows the effect of instrumental resolution on the measured absorbance at the 327.396-nm line of copper. As the spectral resolution increases, the observed peak absorbance increases, until the line is completely resolved. Below an instrumental resolution of 3 pm, the absorbance does not change.

All absorbance measurements made for the determination of the detection limits in Table I were made with an instrumental resolution of 1.00 cm^{-1}; at the copper line this corresponded to 11 pm. Although this resolution did not result in maximum absorption, it was chosen as a compromise. Much longer spectrum acquisition times would have resulted if better resolution was selected. An instrumental resolution of 3 pm yielded a higher absorbance for copper, but the time of acquisition became prohibitive.

One advantage that is realized to some extent is the multichannel capability of FT/AAS. Atomic absorption spectra can be obtained over the profile of the line, as long as the line falls within the selected window of radiation entering the interferometer. This affords the possibility of using the profile of the absorption line for diagnostic purposes, background correction, and for extension of the calibration curve. The capability of extending the linear range of the calibration curve has been demonstrated with continuum source AAS (*26*, *27*). The automatic acquisition of the absorption spectrum that is obtained in FT-AAS allows this type of extension without foresight and preparation. Figure 5 shows the extension of the linear portion of a calibration curve for sodium. Absorption measurements were taken from the spectrum at the

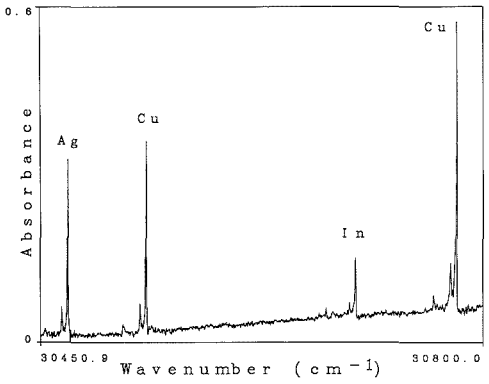

Figure 6. Absorption spectrum of a three-component aqueous solution, 100 μg/mL: 1.00 cm^{-1} resolution and 10-min acquisition time.

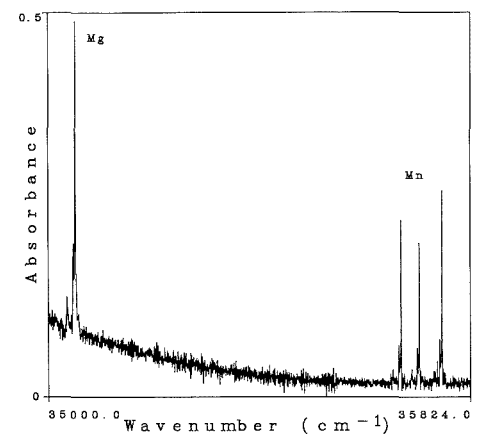

Figure 7. Absorption spectrum of a two-component aqueous solution, 100 μg/mL: 1.00 cm^{-1} resolution and 10-min acquisition time.

peak of the line profile and on the edge of the line profile.

The limited multielement capability is demonstrated by the absorption spectra of Figure 6 and Figure 7. Four absorption peaks corresponding to 100 μg/mL of three elements, Cu, In, and Ag, are shown in Figure 6. At shorter wavelengths, four absorption peaks corresponding to 100 μg/mL of two elements, Mn and Mg, are shown in Figure 7. Clearly the analytical use as a simultaneous method is limited, because only those elements that happen to have absorption lines within the 5-nm spectral window will appear in the spectrum. The use of a grating with poorer dispersion would allow the simultaneous determination of more elements, but S/N would decrease due to the increased total light flux reaching the photomultiplier tube.

CONCLUSION

FT-AAS with a continuum source is limited as an analytical technique since the spectral range, sensitivity, detection power, and acquisition time are interdependent and limited. Nevertheless, the technique may have limited use in specialized analytical applications, especially where ease of background correction and line identification are important and where several selected elements must be measured simultaneously. FT-AAS with a continuum source has had and will continue to have significant use as a diagnostical technique, particularly

for line profile and broadening studies.

LITERATURE CITED

(1) Walsh, A. *Spectrochim. Acta* **1955**, *7*, 108–117.
(2) Winefordner, J. D. *Appl. Spectrosc.* **1963**, *27*, 109–111.
(3) Fassel, V. A.; Mossotti, V. G. *Anal. Chem.* **1963**, *35*, 252–253.
(4) Veillon, C.; Merchant, P., Jr. *Appl. Spectrosc.* **1973**, *27*, 361–365.
(5) Nitis, G. J.; Svoboda, V.; Winefordner, J. D. *Spectrochim. Acta* **1972**, *27b*, 345–363.
(6) Keliher, P. N.; Wohlers, C. C. *Anal. Chem.* **1974**, *46*, 682–687.
(7) Keliher, P. N.; Wohlers, C. C. *Anal. Chem.* **1976**, *48*, 140–143.
(8) Zander, A. T.; O'Haver, T. C.; Keliher, P. N. *Anal. Chem.* **1976**, *48*, 1166–1175.
(9) Cochran, R. L.; Hieftje, G. M. *Anal. Chem.* **1978**, *50*, 791–800.
(10) Marinkovic, M.; Vickers, T. J. *Anal. Chem.* **1970**, *42*, 1613–1618.
(11) Mossotti, V. G.; Abercrombie, F. N.; Eakin, J. A. *Appl. Spectrosc.* **1971**, *25*, 331–341.
(12) Palermo, E. F.; Crouch, S. R. *Anal. Chem.* **1973**, *45*, 1594–1602.
(13) Blackburn, M. B.; Winefordner, J. D. *Can. J. Spectrosc.* **1982**, *27*, 137–140.
(14) Larkins, P. L.; Radziuk, B. Van Loon, J. C. *Spectrochim. Acta* **1983**, *38B*, 473–480.
(15) O'Haver, T. C.; Messman, J. D. *Prog. Anal. Spectrosc.* **1986**, *9*, 483–503.
(16) Harnly, J. M. *Anal. Chem.* **1986**, *58*, 933A–943A.
(17) O'Haver, T. C. *Analyst* **1984**, *109*, 211–217.
(18) Winefordner, J. D.; Avni, R.; Chester, T. L.; Fitzgerald, J. J.; Hart, L. P.; Johnson, D. J.; Plankey, F. W. *Spectrochim. Acta* **1976**, *31B*, 1–19.
(19) Thorne, A. *J. Anal. At. Spectrom.* **1987**, *2*, 227–232.
(20) Hirschfeld, T. *Appl. Spectrosc.* **1976**, *30*, 68–69.
(21) Mertz, Lawrence *Transformations in Optics*; Wiley & Sons: New York, 1965.
(22) Jones, B. T.; Glick, M. R.; Smith, B. W.; Winefordner, J. D. *Spectrochim. Acta*, in press.
(23) Glick, M. R.; Jones, B. T.; Smith, B. W.; Winefordner, J. D. *Appl. Spectrosc.* **1986**, *43*, 342–344.
(24) Cochran, R. L.; Hieftje, G. M. *Anal. Chem.* **1977**, *49*, 2040–2043.
(25) Stubley, E. A.; Horlick, G. *Appl. Spectrosc.* **1985**, *39*, 811–817.
(26) O'Haver, T. C.; Harnly, J. M.; Marshall, J.; Carroll, J.; Littlejohn, D.; Ottaway, J. M. *Analyst* **1985**, *110*, 451–458.
(27) Harnly, J. M.; O'Haver, T. C. *Anal. Chem.* **1981**, *53*, 1291–1298.

RECEIVED for review February 6, 1989. Accepted May 12, 1989. This work was supported by NIH-5R01-GM38434-02. Mark R. Glick thanks BP America for support from a research fellowship.

Mixture Analysis and Quantitative Determination of Nitrogen-Containing Organic Molecules by Surface-Enhanced Raman Spectrometry

J. J. Laserna,[1] A. D. Campiglia, and J. D. Winefordner*

Department of Chemistry, University of Florida, Gainesville, Florida 32611

Surface-enhanced Raman spectrometry (SERS) on a silver-coated filter paper substrate of nitrogen-containing organic molecules is reported. A correction procedure for standardization of measurements is proposed and evaluated to solve the difficult problem of quantitation of adsorbate in SERS. The relative standard deviation obtained through this procedure is around 15%. Linearity ($r = 0.999$) was achieved up to 50 μg/mL aminoacridine. A limited dynamic range is observed, however, due to the limited number of SERS active sites in the substrate. Spectral fingerprinting of three-component mixtures by concentration-dependent selective molecular adsorption on the substrate is also reported.

Investigation of surface phenomena is a key factor for the understanding of subjects of technological interest, such as adhesion, catalysis, corrosion, semiconductor production and characterization, and ultrahigh-vacuum environments. The importance of many aspects of these interfacial phenomena often relies on chemical composition in such a way that techniques capable of providing analytical information on the surface are of concern. These techniques include Auger electron spectroscopy (AES), X-ray photoelectron spectroscopy (XPS), secondary-ion mass spectroscopy (SIMS), and ion-scattering spectroscopy (ISS). By the nature of the effect giving rise to the technique, surface-enhanced Raman spectroscopy (SERS) is a surface analytical technique. In comparison with other surface techniques, SERS can provide information on the chemical form and molecular structure of species situated on a variety of interfaces, including solid–liquid (electrochemical and colloid SERS) (*1*, *2*), solid–vacuum (island film SERS) (*3*), solid–gas (silica and filter paper SERS) (*4*, *5*) and solid–solid (thin-film SERS) (*6*) interfaces. SERS allows studies of the interfacial and conformational behavior of biomolecules and thus enables one to characterize in situ the chemical identity, structure, and orientation of surface species in the adsorbed state (*7*, *8*). In addition, SERS has been shown to be capable of lateral spatial resolution down to the level of 1 μm by means of Raman microprobe instrumentation (*9*) similar to the information available by AES and SIMS. However, in the latter techniques, the sensitivity is much lower (poorer) than the attomole mass sensitivity reported for SERS (*9*).

Among the different materials reported to be SERS active (Ag, Au, Cu, Pd, Li, Na, K, Al, In, AgBr, AgCl, TiO_2, etc.) the metallic form of silver has gained general acceptance for analytical measurements by combining several advantages. It has an appropriate dielectric function, in such a way that the enhancement factor on silver depends to a lesser extent on the excitation wavelength than in other SERS active metals such as gold and copper (*10*). As a result, excitation must be in the red for Cu or Au (*11*), but visible wavelengths may be used with silver (*12*). The metallic form of silver can be easily handled at room temperature and ordinary pressure conditions, which is valuable from a practical standpoint. The analytical applications of SERS on a variety of silver active substrates are rapidly expanding. Sputter-deposited silver surfaces (*13*) have been evaluated for the thiocyanate anion. This substrate can be stored in air for long periods prior to Raman spectral examination in electrochemical and gas-phase

[1] Present address: Department of Analytical Chemistry, Faculty of Sciences, University of Malaga, 29071 Malaga, Spain.

0003-2700/89/0361-1697$01.50/0

media. Silver electrodes have been recently proposed for the analysis of water contaminants (*14*). A limit of detection of 8.5 pg was calculated for pyridine. DNA bases have also been examined in an electrochemical environment (*15*). The combination of a low-power He–Ne laser with a Raman microprobe allows good SERS spectra to be obtained from microscopic areas of the electrode. Silver-coated substrates consisting of latex spheres on glass and filter paper and silica post arrays have also been proposed for the analysis of polynuclear aromatic compounds (*16–18*). Various experimental parameters such as silver layer thickness, particle size, and excitation wavelength were evaluated for maximum sensitivity.

Chemically reduced silver on glass plates (*19, 20*) and filter paper (*5*) has been proposed for the analysis of nitrogen-containing heterocyclic compounds. Chemically reduced (*21–23*) and photoreduced (*24*) silver colloids in batch and flow injection systems (*25, 26*) have been studied. Following this first report of SERS detection in analytical flow systems, a detector for liquid chromatography and flow injection analysis has been developed (*27*).

Only a few attempts to use SERS as a quantitative analytical technique have been reported (*14, 17, 19, 27–29*). The limits of detection are reported to be in the nanogram to picogram range, with a loss of linearity in the SERS response above certain analyte concentrations. In most cases, data on the precision of the measurements are not available. In this paper, several novel analytical aspects of the SERS technique are investigated. On a silver-coated filter paper substrate, fingerprinting of multicomponent samples is reported. The results indicate that depending on the functional groups in the molecule, selective molecular adsorption takes place on the substrate. As a result, unique qualitative information can be obtained from SERS spectra of mixtures. A correction factor to enable standardization of quantitative measurements is reported, providing a relative standard deviation on the order of 15%, a typical precision figure for surface techniques. Quantitative analytical measurements confirm a limited dynamic range for the SERS technique as a result of the limited amount of reactive sites in the substrate. Limits of detection in the picomole level have been found for nitrogen-containing aromatic compounds, including 9-aminoacridine, 1-nitropyrene, and 1,10-phenanthroline.

EXPERIMENTAL SECTION

Instrumentation. The Raman spectrometer consisted of an argon ion laser (Spectra Physics, Model 171) and a 0.22-m double monochromator (Spex Industries, Model 1680B) equipped with a thermoelectrically cooled photomultiplier tube (Hamamatsu, Model R928) and photon counting electronics (SSR Instruments, Model 1105/1120). The analog output signal was directly recorded on a strip chart recorder. A double beam sample compartment (Spex Industries, Fluorolog Series) accommodates the sample holder, which was similar to one described for room-temperature phosphorescence (*30*). Right-angle geometry was used for Raman sampling. The incidence angle of the laser beam on the substrate was 45°. A long-wave pass glass filter (Corion, LG-530) was placed between the sample and the collection optics to remove the exciting light from the scattered radiation, the laser power at the sample was typically 20 mW, and the diameter of the laser beam (TEM_{00} mode) was ca. 1.5 mm. Unfocused, vertically polarized light was used. All spectra reported represent single scans and were obtained at a scan speed of 5 nm min^{-1} with entrance and exit slit settings of 100 μm. The spectrometer resolution was 0.2 nm. The band positions were calibrated with the plasma lines of the Ar^+ laser.

Reagents and Procedure. All chemicals were of analytical reagent grade or equivalent. Distilled, deionized water was used throughout. 9-Aminoacridine hydrochloride monohydrate, *o*-phenanthroline, and 1-nitropyrene were from Aldrich and were used as ethanolic solutions. Working standards were prepared daily from the stock solutions by dilution with ethanol. Whatman No. 1 filter paper was used as substrate and coated with chemically

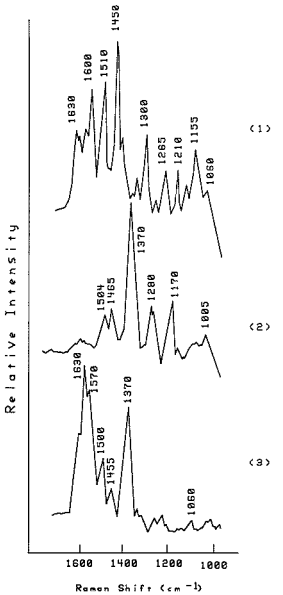

Figure 1. Surface-enhanced Raman spectra on silver-coated filter paper substrate of (1) *o*-phenanthroline, (2) 9-aminoacridine, and (3) 1-nitropyrene. The base lines have been shifted for clarity.

Table I. SERS Spectral Features of *o*-Phenanthroline (OPT), 1-Nitropyrene (NP), and 9-Aminoacridine (AA)

SERS shift,[a] cm^{-1}		
OPT	NP	AA
	980 (vw)	
1005 (w)		1005 (m)
1060 (m)	1060 (w)	1050 (w)
1095 (w)		
1155 (m)		1148 (m)
		1170 (s)
1210 (m)	1210 (w)	
1265 (w)	1260 (w)	1280 (s)
1300 (s)		
	1325 (w)	
	1370 (vs)	1370 (vs)
1430 (w)		
1450 (vs)	1455 (m)	1465 (m)
1510 (s)	1500 (m)	1504 (m)
	1570 (m)	
1600 (s)	1600 (s)	1595 (vw)
1630 (m)	1625 (m)	1625 (vw)

[a] In parentheses, relative intensities are as follows: w, weak; m, medium; s, strong; v, very.

(sodium borohydride) reduced elemental silver by the procedure described elsewhere (*5*). Small portions (1 × 1 cm) of the freshly prepared substrate were placed on the sample holder to which 2 μL of the analytes was added. No evidence of photothermal damage to the substrate during the scan has been observed at the laser power used. For the calculation of SERS intensities, it was estimated that the tails of the SERS peaks contributed negligibly to the background continuum for peaks farther than 20 cm^{-1} from the SERS peaks.

RESULTS AND DISCUSSION

The SERS spectra of 9-aminoacridine (AA), 1-nitropyrene (NP), and *o*-phenanthroline (OPT) are shown in Figure 1. The most prominent spectral features are presented in Table

I. At the concentrations used, the bulk Raman scattering of these analytes is expected to be negligible. The spectra were obtained at an excitation wavelength of 514.5 nm on the surface of a silver-coated filter paper substrate. The morphology of this substrate has been reported elsewhere (*5*). It consists of randomly distributed clusters and dendritic formations of silver, with sizes on the order of 10 μm, deposited on the paper cellulose fibers. The presence of small isolated silver particles with sizes on the order of $\leq$0.1 μm was also noticed. The electromagnetic theory of SERS (*31*) indicates that the plasmon energy depends on the shapes and sizes of the metal particles on the surface, in such a way that by appropriate control of the substrate preparation procedure, the plasmon energy may be shifted into resonance with the exciting radiation, which will maximize the enhancements. It can be thus anticipated that monodisperse systems, with plasmon resonances tuned at the excitation wavelength, would provide maximum and reproducible SERS signals since all the adsorbate molecules present experience the same enhancement factor. However, a polydisperse substrate such as the one used here has the advantage that because of the small dependence of the position of SERS spectral modes with particle size and shape, it is not necessary to strictly control the preparation procedure in order to obtain reproducible spectral features, which is of paramount importance for the implementation of SERS as a qualitative analytical technique. The difficulties associated with the precision of intensities as a result of polydispersity can be handled by adequate standardization procedures, as discussed below.

In the three molecules studied, the π electronic ring system in combination with the presence of heteroatoms and external groups on the ring system seems to be important in determining the SERS behavior. From Figure 1 and Table I, it can be observed that the compounds have a number of spectral coincidences, mainly due to ring stretching vibrations found at wavenumbers around 1000, 1050, 1430, 1600, and 1630 cm^{-1}. Because of the limited rejection capability against Rayleigh scattering of the spectrometer used, the spectral region below 1000 cm^{-1} has not been examined. Consequently, a detailed discussion concerning the orientation of the adsorbed species on the surface has not been attempted. However, some general trends can be outlined. In the case of OPT, the position of the SERS modes shifts slightly to larger wavenumbers once it is adsorbed on the Ag surface, with respect to the conventional Raman spectrum of this compound (*32*). The most important change occurs at the SERS line at 1430 cm^{-1}, which in the conventional Raman spectrum is found at 1397 cm^{-1}. Strong SERS features involving ring stretching vibrations are observed. In the case of AA, as opposed to that of OPT, it is striking that no strong lines are detected above 1550 cm^{-1}, which in conventional Raman spectroscopy are attributed to the central and most rigid part of the molecule, i.e. the carbon–carbon double bond stretching region. One of the interesting aspects of the Raman spectrum of AA is that it could be obtained at all. This compound is a strong fluorescence emitter; it is well-known that, besides the extreme weakness of the Raman effect, the inherent fluorescence of the molecule studied is generally the limiting factor in obtaining reliable Raman spectra. In addition, fluorescence of impurities or solvent is a limiting factor at trace analyte concentration levels. The extreme molecular sensitivity reported here for AA is thus the combination of two effects: the surface enhancement phenomenon and the quenching of fluorescence of the compound itself or of other luminescent concomitants, which is a result of charge transfer (*33*) and radiationless energy transfer (*34*) to the metal surface. The vibrational features of NP at 1570 and 1325 cm^{-1} could be due to the nitro group, on the basis of group frequency assignment (*35*). These peaks are not observed in either AA or OPT.

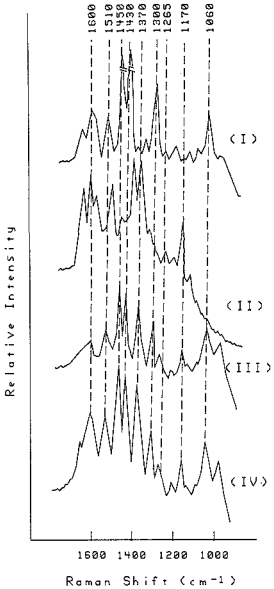

Figure 2. Surface-enhanced Raman spectra of ternary mixtures of *o*-phenanthroline, 9-aminoacridine, and 1-nitropyrene differing in concentration. See Table II for mixture composition.

Table II. Vibrational Bands in the SER Spectra of Mixtures[a]

mixture SER shift, cm^{-1}				
I	II	III	IV	assignment
1005		1005	1005	OPT, AA
1060		1060	1060	OPT, NP, AA
1095		1095	1095	OPT
1155		1150	1150	OPT AA
	1170	1170	1170	AA
1210	1210	1210	1210	OPT, NP
1265	1265	1280	1280	OPT, NP, AA
1300		1300	1300	OPT
	1325			NP
	1370	1370	1370	NP, AA
1430	1405	1430	1430	OPT
1450	1455	1465	1465	OPT, NP, AA
1510	1504	1510	1510	OPT, NP, AA
	1570			NP
1600	1600	1595	1595	OPT, NP, AA
1630	1630	1630	1630	OPT, NP, AA

[a] Mixture composition is as follows. I: OPT, 60 ng; AA and NP, 20 ng each. II: NP, 60 ng; AA and OPT, 20 ng each. III: AA, 60 ng; NP and OPT, 20 ng each. IV: AA, NP, and OPT, 20 ng each.

Selective Molecular Adsorption. The SERS spectra of four mixtures of AA, NP, and OPT obtained at different analyte concentrations are shown in Figure 2. Table II summarizes the vibrational assignments in the mixture analysis. Most of the bands appearing in the mixtures correlate quite well with the vibrational features shown by the isolated compounds. However, even though in a multicomponent mixture characteristic vibrational modes of the individual components can in general be identified, the intensity of the mixture is modulated by the intensity distribution of the compound that is most readily adsorbed. For instance, for mixture II, in which NP is in excess, the intensity in the

Table III. Quantitative Study of SERS of 9-Aminoacridine (AA) and 1-Nitropyrene (NP) on the Silver-Coated Filter Paper Substrate.[a]

analyte	I,[b] counts/s	corrected signals, counts/s		ratios	
		$I - I_{bknd}$[c]	$I - I_{bl}$[d]	I/I_{bknd}	$(I - I_{bl})/(I_{bknd} - I_{bl})$
AA	7496 ± 2425 (32.3)	6459 ± 2218 (34.3)	7176 ± 2365 (32.9)	7.23 ± 1.10 (15.3)	10.01 ± 1.62 (16.2)
NP	7224 ± 3228 (44.7)	3384 ± 2028 (59.9)	6408 ± 3204 (50.0)	1.88 ± 0.28 (14.9)	2.12 ± 0.31 (14.8)

[a] Analyte added, 50 ng. Average of nine replicates. Range expressed as standard deviation. In parentheses, relative standard deviation. [b] Absolute peak intensity (counts per second). [c] Background continuum intensity. [d] Blank signal (silver substrate in absence of analyte).

spectral region below 1200 cm^{-1} is low, as in the case of pure NP. This observation is also true for mixture III (excess of AA), in which the intensity in the region around 1600 cm^{-1} is also similar to that of pure AA.

The spectrum of mixture I, in which OPT is in excess, is virtually identical with that of pure OPT. The strong bands of NP and AA at 1370 cm^{-1} do not appear. The spectral features of NP at 1325 and 1570 cm^{-1}, as well as the AA mode at 1170 cm^{-1}, do not appear either. Therefore, OPT is preferentially adsorbed in this substrate, even in the presence of the other compounds. It should be noted that the OPT mode at 1430 cm^{-1} is heavily enhanced in this mixture with respect to the spectrum of pure OPT. For mixture II where there is an excess of NP, the contribution of the three individual compounds can be easily identified. NP can be identified by the appearance of bands at 1325 and 1570 cm^{-1}, which do not appear in the spectra of the other three mixtures assayed. The OPT band at 1430 cm^{-1} is not observed, while a mode at 1405 cm^{-1} now appears. A complete understanding of this is difficult because it can be a result of a combination of effects including possible interactions between molecules and differences in orientation at the surface, as well as differences in adsorption energies. However, it is recognized (*36*, *37*) that the SERS spectrum of an adsorbed species corresponds to the spectrum of the first adsorbed monolayer, for which shifts in the Raman bands with respect to spectra in solution are often observed. Subsequent layers of adsorbate undergoing enhancement due to long-range electromagnetic effects have the tendency to generate an ordinary Raman spectrum (*36*, *37*). This line of reasoning can explain the new 1405-cm^{-1} band as a shift of the 1430-cm^{-1} mode due to the fact that OPT is separated from the surface to a certain degree by the presence of an increased amount of NP in the mixture considered. The result is that OPT tends to behave as in solution and the 1430-cm^{-1} mode shifts to 1405 cm^{-1}, which is closer to the 1397-cm^{-1} mode in solution. In the case of mixture III, this shift does not take place, indicating that NP was responsible for this effect. When the three compounds are present at the same concentration, the spectrum obtained is similar to that of mixture III except that the intensity in the 1600-cm^{-1} region is now much higher. This study thus suggests the following hierarchy of attachment of the molecules studied and at the concentrations examined to the silver surface: OPT > AA > NP.

Quantitative Study. Efforts were made to standardize the experiments in an attempt to extract quantitative analytical information from SERS on the silver-coated filter paper substrate. Replication of the measurements revealed that the main source of variability for SERS intensities is the magnitude of the background continuum on which the SERS peaks are superimposed. This means that internal standardization should give improved precision by using a molecule showing the SERS effect when adsorbed on the substrate and presenting, consequently, similar variations in the continuum. However, owing to the limited amount of SERS active sites, addition of an internal standard may result in a decrease in the dynamic range of SERS response. This effect has been observed for the quantification of aminoacridine in the presence of nitropyrene as internal standard. An autostandardization can be performed, however. Table III summarizes the SERS intensities averaged for nine samples each of AA and NP (50 ng). Absolute intensities were measured at the most prominent peaks of each compound, 1370 and 1600 cm^{-1}, respectively. As shown, absolute peak intensities and continuum background intensities show relative standard deviations of the order of 30–60%. These results reflect differences in enhancement factors as well as the inhomogeneous distribution of molecules on the surface as a result of difficulties in obtaining a uniform dispersion of the 2-μL sample applied to the substrate. In addition, the evolution with time of the intensities will affect the reproducibility. However, this latter effect was minimized by adherence to a strict control of timing in the measurement process. Since the precision shown by both peak intensities and continuum intensities is similar, corrections based on background subtraction or blank subtraction did not improve the precision. However, Table III shows that by taking the ratio of the peak intensity to the background intensity compensated for the variability of results (both corrected and uncorrected for blank), relative standard deviations of ≈15% are obtained. The reproducibility level obtained with the ratioing procedure probably could be improved by using a more monodisperse substrate or a support providing a smaller diffusion of the applied sample. However, the ease of preparation of this substrate can compensate the moderate level of precision in analytical situations where a rapid screening of samples is needed. Figure 3 shows a calibration curve for AA based on the ratioing correction procedure. It is noteworthy the linear character of the relationship between corrected SERS intensity and analyte concentration, which is consistent with the expression relating Raman intensity and number density of scatter centers (*12*). The correlation coefficient between SERS intensity and AA concentration was 0.999. Above a concentration of 50 μg mL^{-1}, the linearity is lost, reflecting saturation of the SERS active sites in the high coverage regime. Under

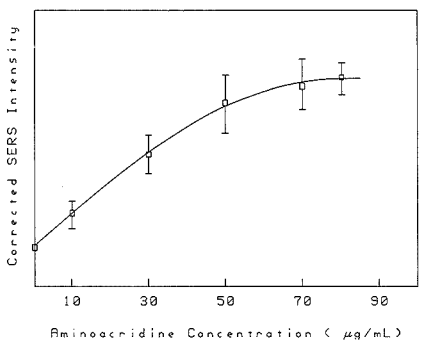

Figure 3. Concentration dependence of SERS intensity of 9-aminoacridine monitored at a Raman shift of 1370 cm^{-1}. Variation bars correspond to standard deviation for triplicate samples. Concentration refers to the sample applied to the substrate.

the circumstances of high surface coverage, it is also possible that dynamic fields from adjacent molecules of the same type lead to mutual depolarization, resulting in reduced SERS intensity (*38*).

The limits of detection for the compounds studied were estimated as follows. It is reasonable to suppose that the 2-μL sample used is distributed homogeneously in the 0.7-cm-diameter substrate and that the SERS signal arises from the molecules at various depths in the silver substrate. Therefore, with a 1.5-mm-diameter laser beam, the sampling efficiency is about $^1/_{20}$ of all analyte molecules applied. For a 2-μL sample of 50 μg mL^{-1} AA, about 1.6×10^{13} molecules are sampled. If the assumption is made that the surface-enhanced cross section for the adsorbate is maintained as the number density of scatterers decreases (*9*), which in turn is consistent with the results of Figure 3, then the absolute limit of detection can be found by calculating the concentration giving a signal-to-noise ratio of $3(2)^{1/2}$ The peak intensity of the 1370-cm^{-1} AA band is 7500 counts and the background (noise) signal is $(2300)^{1/2} = 48$ counts; thus, at the limit of detection, the number of molecules within the laser beam is 4.4×10^{11}, i.e., about 0.7 pmol. The limits of detection for OPT and NP calculated in a similar manner were respectively 1.2 and 1.0 pmol.

CONCLUSIONS

Unlike other spectroscopic techniques in which the spectra of mixtures can be constructed of weighted averages of spectral features of the individual compounds, multicomponent SER spectra on silver show a definite dependence on selective molecular adsorption on the surface. In spite of certain functional-group-dependent SERS features, it is clear that the adsorbate concentration is a key factor for mixture analysis by SERS. Apparently, depending on the SERS active group present, each compound has a different degree of surface adsorption. Molecules whose structure causes them to be strongly adsorbed appear in the SERS spectra of mixtures at lower concentrations. The spectra of these molecules are richer in spectral features as exemplified by *o*-phenanthroline, although no conclusion can be reached with respect to the detectability in view of the limits of detection calculated. The main source of variability for SERS intensities of individual compounds is the background continuum intensity. Quantitative measurements are possible at a reasonable degree of precision using a correction procedure based on ratioing the absolute SERS intensity to the backround intensity. A relative standard deviation of around 15% is thus obtained, which can be compatible with many practical analytical situations.

ACKNOWLEDGMENT

Andres D. Campiglia thanks the Coordenacao de Aperfeicoamento de Nivel Superior-Capes for the grant that is making possible his stay in Gainesville and also thanks the University of Brasilia (Brazil) for permission to leave.

LITERATURE CITED

(1) Otto, C.; de Mul, F. F. M.; Huizinga, A.; Greve, J. *J. Phys. Chem.* **1988**, *92*, 1239.
(2) Wang, J.; Zhang, P.; He, T.; Xin, H.; Liu, F. *J. Phys. Chem.* **1988**, *92*, 1942.
(3) Ishida, H.; Fukuda, H.; Katagiri, G.; Ishitani, A. *Appl. Spectrosc.* **1986**, *40*, 322.
(4) Sequaris, J. M. L.; Koglin, E. *Anal. Chem.* **1987**, *59*, 525.
(5) Laserna, J. J.; Campiglia, A. D.; Winefordner, J. D. *Anal. Chim. Acta* **1988**, *208*, 21.
(6) Parry, D. B.; Dendramis, A. L. *Appl. Spectrosc.* **1986**, *40*, 656.
(7) Koglin, E.; Sequaris, J. M. *Top. Curr. Chem.* **1986**, *134*, 1.
(8) Paisley, R. F.; Morris, M. D. *Prog. Anal. Spectrosc.* **1988**, *11*, 111.
(9) Van Duyne, R. P.; Haller, K. L.; Altkorn, R. I. *Chem. Phys. Lett.* **1986**, *126*, 190.
(10) Wokaun, A.; Gordon, J. P.; Liao, P. F. *Phys. Rev. Lett.* **1982**, *48*, 957.
(11) Pettinger, B.; Wenning, V.; Wetzel, H. *Surf. Sci.* **1980**, *101*, 409.
(12) Van Duyne, R. P. In *Chemical and Biochemical Applications of Lasers*; Moore, C. B., Ed.; Academic Press: New York, 1979; p 101.
(13) Davies, J. P.; Pachuta, S. J.; Cooks, R. G.; Weaver, M. J. *Anal. Chem.* **1986**, *58*, 1290.
(14) Carrabba, M. M.; Edmonds, R. B.; Rauh, R. D. *Anal. Chem.* **1987**, *59*, 2559.
(15) Otto, C.; van den Tweel, T. J. J.; de Mul, F. F. M.; Greve, J. *J. Raman Spectrosc.* **1986**, *17*, 289.
(16) Vo-Dinh, T.; Meier, M.; Wokaum, A. *Anal. Chim. Acta* **1986**, *181*, 139.
(17) Enlow, P. D.; Buncick, M.; Warmack, R. J.; Vo-Dinh, T. *Anal. Chem.* **1986**, *58*, 1119.
(18) Moody, R. L.; Vo-Dinh, T.; Fletcher, W. H. *Appl. Spectrosc.* **1987**, *41*, 966.
(19) Ni, F.; Cotton, T. M. *Anal. Chem.* **1986**, *58*, 3159.
(20) Boo, D. W.; Oh, W. S.; Kim, M. S.; Kim, K. *Chem. Phys. Lett.* **1985**, *120*, 301.
(21) Torres, E. L.; Winefordner, J. D. *Anal. Chem.* **1987**, *59*, 1626.
(22) Laserna, J. J.; Torres, E. L.; Winefordner, J. D. *Anal. Chim. Acta* **1987**, *200*, 469.
(23) Sheng, R. S.; Zhu, L.; Morris, M. D. *Anal. Chem.* **1986**, *58*, 1116.
(24) Ahern, A. M.; Garrell, R. L. *Anal. Chem.* **1987**, *59*, 2813.
(25) Berthod, A.; Laserna, J. J.; Winefordner, J. D. *Appl. Spectrosc.* **1987**, *41*, 1137.
(26) Laserna, J. J.; Berthod, A.; Winefordner, J. D. *Talanta* **1987**, *41*, 605.
(27) Freeman, R. D.; Hammaker, R. M.; Meloan, C. E.; Fateley, W. G. *Appl. Spectrosc.* **1988**, *42*, 456.
(28) Laserna, J. J.; Berthod, A.; Winefordner, J. D. *Microchem. J.* **1988**, *38*, 125.
(29) Rubin, J. C. *J. Electroanal. Chem. Interfacial Electrochem.* **1987**, *220*, 339.
(30) Aaron, J. J.; Andino, M. M.; Winefordner, J. D. *Anal. Chim. Acta* **1984**, *160*, 171.
(31) Gersten, J. I.; Nitzan, A. In *Surface Enhanced Raman Scattering*; Chang, R. K., Furtak, T. E., Eds.; Plenum: New York, 1982.
(32) *Raman / IR Atlas*; Schrader, B., Meier, W., Eds.; Verlag-Chemie: Weinheim, FRG, 1975.
(33) Ritchie, G.; Chen, C. Y. *Pure Appl. Chem.* **1980**, *52*, 361.
(34) Wokavn, A.; Lutz, H. P.; King, A. P.; Wild, U. P.; Ernst, R. R. *J. Chem. Phys.* **1983**, *79*, 509.
(35) Tu, A. T. *Raman Spectroscopy in Biology: Principles and Applications*; Wiley: New York, 1982; p 36.
(36) Moskovits, M.; Dilella, D. P. In *Surface Enhanced Raman Scattering*; Chang, R. K., Furtak, T. E., Eds.; Plenum: New York, 1982.
(37) Fleischmann, M.; Hill, I. R. In *Surface Enhanced Raman Scattering*; Chang, R. K.; Furtak, T. E., Eds.; Plenum: New York, 1982.
(38) Murray, C. A.; Bodoff, S. *Phys. Rev. B.* **1985**, *32*, 671.

RECEIVED for review August 15, 1988. Revised February 1, 1989. Accepted May 12, 1989. This research was supported by NIH-GM11373-25.

Interpreting Mass Spectra of Multiply Charged Ions

Matthias Mann, Chin Kai Meng, and John B. Fenn*

Department of Chemical Engineering, Yale University, New Haven, Connecticut 06520-2159

We describe two algorithms that extract molecular mass information from spectra showing sequences of peaks due to ions with varying numbers of charges. The first, called here the "averaging algorithm", unambiguously assigns charge numbers to the ions associated with the m/z value for each peak in the sequence and then averages the resulting values of M to give a best estimate of the molecular mass. The second, identified as the "deconvolution algorithm", mathematically transforms a spectrum of several peaks for multiply charged ions into one peak corresponding to a singly charged ion. The procedures can be readily implemented with a personal computer and are here applied to representative spectra of small proteins generated by electrospray mass spectrometry. These algorithms are now routinely used in our laboratory for the interpretation of such spectra. They both are fast and convenient, discriminate against background, and take advantage of much of the information contained in a sequence of peaks. Achievable accuracy and sources of error are discussed.

I. INTRODUCTION

The ions produced by the sources traditionally used in mass spectrometry generally comprise singly charged species resulting from the loss or gain of an electron by a parent molecule. Moreover, an appreciable fraction of the ions are often charged fragments of the parent molecule. On the other hand, ions produced by some of the more recently developed sources consist of neutral parent molecules to which small cations or anions are attached. Among these newer and "softer" ionization methods are electrohydrodynamic ionization (EH), fast atom bombardment (FAB), fast ion bombardment (FIB) commonly referred to as secondary ion mass spectrometry (SIMS), laser desorption (LD), plasma desorption (PD), thermospray (TS), and aerospray (AS) originally known as atmospheric pressure ion evaporation (APIE). Due in part to the larger size of the molecules that can be accommodated by these new sources and in part to the nature of their ionization processes, ions containing up to five or six adduct charges have been observed (*1*). However, to our knowledge, except for some preliminary work in our laboratory, no study on how to make efficient use of the peak multiplicity has been reported (*2*).

Recently, with an electrospray (ES) mass spectrometer that has been previously described (*3*), we have been able to obtain the mass spectra shown in Figure 1 for eight small proteins with molecular weights from 5000 to almost 40 000 (*4*, *5*). Analyte samples were dissolved in solvents comprising mixtures of acetonitrile, water, and methanol or 1-propanol. It was necessary to lower the solution pH by addition of small quantities of acetic acid (HAc) or trifluoroacetic acid (TFA). The optimum proportions of these solvent components depended somewhat on the particular sample and were determined by trial and error. Solutions with analyte concentrations ranging from 0.7 to 137 μmol/L, depending upon the species, were injected at flow rates of 8 μL/min. Each of the spectra shown is the result of a single scan requiring 30 s to cover the indicated mass range. The analyzer was a VG Micromass 1212 with a nominal upper limit for m/z for 1500. The analog output from the Channeltron detector was digitized with an analog to digital converter and fed into a homemade data recording and processing system based on an IBM-AT clone. Since our preliminary report at the ASMS Meeting in San Francisco last June, two other groups have confirmed our results (*6*, *7*). Indeed, Edmonds et al. were able to obtain ES spectra for a bovine albumin dimer with a molecular weight of 133 000.

Although the experiment was not optimized for sensitivity, it is apparent from Table I and Figure 1 that very low detection limits can be achieved. For example, the spectrum of lysozyme consumed only about 3 pmol of sample although more was used because processing and manipulation were not very efficient. In each case the spectrum comprises a sequence of peaks with an intensity distribution that is near Gaussian, has a width of around 500 on the m/z scale, and is generally centered at a value between 800 and 1200. The constituent ions of each peak differ from those of its adjacent neighbors by one elementary charge. For the reader's convenience we have shown the number of such charges per ion for two or three peaks in each spectrum. Each such charge is due to an adduct cation from the original solution. Our analyzer did not have sufficient resolution for large ions at these m/z values to permit an unequivocal assertion of unit mass for an adduct ion. However, the need for low pH in the sample solution, along with results obtained for smaller peptides and amino acids, strongly support our assumption that H^+ is the most likely charge carrier in these experiments.

For the eight proteins we studied Table I summarizes the essential features of each spectrum and the information it provides. It is immediately apparent from the figures and the table that the degree of multiple charging in ES ionization is much higher than has been encountered with any other soft ionization method. This feature is very attractive in that it extends the effective mass range of any analyzer by a factor equal to the number of charges per ion. Moreover, because the ions have lower m/z values, they are generally easier to detect and weigh than are singly charged ions of the same mass. On the other hand, peak multiplicity distributes the signal for one species over several channels. But because the number of charges per ion is almost always greater than the number of peaks, the total current carried by one species is greater when there is peak multiplicity than would be the case for a single peak containing the same total number of singly charged ions. Unfortunately, we do not yet know the detector response per charge of a multiply charged ion. We do know, however, that no postacceleration has been required for multiply charged ions that were large enough to require such acceleration had they been singly charged. We also know that the detection sensitivity obtained with ES ionization of large molecules seems to be substantially greater than has been obtained with sources giving rise to ions that are predominantly singly charged (*8*). Moreover, as will emerge in the subsequent discussion, because peak multiplicity allows signal averaging, mass assignment can be made with more precision and confidence than would be the case for a single peak of a singly charged ion. The objective of this paper is to present basic methods for interpreting the sequence of multiply charged peaks and to provide algorithms for retrieving the

0003-2700/89/0361-1702$01.50/0

Table I. Data for the Spectra in Figure 1

	mol wt	concentration g/L	concentration μmol/L	charges	m/z range
insulin (bovine)	5733	0.05	8.8	4–6	950–1450
cytochrome *c* (horse heart)	12360	1.67	137	12–20	600–1100
lysozyme (chicken egg)	14306	0.01	0.71	10–15	900–>1500
myoglobin (equine skeletal muscle)	16950	1.00	58.8	15–27	600–1400
trypsin inhibitor (soybean)	20091	0.10	5.0	16–22	800–1400
α-chymotrypsinogen A (bovine pancreas)	25656	0.50	19.0	17–22	1150–>1500
carbonic anhydrase II (human erythrocytes)	29006	0.50	17.2	23–36	725–1500
alcohol dehydrogenase (horse liver)	39830	0.50	12.5	32–46	800–1300

[a] The molecular weight was determined from the sequence information provided mostly by ref 8 and is an average value based on the natural abundance of isotopes.

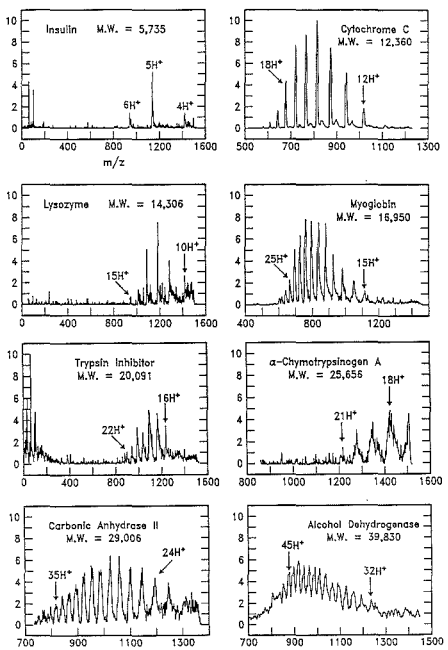

Figure 1. Spectra of multiply charged ions produced with electrospray ionization (ES). Each of the spectra was acquired with a single, 30-s scan. The number of charges *i* are indicated for some representative peaks. Table I gives some data on these spectra. See ref 3 for more details on the experiments.

mass information they contain. Two such algorithms, along with illustrative results obtained by applying them, will be set forth in the following paragraphs. In all the calculations we have assumed that the detector response to any ion did not depend on the number of its charges.

II. AVERAGING ALGORITHM

If one assumes that in a particular spectrum the adduct charges of each ion all have the same identity, and therefore mass, and that any neutral adducts such as solvation species are the same for each ion, then there are three variables associated with each of the peaks in the series: the mass M (numerically equal to the molecular weight M_r) of the parent molecule including neutral adducts, the number of charges i, and the mass m_a of the adduct ions. We use i rather than z to designate the number of charges in order to avoid confusion with the customary m/z scale of mass spectra for which $m = M + im_a$, the total mass of the ion. In general, $z = iq$, where q is an elementary charge and i is unity in conventional spectra for singly charged ions. It should be kept in mind that the units of m/z are properly daltons per elementary charge even though a measured peak position is often loosely expressed simply in daltons (Da) when z is one. All the formulas apply equally well to negatively charged ions with m_a being negative in the case of charge abstraction. Thus one can write for each of the peaks

$$K_i = \frac{M + im_a}{i} = \frac{M}{i} + m_a$$

or

$$(K_i - m_a) \equiv K'_i = \frac{M}{i} \tag{1}$$

where K_i is the apparent value of m/z for the peak position on the scale of the mass analyzer and $K'_i \equiv K_i - m_a$ the peak position m/z minus the adduct ion mass m_a. All masses are isotope averaged and in our examples the positions of peak maxima are used to determine the K_i. With the further constraint that i must be integral, eq 1 for any pair of peaks are in principle enough to determine the three unknowns simultaneously. Elementary manipulation of eq 1 for two charge states i and $i + j$ ($j > 0$) yields for the number of charges i

$$i = j\frac{K'_{i+j}}{K'_i - K'_{i+j}} \tag{2}$$

For example, if the adduct ions are protons ($m_a = 1$) and we observe one peak at $K_i = 1001.0$ and another one two peaks away ($j = 2$) at $K_{i+2} = 834.3$, then we would get $i = 2\,K'_{i+2}/(K'_i - K'_{i+2}) = 1666.6/(1000–833.3) = 10$. That is, the peak at 1001 has 10 charges and the one at 834.3 has 12. The accuracy required in K_i for determining i is low, especially if $K_i - K_{i+j}$ is made large, but increases as i gets larger. From eq 2 it can be shown that an accuracy of one m/z unit in the determination of K_i suffices for i's up to 100 or more (i.e. a 100 kDa molecule if the average value of m/z is around 1000). The value of m_a need not be exact for the determination of i because m_a does not affect the denominator of eq 2 and has only a small effect on the numerator. However, to determine the ion adduct mass directly from the peak positions, we need a substantially higher accuracy in the measured values of K_i. From eq 1 we obtain for m_a

$$m_a = \frac{1}{j}((i + j)K_{i+j} - iK_i) \tag{3}$$

where i and $i + j$ are for any two peaks. A measurement of K_i with an accuracy of about $1/iK_i$ would be required to determine m_a within one dalton (i.e. an accuracy of approximately 0.01 Da if $K_i = 1000$ and $M = 10$ kDa). However, it often happens that possible values of m_a are well separated, e.g. Na^+ at 23 and K^+ at 39. Thus a more modest mass accuracy will usually suffice. For proteins, as mentioned above

and further justified below, an assumption that $m_a = 1$ seems to be appropriate (at least as long as there is not too much sodium in the solution) and will be made in the numerical examples in this paper.

With known charge number, and measured or assumed adduct ion mass m_a, the parent ion mass M can be obtained from any one peak or averaged from a number of peaks

$$M = \frac{1}{n_0}\sum_i iK'_i \tag{4}$$

where the summation is over the i values for the peaks selected for averaging and n_0 is the number of those peaks.

The coherence of the peak sequence makes possible further improvement in the estimate of M given by eq 4. It allows us to identify and ignore peaks that do not belong in the sequence and to evaluate the quality of the spectrum. From eq 1 for any two peaks we obtain

$$\frac{K'_i}{K'_{i+j}} = 1 + \frac{i}{i}$$

$$\frac{1}{i} = \frac{1}{j}\left(\frac{K'_i}{K'_{i+j}} - 1\right) \tag{5}$$

Hence any pair of peaks in an experimental spectrum defines a point with $y = [(K'_i/K'_{i+j}) - 1)/j$ and $x = 1/i$. All such points should fall on the line $y = x$. The scatter of the pair-points around this line is a measure of the quality of the spectrum. If they were all precisely correct, they would all fall precisely on the line. Figure 2a shows such a plot for the cytochrome c spectrum of Figure 1. The seven points at each abscissa value of $1/i$ correspond to the seven possible ratios of K'_i/K'_{i+j} for the eight peaks in the spectrum as $i + j$ goes from 12 to 19. The quality of the experimental results can be readily inferred for each individual peak and for the spectrum as a whole from the departure of the points from the line values. The larger the spread around, or systematic offset from, the $x = y$ line, the less reliable is the measurement. The sensitivity of this quality index is demonstrated in Figure 2b. The points are from the same spectrum of cytochrome c, but the peak at $i = 14$ was deliberately offset by 5 units of m/z. It is apparent that this "stray peak" can be readily distinguished from the sequence peaks by the much larger spread at $i = 14$ of all the points and the cross points at the other values of i. They represent pair combinations with the peak at $i = 14$ when it was displaced by five m/z units. It should be pointed out that this plot is a test for self-consistency of the peaks in a sequence and does not depend on the value of parent mass.

The information on quality of K'_i values obtained from the above procedure can yield a better estimate of M by providing a weighting factor for each peak. In essence the contribution of each K'_i in the averaging process is weighted in accordance with the proximity of its corresponding points to the straight line in a plot such as the one in Figure 2a. Equation 6 defines a relative weighting factor w_i for each peak i

$$w_i = \frac{(i_{max} - i_{min})}{W} \sum_{\substack{j=i_{min}-i \\ j\neq 0}}^{i_{max}-i} \left(\frac{\left| \frac{i}{i+j} - \frac{K'_{i+j}}{K'_i} \right|}{\frac{i}{i+j}} \right)^p \tag{6}$$

where

$$W = \sum_{i_{min}}^{i_{max}} w_i$$

W is the normalizing constant and p is an integer equal to or greater than 2, which specifies the dependence of w on the proximity of the parent point to the straight line in Figure

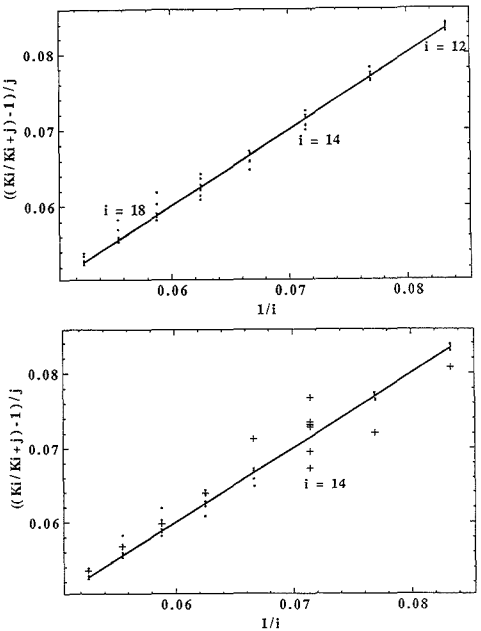

Figure 2. Consistency check on the cytochrome c spectrum of Figure 1. The solid line is the theoretical line: $[(K'_i/K'_{i+j}) - 1]/j = 1/i$. The points are the measured ratios of the peak positions ($K'_i/K'_{i+j} - 1$). See text for further explanation. (a) Measured peak locations from Figure 1. (b) Same as (a) but with the peak for $i = 14$ deliberately offset by 5 mass units to show the increased spread. The peak ratios involving the offset peak are marked by crosses.

2. For a peak whose K'_i has a better than average fit into the sequence pattern, w_i tends to be greater than one. It tends to be less than one if the K'_i value departs from its "ideal" position by an amount greater than the average of all the other peaks. The larger its departure, the smaller will be its weighting factor and its relative contribution to the overall average. Figure 3 shows how the unweighted average differs in behavior from the weighted average obtained with w_i values from eq 6 for $p = 2$. To produce Figure 3, the peak at $i = 19$ in the cytochrome c spectrum (Figure 1) was shifted in increments from −7.5 to +7.5 units from its measured m/z value and at every position we calculated the relative weighting factor w_{19}, the unweighted average, and the weighted average with a value of 2 for p. Evidently a shift of −7.5 mass units in K'_{19} results in a unweighted mass average shift of −17.8 mass units, whereas the weighted average shifts by just −2.6 mass units, only 15% of the mass shift in the unweighted case. The location of the maximum in w_{19} indicates that the measured K'_{19} was one unit too low according to the other peaks of the sequence, corresponding to an error somewhat larger than the standard deviation of ±5 Da in the final mass determination for cytochrome c. Choosing a value for p greater than 2 further enhances the dependence of the weighting factor w_i on the deviation of peak K'_i from the ideal m/z value. The decrease in the weighted standard deviation s_w, which is calculated by multiplying by w_i, the contributions of each K'_i to the error, becomes smaller as p increases. Table II shows this effect for the case of carbonic anhydrase II ($M = 29\,006$): s decreases from ±15.6 mass units for the unweighted average to ±7.9 mass units for $p = 6$. It should be noted that the weighted average does not necessarily change monotonically as p is increased.

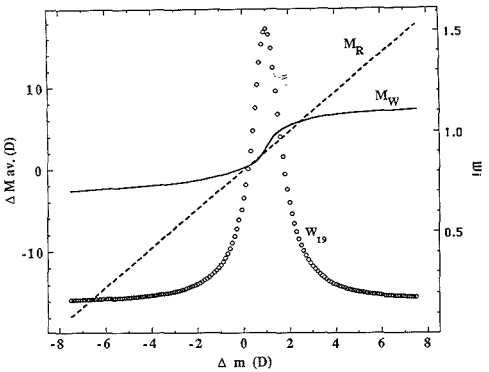

Figure 3. Results of offsetting m/z for the $i = 19$ peak by an amount Δm in the spectrum for cytochrome c. The dashed line shows the effect on unweighted average mass, the solid line on the weighted average. Note that the weighted average is much less affected by the offset peak once that peak is outside its "best position" with respect to the rest of the sequence. The open circles represent (on the right-hand ordinate) the relative weighting factor w_{19} when $p = 2$.

Table II. Comparison of Unweighted and Weighted Averages of Experimental Values for Molecular Weight of Carbonic Anhydrase Whose True (Sequence) Mass is 29 006

weighting index p	$M_{w,p}$ (± std dev)
0	28 982.2 ± 15.6 (unweighted)
2	28 984.2 ± 12.2
3	28 985.6 ± 10.9
4	28 987.3 ± 9.8
5	28 989.1 ± 8.8
6	28 990.8 ± 7.9

In comparing the parent mass obtained by this weighting procedure with the true mass, one has to keep in mind that there are at least two sources of error that contribute to ΔM (i.e. $M_{true} - M_{measd}$). One, the statistical error in ascertaining the individual peak positions is expressed in the unweighted or weighted standard deviation of the measured mass M. The other arises from systematic errors in the calibration of the analyzer mass scale. This latter source of error will obviously not be affected by any weighting procedure. If the error due to mass calibration predominates, weighting the average will not provide a major improvement in mass accuracy. In such a case the standard deviations, weighted or unweighted, do not indicate the experimental accuracy of a measurement but only its precision. A criterion for deciding if mass scale calibration is negligible in determining the error in M is

$$(i_{av})\ \Delta\text{Da} \ll s \qquad (7)$$

where i_{av} is an average number of charges per ion in the sequence of peaks, s is the standard deviation derived from averaging the individual peaks, and ΔDa is the absolute value of the error in daltons of the mass scale calibration. For the example of the cytochrome c spectrum ($i_{av} = 15$, $s = \pm 5$ Da, ΔDa ≈1 Da), the criterion is not fulfilled and the overall error is dominated by ΔDa. Hence in these measurements we would not expect a major decrease in ΔM from the weighting procedure.

Calculating the weighting factors w_i allows a judgement of the quality of a spectrum in much the same way as does noting the scatter of points in a plot such as the one in Figure 2a. In the plot a misassigned peak can be identified by a large difference between y and x values of points in a plot such as the one in Figure 2b. Large differences correspond to low w_i values in the numerical procedure of eq 6. Table III illustrates the results of the numerical procedure for the case of cytochrome c.

Clearly the accuracy with which mass assignments can be made depends directly on the accuracy of the analyzer's mass scale. For unit mass accuracy at 100 kDa the scale error must be smaller than 0.01 m/z units (eq 7). If scale calibration is not a problem (i.e. if eq 7 is satisfied, for example, by peak matching) and the values of K'_i could be determined to within 0.1 mass unit, then unit mass accuracy up to masses of several tens of kilodaltons might be possible even for quadrupole instruments (cf. eq 4 with $i_{av} = 50$ and $n_0 = 25$). Of course, this calculation presupposes that the K'_i values can be determined as exactly for high mass molecules with multiple charges as they can be for singly charged molecules low mass. We have confirmed this presumption only within the limited mass accuracy of our quadrupole (±0.1% at $m/z = 1000$) and for molecules with masses up to 40 kDa. The mass resolution, in contrast to the mass accuracy, would be the same as the nominal resolution for the analyzer, i.e. from 10^3 for many quadrupoles to as high as 10^6 for Fourier transform ICR mass analyzers. For example, to be distinguished with a quadrupole instrument having a resolution of 1000, two substances with $M \approx 30$ kDa would have to differ by 30 mass units.

It should be noted that isotope spread does not contribute appreciably to peak broadening. The contribution of peak half-width from the isotope distribution in a typical protein even at 100 kDa ($C_{4590}H_{6720}N_{1260}O_{1500}S_{30}$, i.e. a scaled-up version of Glucagon) is less than 30 mass units (*9*). The corresponding spread in m/z is less than 0.3 mass unit in a peak for ions with 100 charges.

III. DECONVOLUTION ALGORITHM

Visual interpretation of a spectrum comprising multiply charged peaks, and determination of parent mass, would be

Table III. Peak Positions and Mass Estimates for Horse Heart Cytochrome *c*

i	K'_i[a]	M_i (=iK'_i)	w_i ($p = 2$)	w_i ($p = 4$)	ΔM_i
12	1029.6	12 355.2	1.40	1.58	−5.8
13	950.3	12 353.9	1.49	1.88	−4.5
14	881.4	12 339.6	1.09	0.86	9.8
15	823.2	12 348.0	1.63	2.50	1.4
16	773.1	12 369.6	0.52	0.23	−20.2
17	727.4	12 365.8	0.67	0.36	−16.4
18	685.0	12 330.0	0.54	0.24	19.4
19	649.1	12 332.9	0.67	0.35	16.5
mass from sequence		M_s = 12360.1			
unweighted average		M_r = 12349.4 ± 5.1	ΔM_r = 10.7		$\Delta M_r/M_s$ = 0.087%
weighted average ($p = 2$)		$M_{w,2}$ = 12349.6 ± 4.1	$\Delta M_{w,2}$ = 10.5		$\Delta M_{w,2}/M_s$ = 0.085%
weighted average ($p = 4$)		$M_{w,4}$ = 12350.6 ± 3.1	$\Delta M_{w,4}$ = 9.5		$\Delta M_{w,4}/M_s$ = 0.081%

[a] K'_i is the measured peak position (on the m/z scale) minus adduct ion mass i.e. $K_i - 1$ (because the adduct is a proton). All masses are in terms of u (i.e. daltons).

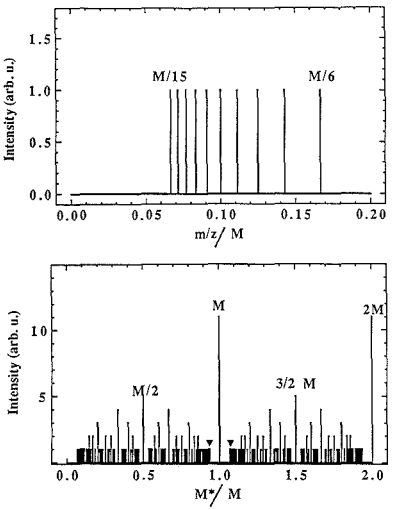

Figure 4. (a) A synthetic sequence of peaks for multiply charged ions with 6 to 15 charges. (b) Deconvolution of (a) using eq 8. The mass scale is in units of the parent mass M.

simplified in the coherent sequence of peaks could be transformed to one singly charged peak located on an m/z scale at the molecular mass M of the parent compound. It will be shown that the following function can provide such a transformation:

$$F(M^*) = \sum_{i=1}^{\infty} f\left(\frac{M^*}{i} + m_a\right) \tag{8}$$

F is the transformation function for which the argument M^* is any arbitrarily chosen trial value of M for which F is to be evaluated. The symbol f represents the distribution function for peak heights in a measured spectrum. For example, if there is a peak of relative intensity 5 at $m/z = 500$ then $f(500) = 5$. m_a is the adduct ion mass, as previously defined. It will be shown below that the function F has its maximum value when M^* = the actual value of M, the parent mass of the ions of the peaks in the sequence. Thus, evaluating F at all values of M^* with $0 \le M^* \le \infty$ yields a transformed or "deconvoluted" spectrum, in which the peak with maximum height corresponds to the parent species with a single massless charge. An example will make it clear how the deconvolution algorithm reconstructs the parent peak from the sequence. For simplicity we assume $m_a = 0$. Figure 4a shows a hypothetical measured spectrum f generated by charging a molecule with mass M with from 5 to 15 massless adduct ions such that the height is unity for every peak in the sequence. These "measured" peaks occur at $M/6$, $M/7$, ..., $M/15$. If F is evaluated at $M^* = M$ the following sum is obtained:

$$F(M) = f\left(\frac{M}{1}\right) + f\left(\frac{M}{2}\right) + \ldots + f\left(\frac{M}{5}\right) + f\left(\frac{M}{6}\right) + \ldots + f\left(\frac{M}{15}\right) + f\left(\frac{M}{16}\right) + f\left(\frac{M}{17}\right) + \ldots$$
$$= 0 + 0 + \ldots + 0 + 1 + \ldots + 1 + 0 + 0 + \ldots = 10$$

Thus, the function F has created a peak at the position $M^* = M$ with a height equal to the sum of the heights of the sequence peaks. As noted earlier we do not yet know how detector response depends on the number of charges per ion. In all the work discussed here we have assumed that the height of any peak in a measured spectrum is related to the abundance of its ions by the same proportionality constant no matter how many charges are on those ions.

If F is evaluated at $M + \epsilon$, a position slightly larger than M, then F will be zero because $(M + \epsilon)$ does not correspond to the position of any of the sequence peaks. However, it is also apparent from the example that the function F will create peaks in the deconvoluted spectrum at more positions than at $M^* = M$. At $M^* = (2/3)M$ the following sum results:

$$F\left(\frac{2M}{3}\right) = f\left(\frac{\left(\frac{2M}{3}\right)}{1}\right) + f\left(\frac{\left(\frac{2M}{3}\right)}{2}\right) + \ldots =$$
$$f\left(\frac{M}{6}\right) + f\left(\frac{M}{9}\right) + f\left(\frac{M}{12}\right) + f\left(\frac{M}{15}\right) = 4$$

Figure 4b shows the results of applying eq 8 to the spectrum of Figure 4a, an ideal sequence of multiply charged ions with $6 \le i \le 15$. It is a property of the spectrum resulting from the transformation F, as shown in Figure 4b, that it comprises a series of calculated peaks containing contributions from the actual peaks in an observed spectrum. By reference to the above procedure, it is easy to infer a number of general features of the deconvoluted spectrum. As we have already noted, its most prominent peak occurs when M^* equals the parent mass M and has a magnitude equal to the sum of the magnitudes of the individual peaks in the sequence. The next highest peak occurs at $M/2$ and it is at most only half as high as the peak at M. In general there are peaks at $(k/i)M$, where $i_{min} \le i \le i_{max}$ and k is any integer. In the sequence of "side peaks" on either side of the parent peak those closest to the parent (maximum) peak M occur at $((i_{max} \pm 1)/i_{max})M$ where i_{max} is the highest number of charges on a single ion. The position of these closest side peaks is indicated by arrowheads in Figure 4b. The height of these side peaks is a factor of $1/(i_{max} - i_{min})$ smaller than the height of the molecular peak at mass M. It also turns out that the deconvoluted spectrum is periodic in M. This periodicity may be viewed physically as being due to synthetic "overtones" of the basic spectrum corresponding to doubling, tripling, etc. of both the parent mass and the number of charges on each peak, and a difference of 2, 3, etc. in the i values of adjacent peaks.

The transformed spectrum changes somewhat in appearance if finite resolution and background are taken into account. To simulate these effects, the shapes of individual peaks in the sequence of Figure 4a are represented in Figure 5a by isosceles triangles with a relative full width at half height (fwhh) of 0.005. Furthermore, a constant background of 10% of the peak height was introduced. The consequences of this treatment are seen in Figure 5b. There is a progressive increase in the magnitude of the "side peaks" because the nonzero peak width in the observed spectrum results in a contribution to F at m/z values on either side of the peak centers. The steady increase in the "base line" is caused by more frequent sampling of the background at higher values of M^*.

This "deconvolution algorithm" has been programmed for both an IBM-AT clone and a Macintosh SE. It was applied to the eight experimental spectra shown in Figure 1 with the assumption that $m_a = 1$. Computation time was usually less than 1 min. Each mass spectrum was represented by 1150 points for a full scan. In the algorithm a linear interpolation between adjacent data points was used. It should be pointed out that this algorithm needs no a priori information about charge states or the number of peaks in the sequence. The only instruction specific to a particular spectrum is the range of m/z in the "window" that spans the peaks to be deconvoluted. Thus the summation of eq 8 goes only from the mimimum to the maximum values of m/z within this window.

Table IV. Summary of Values for Molecular Weight (M) from the Spectra in Figure 1[a]

species	M_a	M_r (unweighted av) $M_r \pm$ std dev	ΔM_r, %	M_{w2} (weighted av, $p = 2$) $M_{w,(2)}$	$\Delta M_{w,(2)}$, %	M_d (by deconvolution) M_d	ΔM_d, %
insulin	5733	5734 ± 14	0.01	5740 ± 12	0.12	5751	0.31
cytochrome c	12360	12349 ± 5	0.09	12350 ± 4	0.08	12352	0.07
lysozyme	14306	14324 ± 15	0.13	14329 ± 10	0.16	14340	0.24
myoglobin	16950	16906 ± 11	0.26	16904 ± 7	0.27	16927	0.26
trypsin inhibitor[b]	20091	19990 ± 37	0.50	20001 ± 28	0.45	20023	0.34
α-chymotrypsinogen A[c]	25656	26131 ± 22	1.8	26130 ± 22	1.8	25939	1.1
carbonic anhydrase II	29006	28982 ± 16	0.08	28984 ± 12	0.08	29005	0.004
alcohol dehydrogenase	39830	39859 ± 25	0.07	39871 ± 17	0.10	39876	0.12

[a] All M values are isotope-averaged. M_a is from sequence (ref 10), M_r is unweighted av. M_{w2} is weighted av ($p = 2$). [b] 75% of the molecules are said to lack the terminal Leu (ref 10). If true in our sample, ΔM's would be much smaller. [c] This may be an atypical case since there are only four broad peaks to average and the mass window extends beyond $m/z = 1500$ (see Figure 1). However, the standard deviation indicates that the measurement error in this spectrum should be only slightly higher than in the other spectra.

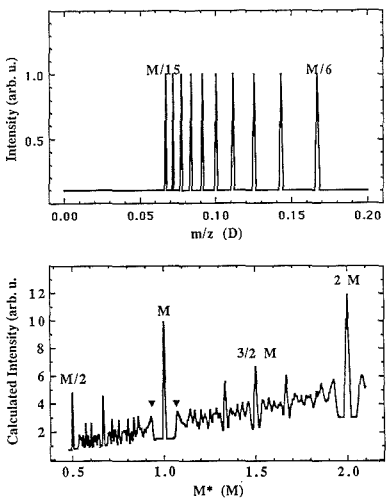

Figure 5. (a) Synthetic sequence of peaks whose shapes are approximated by isosceles triangles (fwhh = 0.5%). There is a constant background that is 10% of the peak height. (b) Transformation of (a) using eq 8. The mass scale is in units of the parent mass M.

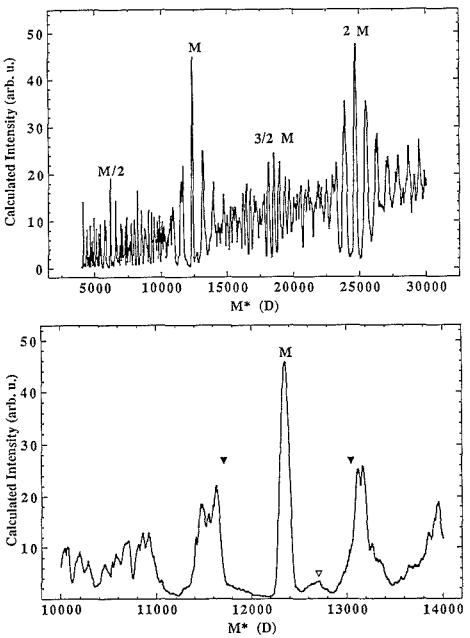

Figure 6. (a) Deconvolution of the cytochrome c (M = 12360) spectrum of Figure 1 using eq 8 with $m_a = 1$. The theoretical positions of the first side peaks are marked by dark triangles. (b) "Zoom" expansion of the spectrum in (a) for the mass range between 10000 and 14000. For explanation of the peak marked by the open triangle see text.

Such a limitation in the range of the summation reduces the noise in the transformed spectrum because background that lies outside the range of interest is not sampled. Figure 6a displays the result of applying the deconvolution procedure to the spectrum of cytochrome c in Figure 1. The transformed spectrum clearly shows the side peaks, the overtone periodicity, and the base line increase discussed above. The parent (largest) peak is magnified in Figure 6b by "zoom" expansion of the mass scale in its vicinity. Figure 7 shows the results of the same treatment for the case of a larger protein, carbonic anhydrase II (M = 29006). Widths at half maximum for both measured and deconvoluted peaks for the other spectra were usually about 1%. Such large spreads resulted in part because effective resolution of our analyzer was only about 300. Table IV summarizes the results for molecular weight determination from the spectra in Figure 1.

It is interesting to note that in general there is a region immediately around the parent peak that is free from artifacts of the deconvolution algorithm. As noted above, this region should extend from $(i_{max} - 1)/i_{max} \times M$ to $(i_{max} + 1)/i_{max} \times M$, where i_{max} is the maximum number of charges found on a molecule. In Figures 4 and 5 the boundaries of this region are marked by black triangles. In the deconvoluted cytochrome c spectrum (Figure 6), however, a small peak (marked with an open triangle) is observed about 340 mass units higher than the molecular peak. Detailed examination of the measured spectrum reveals a small peak just above each main peak in the sequence whose position agrees with the peak found in the deconvolution. This observation indicates that the algorithm can readily detect small peaks close to a parent peak that may be due, for example, to parent species variants with slightly different masses.

The question arises as to the complications introduced when two or more parent species are present in the sample. In some preliminary experiments, with mixtures having two components, e.g. cytochrome c and myoglobin, we have been able to resolve their spectra sufficiently to obtain mass values with

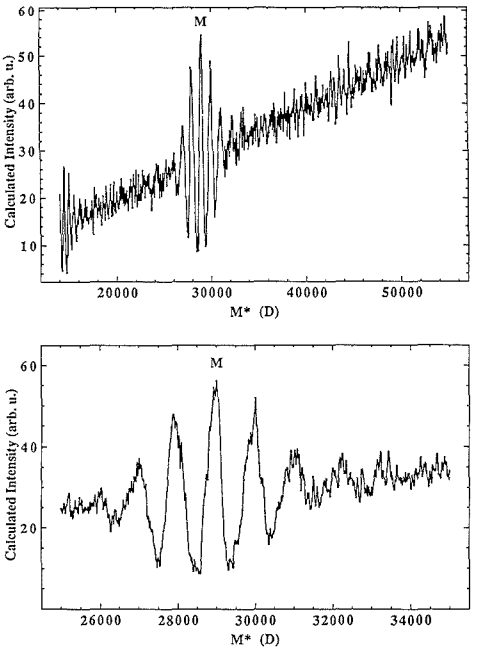

Figure 7. Results as in Figure 6 of applying the deconvolution algorithm to the carbonic anhydrase II (M = 29 006) spectrum of Figure 1.

the same accuracy and confidence as if each component present had been separately analyzed. We plan further experiments with mixtures and will report on them later.

IV. CONCLUSION

Two procedures have been presented for interpreting spectra comprising sequences of peaks for multiply charged ions. One of them establishes unambiguously the number of charges for each measured peak and discriminates against background peaks that do not belong in the sequence. The relevant peaks can then be averaged with confidence to calculate the molecular weight. The other algorithm transforms a measured spectrum and yields directly the peak that would be expected for a parent species with a single massless charge. The methods complement each other. The averaging algorithm will be most useful in dealing with a noisy spectrum having relatively sharp peaks. It will also be the method of choice when a sequence contains only a few large peaks and many small ones because each peak can then be given the same weight in the averaging. A spectrum transformed with the deconvolution algorithm, on the other hand, in effect weights the sequence peaks by their relative magnitude and thus will be most responsive to those with large amplitudes. That algorithm retains some peak shape information and can also resolve mixtures. Often it may be appropriate to use both and to compare their results. For example, if one is not absolutely sure whether a particular peak M in the deconvoluted spectrum is the true parent, one could use the averaging algorithm to decide. Both algorithms discriminate efficiently against background and use much of the information available in the measured spectrum. As we have demonstrated here, ES mass spectrometry combined with each of these procedures generally allows rapid and confident determination of molecular weights for large molecules with an accuracy of a few tenths of a percent or better, even with instruments of modest resolution. With suitable analyzers this accuracy could be significantly increased.

ACKNOWLEDGMENT

Special thanks are due to Shek Fu Wong, Craig M. Whitehouse, Michael Labowsky, Peter Chen, and Walter J. McMurray for many stimulating and fruitful discussions. We also register our appreciation for advice, encouragement, and samples from other colleges at Yale too numerous for a roll call.

LITERATURE CITED

(1) Roepstorff, P.; Sundquist, B. In *Mass Spectrometry in Biomedical Research*; Gaskell, S. J., Ed.; John Wiley & Sons Ltd.: London, 1986; pp 269.
(2) Mann, M.; Meng, C. K.; Fenn, J. B. *Proceedings of the 36th Annual Conference on Mass Spectrometry and Allied Topics* **1988**, 1207.
(3) Whitehouse, C. M.; Dreyer, R. N.; Yamashita, M.; Fenn, J. B. *Anal. Chem.* **1985**, *57*, 675.
(4) Meng, C. K.; Mann, M.; Fenn, J. B. *Proceedings of the 36th Annual Conference on Mass Spectrometry and Allied Topics* **1988**, 771.
(5) Meng, C. K.; Mann, M.; Fenn, J. B. *Z. Phys.* **1988**, *10*, 361.
(6) Covey, T. R.; Bonner, R. F.; Shushan, B. I.; Henion, J. *Rapid Commun. Mass Spectrom.* **1988**, *2*, 249.
(7) Edmonds, C. G.; Loo, J. A.; Barinaga, C. J.; Udseth, H. R.; Smith, R. D. 4th International Symposium on LC-MS, Freiburg, November 1988.
(8) Barber, M.; Green, B. N. *Rapid Commun. Mass Spectrom.* **1987**, *1*, 80.
(9) Yergey, J.; Heller, D.; Hansen, G.; Cotter, R. J.; Fenselau, C. *Anal. Chem.* **1983**, *55*, 353.
(10) *Atlas of Protein Sequence and Structure*; Dayhoff, M. O., Ed.; National Biomedical Research Foundation: Washington, DC, 1972–78; Vol. 5 and Suppl. 1–3.

RECEIVED for review August 15, 1989. Revised manuscript received January 24, 1989. Accepted April 24, 1989. This research was supported by the National Institutes of Health under Grant 5 RO1 Gm31660-3. Partial support was also provided by the donors of the Petroleum Research Fund, administered by the American Chemical Society.

On-Line Electrochemistry/Thermospray/Tandem Mass Spectrometry as a New Approach to the Study of Redox Reactions: The Oxidation of Uric Acid

Kevin J. Volk, Richard A. Yost,* and Anna Brajter-Toth*

Department of Chemistry, University of Florida, Gainesville, Florida 32611

The electrochemical oxidation pathway of uric acid was determined by on-line electrochemistry/thermospray/tandem mass spectrometry. Intermediates and products formed as a result of electrooxidation were monitored as the electrode potential was varied. Several reaction intermediates have been identified and characterized by tandem mass spectrometry. The tandem mass spectrometric results provide convincing evidence that the primary intermediate produced during the electrooxidation of uric acid has a quinonoid diimine structure. The results indicate that once formed via electrooxidation, the primary intermediate can follow three distinct reaction pathways to produce the identified final products. The final electrochemical oxidation products observed in these studies were urea, CO_2, alloxan, alloxan monohydrate, allantoin, 5-hydroxyhydantoin-5-carboxamide, and parabanic acid. The solution reactions that follow the initial electron transfer at the electrode are affected by the vaporizer tip temperature of the thermospray probe. In particular, it was found that at different tip temperatures either hydrolysis or ammonolysis reactions of the initial electrochemical oxidation products can occur. Most importantly, the results show that the on-line combination of electrochemistry with thermospray/tandem mass spectrometry provides otherwise difficult to obtain information about redox and associated chemical reactions of biological molecules such as the structure of reaction intermediates and products, as well as providing insight into reaction pathways.

INTRODUCTION

During the past 15 years, the redox chemistry of many natural and synthetic biologically active compounds including purines has been investigated by using electrochemical methods, frequently in combination with other analytical techniques. The premise of this work has been that the mechanisms observed electrochemically can provide insight into the biological redox reactions of these molecules (*1–12*). In the study of redox reactions, the most successful approaches have used modern electrochemical methods in combination (off-line) with high-performance liquid chromatography (HPLC) (*5, 6*), molecular spectroscopy (*1, 2*), and mass spectrometry (*2, 4, 5*). A combination of these techniques is often required because each technique provides only limited information; as a consequence, no one approach is suitable for all problems.

The analysis of polar and involatile compounds by classical GC/MS methods requires derivatization of samples. The conditions and the time required for derivatization severely limit the use of GC/MS for the identification of electrochemically generated intermediates. Only electrochemically generated compounds of sufficient stability can be analyzed by GC/MS (*11, 12*).

* Authors to whom correspondence should be addressed.

Since the introduction of thermospray as a viable LC/MS interface (*13*), this technique has gained popularity as a soft ionization technique that gives primarily molecular weight information. Hambitzer and Heitbaum (*14*) were the first to successfully combine electrochemistry on-line with mass spectrometry via a thermospray LC/MS interface. These experiments demonstrated the potential for direct detection of electrochemically generated products by monitoring the formation of dimers and trimers upon the electrooxidation of *N,N*-dimethylaniline at a Pt electrode.

In a recent communication from this laboratory (*15*), it has been shown that the on-line coupling of electrochemistry with thermospray/tandem mass spectrometry (EC/TSP/MS/MS) can provide detailed redox information about biologically significant molecules by detecting intermediates and products formed upon electrooxidation. In addition, the use of tandem mass spectrometry allows identification of intermediates and products in a mixture on the basis of their characteristic daughter spectra, a feature important to the identification of structurally related metabolites (*16, 17*). The ability to obtain structural information of each component in an electrolysis mixture without chromatographic separation is a unique feature of EC/TSP/MS/MS. In fact, this allows the necessary time resolution to detect intermediates generated during electrooxidation.

The electrochemical oxidation of uric acid has been extensively studied (*1, 4, 18*). The information obtained in these studies indicates that the electrochemical and enzymatic catalyzed oxidations of uric acid proceed by similar, if not identical, chemical mechanisms (*19*). At pH 7.0 uric acid is known (*1, 4, 11, 12*) to undergo a $2e^-$, $2H^+$ electrochemical oxidation at ca. +0.40 V vs SCE to form an unstable intermediate with a proposed quinonoid diimine structure (Figure 1). Evidence supporting the diimine formation includes the following: its reduction peak in cyclic voltammetry (*4, 20*), intermediates detected by thin-layer spectroelectrochemistry (*12*), and the identification of its partial hydrolysis product, the imine alcohol, by GC/MS (*12*) and recently by EC/TSP/MS/MS (*15*). Controlled potential electrolysis reactions reveal that the final products are allantoin, 5-hydroxyhydantoin-5-carboxamide, urea, and at pH <7.0, alloxan monohydrate and small amounts of parabanic acid (*1*).

The objective of this study was 2-fold. Our major goal was to characterize the capabilities of EC/TSP/MS/MS for on-line characterization of dynamic reactions. Uric acid served as an ideal model and test system. Secondly, we verified that as a result of the coupling of electrochemistry with mass spectrometry, a complete interpretation of the complex redox chemistry of uric acid is possible.

EXPERIMENTAL SECTION

Apparatus. A Finnigan MAT TSQ 45 tandem quadrupole mass spectrometer equipped with a Vestec thermospray LC/MS interface and INCOS data system was used for all studies. The mobile phase was delivered by a LC-2600 ISCO syringe pump at a flow rate of 2.0 mL/min. Samples were injected with a Rheodyne (Model 7410) injector fitted with a 25-μL loop. Al-

0003-2700/89/0361-1709$01.50/0

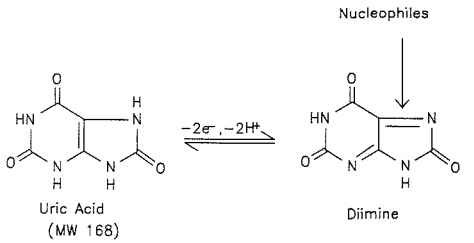

Figure 1. Formation of the primary oxidation intermediate of uric acid, which further reacts by nucleophilic addition.

though the details of the ESA electrochemical cell (Bedford, MA) were described previously (*15*), it is important to note that the palladium reference electrode is a quasi-reference. The peak potentials (E_p) of uric acid and other compounds that were studied vs a palladium reference electrode correspond within ±50 mV to the E_p vs a saturated calomel reference electrode (SCE) under the conditions employed in these studies (0.1 M ammonium acetate supporting electrolyte).

Reagents. Uric acid, 9-methyluric acid, allantoin, alloxan monohydrate, urea, and parabanic acid were obtained from Sigma (St. Louis, MO). The compounds were dissolved in, and then injected into, a mobile phase that consisted of 0.1 M ammonium acetate (pH ~7). Twenty-five microliters of a 100-ppm solution were injected. Methanol was not part of the normal mobile phase and was only added during certain experiments to determine if new intermediates and products formed as a result of methanolysis reactions. For these experiments, percentages of methanol (>15% by volume) were required before methanolysis intermediates and products were observed.

Mass Spectrometry. The thermospray interface (Vestec Corp., Houston, TX) was mounted on a triple-stage quadrupole mass spectrometer (Finnigan MAT Corp., San Jose, CA, Model TSQ 45). Two temperatures were monitored in the experiments: the vaporizer exit temperature (tip temperature) and the source block temperature. In the tip temperature profile studies, the tip temperature was varied while the source temperature was held constant at 290 C. At a flow rate of 2.0 mL/min, the typical operating temperatures were tip, 240 C, and source, 290 C. However, when 0.1 M ammonium acetate/methanol (pH 6.9, 80/20, (v/v)) was used, the optimum operating temperatures were tip, 220 C, and source, 290 C.

Time delay measurements were conducted by simultaneously triggering the mass spectrometer and the potentiometer. This was accomplished by modifying a circuit board in the mass spectrometer that controls acquisition and mass scanning so that the acquisition sequence began at the same time the potential pulse was applied.

Both positive ion and negative ion thermospray mass spectra were obtained by pulsed positive ion/negative ion chemical ionization (PPINICI). Typical conditions for TSP/MS were scan range m/z 125–300 in 0.3 s, electron multiplier voltage 1000 V, and preamplifier gain 10^8 V/A. Although the lower scan range limit of m/z 125 was normally used to avoid background interference from the ammonium acetate reagent ions, several experiments using a lower scan limit of m/z 30 revealed several new products. Selected ion monitoring (SIM) of 1 amu wide windows for 100 ms each was used for all quantitation studies. For MS/MS, the scan range and rates varied, depending upon the m/z of the parent ion. Collisionally activated dissociation (CAD) studies were carried out using nitrogen as the collision gas (2 mTorr) with a collision energy of 30 eV.

The formation of the $[M + H]^+$ and $[M - H]^-$ ions of uric acid was found to be very sensitive to thermospray conditions. The procedure used to promote the production of $[M + H]^+$ and $[M - H]^-$ ions of uric acid is as follows: (1) After normal thermospray operation, the flow of the mobile phase is stopped, and the inlet of the vaporizer probe is fitted with a vacuum-tight plug. (2) The power applied to the vaporizer probe is reduced to zero, but the thermospray probe is allowed to remain inside the heated thermospray source to maintain thermal contact. (3) After about 1 h, the tip temperature is increased to its normal value and the flow is resumed. The pseudomolecular ions of uric acid can then often be observed for about 30 min. It is important to note that when the $[M + H]^+$ and $[M - H]^-$ ions of uric acid are observed in this manner, the total reconstructed ion current (RIC) has increased as well. In other words, the overall sensitivity of thermospray has increased well above the level that was observed before shutting down. Unfortunately, this enhanced sensitivity gradually disappears (<30 min).

Table I. Quantitation Studies with EC/TSP/MS

product	ion monitored	slope (peak area/ng)	mol of product formed/mol of uric acid
alloxan monohydrate	$[M - CO_2 - H]^-$	2.47×10^3	0.21
allantoin	$[M + H]^+$	3.52×10^3	0.18
urea	$[M + H]^+$	9.76×10^3	0.17

RESULTS AND DISCUSSION

Sensitivity of Thermospray and Quantitation in EC/TSP/MS. Thermospray ionization results from the partial or complete vaporization of a liquid (generally an aqueous buffer) as it flows through a heated stainless steel capillary tube into a vacuum (*13*). Although the fundamental processes of thermospray ionization are not completely understood, at least two different mechanisms, direct ion evaporation of preformed ions from the droplets and chemical ionization of neutral sample molecules by the ammonium acetate buffer, may be responsible for ion formation (*21, 22*). Although direct ion evaporation may occur for any molecule that is ionized in aqueous solution, the conditions required to produce ions by direct ion evaporation may be different than those conditions that favor chemical ionization (CI). Because gas-phase ion/molecule reactions such as CI have been shown to influence the thermospray process (*23–26*), the production of sample ions will depend on experimental parameters that affect the vaporization process. These parameters include capillary diameter, tip temperature, and flow rate. The CI process will additionally be affected by gas-phase proton affinities, concentrations of various reagent ions, temperatures, and ion/molecule kinetics. Therefore, in order to obtain reproducible results, it is important to carefully control experimental operating conditions.

In the thermospray process, CI can produce sample ions via gas-phase reactions with reagent ions produced from the ammonium acetate buffer (without filament) if the conditions are favorable for gas-phase proton transfer. Hence, if ammonium acetate buffer is used, any compound (uncharged in solution) with a proton affinity less than that of NH_3 will not be observed as a protonated molecular ion $(M + H)^+$; in negative ion thermospray, any compound with higher gas-phase proton affinity than the acetate ion will not form an $(M - H)^-$ ion. In addition, hydrogen-bonded adduct or cluster ions such as $[M + NH_4]^+$ and $[M + CH_3COO]^-$ can also form and provide useful molecular weight information.

On-line quantitation experiments for allantoin, urea, and alloxan monohydrate indicated that plots of peak area versus amount of injected standard were often not linear over a 10-fold range (450 ng to 4 μg). No attempts were made to optimize thermospray conditions to improve linearity or develop a quantitative method. These experiments were performed simply to provide estimates of conversion and yields of products as well as to demonstrate the compound-dependent nature of the thermospray technique. Selected ion monitoring was used because it provided increased sensitivity.

Table I shows the slopes of the calibration curves for each standard as well as the estimated molar conversion of uric acid to product via on-line electrooxidation. The calculations were

Table II. Positive and Negative Ions Identified in the Electrochemistry/Thermospray/Mass Spectra of Uric Acid

m/z	identity
	Positive Ions
45	$[CO_2 + H]^+$
61	[urea + H]$^+$
120	[urea + acetamide + H]$^+$
121	[urea + urea + H]$^+$
134	[5-hydroxyhydantoin + NH_4]$^+$
141	[bicyclic imidazolone + H]$^+$
143	[alloxan + H]$^+$
158[a]	[2-oxo-4-imino-5-ureidoimidazolidine + H]$^+$
159	[allantoin + H]$^+$
169	[uric acid + H]$^+$
176	[allantoin + NH_4]$^+$
177	[5-hydroxyhydantoin-5-carboxamide + NH_4]$^+$
184[a]	[imine amine + H]$^+$
200	[bicyclic imidazolone + acetamide + H]$^+$
201[a]	[imine amine + NH_4]$^+$
	Negative Ions
88	[oxamic acid − H]$^-$
113	[parabanic acid − H]$^-$
115	[alloxan monohydrate − CO_2 − H]$^-$
139	[bicyclic imidazolone − H]$^-$
141	[alloxan − H]$^-$
156[a]	[2-oxo-4-imino-5-ureidoimidazolidine − H]$^-$
157	[allantoin − H]$^-$
158	[5-hydroxyhydantoin-5-carboxamide − H]$^-$
167	[uric acid − H]$^-$
175	[alloxan monohydrate − CO_2 + acetate]$^-$
182	[imine amine − H]$^-$
183	[imine alcohol − H]$^-$
201	[alloxan + acetate]$^-$

[a] Produced in ammonolysis reactions at tip temperatures <240 °C.

based on the total number of moles of uric acid injected. In the EC/TSP mass spectra of uric acid, the ions corresponding to allantoin, urea, and alloxan monohydrate are of low relative abundance (ca. 30%). However, on a molar basis they account for over 50% of the products and intermediates generated. Therefore, it is clear that intermediates or products that are of much higher abundance in the EC/TSP mass spectra such as the imine alcohol and the bicyclic imidazolone are ionized more efficiently.

The diameter of the stainless steel capillary inside the vaporizer probe appears to play an important role in the vaporization and subsequent ionization processes of uric acid. When the procedure described in the Experimental Section is used, it is reasonable to propose that the diameter of the capillary is reduced by partial clogging due to the deposition of involatile residue from the mobile phase or uric acid, which itself has low solubility. No significant increase in pump back pressure is observed when the procedure described is followed. We propose that the reduction of the diameter of the capillary produces smaller droplets, which evaporate more efficiently.

Effect of Temperature and Mobile Phase on Electrochemistry/Thermospray Mass Spectra. Optimum conditions for the operation of the thermospray interface, such as tip temperature, are traditionally obtained by maximizing the solvent-buffer ion intensities for a given flow rate (*13*, *27*, *28*). Under the conditions employed in this study, a maximum solvent-buffer ion intensity is obtained at a tip temperature of ca. 240 C for a flow rate of 2.0 mL/min. As expected, this tip temperature also produces the most intense reconstructed ion current for samples in EC/TSP/MS. However, in this study we have also identified ions that have maximum responses at lower tip temperatures. At tip temperatures lower than 240 C, additional ions such as 158^+, 184^+, and 182^- are observed in the EC/TSP mass spectra of uric acid which correspond to intermediates formed from ammonolysis reactions (Table II). The relative mass spectral abundances of the ions corresponding to the ammonolysis products (Figures 2 and 3) vary dramatically over a 20 °C range in tip temperature from 230 to 250 °C. This indicates that the ammonolysis reactions may occur inside the vaporizer probe (*29*).

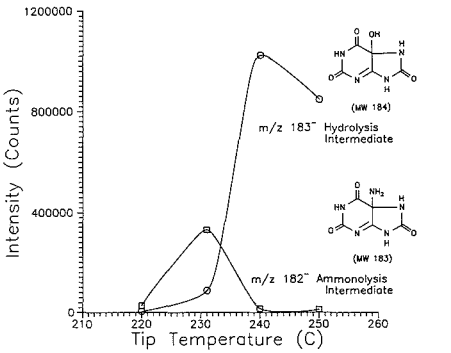

Figure 2. EC/TSP/MS tip temperature study of hydrolysis and ammonolysis reactions of the diimine of uric acid: flow rate of 0.1 M ammonium acetate mobile phase, 2.0 mL/min; source temperature, 290 C.

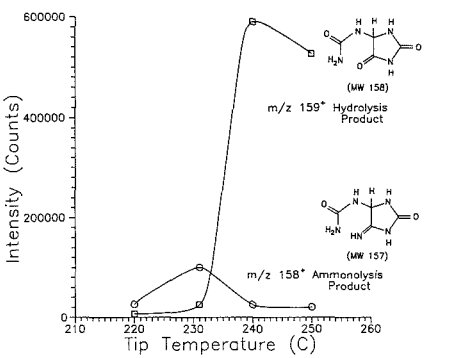

Figure 3. EC/TSP/MS tip temperature study of hydrolysis and ammonolysis reactions of the bicyclic imidazolone of uric acid: flow rate of 0.1 M ammonium acetate mobile phase, 2.0 mL/min; source temperature, 290 C.

The imine double bonds of the primary diimine intermediate make it very susceptible to nucleophilic attack by species such as H_2O, NH_3, methanol, and methylamine (Figure 1). Reactions in which water acts as a nucleophile are well documented (*1*). Attack by one molecule of water produces the hydrolysis intermediate (MW 184), and attack by one molecule of ammonia will, in analogy, produce the ammonolysis intermediate (MW 183). If the mobile phase contains methanol as an organic modifier, then the diimine can also react with one molecule of methanol to produce the methanolysis intermediate (MW 198). As shown in Tables II–IV, EC/TSP/MS and EC/TSP/MS/MS experiments have identified each of these intermediates produced by nucleophilic attack by mobile-phase components on the quinonoid diimine following the electrooxidation of uric acid. In contrast to previous off-line studies (*4*, *12*), this discovery provides convincing evidence to support a quinonoid diimine intermediate after a $2e^-$, $2H^+$ electrooxidation of uric acid.

As can be seen in Figure 2, the intermediates formed as a result of hydrolysis and ammonolysis reactions of the qui-

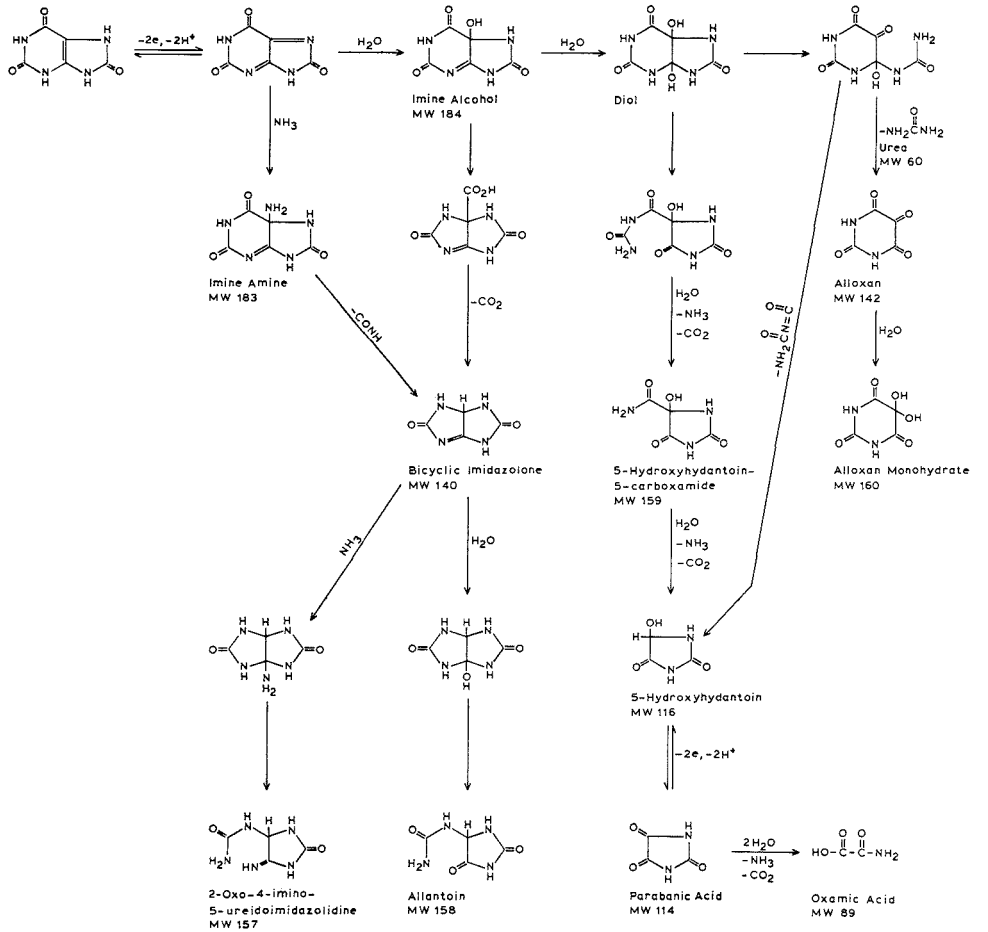

Figure 4. Oxidation pathway of uric acid. The molecular weights are shown for those intermediates and products that have been identified by EC/TSP/MS and EC/TSP/MS/MS.

nonoid diimine (Figure 1) of uric acid have very different optimum tip temperatures. At tip temperatures >240 C, the base peak in the negative ion EC/TSP mass spectrum is m/z 183 corresponding to the $[M - H]^-$ of the imine alcohol hydrolysis intermediate. However, when the tip temperature is lowered to 231 C, the base peak in the negative ion EC/TSP mass spectrum is m/z 182 corresponding to the imine amine ammonolysis intermediate. Figure 3 illustrates the tip temperature dependence of hydrolysis and ammonolysis reactions of another intermediate, the bicyclic imidazolone (Figure 4). The positive $[M + H]^+$ ion at m/z 158 results (Figure 4) from an ammonolysis reaction to form 2-oxo-4-imino-5-ureidoimidazolidine, while the positive ion at m/z 159 results from a hydrolysis reaction of the bicyclic imidazolone to form allantoin, the expected final oxidation product of uric acid. Hydrolysis reactions of intermediates following the electrochemical oxidation of uric acid (Figure 1) are well-known (*1*); therefore, the formation of ammonolysis products under EC/TSP/MS conditions is not surprising, but has not been previously reported.

Mass Spectrometric Hydrodynamic Voltammograms. The on-line combination of electrochemistry with mass spectrometry has been shown to be an extremely powerful tool because of its ability to provide molecular weight information about electrochemically generated intermediates/products (*14, 15*). If the mass spectrometer used is specifically designed to perform MS/MS experiments, then important structural information of the intermediates/products can be obtained (*15*). Another important use of on-line EC/TSP/MS or EC/TSP/MS/MS demonstrated in this paper is in the monitoring of individual species (reactants, intermediates, or products) as a function of electrode potential. Although similar information may be obtained by on-line UV–vis spectrophotometry (spectroelectrochemistry) (*12*), MS/MS is much more likely to permit unambiguous monitoring and identification of individual species.

Figure 5 illustrates the mass spectrometric hydrodynamic voltammograms of uric acid obtained by EC/TSP/MS. As shown by the cyclic voltammogram obtained under normal conditions, oxidation of uric acid begins to occur at ca. +0.0 V and is nearly complete at ca. +0.40 V. This process can also be monitored by mass spectrometry as shown in Figure 5 by noting the intensity of the $[M - H]^-$ ion of uric acid at m/z 167 as a function of the electrode potential. The intensity

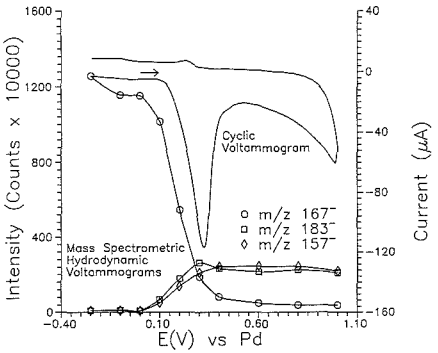

Figure 5. Mass spectrometric hydrodynamic voltammograms of uric acid: flow rate of 0.1 M ammonium acetate mobile phase, 2.0 mL/min; tip temperature, 240 °C; source temperature, 290 °C. Cyclic voltammogram of 300 μM uric acid on rough pyrolytic graphite: scan rate, 200 mV/s; palladium reference electrode; 0.1 M ammonium acetate supporting electrolyte.

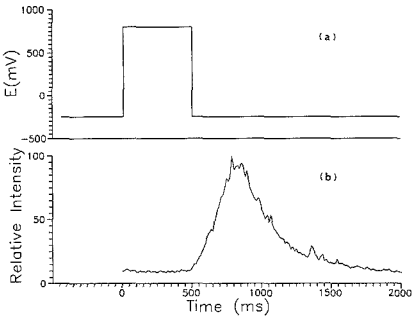

Figure 6. (a) Potential step experiment with 9-methyluric acid: initial potential, −250 mV; step potential, 800 mV; final potential, −250 mV; pulse duration, 500 ms. (b) Relative intensity of ammonolysis intermediate at m/z 196⁻ obtained during a potential step experiment: flow rate of 0.1 M ammonium acetate mobile phase, 2.0 mL/min; tip temperature, 230 C; source temperature, 290 C.

of the 167⁻ ion decreases due to the oxidation as the electrode potential is increased, and the intensity of the ions corresponding to intermediate (imine alcohol, $[M - H]^-$ m/z 183, Figure 5) and product (allantoin, $[M - H]^-$ m/z 157, Figure 5) of uric acid oxidation increases with increasing electrode potential. However, a steady-state situation develops for all ion intensities at potentials >+0.40 V due to the hydrodynamic flow of reactant. It has been shown that steady-state behavior will be produced in all forms of hydrodynamic voltammetry operating in the limiting current region (*30*). Similar hydrodynamic voltammograms are produced in electrochemical HPLC detectors. The design of the cell and the high flow rates (2.0 mL/min) used in these studies will contribute to the steady-state behavior observed. As can be seen in Figure 5, at potentials >+0.40 V the 167⁻ ion drops to ~15% of its original intensity at −0.10 V, indicating that high coulometric efficiencies (ca. 85%) can be obtained with this system. As expected, the formation of the secondary intermediate, the imine alcohol (MW 184), and the final product, allantoin (MW 158), also reaches a steady-state level at ca. +0.40 V. In theory (*30*), the plateau region that beings at +0.40 V in the mass spectrometric hydrodynamic voltammogram of uric acid should roughly correspond to the peak potential of ca. +0.40 V vs Pd obtained in a cyclic voltammetric experiment. As can be seen in Figure 5, the beginning of the steady-state response obtained in the mass spectrometric hydrodynamic voltammogram is in excellent agreement with the peak potential obtained in cyclic voltammetry.

Time Resolution of EC/TSP/MS. One attractive feature of an on-line electrochemistry/identification system is the opportunity to attain sufficient time resolution to detect short-lived intermediates. The delay time (dead volume) between the electrochemical cell and the mass spectrometer is therefore an important parameter and should be as small as possible. Increased dead volume after the cell will not only degrade the time resolution, but will also decrease the probability of detecting important intermediates.

The delay time of our on-line system was determined by two different methods. A delay time of 500 ms at 2.0 mL/min was determined by summing the volume of tubing after the cell (15 μL). The second method used to determine this delay time involved applying a square wave potential step from an initial potential of −250 mV to a final potential of +800 mV for a duration of 500 ms. After 500 ms, the potential was stepped back to the initial potential of −250 mV. Figure 6 illustrates the effect of this potential step experiment on the relative intensity of an ammonolysis intermediate, $[M - H]^-$ at m/z 196, produced during the oxidation of 9-methyluric acid (MW 182). 9-Methyluric acid and uric acid undergo the same oxidation/diimine hydrolysis reactions (*1*). The sample flow rate was 2.0 mL/min, and the intermediate monitored was the partial ammonolysis product of the diimine (MW 197). As can be seen in Figure 6, the delay time before the mass spectrometer starts to respond to the formation of this secondary intermediate is 520 ms, which agrees very well with the time delay of 500 ms calculated from tubing volume. The peak half-width of 500 ms equals the pulse duration. The peak tails, possibly due to adsorption of the intermediate on the electrode surface.

Characterization of Electrochemical Oxidation Products by Tandem Mass Spectrometry. To obtain structural information about reactants and products during electrochemical oxidation, tandem mass spectrometry (MS/MS) was used to produce structurally significant daughter ions by collisionally activated dissociation (CAD) of selected parent ions. MS/MS provides not only structural information but an additional separation stage that enables coeluting components in the electrolysis mixture to be identified.

Figure 7a illustrates the daughter spectrum of the positive ion at m/z 184 ($[M - H]^+$ of the imine amine in Figure 4, the ammonolysis product of the diimine) and is an excellent example of the structural information that can be obtained by MS/MS. Neutral losses of 17 (NH_3) are common for $[M + H]^+$ ions of compounds that contain a primary amine. Although this information is important, additional information is obtained when consecutive neutral losses occur. Thus, the 184⁺ ion initially fragments to 167⁺ (loss of NH_3), which must therefore correspond to the protonated quinonoid diimine (MW 166) and which is further fragmented to the 124⁺ ion (loss of CONH). The parent 184⁺ ion can also initially fragment to 141⁺ (loss of CONH). Both the 141⁺ and 124⁺ ions undergo further consecutive fragmentations which were used to elucidate the structure of the parent ion.

The daughter spectra of an $[M + H]^+$ ion and of its complementary $[M - H]^-$ ion are often very different. The differences in fragmentations between $[M + H]^+$ and $[M - H]^-$ ions can be explained in part by the location of the charge and the stability of the ion. The differences can be illustrated by comparing the daughter spectrum of the positive ion at m/z 184 described previously with the daughter spectrum of its complementary $[M - H]^-$ ion at m/z 182 (Figure 7b). The $[M - H]^-$ ion at m/z 182 initially fragments with a neutral

Table III. Positive Ion Daughter Mass Spectra of Identified Oxidation Intermediates and Products of Uric Acid

m/z (% RA)	structure correlation
$[M + Acetamide + H]^+$ Adduct Ion of Urea at m/z 120	
120 (4)	parent ion
61 (100)	loss of acetamide from 120^+
60 (36)	loss of urea from 120^+
$[2M + H]^+$ Dimer of Urea at m/z 121	
121 (3)	parent ion
61 (100)	loss of urea from 121^+
44 (6)	loss of NH_3 from 61^+
$[M + H]^+$ Ion of Bicyclic Imidazolone at m/z 141	
141 (80)	parent ion
98 (10)	loss of CONH from 141^+
71 (15)	loss of HCN from 98^+
70 (12)	loss of CO from 98^+
55 (8)	loss of CONH from 98^+
43 (100)	loss of HCN from 70^+
$[M + H]^+$ Ion of 2-Oxo-4-imino-5-Ureidoimidazolidine at m/z 158	
158 (10)	parent ion
141 (50)	loss of NH_3 from 158^+
115 (12)	loss of CONH from 158^+
98 (100)	loss of NH_3 from 115^+
71 (15)	loss of HCN from 98^+
61 (70)	loss of 97 from 158^+
55 (25)	loss of CONH from 98^+
44 (20)	loss of NH_3 from 61^+
43 (15)	loss of CO from 71^+
$[M + Acetamide + H]^+$ Adduct Ion of Bicyclic Imidazolone at m/z 200	
200 (3)	parent ion
141 (100)	loss of acetamide from 200^+
98 (8)	loss of CONH from 141^+
70 (8)	loss of CO from 98^+
60 (3)	loss of 140 from 200^+
43 (10)	loss of HCN from 70^+
$[M + NH_4]^+$ Adduct Ion of Imine Amine at m/z 201[a]	
201 (1)	parent ion
184 (35)	loss of NH_3 from 201^+
167 (35)	loss of NH_3 from 184^+
141 (100)	loss of CONH from 167^+
124 (8)	loss of CONH from 167^+
114 (5)	loss of HCN from 141^+
98 (10)	loss of CONH from 141^+
71 (3)	loss of HCN from 98^+
70 (5)	loss of CO from 98^+
55 (8)	loss of CONH from 98^+
43 (4)	loss of CO from 71^+

[a] Produced in ammonolysis reactions at tip temperatures <240 °C.

Table IV. Negative Ion Daughter Mass Spectra of Identified Oxidation Intermediates and Products of Uric Acid

m/z (% RA)	structure correlation
$[M - H]^-$ Ion of Oxamic Acid at m/z 88	
88 (100)	parent ion
44 (70)	loss of CO_2 from 88^-
$[M - H]^-$ Ion of Bicyclic Imidazolone at m/z 139	
139 (100)	parent ion
96 (25)	loss of CONH from 139^-
69 (25)	loss of HCN from 96^-
42 (60)	loss of HCN from 69^-
$[M - H]^-$ Ion of Alloxan at m/z 141	
141 (100)	parent ion
98 (40)	loss of CONH from 141^-
42 (20)	loss of 99 from 141^-
$[M - H]^-$ Ion of 5-Hydroxyhydantoin-5-carboxamide at m/z 158	
158 (50)	parent ion
140 (5)	loss of H_2O from 158^-
115 (100)	loss of CONH from 158^-
97 (15)	loss of H_2O from 115^-
72 (5)	loss of CONH from 115^-
59 (3)	urea anion
42 (20)	loss of 115 from 158^-
$[M - H]^-$ Ion of the Imine Alcohol at m/z 183	
183 (25)	parent ion
140 (100)	loss of CONH from 183^-
112 (8)	loss of CO from 140^-
97 (90)	loss of CONH from 140^-
69 (3)	loss of CO from 97^-
42 (8)	loss of HCN from 69^-
$[M - H]^-$ Ion of Methanolysis Intermediate at m/z 197	
197 (50)	parent ion
196 (20)	loss of H· from 197^-
182 (10)	loss of CH_3· from 197^-
165 (8)	loss of CH_3OH from 197^-
154 (100)	loss of CONH from 197^-
153 (10)	loss of CONH from $196^{\bullet-}$
139 (15)	loss of CH_3· from 154^-
127 (15)	loss of HCN from 154^-
126 (15)	loss of CO from 154^-
122 (10)	loss of CH_3OH from 154^-
111 (10)	loss of CONH from 154^-
97 (8)	loss of CON· from $139^{\bullet-}$
$[M + Acetate]^-$ Adduct Ion of Alloxan at m/z 201	
201 (1)	parent ion
141 (100)	loss of acetic acid from 201^-
98 (4)	loss of CONH from 141^-
59 (4)	loss of 142 from 201^-
42 (10)	loss of 99 from 141^-

loss of 43 (CONH) to produce the 139^- ion. The 139^- ion undergoes competitive fragmentations to produce the 112^- ion (loss of HCN), the 111^- ion (loss of CO), and the 96^- ion (loss of CONH). The negative daughter ion at m/z 96 undergoes further consecutive fragmentations with two losses of HCN to produce the 42^- ion. As can be seen in Figure 7, the positive and negative ion daughter spectra provide structural information that is complementary. For example, only the $[M + H]^+$ ion fragments with a loss of NH_3, indicating the presence of a primary amine. The daughter spectrum of the $[M + H]^+$ ion also clearly shows the presence of three CO groups. This important piece of structural information is confirmed by the daughter spectrum of the $[M - H]^-$ ion.

Other examples of structure elucidation with EC/TSP/MS/MS are summarized in Tables III and IV. Each of the identified ions listed in Tables III and IV produces a unique fragmentation pattern that is characteristic of its structure and that provides the necessary structural information to permit structure elucidation of the parent ion. Losses of small neutral molecules such as NH_3, CONH, HCN, CO, or H_2O are common during the CAD of even-electron species such as $[M + H]^+$ and $[M - H]^-$ ions, as can be seen from Tables III and IV.

The amount (percent relative abundance) of the parent ion remaining after the CAD process depends on parameters such as collision gas pressure and collision energy as well as the stability of the parent ion. The conditions used in this study caused almost complete fragmentation (~5% of the parent ion remaining) of hydrogen-bonded adduct ions such as $[M + NH_4]^+$, $[M + CH_3COO]^-$, and $[M + CH_3CONH_3]^+$, resulting in daughter spectra that contained as their base peak the $[M + H]^+$ or $[M - H]^-$ ion with a corresponding neutral loss of the adduct group (Tables III–V).

For those products (alloxan monohydrate, allantoin, urea, and parabanic acid) that were commercially available, MS/MS was used to confirm their presence in the EC/TSP mass spectra. This was accomplished by comparing the daughter spectra of authentic standards with the daughter spectra of electrochemically generated products. These comparisons are shown in Table V. The agreement between daughter ion

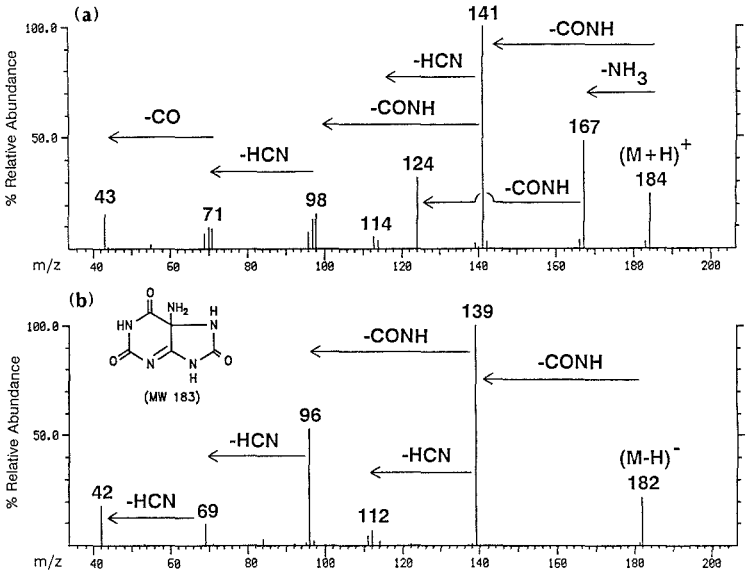

Figure 7. (a) Positive ion daughter spectrum of the $[M + H]^+$ ion of the imine amine ammonolysis intermediate at m/z 184: tip temperature, 230 °C; source temperature, 290 °C. (b) Negative ion daughter spectrum of the $[M - H]^-$ ion of the imine amine ammonolysis intermediate at m/z 182: tip temperature, 230 °C; source temperature, 290 °C.

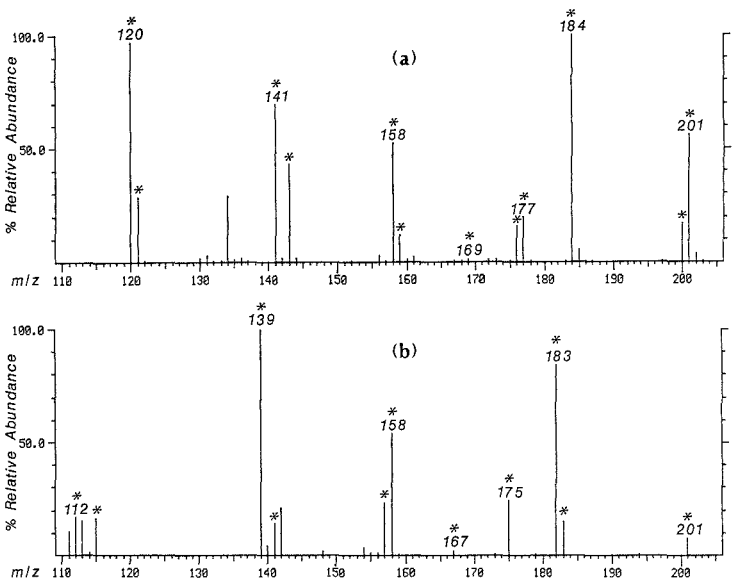

Figure 8. (a) Positive ion EC/TSP/MS spectrum of uric acid: tip temperature, 240 °C; source temperature, 290 °C. (b) Negative ion EC/TSP/MS spectrum of uric acid: tip temperature, 240 °C; source temperature, 290 °C. Identified ions (Table II) are marked with an asterisk.

abundances of standards and electrochemically generated products was generally ±20% relative abundance, as shown in Table V.

Characterization of the Electrochemical Reaction Pathway by TSP/MS/MS. As is clear from the preceding discussion, in order to fully characterize the intermediates and products formed following an electrochemical reaction, both the positive ion and negative ion mass spectra must be considered. This is especially true for compounds formed that have favorable proton affinities to produce only an $[M + H]^+$ or $[M - H]^-$ ion (through proton abstraction by acetate). Still other compounds can undergo both reactions. As shown in Figure 7, the latter case is ideal for the identification of unknown reaction intermediates, because not only is the mo-

Table V. Comparison of Daughter Spectra of Authentic Standards and Electrochemically Generated Products

compd	ion	m/z (% RA) authentic standard	m/z (% RA) EC generated product
urea (MW 60)	$[M + H]^+$	61 (100)	61 (100)
		60 (12)	60 (12)
		44 (80)	44 (80)
		43 (5)	43 (5)
parabanic acid (MW 114)	$[M - H]^-$	113 (100)	113 (100)
		85 (10)	85 (4)
		42 (65)	42 (60)
allantoin (MW 158)	$[M - H]^-$	157 (90)	157 (80)
		140 (10)	140 (10)
		114 (95)	114 (100)
		97 (100)	97 (80)
		71 (10)	71 (8)
		59 (12)	59 (20)
		42 (30)	42 (30)
alloxan monohydrate (MW 160)	$[M - CO_2 + acetate]^-$	175 (3)	175 (3)
		115 (100)	115 (100)
		97 (3)	97 (3)
		72 (6)	72 (6)
		59 (6)	59 (6)

lecular weight confirmed but additional structural information is often obtained as discussed above.

Figure 8 illustrates typical electrochemistry/thermospray positive ion and negative ion mass spectra of the oxidation intermediates and products of uric acid. Table II summarizes the molecular, adduct, and fragment ions identified which are marked with an asterisk in Figure 8. Figure 4 shows the oxidation pathway of uric acid, which is based on these EC/TSP/MS/MS results. As can be seen in Figure 4 and Table II, the intermediates resulting from partial hydrolysis (MW 184) and partial ammonolysis (MW 183) of the quinonoid diimine have been positively identified by their respective fragmentation patterns in EC/TSP/MS/MS.

As can be seen in Figure 4, the formation of parabanic acid from 5-hydroxyhydantoin requires a second oxidation step. Because the quinonoid diimine must undergo several hydrolysis reactions followed by ring opening before 5-hydroxyhydantoin is produced, the production of parabanic acid from 5-hydroxyhydantoin requires each of these intermediates to remain near or at the electrode surface in order for the second oxidation to occur. During off-line bulk electrolysis of uric acid, the formation of parabanic acid is observed because of long electrolysis times in a closed system. However, in a flowing system, because the material is continuously swept out of the electrochemical cell by the mobile phase, parabanic acid will not be produced unless the hydrolysis reactions and ring openings occur on a very short time scale. Adsorption was considered to play a role in the detection of parabanic acid, and the mass chromatograms were examined to determine if any significant time delay existed between the detection of the $[M - H]^-$ ion of the imine alcohol at m/z 183 and the $[M - H]^-$ ion of parabanic acid at m/z 113. The mass chromatograms revealed no significant time delay between the mass spectrometric detection of the negative ions at m/z 183 and m/z 113. This information and time resolution measurements indicate that both species are not adsorbed. Therefore, it is difficult to explain how parabanic acid is produced by direct oxidation.

The identified products, which are listed in Table II, include allantoin, 5-hydroxyhydantoin-5-carboxamide, parabanic acid, and alloxan monohydrate, all of which were identified in previous off-line studies (*1*, *12*) as the final electrochemical oxidation products of uric acid. The positive ions at m/z 159 $[M + H]^+$ and m/z 176 $[M + NH_4]^+$ shown in Figure 8a and the negative ion at m/z 157 $[M - H]^-$ shown in Figure 8b are due to allantoin (MW 158). As can be seen in Figure 4, the ions 139^- and 141^+ must result from the imine alcohol hydrolysis intermediate (MW 184) or the imine amine ammonolysis intermediate (MW 183), which has undergone ring contraction to produce the bicyclic imidazolone (MW 140). Hydrolysis of the bicyclic imidazolone intermediate (MW 140) accompanied by ring opening produces allantoin. The ions 158^+ and 156^- indicate ammonolysis reactions can also occur with the bicyclic imidazolone (Figure 4) to form 2-oxo-4-imino-5-ureidoimidazolidine (MW 157) with a structure similar to that of allantoin.

The results tabulated in Table II include those ions identified when the lower m/z limit was decreased from 120 to 35. Additional ions such as 61^+, 45^+, and 88^- are detected with the lower scan limit (not shown in Figure 8). The positive ion at m/z 61 corresponds to the $[M + H]^+$ of urea. Urea (MW 60) is produced during the formation of alloxan. The 121^+ ion has been identified by MS/MS (Table III) as a proton-bound dimer of urea. Proton-bound dimers have been detected in TSP/MS (*24*, *25*), and their formation has been observed to be dependent on the analyte concentration. The negative ion at m/z 88 has been identified as $[NH_2COCO_2]^-$, the $[M - H]^-$ ion of oxamic acid (MW 89), which results from thermal decomposition of parabanic acid (Table IV).

Table II shows several acetamide adduct ions that have been identified. Smith et al. (*25*) noted intense $(M + 60)^+$ ions for several amino acids studied by TSP/MS, but could not reasonably explain this. It is known (*31*) that acetamide is formed during the dehydration of ammonium acetate; hence the formation of such adduct ions is not surprising. Although the acetamide reagent ion, 60^+, is produced during the thermospray process, the formation of acetamide adducts, as with any adducts, will depend on the basicity of the analyte and the conditions in the TSP source.

The ions 143^+ and 141^- (Table II) have been identified as $[M + H]^+$ and $[M - H]^-$ of alloxan (MW 142). Although only alloxan monohydrate could be obtained as a standard (Table V), the presence of alloxan was inferred from the fragmentation pattern in the daughter spectrum. Alloxan monohydrate (MW 160) is produced from the hydrolysis of alloxan and is the only product identified thus far that does not yield an $(M + H)^+$ or an $(M - H)^-$ ion (Table V); instead it is decarboxylated to produce an $(M - CO_2 - H)^-$ ion at m/z 115 and an $(M - CO_2 + CH_3COO)^-$ ion at m/z 175. When authentic alloxan monohydrate is analyzed by TSP/MS, the sample is completely decarboxylated to produce the negative ions at m/z 115 and 175 (Table V). Because neither an $(M + H)^+$ nor an $(M - H)^-$ ion is observed, these ions are most likely the result of thermal decomposition occurring inside the thermospray vaporizer probe or source, rather than a (gas-phase) mass spectrometric fragmentation of the $[M - H]^-$ or $[M + CH_3COO]^-$ ion. In addition, it is unlikely that a weakly held hydrogen-bonded acetate adduct would remain intact if acetate attachment occurred prior to decarboxylation (mass spectrometric fragmentation).

CONCLUSIONS

The on-line combination of electrochemistry with thermospray/tandem mass spectrometry has provided valuable information about the biologically relevant redox reactivity of uric acid. The main goal, however, was to demonstrate the feasibility and capabilities of this approach as well as to evaluate the potential limitations. In spite of the complexity of the reactions following the electrochemical oxidation of uric acid, EC/TSP/MS/MS allows positive identification of intermediates and products. Although the positive and negative ion mass spectra were extremely helpful in final identification by providing molecular weight information, structural as-

signments required MS/MS because the soft nature of thermospray ionization causes little fragmentation.

All of the previously reported major products of uric acid and several of the intermediates have been identified and characterized by EC/TSP/MS/MS. The intermediates resulting from partial hydrolysis (MW 184) and partial ammonolysis (MW 183) of the quinonoid diimine have been positively identified by their fragmentation patterns. In addition, the ions 139^- and 141^+ in the EC/TSP/MS spectra must result from the hydrolysis intermediate (MW 184) undergoing ring contraction followed by decarboxylation, which produces the bicyclic intermediate. Identification of this bicyclic intermediate confirms that uric acid can follow three different reactions pathways after electrooxidation. Work is now in progress to determine on-line the enzymatic oxidation pathway of uric acid by thermospray/tandem mass spectrometry and to compare it with the results of the electrochemical oxidation.

It is important to recognize that it is the unique operating conditions of EC/TSP/MS/MS which make it possible to detect intermediates as well as final products after electrooxidation. First, the thermospray interface allows direct on-line coupling of the solution-phase electrochemical cell to the mass spectrometer, permitting short-lived intermediates to be observed. Second, MS/MS makes it possible to determine the structure of each of the mixture components, which produce only molecular ions in TSP.

Because the temperature conditions during thermospray change in 500 ms from 25 to 250 °C, the rate constants for the disappearance of intermediates cannot be readily compared to values obtained by room-temperature methods such as spectroelectrochemistry. For example, the imine alcohol intermediate (MW 184) has a half-life estimated by spectroelectrochemistry of ca. 2 min in solution at 25 C. If this rate constant remained unchanged under the elevated temperatures in EC/TSP/MS and with a time delay of only 500 ms, it would not be possible to observe any final products. Therefore, it can be expected that many if not all rate constants will be different under EC/TSP/MS conditions.

LITERATURE CITED

(1) Dryhurst, G. *Electrochemistry of Biological Molecules*; Academic Press: New York, 1977.
(2) McKenna, K.; Brajter-Toth, A. *J. Electroanal. Chem. Interfacial Electrochem.* **1987**, *233*, 49.
(3) Kraske, P. J.; Brajter-Toth, A. *J. Electroanal. Chem. Interfacial Electrochem.* **1986**, *207*, 101.
(4) Goyal, R. N.; Brajter-Toth, A.; Dryhurst, G. *J. Electroanal. Chem. Interfacial Electrochem.* **1982**, *131*, 181.
(5) Childers-Peterson, T. E.; Brajter-Toth, A. *J. Electroanal. Chem. Interfacial Electrochem.* **1988**, *239*, 161.
(6) Childers-Peterson, T. E.; Brajter-Toth, A. *Anal. Chim. Acta* **1987**, *202*, 167.
(7) Astwood, D.; Lippincott, T.; Deysher, M.; D'Amico, C.; Szurley, E.; Brajter-Toth, A. *J. Electroanal. Chem. Interfacial Electrochem.* **1983**, *159*, 295.
(8) Miner, D. J.; Rice, J. R.; Riggin, R. M.; Kissinger, P. T. *Anal. Chem.* **1981**, *53*, 2258.
(9) Rice, J. R.; Kissinger, P. T. *Biochem. Biophys. Res.* **1982**, *104*, 1312.
(10) Andrews, P. A.; Pan, Su-Shu; Bachur, N. R. *J. Am. Chem. Soc.* **1986**, *108*, 4158.
(11) Dryhurst, G.; Kadish, K. M.; Scheller, F.; Renneberg, R. *Biological Electrochemistry*; Academic Press: New York, 1982.
(12) Brajter-Toth, A.; Dryhurst, G. *J. Electroanal. Chem. Interfacial Electrochem.* **1981**, *122*, 205.
(13) Blakley, C. R.; Vestal, M. L. *Anal. Chem.* **1983**, *55*, 750.
(14) Hambitzer, G.; Heitbaum, J. *Anal. Chem.* **1986**, *58*, 1067.
(15) Volk, K. J.; Lee, M. S.; Yost, R. A.; Brajter-Toth, A. *Anal. Chem.* **1988**, *60*, 720.
(16) Rudewicz, P.; Straub, K. M. *Anal. Chem.* **1986**, *58*, 2928.
(17) Perchalski, R. J.; Yost, R. A.; Wilder, B. J. *Anal. Chem.* **1982**, *54*, 1466.
(18) Dryhurst, G. *Bioelectrochem. Bioenerg.* **1985**, *14*, 251.
(19) Brajter-Toth, A.; Goyal, R. N.; Wrona, M. Z.; Lacava, T.; Nguyen, N. T.; Dryhurst, G. *Bioelectrochem. Bioenerg.* **1981**, *8*, 413.
(20) Owens, J. L.; Marsh, H. A.; Dryhurst, G. *J. Electroanal. Chem. Interfacial Electrochem.* **1978**, *91*, 231.
(21) Covey, T. R.; Bruins, A. P.; Henion, J. D. *Org. Mass Spectrom.* **1988**, *23*, 178.
(22) Voyksner, R. D. *Org. Mass Spectrom.* **1987**, *22*, 513.
(23) Bursey, M. M. *Anal. Chem.* **1985**, *57*, 2597.
(24) Alexander, A. J.; Kebarle, P. *Anal. Chem.* **1986**, *58*, 470.
(25) Smith, R. W.; Parker, C. E.; Johnson, D. M.; Bursey, M. M. *J. Chromatogr.* **1987**, *394*, 261.
(26) Parker, C. E.; Smith, R. W.; Gaskell, S. J.; Bursey, M. M. *Anal. Chem.* **1986**, *58*, 1661.
(27) Linberg, C.; Paulson, J. *J. Chromatogr.* **1987**, *394*, 117.
(28) Voyksner, R. D.; Haney, C. A. *Anal. Chem.* **1985**, *57*, 991.
(29) Volk, K. J.; Yost, R. A.; Brajter-Toth, A. *J. Chromatogr.*, in press.
(30) Kissinger, P. T.; Heineman, W. R. *Laboratory Techniques in Electroanalytical Chemistry*; Marcel Dekker, Inc.: New York, 1984.
(31) Pine, S. H.; Hendrickson, J. B.; Cram, D. J.; Hammond, G. S. *Organic Chemistry*, 4th ed.; McGraw-Hill: New York, 1980.

RECEIVED for review December 13, 1988. Accepted April 27, 1989. This research was supported in part by grants from the National Institutes of Health (A.B.T.), U.S. Chemical Research Development and Engineering Center (R.A.Y., A.B.T.), the Division of Sponsored Research at the University of Florida (R.A.Y., A.B.T.), and the Interdisciplinary Center for Biotechnology Research at the University of Florida (A.B.T.). Keven J. Volk thanks Merck-Dohme for a graduate fellowship.

Determination of Serum Cholesterol by a Modification of the Isotope Dilution Mass Spectrometric Definitive Method

Polly Ellerbe,* Stanley Meiselman, Lorna T. Sniegoski, Michael J. Welch, and Edward White V

Center for Analytical Chemistry, National Institute of Standards and Technology (formerly National Bureau of Standards), Gaithersburg, Maryland 20899

An isotope dilution mass spectrometric (ID/MS) method for cholesterol is described that uses capillary gas chromatography with cholesterol-$^{13}C_3$ as the labeled internal standard. Labeled and unlabeled cholesterol are converted to the trimethylsilyl ether. Combined capillary column gas chromatography and electron impact mass spectrometry are used to obtain the abundance ratio of the unlabeled and labeled [$M^{+\cdot}$] ions from the derivative. Quantitation is achieved by measurement of each sample between measurements of two standards whose unlabeled/labeled ratios bracket that of the sample. Seven pools were analyzed by this method: standard reference material (SRM) 1951, which consists of three frozen serum pools with low, medium, and high levels of cholesterol; SRM 1952, which consists of three freeze-dried serum pools with low, medium, and high levels of cholesterol; and SRM 909, a freeze-dried serum pool. The method is a modification of our original definitive method for cholesterol. The modified method uses much better chromatographic separations to assure specificity and a new method of implementing selected ion monitoring on a magnetic mass spectrometer to obtain high-precision measurements of ion intensity ratios on narrow gas chromatographic peaks. The modified method has a coefficient of variation (CV) of 0.22%, which is an improvement over the original method's CV of 0.36%. The measurements were found to be free of interference. The high precision and absence of bias qualify this method as a candidate definitive method.

Heart disease is the number one cause of death in the United States, and epidemiologic studies have shown a strong correlation between coronary heart disease and blood cholesterol levels. Therefore, a major effort, directed by the Cholesterol Education Panel of the National Institutes of Health, is under way to educate physicians and the general public on the importance of having one's blood cholesterol measured and of taking corrective action if the level is elevated.

A wide variety of methods and instrumentation is used to measure serum cholesterol, and the results vary considerably. Proficiency testing programs of clinical laboratories have shown large discrepancies in cholesterol results among the laboratories (*1*). For the cholesterol education program to be effective, the measurements must be accurate enough to allow for proper diagnosis and long-term monitoring. An accuracy base in the form of serum-based materials with known concentrations of cholesterol can provide laboratories with an important component in assuring that patients' samples are accurately measured. To this end, a method of demonstrated accuracy and high precision, i.e., a definitive method, is necessary. Universal acceptance of the requirements for a method to be called definitive has not been achieved. The National Committee for Clinical Laboratory Standards has published guidelines for definitive methods (2), which define a set of rules for the acceptance or rejection of a given method as definitive. Our group at the National Institute of Standards and Technology (NIST) (formerly National Bureau of Standards) has developed methods that are, according to those guidelines, definitive methods for cholesterol (*3*), glucose (*4*), uric acid (*5*, *6*), urea (*7*), and creatinine (*8*) in human serum. Other laboratories have published methods that they describe as definitive for cortisol (*9–11*), cholesterol (*12*), creatinine (*13*), glucose (*14*), and uric acid (*15*).

The first definitive method developed at NIST was for cholesterol (*3*). Many modifications to the instrumentation have been made to improve precision since then (*7*, *8*), and capillary columns have replaced packed columns in the GC. The use of capillary columns leads to relatively narrow chromatographic peaks, which required the development of a new method for multiple ion monitoring (*16*) in order to achieve the required precision. When the need to measure cholesterol again arose, we saw the opportunity of using our modified instrumentation and modern capillary GC columns to improve the previous method.

Isotope dilution mass spectrometry (ID/MS) has been the technique of choice for definitive methods since it does not depend on sample recovery and can be tested for the presence of bias and interferences. Our use of ID/MS is based on spiking a sample with a labeled version of the analyte as an internal standard, equilibrating, processing the sample, and the measuring the ratio of unlabeled to labeled analyte by using gas chromatography/mass spectrometry (GC/MS). Any loss of material after spiking does not affect the results since it is the ratio of unlabeled to labeled analyte that is measured. We tested for bias in sample preparation by preparing independent multiple sets of samples. The probability of undetected interferences was reduced by measuring all samples with the use of a prominent ion from electron impact ionization and then selecting a representative subset of samples to be measured at other prominent ions, with other GC columns, and/or with another mode of ionization. Therefore, for an interfering species to be undetected, it would have to have the same retention time as that of the analyte on the different GC columns, the same ions at all the masses used for measurement in each method of ionization, and the same abundance ratios among these ions as that of either the labeled or unlabeled version of the analyte being measured. These sets of measurements are called the confirmatory measurements.

Standard reference material (SRM) 909, freeze-dried human serum, is certified for only one level of cholesterol, and that level is low compared to normal human serum levels. The present work was done to certify two new human serum SRMs that each consist of three levels and cover a clinically significant range of cholesterol levels for humans.

Our modified ID/MS method for serum total cholesterol fulfills the stringent requirements for a definitive method (2). The method is based on the addition of a known weight of cholesterol-$^{13}C_3$ to a known weight of serum. The cholesterol esters are hydrolyzed, and the mixture of unlabeled and la-

0003-2700/89/0361-1718$01.50/0

beled cholesterol is extracted and converted to their trimethylsilyl ethers. For measurement, the derivative is injected into a GC equipped with a nonpolar fused silica capillary column that has been directly inserted into the ion source of a magnetic sector mass spectrometer. The principal isotope ratio measurements are made from the abundances of the $[M^{++}]$ ions at m/z 458 and 461. Standards are made by combining and derivatizing known amounts of pure unlabeled cholesterol and cholesterol-$^{13}C_3$. Standards with weight ratios slightly higher and slightly lower than that of each sample are measured immediately before and after the sample. Use of this measurement technique, known as bracketing, has produced results of high precision (*3*). Confirmatory measurements made on cholesterol in the same samples using different ions, different chromatographic conditions, and different ionization techniques provided evidence that there was no bias in the measurement process.

EXPERIMENTAL SECTION

Materials. Samples of standard reference material 909, a freeze-dried human serum, were obtained from the Office of Standard Reference Materials (OSRM) at NIST. Other serum pools analyzed were SRM 1951, consisting of three levels of cholesterol in frozen liquid sera, donated by the Centers for Disease Control (CDC), Atlanta, GA; and SRM 1952, consisting of three levels of cholesterol in freeze-dried sera, donated by the College of American Pathologists (CAP), Skokie, IL. SRM 911a cholesterol (cholest-5-en-3-ol (3β)) with a certified purity of 99.8 ± 0.1% was obtained from OSRM. Cholest-5-en-*25,26,27*-$^{13}C_3$-3-ol (3β) with a measured isotopic purity of 99.3 atom % was obtained from MSD Isotopes, St. Louis, MO. Other reagents were of ACS grade and used as is.

Serum Densities. Serum densities were measured according to a procedure described previously (*17*).

Sample Preparation and Derivatization. The procedures used for sample preparation have been previously described (*3*). Briefly, frozen samples were allowed to thaw, and freeze-dried samples were reconstituted by weight (Procedure A)(*18*). A weighed aliquot of an ethanol solution, containing a known quantity of cholesterol-$^{13}C_3$, freshly prepared for each set of samples, was added to a weighed aliquot of each serum sample. The cholesterol esters were hydrolyzed by using KOH in ethanol, and the cholesterol was extracted with hexane. The hexane layer was evaporated and the residue taken up in methanol for storage and handling. This procedure has been shown (*3*) to hydrolyze at least 99.9% of the cholesterol esters in serum. An aliquot of the methanol solution was dried, and bis(trimethylsilyl)acetamide was added to form the trimethylsilyl (TMS) derivative of cholesterol.

Lathosterol–Cholesterol Separation. Lathosterol (5α-cholest-7-en-3β-ol) was derivatized by following the procedure above. Aliquots of the lathosterol derivative and the cholesterol derivative were mixed and examined by GC/MS using the principal measurement conditions described below.

Calibration Standards. Three independent sets, each containing 10 or 11 standards, were prepared. For each set, ethanolic stock solutions of SRM cholesterol and cholesterol-$^{13}C_3$ were prepared by weight. Weighed portions of each solution were combined to provide a series of standard mixtures whose unlabeled:labeled weight ratios ranged from 0.8 to 1.1. Portions of these mixtures were derivatized as needed, following the procedure described above.

GC/MS Instrumentation. The instrumentation consisted of a gas chromatograph combined with a single focusing magnetic sector mass spectrometer controlled by a data acquisition system designed for isotope ratio measurements (*7*). The instrumentation has been substantially modified to permit high-precision measurements to be made on narrow chromatographic peaks. Such high-precision measurements cannot be made on unmodified instrumentation. Measurement of the intensity ratio of unlabeled to labeled analyte was made by selected ion monitoring. The system as previously described (*7*) had serious limitations when applied to the measurement of analytes eluting from capillary columns. In each measurement cycle, there was dead time due to the time necessary for the magnet to settle after switching between ions and due to the use of real-time data display. This dead time was too large to allow the number of measurement cycles necessary for good precision over the 5–20 s wide peaks of the cholesterol TMS derivative eluting from capillary columns.

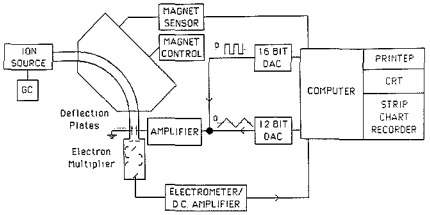

Figure 1. Electric beam switching.

A method suitable for obtaining data on such narrow capillary column peaks has been developed by changing the method of switching between masses and abandoning the display of data as it is acquired. The new means of switching masses eliminates the dead time due to magnet settling (*16*). This is done by selecting the masses of interest by using the pair of deflection plates located after the magnet and before the collector slit, as shown in Figure 1. This pair of plates was previously used only to wobble the ion beam across the collector slit, which allowed the analyst to observe the peak on a peak monitor or oscilloscope. The ion beam passing between these plates is several mass units wide in the mass region used for these measurements. The magnet is set to the lower mass (or between the masses) of interest. Both a square wave signal, which selects the mass, and a triangular wave signal, which sweeps (28 ms/sweep) the selected ion beam across the slit, are applied to the summing point of an amplifier that drives the deflection plates. The square wave voltage from a 16-bit digital to analog converter (DAC) under computer control alternately switches the ion beams through the collector slit. The triangular wave from a 12-bit DAC sweeps about 1 mass unit across the slit for a preset number of times per measurement cycle.

Deflection plate voltages are set such that the unlabeled and labeled ion beams will alternately be switched to the collector slit. The specific hardware used provides a mass range that is about 1.3% of the mass being monitored. The program controlling data acquisition is started before elution of the GC peak of interest. One acquisition is a series of repeated cycles.

The following describes one measurement cycle. The square wave voltage is switched to select the mass of the unlabeled analyte, and acquisition of ion intensity data begins. During acquisition, the triangular wave applied to the deflection plate sweeps the ion beam across the collector slit. Upon completion of a preset number of sweeps (10 for cholesterol measurement), data acquisition is interrupted. The square wave is switched to select the mass for the labeled analyte, and acquisition starts again for the same number of sweeps as set for the unlabeled analyte. When that preset number of sweeps is reached, acquisition is interrupted again, and the next measurement cycle begins.

The process is repeated continuously before and during the elution of the GC peak of interest until the ion intensity signal drops below a preset level, at which time data acquisition is ended. A base line is calculated and subtracted from the intensities measured across the GC peak. The intensities for each mass are then summed across the peak, and an intensity ratio is calculated. The ratios, number of cycles across the peak, and the sum of intensities are then displayed. The total dead time per measurement cycle was reduced from 640 to 80 ms, allowing for enough measurement cycles across chromatographic peaks only a few seconds wide to assure accurate and precise ratio measurements.

GC/MS Conditions. The principal measurements were made on the $[M^{++}]$ ions at m/z 458 and 461 from electron impact (EI) on a nonpolar GC column. Confirmatory measurements were made by using the $[M - (TMS)OC_3H_4]^+$ ions at m/z 329 and 332 from EI and the $[M + NH_4 - (TMS)OH]^+$ ions at 386 and 389 from ammonia chemical ionization (CI) on the same nonpolar GC column and by using the m/z 458/461 from EI on a moderate-polarity column. For measurement under EI conditions, the mass

spectrometer was operated at 70 eV with an emission current of 0.5 mA and an ion source temperature of 200 °C. For measurement under ammonia CI conditions, the emission current was 1 mA, the source manifold pressure (ionization gauge) was 8×10^{-3} Pa (6×10^{-5} Torr), the analyzer pressure was 1×10^{-4} Pa (8×10^{-7} Torr), and the source temperature was 200 °C. For the principal measurements, the confirmatory measurements at m/z 329/332, and the confirmatory ammonia CI measurements, the GC was equipped with a 15 m long, 0.32 mm i.d., nonpolar (95% dimethyl–, 5% phenylmethylpolysiloxane) fused silica capillary column of 1-μm film thickness. An adjustable splitter was placed at the front of the column, and the end of the column was placed directly into the source. The splitter was set to give a vent to column ratio of 10:1, and the GC was operated at a temperature of 270 °C with a helium flow rate of 3 mL min^{-1}. The injection port and interface to the mass spectrometer were maintained at 250–270 °C. Under these conditions the retention time for the cholesterol derivative was about 6 min, and the GC column gave about 1000 theoretical plates per meter. Confirmatory measurements also were made at m/z 458/461 using a 30 m long, 0.32 mm i.d., intermediate-polarity (50% dimethyl–, 50% phenylmethylpolysiloxane) fused silica column of 0.5-μm film thickness. The column temperature was 280 °C, the flow rate was 3 mL min^{-1}, and the retention time of the cholesterol derivative under these conditions was about 8 min.

Measurement Protocol. For the measurement of each sample, two standards were chosen: one whose ion intensity ratio was slightly lower than that of the sample and one whose ion intensity ratio was slightly higher. All the standards in the three sets prepared were considered as one group from which the proper standards for each sample could be chosen. Each standard and sample were measured twice in succession. The two observed intensity ratios were acceptable only if they agreed within 0.5%; if not, a third measurement was made, which had to agree with one of the other two, and the three were averaged. The average constituted one valid measurement. The calculated peak areas for each standard–sample–standard group had to be within a factor of 2 of each other, or the measurement was discarded. Each time a standard was used again in any given half-day, only a single measurement was made, as long as the new ion intensity ratio was within 0.5% of the previous value for that standard.

Measurements were made in the following order: lower (or higher) weight-ratio standard, sample, higher (or lower) weight-ratio standard. Thus, each measurement of a sample was immediately bracketed both in time and ratio by measurements of standards. On a second day the order of standards was reversed and the measurement process repeated. The quantity of analyte in the sample was calculated by linear interpolation of the measured ratio of the sample between the measured ratios of the standards. The weight ratios for each sample for both days had to agree within 0.5%, or a third day's measurement was made. The third measurement had to agree with one of the other days' measurements within 0.5%, or all measurements were discarded. The average of the two (or three if necessary) valid measurements is the reported result.

RESULTS AND DISCUSSION

Instrumentation. The overall precision of the measurements reported here requires that the relative abundances of two ions be determined with a precision of about 0.1% for a sequence of standards and samples. This is accomplished by the combination of a GC/MS instrument specifically modified to produce high-precision results and a rigid measurement protocol which uses that instrument under optimal conditions. Both the protocol and earlier versions of the instrumentation have been previously described (*3*, *7*). The two modes of multiple ion monitoring applicable to our magnetic sector mass spectrometer, accelerating voltage switching and magnetic switching, were extensively investigated. With accelerating voltage switching we have been unable to obtain precisions better than about 1%, but magnetic switching, combined with other instrumental improvements, gave satisfactory precision. Magnetic switching is, however, slow, and as a result does not permit the necessary number of measurements (about 30 for each mass) to produce the required precision when applied to the relatively narrow gas chromatographic peaks eluting from capillary columns. One solution to this problem would be the use of a quadrupole mass spectrometer since these instruments can switch masses rapidly. However, tests on two unmodified commercial quadrupole GC/MS systems gave precisions that ranged from 0.5% to 3%. We therefore implemented a new method of multiple ion monitoring for magnetic sector instruments in which the ion beam is electrically switched between the masses of interest by electric deflection after mass separation (*16*). This method, like accelerating voltage switching, is intrinsically capable of much faster switching rates and lower dead times than magnetic switching. For the present measurements with the present hardware, the switching rate is about 4 times faster than the magnetic switching rate, and the precision is at least as good as we found with peaks from packed GC columns and magnetic switching. The only disadvantage apparent so far, a mass range limited to about 1.3% of the mass to be measured, is the result of the specific hardware used to implement the method.

Choice of Labeled Material. In our previous work on cholesterol using packed columns (*3*), we had used a cholesterol labeled with seven deuteriums as our labeled material (cholest-5-en-*25,26,26,26,27,27,27-d_7*-3-ol (3β)). This labeled material is not suitable for use on capillary columns as it is partially or completely resolved from unlabeled cholesterol, and for high-precision work, the labeled and unlabeled analyte should coelute. We chose to use a carbon-13-labeled material (cholest-5-en-*25,26,27-$^{13}C_3$*-3-ol (3β)) as our labeled cholesterol. No separation of this material from unlabeled cholesterol was detected.

Interferences. Lathosterol is a possible interference because it forms a TMS derivative of identical molecular weight and very similar structure to that of the cholesterol derivative. It did not interfere in our original cholesterol method, but it has interfered in measurements elsewhere (*19*). A mixture of cholesterol-TMS and lathosterol-TMS was examined to see if the two derivatives were resolved. There was 24 s from the computer-calculated cutoff of the cholesterol chromatographic peak to the start of the lathosterol peak when the principal measurement conditions were used. Thus, lathosterol does not interfere with cholesterol in this method. Other likely steroid impurities have different molecular weights and different retention times and should not interfere. The confirmatory measurements described below were run to test for such potential interferences.

Memory Effects. We tested the derivative for memory effects resulting from material remaining in the injector, on the column, or in the source, although none were expected. If a memory effect were present, injections of a sample or standard of one unlabeled:labeled ratio would affect the ratio measured for subsequent injections of sample or standard. We injected sequentially the unlabeled cholesterol derivative, the labeled derivative, and the unlabeled derivative and measured each ratio. The ratios for the injections of the unlabeled material were not significantly different. Even when the ratio differences between consecutive measurements were the most extreme, and any memory effect should be most evident, no memory effect was observed.

Standards Cross-Check. The accuracy of results for serum samples is limited by the accuracy of the standard mixtures used for calibration. For definitive methods we prepare at least two independent sets of standards and test each standard by bracketing with standards from another set. The weight ratio determined by the ID/MS measurements is then compared with the gravimetric weight ratio for that standard. The agreement between these values is an indi-

Table I. Test of Consistency of Two Independently Prepared Sets of Standard Mixtures (SRM 911a Cholesterol and Cholesterol-$^{13}C_3$)

		weight ratios (unlabeled:labeled)		
std[a]	bracketed by[a]	mean measd by ID/MS	weighed in	diff, %
29	4, 5	0.8341	0.8330	−0.13
26	10, 6	0.8686	0.8672	−0.07
23	6, 1	0.9025	0.9037	+0.13
32	6, 1	0.9130	0.9139	+0.10
31	1, 2	0.9344	0.9354	+0.10
24	1, 2	0.9673	0.9663	−0.10
			mean diff	<0.01%

[a] Standards 23–32 were from set 3; standards 1–10 were from set 1.

Table II. Cholesterol in Human Serum SRM 909[a] (mmol L^{-1} g^{-1})

	concentration[b]		
sample	set 1	set 2	set 3
1	4.332	4.341	4.338
2	4.333	4.342	4.336
3	4.329	4.338	4.332
4	4.332	4.331	4.329
5	4.335	4.322	4.342
6	4.330	4.331	4.327
mean	4.332	4.334	4.334
CV, %	0.05	0.18	0.13

Statistical Summary
overall mean = 4.333
CV of single measurement[c] = 0.23%
rel std error of mean = 0.032%

[a] Three independently prepared sets. Three vials per set and two samples per vial. [b] The mean of day 1 and day 2 valid measurements. [c] CV of a single measurement is calculated as $(s^2(\text{sets}) + s^2(\text{vials}) + s^2(\text{aliquots}) + s^2(\text{measurement}))^{1/2}$.

cation of the bias between sets. For cholesterol, three independent sets were prepared and tested by bracketing. The three sets were combined into one group, which was used for all cholesterol measurements. The results of the measurements comparing sets 1 and 3, with set 3 as "samples", are shown in Table I. The mean difference between set 1 and set 2 was −0.01% and between set 2 and set 3 was −0.01% (results not shown).

Serum Results. The results of the principal measurements for cholesterol in SRM 909 are shown in Table II. Three sets of six samples each (two samples from each of three vials) were independently prepared and analyzed. These results indicate the excellent within-set and between-set precision obtainable with this method. The coefficient of variation (CV) for a single measurement was 0.23%, while the relative standard error of the mean was 0.032%. When the original definitive method was last used to analyze SRM 909, the result for cholesterol was 4.341 mmol L^{-1} g^{-1}, which is 0.2% higher than the mean with the modified method. However, at that time we had observed a small, but real, decrease in cholesterol concentration of approximately 0.1% per year, as measured with the original definitive method. Therefore, most of the difference is probably attributable to the time difference of about a year in storage.

The results in Table II are in millimoles of cholesterol per liter of reconstituted serum per gram of dry serum. These concentrations are based on reconstitution of each vial of freeze-dried serum by addition of 10.00 mL of water at 22 °C. Measurements of other analytes in this SRM have shown that the dry material is homogeneous, but that the fill weights of dry serum vary from vial to vial (fill weight CV = 0.5%)(*18*). Therefore, expressing the concentrations per gram of dry serum, rather than per milliliter of serum, corrects the results for fill weight variation.

Table III. Cholesterol in SRM 1951[a] (mg dL^{-1})

	mean[b]			pool	CV of 1	rel SE,[d]
pool	set 1	set 2	set 3	mean	measmt,[c] %	%
70	209.9	210.6	210.7	210.4	0.36	0.010
72	242.1	242.5	242.2	242.3	0.25	0.066
73	282.1	281.7	282.0	282.0	0.23	0.066

[a] Three independent sets, three vials of each pool per set, one sample per vial. [b] Mean of three valid results. [c] CV of a single measurement. [d] Rel SE is relative standard error.

Table IV. Cholesterol in SRM 1952[a] (mmol L^{-1} g^{-1})

	mean[b]			pool	CV of 1	rel SE,[d]
pool	set 1	set 2	set 3	mean	measmt,[c] %	%
1	22.14[e]	22.21	22.22[f]	22.19	0.38	0.120
2	28.26	28.20	28.20	28.22	0.25	0.078
3	35.85	35.78	35.75	35.79	0.26	0.085

[a] Three independent sets, three vials of each pool per set, one sample per vial, except note *e* and *f*. [b] Mean of three valid results. [c] CV of a single measurement. [d] Rel SE is relative standard error. [e] Two vials per set for pool 1 of set 1 only. [f] Three vials total; one from set 3 and two from set 4.

Table V. Cholesterol in Human Serum SRM 909 Measured over 8 Months (mmol L^{-1} g^{-1})

sample[a]	mean	sample	mean	sample	mean
1	4.332	14	4.336	27	4.324
2	4.333	15	4.332	28	4.340
3	4.329	16	4.329	29	4.319
4	4.332	17	4.343	30	4.337
5	4.335	18	4.327	31	4.332
6	4.330	19	4.330	32	4.335
7	4.341	20	4.330	33	4.332
8	4.342	21	4.334	34	4.323
9	4.338	22	4.332	35	4.317
10	4.331	23	4.326	36	4.337
11	4.322	24	4.322	37	4.328
12	4.331	25	4.334		
13	4.338	26	4.330		
mean		4.331			
sample CV, %		0.14			

[a] Samples 1–18 are from the sets to measure SRM 909. Samples 19–30 are the controls from sets in which were also measured SRM 1951 and 1952. Samples 30–37 are the controls from sets in which were measured other samples not reported here.

The results for cholesterol measurements of SRM 1951 are shown in Table III, and results of cholesterol measurements of SRM 1952 are shown in Table IV. Duplicate samples of SRM 909 were analyzed with each set to serve as controls. Results for the SRM 909 samples agreed very well with those given in Table II.

A summary of the results of cholesterol measurements on all vials of SRM 909 run over the 8-month period of method development and sample measurement is shown in Table V. Over this entire period, it was necessary to do only three third-day measurements according to the protocol. The precision of the entire group is excellent. One of the requirements for a definitive method is that the same value for a given analyte in a given material be obtained over a long period of time, assuming stability of the material. We have fulfilled this requirement.

Table VI. Confirmatory Measurements on Samples from SRM 909 Sera (mmol L^{-1} g^{-1})

		results			
set	sample	princpl[a]	EI-329[b]	EI-458[c]	CI[d]
1	9	4.335	4.337	4.328	4.308
1	10	4.330	4.332	4.330	4.334
2	18	4.331	4.349	4.337	4.339
2	19	4.322	4.341	4.330	4.346
3	27	4.332	4.348	4.336	4.330
3	29	4.342	4.331	4.341	4.350
	mean	4.332	4.340	4.334	4.334
	CV, %	0.15	0.18	0.12	0.34
diff from princpl measmt, %			+0.18	+0.05	+0.05

[a] Principal measurements using EI ions at m/z 458/461 and a nonpolar fused silica GC column. [b] Confirmatory measurements using EI ions at m/z 329/332 and a nonpolar fused silica GC column. [c] Confirmatory measurements using EI ions at m/z 458/461 and an intermediate polarity fused silica GC column. [d] Confirmatory measurements using ammonia CI ions at m/z 386/389 and a nonpolar fused silica GC column.

Confirmatory Measurements. Confirmatory measurements are made on selected subsets of the samples to test for bias. Two separate sets of samples were chosen for confirmatory measurements. The first confirmatory set was chosen from the three sets of SRM 909 samples. The samples with the highest and lowest results were selected, plus four samples chosen randomly except that there were two samples from each set selected. The second confirmatory set was chosen from the group of sets containing SRM 1951 and 1952. For this confirmatory set, we chose from SRM 1952 the highest and lowest valued samples, plus four randomly chosen samples except that each pool and set was represented twice. For SRM 1951 the two samples that were the farthest from the mean were low values. These were chosen for the confirmatory set along with four other samples selected randomly except that each pool and each set were represented twice. Finally, since there were no obvious outliers, two of the SRM 909 samples used as controls were chosen randomly.

Each confirmatory set was analyzed in three ways: (1) EI fragment ions at m/z 329/332 on a nonpolar GC column; (2) EI molecular ions at m/z 458/461 on a moderate-polarity GC column; (3) ammonia CI fragment ions at m/z 386/389 on a nonpolar GC column. The complete confirmatory results are shown for SRM 909 in Table VI. For SRM 1951, the average difference between the principal measurements and the confirmatory measurements was +0.12%. For SRM 1952 this average difference was 0.0%. For all samples the differences are small across the different measurement conditions. The overall mean values agree extremely well. Since there are no significant overall biases between results obtained under different measurement conditions, the probability of significant bias in the measurement process is very small.

Error Analysis. While the imprecision of the method is small, and no evidence of bias in the measurement process was found, an analysis of possible sources of bias and imprecision was made. The results for cholesterol in serum are based upon the purity of the unlabeled standard. This material, SRM 911a, is certified to be 99.8 ± 0.1% pure cholesterol. The uncertainty in the purity of SRM 911a, although small, makes a significant contribution to the uncertainty in the result.

Errors in the standards would contribute to errors in the determination of cholesterol levels in serum. The cross-checking of standard sets ensured the absence of significant error. Furthermore, the large numbers of measurements made on each serum pool, with standards from different sets, reduced the effect of random error.

Isotope effects on the extraction and derivatization reaction could lead to bias and imprecision. Possible isotope effects during the extraction of cholesterol are of no consequence since it has been demonstrated that 99% of the cholesterol is recovered (*3*). An isotope effect in the derivatization reaction is not expected because the label in the cholesterol-$^{13}C_3$ is far from the site of reaction. The experimental evidence for negligible isotope effects on the GC column is that the labeled and unlabeled forms of cholesterol-TMS are not measurably separated on a capillary column.

The calculated components of variance for all the data reported here for SRM 909a, 1951, and 1952 are 0.026% for set-to-set and 0.082% for vial-to-vial. The relative standard error of the mean is 0.0322%.

We can compare the sources of error in the modified cholesterol method to the sources of error in the original cholesterol method (*3*). A capillary column provides better resolution and less background column bleed than a packed column, which means fewer possible interferences. In the old method, a small inhomogeneity in the deuterium-labeled cholesterol meant that each set of samples had to be measured with a set of standards prepared from the same stock solution of labeled cholesterol. With the carbon-13-labeled cholesterol there has been no inhomogeneity, so standards to measure any given sample were chosen from the pool of all standards. This decreases the chance that an error in the concentration of the stock solution of the labeled cholesterol could be undetected.

The value for the CV of a single measurement demonstrates the precision of a given measurement method. The CV of a single measurement for the original definitive method is 0.36% (*3*), whereas the CV of a single measurement for the modified definitive method is 0.22%. The modified method is thus more precise than the original method.

Conclusion. The combination of high precision and absence of significant bias qualifies this method as a candidate definitive method for serum cholesterol. This method for certifying cholesterol concentrations in reference materials will be useful in evaluating the accuracy of reference and routine clinical methods.

LITERATURE CITED

(1) Laboratory Standardization Panel. *Clin. Chem.* **1988**, *34*, 193–201.
(2) *Tentative Guidelines for the Development of Definitive Methods in Clinical Chemistry for the National Reference System in Clinical Chemistry, NRSCC1-T*; National Committee for Clinical Laboratory Standards: Villanova, PA, 1982.
(3) Cohen, A.; Hertz, H. S.; Mandel, J.; Paule, R. C.; Schaffer, R.; Sniegoski, L. T.; Sun, T.; Welch, M. J.; White, E., V *Clin. Chem.* **1980**, *26*, 854–860.
(4) White, E., V; Welch, M. J.; Sun, T.; Sniegoski, L. T.; Schaffer, R.; Hertz, H. S.; Cohen, A. *Biomed. Mass Spectrom.* **1982**, *9*, 395–405.
(5) Cohen, A.; Hertz, H. S.; Schaffer, R.; Sniegoski, L. T.; Welch, M. J.; White, E., V. Presented at the 27th Annual Conference on Mass Spectrometry and Allied Topics, Seattle, WA, June 3–8, 1979.
(6) Ellerbe, P.; Meiselman, S.; Welch, M. J.; White, E., V. Presented at the 34th Annual Conference on Mass Spectrometry and Allied Topics, Cincinnati, OH, June 8–13, 1986.
(7) Welch, M. J.; Cohen, A.; Hertz, H. S.; Ruegg, F. C.; Schaffer, R.; Sniegoski, L. T.; White, E., V *Anal. Chem.* **1984**, *56*, 713–719.
(8) Welch, M. J.; Cohen, A.; Hertz, H. S.; Ng, K. J.; Schaffer, R.; Van Der Lijn, P.; White, E., V *Anal. Chem.* **1986**, *58*, 1681–1685.
(9) Sieckmann, L.; Breuer, H. *J. Clin. Chem. Clin. Biochem.* **1982**, *20*, 883–892.
(10) Jonckheere, J. A.; De Leenheer, A. P. *Biomed. Mass Spectrom.* **1983**, *10*, 197–202.
(11) Patterson, D. G.; Patterson, M. B.; Culbreth, P. H.; Fast, D. M.; Holler, J. S.; Sampson, E. J.; Bayse, D. D. *Clin. Chem.* **1984**, *30*, 619–626.
(12) Pelletier, O.; Wright, L. A.; Breckinridge, W. C. *Clin. Chem.* **1987**, *33*, 1403–1411.
(13) Sieckmann, L. *J. Clin. Chem. Clin. Biochem.* **1985**, *23*, 137–144.
(14) Pelletier, O.; Arratoon, C. *Clin. Chem.* **1987**, *33*, 1397–1402.
(15) Sieckmann, L. *J. Clin. Chem. Clin. Biochem.* **1985**, *23*, 129–135.
(16) Meiselman, S.; Ellerbe, P.; Welch, M. J.; White, E., V. Presented at the 34th Annual Conference on Mass Spectrometry and Allied Topics, Cincinnati, OH, June 8–13, 1986.
(17) Sniegoski, L. T.; Moody, J. R. *Anal. Chem.* **1979**, *51*, 1577–1578.
(18) *NBS Certificate of Analysis for SRM 909*. Available from the Office of Standard Reference Material, NIST (formerly NBS), Gaithersburg, MD, 20899.

(19) Schaffer, R.; Sniegoski, L. T.; Welch, M. J.; White, E., V; Cohen, A.; Hertz, H. S.; Mandel, J.; Paule, R. C.; Svensson, L.; Bjorkhem, I.; Blomstrand, R. *Clin. Chem.* **1982**, *28*, 5–8.

RECEIVED for review December 15, 1988. Accepted May 9, 1989. We are grateful to the College of American Pathologists for their support of P.E. Certain commercial equipment, instruments, or materials are identified in this report to specify adequately the experimental procedure. Such identification does not imply recommendation or endorsement by the National Institute of Standards and Technology, nor does it imply that the materials or equipment identified are necessarily the best available for the purpose.

Desorption Chemical Ionization, Thermospray, and Fast Atom Bombardment Mass Spectrometry of Dihydropyridine ⇌ Pyridinium Salt-Type Redox Systems

László Prókai, Bih-Hsiung Hsu, Hassan Farag,[1] and Nicholas Bodor*

Center for Drug Design and Delivery, College of Pharmacy, Box J-497, J. Hillis Miller Health Center, University of Florida, Gainesville, Florida 32610

Trigonellyl-substituted (pyridinium salt type) compounds decompose during sample introduction using desorption chemical ionization (DCI) and thermospray (TSP) ionization. Thermal dequaternization is the main degradation process in DCI, while hydrolytically sensitive bonds are subject to cleavage in the TSP source, and dequaternization and reduction to the dihydropyridine analogues are also observed. Fast atom bombardment (FAB) is the suggested method of ionization because of its ability to provide an intense intact cation. The neutral dihydropyridine analogues can be effectively ionized by DCI and TSP. These methods are recommended, because bombardment-induced oxidation produces artifacts and shows a matrix effect in positive FAB.

INTRODUCTION

Quaternary ammonium salts are considered a class of compounds that are not amenable to the mass spectrometric analysis with methods used for gas-phase neutral molecules, such as electron impact (EI), chemical ionization (CI), and field ionization (FI). Attempts to volatilize the charged quaternary salts prior to analysis generally result in degradation of the salt to nonionic species, which, on the contrary, can be vaporized and ionized. The usual thermal decomposition pathways for quaternary salts are substitution and elimination reactions (*1*). Certain aromatic ammonium salts, however, may undergo other routes of pyrolytic degradation. Reduction to the corresponding neutral dihydropyridine was observed upon heating some pyridinium salts, in addition to the dealkylation and Hoffmann elimination reactions (*2–6*). To overcome the problem of thermal degradation during evaporation prior to ionization, the conversion of pyridinium salts to 1,4-dihydropyridine analogues has been suggested as a derivatization procedure (*7*), but the obtained neutral analogues appeared to be labile themselves in certain cases. Nevertheless, with gas-phase ionization techniques, mass spectra containing the intact cation are obtained from quaternary pyridinium salts due to secondary effects, such as EI-induced fragmentation of the thermally formed dihydropyridine analogues (*8*).

Generation of gas-phase ions from condensed samples including nonvolatile ammonium salts has become possible with the development of desorption ionization methods. Field desorption (FD) mass spectra of pyridinium salts recorded at the "best anode temperature" (BAT) have exhibited high signal intensities of intact cations of the salts and of cluster ions permitting the molecular weight determination (*4*). However, upon heating the emitter above the BAT, the reduction to the corresponding neutral dihydropyridine was observed. Desorption chemical ionization (DCI) has been found to give molecular weight and structural information of a series of pyridinium nucleotide salts (*7*). Secondary ion mass spectrometry can be used as a sensitive method for characterization of quaternary ammonium compounds (*9–13*), but with the inception of fast atom bombardment (FAB) and liquid secondary ion mass spectrometry (liquid SIMS), desorption/ejection of ions from ammonium salt–liquid mixtures upon bombardment with a primary beam of atoms or ions of some kiloelectronvolts energy has produced high ion intensities featuring the intact cation as well as cluster and fragment ions (*14*, *15*). This offers an almost ideal method for molecular weight determination and structural characterization. It has been shown, however, that the matrix can also participate in or promote chemical reactions, such as oxidation–reduction processes (*16*), either in a spontaneous manner or upon primary atom/ion bombardment giving rise to matrix-induced artifacts (*17*) and irrelevant analytical information. Reduction of several aromatic quaternary ammonium salts under FAB and liquid SIMS conditions has been reported (*16*, *18*, *19*, *20*).

Thermospray (TSP) ionization has been evaluated as a possible technique for on-line liquid chromatography/mass spectrometry (LC/MS) for tetraalkylammonium salts (*21*), but it was found to be unsuitable for quantitative analysis owing to the thermal decomposition of the salts by dealkylation under normal operating conditions. On the other hand, TSP mass spectra featuring the intact cations have been obtained from a series of quaternary ammonium salts (*22*), and one-electron reduction of pyridinium salts leading to rather stable radical ions has been described as an important side reaction during ionization. In cases of a direct liquid

*To whom correspondence should be addressed.
[1]Present address: Faculty of Pharmacy, University of Assuit, Assuit, Egypt.

0003-2700/89/0361-1723$01.50/0

Scheme I. Structure of the Compounds Studied

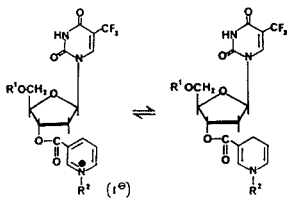

Pyridinium[a] salt	⇌	Dihydropyridine[b] analog	R^1	R^2
1 (416)		2 (417)	H	CH_3
3 (500)		4 (501)	t-BuC(=O)-	CH_3
3a (503)		4a (504)	t-BuC(=O)-	CD_3

[a] Relative mass of the intact cation in parentheses. [b] Relative molecular weight of the compound in parentheses.

introduction (DLI) interface to the CI source of the mass spectrometer, reduction of a quaternary phenanthridinium salt has been observed with acetonitrile solvent, which also served as the reagent gas (*23*).

The improved delivery through biological membranes using a dihydropyridine ⇌ pyridinium salt type redox delivery system has been reported for a wide variety of drugs. The lipophilic compounds formed by coupling the drug with a dihydropyridine type carrier readily diffuse, e.g., into the central nervous system where enzymatic oxidation converts them into the corresponding pyridinium salts, which cannot diffuse out ("locked in") due to its high polarity (*24*, *25*). Hydrolysis of the carrier–drug conjugate then provides a site-specific and sustained drug delivery. A successful example for brain-specific delivery of α,α,α-trifluorothymidine (TFT), an antiviral agent, has been reported recently (*26*, *27*). In the present work, the mass spectral characterization of the compounds (Scheme I) involved in the complex metabolic changes of α,α,α-trifluorothymidine 3′-(1,4-dihydro-1-methyl-3-pyridinecarboxylate)-5′-(2,2-dimethylpropanoate) (**1**) is described with a special emphasis on the comparative evaluation of the potentials and limitations of the title ionization methods and on the possible interconversion of the pyridinium salts and their neutral dihydropyridine analogues during ionization/desorption from condensed phase (solid or liquid) samples.

EXPERIMENTAL SECTION

Mass Spectrometry. All experiments were performed on a MS80RFA double focusing instrument (Kratos Analytical, Manchester, U.K.) operated in various ionization modes. Positive-ion mass spectra were recorded by a Kratos DS90 data system.

Desorption chemical ionization mass spectra were recorded with the standard Kratos DCI probe. A 0.1–0.2-μg sample was coated onto the platinum–iridium coil with an appropriate solvent (usually methanol), then the solvent was allowed to evaporate at room temperature, and the probe was inserted into the combined electron impact/chemical ionization source. Isobutane (99.5+%) or ammonia (99.99+%, Union Carbide Corp., Linde Division, Danbury, CT) were used as reagent gases. The following conditions were applied: ionizing electron energy, 50 eV; emission current, 500 μA; source temperature, 50 °C; source pressure, ~10^{-6} Torr (registered with the standard source vacuum gauge). Positive ion spectra were recorded at 4.0 kV accelerating voltage in the mass range of 100–800 daltons (calibrated with perfluorokerosene in EI mode). The nominal resolution was 1000, a scan speed of 1 s/mass decade was applied. Direct heating of the sample coil was achieved by a programmable power supply unit. The temperature of the coil was raised from 50 to 400 °C at 100 °C/min and then held at the final temperature for 20 s. Mass spectra aquired at the apex of the total ion signal were evaluated.

TSP mass spectrometry was performed by the Kratos thermospray option. The solvent was delivered by a Kratos Spectroflow 400 HPLC pump at 1.0 mL/min flow rate. Aqueous ammonium acetate (0.1 M) (HPLC grade, Fisher Scientific, Fair Lawn, NJ) was used for the quaternary compounds, while a mixture of acetonitrile and 0.1 M ammonium acetate (70:30, v/v) was the solvent for the neutral dihydropyridine analogues. A 0.1–1.0-μg sample dissolved in the thermospray solvent was injected directly (without HPLC column) to the TSP probe with a manual sampler (Kratos Spectroflow 480 injector valve module equipped with a Rheodyne 7125 injection loop, 20 μL). The probe was protected with a 0.5-μm stainless steel in-line frit filter (Supelco, Bellefonte, PA). The temperature of the probe, vaporizer, source, and jet was set to approximately 155, 220, 190, and 210 °C, respectively, and then adjusted to give the signal optimum for the protonated molecular ion of adenosine (m/z 268) with the given thermospray solvent. TSP mass spectra were recorded at 4.0 kV accelerating voltage, nominal resolution of 1000, scan speed of 3 s/decade in the 150–650 daltons mass range. Calibration was established with the positive ions from poly(ethylene glycol), PEG 600.

The FAB gun was an Ion Tech Ltd. (Teddington, Middlesex, U.K.) FAB11NF saddle-field source operated with xenon (99.995%, Union Carbide Corp. Linde Division, Danbury, CT) at 6 keV and 1 mA. Sample introduction was accomplished via placing 3–5 μg of analyte in methanolic solution directly onto the FAB probe and then mixing with 1–2 μL of liquid matrix on the copper target. Different matrices were used including glycerol, thioglycerol, dithioerythritol/dithiothreitol (3:1 mixture, w/w) diethanolamine, triethanolamine, 3-nitrobenzyl alcohol, 2-(octyloxy)nitrobenzene, and poly(ethylene glycol) (PEG 600). The effect of additives was studied by adding 1% (w/w) *p*-toluenesulfonic acid or sodium dithionite to glycerol or by saturating glycerol with lithium iodide at room temperature. FAB mass spectra were collected from 100 to 2400 daltons at 4.0 kV accelerating voltage, nominal resolution of 1500, and scan rate of 10 s/mass decade.

Materials. Synthesis of the analytes is described elsewhere (*28*). Deuteromethyl derivatives (**3a**, **4a**) were obtained by using iodomethane-d_3 (99+ atom % D, Aldrich Chemical Co., Milwaukee, WI) in the appropriate preparative steps.

All solvents were of HPLC grade (Fisher Scientific, Fair Lawn, NJ), matrices and additives were purchased from commercial sources and used without further purification.

RESULTS AND DISCUSSION

The characteristic positive ions obtained by different desorption ionization techniques from the compounds given in Scheme I are listed in Table I. Positive-ion mass spectra are expected to give more relevant results in these cases, since one of the compounds involved in the possible redox system is actually a (preformed) positive organic ion. Desorption methods of ionization usually give detectable signals of intact quaternary ions already existing in the condensed phase, but their intensity is largely determined by the principles used for the generation of gas-phase ions (rapid heating in the presence of a reagent gas plasma in DCI, desorption from heated droplets in TSP, or sputtering from a liquid matrix in FAB, etc.) and the analyte itself. To illustrate the characteristic differences for the title substances, complete bargraph mass spectra obtained by these techniques are given for the **3** ⇌ **4** redox pair in Figures 1 and 2, respectively.

Fast-heating desorption chemical ionization results in the intact cations with low to just detectable intensities for the quaternary salts studied, as exemplified in Figure 1a. Thermal decomposition leading to the corresponding nicotinic acid derivatives (MH^+ quasimolecular ion for **3**, m/z 486) and methyl iodide ($M^{+\cdot}$; m/z 142) is by far the most prevailing process. The decomposition products are then ionized by CI

Table I. Characteristic Positive Ions[a] in Mass Spectra of α,α,α-Trifluorothymidine Derivatives (Scheme I)

structure	DCI-MS[b]	TSP-MS	FAB-MS[c]
1	402 (4), 204 (12), 181 (100), 142 (18), 138 (16)	435 (1), 420 (2), 418 (2), 402 (6), 314 (100)	416 (58), 138 (100)
2	418 (10), 238 (52), 181 (100), 140 (65)	435 (100), 418 (35), 238 (13)	418 (11), 416 (32), 140 (20), 138 (100)
3	500 (0.5), 486 (26), 306 (20), 182 (69), 181 (100), 142 (67), 124 (89)	519 (11), 502 (6), 486 (13), 398 (100), 314 (14)	500 (88), 138 (100)
3a	503 (3), 486 (44), 306 (36), 182 (78), 181 (100), 145 (74), 124 (94)	522 (5), 505 (2), 486 (8), 398 (100), 314 (13)	503 (82), 141 (100)
4	502 (62), 322 (100), 181 (26), 140 (32), 138 (43), 121 (30)	519 (100), 502 (24), 322 (19), 181 (5)	502 (4), 500 (10), 140 (10), 138 (100)
4a	D/H exchange:[d] 505 (12), 504 (35), 503 (28), 502 (25)	522 (100), 505 (41), 322 (10), 181 (2)	505 (5), 503 (12), 143 (11), 141 (100)

[a] m/z, relative intensities (% of base peak) are given in parentheses. [b] Isobutane reagent gas. [c] Glycerol matrix. [d] Sum of MH^+ quasimolecular ion intensities of molecules with different D content are made equal to 100. The spectrum represents a composite of compounds with 0, 1, 2, and 3 deuterium.

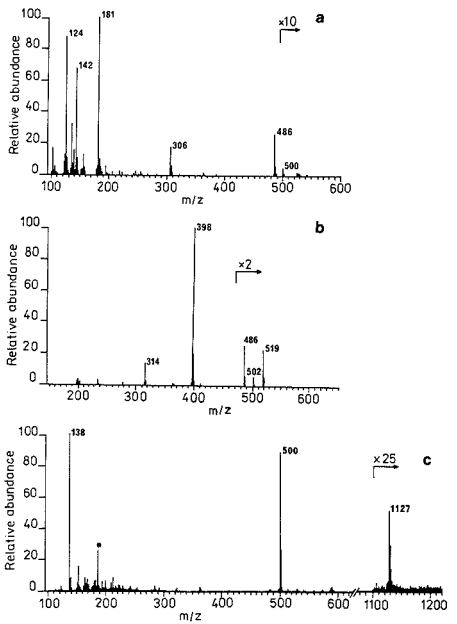

Figure 1. Desorption ionization mass spectra of the quaternary pyridinium salt **3**: (a) DCI (isobutane reagent gas), 10× scaling factor applies from m/z 490; (b) TSP (solvent, 0.1 M aqueous ammonium acetate); (c) FAB (glycerol matrix; asterisk denotes ions from the matrix).

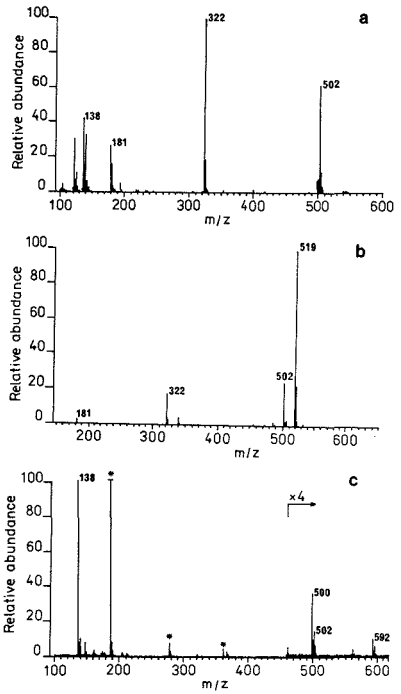

Figure 2. Desorption ionization mass spectra of the dihydropyridine **4**: (a) DCI (isobutane reagent gas); (b) TSP (solvent, acetonitrile/0.1 M aqueous ammonium acetate, 70:30 (v/v); (c) FAB (glycerol matrix; asterisk denotes ions from the matrix).

in the gas phase. This is supported by the observation that in the DCI spectrum of the trideuteromethylpyridinium salt (**3a**) the mass position of the quasimolecular and fragment ions of the nicotinic acid ester is not shifted, and the corresponding methyl iodide formed by degradation of the quaternary salt in the solid phase on the heated wire contains the total amount of the introduced stable isotope label.

Although the 1,4-dihydropyridine analogues exhibit low volatility, they probably produce sufficient vapor pressure under fast-heating DCI conditions to allow gas-phase chemical ionization processes. The prominent MH^+ quasimolecular ion arising from protonation by the reagent ions is accompanied by $[M + NH_4]^+$ adduct ions of nearly equal intensity in ammonia chemical ionization, but the latter one tends to give less abundant fragment ions (*29*). The typical DCI mass spectrum (Figure 2a) shows a number of structure-related fragment ions including the one which corresponds to the loss of the neutral 5-(trifluoromethyl)uracil molecule (BH) from the MH^+ even-electron ion ($[MH - BH]^+$; m/z 322), the protonated 5-(trifluoromethyl)uracil (BH_2^+; m/z 181), and the species representing the dihydropyridine (DHP) unit (m/z 140, 138, and 121), as shown in the simplified fragmentation in Figure 3. These ions indicate that protonation takes place either at the base or at the dihydropyridine unit of the molecule, and it is followed by hydrogen rearrangements and ejection of neutral molecules—the usual fragmentation mechanism of even-electron ions obtained by CI (*30*). A closer resemblance to the CI mass spectral characteristics of nucleosides (*31*) points to the more decisive role of the base

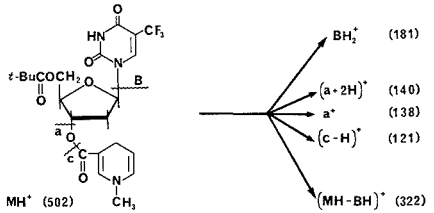

Figure 3. Possible origin of the fragment ions in the DCI spectrum of **4**.

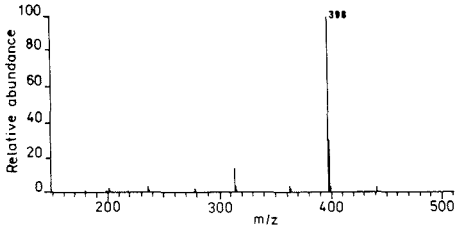

Figure 4. TSP mass spectrum of α,α,α-trifluorothymidine 5′-(2,2-dimethylpropanoate) (solvent, 0.1 M aqueous ammonium acetate).

portion of the molecule in protonation as well as in the subsequent fragmentation. On the other hand, the hydrogen/deuterium exchange observed with the labeled compound (**4a**, see Table I) is thought to be a consequence of the increased isomerization ability of the dihydropyridine ring system under DCI conditions. The platinum–iridium wire might have a catalytic effect to the exchange reaction occurring probably before evaporation/desorption from the condensed-phase sample between the reagent gas plasma and the substance at elevated temperature.

TSP mass spectra show certain similarities to those obtained with DCI. The inability of the ionization technique to give ions corresponding to the intact gas-phase cations for quaternary substances is revealed, as exemplified in Figure 1b. The spectrum appears to represent, however, a more complex mixture than that one can expect as products of a single, well-defined decomposition reaction. Undoubtedly, the ion at m/z 486, similar to that found in the DCI spectrum, arises from thermal dequaternization leading to the nicotinic acid derivative, which is subsequently protonated by the thermospray plume, and possibly its solvent-depleted particles that tend to be overheated in the ion source provide these neutral molecules—identical with those observed upon heating the salt on the surface of a wire. In addition, the quaternary ion is reduced to (1,4- and/or 1,2-) dihydropyridine compounds which are protonated (MH^+, m/z 502) or "cationized" ($[M + NH_4]^+$; m/z 519) in the subsequent ionization step, as inferred from the TSP spectrum presented in Figure 2b. Regions of the ion source possibly contain thermal electrons in significant concentration (*23*) for this chemical reaction to take place. Alternatively, hydrogen radicals or other reactive neutrals may also act as reactant (*32*). Similar to thermal decomposition, the reduction occurs possibly in solvent-depleted particles of the thermospray plume.

Although the remaining ions in the TSP spectrum of quaternary salts **1** and **3**, including the base peaks (m/z 314 and 398, respectively), might have been assigned to fragments formed from the dequaternized or reduced species, this explanation could be argued, since practically no ions were detected at these m/z values in either the corresponding isobutane or ammonia DCI spectra, in which the occurrence of thermal processes were evident, or in the TSP spectra of the dihydropyridine analogues (**2** and **4**). Further studies have suggested another explanation taking a third chemical reaction into account. On the basis of the TSP spectrum of the possible hydrolysis products of **1** (α,α,α-trifluorothymidine) and **3** (α,α,α-trifluorothymidine 5′-pyvalate ester, as shown in Figure 4) registered under identical conditions, hydrolytic cleavage at the trigonellyl ester bond resulting in the formation of these compounds also occurs. Accordingly, the base peaks in the spectra of the quaternary salts can be assigned to the $[M + NH_4]^+$ adduct ions of the neutral molecules described above (m/z 314 for **1**, m/z 398 for **3** and **3a**). This hydrolysis reaction, in contrast to the thermal decomposition and reduction, most probably takes place within the liquid jet droplets of the thermospray plume indicating the stress exerted by the elevated temperature, the pH, and ion concentration of the liquid medium exposed to the analyte during sample introduction, and thus, the hydrolytically sensitive bonds of nonvolatile ions/molecules are also subject to cleavage. Then the reaction products may be ionized according to the mechanism involving ion evaporation from charged liquid droplets (*33*) and/or gas-phase (chemical) ionization following depletion of the droplets from solvent (*34*).

Obviously, the neutral dihydropyridine analogues **2**, **4**, and **4a** can be ionized by TSP due to their (albeit low) volatility that facilitates the presence of intact gaseous neutral molecules in the jet. In comparison with the DCI spectrum obtained with the EI/CI source, a "softer" ionization (less fragmentation) is achieved under thermospray conditions, but the identical fragment ions are indicative of a common (CI) mechanism of ion formation, i.e., gas phase ionization by a reagent ion plasma. A notable difference between the DCI and TSP mass spectra of the deuterium labeled compound **4a** is the lack of hydrogen/deuterium exchange during the ionization with the latter technique. This might be an indication of the heterogeneous (condensed-phase/gas phase) rather than homogeneous (gas-phase) exchange reaction in DCI.

FAB is the only technique studied that is able to provide an intact cation of high intensity from the quaternary salts (Figure 1c). Although of substantially lower intensity, the cluster ion consisting of two cations and an anion (iodide) is readily discernible, and even higher clusters might be detected. The one major fragment ion (m/z 138) is originated from the quaternary substituent. As it has been revealed, FAB is a powerful method for ionization/desorption of preformed ions already existing in the condensed phase (*17*), and the basic function of the matrix might be just to assist the ion evaporation from liquid-phase/gas-phase interface (*35*). Matrix- or bombardment-induced reactions (including reduction) were not observed.

In FAB mass spectra of the neutral dihydropyridine analogues, ions of even higher intensity corresponding in their mass positions to the quaternary ions have been detected, in addition to the expected MH^+ quasimolecular ions (Figure 2c). The intense fragment ion characteristic of the quaternary substituent (m/z 138) is a strong indication of the presence of the ionic substance (**3**). It might have been considered that the preformed cation present as contaminant in the neutral dihydropyridine compound (although the corresponding DCI and TSP spectra revealed only trace amounts of the ionic form) desorbed more efficiently than the MH^+ ion of the latter. Even small amounts of the ionic form would be "overrepresented" in the FAB spectrum when it predominantly occupies, due to the known surface-active feature of quaternary ammonium compounds, the surface regions of the sample/matrix solution, which is directly involved in the sputtering process, resulting in the so-called surface activity discrimination (*36*). In competition for the surface, however, the hydrophobicity/hydrophilicity of the analyte should also

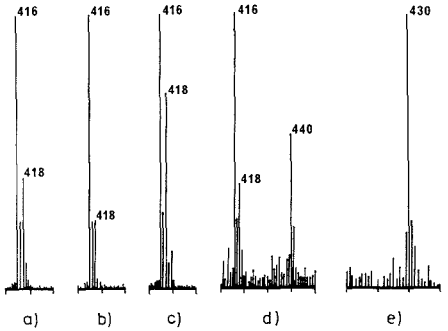

Figure 5. FAB mass spectrum of **2** (molecular ion region): (a) in glycerol; (b) in dithioerithritol/dithiothreitol (3:1); (c) in glycerol + 1% *p*-toluenesulfonic acid; (d) in glycerol + 1% sodium dithionite; (e) in glycerol saturated with lithium iodide.

be evaluated (*37*). Thus, the possible surface activity discrimination of the quaternary pyridinium salt present as a contaminant of the neutral compound may be counterbalanced by the hydrophobic character (*24*, *25*) of the dihydropyridine analogue. Considering these factors and the ion yield of the quaternary salt (**3**) calculated from the respective FAB spectra, the intensity of the cation is exaggerated and cannot be assigned simply as contamination. There should be a chemical reaction, i.e. oxidation, that produces the quaternary ion from the dihydropyridine compound under FAB conditions.

The involvement of the glycerol matrix in the present oxidation process is indicated by the intense $[M - H + \text{glycerol}]^+$ (m/z 592) and $[M + H + \text{glycerol}]^+$ (m/z 594) adducts. Clustering is profoundly less abundant in case of the pure quaternary salts. The reaction may proceed via either direct hydride removal or a sequential electron–proton–electron "hydride-like" oxidation mechanism. On the basis of chemical evidence and theoretical calculations (*38–40*), the direct hydride abstraction (concerted transfer of a proton and two electrons) appears to be more feasible in the matrix media. Another proof of the existence of a chemical reaction is that the rates of competing oxidation and protonation show matrix dependence. In comparison with glycerol (Figure 5a), the ratio of $[M - H]^+/MH^+$ ion intensities of **2** profoundly increases using matrices such as thioglycerol, diethanolamine, triethanolamine, 2-(octyloxy)nitrobenzene, and dithioerythritol/dithiothreitol (Figure 5b), while 3-nitrobenzyl alcohol and PEG 600 produce only slight increase in the relative intensity of the quaternary ion. However, addition of an acid (*p*-toluenesulfonic acid, Figure 5c) evidently enhances the relative intensity of MH^+.

It is interesting to consider the site and extent of oxidation. The practically time-independent intensity ratio of the quaternary ion/protonated molecule during fast atom bombardment suggest that the oxidation takes place at the condensed-phase/vacuum interface characterized as the selvedge region (*41*) and does not involve extensive solution chemistry within the liquid matrix. On the other hand, allowing a matrix, such as thioglycerol, which gives preferentially the ion corresponding to the quaternary compound, to evaporate from the target in the ion source under FAB conditions, then mixing the sample remaining on the probe with glycerol, the intensity ratio characteristic of the latter matrix is obtained again. The procedure (thioglycerol followed by glycerol) can be continued in cycles several times without noticeable changes in the matrix-related intensity ratios. Another proof is that admixing sodium dithionite, a reducing agent of the quaternary compound in solution, to the liquid matrix (glycerol) does not influence the $[M - H]^+/MH^+$ ratio (Figure 5d), although the addition of salt in a smaller amount results in the formation of $[M + Na]^+$ adduct ions as well and is accompanied by an overall decrease in ion intensities. An excess amount of sodium salt suppresses the sputtering process, possibly because of the substantial changes in the nature of the interface region. The cation adduct (m/z 440) induced by the deliberate addition of salt, may, however, help to ascertain the correct molecular weight as the adduct is not affected by artifacts emerging from redox reactions. The known side effect of this approach might be a cation exchange reaction in the liquid matrix (whenever it is feasible, i.e., there are exchangeable hydrogens in the molecule) before desorption giving rise to the appearance of, e.g., $[M - H + 2Li]^+$ ion (m/z 430) in Figure 5e. Unlike the sodium salt, saturation of the matrix with lithium iodide does not suppress the ion formation from the present compound under FAB conditions.

In conclusion, a variety of chemical reactions has been observed during the ionization/desorption of some pyridinium salt ⇌ dihydropyridine redox pairs. Upon crossing the condensed phase/vacuum interface, DCI appears to exert purely thermal stress resulting in dequaternization of the involatile pyridinium salts, while TSP also exhibits species related to hydrolysis and reduction confined to the trigonellyl group. However, both techniques are capable of producing artifact-free mass spectra for the neutral dihydropyridine analogues, and an evaporation–gas-phase ionization sequence is likely to occur under normal operating conditions. On the contrary, FAB provides high-intensity intact cations from the pyridinium salts but results in bombardment-induced oxidation of dihydropyridines. The latter is proposed to be truly interfacial in nature, and its extent is associated with the properties of the liquid matrix. Formation of cation adducts may alleviate the accompanied ambiguities regarding the molecular weight determination, yet the complementary application of these desorption ionization methods is recommended for the title substances.

LITERATURE CITED

(1) Veith, H. J. *Mass Spectrom. Rev.* **1983**, *2*, 419–446.
(2) Hvistendahl, G.; Udheim, K. *Tetrahedron* **1972**, *28*, 1737–1748.
(3) Salzmans, R.; van Binst, G. *Org. Mass. Spectrom.* **1974**, *8*, 357–376.
(4) Larsen, E.; Egsgaard, H.; Holmen, H. *Org. Mass Spectrom.* **1978**, *13*, 417–424.
(5) Ellingsen, P.; Hvistendahl, G.; Udheim, K. *Org. Mass Spectrom.* **1978**, *13*, 455–458.
(6) Ellingsen, P.; Hvistendahl, G. *Org. Mass Spectrom.* **1980**, *15*, 18–21.
(7) Esmans, E. L.; Freyne, E. J.; Vanbroekhoven, J. H.; Alderweidt, F. C. *Biomed. Mass Spectrom.* **1980**, *7*, 377–380.
(8) Lee, T. D.; Anderson, W. R.; Daves, G. D. *Anal. Chem.* **1981**, *53*, 304–308.
(9) Day, R. J.; Unger, S. E.; Cooks, R. G. *J. Am. Chem. Soc.* **1979**, *101*, 501–502.
(10) Ryan, T. M.; Day, R. J.; Cooks, R. G. *Anal. Chem.* **1980**, *52*, 2054–2057.
(11) Unger, S. E.; Ryan, T. M.; Cooks, R. G. *Anal. Chim. Acta* **1980**, *181*, 169–174.
(12) Vincze, A.; Busch, K. L.; Cooks, R. G. *Anal. Chim. Acta* **1982**, *136*, 143–153.
(13) Busch, K. L.; Hsu, B.-H.; Wood, K. V.; Cooks, R. G.; Schwarz, C. G.; Katritzky, A. R. *J. Org. Chem.* **1984**, *49*, 764–769.
(14) Veith, H. J. *Org. Mass Spectrom.* **1983**, *18*, 154–158.
(15) Heller, D. H.; Yergey, A.; Cotter, R. J. *Anal. Chem.* **1983**, *55*, 310–313.
(16) Pelzer, G.; De Pauw, E.; Viet'Dung, D.; Marien, J. *J. Phys. Chem.* **1984**, *88*, 5065–5068.
(17) De Pauw, E. *Mass Spectrom. Rev.* **1986**, *5*, 191–212.
(18) Gale, J. P.; Bentz, B. L.; Chait, B. T.; Field, F. H.; Cotter, R. J. *Anal. Chem.* **1986**, *58*, 1070–1076.
(19) Tondeur, Y.; Sovocool, G. W.; Mitchum, R. K.; Niederhut, W. J.; Donnelly, J. R. *Biomed. Environ. Mass Spectrom.* **1987**, *14*, 733–736.
(20) De Angelis, F.; Doddi, G.; Ercolani, G. *J. Chem. Soc., Perkin Trans. 2* **1987**, 633–637.
(21) Mitchell, D. S.; Jennings, K. R.; Scrivers, J. H. *Proc. ASMS Conf. Mass Spectrom. Allied Top., 35th* **1987**, 427–428.
(22) Schmelzeisen-Redeker, G.; Rollgen, F. W.; Wirtz, H.; Vogtle, F. *Org. Mass Spectrom.* **1985**, *20*, 752–756.
(23) Arpino, P. J.; Schmitter, J.-M. *Org. Mass Spectrom.* **1987**, *22*, 736–739.
(24) Bodor, N.; Brewster, M. E. *Pharm. Ther.* **1983**, *19*, 337–389.

(25) Bodor, N. *Ann. N.Y. Acad. Sci.* **1988**, 289–306.
(26) Rand, K.; Bodor, N.; ElKoussi, A.; Road, I.; Miyake, A.; Houck, H.; Gildersleeve, N. *J. Med. Virol.* **1986**, *20*, 1–8.
(27) ElKoussi, A.; Bodor, N. *Drug Des. Delivery* **1987**, *1*, 275–283.
(28) Miyake, A.; Bodor, N., submitted for publication in *J. Heterocycl. Chem.*
(29) Arpino, P. J.; Devant, G. *Analysis* **1979**, *7*, 348–354.
(30) Harrison, A. G. *Chemical Ionization Mass Spectrometry*; CRC Press: Boca Raton, FL, 1983; pp 65–71.
(31) Wilson, M. S.; McCloskey, J. A. *J. Am. Chem. Soc.* **1975**, *97*, 3436–3444.
(32) McEwan, C. N. *Mass Spectrom. Rev.* **1986**, *5*, 521–547.
(33) Vestal, M. L. *Mass Spectrom. Rev.* **1983**, *2*, 447–480.
(34) Butfering, L.; Schmelzeisen-Redeker, G.; Rollgen, F. W. *J. Chromatogr.* **1987**, *394*, 109–116.
(35) Derrick, P. J. *Fresenius' Z. Anal. Chem.* **1986**, *324*, 486–491.
(36) Ligon, W. V.; Dorn, S. B. *Int. J. Mass Spectrom. Ion Processes* **1984**, *61*, 3113–3122.
(37) Naylor, S.; Findeis, F. A.; Gibson, B. A.; Williams, D. H. *J. Am. Chem. Soc.* **1986**, *108*, 6359–6362.
(38) Bodor, N.; Kaminski, J. J. *J. Mol. Struct.* **1988**, *163*, 315–330.
(39) Bodor, N.; Brewster, M. E.; Kaminski, J. J. *J. Am. Chem. Soc.*, in press.
(40) Bodor, N.; Brewster, M. E.; Kaminski, J. J. *Tetrahedron* **1988**, *44*, 7601–7610.
(41) Cooks, R. G.; Busch, K. L. *Int. J. Mass Spectrom. Ion Phys.* **1983**, *53*, 111–124.

RECEIVED for review October 28, 1988. Accepted May 8, 1989. This work was supported by NIH Grant GM-27167 and presented in part at the 36th Annual Conference on Mass Spectrometry and Allied Topics, San Francisco, CA, June 5–10, 1988.

Potentiometric Homogeneous Enzyme-Linked Competitive Binding Assays Using Adenosine Deaminase as the Label

Thea L. Kjellström and Leonidas G. Bachas*

Department of Chemistry, University of Kentucky, Lexington, Kentucky 40506-0055

Homogeneous enzyme-linked competitive binding assays for biotin are described that are based on the competition between an enzyme–biotin conjugate and free biotin for a fixed number of binding sites of avidin. Unlike conventional homogeneous enzyme immunoassays, in this system the analyte (biotin) is labeled with adenosine deaminase (ADA), an ammonia-producing enzyme. Consequently, potentiometric rather than photometric methods can be used as means of detection. Several ADA–biotin conjugates were prepared and showed as high as 97% inhibition of the enzymatic activity in the presence of avidin. Addition of free biotin reverses this inhibition in an amount proportional to the concentration of analyte. Relatively steep dose–response curves were observed, leading to a precise and accurate assay for biotin. The detection limits of these curves were as low as 1×10^{-8} M. Varying the concentration of the reagents in the assay allowed the detection limit and working range to be altered to a desired value. The proposed method was applied in the determination of biotin in a horse-feed supplement.

INTRODUCTION

Conventional homogeneous enzyme immunoassays are based on the EMIT (enzyme-multiplied immunoassay technique) principle (*1*). In these assays, a ligand-specific antibody binds to an enzyme-labeled ligand (conjugate), modifying its enzymatic activity. Unlabeled ligand reduces the antibody-induced modulation of the enzymatic activity by competing for the specific binder and, therefore, leaving the enzyme-labeled ligand free to react with the substrate(s) (*2–4*). In the commercial EMIT assays the enzyme label used is a dehydrogenase (glucose-6-phosphate dehydrogenase or malate dehydrogenase), and the enzymatic activity is monitored by photometric detection of NADH at 340 nm.

An inherent limitation of assays based on photometric detection is the background absorbance due to the color and turbidity of physiological fluids. A detection system based on a potentiometric rather than a photometric principle circumvents the necessity of sample dilution required to reduce the background absorbance and, therefore, should result in assays with better detection limits.

Although several reports describe the use of electrochemical means of detection in homogeneous enzyme immunoassays (EIAs) (*5*), there is only limited information available concerning the use of ion-selective electrodes to measure enzyme activity in such assays. A homogeneous EIA using a carbon dioxide gas sensor to monitor the inhibition of chloroperoxidase conjugated to IgG by an anti-IgG antibody was reported by Fonong and Rechnitz (*6*). This assay, however, was for a high molecular weight biomolecule. In another EIA, potentiometry was used to monitor the lysis of *Micrococcus lysodeikticus* cells loaded with trimethylphenylammonium ions by a lysozyme–biotin conjugate (*7*). Although quite elegant, this assay showed limited sensitivity; a total change in the signal of approximately 1.5 mV/min was obtained for a change in the concentration of biotin by 3 orders of magnitude.

This report describes a homogeneous competitive binding assay for biotin based on the enzyme adenosine deaminase (ADA) and the strong and specific biotin–avidin interaction. In particular, binding of avidin to an ADA–biotin conjugate reduces the ability of the latter to deaminate adenosine. The competition between biotin in the sample and the ADA-labeled biotin for the avidin controls the enzymatic activity. The ammonia produced can be measured potentiometrically and can be directly related to the activity of the enzyme. Through dose–response curves the production of ammonia can also be related to the amount of biotin in the sample. These curves are extremely steep and therefore provide the basis for a highly sensitive assay for biotin.

It should be mentioned that ADA has been proposed as an enzyme suitable for heterogeneous EIAs (*8, 9*). However, this is the first report of using this enzyme for the development of homogeneous assays. Other heterogeneous electrode-based EIAs have been reviewed recently by Monroe (*10*).

EXPERIMENTAL SECTION

Apparatus. For the static system studies, an Orion ammonia gas-sensing electrode (Model 95-12) was used. Voltages were measured with an Accumet pH/mV meter, Model 825 MP (Fisher

0003-2700/89/0361-1728$01.50/0

Scientific, Cincinnati, OH), interfaced with an Alphacom 1842 printer (Fisher).

The automated ammonia detection system was set up according to the specifications of Fraticelli and Meyerhoff (*11*). The gas dialysis unit consisted of two matched dialysis plates fitted with a GORE-TEX poly(tetrafluoroethylene) gas-permeable membrane (0.2-μm pore size) (W. L. Gore and Associates, Elkton, MD) (*12*). The flow-through electrode unit was constructed with a poly(vinyl chloride) ammonium-selective membrane using nonactin as the ionophore (*11*). Enzymatic activity was measured potentiometrically with the pH/mV meter and recorded on a Fisher Recordall Series 5000 strip-chart recorder.

Reagents. Poly(vinyl chloride), tetrahydrofuran, and dibutyl sebacate were from Polysciences, Inc. (Warrington, PA), Fisher, and Sigma Chemical Co. (St. Louis, MO), respectively. *N*-Hydroxysuccinimidobiotin (NHS-biotin), ADA from calf intestinal mucosa, bovine serum albumin (BSA), and all other chemicals were purchased from Sigma. Deionized distilled water was used to prepare all solutions.

Standard NH_4^+ solutions ranging from 1.00×10^{-2} to 1.00×10^{-6} M were prepared from reagent grade ammonium chloride for the calibration of the detection systems. Calibration of the Orion electrode was performed in a 0.0100 M Tris-HCl buffer, pH 8.5; a 0.100 M citrate buffer, pH 5.5, was used to recondition the electrode (*13*) between measurements. The buffers prepared for the flowing internal electrolyte stream and the sample diluent stream of the automated system were 0.0100 M Tris-HCl, pH 7.5 and 8.5, respectively. The protein buffer consisted of 0.10% (w/v) protein (dialyzed gelatin or BSA) in assay buffer (0.0100 M Tris-sulfate containing 6.5×10^{-5} M ethylenediaminetetraacetic acid (EDTA)). Both the assay and protein buffers were at either pH 8.5 (static system) or pH 7.4 (automated system). Substrate solutions were prepared by dissolving adenosine in the respective assay buffer for each system. All avidin and conjugate dilutions were made with protein buffer.

Preparation and Evaluation of ADA–Biotin Conjugates. Adenosine deaminase was dialyzed in a 0.100 M sodium bicarbonate buffer, pH 8.2. Inosine was added to the enzyme solution in 3000-fold excess to protect the active site during conjugation. For each conjugation, 50 units of enzyme (at 4 °C) was used and enough volume of a NHS-biotin solution (10 mg of NHS-biotin in 1.0 mL of methyl sulfoxide) was added in aliquots to produce various biotin:enzyme ratios in the reaction mixture. Following dialysis against the assay buffer (pH 7.4), each conjugate was diluted to 2.0 mL with the assay buffer.

The ADA–biotin conjugates were characterized with respect to enzymatic activity and inhibition by using the automated system. A volume of 100 μL of the appropriate conjugate was combined with either 200 μL of the protein buffer (activity) or 100 μL each of the protein buffer and avidin (inhibition). The mixture was incubated for 20 min prior to the addition of 1.00 mL of 4.4×10^{-3} M adenosine. The amount of ammonia produced was measured in order to determine the activity and inhibition of the conjugates.

Static System. A pH-dependence study was performed to determine the optimum pH at which the system as a whole (ADA–biotin conjugate coupled with the ammonia gas sensor) produced a maximum change in the millivolt signal. Tris-HCl buffers were used for the pH range 7.5–9.0, and carbonate buffers were used for the pH range 9.5–10.0.

To determine the effect of varying the incubation time, avidin (100 μL) was incubated for various time intervals with specific dilutions of the ADA–biotin conjugate (100 μL) and of the protein buffer (100 μL) in 2.60 mL of assay buffer. Adenosine (200 μL of a 1.6×10^{-2} M solution) was added to the assay beaker, and after the appropriate incubation time, the ammonia produced was monitored for 5 min at 30-s intervals.

A binder dilution curve was generated in order to determine the optimum binder concentration in the assay. One hundred microliters of different concentrations of avidin, 100 μL of ADA–biotin conjugate, 100 μL of protein buffer, and 2.60 mL of assay buffer were incubated together for 15 min; this time was also sufficient for the gas sensor to reach a stable base line. Then, 200 μL of 1.6×10^{-2} M adenosine was added to the assay beaker, and the activity was measured as described above. The percent inhibition was calculated on the basis of the amount of ammonia produced in the presence of avidin relative to that amount produced in the absence of the binder.

Dose–response curves were generated by using the same protocol as that described for the binder dilution study; however, a constant avidin concentration was maintained and 100 μL of the protein buffer was replaced with 100 μL of biotin standards. The percent inhibition was plotted against the logarithm of the concentration of biotin in the standards.

Automated System. To investigate the association kinetics between the conjugate and the binder, 100 μL of an avidin solution (0.5 μg of avidin/mL) was incubated with 100 μL each of the ADA–biotin conjugate (1:200 dilution) and the protein buffer for set time intervals. After each incubation period, 1.00 mL of 6.5×10^{-3} M adenosine was added and allowed to react for 15 min before stopping the reaction with 0.010 M silver nitrate. The ammonia produced was measured, and the percent inhibition was calculated and plotted against the incubation time.

The effect of changing the amount of avidin on the percent inhibition of the conjugate was studied by incubating 100 μL each of the ADA–biotin conjugate (1:200 dilution) and protein buffer and varying amounts of avidin. One thousand microliters of 6.5×10^{-3} M adenosine was added after a 20-min incubation period. The enzymatic activity was measured, and a binder dilution curve was constructed by plotting percent inhibition vs the amount of avidin used in each assay.

The dose–response characteristics of the assay were studied by incubating a range of biotin standards with the ADA–biotin conjugate and avidin. One hundred microliters each of the conjugate, avidin, and biotin standard was incubated for 20 min prior to the addition of 1.00 mL of 6.5×10^{-3} M adenosine. Dose–response curves were prepared by plotting percent inhibition vs the logarithm of the biotin concentration in the standards.

Feed Supplement Analysis. Biotin was extracted from a weighed sample (around 0.10 g) of a horse-feed supplement (Better Hoof from Horse Health Products, Louisville, KY) with 10.0 mL of 1.0 M NaOH. The pH of a 6.00-mL aliquot of this solution was adjusted to between 7 and 8. This solution was further diluted to 10.0 mL with the pH 7.4 assay buffer. The samples for the recovery studies were spiked with a known amount of biotin before extraction. Further dilutions of the supplement preparations and the spiked samples were made with the protein buffer, pH 7.4, so that they fit within the linear portion of the dose–response curve. The protocol for the analysis was that described for the dose–response study using the automated system.

RESULTS AND DISCUSSION

Development of a precise and sensitive homogeneous enzyme-based competitive binding assay is dependent on the use of an enzyme–ligand conjugate that possesses high enzymatic activity and can be inhibited to a great extent. Several conjugates of ADA were prepared from the *N*-hydroxysuccinimide derivative of biotin (*14*), while the active site of the enzyme was protected by an excess of inosine. Such protection minimized the possibility of biotin attachment to lysines at the active site of the enzyme, which may result in a loss of enzymatic activity (*15*).

In order to choose the best conjugate for the homogeneous competitive binding assay, each conjugate was evaluated with respect to percent inhibition, enzymatic activity, and percent residual activity (Table I). As expected, the least conjugated enzyme exhibited the greatest residual activity, 67%. Moreover, the residual activity of the conjugates decreased as the initial biotin:enzyme ratio increased. Contrary, increasing the initial biotin:enzyme ratio led to conjugates whose enzymatic activity can be inhibited by as much as 97% in the presence of avidin. Both of these observations may be attributed to a higher degree of conjugation (i.e., more biotins attached per enzyme molecule) when a higher initial biotin:enzyme ratio was used. Conjugate ADB4, with a 500:1 initial mole ratio of biotin:ADA, showed 31% residual activity and 90% inhibition and was used for the remaining studies.

Although ADA has been used in heterogeneous EIAs (*8*, *9*), this is the first time that a conjugate of this enzyme has

Table I. Characterization of the ADA–Biotin Conjugates

conjugate	initial biotin: enzyme ratio	enzymatic activity,[a] mU	residual activity,[b] %	inhibition,[c] %
ADB1	50:1	4.2	67	28
ADB2	100:1	4.0	64	58
ADB3	200:1	3.2	51	72
ADB4	500:1	1.9	31	90
ADB5	800:1	1.5	25	97

[a] Milliunits, mU, refer to the enzymatic activity of 100 μL of ADA–biotin conjugate. (Unit definition: One unit of ADA deaminates 1.0 μmol of adenosine per minute at pH 7.4.) [b] Percent residual activity was calculated by comparing the activities of the conjugates to the initial activity of the unconjugated enzyme. [c] Percent inhibition was determined by using 1:400 dilutions of the conjugates and an excess of avidin (20 μg). The incubation time was 20 min, in a total volume of 300 μL, after which 1.0 mL of 4.4 × 10^{-3} M adenosine was added. The ammonia produced was monitored with an autoanalyzer system based on a flow-through ammonium-selective electrode.

exhibited a reasonable degree of inhibition. Indeed, attempts to inhibit ADA, highly conjugated with adenosine 3′,5′-monophosphate (cyclic AMP), by an anticyclic AMP antibody were unsuccessful (*16*). Similarly, ADA–folate conjugates were inhibited by less than 10% in the presence of folate binding protein (*17*). A model is proposed here to explain all of the above observations. This model is based on the effect of the depth of the binding site of the various binders on enzyme inhibition. On the basis of electron microscopy studies, it has been reported that upon binding, the carboxylic group of biotin is buried about 9 Å below the surface of avidin (*18*). This distance is approximately 1.5 Å longer than the link provided by the side chain of lysine on the ADA–biotin conjugate. This allows for the avidin to reach the polypeptide backbone of the conjugate, thus forcing a change in the conformation of the enzyme. In comparison with avidin, antibodies have shallower binding pockets (*18*) and therefore are incapable of reaching the surface of the enzyme.

It should be mentioned that conjugates of glucose 6-phosphate dehydrogenase (G6PDH) with either biotin (*14*) or folate (*19*) can be inhibited up to 100% and 70%, respectively, in the presence of their corresponding binding proteins. Similarly, conjugates of this enzyme with other ligands such as therapeutic drugs, drugs of abuse, and hormones can be inhibited in the presence of ligand-specific binders (*20*). Therefore, it appears that it is easier to inhibit conjugates of G6PDH than of ADA. One possible reason for this is that unlike ADA, which needs only one substrate (adenosine), dehydrogenases catalyze redox reactions and require the presence of two substrates. This, along with the fact that NAD is larger than adenosine, implies that the region of the enzyme responsible for substrate recognition is larger in the case of G6PDH and thus more likely to be affected by the binder.

It is customary to include a high concentration of a nonreactive protein in the assay mixtures to prevent nonspecific binding of the biomolecules to the walls of the assay container (*21*). Gelatin was chosen in our initial experiments; however, due to its high ammonia content, it was necessary to dialyze this protein against the assay buffer before use. It was later found that BSA was a more suitable buffer protein. The ammonia background signal due to the BSA buffer was appreciably less, thus eliminating the preassay dialysis step. It was also found that the nature of the protein itself had no effect on the response characteristics of the assay.

In this study, two different types of detection systems were used to measure enzymatic activity. In our initial studies, an Orion ammonia gas-sensing electrode was employed. The

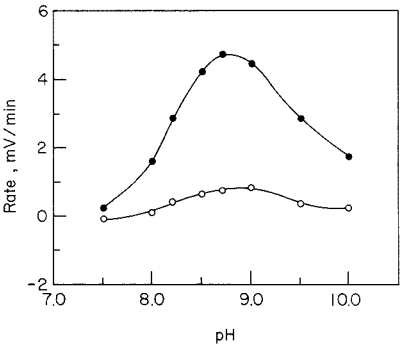

Figure 1. Effect of pH on the enzymatic activity of ADB4 in the absence (●) and presence (○) of 1 μg of avidin. The *y* axis refers to the change in potential per minute due to the production of ammonia. Data points are means of duplicate measurements.

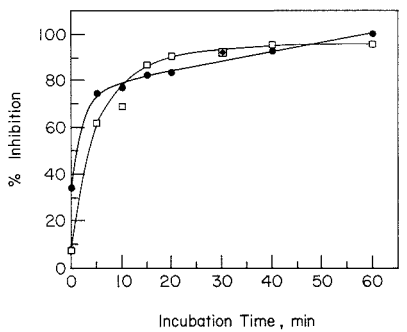

Figure 2. Effect of varying the incubation time between the conjugate and avidin on percent inhibition: (□) 100 μL of a 1:100 dilution of ADB4 and 1 μg of avidin (static system); (●) 100 μL of a 1:200 dilution of ADB4 and 0.5 μg of avidin (automated system). Values shown are averages of duplicate measurements.

optimum pH for ADA is 7.4; however, the Orion electrode has an optimal response at pH 9.5 (*9*). Therefore, in order to find the best conditions for our experiments, it was necessary to evaluate the electrode signal produced as a function of pH. Figure 1 shows the results both in the absence (activity) and presence (inhibition) of avidin. From these data, the optimum pH was determined to be around 8.5. At this pH the electrode detected the greatest difference in the enzymatic rate between the activity and inhibition of the ADA–biotin conjugate. Therefore, controlling the pH at 8.5 should result in more precise assays with better detection limits. A maximum inhibition of 84% was attained in the presence of avidin (the avidin and conjugate were incubated for 15 min). Although a conjugated enzyme (ADB4) was used in these studies, the optimum pH was similar to that reported in an earlier study using unmodified adenosine deaminase with the same detection system (*9*).

To evaluate the association kinetics between the conjugate and avidin, a study was undertaken in which the incubation time was varied (Figure 2). A steep rise in percent inhibition was observed; after an incubation period of 5 min the conjugate was already inhibited by 60%. For the studies based on the ammonia gas sensor, a 15-min incubation period was selected that corresponded to 87% inhibition.

Following optimization of the pH and the incubation time, the effect of changing the amount of avidin on the inhibition of a constant amount of ADB4 was evaluated. As shown in

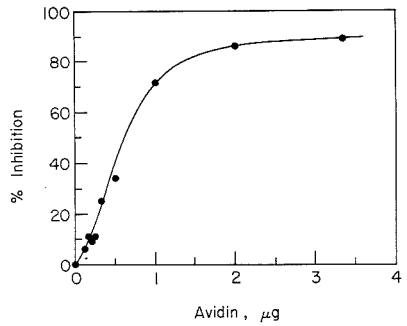

Figure 3. Effect of varying the levels of avidin (micrograms of avidin in the assay mixture) on the inhibition of a 1:100 dilution of ADB4 (static system). Means of duplicate measurements were plotted.

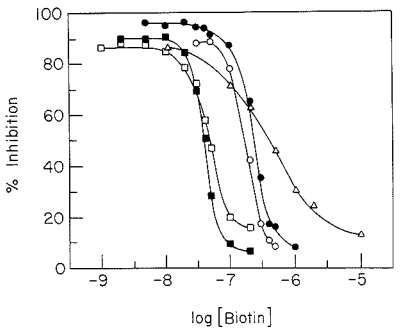

Figure 4. Dose–response curves for biotin: (△) 1:100 dilution of ADB4 in the presence of 1 μg of avidin (static system); (○) 1:200 dilution of ADB4 in the presence of 0.5 μg of avidin (automated system); (□) 1:200 dilution of ADB4 in the presence of 0.25 μg of avidin (automated system); (●) 1:400 dilution of ADB4 in the presence of 0.5 μg of avidin (automated system); (■) 1:400 dilution of ADB4 in the presence of 0.25 μg of avidin (automated system). The *x* axis refers to the molarity of the biotin standards. Curves were generated by plotting means of duplicate measurements.

Figure 3, as the amount of binder increases, the inhibition increases. The least amount of binder that produces a measurable inhibition is around 0.1 μg (equivalent to 1.5×10^{-8} M), which indicates that this method can be used for the sensitive determination of avidin. Further, this curve is useful for the selection of the appropriate concentration of avidin for the biotin assay. Typically, the amount of binder that corresponds to approximately 85% of the maximum inhibition is chosen in order to obtain dose–response curves with the best detection capabilities (*19*, *20*). As shown in Figure 3, 2 μg of avidin produced an inhibition of 86%; however, 1 μg of avidin resulted in an inhibition of 71% and was used for the dose–response studies.

For the latter, free biotin was incubated along with ADB4 and avidin in a single incubation mode of analysis (*22*) before addition of the substrate. Dose–response curves were obtained that related the concentration of biotin in standards to the inhibition of the enzyme–ligand conjugate (Figure 4). The ED_{50} value (effective dose at 50% of maximum response) of this curve is 4×10^{-7} M.

Unfortunately, the use of the commercial gas sensor limits the number of samples that can be analyzed to about three per hour. To circumvent this limitation, an automated gas-sensing detection system was used. The purpose of our initial study with this system was to evaluate the effect of varying the incubation time between avidin and ADB4 (Figure 2). The steepness of the slope between zero and 15 min of incubation time emphasizes the quick response capability of this assay. A value of 75% inhibition was observed at an incubation time as short as 5 min. For the remainder of the studies an incubation period of 20 min, corresponding to 85% inhibition, was chosen.

A binder dilution curve for a 1:200 dilution of ADB4 was then constructed to determine an appropriate amount of avidin to use for the dose–response studies (results not shown). Binder concentrations in the range of 0.25–0.50 μg provided sufficient inhibition of the enzymatic activity and were used to produce a family of dose–response curves (Figure 4). Typically, these curves were steep, which indicates the capability of these assays for the precise and accurate determination of biotin. The steepness of the curves is consistent with theoretial predictions of the response of enzyme immunoassays in cases where the affinity constant of the binder for the free ligand is higher than that for the conjugate (*23*).

Optimization of these assays was undertaken by varying the concentrations of the ADA–biotin conjugate and avidin. Altering these parameters resulted in detection limits as low as 1×10^{-8} M biotin. As evidenced from Figure 4, when the avidin concentration is halved, the resulting curves are shifted to better detection limits by almost an entire decade. Further, at least for the concentrations of binder tested, essentially no effect was observed on the detection limits due to changes in the concentration of ADB4.

In comparison with the automated system, the dose–response curves obtained with the static system (Figure 4) were not as steep since the concentration of the reactants (i.e., conjugate and avidin) was much lower than those used in the automated system. Therefore, the latter system is more sensitive and should result in more precise assays. To quantitate the precision of the assay for biotin using the automated system, the assay was repeated five times with four different biotin concentrations that fall in the steep portion of the curve. The coefficient of variation (CV) for each of the biotin concentrations was calculated, and the average CV was found to be 3.1%.

In order to demonstrate the general applicability of the assay, real sample studies were performed. Biotin is an essential vitamin for both humans and animals, acting as a coenzyme in carboxylation reactions involving ATP (*24*). Horses, for example, need biotin to promote good hoof growth and a healthy coat. Comben et al. have demonstrated through case studies the need for biotin supplementation in a horse's diet, particularly those with badly damaged feet. They claimed that the amount of biotin necessary to sufficiently treat unhealthy hooves is 15 mg/day (*25*).

Horse-feed supplements containing biotin can be purchased from a number of manufacturers. By use of the assay system developed, the amount of biotin in one such feed supplement was determined. Besides biotin, this sample also contained dextrose, gelatin, dried brewer's yeast, calcium phosphate, zinc sulfate, DL-methionine, L-lysine, pyridoxine-HCl, and potassium sorbate. The estimated amount of biotin found was 19% more than that claimed by the manufacturer. Recovery studies were also performed, and the quantities of biotin used to spike the samples before extraction, 48.9 and 24.4 μg, were recovered at 100% and 88%, respectively. These recoveries imply the absence of matrix effects in these determinations.

In conclusion, adenosine deaminase, an ammonia-producing enzyme, was used to develop a homogeneous competitive binding assay for biotin. Steep dose–response curves were observed. By varying the concentrations of the assay reagents, one can adjust the steep portion of the dose–response curve to a desired value over a wide range of biotin concentrations. Finally, the approach presented in this report results in an

essay that allows for potentiometric rather than photometric detection schemes and, therefore, should be advantageous for the determination of blood in turbid and colored samples.

ACKNOWLEDGMENT

nation of the gas permeable membrane.

Registry No. ADA, 9026-93-1; biotin, 58-85-5.

LITERATURE CITED

(1) Ngo, T. T.; Lenhoff, H. M. *Appl. Biochem. Biotechnol.* **1981**, *6*,
(2) Rowley, G. L.; Rubenstein, K. E.; Hulsjen, J.; Ullman, E. F. *J. Biol.*
(3) Ullman, E. F.; Maggio, E. T. In *Enzyme-Immunoassay*; Maggio, E. T.,
(4) Ullman, E. F.; Yoshida, R. A.; Blakemore, J. J.; Maggio, E. T.; Leute, R.
(5) Rehleman, W. R.; Halsall, H. B.; Wehmeyer, K. R.; Doyle, M. J.;
(6) Fortney, T.; Rechnitz, G. A. *Anal. Chem.* **1984**, *56*, 2386–2390.
(7) Gebauer, C. R.; Rechnitz, G. A. *Anal. Biochem.* **1982**, *124*, 330–340.
(10) Monroe, D. *Ann. Biotechnol. Lab.* **1988**, *4*, 28–33.
(11) Freticelli, Y. M.; Meyerhoff, M. E. *Anal. Chem.* **1984**, *56*, 992–997.
(12) Martin, G. S.; Meyerhoff, M. E. *Anal. Chim. Acta* **1986**, *180*, 71–80.
(13) Keeley, D. F.; Walters, F. H. *Anal. Lett.* **1983**, *16*, 1591–1594.
(14) Dewald, S.; Bachas, L. G.; Meyerhoff, M. E. *Anal. Chim. Acta* **1988**, *206*, 45–52.
(15) Lupacchini, A.; Bordelini, A. D.; Ponce, G.; Sognini, D.; Rossi, C. A. *Biochim. Biophys. Acta* **1975**, *385*, 220–227.
(16) Brostrom, S. P. Ph.D. Thesis, University of Michigan, 1984.
(17) Bachas, L. G., University of Michigan, unpublished results, 1986.
(18) [illegible] 1971, *125*, 181–191.
(20) Kabakoff, D. S.; Greenwood, H. M. In *Recent Advances in Clinical* [illegible] 1981; pp 1–30.
(21) [illegible] *130*, 129–135.
(23) Bachas, L. G.; Meyerhoff, M. E. *Anal. Biochem.* **1986**, *156*, 223–230.
(24) Harris, D. C.; Quilty, B.; Langer, P. W. In *The Veterinary Consult*
H., Jr., Harris, R. S., Eds.; Academic: New York, 1966; Vol. II, pp 961–980.
(25) Corbeil, R.; Clark, R. J.; Sutherland, D. J. B. Presented at the Annual Congress of The British Equine Veterinary Association, University of New York, September 5, 1985.

1989. This research was supported by grants from the American Association for Clinical Chemistry (research and En-

(Grant No. R29 GM 40510).

Quantification of Recombinant Interleukin-2 in Human Serum by a Specific Immunobioassay

[illegible]

A sensitive and specific assay for recombinant interleukin-2 (rIL-2) in human serum is described. The assay is based on plate coated with anti-rIL-2 monoclonal antibody (specific for recombinant human IL-2) to capture rIL-2 from serum, and an IL-2 dependent T cell line that proliferates in a dose dependent manner to rIL-2. The assay is 2 units/mL (1 unit = ~50 pg) using 0.1 mL of serum and the calibration curves ranged from 2 to 50 units/mL. Data are presented on the assay specificity, the stability of rIL-2 in serum, and the recovery of rIL-2 from serum. We also report on the use of the procedure to assay clinical samples from patients with [illegible]

INTRODUCTION

Interleukin-2 (IL-2), first described as T-cell growth factor (*1*), is a glycoprotein (15.5 kDa) of 133 amino acids with a [illegible] IL-2 is a lymphokine produced and secreted by T-cells when they are activated with either an antigen or mitogen (*3*). It [illegible] and differentiation of many types of effector cells (*4*).

Recently, attention has focused on the clinical potential of [illegible] clinical as well as clinical studies with IL-2 became possible only after the structural characterization and expression of a cloned gene for human IL-2 in *E. coli* allowed for the [illegible] manufactured IL-2 (recombinant IL-2, rIL-2), differs from the [illegible]

This paper describes an assay for rIL-2 in the serum of patients undergoing treatment with the protein. The assay [illegible] to establish the optimum dosing regimen for the drug and to establish a relationship between serum concentrations of rIL-2 [illegible] of rIL-2 to regulate the proliferation of IL-2 dependent mouse CTLL-2 cells (*7*). It uses a modification of the hybrid assay [illegible] antibody method because we are required to measure the concentration of teceleukin (Roche recombinant IL-2) in serum in patients receiving various concomitant medications. [illegible] the recombinant product as determined by Western blot and by demonstrating that pure glycosylated IL-2 does not bind [illegible] for IL-2 (*2, 6*) in that it utilizes several calibration standards to construct a calibration curve, allows for the direct addition of rIL-2 from potentially interfering compounds, and includes a significant degree of validation.

EXPERIMENTAL SECTION

[illegible] provide aseptic conditions. Cells were maintained in a water jacketed incubator (Forma Scientific Model 3157). Cell counts [illegible] contrast microscope (Nikon). Pipeting into microtiter plates and the washing of plates was done with a Titertek liquid-handling [illegible]

centrifuge (Sorvall, RC-3) was used to pellet cells. A Titertek Multiskan MCC/340 microtiter plate reader (Flow Laboratories, Inc.) was the spectrophotometer used to determine optical densities. A Mini-Orbital shaker (Bellco, Inc.) was used to agitate plates during the affinity isolation step. Corning 96-well tissue culture plates were bound with monoclonal antibody (mAb) and were used in the cell proliferation step. Corning tissue culture flasks (Corning Glass Works) were used to culture CTLL-2 cells. Corning 25942 disposable sterile filter systems (0.22 μm) were used to sterilize the coating buffer, the blocking buffer, and the human AB serum. Falcon Model 2098 graduated conical tubes (50 mL; Becton-Dickinson Laboratories) were used to hold culture supernatant and cells. Immulon-2 flat bottom plates (Dynatech Corp.) were used in the colorimetric determination step. Nunc cryotubes and Sarstedt tubes were used to store frozen calibration standard and quality assurance samples. Radiometric measurements were made with a Model LS-3801 scintillation counter (Beckman Instruments) or a Micromedic Model 28023 gamma counter (Micromedic Systems, Inc.).

Chemicals. $NaH_2PO_4 \cdot H_2O$, $Na_2HPO_4 \cdot 7H_2O$, and NaCl were purchased from Fisher Scientific and were used to make the phosphate buffered saline (PBS). Trizma HCl and Trizma base (reagent grade) were purchased from Sigma Chemical Co. and were used to make the coating buffer. HCl (J. T. Baker Chemical) was used to stop the colorimetric reaction in the lactic acid assay. Glycine buffer, INT (P-iodonitrotetrazolium violet) solution (grade 1), phenazine methosulfate (PMS), β-diphosphopyridine nucleotide (NAD), and lactate dehydrogenase were purchased from Sigma Chemical Co. for use in the lactic acid assay. Hepes buffer (1 M solution), L-glutamine (200 mM), gentamicin sulfate (50 mg/mL), minimal essential medium (MEM), sodium pyruvate and penicillin–streptomycin solution (penicillin 10 000 units/mL and streptomycin 10 000 μg/mL) were obtained from Gibco Laboratories. [^{125}I]-rIL-2 was purchased from New England Nuclear. [^{14}C(U)]-rIL-2 was a gift of R. Crowl (Hoffmann-La Roche, Inc.).

Biologicals. Human IgG (Miles Scientific) and bovine serum albumin (BSA, Sigma Chemical Co.) were used in the blocking buffer. Monoclonal antibodies (5B1 and C-MYC) were gifts of R. Chizzonite (Hoffmann-La Roche, Inc.). The 5B1 monoclonal has an affinity of 1.2×10^9 m^{-1} and is of the IgG$_1$ isotype. The C-MYC monoclonal antibody recognizes amino acid sequence 305–317 of the human C-MYC oncogene protein. The rIL-2 used to prepare the calibration standards and for cell maintenance was provided by the Quality Control Department, Hoffmann-La Roche, Inc. One unit (U) of rIL-2 equals approximately 50 pg of protein. Gelatin, type 1 (approximately 300 bloom from porcine skin), was purchased from Sigma Chemical for use in the blocking buffer. Human serum type AB (Gibco Laboratories) was used to reconstitute the rIL-2 standards. HB101 and HB101 supplement (Du Pont, Inc.) were used to culture the CTLL-2 cell line (American Type Tissue Culture).

Solutions. A vial containing 1000 units of rIL-2 was reconstituted to 500 units/mL with 2 mL of human AB serum, and calibration standards of 2, 5, 10, 20, 25, and 50 units/mL were prepared by diluting with the appropriate amount of human AB serum. A quality assurance pool was made by combining samples from individuals receiving rIL-2.

Serum-free medium was prepared by removing 33.0 mL of medium from a 500-mL bottle of HB101 to which was added 5 mL of 200 mM glutamine, 5 mL of 100 mM sodium pyruvate, 12.5 mL of Hepes buffer, 0.5 mL of gentamicin sulfate (50 mg/mL), 5 mL of penicillin–streptomycin (10 000 units/mL, 10 000 μg/mL), and 5 mL of HB101 supplement which had been reconstituted with 10 mL of sterile distilled water. Monoclonal antibody (mAb) was diluted in coating buffer to give a final concentration of 1 μg/mL. Monobasic phosphate buffered saline (25 mM) was prepared with 3.45 g of $NaH_2PO_4 \cdot H_2O$ and 8.77 g of NaCl in 1 L of distilled H_2O. The dibasic phosphate solution (25 mM) contained 6.7 g of $Na_2HPO_4 \cdot 7H_2O$ and 8.77 g of NaCl in 1 L of distilled H_2O. The dibasic phosphate buffer solution was titrated with the monobasic phosphate buffer solution to pH 7.4, autoclaved to sterilize, and stored at room temperature. Coating buffer for the bioassay was prepared by titrating a solution of 50 mM Trizma HCl and 150 mM NaCl with a solution of 50 mM Trizma base and 150 mM NaCl to pH 4.8, sterilizing the solution by filtration, and storing it at 4 °C. The blocking buffer was prepared by combining 10 g of BSA with 3 g of gelatin dissolved in 1 L of 25 mM PBS (pH 7.4) and was sterilized by filtration. Human IgG (160 mg) was then added aseptically and the final solution stored at 4 °C. The following solutions were used in the colorimetric determination of lactic acid. Glycine buffer–NAD solution was prepared with 50 mg of NAD, 10 mL of glycine buffer, 1 mL of 1% gelatin, and 20 mL of sterile distilled H_2O. The PMS solution was prepared by dissolving 1 mg of phenazine methosulfate in 5 mL of sterile distilled H_2O. The tetrazolium violet solution was prepared immediately prior to use with 10 mL of INT solution, 2.0 mL of phenazine methosulfate solution, and 0.2 mL of lactate dehydrogenase. A 0.35 M HCl solution was used to stop the colorimetric reaction.

Scheme I. Diagram of the Steps in the IL-2 Immunobioassay[a]

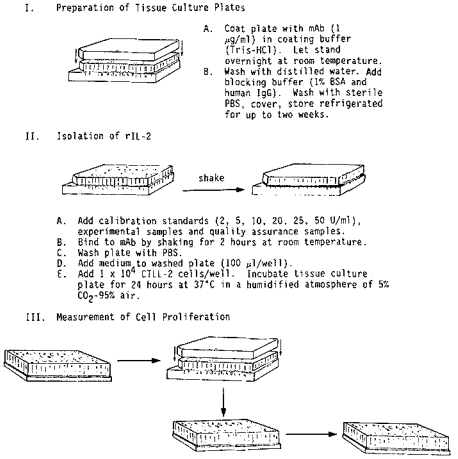

[a] Key: mAb = monoclonal antibody 5B1; BSA = bovine serum albumin; IgG = immunoglobulin G; PBS = phosphate buffered saline; CTLL-2 = cytotoxic T cells derived from a C57B1/6 mouse; NAD = B-diphosphopyridine nucleotide; INT = P-iodonitrotetrazolium violet.

Procedure (Scheme I). Anti-rIL-2 mAb bound tissue culture plates were prepared by coating plates with a fresh solution of 1 μg/mL of mAb in coating buffer (omitting mAb from one column on the plate to serve as a specificity control). Coating buffer (100 μL/well) was added, the plate lids were replaced, and the plates were incubated overnight at room temperature. The following day, the plates were washed 4 times with 400 μL/well of sterile distilled water (Pro/Pette wash cycle). Blocking buffer (100 μL/well) was then added, the plate lids were replaced, and the plates were incubated a minimum of 15 min at 37 °C. The plates were then washed with 400 μL/well of sterile PBS (Pro/Pette wash cycle). The lids were replaced, and the plates were stored at 4 °C for up to 2 weeks.

Recombinant IL-2 was isolated from serum by using the mAb bound capture plates in the following manner. Monoclonal bound tissue culture plates, calibration standards, quality assurance samples, and experimental samples were warmed to 37 °C for 15 min. One hundred microliters of calibration standards (2, 5, 10, 20, 25, and 50 units/mL of rIL-2) were added in triplicate utilizing one set of these standards in the column without mAb as the specificity control. Normal human AB serum (drug-free blank),

quality assurance samples, and experimental samples were also added to the plates. Covered plates were shaken on an orbital shaker at room temperature for 2 h, washed 4 times with 400 μL/well of sterile PBS, and HB101 medium (100 μL/well) was added.

The isolated rIL-2 was then incubated with 100 μL/well of CTLL-2 cells ((1×10^5)/mL) previously washed 3 times in HB101, and viability counted (trypan blue dye exclusion). Cells were used in the assay only when viability exceeded 95%. Plates were covered and incubated for 24 h in an humidified atmosphere of 5% CO_2–95% air at 37 °C.

Cell proliferation in response to isolated rIL-2 in experimental samples and calibration standards was measured by an assay for lactic acid (8). NAD solution (50 μL/well) was added to Dynatech Immulon plates. Cell supernatant from the sample plate (15 μL/well) was transferred to the plate with the NAD solution. The tetrazolium dye solution (50 μL/well) was added, and was allowed to develop for exactly 10 min after which HCl was added to stop the reaction, and the plates were read with a microplate reader at 550 nm.

^{3}H-TdR Method. The procedure was the same as that described above with the following additions. After the cells were incubated at 37 °C for 18 h in an atmosphere of 5% CO_2–95% air, 0.5 μCi of ^{3}H-TdR (25 Ci/mmol) was added to each well for the last 6 h. Then, after 15 μL of supernatant was taken for the colorimetric assay, the cells were harvested on glass filters, and the ^{3}H-TdR incorporated was measured.

Calculations. After the mean optical densities for the lactic acid determinations were calculated, the nonlinear calibration curve was analyzed by use of the computer program NONLIN (9). Calibration curves were generated by fitting the mean optical density (Y) and the concentration (X) of rIL-2 (in units/mL added to control serum) to a weighted ($1/Y$) nonlinear equation $X = (YC - A)/(1 - YB)$, where A, B, and C are constants generated by the nonlinear least-squares program.

Stability Experiments. Bench-top stability was determined by comparing the concentration of samples allowed to stand at room temperature for 0, 3, 6, and 22 h. The long-term stability at −20 °C was determined by duplicate determinations of the same quality assurance pool over a period of 6 months.

Clinical Samples. Serum samples were obtained from three patients administered a 30-min infusion of rIL-2. All patients had Acquired Immunodeficiency Syndrome (AIDS) with documented deficits in cell mediated immunity and all had recovered from at least one opportunistic infection.

RESULTS AND DISCUSSION

IL-2 Dependent Cell Growth. The rIL-2 dependent proliferation of the IL-2 dependent CTLL-2 cell line is illustrated in Figure 1. This cell line was grown in defined HB101 medium to reduce the possibility of non-IL-2 related growth effects. Cells seeded at 7×10^3 cells/mL proliferated to the desired density of 1×10^5 cells/mL after 2–3 days in 100 units of rIL-2/mL of medium. Although CTLL cells survived several days in the absence of IL-2, no significant proliferation was observed. It was also found that the assay worked best when cells were kept in log phase. Thus, cells which grew to densities greater than 2×10^5 cells/mL were not used in the assay or passed. CTLL-2 cells stored at −196 °C could be reconstituted without any difficulty.

Assay. Recombinant IL-2 was isolated from serum by a modified capture-affinity technique (8) that involved coating sterile tissue culture plates with monoclonal anti-rIL-2 antibody to eliminate interferences from non-IL-2 growth factors, comedicants, and inhibitors (10) known to be present in human serum. This mAb has been shown by using the western blot technique (11) to specifically bind to an epitope comprising the first 12 amino acids of rIL-2 in which the threonine at position 3 is non-glycosylated.

For the determination of rIL-2 in human serum, it was necessary to incubate the appropriate serum samples in the prepared microtiter wells. Fortified calibration standards, quality assurance samples, and appropriate controls were

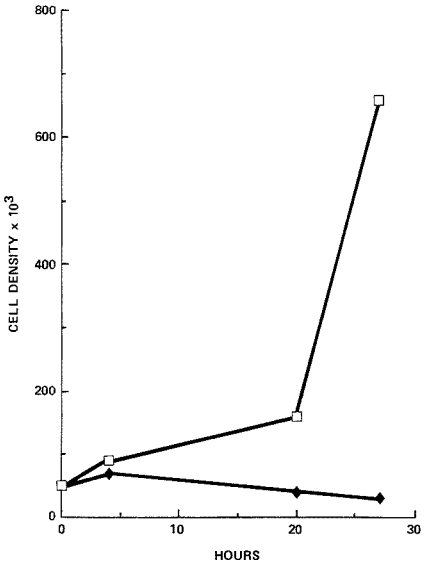

Figure 1. IL-2 dependent response of mouse CTLL-2 cells in HB101 medium to 100 units/mL of rIL-2 over a 26-h time period (□). CTLL-2 cells plus medium with no rIL-2 over the same time period (◆).

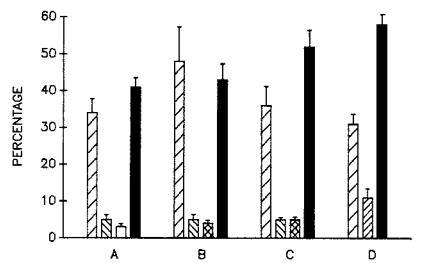

Figure 2. Bar graph represents the percent recovery of [^{125}I]-rIL-2 and [^{14}C(U)]-rIL-2 in the bioassay. Bars labeled A represent recovery percentages from acid elution of bound [^{125}I]-rIL-2. Bars labeled B represent recovery percentages of [^{125}I]-rIL-2 bound by mAb coated at pH 8.0. Bars labeled C represent recovery percentages of [^{125}I]-rIL-2 bound by mAb coated at pH 4.8. Bars labeled D represent recovery percentage of [^{14}C(U)]-rIL-2 bound by mAb coated at pH 4.8. See text for description of bars within each category. Error bars represent one standard deviation in percent.

assayed in addition to experimental samples. Originally rIL-2 was dissociated from the affinity plate with acid (0.2 M acetic acid in 300 mM NaCl) and the neutralized eluent was transferred to tissue culture plates containing the responding CTLL-2 cell line. However, it was discovered, using [^{125}I]-rIL-2 (specific activity 7000 cpm/unit) as a tracer, that only a very small percentage of the counts (5%) were recovered in the neutralized acid eluent (Figure 2A). Because of this finding, the assay was modified in such a way that the cells were added directly to the plate containing anti-rIL-2 and isolated rIL-2. The rationale behind choosing this method will be presented in the section on recovery.

The plates were incubated with the serum samples for 2 h, the microtiter wells were washed, and medium was added to each well followed by the addition of CTLL-2 cells. This mixture was incubated for 24 h after which cell proliferation was measured by a colorimetric determination of lactic acid production in the cell medium (8).

Recovery. Recovery information was obtained by following the above procedure except that control serum was fortified with [^{125}I]-rIL-2. The purity of this tracer (>85%) was determined by cochromatography with unlabeled rIL-2 using reverse-phase HPLC. Tissue culture plates were substituted with Immulon 1 Removawell strips in order to facilitate well by well counting.

Examination of the fate of the labeled rIL-2 was completed by following the label at each step in the assay (Figure 2). Left slanted vertical bars represent material not captured by the mAb and removed with the supernatant. Right slanted bars represent the percent labeled material removed in the first wash. Cross-hatched bars represent the percent label removed in the second wash. Left slanted narrow vertical bar represents the percent labeled material removed in four washes. Clear bar represents percent material removed by acid elution. Black bars represent the percent labeled material bound to the plate by the mAb. In addition, two different pH values (4.8 and 8.0) for coating were compared. After a 2-h incubation, approximately 36% of the label remained in the serum as nonbound material (a higher percentage, 47%, remained unbound if the coating buffer was basic). In these studies 40–50% of the labeled material was recovered bound to the plate and approximately 10% of the total counts eluted in the first two wash steps. Plates treated with no anti-rIL-2 show less than 1% nonspecific binding to the plate.

Evidence for the superiority of coating plates at an acidic pH became apparent when an enzyme linked immunosorbent assay (data not shown) was used to compare the relative amounts of 5B1 monoclonal antibody bound at pH 4.8 and pH 8.0. It was found that 10% (relative) more antibody was found at pH 4.8 than at pH 8.0 when plates were coated at 1 μg/mL (100 μL). In this regard, most reports in which proteins are bound nonspecifically to plastic, basic coating conditions are used.

When [^{14}C(U)]-rIL-2 was used at two concentrations (5 units/mL and 20 units/mL) to determine the recovery from serum under acidic coating conditions, an average recovery at 57.3 ± 3.8% (n = 23) was observed (Figure 2). The percent recoveries at the two concentrations were the same, suggesting that recovery is the same over the concentration range used in our studies. The results presented in Figure 2 indicate that the recovery is very reproducible and that similar recoveries are obtained when either ^{14}C or ^{125}I labeled rIL-2 is used as tracer.

Partitioning. We also used [^{14}C(U)]-rIL-2 to determine the distribution of rIL-2 between blood cells and plasma. The blood cell/plasma concentration ratio (*12*), for a hematocrit of 0.48, was found to be 0.52/1, indicating that approximately one-third of the material is associated with blood cells and two-thirds with the plasma. In addition, when rIL-2 biological activity was compared from serum and plasma in these partitioning experiments, no differences were observed.

Specificity. Serum was fortified with various cytokines (IL-1 α, IL-1 β, IL-4, α-interferon, and tumor necrosis factor) at 1000 units/mL and evaluated in the assay in order to demonstrate assay specificity. As can be seen in Table I, no cell proliferation above the control level occurred in response to these immunomodulators.

5B1 was compared to a monoclonal antibody of the same isotype (C-MYC) to illustrate that rIL-2 was specifically captured by 5B1 anti-rIL-2 antibody. When 50 units/mL of rIL-2 was added to wells that had been coated with this unrelated antibody, no cell proliferation above control levels was observed. Experiments were also undertaken to determine if the antibody capture technique could be eliminated from the assay by adding serum directly. In these experiments, control serum was added directly and compared to results from the highest reference standard (50 units/mL) added directly in HB101 medium. Optical density readings from the lactic acid assay that resulted from the direct addition of control serum were considerably higher (data not shown) than those seen with our highest standard, indicating that serum could not be directly added in our assay. This observation is most likely due to the presence of endogenous lactic acid in serum.

We also compared rIL-2 content measured by the colorimetric determination of lactic acid with the ^{3}H-TdR method from the same experiment (we performed both assays from the same microtiter plate). The mean of the standard deviations in the colorimetric (3.5%) was somewhat lower than that observed in the ^{3}H-TdR method (8.2%). In addition, the content in the Quality Assurance pool sample was closer to the mean amount (4.8 units/mL) when measured by the colorimetric method (4.7 units/mL) than by the ^{3}H-TdR method (3.7 units/mL).

Sensitivity, Precision, Reproducibility, and Stability. It was determined in the above studies that if the monoclonal antibody was bound to the plates at acid pH, it was possible to generate reproducible calibration curves with good dynamic range (Figure 3). Calibration curves were generated by fitting the mean optical densities (Y) determined from the colorimetric lactic acid assay and the concentration (X) of rIL-2

Table I. Optical Densities and Calculated Concentrations from the Analysis of Calibration Standards and Serum Samples Fortified with Other Known Immunomodulators

analyte	concn, units/mL	optical density	IL-2 concn found, units/mL
rIL-2	50	1.117	50.55
	25	0.848	23.74
	20	0.804	20.55
	10	0.646	10.83
	5	0.516	4.43
	2	0.463	2.14
rIFN-αA	1000	0.418	NM
IL-1 α	1000	0.423	NM
IL-1 β	1000	0.426	NM
hrTNF	1000	0.411	NM
hrIL-4	1000	0.434	NM

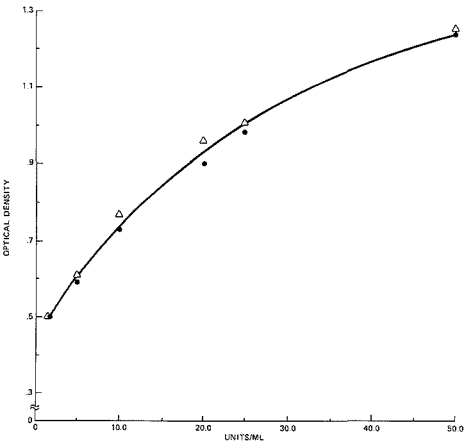

Figure 3. rIL-2 calibration curve (plotting optical densities versus units/mL) from the analysis of six standards. Triangles and dots are duplicate analyses.

Table II. Interassay Precision of the Assay Estimated from the Analysis of the Calibration Standards

added, units/mL	found (mean ± SD), units/mL (n = 17)	rel std dev, %
2[a]	2.0 ± 0.14	7.1
5	5.1 ± 0.29	5.8
10	10.3 ± 0.36	3.5
20	19.6 ± 0.67	3.4
25	24.9 ± 1.25	5.0
50	51.0 ± 1.44	2.8
		4.6%[b]

[a] Significantly different from drug-free serum control at $p > 0.001$ (two-tailed p values obtained from t test, n = 17). [b] Overall relative standard deviation.

Table III. Bench-Top, Room Temperature Stability of IL-2 in Pooled Human Serum

time, h	concn found (mean ± SD, n = 17), units/mL	rel std dev, %
0	4.16 ± 0.29	6.9
3	3.98 ± 0.19	4.8
6	4.16 ± 0.44	10.6
22	4.34 ± 0.35	8.0

(2–50 units/mL) in fortified control serum to the weighted ($1/Y$) nonlinear equation $X = (YC - A)/(1 - YB)$. Concentrations of rIL-2 in experimental samples were calculated by using the above equation, the generated constants and the optical density measurement for the sample.

The interassay precision for the assay, estimated from the fit of the calibration standards to the calibration curve (relative standard deviation of the difference between the found and added concentrations), was 4.6% (17 calibration curves, Table II). Intraassay precision of the assay, estimated as the relative standard deviation of the ratio of duplicate analyses of the calibration standard and the quality assurance sample, was 12.7% (17 calibration curves). The interassay precision at the lower limit of quantitation, 2 units/mL, was 7.1%. Reproducibility of the assay, estimated as the relative standard deviation of multiple analyses of the same quality assurance sample (pooled experimental samples) was 6.9% (17 measurements over a 2-month period). The results of bench-top and long-term stability experiments suggest that rIL-2 is stable under the stated conditions of temperature and time (Tables III and IV).

Human Serum Concentration–Time Profile. Figure 4 illustrates the mean serum concentration–time profile from three AIDS patients who received 1×10^7 units of rIL-2 in a 30-min iv infusion. Concentration data were best fit to a two-compartment intravenous model (Model 8 in PCNONLIN (*13*)). The terminal elimination rate constant (β) was determined (by least-squares regression) from the slope of the natural log serum concentration time plot in postdistribution phase, with the elimination half-life ($t_{1/2}$) calculated by $0.693/\beta$. The calculated $t_{1/2}$ for the three patients ranged from 0.9 to 1.7 h. The calculated clearance (Cl) value for rIL-2 ranged from 7.9 to 15.2 L/h using Cl = dose/$AUC_{0-\infty}$ and the volume of distribution ranged from 19.4 to 22.7 L using V = Cl/β. Details of the human pharmacokinetic studies will be described elsewhere (*14*).

CONCLUSIONS

This paper describes an immunobioassay that is sensitive, reproducible, and specific for the measurement of rIL-2 present in the serum of patients undergoing therapy with this lymphokine. Studies conducted with radiolabeled rIL-2 as tracer indicate that recovery is good utilizing the capture antibody technique. In addition, rIL-2 is quite stable in serum even when stored for many months at −20 °C and for at least a day at room temperature.

Table IV. Long-Term Stability of IL-2 in Pooled Human Serum Samples at −20 °C

date	concn found, units/mL	[(found − mean)/mean] × 100, %
8/12/87	5.18	8.95
9/10/87	4.45	−6.32
10/16/87	5.53	16.32
12/9/87	4.00	−15.79
1/24/88	4.65	−2.11
2/4/88	4.70	−1.05
mean	4.75	8.42
SD (n = 6)	0.54	
RSD,[a] %	11.32	

[a] Relative standard deviation.

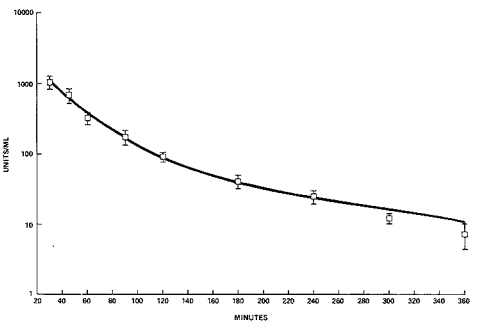

Figure 4. The mean serum concentration–time profile (±1 standard deviation) from three AIDS patients who each received 1×10^7 units of rIL-2 in a 30-min iv infusion.

Our experimental results indicated that this assay is suitable for defining the pharmacokinetic behavior of rIL-2 in patients given doses as low as 5×10^5 units. Currently, the high absorbance of the drug-free samples, representing nonspecific cell growth, limits sensitivity. While the use of the mAb offers a convenient method for isolating rIL-2 from serum, a more uniquely sensitive cell line will be needed before the bioassay could be used to measure lower concentrations of IL-2 with comparable results.

LITERATURE CITED

(1) Morgan, D. A.; Rucsetti, F. W.; Gallo, R. C. *Science* **1976**, *193*, 1007.
(2) Robb, R. J.; Smith, K. A. *Mol. Immunol.* **1981**, *81*, 1087.
(3) Smith, K. A. *Annu. Rev. Immunol.* **1981**, *2*, 319.
(4) Gillis, S.; Mochizuki, D. Y.; Conlon, P. J.; Hefeneider, S. H.; Ramthan, C. A.; Gillis, A. E.; Frank, M. B.; Henney, C. S.; Watson, J. D. *Immunol. Rev.* **1982**, *62*, 167.
(5) Rosenberg, S. A.; Lotze, M. T.; Muul, L. M.; Leitman, S.; Chang, A. E.; Ettinghausen, S. E.; Matory, Y. L.; Skibber, J. M.; Shiloni, E.; Vetto, J. T.; Seipp, C. A.; Simpson, C.; Reichert, C. M. *New Engl. J. Med.* **1985**, *313*, 1485.
(6) Taniquchi, T.; Matsui, H.; Fujita, T.; Takaoka, C.; Kashima, N.; Yoshimoto, R.; Hamuro, J. *Nature* **1983**, *303*, 305.
(7) Gillis, S.; Smith, K. A. *Nature* **1977**, *268*, 154.
(8) Familletti, P. C.; Wardwell-Swanson, J. A. *Biotechnology* **1988**, *6*, 1169.
(9) Metzler, C. M.; Elfring, G. L.; McEwen, A. J. *Biometrics* **1974**, *30*, 562.
(10) Fukushima, T.; Kobayashi, K.; Tsuyoshi, K.; Kasahura, K.; Tabata, M.; Sekine, F.; Negishi, M.; Hirotsuyu, I.; Takahashi, T. *Int. Arch. Allergy Appl. Immunol.* **1987**, *84*, 135.
(11) Chizzonite, R., Hoffmann-La Roche, Inc., personal communication.
(12) Kurata, D.; Wilkinson, G. R. *Clin. Pharmacol. Ther.* **1975**, *16*, 355.
(13) Statistical Consultants, Inc. *Am. Statistician* **1986**, *40*, 52.
(14) Gustavson, L. E.; Nadeau, R. W.; Oldfield, N. F. *J. Biol. Response Modif.*, in press.

RECEIVED for review October 27, 1988. Accepted April 25, 1989.

Conductometric Transducers for Enzyme-Based Biosensors

Susan R. Mikkelsen[1] and Garry A. Rechnitz*[,2]

Department of Chemistry, University of Delaware, Newark, Delaware 19716

The use of alternating current conductometric transducers in biosensing devices has been investigated for urea and D-amino acid sensors using the enzyme systems urease and D-amino acid oxidase/catalase. Transducers with copper and platinum electrodes were constructed and characterized, and two enzyme immobilization methods were tested. Detection limits of 1×10^{-6} M and linear ranges of 2 orders of magnitude were routinely achieved for these model sensors with enzymes covalently immobilized on collagen films.

INTRODUCTION

Biosensors couple the biochemical selectivity of enzymes, antibodies, and chemoreceptors with the sensitivity of optical, electrochemical, thermal, or mass-sensitive transducers that measure local chemical changes at the sensing surface (*1*). The simplest biosensors determine enzyme substrate concentrations and consist of an immobilized enzyme layer at the surface of a transducer that measures the local concentration of a reaction product. This principle has been applied to a wide variety of enzyme/substrate systems and has been the subject of several reviews (*2*, *3*). The electrochemical transduction of local concentrations at the sensing surface into electronic signals is generally accomplished with potentiometric or amperometric devices, where direct current (dc) potential or current values are measured (*4*).

Many enzyme-catalyzed reactions have been studied in homogeneous solution by using conductometric methods. Initial work in this area involved the urea/urease reaction

$$H_2NCONH_2 + 3H_2O \rightarrow 2NH_4^+ + HCO_3^- + OH^- \quad (1)$$

in which the initially uncharged substrate is hydrolyzed to yield four charge-bearing species (*5*). The sensitivity of this method allows the determination of urea at the 30 nM level in 0.1 mM Tris-HCl buffer (*6*), but because the reaction products are NH_4^+ and H_2NCOO^- in Tris buffers (*7*), the detection limit may yet be improved. Conductometric methods may also be used to assess enzyme activity levels at high substrate concentrations (*6*).

Conductometric transducers for biosensing devices have been introduced quite recently by Watson et al. (*8*). Their device consists of an oxidized silicon wafer with serpentined, interdigitated gold electrode pairs on one surface in a planar configuration. The close proximity of the electrodes in each pair allows a small-amplitude sine wave (1 kHz, 10 mV peak-to-peak about 0 V) to induce a measurable alternating current (ac) response. After dc conversion, the resulting signal is linearly related to solution conductance. The transducer was tested with urease immobilized on the sensing surface in a cross-linked albumin–glutaraldehyde gel layer (approximately 1 mm thick) to detect urea in diluted human serum samples. The results correlated well with clinical results, and measurements in the 0.1–10 mM range were feasible in 5 mM imidazole-HCl buffer. The same group has tested the enzymes penicillinase and aryl acyl amylamidohydrolase immobilized on films of cellulose acetate and cellulose nitrate, respectively (*9*). By use of a kinetic method in which the change in ac response was measured over 45 s, nonlinear calibration curves of root mean square current against substrate concentration were obtained for the range 0.05–10 mM. No information regarding the steady-state response or recovery times is available.

In an early paper on conductometric enzyme assays, A. J. Lawrence has listed five properties that, separately or in combination, allow the application of conductometric methods to enzymatic reactions (*10*). They are (i) the generation of ionic groups (e.g. amidases); (ii) the separation of unlike charges (e.g. decarboxylases); (iii) proton migration (e.g. esterases); (iv) changes in the degree of association of ionic groups resulting from chelation (e.g. kinases); and (v) changes in the sizes of charge-carrying groups (e.g. phosphatases).

Because all charge-carrying species are detected simultaneously, conductometric methods are relatively nonselective. Buffers of low ionic strength must be used for the detection of low levels of substrate, since detection limits are ultimately controlled by the ratio $\Delta G/G$, where G is the conductance of the medium and ΔG is the conductance change that results from the enzymatic process (*11*). This same limitation is expected to apply to conductometric biosensors. Ideal biochemical systems with which to test conductometric transducers are thus those processes possessing the highest percentage change in total conductance (conductance coefficients) under identical conditions. Factors i and ii, above, give rise to the largest conductance coefficients (*10*) and will thus be present in the systems of choice.

We report herein the design and characterization of model conductometric biosensors for urea and D-amino acids using the enzymes urease and D-amino acid oxidase, respectively. The D-amino acid oxidase reaction is shown below:

$$\text{D-amino acid} + O_2 + H_2O \rightarrow \text{2-keto acid}^- + H_2O_2 + NH_4^+ \quad (2)$$

Because the hydrogen peroxide produced by the enzyme reaction acts as an inhibitor, it is necessary to coimmobilize catalase to convert the peroxide to water and oxygen. Enzyme immobilization methods include cross-linking in an albumin–glutaraldehyde gel and covalent binding to collagen membranes. The sensors' response times, detection limits, dynamic ranges, and storage stability are discussed.

EXPERIMENTAL SECTION

The design of the conductometric transducer used in this work is shown in Figure 1. The electrodes were constructed from 26 gauge copper (99.5%) or platinum (99.95%) wire and were embedded in a silicone rubber plug (Dow Corning 3112 RTV encapsulant) sealing one end of a plastic tube (the body of an Orion ammonia electrode No. 95-12) of 12.0-mm i.d. and 14.0-mm o.d. The sensing surface consists of four parallel electrodes spaced 2 mm apart, two of 5-mm length at the outside and two inner electrodes of 8-mm length. The electrodes were connected to the two external leads so that the polarity alternated across the sensor surface in order to maximize the resulting cell constant for this

* Author to whom correspondence should be addressed.
[1] Present address: Dept. of Chemistry, McGill University, 801 Sherbrooke St. West, Montreal, Canada H3A 2K6.
[2] Present address: Department of Chemistry, University of Hawaii at Manoa, 2545 The Mall, Honolulu, HI 96822.

0003-2700/89/0361-1737$01.50/0

Table I. Response of Copper and Platinum Transducers to Potassium Chloride[a]

medium	freq, kHz	electrode matl	log–log slope	R
distilled, deionized water	1	copper	0.96	0.998
	1	platinum	0.99	1.000
	10	copper	1.07	0.998
	10	platinum	1.07	0.999
5 mM glycine buffer, pH 8.6	1	copper	0.99	1.000
	1	platinum	0.99	0.997
	10	copper	0.99	1.000
	10	platinum	1.01	1.000

[a] Determined over the range 10^{-6} M < [KCl] < 10^{-2} M.

configuration. This design was chosen for simplicity and ease of construction, although improved analytical characteristics may be achieved with smaller electrode spacings.

The instrumental arrangement consisted of a Wavetek Model 187 function generator connected to the external input of a Princeton Applied Research Model 362 potentiostat in order to apply a voltage sine wave to the transducer. Applied signals were monitored with a Hitachi Model V-302F oscilloscope at the XY outputs of the potentiostat. The current output of the potentiostat was connected to a PAR Model 5101 lock-in amplifier to measure the magnitude of the ac response, with the reference frequency supplied by the function generator. The phase of the waveform sampled by the lock-in amplifier was adjusted for maximum response prior to each measurement. The amplifier output was connected to a Heath/Zenith Model SR-204 strip chart recorder. The potentiostat was operated in the two-electrode mode, with the reference and auxilliary electrode leads connected to one electrode and the working electrode lead connected to the second.

Enzymes were immobilized at the surface of the conductometric transducer with two methods: cross-linking in an albumin–glutaraldehyde gel (method A) and covalent binding to a collagen membrane (method B). Method A used 100 μL of a 15% (w/w) solution of bovine serum albumin (BSA, Sigma No. A4503) to dissolve approximately 2 mg of the solid enzyme preparation. This solution was combined with 25 μL of a 25% solution of glutaraldehyde (Grade 1, Sigma) on the surface of the transducer. The mixture was allowed to react in air for 20 min. The sensor was then placed in a stirred blank buffer solution, and the ac voltage waveform was applied.

Method B required three reaction steps to activate the collagen membrane prior to enzyme immobilization. Collagen films (Yellow Springs Instruments No. 2511, 7.04 mg/cm^2) were treated with 0.2 N HCl in methanol (Fisher, reagent grade) for 48 h at room temperature. The film was rinsed three times with distilled, deionized water and then placed in a 2% (v/v) aqueous solution of hydrazine monohydrate (98%, Aldrich) for 4 h at room temperature. The films were again rinsed and were placed in a freshly prepared solution of 0.2 M $NaNO_2$ (Fisher, reagent grade) and 0.2 M HCl for 5 min at room temperature. This solution generates HONO, which oxidizes the acyl hydrazide groups to acyl azides. The films were rinsed repeatedly and left overnight at 4 C in an enzyme solution containing 25 mg of protein in 10 mL of 0.05 M tetraborate-HCl buffer, pH 8.5. This procedure is similar to that used by Coulet et al. (*12*), who studied a variety of enzymes and found enzyme activities ranging from 7 to 170 munits immobilized per milligram of dry collagen after a 2-h coupling step. The membranes were then rinsed with and stored in the pH 8.5 tetraborate buffer at 4 C. The collagen–enzyme film was rinsed with buffer and held tightly over the surface of the conductometric transducer with an O-ring. The sensor was then placed in a stirred blank buffer solution, and the ac voltage was applied.

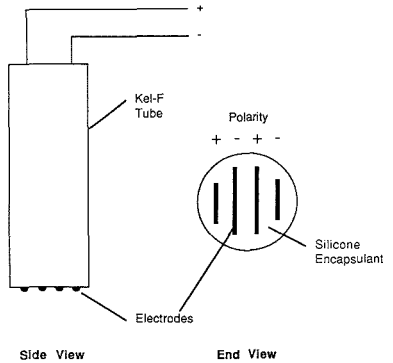

Figure 1. Conductometric transducer design.

For both methods, after the response current base line was established, the buffer was replaced by a known volume of fresh buffer. Substrate additions began after the base line was reestablished.

Buffer solutions were made with chemicals of reagent grade or better in distilled, deionized water. pH measurements were made with a Corning Model 476531 general purpose pH electrode in conjunction with a Corning Model 12 pH/mV meter, which was calibrated before use with pH 7.00 and 10.00 standard buffers (Fisher).

The enzymes urease (EC 3.5.1.5), D-amino acid oxidase (EC 1.4.3.3), and catalase (EC 1.11.1.6) were obtained from Sigma (catalog no. U1500, A1914, and C-10, respectively). Flavin adenine dinucleotide (FAD, disodium salt) was also obtained from Sigma. Stock solutions of urea (Fisher) and various amino acids (Sigma) were prepared in the buffer solutions of interest.

RESULTS AND DISCUSSION

1. Characterization of Copper and Platinum Transducers. Both of the transducers were tested to determine how the phase and amplitude of the response current varies with the frequency of the applied signal and with the conductivity of the solution tested. The amplitude of the applied voltage was maintained at a constant value of 200 mV peak-to-peak about 0 V, and frequencies of 1 and 10 kHz were used. Additions of potassium chloride to 10.0 mL of distilled, deionized water or 5 mM glycine buffer (pH 8.6) were made

Table II. Analytical Characteristics of Conductometric Transducers

medium	electrode matl	freq, kHz	calibrn curve[a] slope, nA/μM	R	p–p noise,[b] nA	detectn[c] lim, μM	cell constant
distilled, deionized water	copper	1	6.95	0.9992	0.71	0.20	2.16
		10	6.53	0.9992	0.39	0.12	2.29
	platinum	1	7.17	0.9999	0.59	0.20	2.08
		10	7.53	0.9997	0.51	0.14	1.99
5 mM glycine buffer, pH 8.6	copper	1	6.78	0.9996	0.78	0.23	2.20
		10	7.11	0.9999	0.59	0.17	2.11
	platinum	1	7.35	0.9994	0.71	0.19	2.04
		10	6.69	0.9991	0.47	0.14	2.23
	Pt–collagen	10	7.08	0.9999	1.8	0.51	2.12

[a] Values determined from regression of seven points obtained over a 1–200 μM range of KCl concentration. [b] Measured in blank medium. [c] Detection limit = 2(p–p noise)/slope.

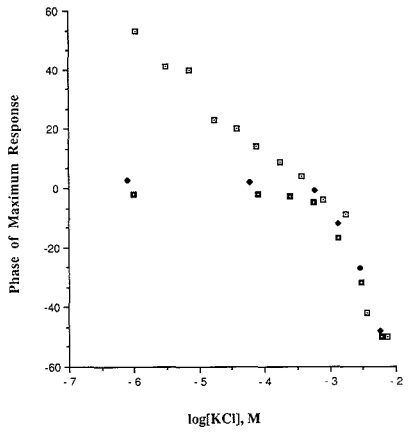

Figure 2. Phase of maximum response (degrees) vs log [KCl] for platinum transducer using 10-kHz, 200-mV peak-to-peak applied signal. Medium: (□) distilled, deionized water; (♦) 5 mM glycine buffer, pH 8.6; (■) 5 mM glycine buffer, pH 8.6, with collagen membrane held over transducer surface.

from concentrated KCl solutions made in the same media. Following each addition, the phase of the measurement made at the lock-in amplifier was adjusted until the maximum response was obtained. The peak response was then recorded.

The results of these tests are given in Tables I and II. As expected from the direct proportionality between conductance and activity, Table I shows that, over 4 decades of specific conductance, linear log–log plots of response current against concentration were obtained in all cases ($R > 0.99$), with slopes ranging from 0.96 to 1.07. In general, the log–log slopes obtained at a 1-kHz applied frequency were slightly less than 1, while those obtained at 10 kHz were slightly greater than 1. The response of the copper transducer in both media at 1 kHz showed considerable drift at KCl concentrations in excess of 2 mM, but was stable when the applied frequency was changed to 10 kHz.

Table II details the analytical characteristics of the transducers over the 1–200 μM range of KCl concentration. Plots of current amplitude against concentration showed good linearity in both distilled water and 5 mM glycine buffer. When a filter of time constant 1 s was employed at the amplifier output, the detection limits for KCl were found to be surprisingly similar for the two media at about 2×10^{-7} M. When a collagen membrane was fixed over the surface of the platinum transducer with a rubber O-ring, the detection limit for KCl was raised by about a factor of 3 because of an increase in the base-line noise; the sensitivity, however, was unchanged in the presence of the collagen membrane.

The phase of the peak in the ac response signal was measured relative to the reference signal at each KCl concentration in distilled, deionized water and the 5 mM glycine buffer. No attempt was made to correct the measured phase values for contributions introduced external to the cell, such as from cable or connector capacitances. With the platinum transducer in distilled water, no dependence of phase on ionic strength was observed for a 1-kHz applied signal. At 10 kHz, however, the phase shifted in the negative direction with increasing ionic strength, as shown in Figure 2. This is believed to result from the increase with ionic strength of the double-layer capacitance values for the four electrode–solution interfaces. In 5 mM glycine buffer, the phase shift is negligible up to KCl concentrations of about 0.5 mM. Above this value, the measured phase approaches the phase values obtained in distilled, deionized water. With a collagen membrane covering the transducer tip and contacting the electrodes, the phase was again approximately constant below 0.5 mM KCl, with a slightly more negative value than that obtained for the exposed transducer.

The phase shifts of the copper transducer were investigated by using the same methods as described above. With a 10-kHz applied signal, the results were essentially identical with those shown for the platinum transducer. At 1 kHz, however, the phase of the response shifted to more positive values with increasing ionic strength. This may be a result of changes in the double-layer capacitance of the copper–solution interface that would occur with the adsorption of ions from solution. Experiments with immobilized enzyme systems were therefore conducted with a 10-kHz applied signal, as copper and platinum showed similar behavior at this frequency.

The transducer cell constants were calculated from the calibration curves of current vs [KCl] by using the relation

$$\text{cell constant} = (\Lambda/1000)(V_p/\text{slope}) \qquad (3)$$

where Λ is the equivalent conductance of KCl (149.9 Ω^{-1}), V_p is the amplitude of the applied voltage (0.1 V for the 200-mV peak-to-peak signal), and the slope is calculated in units of amperes per molar concentration. Equation 3 follows directly from conductometric theory (*13*). The results of these calculations are given in the last column of Table II. No significant difference was found in the cell constants of the copper and platinum transducers; in addition, the cell constants did not depend on the frequency of the applied signal.

2. The Urea Sensor. The urea–urease system was selected for a model sensor so that comparison with the conductometric sensor devised by Watson et al. (*8*) and potentiometric urea sensors (*14–16*) would be possible. This reaction also serves as a model for homogeneous conductometric enzyme assays (*5*).

Immobilization method A was used to cross-link 5 mg of urease and BSA with glutaraldehyde on the surface of the copper transducer. This resulted in a gel layer approximately 1 mm thick. Approximately 3 h in stirred 5 mM glycine buffer (pH 8.0) was required to establish a flat base line, using the 10-kHz, 200-mV peak-to-peak applied signal.

Initial tests were made by adding small volumes from a concentrated urea stock solution to a final urea concentration of 0.1 mM. The sensor's response time was in excess of 3 h, with the initial change in current being linear with time for approximately 60 min. For this reason, a kinetic method was used to characterize the sensor's response to urea. The method, similar to that used by Watson et al. (*8*), involves monitoring the change in the response current for the first 10 min following substrate addition. Subsequent additions allow the construction of a calibration curve, with the initial slope plotted against substrate concentration. Over the 0.01–1.26 mM range of urea concentration, the regression equation (initial slope, nA/min) = 4.4 + 127.5([urea], mM) was followed, with $R = 0.9998$ ($n = 8$). The detection limit, for a 10-min response period, was found to be about 10^{-5} M urea, and this compares favorably with the 10^{-4} M lower concentration studied by Watson et al. (*8*). Although the response depends linearly on substrate concentration, this sensor has no practical value because the recovery time, like the response time, exceeds 3 h. A thin gel layer would be expected to improve the response characteristics, but due to the large area (1.54 cm^2) and uneven surface of the transducer, this method was not attempted.

Immobilization method B was used to covalently link urease to a collagen membrane, which was then held tightly over the surface of the copper transducer with a rubber O-ring. Coulet et al. (*12*) found that this method yielded an immobilized urease activity of 2.1 munits/mg of collagen, with a 2-h enzyme

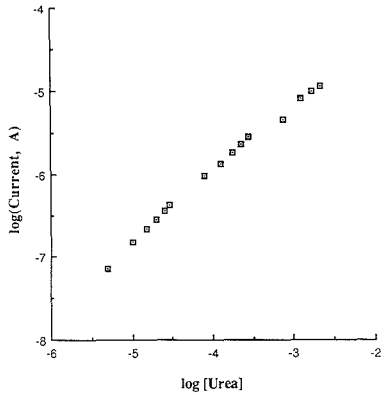

Figure 3. log (current amplitude) vs log [urea] for conductometric urea sensor. Conditions: immobilization method B used; collagen–enzyme membrane held over transducer surface by rubber O-ring; 5 mM glycine buffer, pH 8.0.

Table III. Effect of Ionic Strength on Analytical Characteristics of Urea Sensor

glycine concn, mM	p–p noise,[a] nA	sensitivity,[b] nA/μM	detectn lim,[c] μM
5	1.7	19.2	0.18
50	6.9	8.8	1.6

[a] Measured in blank medium. [b] Measured over a 1–100 μM range of urea concentration. [c] Detection limit = 2(p–p noise)/sensitivity.

coupling step, but they state that this value can be doubled by using longer coupling times. For this reason, coupling times of 15 h or more were used for this work.

This sensor was tested in 5 mM glycine buffer, pH 8.6, by adding urea from concentrated stock solutions to final urea concentrations ranging from 5×10^{-6} to 2×10^{-3} M. The resulting log–log plot of steady-state current vs concentration is shown in Figure 3. From this plot, it is apparent that the dynamic range of this sensor is about 3 orders of magnitude, although the region of direct proportionality, where the log–log slope is equal to 1, has an upper limit of about 1×10^{-4} M.

The effect of ionic strength on the sensor's response was investigated by using pH 8.0 buffers of 5 and 50 mM glycine concentration. The response characteristics are given in Table III. The detection limit is approximately 1 order of magnitude lower in the 5 mM buffer than it is in the 50 mM buffer, as expected from the results of homogeneous conductometric experiments (*11*). The linear range is approximately 2 orders of magnitude in both buffers.

The sensitivity for urea in the 5 mM glycine buffer, 19.2 nA/μM, was found to be more than twice the value of 8.8 nA/μM obtained in the 50 mM buffer. This difference cannot be explained by the sensitivity of the transducer, since the slopes of the calibration curves for KCl were not found to depend upon background ionic strength (Table II). The sensitivity difference can be attributed to local processes at the sensor surface, since the urease reaction produces three ionic species (ammonium, bicarbonate, and hydroxide) that are involved in pH-dependent equilibria. The limited capacity of the 5 mM glycine buffer can be expected to allow local pH changes within the membrane, while the 50 mM buffer will restrict local pH changes to a greater extent. This local pH effect has been studied with a potentiometric urea sensor by Mascini and Guilbault (*14*), who recommend 0.2 M Tris buffers for urea concentrations of 5 mM or less.

The response time of the urea sensor depends upon both substrate concentration and ionic strength. In the 50 mM buffer, the time for 90% response decreased from 12.5 min at 4×10^{-5} M urea to 7.0 min at 1.7×10^{-3} M urea. This is in agreement with theoretical predictions for the transition from first-order to zero-order enzyme kinetics with increasing substrate concentration (*3*) and corroborates published results for potentiometric urea sensors (*16*). In 5 mM buffer, the response time increased from 29 min (5×10^{-6} M) to 37 min (3×10^{-5} M) and then decreased to 13 min at 1×10^{-3} M. This behavior can again be attributed to local pH changes within the membrane that result from the low capacity of the 5 mM buffer, since response times depend upon enzyme kinetics, which, in turn, are pH-dependent.

Despite the lower sensitivity, we thus recommend the 50 mM buffer for fast and reproducible responses. The results obtained with this buffer compare favorably with those reported for Mascini and Guilbault's potentiometric sensor (*14*), which has a detection limit of 5×10^{-5} M and a linear range extending upward to 10^{-2} M urea.

3. The D-Amino Acid Sensor. A conductometric sensor for D-amino acids was constructed by using enzyme immobilization method B and an enzyme coupling solution containing 25 mg of D-amino acid oxidase and 1 mg of catalase. Following the coupling step, the enzyme-coupled collagen membranes were stored in pH 8.5 tetraborate buffer with 0.25 mM FAD added. The FAD was included in the storage buffer because the apoenzyme of D-amino acid oxidase is known to be relatively weakly bound ($K_d = 2.8 \times 10^{-7}$) to its prosthetic group (FAD) and will readily dissociate in buffers containing no FAD (*17, 18*).

Initial blank measurements of transducer responses to D-phenylalanine were made in 5 mM phosphate buffers with no membranes covering the sensing surfaces. As the D-phenylalanine concentration was increased from zero to 0.1 mM (by additions from stock solutions made in the same buffers), negative response currents were observed. The magnitude of these responses was greater for the copper than for the platinum transducer and increased with pH over the 6.0–7.5 pH range. For both transducers, the effect was absent when glycine or Tris buffers were used instead of phosphate. The negative responses observed in the phosphate buffers are thus believed to be due to the adsorption of phenylalanine onto the electrode surface through amine groups, effectively decreasing the electrode areas and the level of the background signal. Amine-containing buffers, such as glycine or Tris buffers, would occupy the available adsorption sites so that the effects of phenylalanine adsorption would not be seen in these media. Because of this effect, the platinum transducer and glycine buffers were used for further work with the D-amino acid sensor.

The membranes were assayed for enzyme activity by measuring the initial change in conductivity (over 4 min) that occurs when a 1.0 cm × 2.0 cm membrane was immersed in 10.0 mL of stirred 5 mM glycine buffer, pH 8.6, containing 4.86 mM D-methionine. The initial slope for the membrane was compared to a calibration curve constructed under the same conditions with varying amounts of homogeneous D-amino acid oxidase in the presence of a 100-fold excess of catalase. The resulting immobilized enzyme activity was calculated as 0.066 ± 0.002 unit for the 2.0-cm^2 membrane, which corresponds to 0.053 unit per sensor.

The pH of the 5 mM glycine buffer was varied between 8.45 and 8.84 in order to determine the optimum pH for the immobilized enzyme system. The response to D-methionine was measured by constructing a three-point calibration curve at each pH over the 5–35 μM concentration range. The slopes

Table IV. Effect of pH on Sensitivity of D-Amino Acid Sensor

pH	sensitivity, nA/μM	pH	sensitivity, nA/μM
8.45	3.24	8.73	4.48
8.57	4.85	8.84	2.55

Table V. Relative Responses of D-Amino Acid Sensor to Various Amino Acids

amino acid	rel response	amino acid	rel response
D-methionine	1.00	D-serine	0.16
D-proline	0.63	D-leucine	0.07
D-phenylalanine	0.17	L-methionine	0.03
D-alanine	0.16	D-valine	0.02

of these calibration curves were calculated by linear regression and are presented in Table IV. The optimum pH for this system is about 8.6, slightly higher than the optimum pH of 8.2 for the homogeneous reaction (*19*).

The selectivity of the D-amino acid sensor was investigated by making duplicate measurements of the response to 25 μM levels of various amino acids in 5 mM glycine buffer, pH 8.6. The average responses to the different substrates, relative to the D-methionine response, are shown in Table V. The magnitude of the response observed with a conductometric biosensor depends upon the kinetics of the enzyme reaction as well as the specific conductances of the reaction products. For most amino acids, the products of the D-amino acid oxidase reaction are ammonium ions and 2-ketocarboxylate species. Proline is an exception, however, with methylammonium and 2-ketobutyrate ions as reaction products. For this reason, D-proline cannot be detected with a potentiometric D-amino acid sensor that uses an ammonium ion-selective transducer (*18*). The conductometric transducer, requiring only the production of ionic species, shows a large response to D-proline. The small response to L-methionine is a result of the pH of the glycine buffer, since a small percentage of the dissolved amino acid will be negatively charged, rather than zwitterionic, at this pH.

The response time of the sensor to D-methionine was measured over a 2 μM to 2 mM concentration range. The time for 90% response varied between 6 and 20 min and depended on substrate concentration. The fastest responses occurred at the lowest substrate concentrations and increased to a maximum at about 0.2 mM. Above this concentration, the response times decreased to a value of 14 min at 2 mM. The response times of potentiometric enzyme electrodes also depend upon substrate concentration, but have been shown, both theoretically (*3*) and experimentally (*20*), to decrease with increasing substrate concentration, with values of 5 min being typical at the 10^{-4} M level. We believe that the unusual response time behavior of this sensor can be attributed to the inhibitory effect of the hydrogen peroxide produced by the D-amino acid oxidase reaction, because the steady-state concentration of this inhibitor within the membrane will vary with substrate concentration even in the presence of coimmobilized catalase. Improvements in the overall response time characteristics may be achieved through improved transducer design, with electrodes embedded in a rigid insulating support material and polished to a flat surface; this would minimize the volume of buffer between the membrane and the sensor surface.

The storage stability of the D-amino acid sensor was investigated over 33 days by measuring responses to D-methionine over the 2 μM to 2 mM concentration range in 5 mM glycine buffer, pH 8.6. The results, shown in Figure 4, indicate that the membranes provide reproducible responses

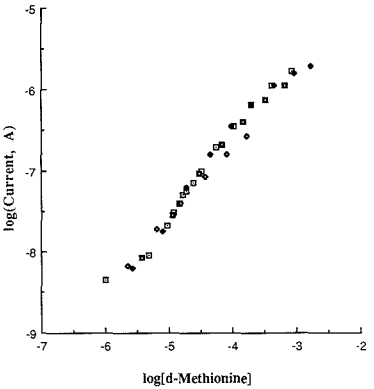

Figure 4. log (current amplitude) vs log [D-methionine] for conductometric D-amino acid sensor at different times following enzyme immobilization. Conditions: method B used to coimmobilize D-amino acid oxidase and catalase to collagen membrane; 5 mM glycine buffer, pH 8.6. Time after enzyme immobilization (days): (□) 3; (♦) 18; (■) 24; (◊) 33.

for 3 weeks following immobilization. The curve obtained on day 33 shows significantly lower responses at high methionine concentrations as a result of the reduced enzyme activity. Coulet et al. (*21*) have tested the enzyme aspartate aminotransferase bound to collagen films that had been lyophilized and reconstituted and observed no loss of enzymatic activity. Storage of the dry membranes may thus be expected to significantly prolong membrane lifetimes.

CONCLUSIONS

Conductometric transducers were investigated for enzymatic urea and D-amino acid biosensors. Detection limits of 10^{-6} M and linear dynamic ranges of 2 orders of magnitude were routinely observed with enzymes covalently immobilized on collagen membranes. Since conductometric transducers respond to ionic strength changes, they do not appear practical for in vivo applications. It has been shown, however, that determinations in diluted biological fluids are possible with the use of a reference sensor containing no immobilized enzyme (*8*). Because of the excellent analytical characteristics of these model sensors, their incorporation into immunological sensing devices is currently under investigation.

LITERATURE CITED

(1) *Biosensors: Fundamentals and Applications*; Turner, A. P. F., Karube, I., Wilson, G. S., Eds.; Oxford University Press: New York, 1987.
(2) Lowe, C. R. *Trends Biotechnol.* **1984**, *2*, 59–64.
(3) Carr, P. W.; Bowers, L. D. *Immobilized Enzymes in Analytical and Clinical Chemistry*; Wiley: New York, 1980; pp 197–310.
(4) Frew, J. E.; Hill, H. A. O. *Anal. Chem.* **1987**, *59*, 933A–944A.
(5) Hanss, M.; Rey, A. *Biochim. Biophys. Acta* **1971**, *227*, 630–638.
(6) Hanss, M.; Rey, A. *Biochim. Biophys. Acta* **1971**, *227*, 618–629.
(7) Jespersen, N. D. *J. Am. Chem. Soc.* **1975**, *97*, 1662–1667.
(8) Watson, L. D.; Maynard, P.; Cullen, D. C.; Sethi, R. S.; Brettle, J.; Lowe, C. R. *Biosensors* **1987**, *3*, 101–115.
(9) Lowe, C. R. PCT International Patent WO 84/03945, 1984; *Chem. Abstr.* **1985**, *103*, P19418.
(10) Lawrence, A. J. *Eur. J. Biochem.* **1971**, *18*, 221–225.
(11) Lawrence, A. J.; Moores, G. *Eur. J. Biochem.* **1972**, *24*, 538–546.
(12) Coulet, P. R.; Julliard, J. H.; Gautheron, D. C. *Biotechnol. Bioeng.* **1974**, *16*, 1055–1068.
(13) Holler, F. J.; Enke, C. G. In *Laboratory Techniques in Electroanalytical Chemistry*; Kissinger, P. T., Heinemann, W. R., Eds.; Marcel Dekker: New York, 1984; pp 238–243.
(14) Mascini, M.; Guilbault, G. G. *Anal. Chem.* **1977**, *49*, 795–798.
(15) Arnold, M. A.; Glazier, S. A. *Biotech. Lett.* **1984**, *6*, 313–318.
(16) Nilsson, H.; Akerlund, A. C.; Mosbach, K. *Biochim. Biophys. Acta* **1973**, *320*, 529–534.
(17) Husain, M.; Massey, V. *Methods Enzymol.* **1978**, *53*, 429–437.
(18) Guilbault, G. G.; Hrabankova, E. *Anal. Chim. Acta* **1971**, *56*, 285–290.
(19) Meister, A.; Wellner, D. In *The Enzymes*; Boyer, P. D., Lardy, H., Myrback, D., Eds.; Academic Press: New York, 1963; Vol. 7, p 639.

(20) Mascini, M.; Liberti, A. Anal. Chim. Acta 1974, 68, 177-184.
(21) Coulet, P. R.; Godinot, C.; Gautheron, D. C. Biochim. Biophys. Acta 1975, 391, 272-281.

RECEIVED for review August 30, 1988. Revised May 3, 1989. Accepted May 3, 1989. The Natural Sciences and Engineering Research Council of Canada is gratefully acknowledged for providing a Postdoctoral Fellowship (S.R.M.). The authors thank the National Science Foundation (Grant CHE-8318192) for financial support.

Immobilized-Metal Affinity and Hydroxyapatite Chromatography of Genetically Engineered Subtilisin

Roman M. Chicz[1] and Fred E. Regnier*

Department of Biochemistry, Purdue University, West Lafayette, Indiana 47907

High-performance immobilized-metal affinity and hydroxyapatite chromatography were employed to investigate the engineered subtilisin S_1 binding site microenvironment. Although these methods are classified as affinity techniques, unlike traditional affinity columns, both are capable of probing the entire surface of a molecule. The metal chelate study employed gradient elution to assemble retention maps for a wide range of mobile-phase pH. Resolution of single substitution variants was achieved at the optimum mobile-phase pH. A total of four metals were applied separately to the metal chelate column to investigate ligand specificity with respect to protein retention. Hydroxyapatite chromatography, albeit an established technique, has only recently been developed as a high-performance chromatographic method. Gradient elution separations were performed to determine selectivity. Immobilized-metal affinity chromatography was found to be the more effective method for the separation of site-specific variants.

INTRODUCTION

Although the development and application of biotechnology to the production of therapeutic proteins has reached an advanced state, analytical procedures essential for quality are still evolving. Problems associated with monitoring the production of proteins by recombinant DNA technology are different than those generally experienced in the pharmaceutical industry, often being of biochemical origin. The unique complication added by genetically engineered organisms is that structural variants of the product protein itself are formed during biosynthesis. Through expression errors, incomplete or incorrect posttranslational modification, or postsynthetic alterations, a series of structural variants can be generated that are extremely similar to the product. This problem is greater in genetically engineered organisms, because expression errors occur at a higher rate than in natural systems (*1*) and enzyme systems for posttranslational modification are different than those in which the product protein is naturally produced. For example, expressed wild-type hemagglutinin has been reported to include between 1% and 5% incorrectly folded proteins (*2*). Other examples of posttranslational errors include incorrect glycosylation and improper oxidation of cysteine residues. The physiological concern with structurally variant proteins is that they may be either of diminished biological activity or immunogenic.

[1] Present address: Department of Biochemistry and Molecular Biology, Harvard University, 7 Divinity Ave., Cambridge, MA 02138.

General complications regarding the purification of genetically engineered products include (i) the formation of undesirable protein variants during biosynthesis, (ii) no way to predict a priori where structural alterations will be found, and (iii) unwanted variant concentrations that occur at lower levels than the product protein. There is a clear need to detect the presence of incorrect variants in therapeutic products that will be administered on a chronic basis. The problem is that we do not know the limits of current analytical methodology to detect these structural alterations. Few methods are known to detect the presence of a single amino acid substitution in proteins of several hundred amino acids. This problem is complicated even further by the absence of model systems to test the discriminating power of various analytical techniques.

It was recently reported that the development of new high-performance liquid chromatography (HPLC) methods for the analysis of proteins offers the greatest near-term opportunities for the advancement of quality control operations (*3*). This paper examines the ability of general affinity chromatographic systems to discriminate between variant proteins. Through the use of site-directed mutagenesis, subtilisin variants were constructed that varied from each other by a single amino acid at a specific location in their three-dimensional structure. These constructs were used to mimic protein variants that could arise by expression errors during biosynthesis and studied chromatographically to determine the discriminating power of HPLC with respect to protein retention.

Although bioaffinity chromatography is known to be superior to other chromatographic modes for resolving mixtures containing different proteins, it targets such a small portion of the protein surface that it does not recognize differences spread over the entire protein surface (*4*). During either step or gradient elution, it is common for structural variants to coelute because their affinity for immobilized ligands is virtually identical under the conditions required for elution. Immobilized-metal affinity chromatography (IMAC), as described by Porath in 1975 (*5*), is a particularly attractive variation of the affinity concept, because the residues recognized by the support are not necessarily clustered together at one location. This method is based on interactions that occur between electron donors (histidine, tryptophan, and cysteine) on the polypeptide surface (*6*) and immobilized metal atoms (Cu(II), Ni(II), Ca(II), Zn(II), Fe(II), and Fe(III)) that act as electron acceptors (*7*). Structural requirements underlying the metal chelate/protein recognition revealed that alkaline mobile-phase specifications are usually applied in IMAC separations because protein adsorption only occurs at a pH where electron donor groups are at least partially unprotonated (*8*).

0003-2700/89/0361-1742$01.50/0

A large number of proteins, some of which are listed in Table I, have been purified by using IMAC. Selectivity is influenced by the number of accessible electron-donating groups on the protein surface, the type of metal immobilized, and mobile-phase pH. Vicinal substitution of amino acids adjacent to primary interaction sites (Trp, Tyr, or His) in oligopeptides demonstrated a decreased retention with negatively charged amino acid replacements (*9*). These results suggest IMAC may be a suitable probe to survey the effects of amino acid substitution on the chromatographic behavior of subtilisin.

Hydroxyapatite chromatography (HAC) resembles affinity chromatography in that a subtle difference in the geometrical arrangement of surface atoms determines retention, but like IMAC, this method probes the entire protein surface. The hydroxyapatite crystal, $Ca_{10}(PO_4)_6(OH)_2$, belongs to the space group $P6_3/m$ and contains two types of main surface faces (a/b or c) (*10*). Located on the a/b crystal face are the positively charged adsorbing sites, formed by two calcium ions and designated as the C sites. On the c surface face, the oxygen atoms of the phosphate ions form the negatively charged adsorbing sites referred to as the P sites (*11*). The fundamental adsorption/desorption mechanism in HAC resembles that of ion exchange, yet due to the unique spatial orientation of the surface faces, the chromatographic selectivity is unlike that of any other ion-exchange sorbent.

Comprehensive studies examining the role of protein structure and charge with respect to the mechanism of interaction between proteins and hydroxyapatite were completed just four years ago (*12–14*). These studies investigated contributions in protein retention as a function of protein pI, ionic nature of the eluant, structural differences between related proteins, and chemical modification of basic and acidic surface residues. By use of two species of β-lactoglobulin differing by one aspartate residue per subunit (two aspartates total), it was demonstrated that this single substitution produced a difference in the elution of these two proteins. Finally, the authors presented a concise and complete mechanism for protein retention on hydroxyapatite supports. With the availability of high-performance columns, and the demonstrated specificity of protein selectivity on hydroxyapatite columns, this technique was chosen to complement the subtilisin IMAC retention study.

EXPERIMENTAL SECTION

Details regarding the variant proteins, equipment, and the assay of enzymatic activity used in this study may be found in the experimental section of the paper reporting the hydrophobic interaction and reversed-phase chromatography of subtilisin (*15*).

Mobile Phase. Mobile-phase buffers used in IMAC were chosen so that the buffer pK_a was within one pH unit of the desired eluent pH: sodium acetate (Mallinckrodt, Paris, KY) (pH 5.0); sodium phosphate dibasic (Fischer Scientific, Fair Lawn, NJ) (pH 6.2 and 7.0); *N*-tris(hydroxymethyl)methyl-2-aminoethanesulfonic acid (TES) (Sigma, St. Louis, MO) (pH 8.0). Buffer A was an aqueous solution with final concentrations of 0.5 M NaCl (Fischer) and 0.02 M of the appropriate salt for the pH range studied. Buffer B contained a final concentration equivalent to buffer A plus 0.02 M imidazole (Aldrich, Milwaukee, WI).

Due to the nature of HAC, only one mobile-phase pH condition was examined. Thus, only one set of buffers were prepared. Buffer A was a 0.01 M aqueous solution of sodium phosphate, while buffer B was comprised of 0.3 M sodium phosphate. Both solutions were adjusted to pH 6.8.

All aqueous solutions were prepared by using deionized water and were adjusted to the desired pH at room temperature with either HCl or NaOH. All solutions were prepared fresh daily, filtered through a Rainin Nylon-66 (0.45-μm) filter (Woburn, MA), and deaerated prior to use.

Chromatography. IMAC was performed on a hydrophilic polymer based, 1000 Å pore diameter, 10-μm particle size TSK Chelate-5PW column (Toyo Soda, Yamaguchi, Japan). Dimensions of the column were 7.5 × 0.75 cm with a coupled IDA concentration of 24 μmol/mL of swollen gel. The column was washed daily with 10 mL (3 bed volumes) of a 0.05 M EDTA, disodium salt (Serva Feinbiochimica, Heidelberg, Federal Republic of Germany), dissolved in 0.02 M sodium phosphate, containing 0.5 M NaCl, pH 7.0, followed by 15 mL of distilled water. To immobilize the metal, 2 mL of 0.2 M metal ion solution in water was injected onto the column immediately after the EDTA/distilled water wash (*16*). The following metals were used in the IMAC study: $CuCl_2$ (General Chemical Co., New York); $NiCl_2$ (J.T. Baker Chemical Co., Phillipsburg, NJ); $ZnSO_4$ (Aldrich); $FeCl_3$ (Matheson, Coleman & Bell, East Rutherford, NJ). Excess Ni(II), Zn(II), and Fe(III) were eluted with 5 mL of deionized water, while 5 mL of 0.1 M sodium acetate containing 0.5 M NaCl, pH 4.0, was used to elute excess Cu(II). The column was next equilibrated with 15 mL of buffer A followed by a blank gradient before chromatographic analysis was attempted. Removal of immobilized metal and subsequent reloading were performed daily to circumvent any changes in ligand density as a result of metal leakage. Samples were examined by gradient elution with a 20-min linear gradient, 0 to 100% buffer B, at a flow rate of 1 mL/min (*17*). Retention maps, for the 5.0 to 8.0 pH range, were assembled from data collected in this manner.

HAC was performed on a 10.0 × 0.8 cm column packed with 3 μm diameter porous spherical particle hydroxyapatite sorbent (Toa Nenryo Kogyo Co., Tokyo, Japan). Prior to chromatographic analysis, the column was equilibrated with buffer B followed by a blank gradient. Samples were chromatographed with a 20-min linear gradient elution from 0 to 100% buffer B at a flow rate of 0.5 mL/min (*18*). At the end of each run, the column was washed for 10 min with 0.3 M phosphate buffer and then equilibrated with 0.01 M phosphate buffer before the next analysis. Modified buffer A solution with a trace of $CaCl_2$ was used in continuous flow overnight. Precipitate was removed from modified buffer A solution by filtration prior to use.

All samples in both modes were chromatographed in duplicate. Injection volumes varied, depending on the variant, between 5 and 70 μL (volume was constant for any one analysis). The solvent perturbation peak in both the UV and conductance detectors was taken as the retention time for unretained protein (t_0).

RESULTS AND DISCUSSION

Immobilized-Metal Affinity Chromatography. As noted above, protein retention in IMAC is dependent on surface-accessible electron-donating groups complexing with the immobilized metal. X-ray crystallographic data on subtilisin (*19*) have shown amino acid residues that are on the surface of the enzyme and capable of interacting with the IMAC sorbent. In the case of tryptophan, all three residues are located on the surface. Trp 106 and Trp 113 are both found in the same α-helix located on the side of the molecule opposite to the active site. Trp 241 and His 238 are near each other in a loop section connecting two helices and lay on the same side of the molecule as Trp 106 and Trp 113. His 226 is positioned in an α-helix near the active site. Of the six histidines found in the wild type enzyme, the active site His 64 as well as His 226 and His 238 are solvent accessible. Cysteine also interacts with immobilized metals but is not present in subtilisin. On the basis of X-ray crystallography it appears that the maximum possible number of amino acid/metal interactions would be six. With a Gly-to-His substitution at position 166, this number increases to seven. Hence, there are effectively three locations on the surface of the molecule, two on the back side and the third in the active site cleft, which can participate in interactions with an IMAC column (Figure 1). An examination of standard protein mixtures on IMAC (*16*) revealed that maximum affinity and resolution of the test proteins for immobilized metal ions followed the order $Cu^{2+} > Ni^{2+} > Zn^{2+}$. For this reason, the initial experiments utilizing IMAC were performed with a Cu(II) metal saturated column.

Retention Maps. To evaluate IMAC as a probe of changes in surface microenvironments, preliminary analyses of re-

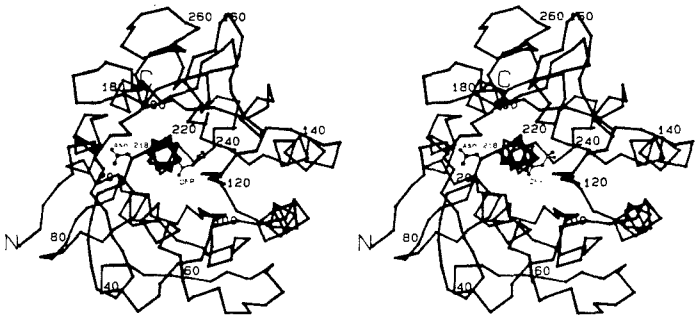

Figure 1. Stereoview of subtilisin backbone structure. Vertices represent α-carbon atoms and each length of rod represents a single residue. This view permits easy recognition of helical regions.

tention and peak shape were carried out using wild-type subtilisin. The wild type enzyme exhibited strong retention with limited peak dispersion from pH 6.2 to 8.0 (Figures 2 and 3A). However, as the mobile-phase pH became increasingly more acidic, retention decreased to the point that subtilisin nearly eluted in the column void volume. The apparent band broadening at pH 5.0 (figure 3B) was partially due to the void volume solvent peak forming a leading shoulder at the base of the subtilisin peak. Collected subtilisin fractions retained over 90% of their original enzymatic activity in all cases. Mobile phase selection for the investigation of variant protein chromatographic behavior was based on these preliminary studies with wild-type subtilisin.

Single substitution variants were used to investigate amino acid contributions to protein retention in IMAC. The location chosen for residue replacement is position 166, the S_1 binding site of subtilisin which contains glycine in the wild-type enzyme. This position is isolated from the back side of the molecule, because it is associated with the substrate binding cleft. In an unrelated study, Russell and Fersht established that amino acid substitutions within a radius of 15 Å influenced the pK_a of His 64 (*20*). Since subtilisin adsorption on an immobilized Cu(II) column is due to interactions with histidine or tryptophan residues, any changes in retention due to amino acid substitutions at position 166 could only be due to some effect on His 64 in the active site of the enzyme, because this is the only electron-donating residue within 15 Å of position 166 (*21*). The retention map of neutral amino acid substitution variants at position 166 (Figure 4) reflected the same general trend found in the multiple substitution variant maps which will be discussed below. Subtle shifts in retention times were observed at pH 6.2. The elution order at this pH, M166 > S166 > Y166 > N166 > V166, reflects the electron-donating power of the heteroatoms (S, O, N) in the side chains of these residues. At other pH conditions, elution of all the neutral variants was virtually the same, with wild-type subtilisin having slightly stronger affinity for the IMAC column below pH 7.0.

Satisfactory separation of only two of the neutral position 166 variants (N166 and V166) from wild type enzyme was achieved. Discriminating the neutral substitution variants from wild type enzyme required a difference of at least 1.60 min in retention time. Attempts to resolve N166 from M166 were ineffective. The N166 peak was seen as a leading shoulder on the M166 peak. With the exception of the wild type and V166, all the neutral substitution variants have an electron donor present in the position 166 amino acid side chain. Therefore, the possibility of direct interaction with the IMAC sorbent exists. Additional interaction between the protein and sorbent normally lengthens the retention time. However, the retention data show the wild-type subtilisin (Gly 166) having the longest retention time, thus discounting additional direct interaction between neutral amino acids substituted at position 166 and the immobilized Cu(II).

The elution order may be explained by changes in the pK_a of the active site histidine, manifested by the different amino acid substitutions at position 166. In a study of neutral amino acid hemoglobin mutants by isoelectric focusing, a single substitution of 138 Gly to Ala in the γ subunit was reported to affect the pK_a of neighboring ionizable groups enough to raise the protein pI by 0.003 of a pH unit (*22*). This was enough to allow the separation of the two mutants using immobilized pH gradient electrophoresis. Perhaps the neutral substitutions for glycine at position 166 affected the His 64 pK_a in a similar manner. This would explain the elution order of the neutral substitution variants. The variant proteins, now with slightly higher pI values compared to the wild type, elute from the IMAC sorbent prior to the wild-type subtilisin due to the increased ionization of the His 64 residue.

The retention map for charged position 166 variants (Figure 5) exhibited the same general trend as the neutral position 166 substitutions except for a significant deviation in chromatographic behavior between the variants at pH 6.2. At this pH, five of the six variants could be separated. The range included a 5-min difference in retention time between H166 and E166. Differences in retention were also recorded for the first time at pH 5.0.

Figure 6 shows the separation of three charged subtilisin variants from the wild type. The two negatively charged substitution variants elute prior to the wild type and H166. Generally, the addition of a negative charge raises the pK_a of the surrounding ionizable groups. This would explain the decrease in retention for the negatively charged substitution variants. In addition to this, a probe of protein hydration showed that water molecules were selectively arranged in the vicinity of ionic regions and that the strength of these water interactions was in the order water–anion > water–cation > water–dipole (*23*). Perhaps the hydration associated with the negative charge at this position complexes with the metal (Figure 7) and decreases the affinity between His 64 and the column.

As expected, the addition of a histidine to subtilisin increased the retention for the H166 variant compared to the wild type. This may be explained by the direct interaction between the substituted histidine and the IMAC support. The elution order of the charged substitution variants at pH 6.2 was consistent with the known retention of charged synthetic peptides (*24*). It has been reported that negatively charged peptides eluted before positively charged peptides, which eluted prior to His, Cys, and Trp containing peptides.

Whereas the selectivity was found to be lower, only four subtilisin proteins could be separated by IMAC compared to

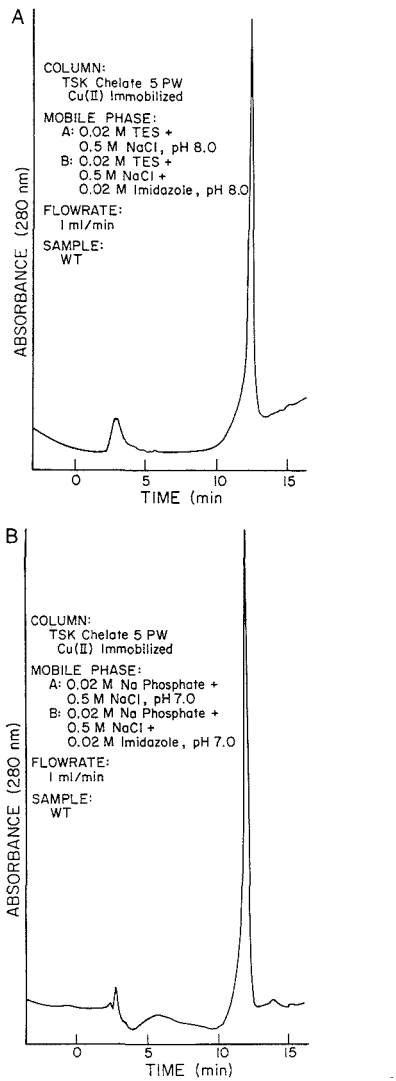

Figure 2. IMAC gradient elution of wild-type subtilisin at alkaline pH. Comparison of sample retention and peak shape using a 20-min linear gradient from 0 to 100% buffer B at (A) a mobile-phase pH of 8.0 and (B) a mobile-phase pH of 7.0.

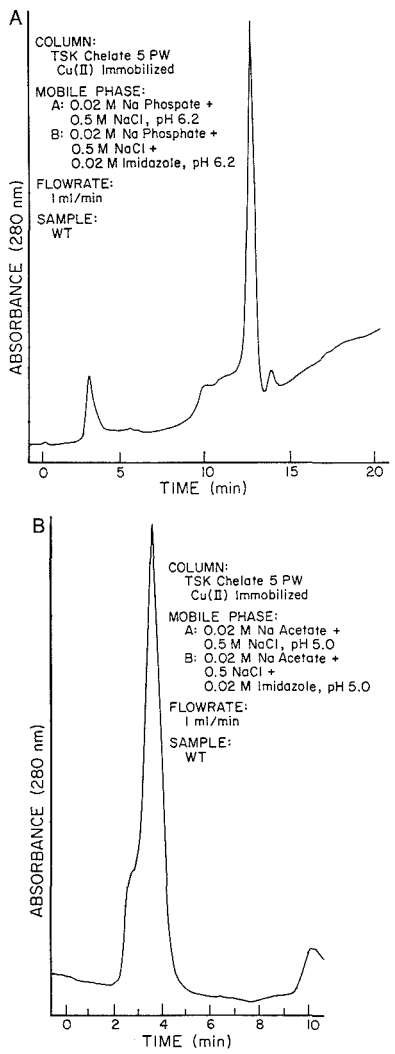

Figure 3. IMAC gradient elution of wild-type subtilisin at acidic pH. Comparison of sample retention and peak shape using the same conditions reported in Figure 2 at (A) a mobile-phase pH of 6.2 and (B) a mobile-phase pH of 5.0.

six for cation-exchange chromatography (CEC) (*21*), the resolving power of IMAC equaled that of CEC with the resolution of the two negatively charged position 166 variants, differing by only a methylene group in a protein with a molecular weight of 27 500. The elution order between these two variants was reversed from that found in CEC.

From these results it may be concluded that IMAC probes the S_1 subsite microenvironment of subtilisin. The selectivity shown at pH 6.2 was probably due to a combination of the net charge differences found in the variant S_1 subsites, incomplete ionization of His 64, partial ionization of the imidazole displacer, and, for H166, the addition of a second histidine which could interact with the support. Conclusive evidence, taken from the retention maps, pointed to pH 6.2 as the optimum pH for subtilisin variant gradient elution separations on the IMAC column.

The results presented here also indicate that strongest affinity was generally obtained at more alkaline pH as reported in the literature. In contrast, the greatest selectivity did not always occur at the conditions giving highest affinity. Perhaps at these conditions, the strong interactions between electron donors and acceptors mask the contributions of adjacent amino acids.

Variants with three to five substitutions were also examined. All of these variants had a phenylalanine for methionine substitution at position 50, a glutamine for glutamate substitution at position 156, and a lysine for glycine substitution

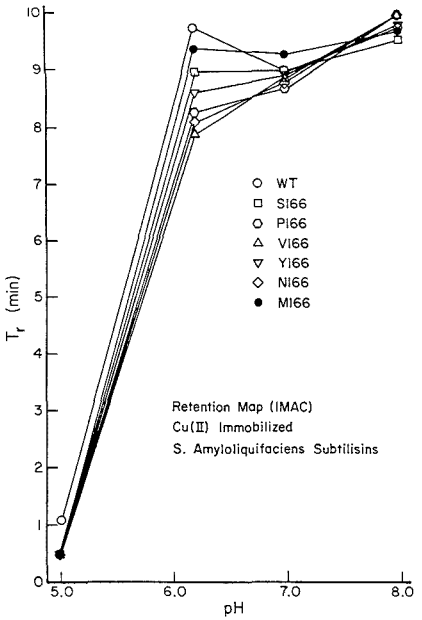

Figure 4. IMAC retention map of wild-type subtilisin and position 166 neutral substitution variants. Retention time plotted against mobile-phase pH using a 20-min linear gradient from 0 to 100% buffer B.

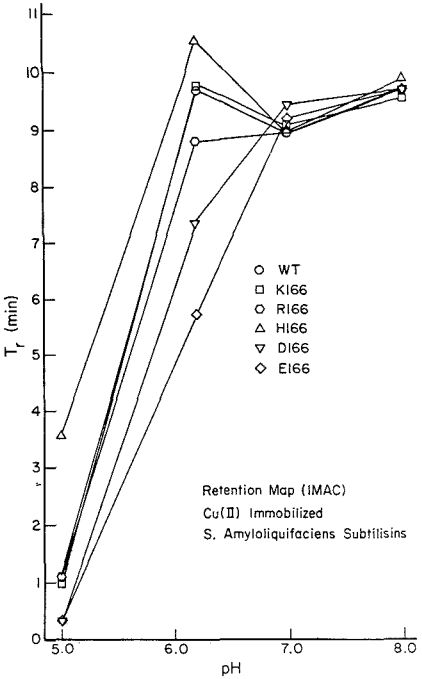

Figure 5. IMAC retention map of wild-type subtilisin and position 166 charge substitution variants. Retention time plotted against mobile-phase pH using a 20-min linear gradient from 0 to 100% buffer B.

at position 166. Subtilisin with these three substitutions will be referred to below as the FQK enzyme. Other subtilisin species examined in this study were FQK R275, FQK R170, FQK R43, and FQK R27-R43, each containing an arginine substitution at the corresponding primary sequence position. The fact that some of these variants were substituted outside the S_1 binding site, particularly on the side of the molecule opposite the catalytic cleft, allowed a more extensive survey of the subtilisin chromatographic contact region in IMAC. The pH retention maps of wild-type and FQK variants (Figure 8) reveal that they are qualitatively similar to those of the single substitution variants with all of the variants coeluting across the entire pH range examined. This means that substitutions made on the back side of the molecule either did not alter the affinity of adjacent electron-donor groups for the immobilized Cu(II) or were not in a favorable location to actively participate in the retention process. A survey of interatomic distances revealed that positions 27, 43, and 170 are all greater than 15 Å away from the surface accessible tryptophan and histidine residues. The carboxy terminal substitution at position 275 is approximately 5 Å away from His 238 and 6 Å away from Trp 241; however, no significant changes in retention were observed with the FQK R275 variant. There are two possible conclusions that can be made from this data: (1) neither His 238 nor Trp 241 are within the subtilisin/IMAC contact surface region, thus the microenvironment perturbation caused by the glutamine to arginine substitution is not chromatographically significant, or (2) the substituted arginine may be interacting with another residue(s) and does not influence either His 238 or Trp 241. In contrast, the wild-type enzyme showed slightly different retention at pH 6.2 compared to FQK variants. This indicates that the active site histidine microenvironment was perturbed by the FQK substitutions. In view of the fact that the position 166 single site substitution of lysine for glycine had little influence on retention, it is probable that either the position 50 phe-

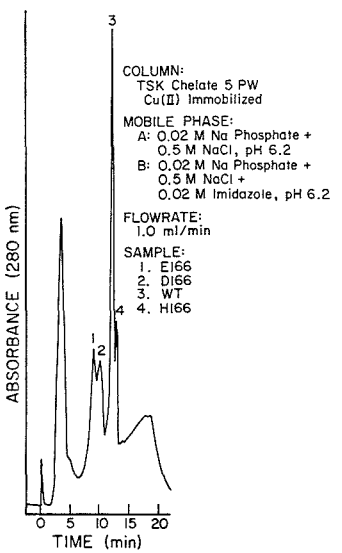

Figure 6. IMAC separation of negatively and positively charged position 166 subtilisin variants from the wild type. 20-min linear gradient from 0 to 100% buffer B.

nylalanine substitution or the position 156 glutamine substitution caused the decrease in retention.

Further examination of the contribution of position 156 was carried out with double substitution variants at positions 156

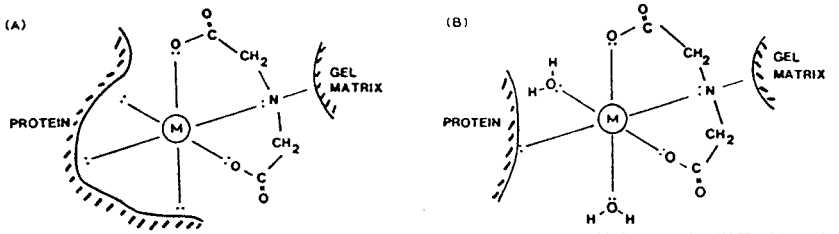

Figure 7. Schematic illustration of IMAC where the chelating group is IDA and the metal ion can bind six ligands. (A) The interaction between metal and protein occurs with the formation of coordination bonds inside the coordination sphere. (B) If the coordination sphere of the ion is unsaturated the coordination sites are temporarily occupied by weakly bound solvent molecules.

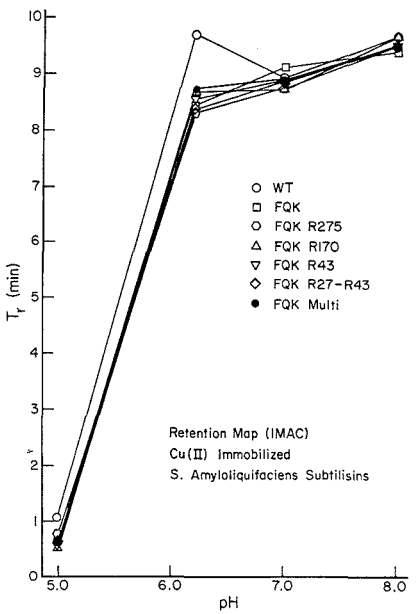

Figure 8. IMAC retention map of wild-type subtilisin and FQK series variants. Retention time plotted against mobile-phase pH using a 20-min linear gradient from 0 to 100% buffer B.

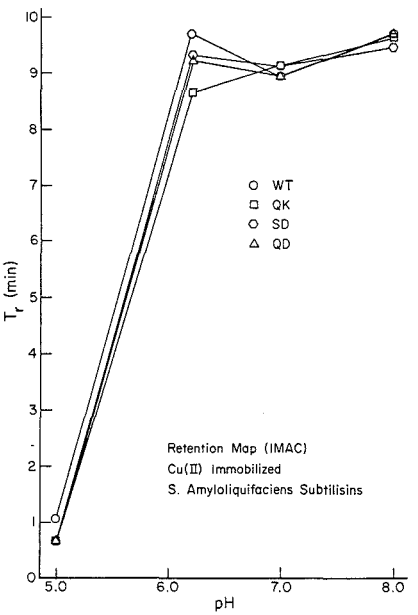

Figure 9. IMAC retention map of wild-type subtilisin and double mutation variants, retention time plotted against mobile-phase pH using a 20-min linear gradient from 0 to 100% buffer B.

and 166. Three variants were used in this study: a position 156 glutamine for glutamate substitution and position 166 lysine for glycine substitution designated the QK variant, a position 156 glutamine for glutamate substitution and position 166 aspartate for glycine substitution designated the QD variant, and a position 156 serine for glutamate substitution and position 166 aspartate for glycine substitution designated the SD variant. As in all the other variants, some discrimination of these double variants was observed at pH 6.2 (Figure 9). It was seen in the single substitution variants that substitution of aspartate for glycine at position 166 decreased retention 2.5 min. However, this substitution in the SD and QD variants had little effect. This means that the position 156 substitution of serine for glutamate in the case of the SD enzyme and glutamine for glutamate in the QD enzyme moderated the contribution of the position 166 substitution. This also indicates that position 156 plays a role in retention. The importance of position 156 is further substantiated by elution of the QK variant 1 min earlier than wild type enzyme. The neutral contribution of lysine at position 166 again implicates position 156 in the retention process.

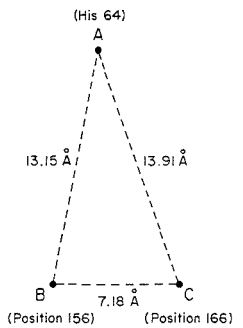

Figure 10. Triangle representing proximity of positions 64, 156, and 166 to each other. The distance was measured from X-ray structure coordinates (25) corresponding to the following atoms: His 64 $C_{\epsilon 1}$, Glu 156 C_{δ}, and Gly 166 C_{α}.

The close proximity of positions 156, 166, and histidine 64 makes it possible to represent these three sites with a triangle

Table I. Some Proteins Purified by IMAC

protein	Me^{2+}	reference
human serum proteins	Zn, Cu	*Nature* **1975**, *258*, 598.
lactoferrin	Cu	*FEBS Lett.* **1977**, *75*, 89.
α_2-SH glycoprotein	Zn	*FEBS Lett.* **1977**, *80*, 351.
α_2-macroglobulin	Zn	*Anal. Biochem.* **1979**, *99*, 415.
plasminogen activator	Zn	*Biochem. Biophys. Acta* **1979**, *580*, 140.
lysozyme	Cu	*Biochem. Biophys. Acta* **1979**, *576*, 385.
D. biflorus lectin	Ca	*FEBS Lett.* **1981**, *130*, 194.
non-histone proteins	Cu	*Anal. Biochem.* **1981**, *115*, 109.
human serum albumin	Cu	*J. Chromatogr.* **1981**, *215*, 333.
phosphotyrosyl-protein phosphatase	Zn	*Biochemistry* **1982**, *21*, 5577.
superoxide dismutase	Cu	*J. Appl. Biochem.* **1982**, *4*, 203.
human serum proteins	Ni	*Biochemistry* **1983**, *22*, 1621.
human serum proteins	Zn, Cd	*J. Chromatogr.* **1984**, *315*, 167.

(ABC) having histidine 64 at vertex A, position 156 at vertex B, and position 166 at vertex C (Figure 10). It has been established in the FQK and position 166 single substitution variants that C → A interactions indirectly alter retention, with the exception of H166 which directly interacted with the IMAC sorbent. The strongest C → A contribution in single substitution variants occurred at pH 6.2 with either aspartate or glutamate at position 166. The effect of these negatively charged substitutions was to decrease retention. In contrast, the strongest C → A effect at pH 5.0 occurred with histidine at position 166.

The question of how position 156 contributes to retention is more difficult to determine. Theoretically the effect could be either direct (B → A) or indirect (B → C → A). Carboxyl–carboxylate interactions in proteins have been reported to partly counteract negative charge (*26*). It is known from X-ray crystallography (*21*) that glutamate 156 is capable of forming a hydrogen bond with aspartate 166 at pH 5.0 and a less ordered bond scheme with glutamate 166. The removal of glutamate at position 156, by means of the double substitution variants, eliminates the hydrogen bonding scheme with the aspartate at position 166. This moderates the effect of the substituted aspartate 166 on histidine 64, as witnessed by the change in variant chromatographic behavior. Therefore, position 156 perturbs the S_1 binding site microenvironment in variable ways depending on the surrounding amino acids. On the basis of the X-ray crystallographic data it is probable that the difference in retention between the wild-type and QK variant is because position 156 has a direct contribution to the microenvironment surrounding His 64.

The final query involving IMAC was to survey the affinity of subtilisin for alternative metal complexes. Although these metals were found to be chromatographically inferior to Cu(II), Ni(II) and Zn(II) have some utility with respect to special protein applications (Table I). A venture was made at both pH 6.2 and 7.5, to retain all the subtilisin variants discussed above on Ni(II), Zn(II), and Fe(III) loaded supports. For all proteins, the attempts were unsuccessful. Subtilisin only interacts with the Cu(II) metal complex.

Hydroxyapatite Chromatography. HAC is a relatively new high-performance chromatographic mode, even though it has an established record for protein purification in soft gels. Figure 11 reviews the possible types of interactions between a protein and a HAC column. With the charged substitutions present at position 166, it was believed that this technique would at least partially resolve certain variants.

The use of a single mobile-phase pH precluded the need

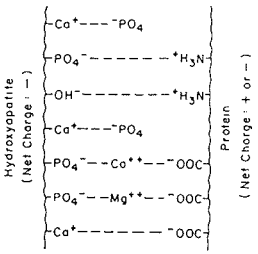

Figure 11. Schematic representation of possible interactions between protein charged residues and a hydroxyapatite sorbent.

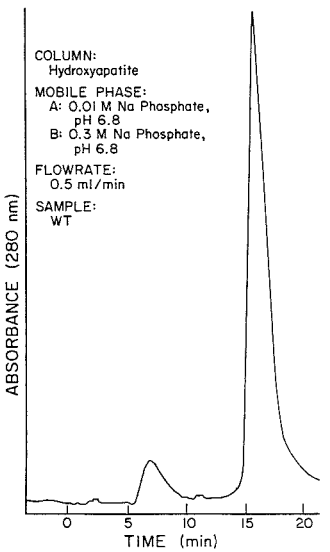

Figure 12. HAC gradient elution of wild-type subtilisin, elution performed using a 20-min linear gradient from 0 to 100% buffer B.

for the assembly of a retention map. Strong retention and good peak shape were recorded for the wild-type subtilisin in Figure 12. Unfortunately, all the variants were retained in exactly the same manner. Retention times varied by a maximum of 0.5 min in a 20-min linear gradient, hardly enough to even form a shoulder away from the main protein peak. Apparently, the S_1 subsite is not part of the subtilisin/HAC contact surface area. Although the results from the HAC study were disappointing, this technique may still discriminate site-specific mutants providing the location of amino acid substitution is recognized by the hydroxyapatite column.

CONCLUSION

These studies have shown that IMAC is superior to HAC in the resolution of subtilisin variants, particularly at position 166. Even though HAC is a powerful chromatographic technique, the chromatographic contact region for the technique apparently falls outside of those areas in subtilisin that were modified in this study. Once again it has been demonstrated that the chromatographic contact region varies between chromatographic methods and that various separation modes probe different parts of a protein's surface.

It is well documented that histidine, tryptophan, and cysteine in polypeptides interact most strongly with immobilized metals (*6*) and that vicinal substitution of charged amino acids in peptides can moderate this interaction (*9*).

From this study it may be concluded that both neutral and charged amino acids in the microenvironment surrounding a histidine center can secondarily influence chromatographic retention of a protein by moderating histidine interaction with an IMAC column. The exact mechanism by which other amino acids moderate the interaction of histidine with an IMAC column remains to be determined.

It may be concluded that IMAC can be a powerful technique for recognizing changes in protein structure within 15 Å of histidine centers in proteins providing the histidine residue is recognized by the IMAC column. Moreover, it has been demonstrated that IMAC is an effective analytical technique for the separation of genetically engineered proteins differing by as little as a single methylene group in a protein of 27 500 M_r.

ACKNOWLEDGMENT

The gracious gift of the subtilisin samples from Genencor, Inc., was appreciated. We are indebted to Tom Porter for his technical assistance.

LITERATURE CITED

(1) Dixon, J., Purdue University, 1988, personal communication. "Therapeutic Peptide and Proteins: Assessing the New Techniques" Banbury Report #29, D. R. Marshad, Ed., 1988.
(2) Gething, M-J.; McCammon, K.; Sambrook, J. *Cell* **1986**, *46*, 939–950.
(3) Garnick, R. L.; Solli, N. J.; Papa, P. A. *Anal Chem.* **1988**, *60*, 2546–2557.
(4) Regnier, F. E. *Chromatographia* **1987**, *24*, 241–251.
(5) Porath, J.; Carlson, J.; Olsson, I.; Belfrage, G. *Nature* **1975**, *258*, 598–599.
(6) Hemdan, E. S.; Porath, J. *J. Chromatogr.* **1985**, *323*, 255–264.
(7) Porath, J.; Olin, B.; Granstrand, B. *Arch. Biochem. Biophys.* **1983**, *225*, 543–547.
(8) Sulkowski, E. *Trends, Biotechnol.* **1985**, *3*, 1–7.
(9) Hemdan, E. S.; Porath, J. *J. Chromatogr.* **1985**, *323*, 265–272.
(10) Kawasaki, T.; Takahashi, S.; Ikeda, K. *Eur. J. Biochem.* **1985**, *152*, 361–371.
(11) Bernardi, G. *Methods Enzymol.* **1973**, *27*, 471–479.
(12) Gorbunoff, M. J. *Anal. Biochem.* **1984**, *136* 425–432.
(13) Gorbunoff, M. J. *Anal. Biochem.* **1984**, *136*, 433–439.
(14) Gorbunoff, M. J.; Timasheff, S. N. *Anal. Biochem.* **1984**, *136*, 440–445.
(15) Chicz, R. M.; Regnier, F. E. *J. Chromatogr.* in press.
(16) Belew, M.; Yip, T. T.; Anderson, L.; Ehrnström, R. *Anal. Biochem.* **1987**, *164*, 457–465.
(17) Nakagawa, Y.; Yip, T.-T.; Belew, M.; Porath, J. *Anal. Biochem.* **1988**, *168*, 75–81.
(18) Yamakawa, Y.; Chiba, J. *J. Liq. Chromatogr.* **1988**, *11*, 665–681.
(19) Wright, C. S.; Alden, R. A.; Kraut, J. *Nature* **1969**, *221*, 235–242.
(20) Russell, A. J.; Fersht, A. R. *Nature* **1987**, *328*, 496–500.
(21) Chicz, R. M.; Regnier, F. E., submitted for publication in *Anal. Chem.*
(22) Cossu, G.; Righetti, P. G. *J. Chromatogr.* **1987**, *398*, 211–216.
(23) Cooke, R.; Kuntz, I. D. *Annu. Rev. Biophys. Bioeng.* **1974**, *3*, 95–126.
(24) Monjon, B.; Solms, J. *Anal. Biochem.* **1987**, *160*, 88–97.
(25) Alden, R. A.; Birktoft, J. J.; Kraut, J.; Robertus, J. D.; Wright, C. S. *Biochem. Biophys. Res. Commun.* **1971**, *45*, 337–344.
(26) Sawyer, L.; James, M. N. G. *Nature* **1982**, 295, 79–80.

RECEIVED for review February 21, 1989. Accepted May 17, 1989. This work was supported by NIH Grant Number 25431. This is paper No. 11929 of the Purdue University Agricultural Experiment Station.

Subambient Temperature Modification of Selectivity in Reversed-Phase Liquid Chromatography

Lane C. Sander* and Stephen A. Wise

Center for Analytical Chemistry, National Institute of Standards and Technology (formerly National Bureau of Standards), Gaithersburg, Maryland 20899

The effect of column temperature on selectivity was studied for the separation of polycyclic aromatic hydrocarbon (PAH) mixtures. Three commercial columns prepared by using monomeric and polymeric surface modification chemistry were employed. Selectivity was evaluated through the use of a three-component PAH mixture previously developed for phase type evaluation. Column selectivity was found to vary continuously with temperature, regardless of the type of phase used. The shape recognition ability of each phase, i.e., the ability of the phase to separate closely related isomers, was observed to be highest at subambient temperatures. A model for the temperature induced selectivity changes is proposed based on the morphology of the bonded phase.

INTRODUCTION

Unlike in gas chromatography, temperature often serves only a minor role in the development of separation methods in liquid chromatography (LC) (*1*). Instead, solute retention is usually controlled by easily adjusted parameters such as mobile phase composition and flow rate. In contrast to gas chromatography, the allowable range for column temperatures in LC is restricted by the properties of the mobile phase. Increased viscosity and freezing are limiting factors at low temperatures; at high temperatures boiling is a limiting consideration (*2*). Separations are commonly carried out under ambient conditions, although greater reproducibility in retention and quantitation result when isothermal conditions are established (*3*). The use of elevated column temperature has been reported as a way of increasing separation efficiency (*4*), particularly for large molecular weight solutes (*5*). Elevated column temperatures have also been used to advantage with solutes with limited solubility in the mobile phase, and in ion-exchange chromatography (*5*).

Thermodynamic aspects of solute retention have been studied in some detail (*6–11*). In general, solute retention is inversely related to temperature, i.e., retention decreases with increasing temperature. Morel and Serpinet (*12–16*) and others (*17–19*) have presented evidence for the existence of phase transitions within the bonded phase, occurring over a narrow temperature interval. The presence of a "break" or offset in a plot of log k' vs $1/T$ (Van't Hoff plot) indicates a change in the way in which the solute interacts with the stationary phase, i.e., a phase transition. Although the effect is of considerable theoretical interest, in practice the shift in retention times caused by the transition is small and does not apply if isothermal conditions are maintained. Other temperature-dependent changes have been reported. Stalcup et al. calculated relative enthalpies and entropies of transfer for

various polycyclic aromatic hydrocarbons (PAHs) to describe retention mechanisms in methanol and acetonitrile environments (*20*). Chmielowiec and Sawatzky (*11*) calculated thermodynamic parameters for PAHs and observed changes in elution order as a function of temperature. These changes were attributed to "entropy dominated retention effects".

Changes in phase morphology that occur with temperature have been investigated by a variety of techniques including calorimetry (*12, 13, 21, 22*), inelastic neutron scattering (*23*), nuclear magnetic resonance (NMR) spectroscopy (*24–28*), and infrared (IR) spectroscopy (*29*). Using an NMR technique, Claudy and co-workers (*13*) concluded that bonded phase chain mobility is increased at elevated temperatures. As might also be expected, chain mobility increases with the distance along the chain from the silica surface (*27*). Sander et al. (*29*) compared the IR spectra of alkyl-bonded silicas at various temperatures to the spectra of the corresponding alkyl silanes and alkanes. Spectral changes resulting from crystal lattice ordering were observed in the neat liquid/solid phase spectra but not in bonded phase spectra. However, overall bonded phase ordering resulting from a reduction in gauche–gauche (tggt, bend), gauche–trans–gauche' (gtg', kink), and end gauche conformations was observed at low temperatures.

In this paper, the effect of column temperature on selectivity will be examined for the separation of PAH mixtures. Observed changes in selectivity will be compared with selectivity differences previously reported for C_{18} phases prepared by monomeric and polymeric surface modification chemistries. A model for temperature induced selectivity changes is proposed based on the morphology of the bonded phase. This representation, which can be considered an extension of the "slot model" (*30, 31*), suggests that changes in selectivity are a result of changes in phase rigidity that occur at different temperatures.

EXPERIMENTAL SECTION

Reagents and Columns. HPLC grade solvents were used in all separations. Phenanthro[3,4-*c*]phenanthrene (PhPh) was obtained from Aldrich Chemical Co. (Milwaukee, WI), 1,2:3,4:5,6:7,8-tetrabenzonaphthalene (TBN, dibenzo[*g,p*]chrysene) was obtained from Rütgers (Castrop-Rauxel, Federal Republic of Germany), and benzo[*a*]pyrene (BaP) was obtained from BCR (Community Bureau of Reference, The Netherlands). Limited quantities of a solution containing these three solutes are available from the authors upon request. A mixture containing 16 priority pollutant PAHs, SRM 1647a, was obtained from NIST (Gaithersburg, MD). Three commercial C_{18} columns were employed in this work: Zorbax C_{18} (a monomeric C_{18} column; MAC-MOD Analytical, Wilmington, DE), Bakerbond wide pore C_{18} (a heavily loaded polymeric C_{18} column; J. T. Baker Chemical Co., Phillipsburg, NJ), and Vydac 201TP C_{18} (a polymeric C_{18} column; The Separations Group, Hesperia, CA). All columns were of the same physical configuration, i.e., 25 cm × 4.6 mm, with 5 μm diameter spherical particles. The Vydac 201TP C_{18} column was packed in our laboratory with commercial C_{18} silica (Vydac 201TP C_{18} phase).

Apparatus. Column temperature was regulated through the use of an insulated column jacket. Ethanol was circulated through the jacket by an external refrigerated fluid bath. Column temperatures within the range of −30 to 55 °C were possible with this apparatus; for temperatures greater than 55 °C, a column block heater was used. Column temperature was measured by using a thermometer immersed in the column jacket and temperatures were maintained to within ±0.2 °C (±1 °C for the block heater). Separations were carried out with a chromatograph consisting of an autosampler with loop injector, reciprocating piston pump, and UV detector (254 nm).

RESULTS AND DISCUSSION

In previous work we have shown that significant differences in selectivity exist among commercial and experimental C_{18} columns for the separation of polycyclic aromatic hydrocarbons (*30–36*). These differences result from variations in a number of parameters in the preparation of the phase, including alkyl chain length (*31*), phase loading (*34, 37, 38*), and, most importantly, the type of surface modification chemistry employed (*32, 39*). Phases prepared under anhydrous conditions, or using monochlorosilane reagents (i.e., "monomeric phases"), have properties distinctly different than phases synthesized using polymeric surface modification procedures (i.e., "polymeric phases"). Typical polymeric synthesis schemes employ trichlorosilane reagents in conjunction with measured quantities of water (*32*). This type of phase is distinct from and should not be confused with cross-linked or immobilized phases of the type used in capillary GC columns.

An empirical classification scheme has been developed for grouping phases with similar selectivity toward PAHs (*35*). The elution order of a mixture of three PAH solutes (PhPh, TBN, BaP; see Experimental Section) varies with bonded phase type and gives an accurate assessment of phase properties for the separation of a wide variety of PAH samples. By calculating the selectivity factor $\alpha_{TBN/BaP}$, a numerical measure of selectivity can be made, and columns can be grouped into similar classes. We have classified phases as follows: $\alpha_{TBN/BaP} \geq 1.7$, "monomeric-like" selectivity; $\alpha_{TBN/BaP} < 1$, "polymeric-like" selectivity; and $1 \leq \alpha_{TBN/BaP} < 1.7$, "intermediate" selectivity.

In the present work, a mixture of PhPh, TBN, and BaP was chromatographed on polymeric (Vydac 201TP C_{18}) and monomeric (Zorbax C_{18}) columns at various temperatures. Dramatic shifts in solute elution were observed over the temperature interval investigated. Characteristic separations for the polymeric phase are illustrated in Figure 1. Separations were carried out at elevated temperatures using 75:25 acetonitrile–water mobile phase; subambient separations were made with 85:15 acetonitrile–water. Under ambient conditions, the mixture was fully resolved with three nearly equally spaced peaks. At elevated temperatures, the elution of BaP decreased relative to TBN; thus the selectivity factor $\alpha_{TBN/BaP}$ increased. By use of the classification scheme described above, phase selectivity was more "monomeric-like" at elevated temperatures. At subambient column temperatures, the opposite trend was observed. The retention of BaP increased relative to TBN, decreasing $\alpha_{TBN/BaP}$. Polymeric-like column selectivity increased with decreasing temperature.

Similar trends were observed for the separation of the phase selectivity test mixture at various temperatures on the Zorbax C_{18} column. Overall column selectivity, as designated by $\alpha_{TBN/BaP}$, became more "polymeric-like" at low temperatures. At elevated temperatures phase selectivity changed only slightly, becoming nearly constant above 45 °C.

Selectivity is plotted as a function of temperature for polymeric and monomeric columns in Figure 2. Monomeric data points reflect measurements carried out at a mobile phase composition of 85:15 acetonitrile–water; polymeric data points are for multiple mobile phase compositions. Selectivity was observed to be nearly independent of mobile phase composition for the polymeric column; however, the slight scatter in the polymeric data in Figure 2 is the result of a minor compositional dependence.

Several trends are apparent in Figure 2. The selectivity of both monomeric and polymeric columns becomes more "polymeric-like" at reduced temperatures. At elevated temperatures, the two columns have similar "monomeric-like" phase selectivity. The selectivity plots suggest that for a finite range of selectivities, column retention behavior of one column type (e.g., polymeric) can be achieved by using a column of the other type (e.g., monomeric) at a different temperature. For example, at ambient temperature (~26 °C) the selectivity

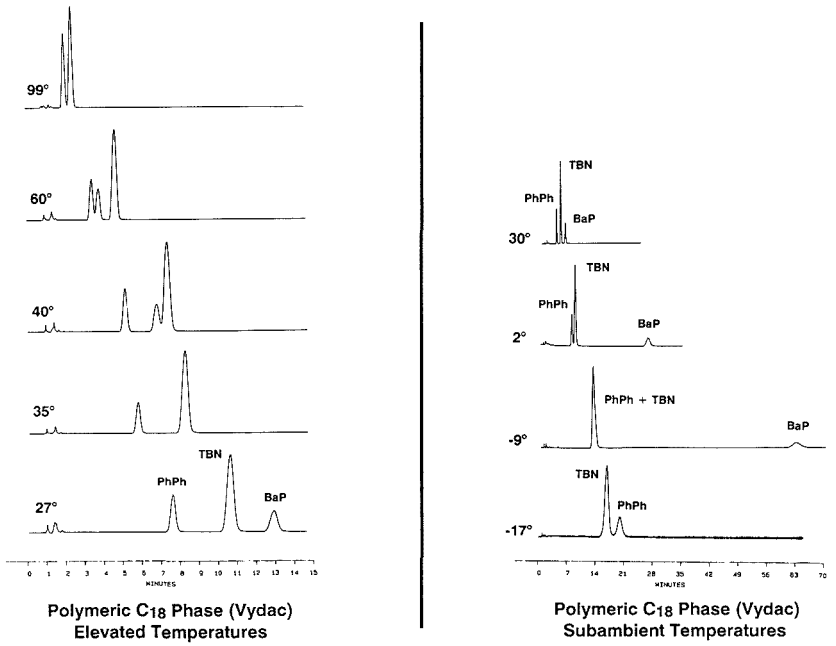

Figure 1. Separation of the phase selectivity test mixture (see text) on a Vydac 201TP C_{18} column at various temperatures.

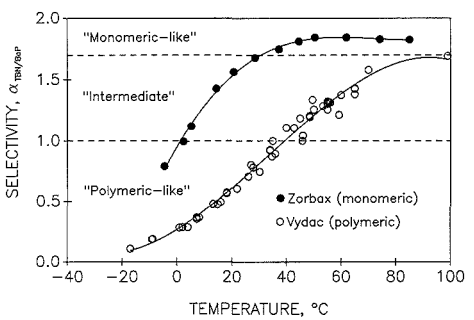

Figure 2. Phase selectivity ($\alpha_{TBN/BaP}$) plotted as a function of temperature for monomeric and polymeric C_{18} columns: mobile phase, Zorbax C_{18}, 85:15 ACN–H_2O; Vydac 201TP C_{18}, various ACN:H_2O compositions.

coefficient $\alpha_{TBN/BaP}$ for the polymeric phase is 0.71. About the same value for $\alpha_{TBN/BaP}$ is obtained for the monomeric phase at −4.6 °C, and it is expected that PAH separations at this temperature would be comparable to separations carried out at ambient conditions on the polymeric column.

To test this idea, a mixture of 16 PAHs was separated on the Zorbax C_{18} column at ambient and subambient conditions (Figure 3). Gradient elution conditions were adjusted in each case to give similar overall retention times. At 25 °C, partial resolution of the components was achieved, characteristic of that observed for most monomeric phases (*32, 36*). Fourteen of the 16 components were resolved at −8 °C, with two early components coeluting (fluorene and acenaphthene). The elution order and overall spacing of the components in the chromatogram are very similar to separations achieved on polymeric C_{18} phases (*32, 36*).

Another possibility is suggested by the selectivity plots in Figure 2. At low temperatures, $\alpha_{TBN/BaP}$ values are reduced and phase selectivity is more "polymeric-like" for both of the phase types. In general, a high degree of shape recognition ability ("shape selectivity") exists for phases with low $\alpha_{TBN/BaP}$ values (*30*). Separations of isomers and other similarly structured compounds can sometimes be achieved with such columns that cannot be achieved for columns with "monomeric-like" selectivity. The use of polymeric phases at low temperatures should result in phase selectivity and shape recognition ability not obtainable in any other way. Although, in theory, comparable phase selectivity might also be obtained with monomeric phases at low temperatures, in practice the temperature necessary to achieve such a change in selectivity is below the working limits for most mobile phase solvents.

To examine this possibility, a mixture of the six possible methylchrysene isomers was used to probe phase shape recognition ability at ambient and subambient temperature conditions. Because these isomers differ only in the ring position of the methyl group, it is difficult to separate all six methylchrysene isomers by liquid and gas chromatography. The quantification of the individual isomers is of some epidemiological interest, since 5-methylchrysene is significantly more carcinogenic than the other isomers. The first attempt to separate methylchrysene isomers by LC was made by Wise and co-workers (*40*). Four of the six isomers were resolved with a Vydac 201TP C_{18} column; however 5- and 6-methylchrysene were not resolved. Separation of all six isomers was first achieved by Markides et al. using capillary GC and experimental smectic (*41*) and nematic (*42*) liquid crystalline polysiloxane stationary phases. Such liquid crystalline GC phases are highly shape selective and in fact have retention properties closely corresponding to polymeric C_{18} phases in LC (*43*). Resolution of these isomers is not possible on more conventional GC phases, e.g., with SE-52 or SE-54 phases.

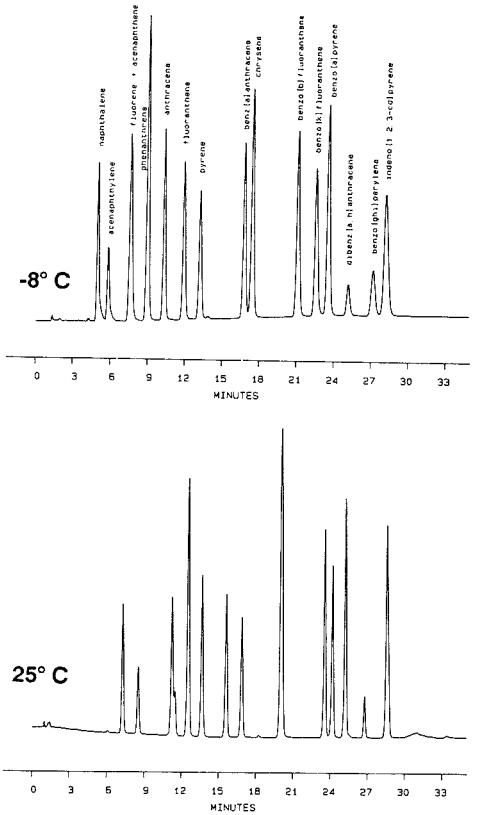

Figure 3. Separation of SRM 1647a, priority pollutant polycyclic aromatic hydrocarbons, at ambient and subambient temperatures on a Zorbax C_{18} column: mobile phase, −8 °C, gradient elution, 80:20 ACN–H_2O to 80:20 ACN–MTBE over 20 min, 1.5 mL/min; 25 °C, gradient elution, 50:50 ACN–H_2O to 100% ACN over 30 min, 1.5 mL/min.

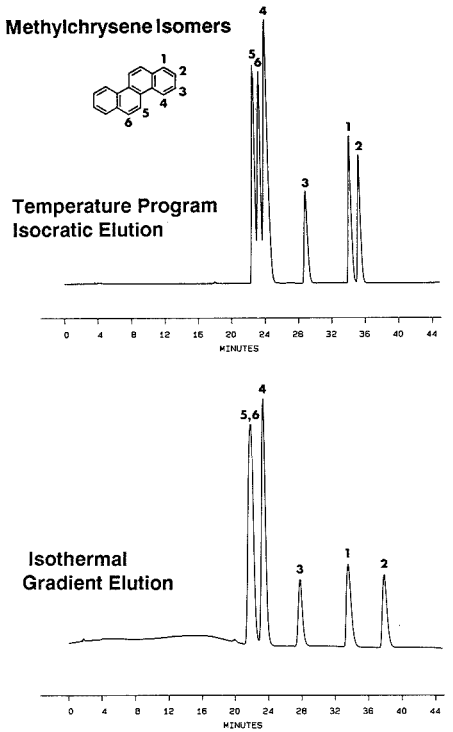

Figure 4. Separation of methylchrysene isomers on a Bakerbond wide pore C_{18} column: (a) temperature 27 °C, gradient elution, 60:40 ACN–H_2O to 85:15 ACN–H_2O over 40 min, 1 mL/min; (b) isocratic elution (100% ACN), temperature program, −25 to 20 °C over 40 min.

Separations of the methylchrysene isomers at ambient and subambient temperatures are illustrated in Figure 4. An isothermal separation of a mixture of the six methylchrysene isomers was carried out at 27 °C, with gradient elution, using a heavily loaded polymeric C_{18} phase (Bakerbond wide pore C_{18}). Four of the six isomers were resolved (5- and 6-methylchrysene coeluted), similar to the separation previously reported (*40*). Under the same conditions, only three isomers were resolved by using the monomeric column (not shown). In Figure 4, all six isomers are resolved with the Bakerbond C_{18} column under isocratic conditions using a subambient temperature program. Separation of 5- and 6-methylchrysene could only be achieved at low temperature. However, under isothermal conditions (−20 °C) the 1-, 2-, and 3-methylchrysene isomers were strongly retained, even using a pure acetonitrile mobile phase. By use of a temperature program, it was possible to separate the critical isomers, while permitting the more easily separated later eluting isomers to be eluted in a reasonable period of time. This separation demonstrates not only an exceptional degree of shape selectivity but the feasibility of temperature programming as an alternative to gradient elution in liquid chromatography.

RETENTION THEORY

In previous studies we have advanced a picture of solute retention referred to as the "slot model" (*30*, *31*). This model suggests that ordering within the bonded phase layer may be represented schematically as slots in a layer. Stated simply, solute penetration into these slots results in retention. Viewed in this way, predictions can be made on the effects that solute shape and bonded phase morphology will have on retention. A few trends can be summarized. Long narrow solutes are retained longer than square solutes of the same molecular weight. Similarly, planar solutes are retained longer than nonplanar solutes with similar overall structure. To view these trends in terms of the model, imagine a surface with a mixture of narrow and wide slots. Long narrow solutes, i.e., solutes with large length-to-breadth ratios (L/B) (*44*), will penetrate a larger number of the slots than square solutes. Because of this enhanced interaction with the bonded phase, retention is increased for long narrow solutes. A similar argument can be made for planar and nonplanar solutes with similar L/B ratios. Nonplanar solutes are more restricted from the slots than corresponding planar solutes. Interaction with the bonded phase is reduced, and retention is decreased for nonplanar molecules.

Phase morphology is an important aspect of this model. It is clear that changes in phase structure in some way affect the chromatographic properties of LC columns. For example, monomeric and polymeric C_{18} phases are both prepared from silanes with the same (C_{18}) alkyl substituents, yet the two

phases differ markedly in selectivity toward PAH and other classes of solutes. In previous work we suggested that these differences originate primarily from phase order (*30, 43*). In a comparison of phase selectivity between selected LC and GC columns, a close correspondence in retention behavior was observed between polymeric C_{18} columns in LC and a smectic liquid crystalline phase in GC (*43*). A high degree of shape recognition ability was observed for each column. Various PAH isomer mixtures were separated, and the elution orders for the two columns were nearly identical. In contrast, little shape recognition ability was found for monomeric C_{18} LC columns or methylsilicone GC columns and little separation of isomers was possible. Liquid crystalline phases have a higher degree of order resulting from alignment of the rodlike substituent molecules. By analogy, this suggests that, as with liquid crystal GC phases, phase ordering within polymeric C_{18} LC phases may be responsible for the selectivity exhibited by these phases. This order may result from loss of alkyl chain mobility within a rigid polymer layer.

Bonded phase length is another aspect affecting phase selectivity. In previous work we have shown that the highest degree of shape recognition was achieved with long chain length alkyl phases (*31*). This trend was observed for both monomeric and polymeric phases but was most dramatic with polymeric phases. As with liquid crystalline GC phases, the more extended alkyl phases exhibited the greatest shape selectivity for PAH isomers. This observation is consistent with the changes in selectivity that result from changes in phase morphology occurring at low temperatures.

The temperature-dependent change in retention behavior for monomeric and polymeric C_{18} phases observed in this study can thus be explained in terms of chain mobility and order. For pure long chain alkanes (e.g., octadecane), chain mobility decreases with temperature, ultimately forming an ordered crystalline solid. In the crystalline state, alkyl chains exist in the all-trans conformation, i.e., fully extended. Such crystalline ordering is not possible for bonded phases since alkyl chain spacing is constrained by the covalent point of attachment to the surface. However, reduction in bonded ligand mobility with temprature has been clearly demonstrated by NMR (*13*) and inelastic neutron scattering (*23*). Furthermore, bonded alkyl chains have been shown to straighten at reduced temperatures (*29*). Bends and kinks in alkyl chains give rise to specific transitions in IR spectra. These transitions decrease as a function of temperature. It can be concluded that alkyl bonded phases become more rigid and more rodlike at low temperatures and thus take on some of the characteristics of liquid crystals. This low-temperature ordering is most pronounced for polymeric bonded phases, for which chain motion is somewhat constrained even at ambient temperature.

It is informative to examine Van't Hoff plots for the three probes used in this work (Figure 5). Evidence for a phase transition is present in the plots for monomeric (Zorbax C_{18}) retention data. The transition appears to occur over an interval from about 40 to 50 °C. This transition temperature is similar to that reported by Morel and Serpinet (*14*) for densely bonded monomeric C_{18} phases. The presence of a transition is not observed for the polymeric phase. The lack of a transition may reveal much about polymeric phase morphology. Over the temperature interval investigated, alkyl chain association does not change abruptly with temperature. This suggests that constraints to chain mobility exist for polymeric phases that do not exist with monomeric phases. In contrast, it appears that sufficient freedom exists in monomeric phases to permit a transition in which alkyl chains are more associated with each other below the transition temperature. Selectivity does not change abruptly as a consequence of the transition. This is contrary to the proposed retention theory of Jinno et al. (*45*). They predicted that a critical change in selectivity toward PAHs would occur near the phase transition, due to a change from "solidlike" to "liquidlike" behavior. We have observed instead gradual changes in shape selectivity over the range −20 to 100 °C, for both monomeric and polymeric C_{18} phases (Figure 2). It should be noted, however, that the probes employed by Jinno et al. are substantially larger than those used in this work, and the results may not be directly comparable. Because changes in selectivity occur continuously as a function of temperature, it seems likely that the presence or absence of a phase transition is of secondary importance to the ordering of individual chains. The possibility of solvent-induced conformational changes for large nonplanar PAH has been advanced by Fetzer (*46*). He suggests that changes in retention behavior may be partly due to such conformational changes for the solute. However, because the conformation of planar PAH would be unaffected by changes in temperature, changes in selectivity for planar solutes that occur as a function of temperature would still be attributed to conformational changes of the bonded phase. A clear example is illustrated in Figure 3 for the separation of chrysene and benz[*a*]anthracene. The elution order observed at −8 °C (benz[*a*]anthracene, chrysene) is characteristic of polymeric C_{18} phases; at 25 °C the solutes coelute (characteristic of monomeric C_{18} phases).

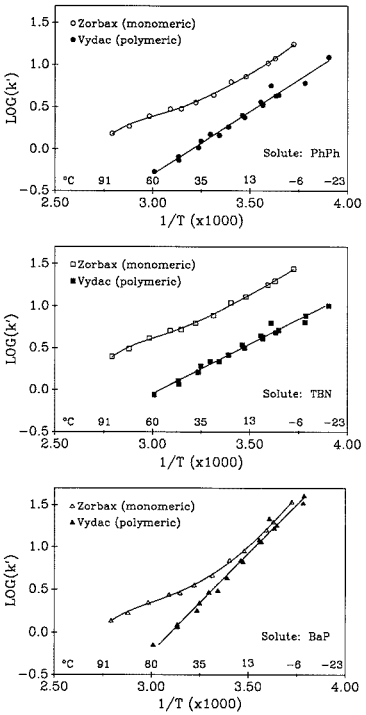

Figure 5. Van't Hoff plots for the phase selectivity test mixture on Zorbax C_{18} (monomeric) and Vydac 201TP C_{18} (polymeric) columns.

Further insight can be obtained through thermodynamic evaluation of the data. $\ln k'$ has been shown to be related to temperature through the following relation:

$$\ln k' = -\Delta H_{m\to s}/RT + \Delta S_{m\to s}/R + \ln \phi$$

where $\Delta H_{m\to s}$ and $\Delta S_{m\to s}$ are respectively enthalpies and entropies of transfer (mobile to stationary phase), R is the ideal gas constant, T is the absolute temperature K, and ϕ is the phase ratio (volume stationary phase/volume mobile phase). The slopes of the curves in Figure 5 are related to the enthalpy of the retention process, whereas the intercepts are related to the sum of the entropy change in solute retention plus the phase ratio. Numerical evaluation of the phase ratio is difficult at best, since the volume of the stationary phase available to the solute during retention must be estimated. Consequently, the calculation of absolute entropies of transfer is probably not justified. Enthalpies of transfer may be calculated without difficulty since knowledge of the phase ratio is unnecessary. Such calculations have been carried out for retention data at elevated temperatures (*20*). Below about 25 °C, slopes of the Van't Hoff plots for PhPh and TBN are similar, indicating that the enthalpies of transfer for these solutes at subambient temperatures are similar for the monomeric and polymeric C_{18} columns. For BaP, this condition is achieved at temperatures lower than 12 °C. Above these temperatures the curves diverge, indicating different enthalpies of transfer, perhaps due to dissociation of bonded phase chains with the monomeric phase at higher temperatures. The slopes of the BaP curves are significantly greater than for the other solutes. Thus, the enthalpy of transfer for BaP is greater than the other solutes. This suggests that BaP is able to interact more strongly with the bonded phase than with the other solutes, perhaps as a result of the planar nature of BaP compared to the nonplanar nature of PhPh and TBN.

The asymptotic nature of the Van't Hoff plots for BaP may be of some consequence, yet the significance is difficult to prove rigorously, since absolute entropies of transfer cannot be calculated. It is interesting, however, to assume that the phase ratios for the monomeric and polymeric columns are about the same. For PhPh and TBN, this means that these solutes are more ordered (i.e., the entropies of transfer are smaller) in the polymeric stationary phase than in the monomeric phase, at any given temperature. For BaP, the degree of ordering would be about the same for both phases, below about 12 °C. This ordering is consistent with the observations presented earlier for the polymeric phase compared to the monomeric phase. It can be stated without assumption that the sum $\Delta S_{m\to s}/R + \ln \phi$ is about the same for BaP on the two columns (<12 °C).

CONCLUSIONS

The variation in column selectivity with temperature is a universal effect that is not specific to a particular column brand or phase type. Because selectivity changes continuously and uniformly with temperature, retention characteristics may be adjusted as required for a given separation. The permissible temperature range is restricted only by the physical properties of the mobile phase employed. To a limited extent, phase selectivity previously attributed to polymeric phases can be mimicked by monomeric phases at low temperatures.

A major application of subambient liquid chromatography is the enhancement of shape selectivity in polymeric C_{18} phases. It has been demonstrated that this technique can be used to separate isomers previously not separable by LC. Evidence suggests that this increase in shape recognition ability is a result of an increase in phase order that occurs at low temperatures. Alkyl chain rigidity and reduced chain mobility result in a phase with liquid-crystal-like retention properties. Although the greatest shape selectivity effects are observed at −10 to −20 °C or lower, practical benefits may be achieved at more modest temperature reductions, e.g., between 0 and 10 °C. This work has concentrated on the effects of temperature on selectivity for polycyclic aromatic hydrocarbons. Studies of changes in selectivity with temperature for other classes of compounds (e.g., carotene isomers) are in progress, and similar trends have been observed.

LITERATURE CITED

(1) Sander, L. C.; Wise, S. A. *CRC Crit. Rev. Anal. Chem.* **1988**, *18*, 299.
(2) Katz, E. D.; Ogan, K. L.; Scott, R. P. W. *J. Chromatogr.* **1983**, *260*, 277.
(3) Gilpin, R. K.; Sisco, W. R. *J. Chromatogr.* **1980**, *194*, 285.
(4) Warren, F. V.; Bidlingmeyer, B. A. *Anal. Chem.* **1988**, *60*, 2821.
(5) Snyder, L. R.; Kirkland, J. J. *Introduction to Modern Liquid Chromatography*, 2nd ed.; Wiley-Interscience: New York, 1979.
(6) Knox, J. H.; Vasvari, G. *J. Chromatogr.* **1973**, *83*, 181.
(7) Melander, W. R.; Campbell, D. E.; Horvath, C. *J. Chromatogr.* **1978**, *158*, 215.
(8) Melander, W. R.; Stoveken, J.; Horvath, C. *J. Chromatogr.* **1981**, *199*, 35.
(9) Szanto, J. I.; Veress, T. *Chromatographia* **1985**, *20*, 596.
(10) Szanto, J. I. *Chromatographia* **1983**, *17*, 27.
(11) Chmielowiec, J.; Sawatzky, H. *J. Chromatogr. Sci.* **1979**, *17*, 245.
(12) Morel, D.; Serpinet, J.; Letoffe, J. M.; Claudy, P. *Chromatographia* **1986**, *22*, 103.
(13) Claudy, P.; Letoffe, J. M.; Gaget, C.; Morel, D.; Serpinet, J. *J. Chromatogr.* **1985**, *329*, 331.
(14) Morel, D. *J. Chromatogr.* **1982**, *248*, 231.
(15) Morel, D.; Serpinet, J. *J. Chromatogr.* **1980**, *200*, 95.
(16) Morel, D.; Serpinet, J. *J. Chromatogr.* **1981**, *214*, 202.
(17) Dawidowicz, A. L.; Rayss, J.; Suprynowicz, Z. *Chromatographia* **1983**, *17*, 157.
(18) Rayss, J. *Chromatographia* **1982**, *15*, 517.
(19) Hammers, W. E.; Verschoor, P. B. A. *J. Chromatogr.* **1983**, *282*, 41.
(20) Stalcup, A. M.; Martire, D. E.; Wise, S. A. *J. Chromatogr.* **1988**, *442*, 1.
(21) Hansen, S. J.; Callis, J. B. *J. Chromatogr. Sci.* **1983**, *21*, 560.
(22) Van Miltenburg, J. C.; Hammers, W. E. *J. Chromatogr.* **1983**, *268*, 147.
(23) Beaufils, J. P.; Hennion, M. C.; Rosset, R. *Anal. Chem.* **1985**, *57*, 2593.
(24) Kelusky, E. C.; Fyfe, C. A. *J. Am. Chem. Soc.* **1986**, *108*, 1746.
(25) Gangoda, M. E.; Gilpin, R. K. *J. Magn. Reson.* **1983**, *53*, 140.
(26) Gilpin, R. K.; Gangoda, M. E. *J. Chromatogr. Sci.* **1983**, *21*, 352.
(27) Sindorf, D. W.; Maciel, G. E. *J. Am. Chem. Soc.* **1983**, *105*, 1848.
(28) Bayer, E.; Paulus, A.; Peters, B.; Laupp, G.; Reiners, J.; Albert, K. *J. Chromatogr.* **1986**, *364*, 25.
(29) Sander, L. C.; Callis, J. B.; Field, L. R. *Anal. Chem.* **1983**, *55*, 1068.
(30) Wise, S. A.; Sander, L. C. *HRC CC, J. High Resolut. Chromatogr. Chromatogr. Commun.* **1985**, *8*, 248.
(31) Sander, L. C.; Wise, S. A. *Anal. Chem.* **1987**, *59*, 2309.
(32) Sander, L. C.; Wise, S. A. *Anal. Chem.* **1984**, *56*, 504.
(33) Sander, L. C.; Wise, S. A. *J. Chromatogr.* **1984**, *316*, 163.
(34) Wise, S. A.; Sander, L. C.; May, W. E. *J. Liq. Chromatogr.* **1983**, *6*, 2709.
(35) Sander, L. C.; Wise, S. A. *HRC CC, J. High Resolut. Chromatogr. Chromatogr. Commun.* **1988**, *11*, 383.
(36) Sander, L. C.; Wise, S. A. *Adv. Chromatogr.* **1986**, *25*, 139.
(37) Wise, S. A.; May, W. E. *Anal. Chem.* **1983**, *55*, 1479.
(38) Sentell, K. B.; Dorsey, J. G. *J. Chromatogr.* **1989**, *461*, 193.
(39) Miller, N. T.; Solak, D. J.; DiBussolo, J. M.; Sagliano, N.; Hartwick, R. A. Chromexpo '89, 1989, Abstract.
(40) Wise, S. A.; Bonnett, W. J.; Guenther, F. R.; May, W. E. In *Polynuclear Aromatic Hydrocarbons: Chemistry and Biological Effects*; Bjørseth, A., Dennis, A. J., Eds.; Battelle Press: Columbus, OH, 1980; p 791.
(41) Markides, K. E.; Nishioka, M.; Tarbet, B. J.; Bradshaw, J. S.; Lee, M. L. *Anal. Chem.* **1985**, *57*, 1296.
(42) Kong, R. C.; Lee, M. L.; Tominaga, Y.; Pratap, R.; Iwao, M.; Castle, R. N. *Anal. Chem.* **1982**, *54*, 1802.
(43) Wise, S. A.; Sander, L. C.; Chang, H.; Markides, K. E.; Lee, M. L. *Chromatographia* **1988**, *25*, 473.
(44) Wise, S. A.; Bonnett, W. J.; Guenther, F. R.; May, W. E. *J. Chromatogr. Sci.* **1981**, *19*, 457.
(45) Jinno, K.; Nagoshi, T.; Tanaka, N.; Okamoto, M.; Fetzer, J. C.; Biggs, W. R. *J. Chromatogr.* **1988**, *436*, 1.
(46) Fetzer, J. C. *Adv. Chem. Ser.* **1988**, *217*, 309.

RECEIVED for review January 19, 1989. Accepted May 2, 1989. Certain commercial equipment, instruments, or materials are identified in this report to specify adequately the experimental procedure. Such identification does not imply recommendation or endorsement by the National Institute of Standards and Technology, nor does it imply that the materials or equipment identified are necessarily the best available for the purpose.

Cycling Technique for the Determination of Femtomole Amounts of Sulfite

Regina Keil

Universität Tübingen, Institut für Botanik, Auf der Morgenstelle 1, D-7400 Tübingen, Federal Republic of Germany

Rüdiger Hampp*

Universität Tübingen, Institut für Botanik, Auf der Morgenstelle 1, D-7400 Tübingen, Federal Republic of Germany

Hubert Ziegler

Technische Universität München, Lehrstuhl für Botanik, Arcisstrasse 21, D-8000 München, Federal Republic of Germany

A micromethod for the fluorometric determination of sulfite is presented. This method is based on a coupled enzyme assay (sulfite oxidase, NADH-dependent peroxidase) the product of which (NAD) is amplified by enzymatic cycling. The assay is linear down to 150 fmol (standards, wine samples). With extracts of freeze-dried needle tissue (*Picea abies* L. (Karst)) the lower limit of detection was 290 fmol.

Sulfite has a long tradition in food chemistry as a preservative, an antioxidant, and an inhibitor of enzymatic and nonenzymatic browning (*1*). Especially in wine production the use of sulfite was customary for several centuries. The effects caused by SO_2 (or sulfite, when dissolved) depend not only on the initial levels applied but also on the actual amounts present in the respective tissue or food product during storage. As sulfite is not considered to be harmless to health (*2*), methods for a sensitive detection of sulfite are necessary.

In additon to its role in food chemistry SO_2 constitutes one of the major air pollutants in industrial and urban areas. It is now well documented that long-term exposures to SO_2, even at concentrations that do not result in any visible signs of injury, cause reductions in plant yield (*3*). Possible interactions of sulfite with metabolic reactions are either deduced from in vitro experiments with cellular organelles or tissue extracts (*4*) or from calculations on model systems (*5*). In order to correlate these observations with in vivo effects the actual concentration of sulfite in polluted tissue has to be known. Methods currently available (and lower limit of detection; 1/mL), such as iodometry (7.5 nmol (*6*)), reaction with 5,5′-dithiobis(2-nitrobenzoic acid) (3 nmol (*7*)) or with 3-methyl-1,2-cyclopentanodione dithiosemicarbazone (10 nmol (*8*)), sulfite oxidase electrode (about 15 nmol (*9*)), HPLC (30 nmol (*10*, *11*), or HPIC (*12*), are not sufficiently sensitive to assay sulfite levels in plant tissue (*4*, *11*). These are obviously very low (*12*).

As we are interested in pollution-dependent alterations in cellular biochemistry (in connection with forest decline) we tried to establish a method for the determination of tissue sulfite with increased sensitivity. In this paper we present an assay which measures sulfite at concentrations of below 200 fmol.

EXPERIMENTAL SECTION

Experimental Rationale. The assay principle is based on the following reactions:

$$SO_3^{2-} + O_2 + H_2O \xrightarrow{\text{sulfite oxidase}} SO_4^{2-} + H_2O_2 \quad (1)$$

$$H_2O_2 + NADH + H^+ \xrightarrow{\text{NADH peroxidase}} 2H_2O + NAD^+ \quad (2)$$

Sulfite oxidation yields H_2O_2 which is then reduced by an NADH-dependent peroxidase. The stoichiometrical consumption of NADH is recorded (*13*). With UV spectroscopy or fluorometry of NADH, the lower limit of detection is between 0.2 and 1 nmol. The sensitivity of this assay can be significantly increased by using the above reactions as a "specific step" which is coupled to an enzymatic cycling procedure for one of the products, i.e., NAD (*14*, *15*).

Reagents. *Enzymes.* Sulfite oxidase (Sulf-OD, EC 1.8.3.1 from chicken liver, 12 units/mL), NADH peroxidase (NADH-POD, EC 1.11.1.1 from *Streptococcus faecalis*, 45 units/mL), and horseradish peroxidase (HRP, EC 1.11.1.7 from horseradish, 250 units/mg), as well as the enzymes used for cycling, were obtained from Boehringer Mannheim. Sulf-OD and NADH-POD were dialyzed against 25 mM TRIS buffer. HRP (lyophilized) was dissolved in reaction buffer.

Buffers. 2-Amino-2-methyl-1-propanol (AMP), *N*-tris(hydroxymethyl)methyl-2-aminoethanesulfonic acid (TES), and 3-(*N*-morpholino)propanesulfonic acid (MOPS) were obtained from Sigma (Deisenhofen, FRG), 2-(*N*-morpholino)ethanesulfonic acid (MES), imidazole, *N*-(2-hydroxyethyl)piperazine-*N*′-2-ethanesulfonic acid (HEPES), triethanolamine hydrochloride (TEA), and tris(hydroxymethyl)aminomethane (TRIS) were from Boehringer Mannheim.

Stabilizing Reagents. Ethylenediaminetetraacetic acid (EDTA) was obtained from Sigma, and water-insoluble poly(vinylpyrrolidone) (PVP) was obtained from Serva (Heidelberg, FRG).

Extraction Medium. MOPS–NaOH (50 mM, pH 7), containing 1.7 mM EDTA, was used for the dilution of sulfite stock solutions or wine samples and for the extraction of lyophilized spruce needle homogenates.

Sulfite Solutions. Sodium sulfite (20 mM, Merck, Darmstadt, FRG) was dissolved in doubly distilled water. This stock solution was used for stability tests and for the assay with HRP. A stock solution with higher stability (4 mM sulfite, containing 18 mM acetaldehyde) was prepared according to Beutler (*16*).

Sulfite Reagent. The reagent stock was made from TEA–NaOH (300 mM, pH 8), NADH (0.1 mM), and EDTA (3 mM). Assay concentrations were obtained by dilution (1:3).

Apparatus. *Spectrophotometry.* Absorption measurements were made with a Uvicon 860 UV-vis spectrophotometer (Kontron, München, FRG). Fluorometry was with a Farrand ratio-2 fluorometer (Farrand, New York). Narrow-band interference filters with a half-width of about 10 nm were used for excitation (340 nm) and emission (450 nm).

Homogenization of frozen needle samples (−80 °C) was under cooling with liquid nitrogen with a Micro Dismembrator II (Braun, Melsungen, FRG). This resulted in an average particle size well below 100 μm.

* Author to whom correspondence should be addressed.

0003-2700/89/0361-1755$01.50/0

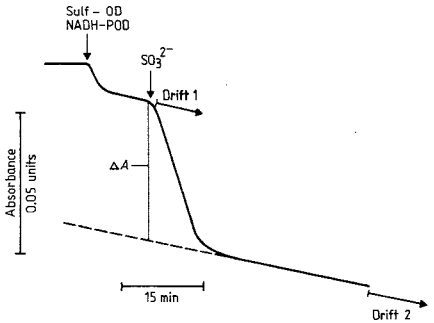

Figure 1. Kinetics of the photometric determination of sulfite. The difference in extinction (ΔA) is determined by extrapolation.

Sampling. Spruce needle material (*Picea abies* L. (Karst.)) was obtained from two open top chambers (University of Hohenheim, FRG) (*17*). In both chambers young spruce trees (about 5 years old) were permanently fumigated with SO_2 (between 0.01 and 0.04 ppm) and sprinkled with water of pH 4 (*17*). Other samples were from spruce trees exposed to environmental levels of SO_2 (Edelmannshof, Welzheimer Forst, near Stuttgart, FRG; 3 h mean values for SO_2 during summer 1986 (May through September) 34–130 $\mu g/m^3$ air = 0.013 to 0.05 ppm). In April, August, and November 1986, needles (up to 3 years old) were collected and metabolically quenched in liquid nitrogen. Homogenization under cooling with liquid nitrogen (see above, 90 s) was in the presence of freshly distilled acetaldehyde. Acetaldehyde forms a stable adduct with sulfite, and this was shown to be a prerequisite for a quantitative recovery of added, internal sulfite standards. Reconstitution of needle lyophilizates resulted in a pH of 4. At this pH the equilibrium in aqueous solution between sulfite, bisulfite, and SO_2 is shifted toward SO_2. Subsequent loss of SO_2 to the gas phase is prevented by acetaldehyde. Two milligrams of the lyophilized powder was mixed with 5 mg of insoluble poly(vinylpyrrolidone) (PVP, Polyclar AT, Serva) and extracted with 1 mL of hot (95 °C) extraction medium (5 min). After cooling on ice insoluble material was pelleted (10 000 g, 8 min, 4 °C).

Wine samples (white German wines Silvaner Scheurebe, Qualitätswein, Riesling, and Morio-Muskat and rosé wine Portugieser rosé) were diluted 1:50 with extraction solution and assayed without further manipulation.

Sulfite Determination. *Spectrophotometric Method, 10^{-9} mol.* The assay described by Beutler and Schütte (*13*) was used in a modified way. The sulfite reagent contained the following (final concentrations in the assay): TEA–NaOH (pH 8), 0.1 M; NADH, 0.033 mM; EDTA, 1 mM. The amounts of enzymes were equivalent to 33 munits (NADH-POD) and 20 munits (Sulf-OD) per milliliter assay volume. A feature of this assay is a background reaction caused by some kind of NADH–oxidase activity which is part of the NADH–POD. This unspecific NADH consumption is independent on the presence of sulfite (Figure 1) and has to be corrected for (compare legend to Figure 1). Efforts to decrease this side reaction (addition of Mn^{2+} as radical scavenger, $Cu^{+/2+}$ (*18*, *19*), ascorbic acid (*18*), reduced glutathione (*20*), and cyanide, H.O. Beutler, personal communication) were not successful (*21*).

In order to get a complete recovery of sulfite which, in the presence of cations such as Fe^{3+} and depending on pH, is easily oxidized (*22*), EDTA was added. EDTA also decreased the unspecific oxidation of NADH to some extent.

Indirect Fluorometry, 10^{-13} mol (Cycling). In this case the specific step (reactions 1 and 2) was combined with an enzymatic amplification of NAD resulting from the NADH–POD reaction.

Oxidation of sulfite with stoichiometric formation of NAD was in a total volume of 30 μL and with decreased amounts of enzymes (munits/mL: NADH–POD, 17; Sulf-OD, 10). Typical sample volumes added to the assay were 2 μL. All pipetting steps were on ice. The reaction was started by rapid warming to 25 °C (water bath). Usually, after 15 min of incubation (complete oxidation of sulfite) the reaction was stopped with HCl (final concentration 0.2 M) and the samples were kept at 95 °C for 5 min. This causes a quantitative breakdown of NADH without affecting NAD.

Two-microliter aliquots were added to 50 μL of NAD cycling reagent (350 mM ethanol, 2.5 mM β-mercaptoethanol, 2.5 mM oxaloacetic acid, 0.025% (w/v) bovine serum albumin (fraction V), 44 units/mL alcohol dehydrogenase (ADH), 15 units/mL malate dehydrogenase (MDH), 125 mM TRIS–HCl (pH 8.0)). In this step, which is performed in fluorometer tubes, the pyridine nucleotide is alternatively reduced (ADH) and oxidized (MDH). The amounts of enzymes added result in about 5000 cycles/h (25 °C). After 1 h the cycling step is stopped by heating the samples in a boiling water bath for 3 min. Malate, formed during cycling, is assayed by oxidation (MDH) and stoichiometric formation of NADH (indicator step). The indicator reagent (1 mL) consisted of glutamic acid (sodium salt), 10 mM, NAD, 0.2 mM, MDH, 3 units/mL, glutamate oxaloacetate transaminase, 0.5 units/mL, and 2-amino-2-methylpropanol hydrochloride, 50 mM (pH 9.9). For more detailed information see ref 14 and 15.

Controls were run either with sample but no Sulf-OD or without sample addition (unspecific NADH oxidation). Recovery of sulfite was routinely checked with internal standards.

All assays were run with at least three parallels.

Table I. Effects of Different Buffers on the Recovery of Sulfite Standards[a]

solvent	pH	recovery, %
Aqua bidest	6.5	18
MES	6.0	80
imidazole	7.0	55
TES	7.0	81
MOPS	7.0	100
HEPES	7.5	79
TRIS	8.0	77
AMP	9.0	98

[a] All solutions were kept at 95 °C for 5 min. Recovery is given in percent of the content of the standardized solution before heating.

RESULTS AND DISCUSSION

Stability of Sulfite in Different Buffers. In Table I the effects of different buffers (50 mM) on the stability of sulfite are compared. Sulfite solutions (1 mM) were prepared with the different buffers and photometrically standardized. These solutions were then used to determine a possible loss of sulfite during the extraction procedure (95 °C, 5 min). The large difference in recovery of sulfite between buffered and unbuffered solutions is evident. Rates of recovery were highest with AMP and MOPS. Because of its lower pK_a value (7.2) MOPS was used for sample extraction.

Substitution of NADH–POD by Horseradish Peroxidase (HRP). Owing to the unspecific NADH oxidation by NADH–POD (Figure 2a) we tested another peroxidase, HRP. Although HRP also exhibits some NADH oxidase activity, this unwanted reaction can be inhibited (*18–20*). With 0.033 mg/mL HRP direct assay) 1 μM Cu^{2+} completely inhibited the unspecific oxidation of NADH without affecting the peroxidation activity of HRP (Figure 2b). However, the combination of this modified specific step with enzymatic cycling was only possible with sulfite standards but not with extracts from spruce needles. Presumably, residual phenols contained in the needle extract (not completely removed by PVP) are responsible for this effect. According to Yang (*23*) the peroxidase–H_2O_2 enzyme complex promotes the oxidation of phenols to phenoxy radicals. With these radicals sulfite will start a chain reaction which leads to the complete oxidation of sulfite. Extremely reactive intermediates of this process can cause the destruction of NADH without producing NAD. Thus, needle extracts were assayed with the NADH–POD system.

Cycling Assay. In order to check for interferences of specific step components with the NAD cycle, the fluores-

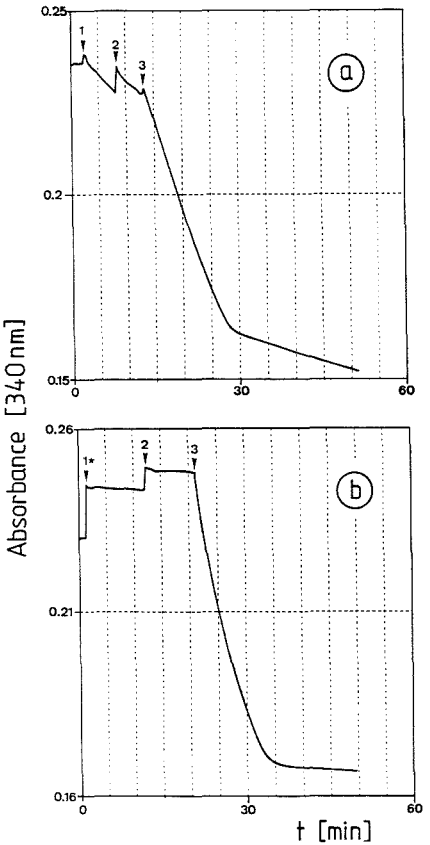

Figure 2. Kinetics of the sulfite oxidation with the NADH–POD system (a) and the HRP system (including 1 μM $CuCl_2$) (b). In b there is no unspecific background reaction. Numbers indicate addition of (1) NADH-POD, (1*) HRP, (2) Sulf-OD, and (3) sulfite standard (10 nmol).

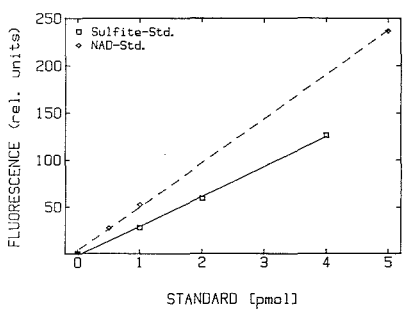

Figure 3. Cycling assay for sulfite, fluorescence yield with sulfite (□) and NAD standards (◇).

cences resulting from sulfite and NAD standards at identical concentrations were compared. Figure 3 shows that NAD standards (0.5–5 pmol) added to the cycling system without the introduction of a specific step aliquot resulted in a higher fluorescence yield compared to the cycling of NAD resulting from sulfite oxidation (a 2-μL aliquot of the specific step is

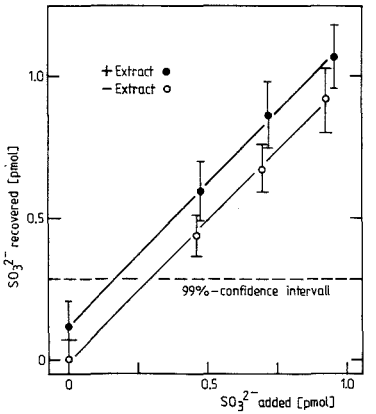

Figure 4. Cycling assay for sulfite. Sulfite standards (0.5 to 1 pmol) were assayed in the absence (○) and presence (●) of spruce needle extract. The difference between both curves (± extract), which is 112 fmol, results from sample sulfite.

introduced into the cycling assay). This decrease in cycling rate (about 40%; compare Figure 3) should thus be caused by a transfer of specific step solutes. However, due to internal standardization of the specific step reaction, this interference is not a problem.

Linearity of the Sulfite Determination. Sulfite standards with and without extracts from spruce needles (control needles: from trees showing no signs of pollution effects) were measured in order to check for linearity of the coupled assay. Figure 4 shows that under both conditions the fluorescence increase with increasing concentrations of sulfite was linear, with correlation coefficients higher than 0.999 (slopes, 1.01 (plus extract), 1.0 (without extract); intercepts, 120 fmol (plus extract), 8 fmol (without extract)). The difference in both intercepts (112 fmol) should result from sample sulfite. As in the presence of needle extract the limit of detection (99% confidence interval) was 290 fmol, this sample content cannot be reliably determined. In the absence of needle extract the limit of detection was as low as 130 fmol of sulfite. For wine the lower limit was found to be in the same range as with buffer only (140 fmol). Linearity was maintained up to 10 pmol. Possibly owing to extract constituents, increasing both the volume of the extract added to the specific step or the extract concentration above the values given in this paper resulted in a decrease in yield.

Recovery of internal sulfite standards added to needle homogenates with the extraction buffer was about 90%.

Sulfite in Spruce Needle Material. None of the samples (1- to 3-year-old needles) contained amounts of sulfite sufficiently high to permit its detection within the 99% confidence interval.

With a level of probability of 95% sulfite was detected in 1-year-old needles from the open top chambers and in two samples (1-year-old and 3-year-old needles) taken from spruce trees at their natural location (Welzheimer Forst). The amount of sulfite detected in these samples was 1.1 to 1.3 nmol/mg dry weight (needle dry weight was about 45% of fresh weight). This amount corresponds to a cell sap concentration of about 1 mM. In spite of the high sensitivity of the assay, tissue levels of sulfite of less than 1 nmol/mg dry weight cannot be reliably assayed. However, tissue concentrations of sulfite are more likely to be in the micromolar range (*12*). Thus the results given here for needle extracts indicate that only under increased levels of SO_2 pollution (or slow

decomposition of SO_2 within the tissue) sulfite can be detected with minor significance.

Sulfite in Wine. With wine samples "sulfite cycling" worked without problems. Using this technique we were able to detect significant amounts of sulfite in different provenances of wine which were declared as sulfite free (according to current determination methods). These wines contained between 50 and 90 μM sulfite.

A comparison between the limits of detection of sulfite in the original method (15 nmol) and in the cycling assay (130 fmol) shows that the method reported in this communication offers an increase in sensitivity by a factor of 10^5. However, the degree to which this increase in sensitivity can be utilized depends on the sample properties. The determination of SO_3^{2-} in spruce needle extracts is restricted to values of more than 1 nmol/mg dry weight. This is possibly due to phenolic compounds or other ingredients. Nevertheless with this method the amount of sulfite in SO_2-stressed plants can be determined. This may open access to other complex sample matrices.

ACKNOWLEDGMENT

We wish to thank Dr. T. Benz for constructive advice.

Registry No. SO_3^{2-}, 14265-45-3.

LITERATURE CITED

(1) Joslyn, M. A.; Braverman, J. B. S. *Adv. Food Res.* **1954**, *5*, 96.
(2) Baker, G. J.; Collett, P.; Allen, D. H. *Med. J. Aust.* **1981**, *2*, 614.
(3) Roberts, T. M.; Darrall, N. M.; Lane, P. *Adv. Appl. Biol.* **1984**, *9*, 1.
(4) Ziegler, I. *Res. Rev.* **1975**, *56*, 79.
(5) Pfanz, H.; Martinoia, E.; Lange, O.-L.; Heber, U. *Plant Physiol.* **1987**, *85*, 928.
(6) Rebelein, H. *Chem. Mikrobiol. Technol. Lebensm.* **1973**, *2*(4), 112–121.
(7) Humphrey, R. E.; Ward, M. H.; Hinze, W. *Anal. Chem.* **1970**, *42*(7), 698–702.
(8) Laila, A. *Anal. Lett.* **1987**, *20*(9), 1333–1345.
(9) Smith, V. J. *Anal. Chem.* **1987**, *59*, 2256–2259.
(10) Schwedt, G.; Bäurle, A. *Fresenius' Z. Anal. Chem.* **1985**, *322*, 350–353.
(11) Grill, D.; Esterbauer, H. *Phyton (Austria)* **1973**, *15*(1-2), 87–101.
(12) Wellburn, A. R. *New Phytol.* **1985**, *100*, 329–339.
(13) Beutler, H. O.; Schütte, I. *Deutsche Lebensm. Rundsch.* **1983**, *79*(10), 323–330.
(14) Lowry, O. H.; Passonneau, J. V. *A Flexible System of Enzymatic Analysis*; Academic Press: New York, 1972.
(15) Kato, T.; Berger, S. J.; Carter, J. A.; Lowry, O. H. *Anal. Biochem.* **1973**, *53*, 86–97.
(16) Beutler, H. O. "Sulfit. UV-Test". In *Methoden der biochemischen Analytik und Lebensmittelanalytik mit Test-Combinationen*; Boehringer Mannheim GmbH: Mannheim, 1986; pp 116–117.
(17) Seufert, G.; Arndt, U. *AFZ, Allg. Forst Zeitschrift* **1985**, 1/2, 13–18.
(18) Klebanoff, S. J. *J. Biol. Chem.* **1959**, *234*(9), 2480–2485.
(19) Akazawa, T.; Conn, E. E. *J. Biol. Chem.* **1958**, *232*, 403–415.
(20) Klebanoff, S. J.; Yip, C.; Kessler, D. *Biochim. Biophys. Acta* **1962**, *58*, 563–574.
(21) Keil, R. "Biochemische Untersuchungen an gesunden und geschädigten Fichtennadeln (Picea abies) in Abhängigkeit von Nadelalter und Vegetationsperiode: Sulfit, Malat, Pyridinnukleotide", Dissertation, Fakultät f. Biologie der Eberhard-Karls-Universität, Tübingen, F. R.G., 1988, pp 52–54.
(22) Cotton, F. A.; Wilkinson, G. *Advanced Inorganic Chemistry*; Wiley & Sons: New York, 1980; pp 532–533.
(23) Yang, S. F. *Arch. Biochem. Biophys.* **1967**, *122*, 481–487.

RECEIVED for review January 25, 1989. Accepted May 1, 1989. This project was financed by grants from the "Projekt Europäisches Forschungszentrum für Massnahmen zur Luftreinhaltung" (PEF) and the European Community.

Determination of Lead in Antarctic Ice at the Picogram-per-Gram Level by Laser Atomic Fluorescence Spectrometry

Michail A. Bolshov,[1] Claude F. Boutron,*[2] and Aleksandr V. Zybin[1]

Institute of Spectroscopy, USSR Academy of Sciences, Troitzk, 142092 Moscow Region, USSR, and Laboratoire de Glaciologie et Géophysique de l'Environnement du CNRS, Domaine Universitaire, 2, rue Molière, B.P. 96, 38402 St. Martin d'Hères Cedex, France

We present here preliminary results of the measurement of Pb in ancient Antarctic ice down to the sub-pg/g level by laser excited atomic fluorescence spectrometry with electrothermal atomization. Detailed calibration of the spectrometer was successfully achieved down to the sub-pg/g level by using ultralow concentration Pb standards. The ice core samples, which had previously been mechanically decontaminated, were directly analyzed for Pb by using very small volumes (20 μL only), without any preconcentration step or chemical treatment. The results are in very good agreement with those previously obtained for the same ice samples by isotope dilution mass spectrometry.

1. INTRODUCTION

For 20 years there has been a growing interest in the investigation of the occurrence of Pb (and of several other heavy metals such as Cd, Cu, Zn, Hg, ...) in the well-preserved dated snow and ice layers deposited in the central areas of the remote Antarctic and Greenland ice sheets (*1–14*). This is indeed a unique way to reconstruct the past natural tropospheric fluxes of this highly toxic heavy metal on a global scale and to determine to what extent these fluxes are now influenced by human activities.

Such investigation has unfortunately proved to be very difficult because of the extremely low concentrations to be measured. As an illustration, Pb concentrations in Holocene Antarctic ice have recently been shown to be as low as about 0.4 pg of Pb/g (*6, 9*). First of all, it is mandatory to decontaminate the snow or ice samples before final analysis, since most available samples are more or less contaminated on their outside, regardless of the precautions taken to collect them cleanly in the field (*2–4, 6–9, 11–14*). Ultrasensitive analytical techniques must then be used. Due to the extremely low concentrations involved, ultraclean procedures are required throughout the entire analytical procedure, from sample decontamination to final analysis (*11, 14–16*).

Up to now, the analytical techniques that have been used for the final analysis of the decontaminated samples are either

* Author to whom correspondence and reprint requests should be addressed.
[1] Institute of Spectroscopy.
[2] Laboratoire de Glaciologie et Géophysique de l'Environnement.

0003-2700/89/0361-1758$01.50/0

isotope dilution mass spectrometry (IDMS) (*1–3, 6–9*) or flameless atomic absorption spectrometry (FAAS) (*4, 5, 10, 13*). The first one of these two methods has the advantage of being absolute. Unfortunately, these two techniques do not allow a direct measurement of Pb at the extremely low concentration levels involved. For IDMS, a complicated chemical treatment, including an extraction into $CHCl_3$ and dithizone, is required (*1–3, 6–9, 15*). For FAAS, a preconcentration (by nonboiling evaporation or by adsorption onto tungsten wire loops) is necessary (*4, 10, 13, 17, 18*). These time-consuming chemical treatments or preconcentrations are especially difficult to perform at the pg/g level, and rather large samples (~30 to 500 g) are required in order to get high enough Pb amounts for the final analysis and to keep these amounts higher than the contamination contributions from reagents and ware.

The newly developed technique of laser excited atomic fluorescence with electrothermal atomization (LEAF-ETA) (*19–29*) offers a promising way to allow a direct and fast analysis of the decontaminated samples, using very small samples, without any preliminary chemical treatment or preconcentration. We present here the results of the first direct LEAF-ETA analyses of Pb down to sub pg of Pb/g concentration levels in Antarctic ancient ice using very small aliquots (20 μL only). These results are compared with those previously obtained for the same ice samples by IDMS (*6, 9*).

2. SAMPLE PREPARATION

The samples analyzed by LEAF-ETA in this work are 14 sections of the 905 m Dome C deep Antarctic ice core (*30*). This core, which covers the past 40 000 years (*31*) was thermally drilled at Dome C (77°39′S, 124°10′E) in a dry hole that had not been filled with a wall-retaining fluid. They were decontaminated and prepared inside Patterson's clean laboratory (*15*) at the California Institute of Technology (Caltech, Division of Geological and Planetary Sciences), Pasadena, CA.

Each core section (diameter 10.5 cm, length 15–30 cm) was transported frozen from Antarctica to Caltech packed in double, sealed polyethylene bags. It was then decontaminated inside the Caltech clean laboratory by mechanically chiseling successive veneers of ice progressing from the outside to the interior of the core using ultraclean stainless steel chisels, inside a cooled double-walled nitrogen-flushed ultraclean polyethylene tray. The chiseling procedure has been described in detail elsewhere (*3, 6, 12*). The remaining inner core so obtained was 2 to 4 cm in diameter. Only these 14 inner cores were analyzed by LEAF-ETA.

Each inner core was melted overnight at room temperature inside the Caltech clean laboratory in ultraclean 1-L conventional polyethylene beakers. Twice distilled ultrapure HNO_3 prepared at the U.S. National Institute of Standards and Technology (NIST) (*32, 33*) was then added to make a 0.1% HNO_3 solution. The Pb content of the batch of acid had previously been shown by IDMS to be 8 pg of Pb/g (*6, 7*). The acidified solution was allowed to sit for 2 h. A 50–100-mL aliquot was then taken into 250-mL conventional polyethylene bottles packed inside acid-cleaned polyethylene bags. It was immediately refrozen and transported frozen to the Laboratoire de Glaciologie et Géophysique de l'Environnement (LGGE), Saint Martin d'Hères, France.

Inside the LGGE clean laboratory (*17*), these aliquots were melted at room temperature, and a 5–10-mL subaliquot was taken into 30-mL conventional polyethylene bottles packed inside acid-cleaned polyethylene bags. These subaliquots were then transported frozen to the Institute of Spectroscopy in Troitzk, USSR. Great precautions were taken during these successive aliquotings in order to ensure an even distribution of the solid microparticles which might be present in the ice.

The 1-L conventional polyethylene beakers and the 250-mL conventional polyethylene bottles had been cleaned inside the Caltech clean laboratory by a $CHCl_3$ rinse, at least 3 days at 55 °C in 25% reagent grade HNO_3 (Baker), at least 3 days at 55 °C in 0.1% HNO_3 (NIST twice distilled diluted in Caltech quartz distilled water (QDW); the Pb content of this water is 0.16 pg of Pb/g (*34*)), and finally at least 3 days in another 0.1% NIST HNO_3 bath at 55 °C. The beakers were kept in the last bath for several months untill use. The bottles were kept filled with 0.1% NIST HNO_3 diluted in QDW for several months at room temperature before use.

Table I. Graphite Cup Atomizer: Working Conditions for Pb

step	temp, °C	ramp rate, °C/s	duration, s
evaporation	95	40	30
ashing	600	80	10
atomization	1600	700	4
firing	2000	700	5
cooling	2000–20		20

The 30-mL conventional polyethylene bottles had been cleaned inside the LGGE clean laboratory with a procedure similar to that described in the previous section. The LGGE acid baths were however made from the LGGE Maxy ultrapure water (the Pb content of this water has been shown by IDMS to be 0.27 pg of Pb/g (*34*)), and the bottles were allowed to sit in each of the three successive baths for at least 2 weeks.

Pb contamination introduced during the mechanical chiseling, from the NIST HNO_3, from the walls of the beakers, bottles, and micropipets, and from the air in the clean laboratories was accurately determined from numerous blank determinations. For the 20-μL samples which will be used for the LEAF-ETA measurements, the corresponding Pb contamination value is found to be about 0.11 pg of Pb/g, originating mainly from chiseling (about 0.1 pg of Pb/g) and from HNO_3 (0.01 pg of Pb/g). This represents from 0.5 to 30% of total Pb present in these 20-μL samples, depending on concentrations. It must be emphasized that for the IDMS measurements of the same ice samples (*6, 9*), the relative contribution of the Pb contamination to the total Pb present in the IDMS sample was higher (from 5 up to 75%) (*6, 9*) because the chemical treatment from sample melting to the final sample of isolated Pb on the filament of the mass spectrometer is much more complicated than for the LEAF-ETA measurements.

3. LASER EXCITED ATOMIC FLUORESCENCE SPECTROMETER

The LAFAS-1 spectrometer used in this work comprises four basic units: a radiation source, an electrothermal atomizer, a recording system, and a computer control system. Each of the four basic units is described in detail elsewhere (*29*). We give here only brief descriptions of these units.

The radiation source consists of a tunable dye laser (DL) pumped by a XeCl excimer laser. An oscillator–amplifier scheme of DL is used. An original grating assembly and a control unit (*35*) enable tuning of the DL wavelength by a microcomputer. Second harmonic generation of the DL in a temperature-stabilized KDP crystal is used to obtain tunable UV radiation. The maximum power of the second harmonic generation is about 3 kW. Pb atoms are excited at the 283.3-nm line (transition 6 $p^2 {}^3P_0$–7 $s^3 P_1^0$); fluorescence is recorded at 405.8 nm (transition 6 $p^2 {}^3P_2$–7 $s^3 P_1^0$). The graphite cup of the atomizer is pyrotically coated. Argon is used as purge gas (2 L/min). The heating regimes for the graphite cup atomizer are shown in Table I.

Fluorescence radiation is collected at an angle of 90° by a telescopic system on the entrance slit of the compact monochromator (relative aperture 1:3.7, reciprocal linear dispersion of 6.3 nm/mm). Fluorescence is recorded by a photomultiplier tube (PMT) FEU-130 (or FEU-100) and a charge sensitive analog to digital converter (ADC). The ADC output code A (numerical value) is fed to the computer for further processing. Commercial neutral light filters are used before the entrance slit of the monochromator to attenuate the fluorescence signal.

To reduce contamination problems, the whole spectrometer was located inside a specially designed room supplied with filtered air. Moreover, the electrothermal atomizer, the recording system, and a small table covered with polyethylene film onto which the samples and standards were handled were placed inside a clean chamber (2.5 × 1.7 × 2.8 m). The ventilation system of the chamber provided the high efficiency filtering of the air and

Table II. Preparation of the Very Low Concentration Multielemental Standards for LEAF-ETA

element	chemical form	solvent	volume diluted in the 200-mL flask, μL	concn ranges in the final standards, pg/g
Ag	metal	HNO_3	20	0.2–100
Al	metal	HCl	2000	20–10000
As	metal	HNO_3	10	0.1–50
Ca	carbonate	HNO_3	500	5–2500
Cd	metal	HNO_3	10	0.1–50
Co	metal	HNO_3	10	0.1–50
Cu	metal	HNO_3	100	1–500
Fe	metal	HNO_3	2000	20–10000
Hg	chloride	H_2O	200	2–1000
K	nitrate	HNO_3	500	5–2500
Mg	oxide	HNO_3	500	5–2500
Mn	metal	HNO_3	100	1–500
Mo	metal	aqua regia	10	0.1–50
Na	bicarbonate	HNO_3	500	5–2500
Ni	metal	HNO_3	100	1–500
Pb	oxide	HNO_3	100	1–500
Se	dioxide	H_2O	10	0.1–50
Ti	metal	HCl	20	0.2–100
Vd	pentaoxide	HCl	20	0.2–100
Zn	metal	HNO_3	20	0.2–100

laminar vertical flow of clean air inside the chamber.

Both the samples and the standards were introduced into the graphite cup of the atomizer with a 20-μL Eppendorf micropipet. The polypropylene tips of the micropipet were cleaned by dipping them for a few minutes into concentrated reagent grade HNO_3 and then several successive rinsings with 1% HNO_3 (NIST twice distilled diluted in LGGE ultrapure water). The operator wore full clean room clothing and polyethylene gloves.

4. RESULTS AND DISCUSSION

4.1. Calibration of the Spectrometer. Detailed calibration was performed with synthetic acidified (0.1% NIST HNO_3) multielemental standards. These standards contained 19 elements, Table II, according to typical elemental concentration ratios of Antarctic ice. They were prepared inside the LGGE clean laboratory from Baker or Fisher certified atomic absorption standards (1000 ppm solutions). An intermediate solution containing all the 19 elements was first prepared by diluting 10–500 μL of these standards in 200 mL of LGGE ultrapure water in a 200-mL polypropylene volumetric flask, Table II. The low concentration standards were then made by diluting 2–1000 μL of this intermediate solution in 1000 mL of LGGE ultrapure water in a preconditionned ultraclean 1000-mL conventional polyethylene bottle. The standards were immediately acidified inside the bottle by adding 1 mL of NIST HNO_3 (measured in a specially designed FEP Teflon graduated cylinder). The standards were then stored frozen in 30-mL preconditionned conventional polyethylene bottles packed inside acid-cleaned sealed polyethylene bags. Cleaning procedures for the bottles and for the micropipet's tips were similar to those described in the previous section. Pb concentration in the standards ranged from 1 to 500 pg of Pb/g. The corresponding concentration ranges for the 18 other elements are given in Table II.

Each of the standards was measured 2 to 3 times. Results of these determinations are shown in Table III. A regression line was constructed by using the least-squares method, in the form

$$\log A_i = \log a + b \log C_i \qquad (1)$$

where A_i is the ADC code proportional to the intensity of the fluorescence (arbitrary units), C_i is the Pb concentration in the i^{th} standard, and b is the slope of the regression line.

Table III. Calibration of the Spectrometer: Measured Analytical Signals and Mean Calculated Net Signals for Each of the Standards[a]

Pb concn in std, pg/g	analytical signal A, AU	mean net signal S,[b] AU
(0.28)[c]	272, 69, 229, 145	76
1	527, 270, 417	302
2.5	570, 790	577
5	1175, 1040	1005
7.5	1453, 1230, 1256	1210
10	2225, 2202, 2344	2154
25	4120, 4700, 4446	4319
50	9104, 7843	8371
100	15650, 16494	15969
250	40447, 38874	39558

[a] The signals obtained for LGGE ultrapure water are also given. [b] The net signal is calculated using relation $S = \bar{A} - \bar{B}$ where $\bar{A}$ represents the mean analytical signal and $\bar{B}$ the mean background value ($\bar{B}$ = 103 AU). [c] LGGE ultrapure water.

Table IV. Comparative Determination of Pb in the Inner Core of 14 Sections of the Dome C 905 m Antarctic Ice Core by LEAF-ETA and IDMS

sample depth,[a] m	measured Pb concn,[b] pg/g LEAF-ETA	CI[c]	IDMS[d]
172.8	1.44	0.7	0.76
300.6	0.69	0.45	0.47
373.9	0.84	0.5	0.94
451.9	0.32	0.2	0.43
476.3	0.16	0.2	0.32
500.5	4.6	2.2	3.81
527.2	6.8	3.1	10.5
545.1	7.3	3.3	10.2
602.2	9.9	4.4	11.4
658.2	13.8	6.1	14.0
670.5	19.7	8.8	29.3
704.2	13.4	5.9	15.2
775.7	6.2	2.8	7.2
796.9	1.84	1.0	1.25

[a] Age of the ice ranges from 3800 to 34 000 years BP (*31*). [b] Both LEAF-ETA and IDMS concentrations have been corrected for blanks. [c] Confidential interval at the 0.95 confidence level calculated by using eq 2, see text. [d] Pb concentrations measured in the same samples by IDMS (*6*, *9*).

When the regression line was constructed, the points 1 pg/g and 7.5 pg/g were not taken into account. The value measured for the 1 pg/g standard lies indeed significantly above the curve, because at this extremely low concentration level, the Pb content of the LGGE ultrapure water used for the preparation of the standards (0.27 pg of Pb/g (*34*)) becomes significant and must be taken into account. The true Pb content in this 1 pg/g standard determined from the regression line, 1.28 pg/g, is indeed in excellent agreement with that calculated when adding the Pb content of this water (*34*) to that introduced into the standard. The 7.5 pg/g standard gave systematically low values in all series of experiments, possibly because of errors in its preparation (the Pb content in this standard calculated from the regression line is 5.4 pg/g instead of 7.5 pg/g).

As an additional standard, we also analyzed LGGE ultrapure water 3 times, Table III. The Pb content of this water determined from the regression line is found to be 0.28 pg/g. This value is in excellent agreement with that previously determined for that water by IDMS (*34*).

4.2. Dome C Antarctic Ice Samples. Pb concentrations directly measured by LEAF-ETA in the inner cores of the 14 sections of the Dome C ice core using sample volumes of 20

μL are shown in Table IV (after correction for chiseling and nitric acid blanks, see section 2). Each inner core was measured only once. The calibration was based on the two standards 2.5 pg/g (which was measured 2 times) and 25 pg/g (3 times).

The confidential intervals (CI) given in Table IV were calculated by using the equation

$$CI = t_{P,f} S_{r,c} \bar{C}_x / N^{1/2} \quad (2)$$

where $\bar{C}_x$ represents the mean measured Pb concentration in the ice sample, $t_{P,f}$ the Student's coefficient, N the number of parallel measurements of concentration C_x, $S_{r,c}$ the relative standard deviation of the measured values C_x, P the confidential level ($P = 0.95$), m the number of points used to construct the calibration curve, and f the number of degrees of freedom ($f = m - 2$).

$S_{r,c}$ is calculated by using eq 8 of ref 36

$$S_{r,c} = \frac{2.35 S_0^2}{b}\left[1 + \frac{1}{m} + \frac{(\log A_x - \overline{\log A})^2}{b^2[\sum_{i=1}^{m}(\log C_i)^2 + m(\overline{\log C})^2]} + 0.189\left(1 + \frac{1}{n_b}\right)\frac{S_{I_b}^2}{S_0^2 A_x^2}\right]^{1/2} \quad (3)$$

where b is the slope of the calibration curve, n_b the number of background measurements, S_{I_b} the standard deviation of the background, A_x the analytical signal for the x_{th} sample, and S_0, $\overline{\log A}$, and $\overline{\log C}$ are defined by the following equations:

$$S_0^2 = \frac{\sum_{i=1}^{m}(\log A_{i,exp} - \log A_{i,calib.})^2}{m - 2} \quad (4)$$

$$\overline{\log A} = \frac{1}{m}\sum_{i=1}^{m} \log A_i \quad (5)$$

$$\overline{\log C} = \frac{1}{m}\sum_{i=1}^{m} \log C_i \quad (6)$$

The first three members of eq 3 represent the part of total relative standard deviation originating from the fluctuations of the experimental points around the calibration curve. The last one is the part caused by the precision of the background measurements.

It can be seen that the CI values given in Table IV at the 95% confidence level are rather large: they range from about 30% up to 50% of the measured concentrations. These wide CI values are mainly due to the small number of measurements of the samples, the small amount of experimentally measured standards (m), and the small amount of background measurements. Indeed, we preferred to analyze a larger number of ice samples with wide CI values, rather than to analyze a small number of samples with smaller CI values. In this first use of LEAF-ETA for the direct measurement of Pb in Antarctic ice, the main goal was indeed to compare the results with those previously obtained by IDMS (see section 4.3) for a range of concentration as large as possible and for samples taken from different parts of the Dome C core (there might have been systematic differences since the speciation of Pb might not be the same during the Holocene (depths smaller than about 480 m) and during the Last Glacial Maximum (depths between about 480 and 780 m). Obviously, it will be necessary in the future to perform much more numerous measurements both for the samples and for the standards and the background fluctuations, in order to get smaller CI values.

The lowest Pb concentration values we measured with the spectrometer for the Dome C core were 0.27 pg/g (depth 476.3 m) and 0.43 pg/g (451.9 m). After substraction of the 0.11 pg/g blank (see section 2), this gave final net concentration values of 0.16 and 0.32 pg/g, respectively, Table IV. The sample volume introduced into the spectrometer being only 20 μL, the absolute Pb mass that was detected in these two core sections was as low as about 5–8 fg (or $\sim$(1.5–2) $\times 10^7$ Pb atoms). This confirms the outstanding sensitivity of the LEAF-ETA technique, which is several orders of magnitude more sensitive for Pb than any other available analytical technique.

4.3. Comparison with the IDMS Data. The inner cores of the 14 sections of the Dome C core that we measured by LEAF-ETA had previously been analyzed for Pb by the ultraclean IDMS technique in Patterson's laboratory at the California Institute of Technology (*6*, *9*). In that procedure, 50- to 200-g samples had to be used. Ultrapure NIST HNO_3 was first added to make a 0.1% HNO_3 solution. A ^{208}Pb spike was added and then the solution was allowed to equilibrate for 2 h. The pH was adjusted to 8–9 with high-purity ammonium hydroxide. Then Pb was extracted into 19.5 mL of ultrapure $CHCl_3$ and 0.5 mL of ultrapure dithizone. The $CHCl_3$ layer was acid stripped into 5 mL of 5% ultrapure HNO_3; this acid solution was washed with 5 mL of ultrapure $CHCl_3$ and then evaporated to dryness. The residue was transferred to a rhenium filament with ultrapure water, treated with purified silica gel and H_3PO_4. The filament was then inserted into a thermal ionization mass spectrometer, and the $^{208}Pb/^{207}Pb$ ratio was measured to determine Pb concentration in the samples from the weights of the sample and the spike and the $^{208}Pb/^{207}Pb$ ratios in them. Each analysis was very carefully corrected for total Pb contamination from labware, reagents, and operations, as described in details in ref 3 and 6–9. The precision of these IDMS data, which are shown in Table IV, was estimated to range from about 50% (for the very low concentrations at the 0.5 pg/g level) down to about 10% (for the high concentrations at the 5–30 pg/g level).

As shown in Table IV and Figure 1, LEAF-ETA and IDMS data are in very good agreement, which strongly supports the accuracy of both sets of data. It must however be emphasized again that for the LEAF-ETA measurements only 0.02-g samples were required even at the pg/g concentration level and that there was no need for any preconcentration or chemical treatment; one sample determination took only 3–5 minutes. For the IDMS measurements on the other hand, 50–200-g samples were required at the pg/g concentration level, and a difficult and time-consuming chemical treatment was required; one sample determination took at least half a day.

5. CONCLUSION

Our preliminary data confirm that LEAF-ETA is a very promising technique for the direct measurement of Pb at extremely low concentration levels in decontaminated samples of ancient Antarctic ice, using very small volumes of sample. It will be however necessary in the future to get better analytical precisions by increasing the number of measurements both for the standards and for the samples.

It will also be interesting to investigate the possibility of using LEAF-ETA for the direct measurement of other heavy metals such as Cd, Hg, and Bi at very low concentration levels in Antarctic and Greenland ice and snow. Finally, it will also be interesting to investigate the possibility of using laser photoionization spectroscopy (*37–40*) for the direct analysis of heavy metals and possibly of Pb isotopes in these samples

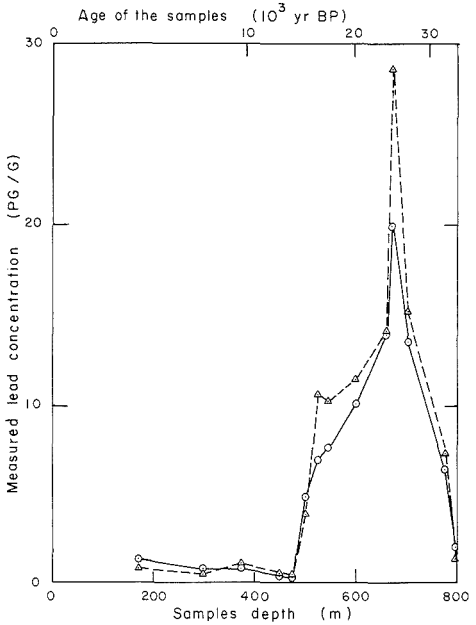

Figure 1. Comparative analysis of the inner core of various sections of the Dome C deep Antarctic ice core by LEAF-ETA: this work (open circles, solid line) and by IDMS (*6*, *9*) (triangles, dashed line).

at very low concentration levels.

ACKNOWLEDGMENT

We thank V. G. Koloshnikov for his continuous interest and help in this work, C. C. Patterson for his participation in the sample preparation and in the IDMS analyses at California Institute of Technology, and F. Hartmann and G. Mavel for their help in initiating this research.

Registry No. Pb, 7439-92-1; H_2O, 7732-18-5.

LITERATURE CITED

(1) Murozumi, M.; Chow, T. J.; Patterson, C. C. *Geochim. Cosmochim. Acta* **1969**, *33*, 1247–1294.
(2) Ng, A.; Patterson, C. C. *Geochim. Cosmochim. Acta* **1981**, *45*, 2109–2121.
(3) Boutron, C. F.; Patterson, C. C. *Geochim. Cosmochim. Acta* **1983**, *47*, 1355–1368.
(4) Wolff, E. W.; Peel, D. A. *Ann. Glaciol.* **1985**, *7*, 61–69.
(5) Wolff, E. W.; Peel, D. A. *Nature* **1985**, *313*, 535–540.
(6) Boutron, C. F.; Patterson, C. C. *Nature* **1986**, *323*, 222–225.
(7) Boutron, C. F.; Patterson, C. C.; Petrov, V. N.; Barkov, N. I. *Atmos. Environ.* **1987**, *21*, 1197–1202.
(8) Boutron, C. F.; Patterson, C. C. *J. Geophys. Res.* **1987**, *92*, 8454–8464.
(9) Boutron, C. F.; Patterson, C. C.; Lorius, C.; Petrov, V. N.; Barkov, N. I. *Ann. Glaciol.* **1988**, *10*, 5–9.
(10) Wolff, E. W.; Peel, D. A. *Ann. Glaciol.* **1988**, *10*, 193–197.
(11) Boutron, C. F. In *National Perspectives on Global Metal Cycling*; Hutchinson, T. C., Gordon, C. A., Meema, K., Eds.; Scope Rpt 31; Wiley Eastern Ltd.: New Delhi, India, in press.
(12) Boutron, C. F.; Patterson, C. C.; Barkov, N. I. In *Proceedings of the International Workshop on Ice Core Drilling*; Grenoble, Sept 1988, in press.
(13) Batifol, F.; Boutron, C. F.; De Angelis, M. *Nature* **1989**, *337*, 544–546.
(14) Peel, D. A. In *The Environmental Record in Glaciers and Ice Sheets*; Oeschger, H., Langway, C. C., Jr., Eds.; Dahlem Konferenzen; John Wiley: New York, 1989, pp 207–223.
(15) Patterson, C. C.; Settle, D. M. In Accuracy in Trace Analysis: Sampling, Sample Handling and Analysis. *Natl. Bur. Stand. (U.S.), Spec. Publ.* **1976**, *422*, 321–351.
(16) Murphy, T. J. In Accuracy in Trace Analysis: Sampling, Sample Handling and Analysis. *Natl. Bur. Stand. (U.S.), Spec. Publ.* **1976**, *422*, 509–539.
(17) Boutron, C. F.; Martin, S. *Anal. Chem.* **1979**, *51*, 140–145.
(18) Wolff, E. W.; Landy, M. P.; Peel, D. A. *Anal. Chem.* **1981**, *53*, 1566–1570.
(19) Omenetto, N.; Winefordner, J. D. In *Analytical Laser Spectroscopy*; Omenetto, N., Ed.; John Wiley: New York, 1979.
(20) Bolshov, M. A. In *Laser Analytical Spectrochemistry*; Letokhov, V. S., Ed.; Adam Hilger: Bristol, 1986; pp 52–97.
(21) Hohimer, I. P.; Hargis, P. J., Jr. *Anal. Chim. Acta* **1978**, *97*, 43–49.
(22) Epstein, M. S.; Bradshaw, J.; Bayer, S.; Bower, J.; Voigtman, E.; Winefordner, J. D. *Appl. Spectrosc.* **1980**, *34*, 372–376.
(23) Bolshov, M. A.; Zybin, A. V.; Koloshnikov, V. G.; Vasnetsov, M. V. *Spectrochim. Acta* **1981**, *36B*, 345–350.
(24) Bolshov, M. A.; Zybin, A. V.; Smirenkina, I. I. *Spectrochim. Acta* **1981**, *36B*, 1143–1152.
(25) Omenetto, N.; Human, H. G. C.; Cavalli, P.; Rossi, G. *Spectrochim. Acta* **1984**, *39B*, 115.
(26) Smith, B. W.; Omenetto, N.; Winefordner, J. D. *Spectrochim. Acta* **1984**, *39B*, 1389–1394.
(27) Preli, F. R.; Dougherty, J.; Michel, R. G. *Anal. Chem.* **1987**, *59*, 1784–1789.
(28) Omenetto, N.; Cavalli, P.; Broglia, P.; Qi, P.; Rossi, G. *Anal. At. Spectrosc.* **1988**, *3*, 231.
(29) Apatin, V. M.; Arkhangelskii, B. V.; Bolshov, M. A.; Ermolov, V. V.; Koloshnikov, V. G.; Kompanetz, O. N.; Kutznetsov, N. I.; Mikhailov, E. L.; Shishkovskii, V. S.; Boutron, C. F. *Spectrochim. Acta* **1989**, *44B*, 253–262.
(30) Lorius, C.; Merlivat, L.; Jouzel, J.; Pourchet, M. *Nature* **1979**, *280*, 644–648.
(31) Jouzel, J.; Raisbeck, G.; Benoist, J. P.; Yiou, F.; Lorius, C.; Raynaud, D.; Petit, J. R.; Barkov, N. I.; Korotkevich, Y. S.; Kotlyakov, V. M. *Quaternary Res.* **1989**, *31*, 135–150.
(32) Kuehner, E. C.; Alvarez, R.; Paulsen, P. J.; Murphy, T. J. *Anal. Chem.* **1972**, *44*, 2050–2056.
(33) Paulsen, P. J.; Beary, E. S.; Bushee, D. S.; Moody, J. R. *Anal. Chem.* **1988**, *60*, 971–975.
(34) Boutron, C. F.; Patterson, C. C., Pasadena, 1985, unpublished work.
(35) Kompanetz, O. N.; Mishin, V. I.; Nesteruk, I. N. *Sov. Quant. Electr.* **1988**, *15*, 455–459.
(36) Bolshov, M. A.; Dashin, S. A.; Zybin, A. V.; Koloshnikov, V. G.; Maiorov, I. A.; Smirenkina, I. I. *Z. Anal. Chem.* **1986**, *41*, 1862–1870.
(37) Bekov, G. I.; Letokhov, V. S. *Appl. Phys.* **1983**, *30*, 161–176.
(38) Bekov, G. I.; Letokhov, V. S.; Radaev, V. N. *J. Opt. Soc. Am.* **1985**, *2*, 1554–1560.
(39) Bekov, G. I.; Kudryavtsev, Yu. A.; Auterinen, I.; Likonen, J. *Inst. Phys. Conf. Ser.* **1987**, *84*, 97–102.
(40) Bekov, G. I.; Letokhov, V. S.; Radaev, V. N.; Badyukov, D. D.; Nazarov, M. A. *Nature* **1988**, *332*, 146–148.

RECEIVED for review March 8, 1989. Accepted May 5, 1989. This work was supported in France by the Ministère de l'Environnement, the Terres Australes et Antarctiques Françaises, the Expéditions Polaires Françaises, and the Ministère des Relations Extérieures. The Dome C deep drilling in Antarctica and the ice cores decontamination at California Institute of Technology were supported by the U.S. National Science Foundation. This research was part of the collaboration between the Institute of Spectroscopy and the Laboratoire de Glaciologie et Géophysique de l'Environnement established within the framework of the French–Soviet Commission.

Cyclic Voltammetry at Microhole Array Electrodes

Koichi Tokuda*

Department of Electronic Chemistry, Graduate School at Nagatsuta, Tokyo Institute of Technology, Nagatsuta, Midori-ku, Yokohama 227, Japan

Ken-ichi Morita[1] and Yoshihiro Shimizu

Basic Research Laboratories, Toray Industry, Inc., 1111 Tebiro, Kamakura 248, Japan

Microhole array electrodes have a unique characteristic of exhibiting steady-state current. Cyclic voltammograms at microhole array electrodes are treated theoretically for a reversible redox-electrode process, and analytical expressions for current–potential curves are presented. Cyclic voltammetry of a $[Fe(CN)_6]^{4-/3-}$ couple is carried out at these microhole array electrodes constructed from a carbon fiber–epoxy composite. The theoretical results are applied to the analysis of the experimental results, and a reasonable value for the diffusion coefficient is obtained from the analysis of the ratios of maximum (peak) currents of cyclic voltammograms to the steady-state currents.

Microhole array electrodes, which can be fabricated by electrochemical etching of a carbon fiber–epoxy composite, have proved to be promising as an oxygen sensor (*1*), a biosensor (*2*), and a flowmeter (*3*). One of the most important features of the microhole array electrodes is that the steady-state current is readily reached. This is because the convection of the bulk solution has little effect on the mass transfer within the microholes, and thus a linear concentration gradient of the electroactive species is established when its concentration just outside of the microholes is kept constant by stirring the solution. Extensive applications of these electrodes for electroanalytical purposes are under consideration, and their design also shows promise in the analysis of kinetic studies. However, since an easy means of construction has only recently been achieved (*1*), the theory for various voltammetric methods including kinetics with these electrode has not been solved as yet. Understanding of the fundamental characteristics of such microhole array electrodes is desirable for their use in the sensors mentioned above as well as in other fields.

Recently Bond et al. (*4*) reported a comparison of the chronoamperometric response at inlaid and recessed disk electrodes. They obtained equations for the transient current response at a single recessed disk electrode under conditions of stirred and quiescent solution. The microhole array electrode fabricated from the carbon fiber–epoxy composite can be regarded as an ensemble of a number of such recessed disk electrodes. This allows amplification of signals.

Cyclic voltammograms obtained with the microhole array electrodes are quite similar in shape to those for stationary rotating disk, ultramicrosphere or ultramicrodisk electrodes. In other words, sigmoidal voltammograms are obtained at slow potential sweep rates, which is expected from the linear concentration gradient in the microholes at the steady state (*1*, *4*).

This paper is devoted to the derivation and the calculation of reversible current–potential curves at microhole array electrodes and presents analytical expressions for all sweep rates. Theoretical results have been compared with experimental ones obtained for the redox-electrode reaction of hexacyanoferrate(II/III) at carbon fiber microhole array electrodes of various depths. Relatively good agreement between experimental and theoretical results has been obtained.

[1] Present address: Toin University of Yokohama, 1614 Kurogane-cho, Midori-ku, Yokohama 227, Japan.

THEORY

Mathematical Model of the Electrodes. We consider the microhole array electrode as an ensemble of N recessed microdisk electrodes of equal diameter d and depth L as shown in Figure 1A. Although the scanning electron micrographs of the etched carbon fibers (*1*) have revealed that the surfaces of the carbon fibers are not flat but conical or bullet shaped as schematically shown in Figure 1B, it is assumed in the model that each microhole electrode has a surface area equal to the cross-sectional area of the carbon fiber or that of the microhole. Thus the total geometric surface area of the electrode A is equal to $N(\pi d^2/4)$. Since each microhole electrode is regarded as an independent unit, it may suffice to consider mass transport in the single microhole and then the total current will be obtained from multiplying the current density by the total electrode area A. When the solution is well stirred, the concentration of the electroactive species at the mouths of the microholes may be maintained at its initial value.

Consider a simple redox-electrode reaction

$$R \rightleftarrows O + ne^- \tag{1}$$

for which we make the following assumptions: (a) both species R and O are soluble in solution; (b) the reaction proceeds so rapidly that the Nernst equation holds at the electrode surface; (c) these species have equal diffusion coefficients D; (d) the solution contains an excess of the supporting electrolyte; (e) before electrolysis only the reduced form R of the redox couple is present in the solution, the concentration of which is denoted by c_R°; and (f) initially the electrode potential E is set at a value E_i which is sufficiently less positive than the formal potential $E^{\circ\prime}$ of reaction 1 so that virtually no faradaic current flows in the cell.

The potential sweep is performed according to the program

$$E = E_i + vt \qquad \text{for } 0 \le t \le t_r \text{ (forward sweep)} \tag{2}$$

and

$$\begin{aligned} E &= E_r - v(t - t_r) \\ &= E_i - vt + 2vt_r \text{ for } t \ge t_r \text{ (reverse sweep)} \end{aligned} \tag{3}$$

where v is the potential sweep rate, t_r is the switching time when the direction of the potential sweep is reversed, and E_r is the switching potential given by

$$E_r = E_i + vt_r \tag{4}$$

which may be chosen to be sufficiently positive of $E^{\circ\prime}$.

We seek expressions for reversible current–potential curves for forward and reverse sweep separately.

0003-2700/89/0361-1763$01.50/0

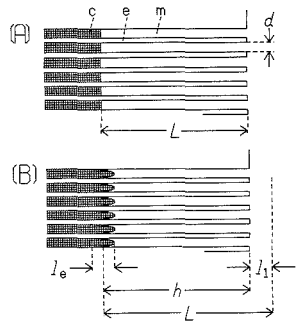

Figure 1. (A) Schematic diagram of the mathematical model of microhole array electrodes used for theoretical treatment of the diffusion problems: (c) carbon fiber, (e) epoxy resin, and (m) microhole. (B) Schematic illustration of the model used in the analysis of experimental data, where l_e is length of the etched electrode, l_1 is the thickness of diffusion boundary layer, and h is the depth of microholes.

Forward Potential Sweep. Since diffusion is the only mode of mass transfer of species R and O in the microholes, we can utilize the one-dimensional diffusion equation

$$\partial c_B/\partial t = D\partial^2 c_B/\partial x^2 \qquad (B = R, O) \tag{5}$$

where c_B denotes the concentration of species B, t is the time elapsed from the beginning of the potential sweep, and x is the distance measured from the electrode surface along the hole. If we introduce, for convenience, new variables defined by

$$\tau = Dt/L^2 \quad \text{and} \quad \xi = x/L \tag{6}$$

where L is the depth of microholes, then eq 5 may be rewritten as

$$\partial c_B/\partial \tau = \partial^2 c_B/\partial \xi^2 \tag{7}$$

The initial conditions are given by

$$c_R = c_R^\circ, \; c_O = 0 \quad \text{for } \xi \geq 0, \; \tau = 0 \tag{8}$$

The boundary conditions for a position just outside of the microholes are

$$c_R = c_R^\circ, \; c_O = 0 \quad \text{for } \xi = 1, \; \tau > 0 \tag{9}$$

The other boundary condition is given by the Nernst equation

$$c_O/c_R = \exp\{(nF/RT)(E - E^{\circ\prime})\} \quad \text{for } \xi = 0, \; \tau > 0 \tag{10}$$

where E is the electrode potential and other symbols have their usual significance. The final boundary condition is given by the relation between the fluxes and the current density i/A

$$\partial c_R/\partial \xi = -\partial c_O/\partial \xi = iL/nFAD \quad \text{for } \xi = 0, \; \tau > 0 \tag{11}$$

This boundary value problem is solved by using the Laplace transformation (5), as explained in Appendix 1. The concentrations of R and O at the electrode surface are given by

$$c_R^s = c_R^\circ - \int_0^\tau \theta_2(0; \tau - u)\{i(u)L/nFAD\}\, du \tag{12}$$

$$c_O^s = \int_0^\tau \theta_2(0; \tau - u)\{i(u)L/nFAD\}\, du \tag{13}$$

where superscript s indicates that c is taken at the electrode surface and $\theta_2(0;\tau)$ is one of the theta functions (6).

Substituting eq 12 and 13 into the Nernst equation (10) and rearranging give

$$\int_0^\tau \theta_2(0; \tau - u)[i(u)L/nFAD]\, du = c_R^\circ\{1 + \exp(-\zeta)\}^{-1} \tag{14}$$

where u is an auxiliary variable and ζ is a dimensionless potential defined by

$$\zeta = (nF/RT)(E - E^{\circ\prime}) \tag{15}$$

Combining eq 2 and 6 with eq 15 yields

$$\zeta = \zeta_i + p\tau \tag{16}$$

where

$$\zeta_i = (nF/RT)(E_i - E^{\circ\prime}) \tag{17}$$

and

$$p = nF\upsilon L^2/RTD \tag{18}$$

Integral eq 14 can be solved as shown in Appendix 2 and the result is

$$i = (nFAD/L)\int_0^\tau \theta_3(0; \tau - u) \times (d/du)(c_R^\circ[1 + \exp\{-\zeta(u)\}]^{-1})\, du \tag{19}$$

where $\theta_3(0;\tau)$ is also one of the theta functions and is given by (6)

$$\theta_3(0;\tau) = (\pi\tau)^{-1/2}[1 + 2\sum_{j=1}^{\infty} \exp(-j^2/\tau)] \tag{20}$$

or, in the alternative representation, by

$$\theta_3(0;\tau) = 1 + 2\sum_{j=1}^{\infty} \exp(-j^2\pi\tau) \tag{21}$$

In general, the behavior of the voltammograms is independent of the choice of E_i as long as E_i has sufficiently negative value compared to $E^{\circ\prime}$ as discussed in a previous paper (7). Thus changing the variable as $y = \tau - u$ and letting $\zeta_i \to -\infty$ ($E_i \to -\infty$) (7), we have an expression for the forward sweep voltammogram (the anodic wave):

$$i_a = (nFADc_R^\circ/L)\int_0^\infty \theta_3(0;y)\exp(\zeta - py) \times \{1 + \exp(\zeta - py)\}^{-2}\, dy \tag{22}$$

Subscript a has been added in order to denote that current is anodic or potential sweep is in the position direction. The value of the integral in eq 22 is unity for large values of ζ, as will be shown below, and steady-state current i_{ss} is attained

$$i_{ss} = nFADc_R^\circ/L \tag{23}$$

It is interesting to note that eq 22 is exactly the same as the expression for the anodic current in potential sweep voltammetry at a thin-layer cell where two opposing parallel electrodes separated by a distance L serve as the working and the auxiliary electrodes and the regeneration of one of the redox couple consumed at the work electrode takes place at the auxiliary electrode (8).

Reverse Potential Sweep. If the potential is swept up to a value sufficiently positive of $E^{\circ\prime}$, then a steady state is established for the current and for the concentration distribution in the microholes. If we select such a potential as the switching potential E_r, then the corresponding switching time may be regarded as an initial time for the calculation of current for the reverse potential sweep. Then, the initial condition for eq 7 is given by

$$c_R = c_R^\circ\xi \quad \text{and} \quad c_O = c_R^\circ(1 - \xi) \quad \text{at } \tau = 0 \tag{24}$$

The boundary conditions are as follows:

$$\partial c_R/\partial \xi = -\partial c_O/\partial \xi = iL/nFAD \qquad \text{for } \xi = 0, \; \tau > 0 \tag{25}$$

$$c_O/c_R = \exp\{(nF/RT)(E_r - E^{\circ\prime}) - p\tau\} \qquad \text{for } \xi = 0, \; \tau > 0 \tag{26}$$

and

$$c_R = c_R^\circ, \quad \text{and } c_O = 0 \qquad \text{for } \xi = 1, \; \tau > 0 \tag{27}$$

This boundary value problem is also solved using the Laplace transformation as shown in Appendix 3. The concen-

trations of R and O at the electrode surface are given by

$$c_R^s = \int_0^\tau \theta_2(0; \tau - u)\{c_R^\circ - i(u)L/nFAD\}\, du \quad (28)$$

$$c_O^s = c_R^\circ - \int_0^\tau \theta_2(0; \tau - u)\{c_R^\circ - i(u)L/nFAD\}\, du \quad (29)$$

Introducing eq 28 and 29 into eq 26 and following the procedure similar to that employed for the forward potential sweep, we obtain an expression for the reverse sweep voltammogram (the cathodic wave)

$$i_c = (nFADc_R^\circ/L)\Big[1 - \int_0^\infty \theta_3(0;y)\exp(\zeta + py) \times \{1 + \exp(\zeta + py)\}^{-2}\, dy\Big] \quad (30)$$

Thus, analytical expressions for current–potential curves have been evaluated and can be used for all sweep rates.

EXPERIMENTAL SECTION

Microhole array electrodes were prepared from high strength carbon fibers (TORAYCA T-300; the number of fibers in a single electrode is 1000; 6.93 μm in diameter) using fabrication techniques described in the previous paper (*1*). Depths of microholes were controlled by the amount of charge used during the etching process of the carbon fibers. Seven microhole array electrodes of different depths were employed in the present work. After the electrochemical measurements were finished, the actual depth of the microholes were determined from the scanning electron micrographs of the cross-sectional view of the microhole array electrodes.

Solutions of 1.0 mmol/dm^3 potassium hexacyanoferrate(II) in 0.4 mol/dm^3 potassium sulfate were prepared from reagent grade chemicals without further purification in water purified with an ultrapure water supplier (TORAYPURE LV-08).

Electrochemical measurements were carried out by use of a potentiostat (Model HA-301, Hokuto Denko, Tokyo) and a function generator (Model HB-104, Hokuto Denko, Tokyo) with an x–y recorder (Type 3086, Yokogawa Hokushin Electric, Mitaka, Japan). The electrochemical cell used was a 100-mL beaker with a silicone rubber lid having holes for installation of electrodes and for a nitrogen inlet tube. A saturated calomel electrode (SCE) was used as the reference electrode and all potentials were referred to this electrode. The auxiliary electrode was a platinum wire. The solutions were deaerated with nitrogen. They were stirred by a magnetic bar covered with Teflon during the measurements. Electrochemical measurements were conducted at 30 ± 0.5 °C.

Scanning electron micrographs of cross-sectional view of the microhole array electrodes were obtained with a Hitachi S-800 scanning electron microscope with a field emission gun.

RESULTS AND DISCUSSION

Characteristics of Cyclic Voltammograms. Theoretical cyclic voltammograms were calculated from eq 22 and 30 on a personal computer (NEC PC-9801RA). The integral from 0 to ∞ was evaluated by dividing it into three integrals over the subintervals [0, 0.04], [0.04, 1.4] and [1.4, ∞]. Though $\theta_3(0;y)$ is singular at $y = 0$, we can avoid the singularity by replacing $\theta_3(0;y)$ by $(\pi y)^{-1/2}$ in the region of $0 < y \leq 0.04$ (see eq 20) and by integrating by parts. In the region of $y \geq 1.4$, $\theta_3(0;y)$ is virtually equal to 1 (see eq 19) and the integration is trivial. Other integrals were evaluated by using Simpson's 1/3 rule. The current–potential curves thus calculated are shown in Figure 2 for several values of $p = nFvL^2/RTD$. It should be noted that the anodic and the cathodic waves are symmetric with respect to the point $(E^{\circ\prime}, nFAc_R^\circ D/2L)$. This will be apparent from the relation

$$i_a(\zeta) + i_c(-\zeta) = nFAc_R^\circ D/L \quad (31)$$

which can readily be derived from eq 22 and 30.

When p is less than 0.02, the voltammograms are independent of p, indicating steady-state behavior. Traces of the forward (anodic) sweep and the reverse (cathodic) seeep

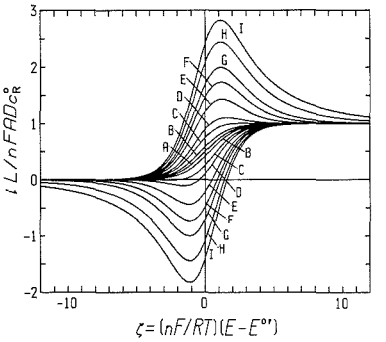

Figure 2. Theoretical cyclic voltammograms for a reversible redox-electrode process. Values of p are (A) ≤0.02, (B) 1.0, (C) 3, (D) 5, (E) 10, (F) 15, (G) 20, (H) 30, and (I) 40.

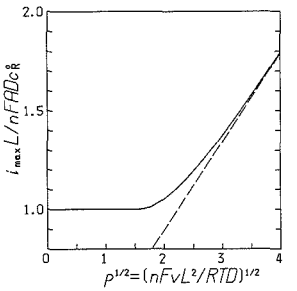

Figure 3. Dependence of the normalized maximum current or the ratio of i_{max} to i_{ss} on square root of p. Dashed line corresponds to the case of the semiinfinite linear diffusion conditions.

voltammograms are completely identical and these can be expressed by

$$i = (nFAc_R^\circ D/L)/[1 + \exp\{-(nF/RT)(E - E^{\circ\prime})\}] \quad (32)$$

Thus the current–potential curves are sigmoidal in shape and the limiting current plateau, i.e., the steady-state current i_{ss}, is easily obtained. This behavior is the same as that for conventional polarograms and rotating disk voltammograms or at ultramicroelectrodes. In this case the half-wave potential $E_{1/2}$ equals $E^{\circ\prime}$ since $D_R = D_O = D$.

With an increase in the value of p, $E_{1/2}$ of the anodic wave moves from $E^{\circ\prime}$, toward less positive values and the cathodic half-wave potential moves toward more positive values. It has been found theoretically that if $p \leq 2$, then the sigmoidal form is retained and the reciprocal slope of the conventional logarithmic plot, i.e., plot of log $\{i/(i_{ss} - i)\}$ vs E, is equal to $2.3RT/nF$. The shift of $E_{1/2}$ is not due to the change in reversibility but is caused by the transition from the steady-state mass transport condition (i.e., a fixed diffusion layer thickness) to a time-dependent diffusion layer thickness. When p is less than 2, the maximum current i_{max} is equal to i_{ss}.

When the value of p exceeds ca. 2.5, peaks appear on both the forward sweep and the reverse sweep waves. In this case we denote the peak current i_p as i_{max}. Figure 3 shows variation of $i_{max}L/nFADc_R^\circ$ or i_{max}/i_{ss} with $p^{1/2}$. When $p \geq 15$, i_{max}/i_{ss} is proportional to $p^{1/2}$ and the slope is equal to 0.446. Then we have

$$i_p/i_{ss} = i_{max}L/nFADc_R^\circ = 0.446p^{1/2} \quad (33)$$

or using eq 18

$$i_p = 0.446nFAc_R^\circ D^{1/2}(nF/RT)^{1/2}v^{1/2} \quad (34)$$

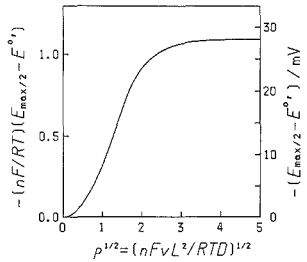

Figure 4. Dependence of the potential of the half-maximum current $E_{max/2}$ on $p^{1/2}$ (anodic wave). Right ordinate is for n = 1 and 25 °C.

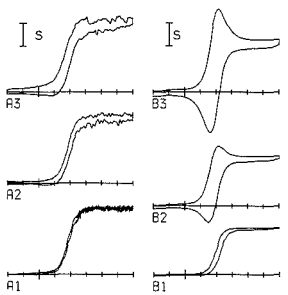

Figure 5. Cyclic voltammograms for oxidation and rereduction of $[Fe(CN)_6]^{4-}$ in 0.4 mol/dm^3 K_2SO_4 aqueous solution at microhole array electrodes of h = 11 μm (A) and h = 156 μm (B): potential range, −0.20 to +0.60 V; potential sweep rate (A1) 5 mV/s, (A2) 20 mV/s, (A3) 50 mV/s, (B1) 1 mV/s, (B2) 5 mV/s, and (B3) 10 mV/s; S = 50 nA (A) and S = 10 nA (B).

This is the same equation as for the peak current of the reversible potential sweep voltammogram under semiinfinite diffusion conditions (*9*, *10*), indicating that when the potential sweep rate v is high enough or the depth of microholes L is deep enough to satisfy $p \geq 15$, then the diffusion layer thickness is less than L at the time the peak appears.

The shape of voltammograms is also characterized by the potential of the half-maximum current $E_{max/2}$, the dependence of which on $p^{1/2}$ is shown in Figure 4 for anodic wave. For values of $p \leq 0.25$, $E_{max/2} = E^{o\prime}$ within $(2/n)$ mV at 25 °C, which corresponds to the steady-state condition. When $p \geq 15$, on the other hand, $E_{max/2} = E^{o\prime} - 1.09(RT/nF)$. This corresponds to the half-peak potential for semiinfinite diffusion. This behavior is the same as that in the thin-layer cell mentioned above (*8*).

In order to apply the theoretical results, the redox-electrode reaction of hexacyanoferrate(II/III) was chosen as a reversible system. Typical cyclic voltammograms obtained experimentally for oxidation of 1.0 mmol/dm^3 $[Fe(CN)_6]^{4-}$ in aqueous 0.4 mol/dm^3 K_2SO_4 solutions are shown in Figure 5 for the microhole array electrodes having depths of about 10 and 150 μm.

At the electrode of 10 μm depth, sigmoidal current–potential curves were obtained for the sweep rate range between 2 and 50 mV/s. Some noise seen on the limiting current plateau was due to the turbulent flow caused by the agitation of the solution. Noise of less amplitude was observed at the electrode of 20 μm depth but could not be seen at the 50 μm depth. Since the solution was stirred with a magnetic bar stirrer, the flow in the cell was turbulent. When the electrodes were placed in a laminar flow, such noise was found to be greatly reduced.

The traces of the forward and the reverse sweep completely overlapped and showed no hysteresis at the sweep rate of 2 mV/s (10 μm depth), indicating that the redox-electrode process of the hexacyanoferrate couple is reversible under the conditions employed. Although the effect of charging current became more apparent in the higher sweep rate range, the limiting current values were found to be the same when a correction of the charging current was made as described below. The fact that the steady-state behavior is observed at the microhole array electrode of 10 μm depth is predicted from the theoretical results because the value of p lies in the region from 0.01 to 0.38 for 2 mV/s $\leq v \leq$ 50 mV/s and for representative D values ranging from 5×10^{-6} to 1×10^{-5} cm^2/s.

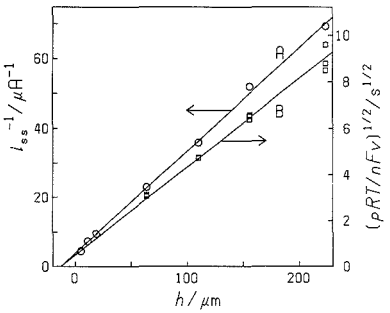

Figure 6. Plots of reciprocal of steady-state current against depth of the microhole h (A) and plots of $(pRT/nFv)^{1/2}$ obtained from peak current against h (B).

Cyclic voltammograms at the microhole array electrode of 150 μm depth showed well-defined peaks on both anodic and cathodic waves for $v \geq 2$ mV/s, but the voltammogram recorded at v = 1 mV/s was almost sigmoidal. These voltammograms were almost symmetric as expected from the theoretical results.

Analysis of the Steady-State Current. The reciprocal of the steady-state current is expected from eq 23 to be proportional to the depth of microholes. In order to compare the theoretical and experimental voltammograms, it is desirable to have values of the depths of the microholes. Although the depth of the microholes can approximately be controlled by the amount of electricity consumed in the etching process as mentioned previously (*1*), a more reliable value of the actual depth is determined from the scanning electron micrographs of the cross-sectional view of the microholes. The etched tips of carbon fibers were not flat but had a shape like a bullet head as shown in Figure 1 of the previous paper (*1*) and schematically in Figure 1B, and the average length l_e of the etched carbon fiber tips ranged from 2.5 to 13 μm depending on the total microhole depth; the larger the total depth, the larger l_e. We will define the depth of microholes h as a sum of the average distance from the mouths to the tipe of the carbon fibers and half of l_e as shown in Figure 1B.

Figure 6 shows plots of the reciprocal of the steady-state current against the microhole depth. The steady-state current values were determined from the chronoamperometric experiments but they agree completely with the limiting current values obtained from cyclic voltammograms with a correction of the charging current. This correction was carried out on the voltammograms by subtracting the current value calculated from the linear extrapolation of the residual current curve preceding the initial rise of the wave, and was used throughout this work. These plots fall on a straight line (line A) which has an intercept at −13 μm on the abscissa. Thus we may write as

$$1/i_{ss} = (h + l_1)/nFADc_R^{\circ} \qquad (35)$$

where l_1 may be regarded as a length which must be taken into account to include the effect of a layer outside of the mouths of microholes on the diffusion process. This behavior is the same as that for oxygen reduction reported in the previous paper (*1*) and l_1 was considered to be the thickness of the diffusion boundary layer formed on the surface of microhole array under the stirring condition. Thus the thickness of the diffusion layer L is regarded as the sum of h and l_1 as shown in Figure 1B. The value of 13 μm for l_1 found in this work is somewhat larger than the average value of 7.6 μm found in the previous work for the reduction of oxygen (*1*). However, a range of l_1 values from 4.1 to 12.8 μm was observed in the previous work (*1*), and the discrepancy may result from possible variation of stirring conditions in the solution.

From the slope value of line A in Figure 6, the product of the diffusion coefficient by the total area was evaluated to be 3.46×10^{-9} cm^4/s. If we assume that the diameter of the microholes is equal to that of carbon fibers and the tips of the carbon fibers are flat, the total electrode surface area A is estimated to be 3.8×10^{-4} cm^2, which yields $D = 9.1 \times 10^{-6}$ cm^2/s. Inspection of micrographs of the surfaces of microhole array electrodes revealed that some neighboring microholes were connected to each other by thin crevices formed in the epoxy resins during the electrochemical etching process. If we take this observation into account, then, since the effective surface area is larger, the value of D would become somewhat smaller than 9.1×10^{-6} cm^2/s.

It is also necessary to consider the effect of the difference in the surface areas of the real electrodes and of the electrode model in Figure 1A on the current intensity. As mentioned above, the real surface area of the electrode is obviously larger than the one estimated above since the carbon fiber tipes have a shape like a bullet. At the early stage of the electrolysis, the diffusion layer has not developed and thus the current value reflects the real surface area. As time passes, however, the diffusion layer develops, the thickness eventually well exceeds l_e, and the steady-state current i_{ss} would become insensitive to l_e. Thus it is expected that the effect of l_e on i_{ss} or on the D value evaluated from i_{ss} would be relatively insignificant and i_{ss} may be determined by the geometric cross-sectional area of the microholes. However, since it has not been clarified quantitatively how large this effect is, exploration of etching methods to make flat carbon fiber tips is under way.

An alternate means of estimating the D value, which is independent of the surface area value, is described below.

Analysis of the Cyclic Voltammograms. When cyclic voltammograms show peaks, we can evaluate p values from the ratio of the peak current to the steady-state current, i_p/i_{ss}, using the working curve shown in Figure 3. Values of $(pRT/nFv)^{1/2}$ thus calculated are plotted against h in Figure 6. These plots also fall on a straight line (line B), which has an intercept at about −13 μm on the abscissa. It is interesting to note that both intercept values of lines A and B are almost the same. This linearity is expected from eq 18 when we write $L = h + l_1$

$$(pRT/nFv)^{1/2} = D^{-1/2}(h + l_1) \tag{36}$$

From the slope of this line, D is evaluated to be 6.7×10^{-6} cm^2/s.

A value of 5.9×10^{-6} cm^2/s has been reported for D of $[Fe(CN)_6]^{4-}$ in 0.4 mol/dm^3 K_2SO_4 at 25 °C (*11*). If we take into account a temperature coefficient of about +2%/°C for diffusion coefficients in aqueous solution (*12*), then we have 6.5×10^{-6} cm^2/s at 30 °C. This value is very close to that evaluated from the ratio of i_{max}/i_{ss}.

There is some discrepancy (about 30%) between the D value obtained from the steady-state current measurement (line A) and that from cyclic voltammetry (line B). Evaluation of the D value from i_{ss} requires the value of the electrode surface area A, and thus some uncertainty in A directly influences the estimated D value. The higher value of D obtained from i_{ss} may partly result from the used value of A which would be smaller than the real one.

When i_{max} is attained, the diffusion layer has well-developed although the development is not complete as in the steady state. Thus the shape of carbon fiber tips may affect more or less equally both i_{ss} and i_{max}. The effect of uncertainty of the electrode surface area on the evaluated value of p from i_{max}/i_{ss} is ruled out because only the ratios of experimental values are used and this may be the reason why a reasonable value of D was obtained from line B in Figure 6.

It is concluded that relatively good agreement has been obtained between the theoretical and experimental results for reversible cyclic voltammograms at microhole array electrodes. Extension of the work to examine kinetically controlled systems is also being considered.

The amplified current at the microhole array electrode is a great advantage over the single hole electrode (*4*). The microhole array electrode may be most suited for measurements in stirred solutions or in flow-through systems. Under these conditions, concentrations of the species outside the holes are regarded to be uniform and thus there is no complexity resulting from the overlapping of diffusion layers, which must be taken into account in the case of ensembles of inlaid microdisk electrodes. Application of the microhole array electrode to electrochemical detectors in liquid chromatography and flow injection analysis is under way.

APPENDIX

Appendix 1. Application of the Laplace transformation with respect to τ to eq 7, 9, and 11 yields

$$d^2L[c_B]/d\xi^2 = (s/D)L[c_B] - c_B^\circ/D \tag{A1}$$

with

$$dL[c_R]/d\xi = -dL[c_O]/d\xi = L[iL/nFAD] \text{ for } \xi = 0 \tag{A2}$$

$$L[c_R] = c_R^\circ/s,\ L[c_O] = 0 \text{ for } \xi = 1 \tag{A3}$$

where $L[f]$ denotes the Laplace transform of function f and s is the dummy Laplace variable. General solutions of eq A1 for B = R and O may be written as

$$L[c_R] = c_R^\circ/s + A_R \exp(-s^{1/2}\xi) + B_R \exp(s^{1/2}\xi) \tag{A4}$$

$$L[c_O] = A_O \exp(-s^{1/2}\xi) + B_O \exp(s^{1/2}\xi) \tag{A5}$$

where coefficients A_R, B_R, A_O, and B_O are functions of s to be determined from the boundary conditions. Using eq A2–A3, we have

$$A_R = -A_O = -L[iL/nFAD]s^{-1/2}\{1 + \exp(-2s^{1/2})\}^{-1}$$

$$B_R = -B_O = L[iL/nFAD]s^{-1/2}\{1 + \exp(2s^{1/2})\}^{-1}$$

Substituting these equations into eq A4–A5 and rearranging the resulting equation yield

$$L[c_R] = c_R^\circ - s^{-1/2} \sinh\{s^{1/2}(1 - \xi)\} \operatorname{sech}(s^{1/2})L[iL/nFAD] \tag{A6}$$

$$L[c_O] = s^{-1/2} \sinh\{s^{1/2}(1 - \xi)\} \operatorname{sech}(s^{1/2})L[iL/nFAD] \tag{A7}$$

At the electrode surface (i.e., $\xi = 0$), these equations reduce to

$$L[c_R^s] = c_R^\circ - s^{-1/2} \tanh(s^{1/2})L[iL/nFAD] \tag{A8}$$

$$L[c_O^s] = s^{-1/2} \tanh(s^{1/2})L[iL/nFAD] \tag{A9}$$

The Laplace inversion transform of eq A8 and A9 by use of the relation (5)

$$L^{-1}[s^{-1/2} \tanh (as^{1/2})] = a^{-1}\theta_2(0;\tau/a^2) \quad (a, \text{constant}) \tag{A10}$$

yields eq 12 and 13, respectively. In the above equation, L^{-1} is the inverse Laplace transform operator.

Appendix 2. Applying Laplace transformation to eq 14 and rearranging, we have

$$L[i(\tau)L/nFAD] = s^{-1/2} \coth (s^{1/2})sL[c_R^\circ\{1 + \exp(-\xi)\}^{-1}] \tag{A11}$$

Inverse transform of eq A11 is obtained by making use of relations (5)

$$sL[f(\tau)] = L(df(\tau)/d\tau] + f(0)$$

and

$$L^{-1}[s^{-1/2} \coth (as^{1/2})] = a^{-1}\theta_3(0;\tau/a^2) \quad (a, \text{constant}) \tag{A12}$$

and we have eq 19.

Appendix 3. Application of the Laplace transformation with respect to τ to eq 7, 25, and 27 using eq 24 yields

$$d^2L[c_R]/d\xi^2 = (s/D)L[c_R] - c_R^\circ\xi/D \tag{A13}$$

$$d^2L[c_O]/d\xi^2 = (s/D)L[c_O] - c_R^\circ(1 - \xi)/D \tag{A14}$$

with

$$dL[c_R]/d\xi = -dL[c_O]/d\xi = L[iL/nFAD] \text{ for } \xi = 0 \tag{A15}$$

$$L[c_R] = c_R^\circ/s,\ L[c_O] = 0 \text{ for } \xi = 1 \tag{A16}$$

Following the procedure similar to Appendix 1, we obtain

$$L[c_R] = c_R^\circ\xi/s - s^{-1/2} \sinh \{s^{1/2}(1 - \xi)\} \operatorname{sech} (s^{1/2})\{L[iL/nFAD] - c_R^\circ/s\} \tag{A17}$$

$$L[c_O] = c_R^\circ(1 - \xi)/s + s^{-1/2} \sinh \{s^{1/2}(1 - \xi)\} \operatorname{sech} (s^{1/2})\{L[iL/nFAD] - c_R^\circ/s\} \tag{A18}$$

Letting $\xi = 0$ in eq A17 and A18 and inverse transforming by use of eq A10 gives eq 28 and 29.

ACKNOWLEDGMENT

Helpful discussion with Dr. J. F. Cassidy is gratefully acknowledged.

Registry No. $Fe(CN)_6^{4-}$, 13408-63-4; $Fe(CN)_6^{3-}$, 13408-62-3; $KFe(CN)_6$, 13943-58-3; dipotassium sulfate, 7778-80-5.

LITERATURE CITED

(1) Morita, K.; Shimizu, Y. *Anal. Chem.* **1989**, *61*, 159.
(2) Shimizu, Y.; Morita, K., submitted for publication in *Anal. Chem.*
(3) Morita, K.; Sugiyama, T.; Ohaba, M., unpublished results.
(4) Bond, A. M.; Luscombe, D.; Oldham, K. B.; Zoski, C. G. *J. Electroanal. Chem.* **1988**, *249*, 1.
(5) Roberts, G. E.; Kaufman, H. *Table of Laplace Transforms*; W. B. Saunders Company: Philadelphia, PA, 1966.
(6) Spanier, J.; Oldham, K. B. *An Atlas of Functions*; Hemisphere Publishing Corporation: Washington, DC, 1987; Chapter 27.
(7) Aoki, K.; Tokuda, K.; Matsuda, H. *J. Electroanal. Chem.* **1983**, *146*, 417.
(8) Daruházi, L.; Tokuda, K.; Farsang, G. *J. Electroanal. Chem.*, in press.
(9) Matsuda, H.; Ayabe, Y. *Z. Elektrochem.* **1955**, *59*, 494.
(10) Nicholson, R. S.; Shain, I. *Anal. Chem.* **1964**, *36*, 706.
(11) Bruckenstein, S.; Tokuda, K.; Albery, W. J. *J. Chem. Soc. Faraday Trans. 1* **1977**, *73*, 823.
(12) Sawyer, D. T.; Roberts, J. L., Jr. *Experimental Electrochemistry for Chemists*; John Wiley: New York, 1974; p 153.

RECEIVED for review December 28, 1988. Accepted May 9, 1989.

Fiber-Optic Time-Resolved Fluorescence Sensor for the Simultaneous Determination of Al^{3+} and Ga^{3+} or In^{3+}

Mary K. Carroll, Frank V. Bright,[1] and Gary M. Hieftje*

Department of Chemistry, Indiana University, Bloomington, Indiana 47405

A fiber-optic fluorescence sensor for simultaneous two-elemental determinations has been developed. The sensor is based on the formation of a complex between specific metal ions and a metal ion chelator. Several chelator–ion systems and several means of chelator immobilization were studied. The successful fiber-optic sensor design is based on a pool of chelator solution trapped behind a membrane made of Nafion. The chelator ultimately chosen, lumogallion, forms strongly fluorescent complexes with trivalent aluminum, gallium, and indium ions. Because of the difference in fluorescence lifetimes of the various lumogallion complexes, time-resolved fluorometry enables simultaneous determination of two of these ions.

* Author to whom correspondence should be addressed.
[1] Current address: Department of Chemistry, State University of New York at Buffalo, Buffalo, NY.

INTRODUCTION

Many chelators form strongly fluorescent complexes with metal ions. Often, the fluorescence of the chelator itself is weaker than that of its complexes. As a result, the extent of complexation and, thus, the concentration of an ion in solution can be found from a measurement of fluorescence intensity. However, a chelator will frequently form complexes with several different ions, and the emission spectra of the different complexes are sometimes similar. Hence, interferences plague the determination of any particular metal ion in the presence of one or more of the others.

This report describes the development of a fiber-optic-based fluorescence sensor capable of simultaneous two-element determinations under the conditions described above.

Others have developed fiber-optic sensors for the determination of metal ions (*1–5*). Generally, these sensors are fabricated by immobilizing a metal indicator or chelator on

0003-2700/89/0361-1768$01.50/0

the distal end of the fiber and measuring the fluorescence of the complex formed when the optrode contacts an appropriate ion-containing solution. Seitz and co-workers have published data on sensors of this type based on the complexes of morin, calcein, and quinolin-8-ol sulfonate (*1–4*). Unfortunately, these sensors are subject to severe interferences from ions other than the one targeted.

In this paper, we avoid these interferences through the use of time-resolved fluorometry. Lytle and co-workers have shown that this method can be used to determine two or more metal ions in solution when the lifetimes of their fluorescent complexes are different (*6, 7*). Vitense and McGown have performed simultaneous determinations of metal ions through the use of phase-resolved fluorometry (*8, 9*). We have combined the advantages of fiber-optic sensors with the method of time-resolved fluorometry to create a sensor that is capable of simultaneously determining the concentrations of Al^{3+} and Ga^{3+} or Al^{3+} and In^{3+} ions in solutions containing a mixture of these ions. Detection limits obtained for aluminum, gallium, and indium ions by using this sensor are 2×10^{-8}, 2×10^{-7}, and 3×10^{-6} M, respectively, and dynamic ranges are between 2 and 3 orders of magnitude. Relative errors encountered when mixtures of ions are determined range from 4 to 20%. Response times of a new chelator-pool sensor lie in the range of 4–5 min.

THEORY

The method employed to determine fluorescence lifetimes is called the phase-plane method, described in detail by Demas and co-workers (*10, 11*). When applied to a mixture of chelator–ion complexes with overlapping fluorescence spectra, the phase-plane method utilizes simultaneous equations and the fluorescence lifetime for each complex to calculate the contribution of each complex to the observed emission intensity (*11*).

EXPERIMENTAL SECTION

Reagents. Lumogallion was purchased from Pfalz and Bauer. Perfluorinated ion-exchange powder, 5% solution by weight, and morin hydrate were purchased from Aldrich Chemical Co. Gallium(III) chloride and indium(III) chloride were obtained from Aesar; aluminum(III) nitrate nonahydrate was obtained from Fisher Scientific Co. All of the above reagents were used without further purification. Mordant Blue 31 was synthesized following the procedure outlined by Hiraki (*12*). Fluorescein (Sigma Chemical Co.) and Rhodamine 6G (Exciton) were used as reference fluorophores for the time-resolved measurements. Solutions were prepared by using distilled, deionized water, spectral grade acetone (Fisher Scientific), absolute ethanol (Aaper Alcohol and Chemical Co.), or a combination of these solvents. Commercial buffers (Fisher Scientific) were used for the pH study.

Immobilization Procedures. Morin and the morin–Al^{3+} complex were immobilized on microcrystalline cellulose (J. T. Baker Chemical Co.) following the procedure of Saari and Seitz (*2, 3*). The immobilized morin was compared with a sample donated by W. R. Seitz and was found to have the same emission spectrum.

Lumogallion, its aluminum, gallium, and indium complexes, and morin and its complexes were immobilized by soaking AG1-X4 ion-exchange resin (Bio-Rad) in a solution of chelator or complex.

Conventional Fluorescence Measurements. The instrument used for conventional fluorescence measurements is shown in Figure 1. The beam (150–250 mW of the 514.5-, 488.0-, or 457.9-nm line) from a Spectra-Physics Model 171 argon ion laser is reflected from two mirrors, M1 and M2, passes through an iris, I, and is focused by lens L1 into one end of a 0.5-m-long bifurcated optical fiber (200-μm diameter, donated by Galileo Electro-Optics). Fluorescence from the sample is collected by the other end of the optical fiber and is carried 0.5 m to a Spex double monochromator (Model 1680B). A Hamamatsu R928 photomultiplier tube in a Pacific Model 3150,S PMT housing collects the emission signal. The PMT is powered by a Pacific Photometric Instruments Model 203 high-voltage power supply, operated at −1000 V dc, and its

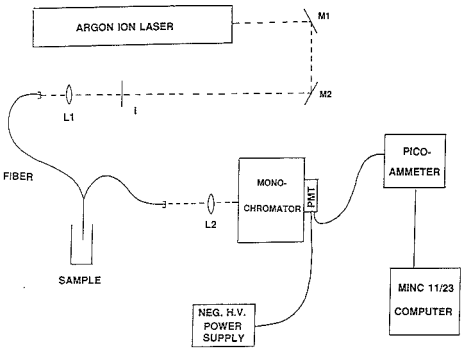

Figure 1. Schematic design of instrument used for conventional fluorescence measurements: M, mirror; I, iris; L, lens.

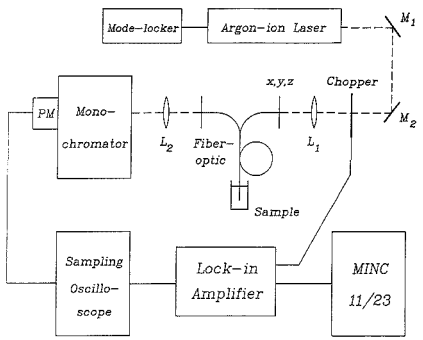

Figure 2. Schematic design of instrument used for time-resolved fluorescence measurements: M, mirror; L, lens; xyz, translation mount; PM, photomultiplier tube.

output is sent to a Keithley 414S picoammeter. The output of the picoammeter is connected to a DEC MINC-11/23 computer. The computer also functions to drive the monochromator. No attempt was made here to improve signal-to-noise ratios in the steady-state spectra by means of computer-based time averaging. Indeed, if the spectra were plotted on a strip chart recorder the apparent signal-to-noise ratio would be higher.

Time-Resolved Fluorescence Measurements. Figure 2 shows the instrument used for fluorescence lifetime measurements. A similar instrument has been described previously (*13*), and only its general features will be outlined here. The 514.5-, 488.0-, or 457.9-nm output of a mode-locked Spectra-Physics Model 171 argon ion laser (Spectra-Physics Model 342 mode-locker, Model 452 mode-locker driver) is reflected from two mirrors, M1 and M2, mechanically chopped, and focused by L1 into one end of a bifurcated optical fiber (200 μm diameter, Galileo Electro-Optics). The beam travels 0.5 m through the fiber to the sample (either an optrode or a solution). The resulting fluorescence is collected through another 0.5-m length of fiber and carried to a Kratos Model GM100-1 monochromator set to the wavelength of maximum emission for the compound being studied. Detection of this fluorescence is accomplished with a Hamamatsu R928 PMT in a Pacific Model 3150,S PMT housing. The output of the PMT is sent to a sampling oscilloscope (Tektronix Model 7844 mainframe, Model S4 sampling head, Model 7S11 sampling unit), which is triggered by the mode-locker driver. The fluorescence decay of the sample is recorded by the oscilloscope, the output of which is sent to an EG&G Princeton Applied Research Model 5101 lock-in amplifier. The lock-in amplifier, used to reduce noise introduced by the sampling oscilloscope, is referenced to the mechanical chopping frequency. The output of the lock-in amplifier is sent to a MINC-11/23 computer for data collection. The computer controls the scan rate of the oscilloscope time base; thus,

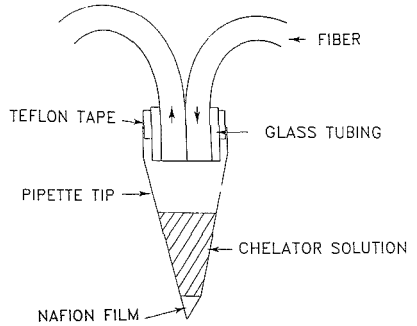

Figure 3. Chelator pool optrode; original design. Not to scale.

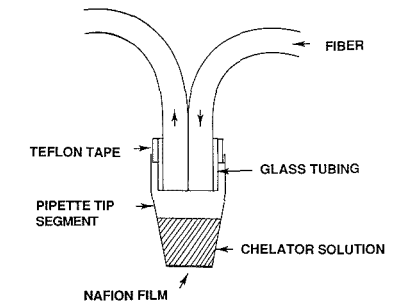

Figure 4. Improved version of chelator pool optrode. Not to scale.

independent monitoring of individual points on the fluorescence decay curve can be performed.

OPTRODE DESIGN

Figure 3 is a schematic diagram of a new kind of chemical sensor based on a pool of chelator solution trapped behind an ion-permeable membrane. A solution of anionic chelator, placed behind a plug of Nafion film, cannot pass through the film into the sampled metal ion solution, because Nafion contains anionic "pores". In contrast, the positively charged metal ions can diffuse through the membrane into the chelator pool where complexation occurs.

To prepare the optrode of Figure 3, a drop of Nafion solution is suspended in the tip of an inverted 250-μL plastic disposable pipet tip (Rainin, Inc.). The solvent is allowed to evaporate, leaving a plug of Nafion in the tip. A razor is then used to cut through the Nafion plug to obtain a thinner film of Nafion. It is necessary to cut the plug at an angle to avoid shattering the rather brittle Nafion film. The pipet tip is then righted and a pool of chelator solution added to it (typically, 125 μL is added). The optrode is fixed onto the end of the bifurcated fiber optic by Teflon plumbing tape. A hole is punched out of the side of the pipet to relieve back pressure and to enable ions to traverse through the membrane without producing a pressure differential.

This preliminary design suffered from sensor-to-sensor irreproducibility, as discussed later. A modified chelator pool optrode was therefore designed (see Figure 4). The top segment of a 250-μL plastic disposable pipet tip is set upright on a Parafilm-covered microscope slide. The Nafion film is then formed by adding a fixed amount, generally 50 or 60 μL, of Nafion solution to the pipet tip segment and letting the solvent evaporate. The Nafion film thus prepared is about 35 μm in thickness. The sensor is peeled off the Parafilm, leaving the Nafion film intact across the end of the pipet tip segment.

Table I. Fluorescence Lifetimes of Selected Chelator–Ion Complexes

complex	lifetime, ns	std dev, ns
morin-Al(III)	4.11	0.13
morin-Ga(III)	4.07	0.21
morin-In(III)	3.92	0.24
lumogallion-Al(III)	2.41	0.10
lumogallion-Ga(III)	1.33	0.20
lumogallion-In(III)	0.94	0.16
Mordant Blue 31-Al(III)	1.65	0.16
Mordant Blue 31-Ga(III)	0.96	0.13
Mordant Blue 31-Mg(II)	1.54	0.08

RESULTS AND DISCUSSION

Several chelator–ion chemical systems have been tested. The requirements are that the chelator be relatively nonfluorescent and that it form complexes with metal ions that are strongly fluorescent. The fluorescence lifetimes of the various complexes must be sufficiently different to allow distinction among their individual contributions to a total fluorescence signal. We have found that, for our instrumental system, the lifetimes must differ by at least 1 ns to meet this criterion. In addition, the 12.2-ns interpulse spacing of the mode-locked laser renders examination of lifetimes greater than 10 ns difficult.

Morin. Morin is a metal ion chelator that has been used successfully in previous fiber-optic sensors (*2, 3*). Morin is known to form complexes with a variety of metal ions, including Al^{3+}, Ga^{3+}, and In^{3+}. These specific complexes, in 5 μM concentration, visibly fluoresce when exposed to ordinary room lighting. Morin is itself only weakly fluorescent when excited with the 457.9-nm argon ion laser line. The Al^{3+}, Ga^{3+}, and In^{3+} complexes of morin all show emission maxima at about 525 nm when excited with 457.9-nm light and in a 1:1 morin:ion concentration ratio in absolute ethanol. These spectra all overlap strongly, and the morin complexes are therefore difficult or impossible to distinguish by conventional fluorometric techniques.

Lifetime measurements for the three morin complexes in solution were obtained with time-resolved fluorometry. The fluorescence lifetimes of the species, calculated from the decay curves, are listed in Table I. Our instrument cannot be used to determine one ion in the presence of either of the others, because the lifetimes of the three species are so similar (within 0.2 ns).

Morin immobilized on cellulose (*2, 3*) produces a relatively weak fluorescence signal. Moreover, the fluorescence lifetimes of the morin–ion complexes do not change appreciably when the complexes are immobilized. Thus, a sensor based on morin and the formation of its complexes with Al^{3+}, Ga^{3+}, and In^{3+} is not suitable for multielemental determinations using time-resolved fluorometry.

Lumogallion. Lumogallion (LMG) by itself can be excited by using the 488.0-nm argon ion laser line. In pH 5.0 acetate buffer solution, the wavelength of maximum emission is found to be about 595 nm (Figure 5). Although lumogallion itself fluoresces, it forms complexes with group IIIA elements (*9, 14–20*) that are at least 2 orders of magnitude more strongly fluorescent. The LMG–Al^{3+} complex exhibits the greatest intensity, followed by the LMG–Ga^{3+} complex and the LMG–In^{3+} complex. The fluorescence spectra of all three complexes are quite similar (see Figure 6), so determination of one ion in the presence of the others is difficult or impossible by conventional fluorescence measurements.

Fluorescence decay curves for the 20-μM lumogallion complexes are shown in Figure 7 and the corresponding lifetimes collected in Table I. The fluorescence lifetime of the LMG–Al^{3+} complex, 2.41 ns, is at least 1 ns longer than that of either

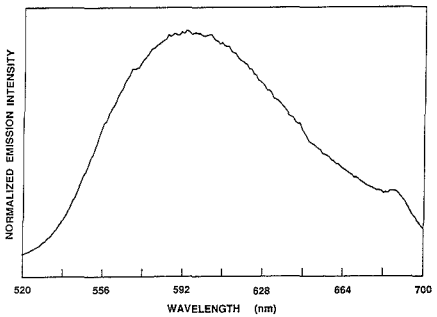

Figure 5. Fluorescence spectrum of lumogallion in pH 5.0 acetate buffer. Excitation wavelength = 488.0 nm.

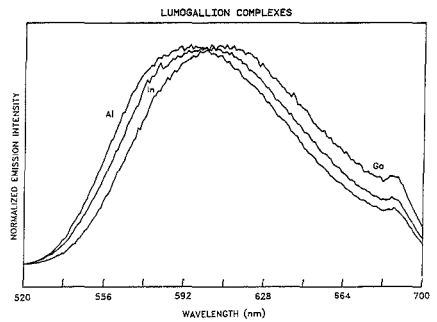

Figure 6. Fluorescence spectra of lumogallion–ion complexes in pH 5.0 buffer: excitation wavelength, 488.0 nm; lumogallion concentration, 2.5×10^{-5} M; cation concentration, 5×10^{-4} M; relative vertical scale, 30:100:1000 In:Ga:Al complexes, taking intensity of LMG alone equal to 1 (in Figure 5).

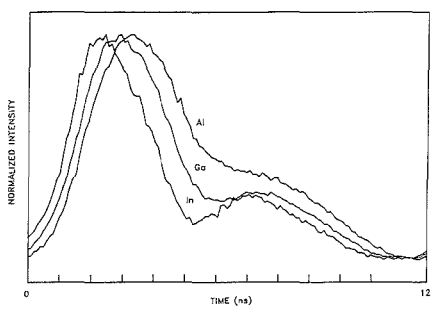

Figure 7. Fluorescence decay curves for lumogallion–ion complexes: concentration of LMG, 8.0×10^{-5} M; of Al^{3+}, 3.1×10^{-4} M; of Ga^{3+}, 7.7×10^{-4} M; and of In, 3.7×10^{-4} M.

the Ga^{3+} or In^{3+} complexes. Thus, the contributions of the individual complexes should be discernible with our instrument through time-resolved fluorometry.

Immobilization of Lumogallion. Although lumogallion can be immobilized on Bio-Rad AG1-X4 anion-exchange resin, the immobilized LMG does not then form complexes with Al(III), Ga(III), or In(III) ions. Presumably, the active chelating site is sequestered by immobilization. Alternatively, lumogallion complexes can be immobilized on AG1-X4 resin and the metal ions subsequently removed by immersion of the resin in a basic solution. Even then, the chelating agent

Table II. Determination of Mixtures of Aluminum and Gallium[a]

prepared, μM		found, μM	
Al(III)	Ga(III)	Al(III)[b]	Ga(III)[c]
1	10	1.3	9.2
1	20	1.2	18.6
2	5	1.8	5.1

[a] Conditions: lumogallion concentration, 30 μM; pH 5; excitation wavelength, 457.9 nm; emission wavelength, 600 nm; laser average power, 160 mW. [b] Average relative error for Al(III) was 20%. [c] Average relative error for Ga(III) was 4%.

Table III. Determination of Mixtures of Aluminum and Indium[a]

prepared, μM		found, μM	
Al(III)	In(III)	Al(III)[b]	In(III)[c]
1	40	1.06	43
1	90	0.90	97
2	20	1.92	23

[a] Conditions: lumogallion concentration, 30 μM; pH 5.0; excitation wavelength, 457.9 nm; emission wavelength, 600 nm; laser average power, 160 mW. [b] Average relative error for Al(III) was 7%. [c] Average relative error for In(III) was 9%.

remaining on the resin will not form complexes with the trivalent ions when it is subsequently immersed in a buffered solution containing them.

It is for these reasons that the pool optrodes of Figures 3 and 4 were designed. They are inexpensive and relatively easy to prepare. One optrode can be used many times and is readily regenerated simply by rinsing out the pool of lumogallion and soaking the optrode in acid to remove any ions that remain in the membrane. The optrode is very sensitive and gives steady-state (single-ion) detection limits of 2×10^{-8}, 2×10^{-7}, and 3×10^{-6} M for aluminum, gallium, and indium ions, respectively. (The detection limit is defined here as the concentration of analyte that yields a signal equal to 3 times the standard deviation of the background fluctuation.) A linear dynamic range of 3 orders of magnitude is obtained for both aluminum and indium complexes, and a range of 2 orders of magnitude is obtained for gallium.

The principal disadvantage of the design of Figure 3 is its slow response time. Figure 8A shows that its response begins to level off only after 20 min of immersion is a metal-ion-containing solution. Another disadvantage of the sensor design of Figure 3 is that a reproducible Nafion film thickness could not be guaranteed.

The design of Figure 4 performs as well as the sensor shown in Figure 3 but has a response time of under 5 min (see Figure 8B) and exhibits good sensor-to-sensor film thickness reproducibility.

A previous study has described the pH-dependence of fluorescence intensities and lifetimes of the lumogallion–ion complexes (*9*). Here, the effect of pH on the chelator pool optrode is minimal. Buffered solutions covering the range from pH 3.0 to 8.0 were used as the matrix for both the lumogallion pool optrode and the aluminum-ion-containing sample solution. In all cases, the ions traverse the Nafion membrane and form fluorescent complexes with lumogallion. The response time of the sensor is less than 10 min at every pH. No leakage of lumogallion is noted at any pH. Thus, the sensor is useful over a wide range of solution pH.

Multielemental Determinations. It can be seen in Table II that the values calculated by using the time-resolved fluorometry technique are within 2–20% of the true values for the aluminum and gallium mixture. Results for the si-

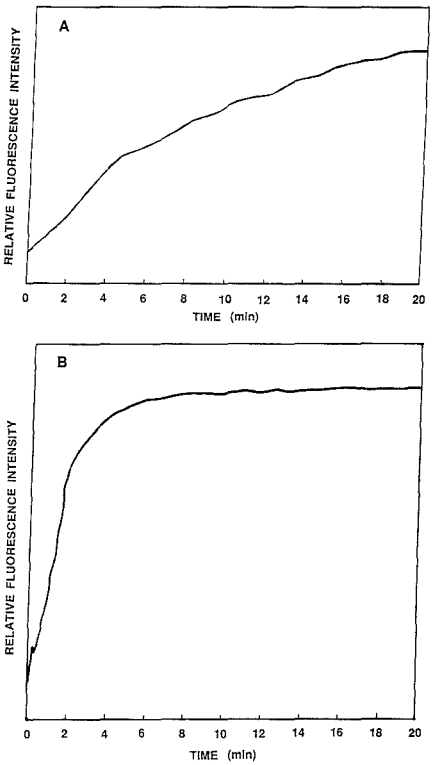

Figure 8. (A) Time response of a typical chelator pool optrode of the design shown in Figure 3. (B) Time response of a typical chelator pool optrode of the design shown in Figure 4.

multaneous determination of aluminum and indium ions are even better (all within 10%), as seen in Table III.

Application to Other Chemical Systems. The chelator pool optrode described here for lumogallion should be useful for other complexing reactions that involve an anionic chelator. For example, Mordant Blue 31 is similar in structure to lumogallion. As a result, it is likely to undergo a conformational change when it forms a complex with metal ions such as Al(III), Ga(III), and Mg(II). Unfortunately, synthesis of Mordant Blue 31 in our laboratory has resulted in a very impure product, due to significant amounts of NaCl contamination. Nonetheless, conventional fluorescence spectra obtained from an unknown concentration of Mordant Blue 31 and excess metal ions agree well with those reported in the literature (*12*). Also, measurements of the fluorescence lifetimes of the Mordant Blue 31 complexes indicate that time-resolved fluorometry could be used to determine aluminum and either gallium or magnesium in a mixture (see Table I). Further purification will be necessary before simultaneous determination of the ions is possible; the concentrations of the Mordant Blue 31 solutions are as yet unknown. Nonetheless, the Mordant Blue 31 system appears to be well-suited for use in the chelator pool optrodes.

ACKNOWLEDGMENT

We are grateful to Dean Geraci and Galileo Electro-Optics for donating the optical fibers used in this investigation. We thank W. R. Seitz (University of New Hampshire) for donating samples of morin immobilized on cellulose.

LITERATURE CITED

(1) Saari, L. A.; Seitz, W. R. *Anal. Chem.* **1984**, *56*, 810–813.
(2) Saari, L. A.; Seitz, W. R. *Anal. Chem.* **1983**, *55*, 667–670.
(3) Saari, L. A.; Seitz, W. R. *Analyst* **1984**, *109*, 655–657.
(4) Zhujun, Z.; Seitz, W. R. *Anal. Chim. Acta* **1985**, *171*, 251–258.
(5) Zhujun, Z.; Mullin, J. L.; Seitz, W. R. *Anal. Chim. Acta* **1986**, *184*, 251–258.
(6) Craven, T. L.; Lytle, F. E. *Anal. Chim. Acta* **1979**, *107*, 273–278.
(7) Craven, T. L.; Lytle, F. E. *Spectrosc. Lett.* **1979**, *12*, 559–566.
(8) Vitense, K. R.; McGown, L. B. *Anal. Chim. Acta* **1987**, *193*, 119–125.
(9) Vitense, K. R.; McGown, L. B. *Analyst* **1987**, *112*, 1273–1277.
(10) Demas, J. N. *Excited State Lifetime Measurements*; Academic Press: New York, 1983; pp 130–134.
(11) Carraway, E. R.; Hauenstein, B. L., Jr.; Demas, J. N.; DeGraff, B. A. *Anal. Chem.* **1985**, *57*, 2304–2308.
(12) Hiraki, K. *Bull. Chem. Soc. Jpn.* **1972**, *45*, 789–793.
(13) Bright, F. V.; Vickers, G. H.; Hieftje, G. M. *Anal. Chem.* **1986**, *58*, 1225–1227.
(14) *CRC Handbook of Organic Analytical Reagents*; Cheng, K. L., Ueno, K., Imamura, T., Eds.; CRC Press, Inc.: Boca Raton, FL, 1982; pp 139–157.
(15) Fernandez-Gutierrez, A.; Munoz de la Pena, A. In *Molecular Luminescence Spectroscopy: Methods and Applications: Part 1*; Schulman, S. G., Ed.; "Chemical Analysis"; Elving, P. J., Winefordner, J. P., Kolthoff, I. M., Eds.; John Wiley and Sons: New York, 1985; Vol. 77, Chapter 4.
(16) Haugen, G. R.; Steinmetz, L. L.; Hirschfeld, T. B.; Klainer, S. M. *Appl. Spectrosc.* **1981**, *35*, 568–571.
(17) Imasaka, T.; Harada, T.; Ishibashi, N. *Anal. Chim. Acta* **1981**, *129*, 195–203.
(18) Ishibashi, N.; Kina, K.; Goto, Y. *Anal. Chim. Acta* **1980**, *114*, 325–328.
(19) Hydes, D. J.; Liss, P. S. *Analyst* **1976**, *101*, 922–931.
(20) Kina, K.; Ishibashi, N. *Microchem. J.* **1974**, *19*, 26–31.

RECEIVED for review August 19, 1988. Revised April 20, 1989. Accepted May 1, 1989. The authors acknowledge financial support of this work by the Office of Naval Research, the Upjohn Company, and the National Science Foundation through Grant CHE 87-22639. This material is based upon work supported under a National Science Foundation Graduate Fellowship, granted to M.K.C., who also acknowledges support by an Indiana University Graduate Fellowship.

Split Zone Flow Injection Analysis: An Approach to Automated Dilutions

Gregory D. Clark, Jaromir Ruzicka, and Gary D. Christian*

Center for Process Analytical Chemistry, Department of Chemistry, BG-10, University of Washington, Seattle, Washington 98195

A simple, automated, on-line dilution system based on flow injection analysis (FIA) has been developed. The method relies on the reproducible cleavage of a dispersed sample zone, thereby attenuating the resulting peak's area and increasing its dispersion coefficient. Salient and practical features of previous dilution systems, developed by this and other groups, have been incorporated, making this system versatile and practical. Four methods for achieving dilutions were studied. These systems were evaluated for durability, reproducibility, range of dilution, and speed. A 0.0023 M solution of bromocresol green dye was used as a test solution for the dilutions. Other factors that might affect the dilutions, such as viscosity, were studied. A method for calculating the delay time required for a given dilution factor is discussed.

Flow injection analysis (FIA) is widely accepted as a means to perform rapid analyses. However, the samples that are used to test the method are often formulated to be as uncomplicated as possible, which allows examination of the chemistry of the analysis. For example, the test sample is usually present in concentration ranges amenable to direct determination and the matrix typically has a low viscosity. However, to analyze a sample of industrial origin, for example, manual pretreatment is often necessary prior to performing the analysis. The time necessary for such pretreatment increases the turnaround time accordingly. Furthermore, manual pretreatment is often a source for experimental error and is undesirable when the sample is toxic or originates from a hostile environment. Inasmuch as this work was initiated to develop a rapid method for the determination of a highly concentrated, highly viscous photographic dye, a method was needed to perform an extensive, adjustable dilution with simultaneous detection.

FIA is suitable for automated sample handling and pretreatment through reproducible manipulation of the concentration gradient of the injected sample. In a single-line FIA system the most common methods to perform a dilution are to increase the dispersion coefficient by decreasing the sample volume or by increasing the radius or length of the flow system tubing (*1*) or to utilize gradient dilution (*2*). Using a gradient chamber-based system is a practical means to achieve high dispersion coefficients in a single-line system (*1, 3, 4*). The use of a multiline FIA system, however, enables one to sample a portion of the concentration profile or add diluent to the sample. Zone sampling (*5*), cascade dilution (*6*), and gradient chamber-based zone sampling (*7, 8*) utilize the multiline advantage of FIA.

In this paper we describe an automated dilution system using FIA based on a variant to zone sampling, which relies on the reproducible cleavage of a portion of the trailing edge of the sample's concentration profile. Dilutions may be achieved by cleaving a portion of the trailing edge of the sample zone. The dilutions may be expressed in terms of the dispersion coefficient or the inverse mole fractions. Salient features of previous designs were incorporated into the current design. A means to calculate the parameters required to preset the dilution factor is discussed.

EXPERIMENTAL SECTION

Reagents. A 0.01 M sodium tetraborate solution (borax) was used throughout as the carrier and diluent streams as well as solvent for the dye samples.

A 0.0023 M bromocresol green (BCG) stock solution was prepared by dissolution of 0.8 g of the indicator in 30 mL of 0.01 M NaOH and diluting to nearly 500 mL with the stock borax solution. The pH of the resulting solution was measured with a Radiometer glass pH meter, and was adjusted to pH 8.5 using 6 M NaOH. The final volume of 500 mL was made up with the stock borax solution. The pH transition range (yellow to blue) of BCG is 3.8–6.4 (*9*). By the above adjustment of pH, less than 1% of the BCG is in the protonated, yellow form. Any change of peak height or area is assured to be due to dilution or dispersion instead of chemical conversion by the basic borax solution.

Dilutions of 25-fold to 1000-fold were made of the 0.0023 M BCG stock solution for calibration purposes. The appropriate volume of the stock BCG solution was added to a 10-mL volumetric flask, and the final volume made up with the stock borax solution.

Samples of BCG with viscosities ranging from 1 to 167 cP were prepared by adding an appropriate weight of glycerol (*9*) to a tared 50-mL volumetric flask to which was added 5 mL of the 0.0023 M BCG solution. A volume of nearly 50 mL was made up with the stock borax solution, and then the pH of the solutions was adjusted to 8.5 by using 6 M NaOH. The final volume of 50 mL was made with the stock borax solution.

Apparatus. Optical and Digital Components. The flow injection systems used were similar to one described previously (*10, 11*). The microconduits manifolds used in this study are shown in Figures 2–5.

An IBM PC/XT personal computer was used for data acquisition and experiment control. A computer program, described in ref 11, controlled the pumps and collected data beginning at the time of injection. The program also managed data storage, display, and calculation of pertinent run parameters such as area or first moment. An IBM data acquisition and control adapter (DACA) was used to interface the computer with the pumps for speed and direction control, with the detector via an amplifier/filter for data acquisition, and with a microswitch on the injection valve to start the experiment.

Flow Conduits and Experimental Operation. Two manifolds were used in this study and were individually configured for the four flow systems studied. They were prepared by pressing the flow pattern into a PVC block (for more details see ref 10, p 248). In one, the three flow systems shown in Figures 2–4 were constructed. The use of one manifold for the three flow systems conserved the channel geometry and the total reactor volume between the three systems. In the other manifold, the gradient chamber-based system shown in Figure 5 was developed. A 25-μL injection volume was used throughout. The reagents were propelled by using Tygon pump tubing from Cole-Parmer and Alitea C6-V peristaltic pumps provided by Alitea USA (P.O. Box 26, Medina, WA 98039). Micro-Line tubing, with an inside diameter of 0.51 mm, was used as connection tubing throughout.

A confluence point between P1 and P2 (in the first three systems) was created by using a tee with the confluent channels merging at a 60° angle and the exit stream juxtaposed between the two confluent streams, such that the angles between the inlet

0003-2700/89/0361-1773$01.50/0

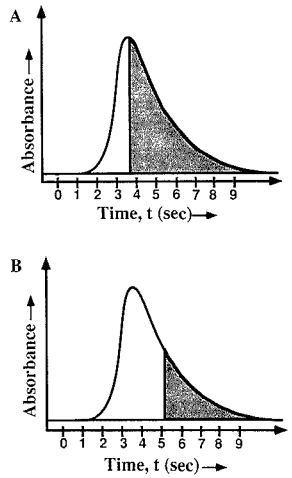

Figure 1. Two computer-generated peaks demonstrating split zone dilution method: (A) peak with zone split 3.5 s after injection (t_{del} = 3.5 s); (B) peak with zone split 5.4 s after injection (t_{del} = 5.2 s). The shaded area in each profile is sampled.

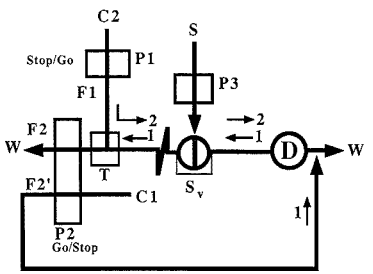

Figure 2. Schematic of the split zone (SZ) dilution system. P1, P2, and P3 are peristaltic pumps. S is the sample or standard, with sample volume S_v. D is the flow cell-detector apparatus. T denotes the confluent tee. C1 and C2 are carrier solutions (same solution as C or a separate reagent). W is waste. Go/Stop and Stop/Go indicate timed on/off and off/on cycles of the pumps, P2 and P1, respectively. The thin arrows denote liquid flow. F1, F1′, and F2 are flow rates (see text for further information). Not diagrammed for clarity are data and control connections to the computer via the DACA board.

and outlet streams are 30°. This arrangement has been found to ensure optimal mixing conditions (*12*).

Procedure. The dilution method relies on the cleavage of the sample concentration profile into a portion that is analyzed and a portion that is discarded. This process is illustrated in Figure 1. The shaded area in parts A and B of Figure 1 indicates the fraction of the initial concentration profile to be sampled, while the unshaded portion is discarded. The process of splitting the sample zone reduces the number of moles in the detected, analyzed zone. Figure 1A shows a peak undergoing cleavage at a time that corresponds to roughly the peak maximum, while in Figure 1B the peak is being cleaved at a time corresponding to a height of 1/3 peak maximum.

After the sample is injected, the sample proceeds toward the tee or gradient chamber, as dictated by the experiment. After a preset time following the injection, t_{del}, the computer stops pump 2 (P2) and the fraction of the zone still between the injection valve and the tee (or still in the gradient chamber) is propelled to the detector and analyzed. The individual system configurations are discussed below.

Split Zone (SZ) System (Figure 2). Prior to t_{del}, P1 is off and P2 is on. The sample is injected into a carrier stream labeled

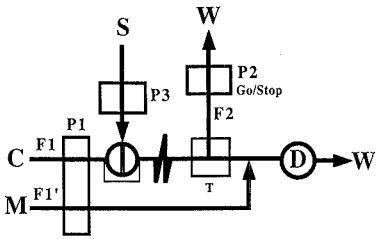

Figure 3. Schematic of the SZCS dilution system. C is the carrier solution. M is the make-up stream (same solution as C or a separate reagent). Other nomenclature is identical with that found in caption to Figure 2.

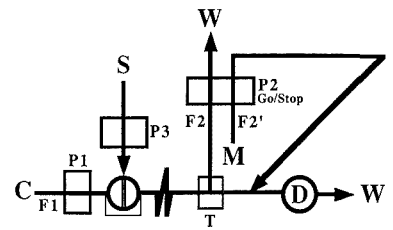

Figure 4. Schematic of the SZRS dilution system. Nomenclature is identical with that found in caption to Figure 3.

C1. The sample is being aspirated toward the confluence tee by the aspirant stream at a flow rate F2 = 1.05 mL/min. (In Figure 2 this is shown to be to the left, direction 1.) The flow rate (F2′) of C1, is 1.85 mL/min. F2′ is set greater than F2 so that some carrier is always perfusing the detector (which is important in some detectors such as atomic absorption spectrometers). At the delay time, t_{del}, when the desired fraction of the sample zone is between the tee and the injection valve, a second carrier stream, C2, is started and the aspirating stream and C1 are stopped. The carrier flow direction is effectively reversed (direction 2) and the fraction of the original sample zone remaining between the tee and the injector proceeds to the detector and waste. The flow rate of C2 is set to be 1.0 mL/min. This and the other flow rates were measured by collecting the output from the Tygon pump tubing for 3 min and calculating the average flow rate.

If a dilution corresponding to Figure 1B is desired, the delay time for stopping P2 and starting the P1 would be approximately 5.2 s. The peak height and area of the resulting zone (shaded gray in Figure 1) would be recorded. For this study the delay times were chosen to be longer than the time at peak maximum, for reasons discussed below. Methods for quantification of the dilution provided are described below.

Split Zone Confluent Streams (SZCS) System (Figure 3). The manifold from the SZ system was modified for the SZCS system. P1 and P2 are both on initially, with flow rates F1 = 1.0 mL/min, F1′ = 4.0 mL/min, and F2 = 1.5 mL/min. The sample and carrier (C) flow through P2 to waste. The differences in flow volumes between F1 and F2 are made up by the make-up stream, M, with a flow rate of F1′ = 4.0 mL/min. At the appropriate time, P2 is stopped. The sample remaining between the injector and tee is directed toward the detector. It undergoes confluence with the make-up stream, M, and is further diluted.

Split Zone Reagent Saver (SZRS) System (Figure 4). The SZRS system is essentially identical with the SZCS system, except that the make-up stream is propelled by P2. The make-up stream is thereby stopped at the delay time. This serves to conserve carrier solution, which is continually used in the SZCS system. The decreased carrier consumption volume is, however, gained at the loss of the extra dilution that would be provided by the confluence point.

Split Zone Gradient Chamber (SZGC) System (Figure 5). The SZGC system, employing a gradient chamber was used in the fourth part of this study. It was constructed so that the

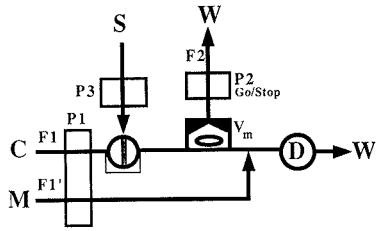

Figure 5. Schematic of the SZGC dilution system. V_m is the volume of the gradient chamber. Other nomenclature is identical with that found in caption to Figure 3.

distance from the injection valve to the gradient chamber was minimized.

Construction and Characterization of the Gradient Chamber. The gradient chamber was created by milling a circular domed depression in a microconduit block. Inlet and outlet channels were prepared by pressing the pattern in the PVC block. A channel to P2 was created by drilling a 0.72 mm diameter hole in the dome of the gradient chamber. Micro-Line tubing was inserted and the end was cut flush with the ceiling of the chamber. A miniature stir bar was placed in the chamber. The conduit was sealed with silicone rubber and held rigid with a FIAlab device (Alitea USA). A magnetic stirrer was mounted in the FIAlab device, underneath the conduit to provide stirring. The volume of the chamber was calculated by using eq 1 (ref 10, p 32)

$$V_m = \frac{C^\circ}{C^{max}} S_v \tag{1}$$

The steady-state absorbance value (C°) of the 1.15×10^{-5} M bromocresol green sample was 0.606. A 25.0-μL sample (S_v) was injected and a peak height (C^{max}) of 0.0244 was measured. The volume of the chamber (V_m) was then calculated to be 680 μL.

Experimental Operation. Initially P1 and P2 are running. The carrier flow rate, F1, is 1 mL/min, and the make-up stream flow rate, F1′, is 4.98 mL/min. The flow rate of the aspirant stream, F2, is 1.4 mL/min. All of the sample and carrier stream is directed through P2 to waste. At the appropriate time P2 is stopped. The remaining sample is cleared from the gradient chamber and undergoes further dilution at the confluence tee by the makeup stream flowing at F1′ and is detected.

Numerical Considerations For the SZGC System. One can measure the height and area of the resulting peaks. The dispersion coefficient may be taken as an expression of the dilution occurring in the FIA stream. Whitman and Christian (*6*) introduced a term that also defines dilution and that is valid for an open or multiline system. They defined the dilution in terms of the inverse mole fraction X^{-1}, given as the ratio of the number moles injected (n°) to the number of moles detected (n_{det})

$$X^{-1} = n^\circ / n_{det} \tag{2}$$

The area of a peak is proportional to the number of moles, and if a sample of known concentration is prepared by a k-fold dilution of the calibration standard, eq 2 can be written in terms of the areas of the resulting peaks

$$X^{-1} = kA^\circ / A_{det} \tag{3}$$

where A° is the area of the peak for the manually diluted calibration standard detected without further dilution and A_{det} is the area of the calibration standard peak recorded after dilution of the original sample by the system.

If the exact function of the concentration profile were known at the tee, X^{-1} for a given t_{del} could be easily calculated. Gisen et al. (*4*) suggested concentration profiles for a gradient chamber, for which the dilution model will be discussed here

$$C = \frac{\upsilon}{(1 - 2\upsilon)}(e^{-\theta/(1-\upsilon)} - e^{-\theta/\upsilon}) \tag{4}$$

where θ is the reduced time, given by $\theta = (Q/V_t)t$, and the reduced volume, υ, is given by $\upsilon = V_i/V_t$. Q is the volumetric flow rate, V_i is the injected volume. V_t is the total volume, $V_t = V_i + V_g$, where V_g is the volume of the dominant dispersing unit (gradient chamber).

Integrating the concentration profile in eq 4, from the injection time to the long time limit of the experiment, yields the area for the nondiluted (full) peak

$$A_{tot} = \frac{\upsilon}{1 - 2\upsilon}\int_0^\infty (e^{-\theta/(1-\upsilon)} - e^{-\theta/\upsilon})\, dt = \frac{\upsilon V_t}{Q(1 - 2\upsilon)}(1 - 2\upsilon) \tag{5}$$

Likewise, integrating eq 4 from the delay time, t_{del}, to the long time limit of the zone yields the area of the resultant profile (the area of the shaded region in Figure 1)

$$A_{del} = \frac{\upsilon V_t}{Q(1 - 2\upsilon)}((1 - \upsilon)e^{-Qt_{del}/(V_t(1-\upsilon))} - \upsilon e^{-Qt_{del}/(V_t\upsilon)}) \tag{6}$$

Dividing eq 5 by eq 6 yields an expression for X^{-1}

$$X^{-1} = \frac{1 - 2\upsilon}{(1 - \upsilon)e^{-Qt_{del}/V_t(1-\upsilon)} - \upsilon e^{-Qt_{del}/\upsilon V_t}} \tag{7}$$

When no cleavage is made, corresponding to a delay time of zero, the inverse mole fraction (dilution factor) is calculated to be unity, using eq 7. Conversely, for a large delay time, the inverse mole fraction is very large. It is important to remember that this model (eq 4–7) is valid only for the gradient dilution chamber-based system, the trailing portion of the zone profile being an exponentially decreasing one.

RESULTS AND DISCUSSION

The 25-fold to 1000-fold diluted BCG standards were injected into a carrier stream flowing directly into the detector. Heights and areas of the resulting peaks were recorded. A quadratic regression was performed relating the peak heights as a function of concentration. The resulting calibration equation was

$$\text{PkHt} = (6.524 \times 10^{-3}) + 8623[\text{BCG}] - (2.455 \times 10^{-5})[\text{BCG}]^2 \tag{8}$$

where PkHt is the peak height and [BCG] is the concentration of the calibrant in μM. The heights of the peaks resulting from the dilution system are used to calculate C_{max}, the concentration of the analyte at the peak maximum. The dispersion coefficients are then calculated by dividing the concentration of the injected material by C_{max}

$$D = C^\circ / C_{max} \tag{9}$$

The inverse mole fractions, X^{-1}, for the peaks obtained by using the dilution system are more precisely calculated than D values for the two-line system since the inverse mole fraction calculations are based on mass balance. A 75-fold dilution was made of the 0.0023 M calibrating standard and this diluted sample was injected into the FIA system without the dilution system. The area, A°, was found to be 0.867. When an area is found of a peak with unknown dilution, eq 3 can then be used setting $k = 75$ and $A^\circ = 0.867$.

SZ, SZCS, and SZRS Systems. The SZ, SZCS, and SZRS systems described above were evaluated for range and precision of dilution, dependence on concentration of analyte, and sample viscosity. The different approaches were taken to develop systems with certain characteristics for flexible use, such as for low reagent consumption and low viscosity dependence, among others.

Figure 6 shows the resulting dispersion coefficients as a function of the delay time for the SZ, SZCS, and SZRS systems. A plot of the inverse mole fractions, X^{-1}, as a function of the delay time for these systems results in similar curves with numerical values about one-fourth of those for D. From these two plots it is shown that the SZCS system provides the highest dilution (expressed in dispersion coefficient, D, and

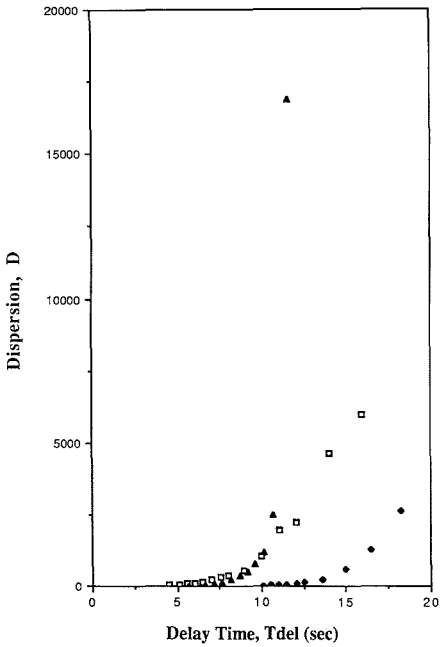

Figure 6. Dispersion coefficient versus delay time in the three nongradient device dilution systems (SZ, SZCS, and SZRS): filled triangle, SZCS; open square, SZ; filled diamond, SZRS.

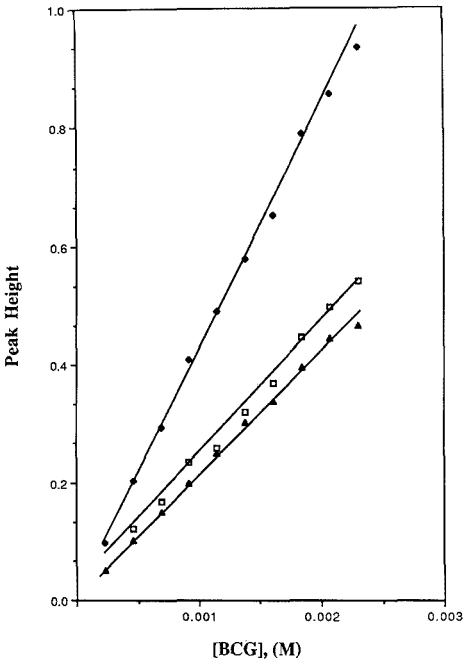

Figure 7. Peak height vs concentration of bromocresol green dye in the three nongradient device dilution systems (SZ, SZCS, SZRS): open square, SZ (40-fold dilution); filled diamond, SZRS (15-fold dilution); filled triangle, SZCS (45-fold dilution).

inverse mole fraction, X^{-1}). All three provide reproducible dilutions with low relative standard deviations (RSD).

As the dilution factors increase (increasing delay times) the RSD increases. A practical limit of the RSD was chosen as 3%. The SZ, SZRS, and SZCS maintained RSD's below this limit for dispersions up to 300, 2600, and 5000, respectively.

Samples with BCG concentrations between 0.000 23 and 0.0023 M were subjected to dilution by using the SZ, SZCS, and SZRS systems. These systems each had a set delay time; however this time was not the same for each because the residence time of the sample to the splitting tee varied between the systems. Figure 7 shows a plot of the resulting peak heights for each of these samples (after dilution) as a function of concentration. The plot shows no dependence of the dilution on sample concentration.

Viscosity Effects. The SZ, SZCS, and SZRS systems were tested for viscosity dependence. There was no viscosity effect on the dilution for samples with viscosities less than 10 cP. However, for samples with identical concentrations of BCG but with increasing viscosities greater than 10 cP, the resultant peak heights for these three systems decreased. This indicated that the increasing viscosity affected the development of the sample's concentration profile, leading to changed cleavage of the sample zone. Vanderslice et al. demonstrated that when the diffusion coefficients vary, even by a factor of 5, the bolus shape is changed dramatically (*13*). According to the Wilke–Chang formula for the diffusion coefficient, the diffusion coefficient is inversely proportional to the viscosity (*14*). Thus the change in sample viscosity would affect the development of its concentration profile in an FIA experiment. Since the three systems rely on reproducible development and cleavage of the concentration profile, it is not expected that they perform the same when the viscosity changes. Nor is it expected that these three methods will dilute samples reproducibly which have solutes of varying molecular weights or shapes, since both are known to affect the molecular diffusion coefficient (*15*).

The SZGC System. Our sample requirements dictated that the dilution technique under development must function well for sample viscosities which range from 1 to 167 cP. This range of viscosities corresponds to a range of diffusion coefficients that vary over 2 orders of magnitude. Accordingly, and to provide greater dilutions, the split zone gradient chamber (SZGC) approach was developed. The gradient chamber provides an external source of mixing which reduces the impact of the sample viscosity on the concentration profile which develops.

The same standards used to test the other systems were subjected to the SZGC dilution system. The experimental peak areas and inverse mole fractions for the SZGC system are plotted as a function of the delay time in parts A and B of Figure 8, respectively. A plot of dispersion coefficients results in a curve similar to Figure 8B, with numerical values about 10-fold greater. A dispersion coefficient of 15 000 is accomplished in under 2 min with an RSD of 3%.

Larger dispersion coefficients and inverse mole fractions were achieved with the SZGC system than with the other three systems discussed above, and precision was greater for higher dilutions. However, the increased dilution and precision were gained at the expense of increased residence times. Two minutes was often required between injections. The volume of reagent consumed was also much larger than for the previous three systems. Sample peaks for the SZGC system are shown in Figure 9. The decaying exponential feature of the peaks is clearly evident, as well as the increased peak width. The trailing edges are qualitatively similar, as expected. The gradient chamber is the dominant dispersing unit, and the injected bolus is cleaved at varying times along its trailing edge.

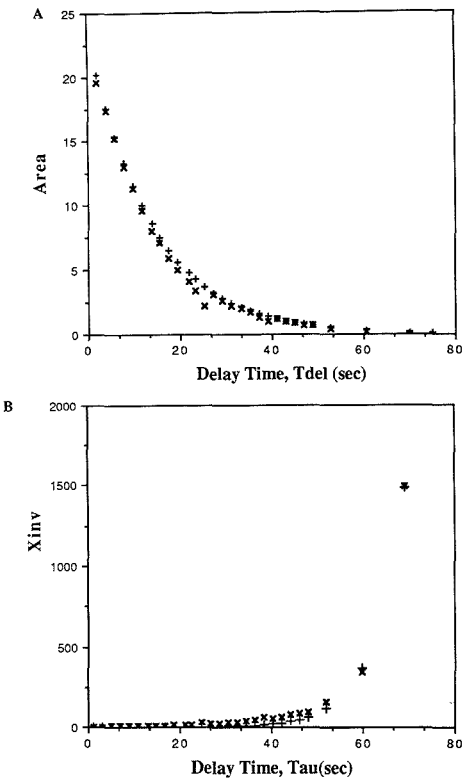

Figure 8. (A) Peak area versus delay time for SZGC (×). Also plotted are points (+) calculated by nonlinear regression using eq 10. (B) Inverse mole fraction versus delay time for SZGC (×). Also plotted are points (+) calculated by nonlinear regression using eq 11.

Table I. Fitted Parameters and Regression Coefficients for SZGC System Model

	A	B	C	D	R^2
area (eq 10)	22.09	0.0728	−12.68	4.405	0.9993
X^{-1} (eq 11)	18.497	0.1479	163.8	4.400	0.9963

Therefore, all material left in the chamber after the delay time is flushed to the detector and empties at a decaying exponential rate (*16*).

The curves reflect an exponential increase in X^{-1} and D values with increasing delay times. Equation 6 reflects exponential increases in X^{-1} for the SZGC system using mass balance relationships. Nonlinear regressions based on eq 6

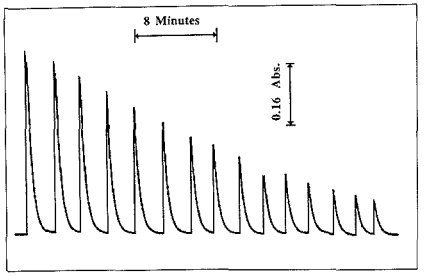

Figure 9. Typical SZGC peaks. Shown are dilutions using delay times ranging from 1.95 to 29.30 s, corresponding to dispersion coefficients of 24.1–226, respectively. The inverse mole fractions for these peaks are 3.35–25.2, respectively.

and 7 were performed. The nonlinear regression for eq 6 was calculated by using eq 10

$$A_{det} = Ae^{-Bt_{del}} - Ce^{-Dt_{del}} \quad (10)$$

Likewise, nonlinear regression calculation for eq 7 was performed by using eq 11

$$X^{-1} = \frac{1}{Ae^{-Bt_{del}} - Ce^{-Dt_{del}}} \quad (11)$$

The regression coefficients A, B, C, and D in eq 10 and 11 are listed in Table I. The value for D in both cases is approximately 4.4, which effectively removes the contribution of the second exponential from the equation. The contribution of the first exponent in each equation is simply the integral of the decaying exponential function which approximates the decaying portion of the gradient chamber concentration profile (*1*, *4*).

In any case, these equations allow the calculation of the dilution factor (X^{-1}) achieved for a specific delay time or the delay time required to achieve a particular dilution. This result is especially useful if the sample presented is too concentrated for measurement at a preestablished dilution factor and if the dilution factor needs to be adjusted. The dilution factor required to achieve a measurable response could be calculated by using this equation. This would also allow back-calculation of the concentration of the sample. Calculated areas and dilution factors are compared with experimental values in Figure 8. Good agreement between the experimental and calculated points is seen.

The SZGC approach was examined for dependence on the viscosity of the sample. With the exception of experimental error, no variation in the peak height was seen at sample viscosities up to 167 cP. The mechanical radial stirring is assumed to be responsible for reducing viscosity dependence which was dramatic in the other three systems.

Gisen et al. (*4*) pointed out that experiments which exploit the gradient do so with greater reproducibility when using the trailing edge rather than the leading edge since the trailing edge has smaller gradient than the leading edge. It was also

Table II. Merits and Drawbacks of Each Dilution Method

system	figure no.	merits	dilution range	drawbacks
SZ	2	provides rapid means for medium dilution	300	large viscosity dependence, sensitive to dead volume errors
SZCS	3	provides large, rapid dilutions	5000	large viscosity dependence, large reagent consumption
SZRS	4	provides moderate dilution with low reagent consumption	2600	large viscosity dependence, residence times somewhat longer than SZCS
SZGC	5	provides very large, precise dilutions, with no viscosity dependence	15 000	high reagent usage, very long residence times (on order of 1.5–2 min/sample)

shown (*4*) that precision associated with peaks obtained by using a gradient chamber as the primary dispersing component surpasses the precision associated with peaks originating in a capillary tube. These two observations clearly manifest themselves in this technique. The trailing edge of the peak is always used and the SZGC system provided the highest dilutions with the best precision.

CONCLUSION

When the dilution systems are compared for use, several aspects must be considered: speed, reproducibility, range of dilution, and ability to set or calculate dilution factors for analyte calibration. By far the most simple dilution system offered to date is a simple single-line system or one with a gradient chamber. The D values for these gradient chamber systems have a practical limit of 1000 and are fixed for a particular configuration. They have the added advantage of not requiring computer control. The cascade dilution system (*6*) also has the advantage of not requiring computer control and adds a further advantage in offering a range of dilutions that may be calculated by knowing the flow rates of the diluent and aspirant streams. The dilutions provided are on the order of 500-fold. Reis et al. reported total dispersions near 1000 obtained by using the original zone sampling approach (*5*). The zone sampling as well as the split zone methods require a source of timing, making the systems inherently more complicated. Using a zone sampling method that was modified to include two gradient chambers, an automated injection valve, and buret pumps, Garn and co-workers (*8*) were able to achieve dispersion coefficients on the order of 10^6-fold, clearly the largest dilutions provided by FIA thus far. The split zone systems here, however, using a manually controlled injection valve and peristaltic pumps, offered dispersion coefficients on the order of 10^4. While their use has sometimes been questioned, peristaltic pumps are more commonly used in FIA than alternative fluid propulsion devices. The current method was designed and optimized for the most common of experimental configurations.

The relative precision of the dilutions as a function of the delay time is similar among the first three of our systems, usually better than 3%, while the gradient chamber system generally provides somewhat improved precision for a given dilution. Increasing delay times are needed to provide larger dilutions, and the precision decreases at large delay times. This is likely due to small, random fluctuations of analyte concentration at the trailing edge of the zone. Practical limits for dilutions are listed in Table II for the systems using 3% RSD as a cutoff. Also noted in Table II are the advantages and disadvantages each system offers. The following guidelines are suggested for the use of these systems:

1. The time base of the dilution could be adjusted to a particular need by adjusting the flow rate. In any case the dilution provided will have to be calibrated for the individual system.

2. For moderate dilutions ($D < 2500$) with minimal reagent usage, the split zone reagent saver (SZRS) system should be used. There is at least a 50% reduction in carrier reagent usage compared with the SZCS system.

3. For moderate to high ($D < 15000$) and fast dilutions ($t_{del} < 12$ s) the split zone confluent streams system (SZCS) should be used. This approach is the method of choice when the samples have low viscosity. This approach also provides a means to employ a second carrier for further reactions.

4. For very high dilutions and when sample viscosities are greater than 10 cP, the split zone gradient chamber system (SZGC) should be used. This method, however, requires a longer time, on the order of 2 min, between samples. This time can be somewhat shortened by increasing the flow rate after cleavage of the sample zone has occurred. It was shown by Gisen et al. (*4*) that increasing the flow rate of samples eluted from gradient chambers resulted in no loss in precision.

LITERATURE CITED

(1) Ruzicka, J.; Hansen, E. H. *Anal. Chim. Acta* **1978**, *99*, 37.
(2) Olsen, S.; Ruzicka, J.; Hansen, E. H. *Anal. Chim. Acta* **1982**, *136*, 101.
(3) Stewart, K. K.; Rosenfeld, A. G. *Anal. Chem.* **1982**, *54*, 2368.
(4) Gisen, M.; Thommen, C.; Mansfield, K. F. *Anal. Chim. Acta* **1986**, *179*, 149.
(5) Reis, B. F.; Jacintho, J.; Moratatti, J.; Krug, F. J.; Zagatto, E. A. G.; Bergamin, F°, H.; Pessenda, L. C. R. *Anal. Chim. Acta* **1981**, *123*, 221.
(6) Whitman, D. A.; Christian, G. D. *Talanta* **1989**, *36*, 205.
(7) Toei, J. *Anal. Lett.* **1988**, *21*, 1633.
(8) Garn, M. B.; Gisin, M.; Gross, H.; King, P.; Schmidt, W.; Thommen, C. *Anal. Chim. Acta* **1988**, *207*, 225.
(9) *CRC Handbook of Chemistry and Physics*, 64th ed.; Weast, R. C., Ed.; CRC Press, Inc.: Boca Raton, FL, 1983; p D-150.
(10) Ruzicka, J.; Hansen, E. H. *Flow Injection Analysis*, 2nd ed.; Wiley: New York, 1988.
(11) Clark, G. D.; Christian, G. D.; Ruzicka, J.; Anderson, G. F.; van Zee, J. A. *Anal. Instrum.*, in press.
(12) Clark, G. D.; Hungerford, J. M.; Christian, G. D. *Anal. Chem.* **1989**, *61*, 973.
(13) Vanderslice, J. T.; Rosenfeld, A. G.; Beecher, G. R. *Anal. Chim. Acta* **1986**, *179*, 119.
(14) Giddings, J. C. *Dynamics of Chromatography, Part I, Principles and Theory*; Dekker: New York, 1965.
(15) Berry, R. S.; Rice, S. A.; Toss, J. *Physical Chemistry*; Wiley: New York, 1980; p 1104.
(16) Pardue, H. L.; Fields, B. *Anal. Chim. Acta* **1981**, *124*, 39.

RECEIVED for review November 28, 1988. Accepted May 15, 1989.

Titanium Dioxide Based Substrate for Optical Monitors in Surface-Enhanced Raman Scattering Analysis

Job M. Bello, David L. Stokes, and Tuan Vo-Dinh*

Advanced Monitoring Development Group, Health and Safety Research Division, Oak Ridge National Laboratory, Oak Ridge, Tennessee 37831-6101

An optical monitor was investigated for in situ surface-enhanced Raman scattering (SERS) analysis. This optical monitor consists of a solid surface such as a glass plate coated with TiO_2 and covered with a silver layer. The TiO_2 provides the necessary surface submicrometer roughness for the SERS process; the nominal particle diameter of TiO_2 used in this study is 0.2 μm. The effect of substrate conditions such as silver thickness and amount of TiO_2 on SERS intensity was investigated. Other experimental parameters including the solvent, the laser power, and the excitation geometry were found to have an effect on the SERS intensity of the model compound in solution. It was also shown that the solution SERS signal obtained with this method was very stable with time, and the SERS intensity did not appear to be affected significantly by exposure to laser radiation. The analytical figures of merit of this technique such as spectral features, signal reproducibility, and limits of detection were investigated to demonstrate the analytical potential of this new substrate that can be used as an optical monitor for in situ analysis of liquid samples.

INTRODUCTION

The discovery of an enhancement in the Raman scattering efficiency of molecules on electrochemically roughened electrodes by factors up to 10^7 has sparked renewed interest in the field of Raman spectroscopy during the past decade. Numerous reports have been published on the theoretical aspects of the surface-enhanced Raman scattering (SERS) phenomenon. Several models have been proposed to explain the SERS effect. One model attributes the SERS enhancement to the modification of the molecular polarizability caused by complex formation between the molecule and the atom of the metal surface (*1*). Another chemical concept called "adatom" involves the chemical adsorption between the analyte and the substrate (*2*). A third model attributes the SERS enhancement to increased local electric fields at the metal surface. This increased field strength is a result of excitation of the collective oscillations of the conduction electrons (surface plasmons) on the metal surface (*3–5*).

Recently, several analytical applications of SERS have appeared in the literature. The analytical usefulness of SERS as a new spectrochemical tool for the analysis of polycyclic aromatic compounds has been reported (*6*). SERS was also used to analyze organophosphorus chemical agents (*7*) and chlorinated pesticides (*8*). A SERS postcolumn detection system for high-performance liquid chromatography using a silver sol substrate has also been developed (*9*). Other applications of SERS with silver particles on quartz posts (*10, 11*), metal island films (*12*), and silver sols (*13*) have also been reported.

In most previous works involving SERS-active solid substrates (6–8, 10, 11), the sample was spotted on the substrates, was allowed to dry, and then was subjected to measurements. In this paper, a new approach to performing in situ SERS measurements using SERS-active solid substrates is reported for several carboxyl aromatic compounds. This technique allows in situ measurement of the SERS signal of an ethanolic solution of the analyte. The development of a new type of SERS optical sensor consisting of a glass plate coated with silver-coated TiO_2 is also described. Experimental conditions and the analytical aspects of this technique were investigated in detail.

EXPERIMENTAL SECTION

Instrumentation. SERS measurements were conducted with a SPEX Model 1403 double-grating spectrometer equipped with a gallium arsenide photomultiplier tube (RCA, Model C31034) operated in the single-photon counting mode. A SPEX Datamate computer was used for data storage and processing. A detailed description of the experimental setup has been described previously (*10*). The 514.5-nm line of an argon ion laser (Spectra Physics Model 166) was used for excitation. The laser power was set at 50 mW for most of the experiments. A right angle geometry of the laser excitation source and the scattered radiation was used. The monochromator bandpass was 2 cm^{-1}.

Chemicals. TiO_2 (Titanox 1000) was provided by N. L. Chemicals (Highstown, NJ). Terephthalic acid (Pfaltz and Bauer), *p*-aminobenzoic acid (Aldrich), gallic acid (Eastman Kodak), phthalic acid (Aldrich), and isophthalic acid (Pfaltz and Bauer) were used without further purifications. Sample solutions were prepared in spectroscopic grade ethanol (Warner-Graham Co.).

Procedure. SERS optical sensors were prepared in the following manner. Microscope slides were cut into rectangular strips, cleaned with dilute nitric acid, distilled water, and ethanol, and finally dried in an oven before use. Drops of an aqueous suspension of TiO_2 were delivered on the glass slide, which was then spun at 2000 rpm for 20 s with a spin-coating device to uniformly spread the TiO_2 on the surface of the glass. Silver was then thermally evaporated onto the TiO_2-coated glass strips under vacuum (*6*). Approximately 1 mL of the sample solution was pipetted into a standard fluorescence cuvette. Then, the silver-coated TiO_2 SERS substrate was inserted directly into the cuvette, and the SERS spectrum was recorded.

RESULTS AND DISCUSSION

SERS has been observed from various solid substrates such as metal electrodes, metal island films, and glass or cellulose coated with silver-coated microparticles. However, with the exception of metal electrodes, studies performed to date with solid substrates have been limited to dry-state analysis. The need for easily fabricated SERS-active optical monitors that can be used in solution is important for the application of SERS in in situ analyses. Although metal electrodes have been used in solution SERS studies, the difficulty in obtaining reproducible surface roughness from one electrode to another can be a problem with this substrate. Another medium where SERS enhancement can be observed is the silver sol solution. Although a very low SERS limit of detection can be obtained with silver sols, a very elaborate and precise procedure is usually required to obtain the right silver particle size in the sol necessary to induce the SERS signal. Hence, glass or cellulose coated with silver-coated microparticles should be ideal substrates for in situ SERS analysis because these

*Author to whom correspondence should be addressed.

0003-2700/89/0361-1779$01.50/0

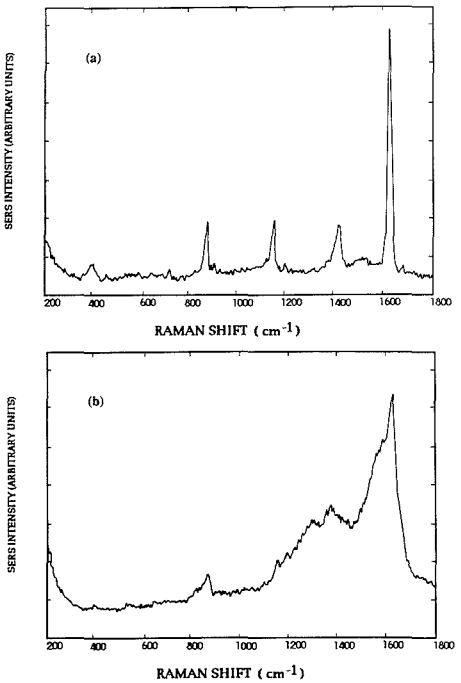

Figure 1. (a) In situ SERS spectrum of 500 ppb TPA in ethanol obtained with TiO_2 optical sensor. Laser power was 50 mW. (b) Dry-state SERS spectrum of 500 ng of TPA adsorbed on TiO_2 substrate. Laser power was 50 mW.

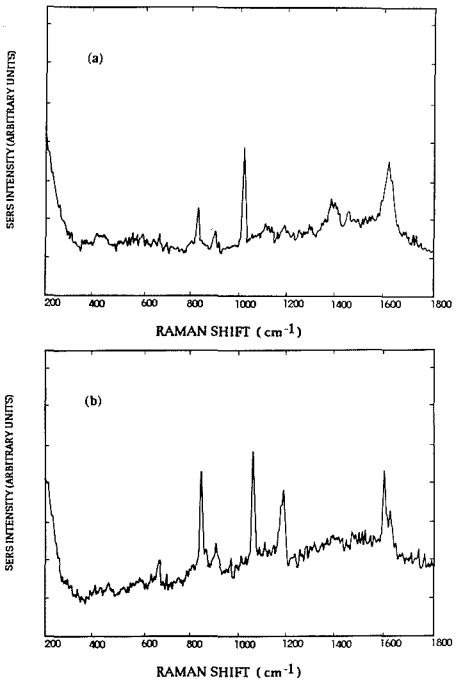

Figure 2. (a) In situ SERS spectrum of 8 ppm isophthalic acid obtained with TiO_2 optical sensor. Laser power was 50 mW. (b) In situ SERS spectrum of 8 ppm phthalic acid obtained with TiO_2 substrate. Laser power was 50 mW.

substrates usually give a good, reproducible SERS signal and are easily fabricated. Furthermore, a large number of compounds have been shown to exhibit a SERS signal on these substrates.

SERS Spectrum with TiO_2-Based Substrate. Figure 1a shows the in situ SERS spectrum of a 500 ppb ethanol solution of terephthalic acid (TPA), obtained with a TiO_2-based substrate. As shown in Figure 1a, the SERS spectrum of TPA shows five sharp bands, with the strongest band at 1618 cm^{-1}. The bands observed at 1618, 1142, 868, and 400 cm^{-1} correspond to A_g mode vibrations of TPA (*14*). On the other hand, the band at 1406 cm^{-1} corresponds to a symmetric OCO stretch (*15*). It is also noteworthy that the characteristic CO stretching-vibration band at about 1650 cm^{-1} is noticeably absent in the solution spectrum of TPA (Figure 1a). This indicates that the carboxylate form of TPA was the one adsorbed on the metal surface (*15*). In addition, the spectrum of TPA shown in Figure 1a is very similar to the one described in the literature for terephthalate ion adsorbed onto metal surfaces (*14*). The solution (ethanol) SERS spectrum of TPA was also obtained by using a silver-coated polystyrene bead (0.364 μm) on glass. The SERS spectrum of TPA obtained with this substrate was exactly the same as that obtained with the TiO_2-based substrate (Figure 1a).

The excitation beam used to obtain the in situ SERS spectrum of TPA shown in Figure 1a was the 514.5-nm line of the argon ion laser with a power of 50 mW. It has been reported in the literature that a broad background band occurring at the 1300–1600-cm^{-1} region is usually found in the dry-state SERS spectra of compounds such as phthalic acid and benzoic acid adsorbed on silver-coated microspheres on glass when the samples are excited with the 514.5-nm line, even with 30-mW laser power (*16*). These broad bands centered at 1337 and 1587 cm^{-1} have been attributed to Raman scattering from an amorphous carbon layer produced by the laser decomposition of an organic monolayer. The presence of the carbon bands in this region is a problem because they can obscure the SERS bands of the analyte that may occur in the 1300–1600-cm^{-1} region of the spectrum. Figure 1b shows the dry-state SERS spectrum of 500 ng of TPA adsorbed on silver-coated TiO_2 on glass, obtained with the 514.5-nm line and 50 mW of laser power. It is evident in Figure 1b that the carbon layer Raman scattering is present in the dry-state SERS spectrum of TPA on the TiO_2-based substrate and that some of the SERS bands of TPA were obscured by the carbon bands (1142 and 1406 cm^{-1}). With the in situ SERS method, however, the amorphous carbon Raman bands are noticeably absent. As shown in Figure 1a, the solution SERS spectrum of TPA does not show any bands at 1337 and 1587 cm^{-1}. The solution SERS spectra of other compounds that were investigated, such as isophthalic acid and phthalic acid, shown in parts a and b of Figure 2, respectively, also did not show the amorphous carbon bands at 1300–1600 cm^{-1}. The characteristic SERS bands of isophthalic acid and phthalic acid in the 1300–1600-cm^{-1} region were clearly visible in the in situ SERS spectra of these compounds (Figure 2). Several factors may account for the absence of amorphous carbon bands in the SERS spectrum obtained with the in situ technique. One explanation for the absence of the amorphous carbon bands is that any substrate surface heating that may have been caused by the incident laser beam would have been dissipated immediately since the substrate was in contact with the liquid medium, which served as a heat sink. Furthermore, when any photodecomposition of the sample occurred at the substrate

Table I. In Situ SERS Intensities of a 500 ppb Ethanol Solution of TPA as a Function of TiO_2 Suspensions Used To Produce the SERS-Active Substrates

% TiO_2	rel intens[a]	% TiO_2	rel intens[a]
5	1.0	20	3.3
10	2.0	25	2.8
15	2.4		

[a] Results of two determinations.

surface, the decomposed sample molecule could have diffused into the sample solution while being replaced by another TPA molecule from the bulk solution.

Silver Thickness. In this study, a glass coated with silver-coated TiO_2 was investigated as an SERS optical sensor for in situ SERS determination. TiO_2 is an ideal substrate for SERS because it is a relatively good insulator and also yields about the right grain of surface roughness (0.025–0.5 μm). These two aspects of TiO_2 are important parameters influencing the SERS signal. The TiO_2 material used in this work is only available in one particle size. The manufacturer listed the nominal particle diameter of the TiO_2 to be 0.2 μm. Since TiO_2 is a new substrate, it was necessary to find the optimum substrate conditions for inducing SERS. With TPA used as the model compound, the silver thickness needed to coat the TiO_2 on the glass surface was optimized to yield the strongest SERS signal. The determination of the optimum substrate conditions was carried out in situ using a 500 ppb ethanol solution of TPA. The 1618-cm^{-1} SERS band of TPA was used as the SERS reference signal. Silver-coated TiO_2 substrates with three different silver thicknesses were prepared and used for comparative SERS measurements. The relative SERS intensities of TPA on substrates having silver thicknesses of 250, 1250, and 1500 Å were found to be 1.0, 1.1, and 1.1, respectively. These results indicated that the SERS intensity of the model compound was constant for the various silver thickness layers investigated. Thus, all of the measurements performed in this study were made on a substrate having a 1200-Å silver layer.

Effect of TiO_2 Concentration. It has been shown with substrates such as fumed silica that the concentration of microbodies on the surface has an effect on SERS intensity (*17*). For example, a low-concentration solution of the substrate may not be sufficient to form a uniform layer of the microparticle, while a very high concentration solution may lead to the formation of aggregates, both of which may cause the SERS intensity to be less than optimal. We have therefore performed extensive studies to determine the optimal concentration of TiO_2 for SERS analysis. The amount of TiO_2 deposited onto the glass plate was varied, and comparative SERS measurements were conducted. Table I lists the SERS relative intensity of the 1618-cm^{-1} band of an ethanol solution of TPA, obtained with substrates produced with TiO_2 suspension concentrations of 5%–25% TiO_2 (w/v). TiO_2 suspensions greater than 25% give a very viscous solution and do not spread out uniformly onto the glass support; therefore, suspensions greater than 25% TiO_2 were not used in this study. Table I shows that an increase in the SERS intensity of the model compound was observed between 5% and 20% TiO_2. The most intense SERS signal was observed when substrates with 20% and 25% TiO_2 were used. Thus, for a TiO_2 substrate, at least a 20% TiO_2 solution should be used in order to obtain the optimum SERS intensity.

Monitor Excitation Using Back-Side Geometry. Another aspect of in situ SERS analysis that has a major effect on SERS intensity is the geometry of the substrate with respect to the laser beam. Figure 3 shows the geometry that was used with in situ solution SERS determination (Figure 3a) and the geometry used normally with dry-state SERS analysis (Figure 3b). It was found that directing the laser beam onto the back side of the substrate and collecting the scattered radiation also from the back side of the substrate (Figure 3a) increased the SERS intensity obtained in solution by approximately 11-fold. This is an interesting result because usually dry-state SERS measurements are done by focusing the laser beam onto the silver-coated side of the substrate (Figure 3b). We have also observed a similar effect for the in situ SERS analysis of benzo[*a*]pyrene–tetrol obtained with a silver-coated microsphere substrate (*18*). Jennings et al. (*19*) also reported that the SERS intensity for copper and zinc phthalocyanine complexes adsorbed on silver-island films was greater if a back-side geometry was used. They attributed this to the discontinuous nature of the silver film, whereby excitation from the back side of the substrate results in the observed scattering being mainly due to molecules forming the first monolayer of the analyte. Although a 1200-Å continuous layer of silver was used in our work, our results suggest that the laser beam was able to penetrate the silver layer and that the Raman radiation could be transmitted through the silver layer. However, it should be emphasized that further studies are still needed to explain this enhancement observed from the back-side geometry. The excitation of the molecules forming the first monolayer may be only one contributing factor to the observed enhanced SERS intensity obtained with this geometry (Figure 3a). At present, we are studying various conditions that may be important factors in the SERS enhancement effect observed from the geometry shown in Figure 3a.

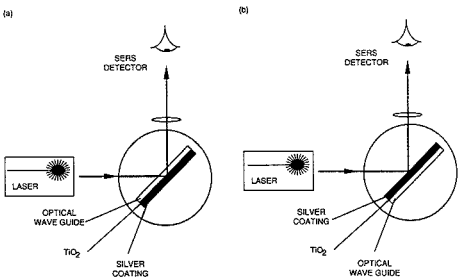

Figure 3. Top view of the excitation–detection geometries used for SERS measurements: (a) in situ SERS analysis; (b) dry-state SERS analysis.

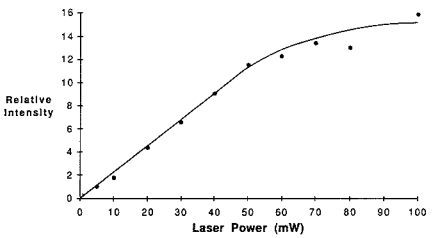

Figure 4. SERS relative intensity of 500 ppb TPA in ethanol as a function of laser power in milliwatts.

Excitation Laser Power. The effect of the strength of the excitation laser beam on SERS intensity was also investigated. Figure 4 shows a plot of the laser power in milliwatts as a function of the in situ SERS intensity of TPA in ethanol. It is evident from the results in Figure 4 that the SERS intensity increased linearly between 0 and 50 mW, and then beyond 50 mW, the SERS intensity increased slightly and appeared to level off. The leveling off of signal for laser power

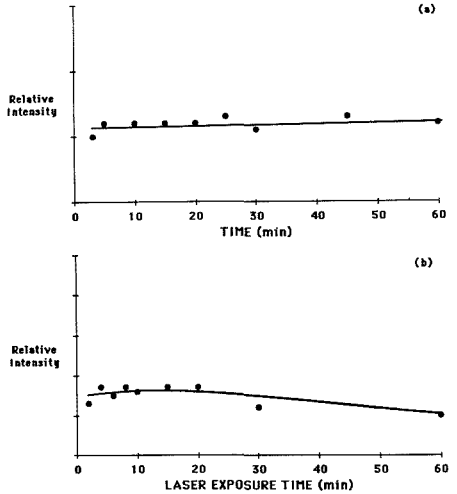

Figure 5. SERS relative intensity of 500 ppb TPA in ethanol as a function of time: (a) equilibrium rate study; (b) photostability study. Laser power was 50 mW.

greater than 50 mW is most likely caused by thermal decomposition of the molecule at these laser powers and with the beam focused to a small spot. It is also worth noting that even at only 5-mW laser power, the SERS intensity of TPA was still useful analytically. This is an important aspect of this technique for practical applications because of the possibility of using low-power, compact, and inexpensive lasers for field applications.

Response Time and Stability of the in Situ SERS Intensity. Response time and stability of the SERS signal with time are two important analytical parameters. Figure 5a shows the results of an experiment determining how fast TPA molecules would adsorb onto the surface of the SERS substrate. The procedure used to obtain the data in Figure 5a involved exposing the sample solution containing the SERS-active substrate to the laser beam for 1 min prior to data acquisition and then blocking the laser beam after each measurement to avoid sample exposure to laser irradiation between each data acquisition, thus preventing any photodecomposition of the analyte. The abscissa in Figure 5a refers to the time elapsed after the substrate was immersed into the sample solution. As shown in Figure 5a, the SERS intensity of TPA was stable throughout the entire time range of the experiment (3–60 min). The data shown in Figure 5a indicate that the rate of equilibrium of the TPA molecules between the ethanol solution and the SERS-active substrate was very fast, since the maximum SERS signal was reached in less than 3 min. Therefore, with this method the analyst only has to wait for a maximum of a few minutes prior to the start of data acquisition to obtain the optimum SERS intensity.

Figure 5b shows the photostability of the SERS intensity of TPA in ethanol. To obtain the data in Figure 5b, sample exposure to the laser beam and the start of data acquisition was initiated at 10 min after the substrate was immersed into the sample solution. This was done in order to let the TPA molecules equilibrate between the ethanol solution and the substrate. In addition, the sample was also not exposed to the laser beam during the equilibration period to prevent any photodecomposition that may occur during this period. It can be seen in Figure 5b that the SERS intensity of TPA was stable between 2- and 20-min laser exposures, and then the signal slightly dropped off beyond 20 min. This result indicates that TPA molecules were not thermally degraded by the laser beam with time.

Table II. Solution SERS Limits of Detection (LOD) of Carboxyl Aromatics in Ethanol Obtained with a Silver-Coated TiO_2-Based Substrate

compound	LOD,[a] ppb	LOD,[a] M
p-aminobenzoic acid	130	9.48×10^{-7}
isophthalic acid	1020	6.14×10^{-6}
phthalic acid	980	5.95×10^{-6}
gallic acid	932	4.05×10^{-6}
terephthalic acid	17	1.02×10^{-7}

[a] Relative standard deviation ~10%.

Analytical Figures of Merit. The signal reproducibility of in situ SERS analysis was also investigated. With the 1618-cm^{-1} SERS band of TPA used as the reference signal, the SERS intensity of TPA was obtained with 10 different silver-coated TiO_2 substrates for an ethanolic solution of TPA (500 ppb). The result of our measurements shows that the SERS signal obtained with this technique has good reproducibility. The relative standard deviation (RSD) of the 10 signals of TPA is ±10%. This RSD represents a significant improvement over that of dry-state SERS measurements, where typical RSDs were 20%–30%.

Table II lists the in situ SERS limits of detection (LOD) of five carboxyl aromatic compounds in ethanol obtained with the silver-coated TiO_2 substrate. LOD values were determined from the SERS spectrum (by using the most intense band of the analyte and the noise associated in this region of the spectrum) of a solution of the analyte in the linear range of the calibration curve. In addition, the definition of LOD employed was the concentration of the analyte that would give a signal-to-noise ratio of 3 ($S/N = 3$). As indicated in Table II, the LODs of the five carboxyl aromatics are excellent. The LOD range of the five compounds is from the low-parts-per-billion ($\sim 1 \times 10^{-7}$ M) to the low-parts-per-million ($\sim 6 \times 10^{-6}$ M). The wide range of LOD is most likely due to the degree of adsorption of the different compounds onto the SERS substrate.

LITERATURE CITED

(1) Furtak T. E. *J. Electroanal. Chem. Interfacial Electrochem.* **1983**, *150*, 375.
(2) Otto, A. *Appl. Surf. Sci.* **1980**, *6*, 309.
(3) Gersten, J.; Nitzan, A. *J. Chem. Phys.* **1980**, *73*, 3023.
(4) Kerker, M.; Wang, D. S.; Chew, H. *Appl. Opt.* **1980**, *19*, 4159.
(5) Ferrell, T. L. *Phys. Rev. B: Condens. Matter* **1982**, *25*, 2930.
(6) Vo-Dinh, T.; Hiromoto, M. Y. K.; Begun, G. M.; Moody, R. L. *Anal. Chem.* **1984**, *56*, 1667.
(7) Alak, A. M.; Vo-Dinh, T. *Anal. Chem.* **1987**, *59*, 2149.
(8) Alak, A. M.; Vo-Dinh, T. *Anal. Chim. Acta* **1988**, *206*, 333.
(9) Freeman, R. D.; Hammaker, R. M.; MeLoan, C. E.; Fateley, W. G. *Appl. Spectrosc.* **1988**, *42*, 456.
(10) Vo-Dinh, T.; Meier, M.; Wokaun, A. *Anal. Chim. Acta* **1986**, *181*, 1843.
(11) Enlow, P. D.; Buncick, M.; Warmack, R. J.; Vo-Dinh, T. *Anal. Chem.* **1986**, *58*, 1119.
(12) Jennings, C.; Avoca, R.; Hor, A.; Loufyt, R. O. *Anal. Chem.* **1984**, *56*, 2033.
(13) Berthod, A.; Laserna, J. J.; Winefordner, J. D. *Appl. Spectrosc.* **1987**, *41*, 1137.
(14) Boerio, F. J.; Roth, P. G. *Appl. Spectrosc.* **1987**, *41*, 463.
(15) Pagannone, M.; Formio, B.; Mattei, G. *Spectrochim. Acta* **1987**, *43A*, 621.
(16) Goudonnet, J. P.; Begun, G. M.; Arakawa, E. T. *Chem. Phys. Lett.* **1982**, *92*, 197.
(17) Vo-dinh, T.; Alak, A. M.; Moody, R. L. *Spectrochim. Acta* **1988**, *415*, 605.
(18) Vo-Dinh, T.; Miller, G. H.; Bello, J.; Johnson, R.; Moody, R. L.; Alak, A. M.; Fletcher, W. H. *Talanta* **1989**, *36*, 227.
(19) Jennings, C.; Aroca, R.; Hor, A.; Loutfy, R. O. *Anal. Chem.* **1984**, *56*, 2035.

RECEIVED for review December 5, 1988. Revised manuscript received May 2, 1989. Accepted May 18, 1989. This work was sponsored by the Office of Health and Environmental Re-

search under Contract DE-AC05-840R21400 with Martin Marietta Energy Systems, Inc., and the ORNL Director R & D Fund. This research was also supported in part by the appointment of J.M.B. to the Postgraduate Research Training Program under Contract DE-AC05-760R00033 between the U.S. Department of Energy and Oak Ridge Associated Universities and of D.L.S. to the SCUU Science Semester under Contract DE-AC05-840R21400 between the U.S. Department of Energy and Martin Marietta Energy Systems, Inc.

CORRESPONDENCE

Exchange of Comments on the Simplex Algorithm Culminating in Quadratic Convergence and Error Estimation

Sir: When they proposed their well-known simplex algorithm for minimizing an arbitrary nonlinear function of n parameters, Nelder and Mead (*1*) suggested that a suitable way to end their procedure would be to fit the $n + 1$ function values of the final simplex to a quadratic equation. The necessary theory had been derived earlier by Spendley et al. (*2*). Recently, Phillips and Eyring (*3*) have reiterated this suggestion, stressing that, for least-squares problems, the quadratic approximation provides a sound basis for estimating the uncertainties in the optimized parameter values.

The chief purposes of this contribution are (a) to correct a number of serious errors in the literature; (b) to draw attention to a particularly efficient method of implementing the quadratic approximation that is applicable in dealing with least-squares problems; (c) to stress the value of the quadratic approximation in locating the precise minimum after the simplex algorithm has progressed to a suitable point; and (d) to point out that under certain circumstances the quadratic approximation is unsuccessful, although the simplex algorithm itself very rarely fails.

ERRORS IN THE LITERATURE

The expression given by Phillips and Eyring (*3*) in their Table I, for calculating the elements of the matrix $\mathbf{Q}$, is incorrect and should be eq 1. In other words the *ith* column

$$q_{ji} = \theta_{i,j} - \theta_{0,j} \tag{1}$$

of $\mathbf{Q}$ is equal to $\vec{\theta}_i - \vec{\theta}_0$. Equations 5–7 in the paper of Phillips and Eyring are also incorrect. To be consistent with their definition of $\bar{\mathbf{a}}$, the term $\mathbf{QB}^{-1}\bar{\mathbf{a}}$ in eq 5 ought to be multiplied by $^1/_2$. In eq 6, the constant should be 4, not $^1/_4$. Equation 7 reiterates an error, or possibly a misprint, in ref 1; the multiplier 2 is not required. It may be shown that the matrix $(\mathbf{Q}^{-1})^t\mathbf{BQ}^{-1}$ is equal to the curvature matrix, α, as defined by Bevington (*4*), not as incorrectly defined in ref 3. It follows on the basis of equations derived in ref 4 that the multiplier 2 is not required.

These corrections are incorporated in Table I and eq 2–4 of this paper. Here and subsequently, the symbols used by Nelder and Mead (*1*) are mainly adhered to. For example, the parameter vector at vertex i is $\mathbf{p}_i = (p_{i1}, \ldots, p_{in})$, and the corresponding function value is y_i. An exception is $\mathbf{a}$, which conforms with the definition of Spendley et al. (*2*), not that of Nelder and Mead (*1*). Before $\mathbf{a}$, $\mathbf{B}$, and $\mathbf{Q}$ are calculated according to Table I, the indexing is adjusted so that y_0 is the minimum function value (the other y_i need not be sorted), and the function values $y_{ij} (i \neq j)$ at the halfway points (i.e. midway along the sides of the simplex) are computed.

Table I. Rules for Calculating the Elements of Vector a and Matrices B and Q

$a_i = 4y_{0i} - y_i - 3y_0$	$i = 1, \ldots, n$
$b_{ii} = 2(y_i + y_0 - 2y_{0i})$	$i = 1, \ldots, n$
$b_{ij} = 2(y_{ij} + y_0 - y_{0i} - y_{0j})$	$i \neq j$
$q_{ji} = p_{ij} - p_{0j}$	$i = 1, \ldots, n; j = 1, \ldots, n$

The parameter vector corresponding to the minimum of the quadratic function is given by eq 2.

$$\mathbf{p}_{min} = \mathbf{p}_0 - {}^1/_2\mathbf{QB}^{-1}\mathbf{a} \tag{2}$$

If the quadratic approximation is satisfactory, the calculated $\mathbf{p}_{min}$ ought to lie within the parameter space adequately mapped by the simplex. This requirement is expressed by the inequality (*3*). The constant 4 in inequality 3 corresponds

$$(\mathbf{B}^{-1}\mathbf{a})^t(\mathbf{B}^{-1}\mathbf{a}) < 4 \tag{3}$$

to a suggestion made in ref 2: The inequality could be made slightly less restrictive by substituting a larger constant, say 16.

For a least-squares problem, σ^2 is calculated as $y_{min}/(N - n)$ (where N is the number of observations), and the variance–covariance matrix, ϵ, is calculated by using eq 4. The

$$\epsilon = \sigma^2\mathbf{QB}^{-1}\mathbf{Q}^t \tag{4}$$

uncertainties in the parameters may now be calculated as the square roots of the diagonal elements of ϵ.

LEAST-SQUARES PROBLEMS

Experimentalists are frequently concerned with the differences between observed and calculated quantities. These differences are sometimes named residuals. In least-squares problems, the aim is to minimize the sum of the squares of the residuals. Equations 2–4 may be used to deal with least-squares problems, but their use is inefficient. For this type of problem, the quadratic approximation implies that the residuals vary linearly with respect to the parameters. It follows that function evaluations at the $n + 1$ points of the simplex are sufficient to define the quadratic function, and it is unnecessary to calculate the additional $n(n + 1)/2$ function values at the halfway points. The following procedure is based on theory given by Spendley (*5*). The simplex procedure may require minor surgery, since it is necessary to retain in memory the N residuals, $f_k(\mathbf{p}_i)$ $(k = 1, \ldots, N)$, as well as the function value $y_i = \sum_{k=1}^{N}\{f_k(\mathbf{p}_i)\}^2$, associated with each of the $n + 1$ vertices of the simplex. On exit from the simplex algorithm, the first step is to adjust the indexing so that y_0 is the minimum function value. One then calculates elements $M_i^{(k)}$ $(i = 1, \ldots, n; k = 1, \ldots, N)$ using eq 5. The

0003-2700/89/0361-1783$01.50/0

$$M_i^{(k)} = f_k(\mathbf{p}_i) - f_k(\mathbf{p}_0) \quad (5)$$

elements $M_i^{(k)}$ may be stored in the array previously used for the residuals, ensuring that the $f_k(\mathbf{p}_0)$ are not overwritten. Next, one constructs an $n \times n$ matrix, Ω, using eq 6 and an

$$\Omega_{ij} = \sum_{k=1}^{N} M_i^{(k)} M_j^{(k)} \quad (6)$$

n-element column vector, $\mathbf{F}_0$, using eq 7. Like $\mathbf{B}$ and $\mathbf{a}$, Ω

$$F_{0i} = \sum_{k=1}^{N} f_k(\mathbf{p}_0) M_i^{(k)} \quad (7)$$

and $\mathbf{F}_0$ contain the coefficients of a quadratic approximation in a convenient coordinate system, but whereas Ω is directly comparable to $\mathbf{B}$, $\mathbf{F}_0$ is comparable to $-^1/_2\mathbf{a}$. In terms of Ω and $\mathbf{F}_0$, eq 2–4 are replaced by eq 8–10, respectively Equations 8–10 have the advantage over the analogous eq 2–4 in that their use avoids the need to calculate the function values at the halfway points. A possible disadvantage is that the N residuals at the $n + 1$ vertices must be stored in memory—when microcomputers are used to analyze large data sets, this can pose a problem.

$$\mathbf{p}_{\min} = \mathbf{p}_0 + \mathbf{Q}\Omega^{-1}\mathbf{F}_0 \quad (8)$$

$$(\Omega^{-1}\mathbf{F}_0)^t(\Omega^{-1}\mathbf{F}_0) < 1 \quad (9)$$

$$\epsilon = \sigma^2\mathbf{Q}\Omega^{-1}\mathbf{Q}^t \quad (10)$$

THE FLOW DIAGRAMS

Flow diagrams applicable to any minimization problem and exclusively to least-squares problems are shown in Figure 1 and 2, respectively. In these diagrams some of the Fortran variable names that were employed by O'Neill (*6*) are used.

The upper part of Figure 1 is a slightly simplified version of the flow diagram of Nelder and Mead (*1*), to which a few minor corrections have been made. α, β, and γ are coefficients for which values of 1, $^1/_2$, and 2 were recommended (*1*). The simplification, which has been used by other workers (*7*), is that whenever a contracted vertex is calculated, it always replaces the previous worst vertex. This simplification had no effect on the rate of convergence with five of the six test functions listed in the following section, but with test function 4, it led to a worthwhile reduction in the number of function evaluations. After an expansion, Nelder and Mead incorporated the expanded (as opposed to the reflected) vertex if $y^{**} < y_l$. It has been suggested (*8*, *9*) that the appropriate condition ought to be $y^{**} < y^*$. It is not clear that this modification is an improvement, when one considers the desirability of shifting the simplex as rapidly as possible in a moderately good direction. With the six test functions listed in the following section, the modification was advantageous in two cases, was detrimental in two cases, and in two cases did not influence the rate of convergence. The modification has not been incorporated into Figure 1.

A feature of Nelder and Mead's original flow diagram is that, with each cycle through the procedure, the value of y_l does not necessarily improve (decrease). For practical purposes, it seems useful to distinguish between such a cycle and an iteration, meaning a succession of cycles culminating in a lowering of y_l. In a computer program written by Daniels (*10*) an iteration was considered complete only when an expansion was attempted; however, this overlooks the fact that a succession of cycles in which an expansion is not attempted may result in a lowering of y_l. In Figure 1, after each cycle a check is made to determine whether y_l has decreased. Only if y_l has decreased is a check made to see if a further iteration is required. This is an alternative approach to that of O'Neill (*6*), who checked the convergence criteria every KONVGE cycles, where KONVGE was a number supplied by the user.

One should aim to proceed to the final stage of fitting the y_i values to a quadratic function as soon as the vertices of the simplex are sufficiently close to the desired minimum for the quadratic approximation to be satisfactory. How does one determine when this point has been reached? A good compromise between rigor and efficiency seems to be provided by monitoring the variance of function values, calculated as $(\sum_{i=1}^{n+1}(y_i)^2 - (\sum_{i=1}^{n+1}y_i)^2/(n+1))/n$. When this quantity becomes smaller than a preset value (named REQMIN, in conformity with O'Neill), the simplex iterations are stopped. REQMIN should be neither too large, in which case the quadratic approximation may be unsatisfactory, nor too small, when round-off errors may be a problem. Practical experience is helpful in selecting a suitable value, and some pertinent data is given in the following section of this paper.

Figure 1 includes an addendum, below the broken line, which exploits eq 2–4 and is applicable to any kind of unconstrained minimization problem. Figure 2 shows an alternative addendum that exploits eq 8 and 10 and is restricted to least-squares problems. These addenda are intended to show possible ways in which the principles may be applied. Clearly, the details will depend on the intended application—for example a program unit intended for interactive use will differ from a program unit for use in batch mode. Equation 8, since its use does not require additional function evaluations, can be incorporated into the simplex algorithm as an additional search strategy; this subject has been discussed by Spendley (*5*).

PERFORMANCE OF THE PROGRAMS

Computer programs to implement the flow diagrams shown in Figures 1 and 2 were written for the IBM PC in ASYST (a trademark of Asyst Software Technologies, Inc.). Program P1 implemented the simplex algorithm above the broken line in Figure 1. Program P2 implemented the whole of the flow diagram. Program P3 combined the simplex algorithm with the addendum shown in Figure 2.

ASYST uses the 8087 coprocessor, with an internal accuracy of about 18 digits, for all arithmetic. Because of this, calculations are not significantly faster using single-precision variables (accuracy: 7 digits) than using double-precision variables (accuracy: 16 digits). For this reason, programs P1, 2 used double precision throughout. To implement Figure 2, a large amount of memory is often needed to store the $N(n + 1)$ residuals, as mentioned above. To alleviate this problem, in P3 the residuals were stored in single precision, although double precision was used for all other floating point variables. Fortran subroutines that use the same principles as P1–3 were also written and tested initially on a VAX-11: Single-precision versions of these subroutines did not always give the same numerical results as P1–3, possibly because of errors in calculating the variance of function values (*11*), but when they were converted to double precision the output was almost identical with that of P1–3. The double-precision subroutines were also compiled and run on an IBM PC (with 8087), with satisfactory results.

The following six test functions were used:

(1) $y = (x_1^2 + 3\cos x_2 - 2)^2 + (\cos x_1 + 2x_1x_2 - 4)^2$; starting point 1,1. See ref 10.

(2) $y = 100(x_2 - x_1^2)^2 + (1 - x_1)^2$; starting point −1.2,1. Test function 1, ref 6.

(3) $(x_1 + 10x_2)^2 + 5(x_3 - x_4)^2 + (x_2 - 2x_3)^4 + 10(x_1 - x_4)^4$; starting point 3,−1,0,1. Test function 2, ref 6.

(4) $y = 100\{x_3 - 10\theta(x_1,x_2)\}^2 + \{\sqrt{(x_1^2 + x_2^2)} - 1\}^2 + x_3^2$; when $x_1 > 0$, $2\pi\theta(x_1,x_2) = \arctan(x_2/x_1)$; when $x_1 < 0$, $2\pi\theta(x_1,x_2) = \pi + \arctan(x_2/x_1)$; when $x_1 = 0$ and $x_2 = 0$, $y = 10000$; starting point −1,0,0. Test function 3, ref 6.

(5) $y = \sum_{i=1}^{10} x_i^4$; starting point 1,1, ..., 1. Test function 4, ref 6.

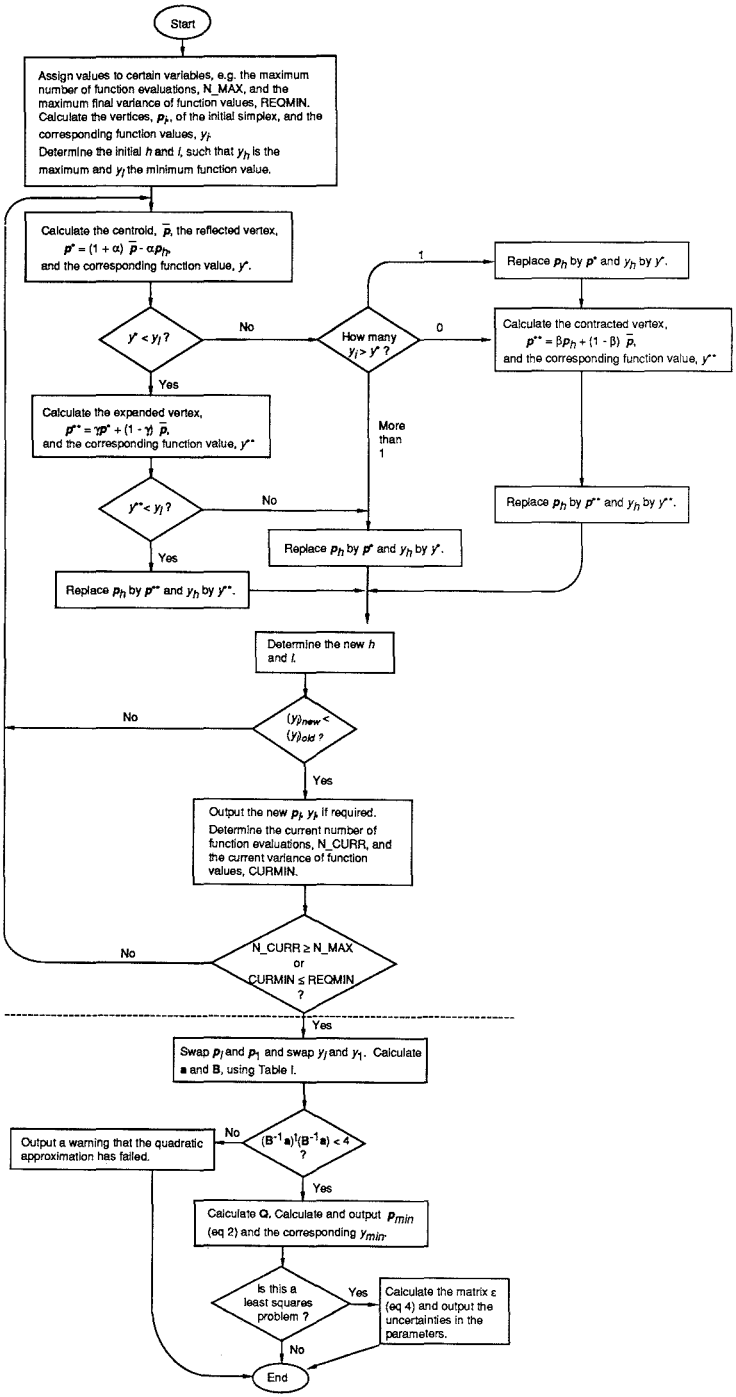

Figure 1. Flow diagram showing a slightly modified Nelder–Mead simplex algorithm with an addendum (below the broken line) exploiting eq 2–4.

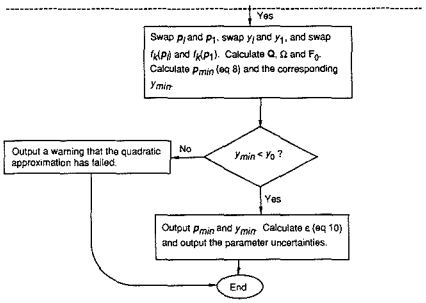

Figure 2. An addendum to the simplex algorithm (above the broken line in Figure 1) that exploits eq 8 and 10.

Table II. Performance of Programs P1 and P2 with Five Test Functions

function	program	REQMIN	no. of function evaluations	function min
1	P1	10^{-13}	60	3.8×10^{-8}
	P2	10^{-10}	49	9.1×10^{-13}
2	P1	10^{-13}	151	3.1×10^{-9}
	P2	10^{-10}	142	1.7×10^{-9}
3	P1	10^{-13}	206	1.1×10^{-7}
	P2	10^{-10}	203	*a*
4	P1	10^{-13}	238	1.9×10^{-7}
	P2	10^{-10}	230	5.5×10^{-10}
5	P1	10^{-13}	457	8.2×10^{-7}
	P2	10^{-10}	349	*a*

[a] Quadratic approximation failed.

(6) $y = \sum_{i=1}^{N}[A_i - x_1(1 - \exp(-x_2 t_i))]^2$; starting point 1,1. This corresponds to the least-squares problem defined in ref 12, where the 18 observed values of A and t are listed.

For these test runs the side length of the initial simplex was 1, and the maximum number of function evaluations allowed (N_MAX) was 1000. For the maximum allowed variance of function values, REQMIN, various values were tried: It was found that with program P1 a suitable value was 10^{-13}, and with programs P2 and P3 a suitable value was 10^{-10}. Results with functions 1–5 are reported in Table II. These functions all have minima of zero. The table shows that whenever the quadratic approximation did not fail, P2 achieved a lower function minimum after a smaller number of function evaluations than P1. Of course, the value of REQMIN could be adjusted so as to achieve a different trade-off between speed and accuracy.

Functions 3 and 5 do not approximate to a quadratic form, even in the close vicinity of the minimum. In both cases the failure of the quadratic approximation was clearly shown by the fact that the inequality (3) was not satisfied. It seems likely that this kind of situation would be rare in dealing with least-squares problems; if it did arise, one would clearly need to disregard any errors derived via eq 4 or eq 10.

Phillips and Eyring (*3*) did not use the quadratic approximation to help locate the function minimum, but only as a means of estimating errors. With their method, a relatively small value of REQMIN must be used to locate the minimum precisely. As Table II shows, the method is less efficient than the kind of strategy used in P2, except when the quadratic approximation fails. Because of the smallness of REQMIN, the variations in y_i (at any rate when calculated by using single precision) may be strongly influenced by round-off errors, necessitating enlargement of the simplex before proceeding with the quadratic approximation, as originally suggested by Nelder and Mead (*1*). Such an enlargement compounds the inefficiency of the method, because of the additional function evaluations needed.

Table III. Performance of Programs P1, P2, and P3 with Test Function 6

program	REQMIN	no. of function evaluations	function min	param uncertainties
P1	10^{-13}	76	0.003 602 958 9	
P2	10^{-10}	67	0.003 602 812 0	0.0088; 0.0104
P3	10^{-10}	64	0.003 602 809 0	0.0083; 0.0098

Results with function 6 are reported in Table III. This function has a minimum of 0.0036028045.... Clearly P2 and P3 are superior to P1, both in rate of convergence and in providing estimates of the errors. P2 and P3 give similar results, but P2, unlike P3, requires $n(n + 1)/2$ function evaluations at the halfway points. This is not a problem for simple functions such as 6, but for complex functions of many parameters it can be a problem. We regularly use a program similar to P3 to adjust spectral parameters so as to minimize the deviation between calculated and observed electron spin resonance spectra (*13*). In a typical example the number of parameters might be 13, and a function evaluation might take 40 s, using an IBM PC. In this situation the additional $n(n + 1)/2$ function evaluations required by P2 would take about 1 h.

LITERATURE CITED

(1) Nelder, J. A.; Mead, R. *Comput. J.* **1965**, *8*, 308.
(2) Spendley, S. N.; Hext, G. R.; Himsworth, F. R. *Technometrics* **1962**, *4*, 441.
(3) Phillips, G. R.; Eyring, E. M. *Anal. Chem.* **1988**, *60*, 738.
(4) Bevington, P. R. *Data Reduction and Error Analysis for the Physical Sciences*; McGraw-Hill: New York, 1969; eq 8–24, 11–13, 8–30.
(5) Spendley, W. In *Optimization: Symposium of the Institute of Mathematics and its Applications, University of Keele, England, 1968*; Fletcher, R., Ed.; Academic: New York, 1969; p 259.
(6) O'Neill, R. *Appl. Stat.* **1971**, *20*, 338.
(7) Deming, S. N.; Parker, I. R. *CRC Crit. Rev. Anal. Chem.* **1978**, *7*, 187.
(8) Benyon, P. R. *Appl. Stat.* **1976**, *25*, 97.
(9) Aberg, E. R; Gustavsson, A. G. T. *Anal. Chim. Acta* **1982**, *144*, 39.
(10) Daniels, R. W. *Introduction to Numerical Methods and Optimization Techniques*; North-Holland: New York, 1978.
(11) Chambers, J. M.; Ertel, J. E. *Appl. Stat.* **1974**, *23*, 250.
(12) Deming, S. N.; Morgan, S. L. *Anal. Chem.* **1973**, *45*, 278A.
(13) Beckwith, A. L. J.; Brumby, S. *J. Magn. Res.* **1987**, *73*, 252.

Steven Brumby

Research School of Chemistry
Australian National University
G.P.O. Box 4, ACT 2601, Australia

RECEIVED for review July 28, 1988. Accepted April 17, 1989.

Sir: In an earlier paper (*1*), we discussed a method proposed by Nelder and Mead (*2*) for estimating parameter errors in nonlinear least-squares data analysis using the sequential simplex method. There were several errors in the paper, and a correction has appeared in print (*3*). In the preceding paper Brumby (*4*) discusses a second approach to this problem due

0003-2700/89/0361-1786$01.50/0

to Spendley (5) and corrects some mistakes in the literature. It should be noted that ref 3 and 4 use different definitions in Table I.

It is the purpose of this comment to clarify several misrepresentations of our article (1), not to dispute the validity of Brumby's approach. The following discussion will use the notation of ref 4. In this notation, P1 is a modified simplex method without quadratic convergence (5), P2 uses P1 plus the method of ref 1–3, and P3 uses Brumby's method added to P1.

(1) Reference 4 states that single- and double-precision versions of programs P1–3 did not always give the same results "possibly because of errors in calculating the variance of function values". It should be noted that ref 1 codes the simplex algorithm in single precision except for the function values, y_i, and variance calculations, which are done in double precision to avoid round-off errors. The work of Chambers and Ertel (6) was cited in ref 1 to reinforce this point.

(2) Reference 4 incorrectly states that Phillips and Eyring use the quadratic approximation only for error estimation, and not in locating the precise minimum of the function.

(3) Brumby is also mistaken when he states that P2 requires an extremely small value of REQMIN to locate the precise minimum. For example, the six test functions considered in ref 4 used the same value of REQMIN for P2 and P3 and a value 3 orders of magnitude smaller for P1.

(4) It is not our contention that the simplex must be contracted until round-off error strongly influences the result, and the simplex then enlarged. The simplex is enlarged only if required to obtain reliable error estimates.

Finally, a general comment concerning execution times is in order. The last paragraph of ref 4 discusses the routine use of P3 to fit a 13-parameter function. Results in ref 2, 4, and 7 suggest such a problem will require several hundred iterations and several hours for minimization and is not a typical example. Simplex routines are fairly competitive with other methods for a small number of parameters, but become much less efficient than Newton–Raphson or quasi-Newton routines for more than five parameters (6–11).

LITERATURE CITED

(1) Phillips, G. R.; Eyring, E. M. *Anal. Chem.* **1988**, *60*, 738–741.
(2) Nelder, J. A.; Mead, R. *Comput. J.* **1965**, *8*, 308–313.
(3) Phillips, G. R.; Eyring, E. M. *Anal. Chem.* **1988**, *60*, 2656.
(4) Brumby, S. *Anal. Chem.*, preceding paper in this issue.
(5) Spendley, W. In *Optimization: Symposium of the Institute of Mathematics and its Applications, University of Keele, England, 1968*; Fletcher, R., Ed.; Academic Press: New York, 1969.
(6) Chambers, J. M.; Ertel, J. E. *Appl. Stat.* **1974**, *23*, 250–251.
(7) Reddy, B. R. *Appl. Spectrosc.* **1985**, *39*, 480–484.
(8) Powell, M. J. D. *SIAM Rev.* **1970**, *12*, 79–97.
(9) Chambers, J. M. *Biometrika* **1973**, *60*, 1–13.
(10) Olsson, D. M.; Nelson, L. S. *Technometrics* **1975**, *17*, 45–51.
(11) Bard, Y. *Nonlinear Parameter Estimation*; Academic Press: New York, 1974.

G. R. Phillips
E. M. Eyring*

Department of Chemistry
University of Utah
Salt Lake City, Utah 84112

RECEIVED for review February 27, 1989. Accepted April 17, 1989. This research was supported in part by the Office of Naval Research.

TECHNICAL NOTES

Construction of an Optically Transparent Thin-Layer-Electrode Cell for Use with Oxygen-Sensitive Species in Aqueous and Nonaqueous Solvents

Matthew B. G. Pilkington, Barry A. Coles, and Richard G. Compton*

Physical Chemistry Laboratory, Oxford University, South Parks Road, Oxford OX1 3QZ, England

We present a design for a reusable optically transparent thin-layer-electrode (OTTLE) cell, which is easy to assemble and does not require technical skills or services. All the complex parts are obtainable as standard items from the manufacturers quoted (vide infra). Designs for O_2-free nonaqueous OTTLE cells have appeared in the literature (1–8). However, unlike the cell reported here, these all required instrument-making facilities for construction. The cell can be reused without dismantling for either aqueous or nonaqueous work. Leakage is not a problem over the lifetime of several experiments, and an additional advantage is the ability to thermostat the cell (0–40 °C).

EXPERIMENTAL SECTION

The main cell body was an Hellma optically transparent flowthrough cell available in UV–visible and IR quartz glass (catalog no. 136K, light path lengths of 100, 200, and 500 μm, Hellma (England), Ltd., Westcliffe-on-Sea, Essex, England). The working chamber was formed by sandwiching a semitransparent gold minigrid (100 wires/in., 80% transmittance, Buckbee Mears Co., St. Paul, MN) between the two cell plates (Figure 1). The solution under investigation could flow in the direction indicated. This aided cleansing and drying of the cell for experimentation on different solutions. The dimensions of the working chamber were as shown (Figure 1). In order to prevent leaks due to the Au minigrid passing out through the gap between the cell plates, the cell was heated while being held together firmly by a Hellma metal flowthrough cell holder (catalog no. 013.000) and low-melting wax (facial depilatory wax, Vychem, Ltd., Poole, Dorset, England) fed into the gap by capillary action. This wax has excellent adhesion to silica, melts at 50 °C, sets rigidly on cooling, and dissolves (for dismantling/cleaning purposes) in ethanol. This provided an adequate seal for acetonitrile, dichloromethane, and water. The cell was jacketed with flowing argon to prevent O_2 from diffusing through the wax seal. A slot could be ground with simple glassworking facilities to allow the electrode to be introduced without altering the path length of the original cell, but an O_2-free seal would still be required at the point of entry of the minigrid. The use of a thermoplastic material for sealing allows easy assembly and disassembly with little risk of breakage—an important consideration with silica components—and justifies

0003-2700/89/0361-1787$01.50/0

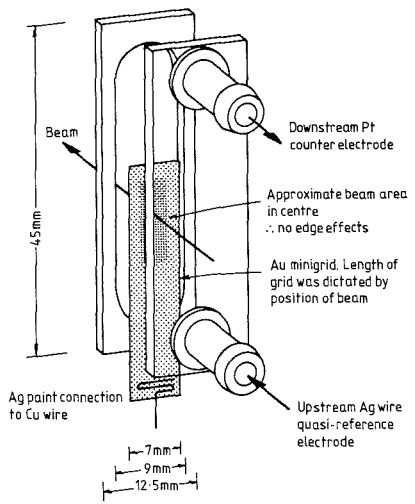

Figure 1. Diagram of a Hellma flow-through cell converted for spectroelectrochemistry.

the acceptance of a finite life for the seal. The wax seal is slowly degraded with a lifetime of at least 1 h of continuous experimentation in dichloromethane, 10 h in acetonitrile, and longer with water. Intermittent use may extend over a long period if the flow system is drained by drawing dry air through after each experimental session. Some solvents (e.g. dimethylformamide) or higher temperature experiments would require a different sealant, but we would expect to use the same method. We have found no evidence of electroactivity caused by exposure of these solutions to the wax. Optical absorption for dissolved wax in acetonitrile, dichloromethane, and water is too low at the concentrations involved to affect the UV–vis spectrum at $\lambda \geq 250$ nm.

The cell and cell holder assembly fits a standard water thermostated Perkin-Elmer cell holder (Europe catalog no. B008-0819) and was used mounted in a Perkin-Elmer Lambda-5 spectrometer. The OTTLE cell plus holder have the same external cross sectional dimensions of 12.5 × 12.5 mm as a standard 10 mm path length UV–vis cell. The cell was fed via a gravity feed reservoir mounted outside the spectrometer where degassing of O_2-sensitive solutions with argon could take place. Connection from the reservoir to the cell was via 1.5 mm bore Altex poly(tetrafluoroethylene) (PTFE) tubing (Anachem, Luton, England). This was jacketed with an argon-purged tube to prevent ingress of O_2. The electrical connection to the Au minigrid was made by silver paint (RS Components, part no. 555-156) to a copper wire. A silver wire quasi-reference electrode was placed within the PTFE tubing close to and upstream of the cell but sufficiently close to avoid excessive ohmic drop. This electrode was brought out for connection via an Altex "tee" connector and an Araldite seal. The PTFE flow tubing was connected to the cell by using short lengths of Ar jacketed silicone rubber tubing. The Pt counter electrode was placed in a wider section of tubing downstream from the cell to prevent interference by counter-electrode products in the working electrode chamber. The Pt was in the form of a 60 × 20 mm, 52-mesh gauze of 0.1-mm wire coiled into a spiral. Electrochemical measurements were made with a potentiostat, scan generator, and potential step module (Oxford Electrodes, England, Ltd.).

1-Bromo-9,10-anthracenedione (BA) and 1-iodo-9,10-anthracenedione (IA) were prepared by D. Bethell at Liverpool University to 99% purity. Acetonitrile was triply distilled and dried over calcium hydride pellets and stored over 4A grade activated molecular sieves under dry N_2. Tetra-*n*-butylammonium perchlorate (TBAP) was dried as received (Fluka, purum) under vacuum for 24 h prior to use. The solutions were prepared in a drybox and were degassed by purging with dry O_2-free Ar.

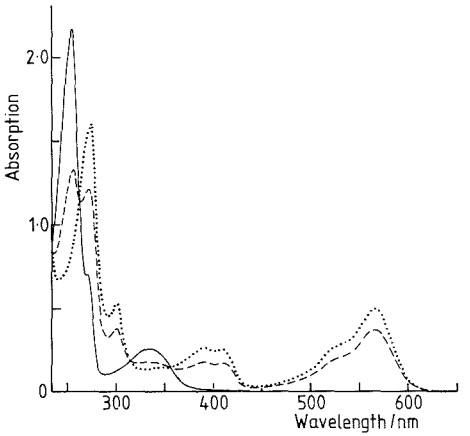

Figure 2. Development of the thin-layer spectrum with time for the reduction of 1.1×10^{-3} M BA in acetonitrile with 0.1 M TBAP at 25 °C: (—) BA at $t = 0$, (---) BA and $BA^{\bullet-}$ at $t < 130$ s and (...) $BA^{\bullet-}$ at $t \geq 130$ s. The time elapsed to reach exhaustive electrolysis was 130 s.

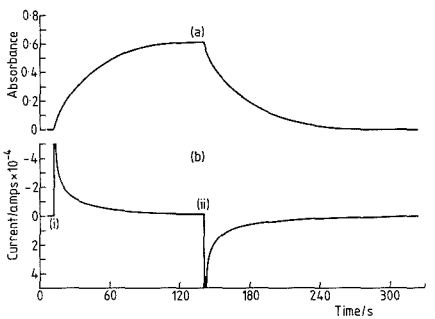

Figure 3. Parallel current and absorption transients in a stationary solution: (a) absorption against time at 565 nm; (b) current against time. At (i) the potential was stepped from 0 to −0.9 V vs an Ag wire pseudo reference electrode, and at (ii) the potential was stepped back to 0 V. This corresponded to stepping from a zero current to what would be a limiting current potential under flowing conditions.

RESULTS AND DISCUSSION

The performance of the 500-μm cell was evaluated by using the $BA/BA^{\bullet-}$ redox couple. BA undergoes a one-electron reversible reduction to $BA^{\bullet-}$ on gold in 0.1 M TBAP in dry acetonitrile (*9*). The electrochemistry was carried out while solution was flowing through the cell at 10^{-3} cm^3 s^{-1}. Potential was slowly swept in a cathodic direction until a limiting current was reached. The solution and potential were then held stationary, and the spectrum was observed to change. The current decayed to zero as exhaustive electrolysis occurred over a time scale of about 130 s. The spectra displayed (Figure 2) describe the change in absorption as the parent molecule BA underwent 1-e^- reduction to $BA^{\bullet-}$. Absorption/current transients were produced by potential steps (Figure 3). The cell thickness was confirmed from the absorption of BA at 335 nm ($\epsilon = 4.01 \times 10^{-3}$ M^{-1} cm^{-1} (*9*)) using the Beer–Lambert law. The optical path length was 560 μm, longer than the original cell path length due to the Au minigrid. The 100-μm cell was similarly found to have a 160-μm optical path length with the minigrid in place. The 100-μm cell was used to observe the spectrum of the unstable $IA^{\bullet-}$ radical. IA undergoes a 1-e^-

reduction to $IA^{\bullet-}$ on gold in 0.1 M TBAP in dry acetonitrile. The UV–visible absorption spectrum of $IA^{\bullet-}$ was not observed with the 560-μm cell, but was observed with the 160-μm cell. When stationary IA solution was reduced in the 100-μm cell, the $IA^{\bullet-}$ spectrum grew to a maximum over 10 s and disappeared over a total period of 35 s. Decreasing the cell thickness (l) from 560 to 160 μm produced a 12-fold decrease in the time taken (t) to achieve exhaustive electrolysis for electroactive species with similar diffusion coefficients (D). This agrees with the approximate relation

$$t \propto l^2/D$$

The compound under observation must have a molar extinction coefficient above a certain limit, with the minimum requirements being $\epsilon > 200$ M^{-1} cm^{-1} for the 560-μm cell and $\epsilon > 600$ M^{-1} cm^{-1} for the 160-μm cell. The flow operation of this system permits cleaning and O_2 removal so that the cell need not be removed from the spectrometer between experiments on different solutions. Thus the cell has an application for photoelectrochemical detection in high-performance liquid chromatography and for flow injection analysis (*10*, *11*).

To conclude, we have shown that a well controlled spectroelectrochemical system may be constructed without instrument workshop facilities, thus making the technique much more widely available.

ACKNOWLEDGMENT

We thank D. Bethell for providing samples of 1-bromo-9,10-anthracenedione and 1-iodo-9,10-anthracenedione.

Registry No. BA, 632-83-7; $Ba^{\bullet-}$, 121176-25-8; IA, 3485-80-1; $IA^{\bullet-}$, 121176-26-9; Au, 7440-57-5.

LITERATURE CITED

(1) Murray, R. W.; Heineman, W. R.; O'Dom, G. W. *Anal. Chem.* **1967**, *39*, 1666.
(2) Yildiz, A.; Kissinger, P. T.; Reilley, C. N. *Anal. Chem.* **1968**, *40*, 1018.
(3) Heineman, W. R.; Burnett, J. N.; Murray, W. M. *Anal. Chem.* **1968**, *40*, 1974.
(4) Muth, E. P.; Fuller, J. E.; Doane, L. M.; Blubaugh, E. A. *Anal. Chem.* **1982**, *54*, 604.
(5) Porter, M. D.; Dong, S.; Gui, Y.-P.; Kuwana, T. *Anal. Chem.* **1984**, *56*, 2263.
(6) Sanderson, D. G.; Anderson, L. B. *Anal. Chem.* **1985**, *57*, 2388.
(7) Nevin, W. A.; Lever, A. B. P. *Anal. Chem.* **1988**, *60*, 727.
(8) Zhang, C.; Park, S.-M. *Anal. Chem.* **1988**, *60*, 1639–1642.
(9) Compton, R. G.; Pilkington, M. B. G.; Bethell, D., unpublished work, Physical Chemistry Laboratory, Oxford University, November 1988.
(10) Dewald, H. D.; Wang, J. *Anal. Chem.* **1984**, *166*, 163.
(11) LaCourse, W. R.; Krull, I. S. *Anal. Chem.* **1985**, *57*, 1810.

RECEIVED for review December 19, 1988. Accepted March 27, 1989. M.B.G.P. thanks the SERC for a studentship.

Application of a Nested-Loop System for the Simultaneous Determination of Thorium and Uranium by Flow Injection Analysis

José Luis Pérez Pavón, Bernardo Moreno Cordero,* Jesús Hernández Méndez, and Rosa Maria Isidro Agudo

Department of Analytical Chemistry, Bromatology and Food Sciences, University of Salamanca, Salamanca, Spain

Numerous methods have been described for the determination of uranium (*1–6*) and thorium (*7–11*), most of them colorimetric. However, owing to the low concentrations in samples of interest and the presence of interferents, direct determinations are difficult, and separation or preconcentration techniques such as liquid–liquid extraction, ion-exchange chromatography, and extraction columns are always employed prior to analytical measurement.

Continuous automated or semiautomated analytical techniques are to be preferred over wet methods when one is dealing with hazardous materials or when large numbers of samples have to be analzyed. Several flow injection analysis (FIA) procedures have been proposed for the determination of uranium (*12–15*) and thorium (*16*); in this work we propose for the first time a sensitive and selective FIA method for the simultaneous determination of thorium and uranium without previous separation from the matrix; Arsenazo III is used as the reagent, with monitoring of the systems at $\lambda = 665$ nm.

The proposed FIA system is a two-channel manifold with a two-valve nested-loop injection system, the loop of one valve being a lead powder reducing column (Figure 1). The injected sample is split into two sections, one of them passing through the reducing column.

EXPERIMENTAL SECTION

Reagents. Stock solutions of uranium and thorium at a concentration of 2.0×10^{-3} M were prepared by dissolving appropriate amounts of uranyl nitrate hexahydrate (Merck) and thorium nitrate pentahydrate (Merck) in water. Stock solutions of Arsenazo III were prepared by dissolving 0.4100 g of the solid product (Fluka) in 250 mL of water. Aqueous 10% (w/v) solutions were of Triton X-100 (Analema). The reagent solution was prepared by mixing 25.0 mL of the stock Arsenazo III solution, 25.0 mL of the 10% (w/v) solution, and 75 mL of concentrated HCl and then diluting with water up to 250 mL. All chemicals reagents were of analytical grade.

Apparatus. The flow system comprised a peristaltic pump (Gilson Minipuls 2 HP-4) and a Perkin-Elmer Coleman 55 with a 1-cm flowthrough cell (18 μL, Hellma 178 12-QS). All connections were 0.5 mm i.d. Teflon tubing.

Injection System (Figure 1). Dasgupta and Hwang (*17*) report a configuration of a six-port injection valve installed within the loop of another six-port injection valve for the determination of aqueous peroxides; the loop of the nested (inner) valve contains an immobilized packed reactor with differentiating action on the analyte components. We have adapted this system for the simultaneous determination of thorium and uranium; the loop of the inner valve contains a lead reductor minicolumn. The minicolumn was a 5-cm length of 2 mm i.d. glass tubing; it was packed with lead powder (0.1–0.3 mm) with small glass wool beds at each end to prevent the escape of the material.

How the nested-loop device should be handled is described in the original paper (*17*) and summarized in our procedure. The resulting detector output is two separate sequential signals. When a uranium solution is injected into the system, the first peak (section L_1, nonreduced sample) is much lower than the second peak due to the low molar absorptivity of the U(VI)–Arsenazo III complex; the second peak (section L_2, reduced sample) corresponds to the U(IV)–Arsenazo III complex and is similar to the peaks obtained when a thorium solution is injected into the system.

Procedure. The system is started with both valves in the inject mode; this allows the filling of the column and R_1 with carrier solution. Later, both valves are switched to the loading mode and the sample (thorium and/or uranium, 3.6 M HCl) is pumped to fill L_1 and L_2. Then, V_2 is switched first, followed by V_1, and the carrier solution (3.6 M HCl) directs the sample toward the reagent stream (2.0×10^{-4} M Arsenazo III, 3.6 M HCl, 1% (w/v) Triton X-100); the signal is recorded at $\lambda = 665$ nm.

The conditions under which these determinations were carried out were as follows: carrier, 3.6 M HCl; reagent, 2.0×10^{-4} M Arsenazo III (3.6 M HCl, TX-100 1%); $L_1 = 143$ μL; $L_2 = 254$ μL;

0003-2700/89/0361-1789$01.50/0

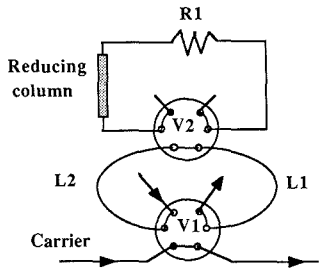

Figure 1. Injection system.

R_1 = 100 cm; R_2 = 50 cm; lead column length = 5.5 cm; Q_t = 3.1 mL/min, with flow rates kept the same in both branches of the setup.

RESULTS AND DISCUSSION

Arsenazo III is only sparingly soluble in concentrated acid media, but its solubility increases upon addition of Triton X-100 to the solutions. A 1% (w/v) concentration of the surfactant is sufficient to stabilize 2.0×10^{-4} M Arsenazo III; for more concentrated solutions 2% Triton X-100 is recommended. Preliminary studies showed that the presence of surfactant does not cause any modifications in the complex or spectra of the reagents.

As a previous reduction process was necessary to obtain U(IV) from the uranyl cation, lead was chosen as the reducing agent (powder packed in a minicolumn) since it quantitatively reduces U(VI) to U(IV) without the production of hydrogen bubbles up to proton concentrations close to 4 M. A 3.6 M concentration of HCl was used for all the experiments.

Influence of Variables. The effect of chemical and hydrodynamic variables was studied by using four different column lengths (4.0, 5.5, 9.0, and 15.5 cm); the signals did not vary appreciably. Regarding the influence of Arsenazo III concentration, the results show that the signal reaches a constant value when the reagent concentration was about 10-fold that of the cation. For the rest of the variables studied (L_1, L_2, R_1, R_2, and Q_t) the results were just as predictable. Final optimized values are reported in the Experimental Section.

Analytical Characteristics of the Determination. For cation concentrations ranging between 1.0×10^{-7} and 2.0×10^{-5} M, when two columns of different lengths (5.5 and 9.0 cm) and two concentrations of Arsenazo III (2.0×10^{-4} and 4.0×10^{-4} M) were used, the signal was found to be proportional to the cation concentration. The increase in column length or in the concentration of Arsenazo III did not lead to significant increases in linearity or in the intensity of the signal, although it did cause an increase in the stability of the base line, such that it was preferable to use short columns and the minimum concentration of reagent that would ensure linearity within the concentration range studied.

Under the optimum experimental conditions straight lines were obtained for the following calibrations:

uranium

$$h_1 = 1832[\mathrm{U}] + 0.002 \ (r = 0.9973);$$
$$h_2 = 32507[\mathrm{U}] + 0.001 \ (r = 0.9997)$$

thorium

$$h_1 = 42553[\mathrm{Th}] + 0.005 \ (r = 0.9997);$$
$$h_2 = 37157[\mathrm{Th}] + 0.0002 \ (r = 0.9997)$$

(h_1: nonreduced sample; h_2: reduced sample)

In order to determine the precision of the method, triplicate injections of 10 identical solutions of each of the cations were made (2.0×10^{-6} M) for all the experimental conditions under which the straight lines for the calibrations were obtained. For the column of 5.5-cm length and Arsenazo III at 2.0×10^{-4} M, the relative standard deviation for the second peak was 2.1% for U and 0.9% for Th. No significant differences were found under the other experimental conditions.

Calculation of the detection limits was carried out from the measurements of noise (width of the base line), considering as the minimum amount detectable that which yielded a signal double the width of the base line. With this criterion, the values obtained were 1.23×10^{-7} M for uranium and 9.4×10^{-8} M for thorium.

Table I. Simultaneous Determination of Thorium and Uranium in Synthetic Mixtures

metal added/ppm		metal recovered/ppm	
Th	U	Th	U
0.93		0.94	−0.03
	0.95	−0.01	0.97
0.93	0.47	0.92	0.47
0.46	0.95	0.45	0.96
0.23	1.43	0.22	1.37
1.39	0.24	1.36	0.26
0.09	1.43	0.09	1.43
1.39	0.09	1.36	0.10
1.39	0.47	1.36	0.46

Simultaneous Determination of Thorium and Uranium. Nine synthetic mixtures of varying composition were used as unknown samples for the determination. In order to check the validity of the procedure for ores, analysis was performed on a standard ore (pitchblende S-12) supplied by the Atomic Energy Agency and prepared by the Junta de Energía Nuclear (Madrid, Spain) for contrast analysis in which only the content of uranium was specified (0.014%).

The procedure followed by attacking the rock was as follows: 0.5 g of rock was treated with 5 mL of HNO_3 and heated until dry. The residue obtained was treated with HCl and brought to dryness again. The new residue was suspended in 0.1 M HCl, filtered, washed, and brought up to volume in a 50-mL flask after addition of HCl to adjust the acid concentration to 3.6 M.

After determination of the straight lines of the corresponding calibrations, a system of equations was postulated as follows:

$$h_i = \sum m_{ij} c_j$$

where h_i is the height of the two peaks obtained on injecting mixtures and m_{ij} are the slopes of the straight lines of the corresponding calibrations. With this system of equations it was possible to calculate the concentration of each of the components of the sample.

From the results obtained for the synthetic mixtures (Table I), the proposed method may be used for the determination of small amounts of thorium (0.09 ppm) even in the presence of amounts uranium up to 16-fold higher. It is possible to determine uranium in the presence of thorium for ratios of the same order.

The results obtained in the case of the standard ore were as follows: found, % U_3O_8 = 0.0147 and % Th = 0.0005; reference, % U_3O_8 = 0.014; % Th, not certified.

Registry No. U, 7440-61-1; Th, 7440-29-1.

LITERATURE CITED

(1) John, F. W.; Black, R. A. *Anal. Chem.* **1953**, *25*, 1200–1204.
(2) Clinch, J.; Guy, M. J. *Analyst* **1957**, *82*, 800–807.
(3) Foreman, J. K.; Riley, C. J.; Smith, T. D. *Analyst* **1957**, *82*, 89–95.
(4) Baltisberger, R. J. *Anal. Chem.* **1964**, *36*, 2369–2370.
(5) Borak, J.; Slovak, Z.; Fischer, J. *Talanta* **1970**, *17*, 215–229.
(6) Kadam, B. V.; Maiti, B.; Sathe, R. M. *Analyst* **1981**, *106*, 724–726.

(7) Sarma, D. V.; Raghava Rao, B. S. *Anal. Chim. Acta* **1955**, *13*, 142–149.
(8) Purushottam, A. Z. *Anal. Chem.* **1955**, *145*, 245–248.
(9) Fletcher, M. H.; Milkey, R. G. *Anal. Chem.* **1956**, *28*, 1402–1407.
(10) Arnfelt, A. L.; Edmundsson, I. *Talanta* **1961**, *8*, 473–476.
(11) Onishi, H.; Sekine, K. *Talanta* **1972**, *19*, 473–478.
(12) Lynch, T. P.; Taylor, A. F.; Wilson, J. N. *Analyst* **1983**, *108*, 470–475.
(13) Silfwerbrand-Lindh, C.; Nord, L.; Danielsson, L. G.; Ingman, F. *Anal. Chim. Acta* **1984**, *160*, 11–19.
(14) Jones, E. A. *Anal. Chim. Acta* **1985**, *169*, 109–115.
(15) Atallah, R. H.; Christian, G. D.; Hartenstein, S. D. *Analyst* **1988**, *113*, 463–469.
(16) Baban, S. B. *Anal. Proc.* **1980**, *17*, 535–537.
(17) Dasgupta, P. K.; Hwang, H. *Anal. Chem.* **1985**, *57*, 1009–1012.

RECEIVED for review January 3, 1989. Accepted April 3, 1989.

On-Line Dilution Scheme for Liquid Chromatography

Javier N. Oquendo*[,1] and Joseph A. Leone*

ARCO Oil and Gas Company, Research and Technical Services, Plano, Texas 75075

INTRODUCTION

In our laboratories, dilution is the most frequent pretreatment for the ion chromatographic analysis of samples. A commercial dilutor, whose operation was independent of that of an automated ion chromatograph, was used to handle a large number of samples. The advantages of operating both pieces of equipment as a single unit were obvious and prompted an investigation into an on-line dilution scheme.

On-line dilution is the subject of several publications dealing with spectroscopic techniques (*1–5*). However, the idea does not appear to have been exploited in liquid chromatography. The on-line chromatographic dilution scheme utilized in this work combines a sample stream, provided by a stepper motor driven syringe, with that of the eluent after it has passed through the column or the detector.

EXPERIMENTAL SECTION

Apparatus. A schematic diagram of the ion chromatographic system used in this work is shown in Figure 1. The equipment consisted of a Model 2120 dual channel ion chromatograph equipped with autoion 300 software (Dionex, Sunnyvale, CA), a Model 401 stepper motor driven syringe (Gilson Medical Electronics Inc., Middleton, WI), a Model 212B syringe controller (Gilson Medical Electronics Inc., Middleton, WI), and a Model 32297 autosampler (Dionex, Sunnyvale, CA).

Modifications and optional parts for the ion chromatograph, all Dionex brand unless otherwise indicated, were as follows. Two injection valves (P/N 35913) placed in series and referred to here as valves A and B, an in-line filter (P/N 35331), a 250 × 3 mm anion separator (HPIC-AS4A, P/N 037041), an anion micromembrane suppressor (P/N 038019), and a mixing tee (P/N 24313). Valve C was a two-stack four-way valve (P/N 35914) with plugs as shown in Figure 1. The volumes of injection of valves A and B were 25 and 10 μL, respectively. The mixing coil was a 50 cm long piece of tubing packed with glass beads that was prepared by cutting a reaction coil (P/N 37556) used for postcolumn derivatizations. Tubing connections between the autosampler and the sample waste were made with 0.5 mm i.d. Teflon tubing (P/N 35519). All other liquid connections utilized 0.3 mm i.d. Teflon tubing (P/N 35548).

A computer program was written for the syringe controller that allows the user to select among several modes of operation. The operation of the syringe controller was synchronized to that of the ion chromatograph by means of a contact closure relay. All work was performed with a 1.0-mL glass syringe.

The analytical pump was operated in the constant flow/constant pressure mode. All ion separations were carried out with a solution of 2.2 mM $NaHCO_3$ and 0.8 mM Na_2CO_3 as eluent at a flow rate of 2.0 mL/min. The regenerant solution was 0.025 N H_2SO_4.

[1] Present address: South American Petrolite of Venezuela, Apartado 5685, Caracas 1010A, Venezuela.

Procedures. Unless otherwise stated, the syringe operates at 250 μL/s. With valves A and B in the load position, and valve C positioned so as not to allow any mixing, the syringe pumps 2.0 mL of sample in four aliquots of 0.5 mL. For a given total volume of sample, carryover decreases with the volume of these aliquots. At this stage, nondiluted samples can be injected via valve A. If the mode of operation calls for sample dilution, the syringe draws a volume of sample that equals 70 μL plus the sample dilution flow rate times a constant (*55*). Next, valve C is positioned so as to allow the combination of the sample and eluent streams while the syringe pumps 70 μL of sample at 7 μL/s, and the remaining volume at the rate selected by the user. Carryover in the lines between valve C and the mixing tee is largely reduced by pumping sample at an initial flow rate much higher than that required for the on-line dilution of the sample. One minute later, valve C is switched to the nonmixing position and the diluted sample injected via valve B. Eluent dilution flow rates different from that used for the ion separation can be utilized after allowing sufficient time for equilibration (~30 s).

RESULTS AND DISCUSSION

The performance of the instrument was evaluated with brines since brine characterization is of considerable interest in the oil industry.

Dilution factors (DF) were calculated from

$$DF = (Qs + Qe)/Qs \quad (1)$$

where Qs and Qe are the sample and eluent dilution flow rates, respectively. A plot of peak area of the on-line diluted samples of a 20 000 ppm chloride solution versus the inverse of the dilution factors obtained from all combinations of sample dilution flow rates (6, 12, 24, 48, 96, 192, and 384 μL/min) and eluent dilution flow rates (1.00, 2.00, and 3.00 mL/min) was linear. The resulting linear equation was peak area = (396 ± 0.3)DF^{-1} − (0.7 ± 0.3), with a correlation coefficient (r) of 0.999. Peak-area relative standard deviations (RSDs) of six consecutive injections of each of these samples ranged from 0.4% to 3.0% and were under 2.1% for dilution factors of up to 250. RSDs of similar samples diluted manually with an adjustable pipet were in the range from 0.6% to 2.2%.

The system is capable of handling the dilution of highly concentrated samples. A plot of peak area versus the concentration of the solutions placed in the autosampler was linear for concentrations of chloride of 0.5, 1.0, 2.0, 5.0, and 10.0% when operating with fixed eluent and sample dilution flow rates of 2.00 and 0.06 mL/min, respectively. The corresponding linear equation was peak area = (64.8 ± 0.4)C1(%) − (0.31 ± 0.08) with a correlation coefficient (r) of 1.000.

"Water dips" for samples diluted with the nonsuppressed eluent were much smaller than those of samples diluted with the suppressed eluent. This observation is consistent with

0003-2700/89/0361-1791$01.50/0

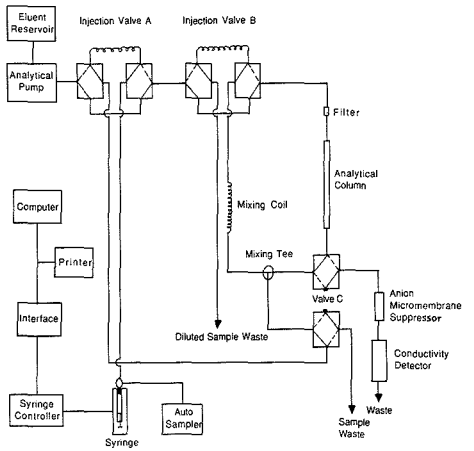

Figure 1. Schematic diagram of the ion chromatographic system. In some instances, valve C was placed after the detector.

the reduced levels of CO_2 present in the suppressed eluent (6).

The placement of valve C after the detector and the use of a similar dilution and separation eluent flow rates turned out to be advantageous. Sample throughput could then be increased by diluting a sample while simultaneously recording the chromatogram of a previous sample. In this mode of operation sample dilution had a negligible effect on the detector response and was carried out without contamination from the ions of the injected sample.

In a series of experiments, oil-producing sands were placed along with concentrated solutions of NaCl in an autoclave and subjected to conditions that simulate those of EOR processes. The resulting brines contained anions at vastly different concentrations. Changes in the chloride concentration and the presence of other anions such as bromide, nitrate, phosphate, and sulfate at low concentration provided an indication of sand reactivity. Following the on-line dilution of the sample, the time controlled injection of the nondiluted and diluted samples allowed us to determine both major and minor components in a single run. Figure 2 shows the chromatogram of a standard solution obtained when operating in this manner. The subscripts A and B are used to identify a peak as coming from injection valves A and B, respectively. The relative position of the chloride B peak can be changed by adjusting the time elapsed (Δt) between the moments the nondiluted and diluted samples are injected.

Advantages of the above mode of operation over the usual approach of determining major and minor components in

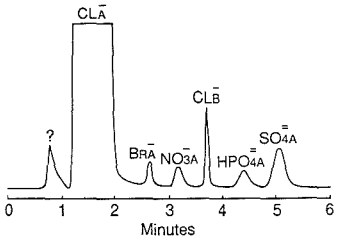

Figure 2. Chromatogram of a standard solution containing 10 000 ppm of chloride, 20 ppm of each bromide and nitrate, 50 ppm of phosphate, and 40 ppm of sulfate (Qe = 2.00 mL/min, Qs = 0.03 mL/min, Δt = 2.49 min).

different runs without on-line dilution were (1) savings in analysis time and disk memory, (2) a single set of standard solutions sufficed for the determination of all components, (3) the autosampler could be loaded with twice the number of nondiluted samples, (4) results for all components were obtained in a single computer printout, and (5) a single chromatogram showed how all components were determined.

CONCLUSIONS

This work shows that a number of advantages can result from replacing the sample pump of an automated liquid chromatographic system with a stepper motor driven syringe and appropriate valve configuration. Our test results also show that this system can be used for the analysis of samples needing preconcentration.

It is possible to interface the syringe to the computer, in which case there is no need for a syringe controller. This modification would lower the cost of a similar chromatographic system.

ACKNOWLEDGMENT

We wish to thank ARCO Oil and Gas Company for permission to publish this paper. The authors also thank Hernan Prieto of INTEVEP, S.A., and the reviewers for valuable suggestions.

LITERATURE CITED

(1) Habig, R. L.; Williamson, W. R. *Clin. Chem.* **1970**, *16*, 251–253.
(2) Ruddel, M. E.; McClean, S. W. *Anal. Chem.* **1981**, *53*, 1946–1949, and references therein.
(3) Ramsey, M. H.; Thompson, M. *Analyst* **1982**, *107*, 232–234.
(4) Moore, G. L.; Watson, A. E.; Humphries-Cuff, P. *Spectrochim. Acta, Part B* **1982**, *37B*, 835–837.
(5) Bysouth, S. R.; Tyson, J. F. *J. Anal. At. Spectrom.* **1987**, *2*, 217–220.
(6) Dasgupta, P. K. *Anal. Chem.* **1984**, *56*, 96–103.

RECEIVED for review February 8, 1988. Resubmitted April 13, 1989. Accepted May 1, 1989.

For Over Six Decades...

The Leader in the Field.

ANALYTICAL CHEMISTRY, the world's foremost publication in the vital field of measurement science, comes to you semi-monthly packed with *more* research articles, special features and application papers.

Keeping pace with the changes has continued to make *ANALYTICAL CHEMISTRY* the pinnacle of publications in the field . . . for over 6 decades.

For your personal subscription:

CALL TOLL FREE (800) 227-5558 (U.S. only)
Outside U.S. (202) 872-4363

Telex: 440159 UI
89 2582 ACSPUBS

American Chemical Society
1155 16th St., NW
Washington, DC 20036

Bring your micro CHN analyses into the 1990's with the CHN-900 Carbon/Hydrogen/Nitrogen Elemental Determinator from LECO®

The LECO® CHN-900, thru its speed and precision, can make your current micro CHN analysis methods obsolete. The CHN-900 features a nominal 4-minute analysis time with precision of 0.001% for carbon and 0.01% for both hydrogen and nitrogen.

A 16-bit microprocessor coupled to icon-driven, touch-screen software, makes the CHN-900 one of the easiest-to-operate micro-CHN instruments available. The system comes complete with a high speed (300 cps) printer for hard-copy printouts of data and a standard 19-sample autoloader which reduces operator interface by allowing a number of samples to be analyzed automatically.

The CHN-900 is more than just another laboratory instrument, the self-contained data base with built-in archival, statistical and sort routines, allows the CHN-900 to be used as a lab management system. Compare the LECO® CHN-900 to other systems and you will see that it is the instrument for you in the 1990's and beyond.

Optional LECO® 450 Electronic Micro-Balance

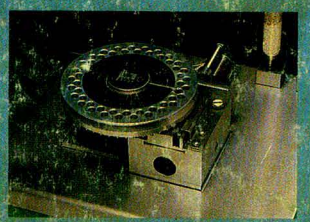

Optional 49-sample autoloader

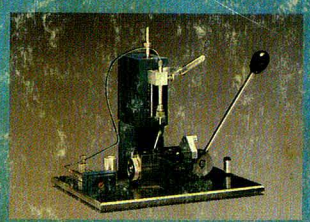

Optional CP-100 Capsule Press

To learn more about this new LECO® system, call or write today!

LECO CORPORATION 3000 Lakeview Avenue
St. Joseph, MI 49085-2396 U.S.A. Phone: (616) 983-5531

CIRCLE 90 ON READER SERVICE CARD